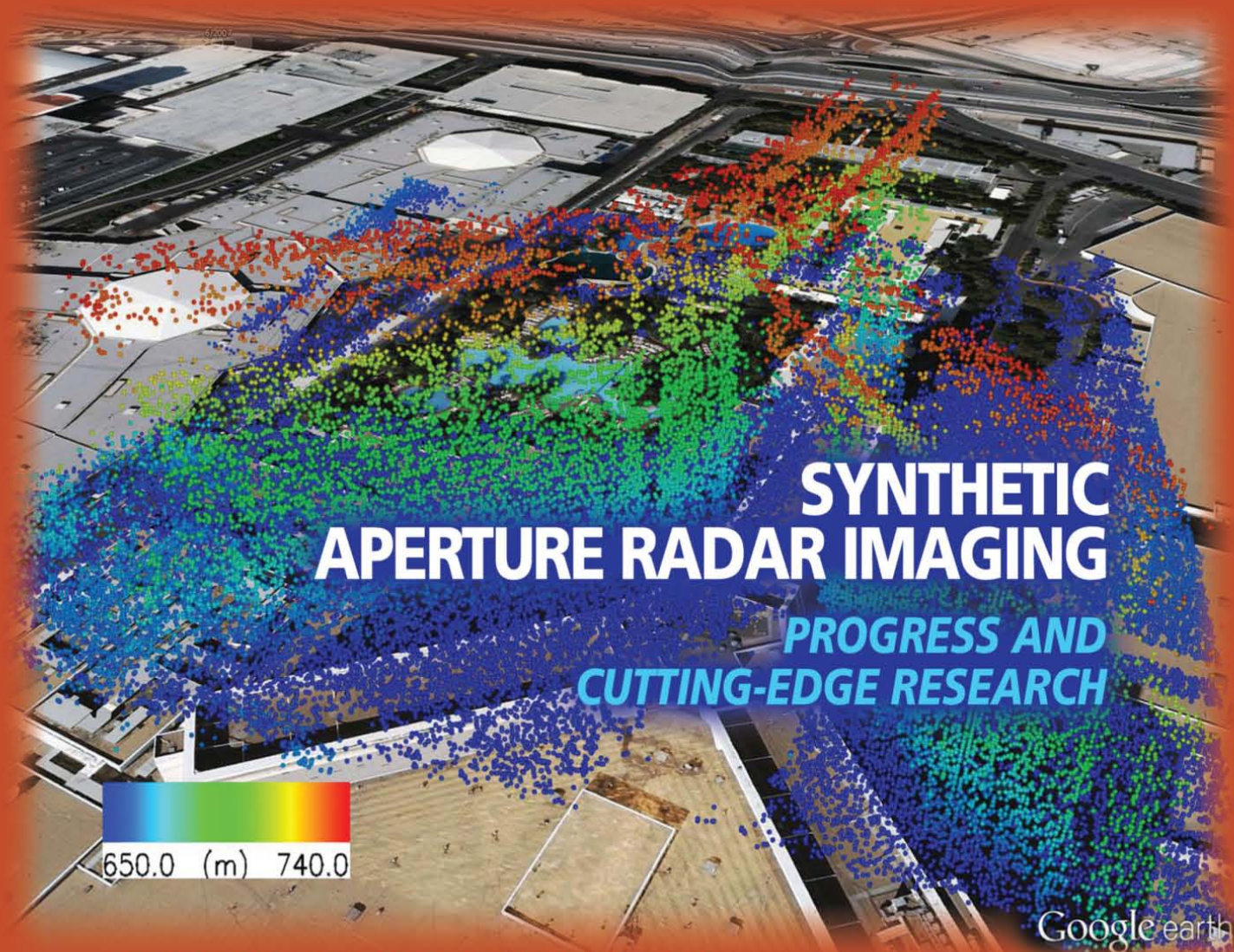


IEEE Signal Processing MAGAZINE

[VOLUME 31 NUMBER 4 JULY 2014]



SYNTHETIC APERTURE RADAR IMAGING

PROGRESS AND CUTTING-EDGE RESEARCH



LONG-WAVE INFRARED HYPERSPECTRAL REMOTE SENSING OF CHEMICAL CLOUDS

EFFECTIVE FEATURE EXTRACTION AND DATA REDUCTION IN REMOTE SENSING USING HSI

OPTIMAL MULTIUSER TRANSMIT BEAMFORMING





Ultra Small 2x2mm

2W ATTENUATORS DC-20GHz from \$1.99 ea. (qty. 1000)

Save PC board space with our new tiny 2W fixed value absorptive attenuators, available in molded plastic or high-reliability hermetic nitrogen-filled ceramic packages. They are perfect building blocks, reducing effects of mismatches, harmonics, and intermodulation, improving isolation, and meeting other circuit level requirements. These units will deliver the precise attenuation you need, and are stocked in 1-dB steps from 0 to 10 dB, and 12, 15, 20 and 30 dB.

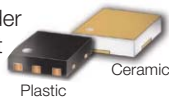
The ceramic hermetic **RCAT** family is built to deliver reliable, repeatable performance from DC-20GHz under the harshest conditions. With sample prices starting at

only \$4.95 ea. (qty. 20), these units are qualified to meet MIL requirements including vibration, PIND, thermal shock, gross and fine leak and more, at up to 125°C!

The molded plastic **YAT** family uses an industry proven, high thermal conductivity case and has excellent electrical performance over the frequency range of DC to 18 GHz, for prices as low as \$2.99 ea. (qty. 20).

For more details, just go to minicircuits.com – place your order today, and you can have these products in your hands as soon as tomorrow!

 RoHS compliant



FREE Simulation Models! 

<http://www.modelithics.com/mvp/Mini-Circuits/>

Mini-Circuits®

www.minicircuits.com P.O. Box 350166, Brooklyn, NY 11235-0003 (718) 934-4500 sales@minicircuits.com

515 rev D

CONTENTS

[VOLUME 31 NUMBER 4]

SPECIAL SECTION—SYNTHETIC APERTURE RADAR IMAGING

15 FROM THE GUEST EDITORS

Joachim Ender, Moeness G. Amin,
Gianfranco Fornaro,
and Paul A. Rosen

16 WIDE-ANGLE SYNTHETIC APERTURE RADAR IMAGING

Joshua N. Ash, Emre Ertin,
Lee C. Potter, and Edmund G. Zelnio

27 SPARSITY-DRIVEN SYNTHETIC APERTURE RADAR IMAGING

Müjdat Çetin, Ivana Stojanović,
N. Özben Önhon, Kush R. Varshney,
Sadeq Samadi, W. Clem Karl,
and Alan S. Willsky

41 TOMOGRAPHIC PROCESSING OF INTERFEROMETRIC SAR DATA

Gianfranco Fornaro, Fabrizio
Lombardini, Antonio Paucullo,
Diego Reale, and Federico Viviani

51 SUPERRESOLVING SAR TOMOGRAPHY FOR MULTIDIMENSIONAL IMAGING OF URBAN AREAS

Xiao Xiang Zhu and Richard Bamler

59 CONTEXTUAL INFORMATION-BASED MULTICHANNEL SYNTHETIC APERTURE RADAR INTERFEROMETRY

Fabio Baselice, Giampaolo Ferraioli,
Vito Pascazio, and Gilda Schirinzi

69 EXPLOITING PATCH SIMILARITY FOR SAR IMAGE PROCESSING

Charles-Alban Deledalle,
Loïc Denis, Giovanni Poggi,
Florence Tupin, and Luisa Verdoliva

79 MODELING AND INTERPRETATION OF SCATTERING MECHANISMS IN POLARIMETRIC SYNTHETIC APERTURE RADAR

Si-Wei Chen, Yong-Zhen Li,
Xue-Song Wang, Shun-Ping Xiao,
and Motoyuki Sato

90 SAR IMAGING ALGORITHMS AND SOME UNCONVENTIONAL APPLICATIONS

Raffaele Solimene, Iliaria Catapano,
Gianluca Gennarelli, Antonio Cuccaro,
Angela Dell'Aversano,
and Francesco Soldovieri

99 THE TIME-REVERSAL TECHNIQUE FOR SAR FOCUSING OF BURIED TARGETS

Robert Kedzierawski,
Jean-Marc Le Caillec,
and Witold Czarnecki

110 MULTIPATH EXPLOITATION AND SUPPRESSION FOR SAR IMAGING OF BUILDING INTERIORS

Michael Leigsnering,
Moeness G. Amin, Fauzia Ahmad,
and Abdelhak M. Zoubir

FEATURE

120 LONG-WAVE INFRARED HYPERSPECTRAL REMOTE SENSING OF CHEMICAL CLOUDS

Dimitris G. Manolakis,
Steven E. Golowich,
and Robert S. DiPietro

COLUMNS

4 FROM THE EDITOR

Signal Processing: Is it Time
to Change the Society's Name?
Abdelhak Zoubir

6 PRESIDENT'S MESSAGE

At the Forefront in Technical
Publications
Alex Acero

8 READER'S CHOICE

Top Downloads in IEEE *Xplore*

10 SPECIAL REPORTS

Signal Processing: On the Edge
of Astronomy's New Frontier
John Edwards

Health Alliance Boosts Influence
in Standards Development
Ron Schneiderman

142 LECTURE NOTES

Optimal Multiuser Transmit
Beamforming: A Difficult Problem
with a Simple Solution Structure
Emil Björnson, Mats Bengtsson,
and Björn Ottersten

149 APPLICATIONS CORNER

Effective Feature Extraction and Data
Reduction in Remote Sensing Using
Hyperspectral Imaging
Jinchang Ren, Jaime Zabalza,
Stephen Marshall, and Jiangbin Zheng

155 LIFE SCIENCES

Signal Processing in Visual Optics
D. Robert Iskander

DEPARTMENT

159 DATES AHEAD

IEEE SIGNAL PROCESSING magazine

IEEE SIGNAL PROCESSING MAGAZINE

Abdelhak Zoubir—*Editor-in-Chief*
Technische Universität Darmstadt, Germany

AREA EDITORS

Feature Articles
Marc Moonen—KU Leuven, Belgium

Columns and Forum

Andrea Cavallaro—Queen Mary, University
of London, United Kingdom

Andres Kwasinski—Rochester Institute
of Technology, United States

Special Issues

Fulvio Gini—University of Pisa, Italy

e-Newsletter

Christian Debes—AGT International, Germany

EDITORIAL BOARD

Moeness G. Amin—Villanova University,
United States

Sergio Barbarossa—University of Rome
"La Sapienza," Italy

Mauro Barni—Università di Siena, Italy

Helmut Bölcskei—ETH Zürich, Switzerland

A. Enis Cetin—Bilkent University, Turkey

Patrick Flandrin—CNRS chez ENS Lyon, France

Bastiaan Kleijn—Victoria University
of Wellington, New Zealand

Visa Koivunen—Aalto University, Finland

Hamid Krim—North Carolina State University,
United States

Ying-Chang Liang—Institute for Infocomm
Research, Singapore

V. John Mathews—University of Utah,
United States

Satoshi Nakamura—Nara Institute
of Science and Technology, Japan

Kuldip Paliwal—Griffith University, Australia

Béatrice Pesquet-Popescu—Télécom ParisTech,
France

Eli Saber—Rochester Institute of Technology,
United States

Ali Sayed—University of California, Los Angeles,
United States

Hing Cheung So—City University of Hong Kong,
Hong Kong

Victor Solo—University of New South Wales,
Australia

Sergios Theodoridis—University of Athens,
Greece

Isabel Trancoso—INESC-ID/Instituto
Superior Técnico, Portugal

Michail K. Tsatsanis—Entropic Communications

Min Wu—University of Maryland

Pramod K. Varshney—Syracuse University,
United States

Z. Jane Wang—The University of British Columbia,
Canada

ASSOCIATE EDITORS—
COLUMNS AND FORUM

Rodrigo Capobianco Guido —
University of Sao Paulo, Brazil

Aleksandra Mojsilovic —
IBM T.J. Watson Research Center

Douglas O'Shaughnessy — INRS, Canada

Gene Cheung — National Institute
of Informatics

Alessandro Vinciarelli — IDIAP-EPFL

Michael Gormish — Ricoh Innovations, Inc.

Xiaodong He — Microsoft Research

Fatih Porikli — MERL

Stefan Winkler — UIUC/ADSC, Singapore

Saeid Sanei, — University of Surrey,
United Kingdom

Azadeh Vosoughi — University of Central Florida

Danilo Mandic — Imperial College,
United Kingdom

Roberto Togneri — The University of Western
Australia

Gail Rosen — Drexel University

ASSOCIATE EDITORS—
E-NEWSLETTER

Gwenael Doerr—Technicolor, France

Vítor Nascimento—University of São Paulo, Brazil

Shantanu Rane—MERL

Yan Lindsay Sun—University of Rhode Island

IEEE SIGNAL PROCESSING SOCIETY

Alex Acero—*President*

Rabab Ward—*President-Elect*

Konstantinos (Kostas) N. Plataniotis—*Vice
President, Awards and Membership*

Wan-Chi Siu—*Vice President, Conferences*

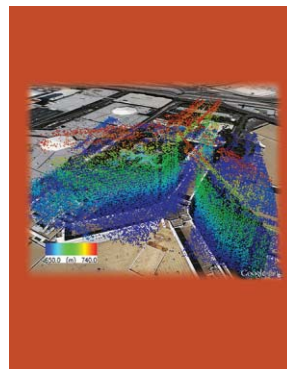
Alex Kot—*Vice President, Finance*

Mari Ostendorf—*Vice President, Publications*

Charles Bouman—*Vice President,
Technical Directions*

COVER

IMAGE COURTESY OF CNR-IREA AND DLR-IMF

IEEE PERIODICALS
MAGAZINES DEPARTMENT

Jessica Barragué
Managing Editor

Geraldine Krolin-Taylor
Senior Managing Editor

Susan Schneiderman
Business Development Manager
+1 732 562 3946 Fax: +1 732 981 1855

Felicia Spagnoli
Advertising Production Manager

Janet Dudar
Senior Art Director

Gail A. Schnitzer
Assistant Art Director

Theresa L. Smith
Production Coordinator

Dawn M. Melley
Editorial Director

Peter M. Tuohy
Production Director

Fran Zappulla
Staff Director, Publishing Operations

IEEE prohibits discrimination, harassment, and bullying.
For more information, visit
<http://www.ieee.org/web/aboutus/whatis/policies/p9-26.html>.

IEEE SIGNAL PROCESSING MAGAZINE (ISSN 1053-5888) (ISPREG) is published bimonthly by the Institute of Electrical and Electronics Engineers, Inc., 3 Park Avenue, 17th Floor, New York, NY 10016-5997 USA (+1 212 419 7900). Responsibility for the contents rests upon the authors and not the IEEE, the Society, or its members. Annual member subscriptions included in Society fee. Nonmember subscriptions available upon request. Individual copies: IEEE Members US\$20.00 (first copy only), nonmembers US\$201.00 per copy. Copyright and Reprint Permissions: Abstracting is permitted with credit to the source. Libraries are permitted to photocopy beyond the limits of U.S. Copyright Law for private use of patrons: 1) those post-1977 articles that carry a code at the bottom of the first page, provided the per-copy fee indicated in the code is paid through the Copyright Clearance Center, 222 Rosewood Drive, Danvers, MA 01923 USA; 2) pre-1978 articles without fee. Instructors are permitted to photocopy isolated articles for noncommercial classroom use without fee. For all other copying, reprint, or republication permission, write to IEEE Service Center, 445 Hoes Lane, Piscataway, NJ 08854 USA. Copyright ©2014 by the Institute of Electrical and Electronics Engineers, Inc. All rights reserved. Periodicals postage paid at New York, NY, and at additional mailing offices. Postmaster: Send address changes to IEEE Signal Processing Magazine, IEEE, 445 Hoes Lane, Piscataway, NJ 08854 USA. Canadian GST #125634188 Printed in the U.S.A.

Digital Object Identifier 10.1109/MSP.2014.2311860



Now... 2 Ways to Access the IEEE Member Digital Library

With two great options designed to meet the needs—and budget—of every member, the IEEE Member Digital Library provides full-text access to any IEEE journal article or conference paper in the IEEE Xplore® digital library.

Simply choose the subscription that's right for you:

IEEE Member Digital Library

Designed for the power researcher who needs a more robust plan. Access all the IEEE content you need to explore ideas and develop better technology.

- 25 article downloads every month

IEEE Member Digital Library Basic

Created for members who want to stay up-to-date with current research. Access IEEE content and rollover unused downloads for 12 months.

- 3 new article downloads every month

Get the latest technology research.

Try the IEEE Member Digital Library—FREE!

www.ieee.org/go/trymdl



IEEE Member Digital Library is an exclusive subscription available only to active IEEE members.

[from the **EDITOR**]Abdelhak Zoubir
Editor-in-Chief

zoubir@spg.tu-darmstadt.de
<http://signalprocessingsociety.org/publications/periodicals/spm>

Signal Processing: Is it Time to Change the Society's Name?

On 10 April 2014, I received an e-mail from Petar M. Djurić that was sent to all members of the IEEE Signal Processing Society (SPS), with the subject title, “The Power of a Name” [1]. The message provides a brief description of the evolution of the Society before suggesting that the time has come for another Society name change.

At the Board of Governors meeting in December 2013, a committee was formed (Philip Chou, Walter Kellermann, Anthony Kuh, Anna Scaglione, and Petar M. Djurić) to explore the possibility of changing the Society's name, an issue that has been a topic of discussion for quite a long time. But what is the motivation for such a change?

There has been a series of columns and editorials published in *IEEE Signal Processing Magazine (SPM)* over the last decade that have addressed the important issue of what signal processing conveys for a layperson [2], [3]. More recently, in the new *SPM* column, “Reflections,” José M.F. Moura et al. shared their “reflections” on this thought-provoking topic, i.e., signal processing inside [4].

There is no doubt in my mind that we must do something to increase awareness about our profession among the public at large. The fundamental question we should ask is whether a name change alone would achieve this goal. Clearly, a change of name would help, but to what? The e-mail Petar M. Djurić sent on behalf of the committee can be found in [1]. It invites all SPS members to provide feed-

back on this topic and offers suggestions for some new names.

I took the time to read the many comments made by colleagues, and I found the exercise worthwhile. Some of the critics provide good arguments as to why the Society should stick with the name “Signal Processing.” One strong argument against a name change is that “The public (as a whole) has little awareness of what most professions really involve, or what they're called. That is no reflection on the names or the crafts involved, and very clearly doesn't matter...” The many in favor of a name change argue that they are “in favor of changing the name if the name chosen is broadening the domain of interest of SPS members in the sense of representing current (and eventually future) research and professional activities...”

The page is still available for comments, and we are interested in receiving feedback. So far, there seems to be interest in adding the word “Information” to “Signal.” It is the committee's responsibility to evaluate the many comments provided and to draw conclusions.

My personal view is that a name change would help, indeed. More importantly, however, is to raise awareness about our profession among the laypeople. In my editorial in the May 2013 issue of *SPM* [5], I wrote, “My personal view is that we have to be more active in disseminating success stories of signal processing, not only to the decision makers, but also to the public at large.” One of the commentators in [1] wrote, “When people ask ‘What is SP?’ I say it is everything that goes on inside a smartphone and their eyes suddenly light up.”

Our mandate is to increase awareness to the point where the public no longer questions what signal processing is. If we

were to change the name, and the public still does not know what our profession involves, it would solidify what the observer before wrote, “The public (as a whole) has little awareness of what most professions really involve.” This would not help the Society, and we would start the very same exercise years down the road. The real challenge is to actively promote our discipline so that just the mention of signal processing without any explanation would cause the public's eyes to light up.

SPM is an outstanding vehicle to raise awareness among professionals in signal processing and among professionals in cognate areas through columns, forum, and the eNewsletter. It gives me great pleasure to introduce the new area editor (eNewsletter), Dr.-Ing. Christian Debes, whose mandate is to reshape the eNewsletter in this new area of communication. He will replace Z. Jane Wang, whom I thank for her hard work as area editor and who will support *SPM* in her new role as a member of the Senior Editorial Board.

REFERENCES

- [1] P. M. Djurić. The Power of a Name. [Online]. Available: http://www.signalprocessingsociety.org/uploads/email/power_of_a_name.html
- [2] K. J. R. Liu, “Signal processing inside?” *IEEE Signal Processing Mag.*, vol. 21, no. 5, p. 2, Sept. 2004.
- [3] J. M. F. Moura, “What is signal processing?” *IEEE Signal Processing Mag.*, vol. 26, no. 6, p. 6, Nov. 2009.
- [4] J. M. F. Moura, J. L. Flanagan, and N. S. Jayant, “The discipline of signal processing,” *IEEE Signal Processing Mag.*, vol. 30, no. 6, pp. 174–176, Nov. 2013.
- [5] A. M. Zoubir, “Dissemination of research findings: What role can we play?” *IEEE Signal Processing Mag.*, vol. 30, no. 3, p. 2, May 2013.

[SP]

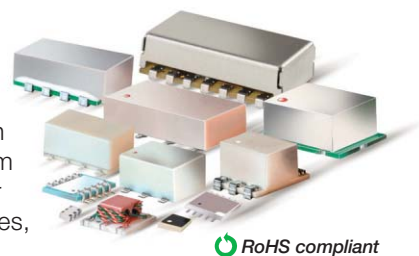
Digital Object Identifier 10.1109/MSP.2014.2311862
Date of publication: 13 June 2014



90° SPLITTERS

5 MHz to 8 GHz **\$199**
from ea. qty. 1000

With over 70 different models, our two-way 90° splitters make the perfect building blocks for many designs including balanced amplifiers, IQ modulator/demodulators, single sideband modulators, image rejection mixers, voltage variable attenuators, phase shifters, and more! Use them for signal processing designs requiring 90° phase offset or to insulate your circuit from reflective elements. The industry's widest range of frequencies, extra low amplitude and phase unbalance, and packages as small as 0.08 x 0.05" make these hybrids essential tools for your RF design toolbox.



RoHS compliant

Tiny, robust, low-cost LTCC models are now available in small quantity reels, with standard counts of 20, 50, 100, 200, 500, 1000, or 2000 at no extra cost! For full performance details and product availability, visit minicircuits.com.

Order online today and have units in-hand as soon as tomorrow!

 **Mini-Circuits®**

www.minicircuits.com P.O. Box 350166, Brooklyn, NY 11235-0003 (718) 934-4500 sales@minicircuits.com

463 rev K

[president's MESSAGE]

Alex Acero
2014–2015 SPS President
a.acero@ieee.org



At the Forefront in Technical Publications

The IEEE publishes nearly one third of the world's technical literature in electrical engineering, computer science, and electronics. This includes more than 154 transactions, journals, and magazines published annually. The IEEE Signal Processing Society (SPS) produces seven of those publications: *IEEE Transactions on Signal Processing*, *IEEE Signal Processing Magazine*, *IEEE Transactions on Image Processing*, *IEEE Signal Processing Letters*, *IEEE Transactions on Audio, Speech, and Language Processing*, *Journal on Selected Topics on Signal Processing* and *IEEE Transactions on Information Forensics and Security*.

Included in the tier-2 Society membership fee of US\$35 a year, you receive electronic access to all seven of these publications. In 2013, these seven publications produced 20,052 pages, a significant increase over the 14,419 pages published in 2008.

All of these IEEE journals are hybrid open access, meaning that authors of manuscripts accepted for publication are given the choice of paying to have their articles made freely available to all readers. These open access papers go through the identical peer-reviewed quality standards as conventional articles. This mechanism is valuable for authors whose research was funded by a government grant that requires open access publications.

The SPS is the fourth-largest Society by membership and second in publishing volume. This is a huge enterprise that requires many authors submitting manuscripts, numerous volunteers reviewing them, and staff putting it all together. I would like to offer my most sincere “thank you” to all. For those of you who are

experts in one of our published fields, we welcome your assistance in helping us review qualified papers.

While quantity is an important metric, quality is even more important. Quality is a multidimensional assessment evaluated with metrics such as timeliness and impact factor. Timeliness is measured as average time from submission to publication. The impact factor of a journal is the average number of citations received per paper published in that journal during the two preceding years. The IEEE is also using additional metrics to measure the stature of a journal in a field.

The IEEE Periodicals Review Committee is tasked with ensuring quality, reviewing all IEEE journals and magazines every five years. In 2014, it was our turn. This process started with a thorough report prepared by the Society's vice president of publications, publications board, and staff. In February, the Review Committee reviewed the reports and spent about 45-min per publication asking questions of the Society leadership and the publications' editors-in-chief. Their overall feedback was quite positive. Many of our publications have an impact factor over “3,” while *IEEE Transactions on Signal Processing* ranks fifth in total citations and *IEEE Signal Processing Magazine* has consistently been in the top five in impact factor. The average time from submission to publication across all our periodicals is under a year, with the fastest being about three months for *IEEE Signal Processing Letters*. The Review Committee was also complimentary of our publications processes, especially our recent policy of allowing papers in *IEEE Signal Processing Letters* to be presented at conferences.

In addition to our own publications, SPS manages *IEEE Transactions on Multimedia*, and we cosponsor other periodicals

covering topics such as cloud computing, big data, wireless communications, sensors, life sciences, the Internet of Things, and much more.

Reflecting the needs of our members in a fast-growing field, we have obtained approval for a new 2015 journal: *IEEE Transactions on Computational Imaging*. The IEEE Engineering in Medicine and Biology, IEEE Circuits and Systems, and IEEE Geoscience and Remote Sensing Societies are participating with us in this new journal, which we will manage. According to its approved scope, “The *IEEE Transactions on Computational Imaging* will publish articles where computation plays an integral role in the image formation process. Papers will cover all areas of computational imaging ranging from fundamental theoretical methods to the latest innovative computational imaging system designs. Topics of interest will include advanced algorithms and mathematical techniques, model-based data inversion, methods for image and signal recovery from sparse and incomplete data, techniques for nontraditional sensing of image data, methods for dynamic information acquisition and extraction from imaging sensors, software and hardware for efficient computation in imaging systems, and highly novel imaging system design.” I encourage all interested authors to submit high-quality papers to this journal.

Unwilling to rest on our laurels, I continue to appreciate your suggestions for further improving our publications processes and content.

Digital Object Identifier 10.1109/MSP.2014.2311863

Date of publication: 13 June 2014



Instant Access to IEEE Publications

Enhance your IEEE print subscription with online access to the IEEE Xplore® digital library.

- Download papers the day they are published
- Discover related content in IEEE Xplore
- Significant savings over print with an online institutional subscription

Start today to maximize your research potential.

Contact: onlinesupport@ieee.org
www.ieee.org/digitalsubscriptions

"IEEE is the umbrella that allows us all to stay current with technology trends."

Dr. Mathukumalli Vidyasagar
Head, Bioengineering Dept.
University of Texas, Dallas



 **IEEE**
Advancing Technology
for Humanity

[reader's **CHOICE**]

Top Downloads in IEEE *Xplore*

This issue's "Reader's Choice" column contains a list of articles published by the IEEE Signal Processing Society (SPS) that ranked

among the top 100 most downloaded IEEE *Xplore* articles through December 2013. The table below contains the citation information for each article and the rank obtained in IEEE *Xplore*. The

highest rank obtained by an article in this time frame is indicated in bold. Your suggestions and comments are welcome and should be sent to Associate Editor Michael Gormish (gormish@ieee.org).

TITLE, AUTHOR, PUBLICATION YEAR IEEE SPS PUBLICATIONS	ABSTRACT	RANK IN IEEE TOP 100 (2013)							N TIMES IN TOP 100 (SINCE JAN 2011)
		DEC	NOV	OCT	SEP	AUG	JUL		
A TUTORIAL ON PARTICLE FILTERS FOR ONLINE NONLINEAR/NON-GAUSSIAN-BAYESIAN TRACKING Arulampalam, M.S.; Maskell, S.; Gordon, N.; Clapp, T.; <i>IEEE Transactions on Signal Processing</i> vol. 50, no. 2, 2002, pp. 174–188	This paper reviews optimal and suboptimal Bayesian algorithms for nonlinear/non-Gaussian tracking problems, with a focus on particle filters. Variants of the particle filter are introduced within a framework of the sequential importance sampling (SIS) algorithm and compared with the standard EKF.	8	6	25	8	4	4	33	
AN INTRODUCTION TO COMPRESSIVE SAMPLING Candes, E.J.; Wakin, M.B. <i>IEEE Signal Processing Magazine</i> vol. 25, no. 2, Mar. 2008, pp. 21–30	This article surveys the theory of compressive sampling, also known as compressed sensing or CS, a novel sensing/sampling paradigm that goes against the common wisdom in data acquisition.	10	11	10	15	13	19	35	
IMAGE QUALITY ASSESSMENT: FROM ERROR VISIBILITY TO STRUCTURAL SIMILARITY Wang, Z.; Bovik, A.C.; Sheikh, H.R.; Simoncelli, E.P. <i>IEEE Transactions on Image Processing</i> vol.13, no. 4, 2004, pp. 600–612	This paper introduces a framework for quality assessment based on the degradation of structural information. Within this framework a structure similarity index is developed and evaluated. MATLAB code available.	28	24	33	37	38	30	15	
IMAGE SUPER-RESOLUTION VIA SPARSE REPRESENTATION Yang, J.; Wright, J.; Huang, T.S.; Ma, Y. <i>IEEE Transactions on Image Processing</i> vol. 19, no. 11, 2010, pp. 2861–2873	This paper presents an approach to single-image superresolution, based upon sparse signal representation of low- and high-resolution patches.	31	44	51	51	82	68	7	
SUPER-RESOLUTION IMAGE RECONSTRUCTION: A TECHNICAL OVERVIEW Cheol Park, S.; Kyu Park, M.; Gi Kang, M. <i>IEEE Signal Processing Magazine</i> vol. 20, no. 3, 2003, pp. 21–36	This article introduces the concept of super resolutions (SR) algorithms and presents a technical review of various existing SR methodologies and models the low-resolution image acquisition process.	34	45	90				16	

Digital Object Identifier 10.1109/MSP.2014.2312184

Date of publication: 13 June 2014

TITLE, AUTHOR, PUBLICATION YEAR IEEE SPS PUBLICATIONS	ABSTRACT	RANK IN IEEE TOP 100 (2013)						N TIMES IN TOP 100 (SINCE JAN 2011)
		DEC	NOV	OCT	SEP	AUG	JUL	
COMPRESSIVE SENSING [LECTURE NOTES] Baraniuk, R.G. <i>IEEE Signal Processing Magazine</i> vol. 24, no. 4, 2007, pp. 118–121	This lecture note presents a new method to capture and represent compressible signals at a rate significantly below the Nyquist rate. This method, called compressive sensing, employs nonadaptive linear projections that preserve the structure of the signal; the signal is then reconstructed from these projections using an optimization process.	39	58	60	95	71		9
SCALING UP MIMO: OPPORTUNITIES AND CHALLENGES WITH VERY LARGE ARRAYS Rusek, F.; Persson, D.; Buon Kiong L.; Larsson, E.G.; Marzetta, T.L.; Edfors, O.; Tufvesson, F. <i>IEEE Signal Processing Magazine</i> vol. 30, no. 1, 2013, pp. 40–60	The more antennas the transmitter/receiver is equipped with, and the more degrees of freedom that the propagation channel can provide, the better the performance in terms of data rate or link reliability. This article quantifies the reliability and achievable rates.	43	75		73			10
THE DISCIPLINE OF SIGNAL PROCESSING: PART 2 [REFLECTIONS] Kwasinski, A.; Kaveh, M.; Deng, L. <i>IEEE Signal Processing Magazine</i> vol. 31, no. 1, 2014, pp. 157–159	This article discusses the field of signal processing engineering and reports on applications and technologies supported by its use.	62						1
IMAGE PROCESSING USING SMOOTH ORDERING OF ITS PATCHES Ram, I.; Elad, M.; Cohen, I. <i>IEEE Transactions on Image Processing</i> vol. 22, no. 7, 2013, pp. 2764–2774	This paper extracts overlapping image patches, orders these patches and applies one dimensional filtering to the reordered set of pixels. These techniques are applied to denoising and inpainting.	63	90	36	12	9	15	7
IMAGE INPAINTING: OVERVIEW AND RECENT ADVANCES Guillenot, C.; Le Meur, O. <i>IEEE Signal Processing Magazine</i> vol. 31, no. 1, 2014, pp. 127–144	A survey of the processes of restoring missing or damaged areas in an image.	94						1
VECTOR-VALUED IMAGE PROCESSING BY PARALLEL LEVEL SETS Ehrhardt, M.J.; Arridge, S.R. <i>IEEE Transactions on Image Processing</i> vol. 23, no. 1, pp. 9–18	This paper considers the components of an image as a vector. By minimizing large angles, parallel level sets are obtained and used for demosaicking.	98						1
ROBUST PART-BASED HAND GESTURE RECOGNITION USING KINECT SENSOR Ren, Z.; Yuan, J.; Meng, J.; Zhang, Z. <i>IEEE Transactions on Multimedia</i> vol. 15, no. 5, 2013, pp. 1110–1120	This paper focuses on building a robust part-based hand gesture recognition system using Kinect sensor. To handle the noisy hand shapes obtained from the Kinect sensor, we propose a novel distance metric, finger-Earth mover's distance, to measure the dissimilarity between hand shapes.			93				1
A GENERALIZED MEMORY POLYNOMIAL MODEL FOR DIGITAL PREDISTORTION OF RF POWER AMPLIFIERS Morgan, D.R.; Ma, Z.; Kim, J.; Zierdt, M.G.; Pastalan, J. <i>IEEE Transactions on Signal Processing</i> vol. 54, no. 10, 2006, pp. 3852–3860	This paper reviews predistortion models based on memory polynomials and proposes a new generalized memory polynomial with results measured using a real 30-W, 2-GHz power amplifier.				1			1

Signal Processing: On the Edge of Astronomy's New Frontier

Digital signal processing (DSP) plays several important roles in modern radio astronomy, such as processing data to create high-resolution radio images, isolating weak emissions from celestial sources, and reducing distortions in incoming signals. DSP can also manage beam-forming, a complex process that allows radio signals to be received from across the sky from any direction, and even multiple directions simultaneously.

Many astronomy projects are now relying on advanced signal processing techniques to probe the edges of the universe to extend humanity's understanding of its origins, scan the skies to image exoplanets—worlds outside our solar system—and investigate many of the major outstanding questions in astronomy. Here's a look at two of them.

MORE ANTENNAS, MORE RECEIVERS

Radio astronomy is currently undergoing a fundamental change, perhaps its most important development since amateur radio operator and pioneer radio astronomer Grote Reber built the first parabolic dish radio telescope (measuring 9 m in diameter) in his Illinois backyard in 1937. In the years that followed, very large telescope dishes became icons of radio astronomy research.

Now, however, radio astronomy is moving toward antennas systems concentrated among individual receivers. The 2010 Low Frequency Array (LOFAR) project, for example, uses approximately 50 stations, each consisting of at least 96 low band antennas and 768 high band antennas concentrated among approximately

48 receiving stations. Extending this approach even further is the Square Kilometre Array (SKA), planned for full operation by 2030.

SKA's designers anticipate deploying somewhere in the neighborhood of 50,000 networked receivers and perhaps as many as 2.5 million antennas. Many of the receivers will be located inside an inner core measuring approximately 100 km in length. Some receivers, however, will be arranged into a set of spiral arms measuring 1,500 km in length. With the help of interferometry signal processing, a collection of relatively small radio telescopes will be able to operate as single, gigantic "virtual" instrument possessing a maximum reception area equal to the combined area of the individual dishes (which for SKA, as its name indicates, is a square kilometer) (Figure 1). The system's baseline—a measure of the telescope's resolving power—will be equal to the distance between the furthest individual components, roughly 200 km. "We have about 350 people involved in the current phase, the preconstruction phase, and we have a huge amount of interest from industry, from signal processing companies—companies that make field-programmable gate arrays (FPGAs), for example," says Tim Cornwell, SKA's architect.

SKA will be built in the southern hemisphere with cores in South Africa and Australia, locations where the view of the Milky Way Galaxy is best and radio interference is less of a problem. Upon completion, SKA promises to be approximately 50 times as sensitive as existing radio telescopes and capable of surveying the sky about 10,000 times faster. The telescope is also expected to generate a torrent of data—up to 160 Gb/s second from each antenna. Much of that information will be used to help researchers

find answers to some of the biggest outstanding questions in astronomy. SKA is being designed, for example, to help astronomers search for gravitational waves, the ripples in the structure of space-time predicted by Albert Einstein's general relativity. "If you have a large number of pulsars all over the sky, you can use them to look for gravitational waves," Cornwell shares. "That's one of the projects that will be done, a survey of the entire sky looking for pulsars."

The system also promises to allow more astronomers to join the hunt for exoplanets, using an investigative tool with far greater resolving power than existing radio telescopes. Even more tantalizing is the prospect of using SKA to look back in time to the universe's so-called Dark Ages—a period extending up to some 400 million years after the Big Bang—an era of darkness that existed before the first stars and galaxies were formed and about which very little is directly known.

WHAT'S OLD IS NEW

Utilizing interferometry as a technique to enhance a radio telescope's resolving power isn't a new idea. Many existing radio telescopes, including LOFAR, are integrated into such networks. SKA, however, takes the approach to a new level. Planners envision a Very Long Baseline Interferometry Network (VLN) that will combine telescopes separated by thousands of kilometers to form a radio interferometer with resolution comparable to a single dish measuring thousands of kilometers in diameter. "Digital signal processing will enable us to collect the very large amount of data that we need and to process it to get all the information out," Cornwell notes. "Radio astronomy has always been at the

Digital Object Identifier 10.1109/MSP.2014.2312176

Date of publication: 13 June 2014

forefront of digital signal processing because of this very factor.”

Interferometry is used to obtain high-resolution information about a particular radio source. “At its heart, interferometry is just a statistical technique,” Cornwell explains. “The noise signals at two or more antennas are correlated via one of a number of techniques (mostly digital/computer now).” If the signals are totally correlated then there must be a small source on the sky producing the same signal in different antennas. “The difference in time between the signal landing at each telescope gives information about the location of the radio source on the sky,” Cornwell says. If the correlation shows more complex behavior than the source itself must be complicated. “A two-dimensional inverse Fourier transform (FT) will produce an image of the source,” Cornwell remarks.

Data from each SKA telescope will be transmitted to a system central correlator linked to high-speed computers that are designed to merge signals from multiple telescopes. The correlator will be situated near the array's core, where the data will be combined and synchronized. Filters will then be used to separate the radio frequency signals required for astronomy from any interfering radio frequency signal that would contaminate the data.

“Basically in radio, if you want to see objects at a very great distance, you have to deal with very faint signals and you have to collect a lot of those signals,” Cornwell says. “In modern processing, we find that to get high-accuracy information out, we have to do DSP,” he adds.

Data from the correlator will be sent to another location for processing. “In South Africa one option would be in Cape Town,” Cornwell says. “In Cape Town there will be a supercomputer, and it will take all of this data and make an image from the information over the region you're looking at.”

Images will also have to be stored inside a massive database, a system that has yet to be developed. “The astronomer will connect to the archive and download the image and look at it and do astrophysics,” Cornwell says “By the time we're up and running on our network internally,



[FIG1] An artist's rendition of the SKA dish arrays in operation at night. Using a technique known as interferometry, they will be able to combine their data to create an image that would be the same as one created by a much larger single aperture instrument. (Photo courtesy of the SKA Organisation.)

we'll have something like an order of magnitude more data flowing than is on the entire global Internet today.”

SKA will also utilize beamforming, the critical signal processing technique used in radio astronomy to observe radio signals from specific regions of the sky. While radio dishes mechanically turn to observe an area of sky, SKA's aperture array antennas will have no moving parts, so the beams must be electronically steered to allow the observation of specific sky regions.

SKA will also use signal processing to automatically detect the repetitive pulsed signal of objects such as pulsars buried in the data. Besides pulsars, the SKA will be able to automatically detect transient astronomical events, including supernovae, gamma-ray bursts, and microlensing events, which can temporarily brighten objects in the far reaches of the universe due to the gravity of a foreground object acting as a lens. Both methods of autodetection are time-frequency-based observations and require high time resolution data.

Cornwell notes that SKA will challenge signal processing algorithm development in two key areas. Faster and better ways will have to be developed to make the high dynamic range images required for SKA science (a ratio of $10^6:1$ to $10^7:1$). Effective radio interference mitigation algorithms will also be needed to enable observations across wide segments of the radio spectrum. The algorithms used will need to be as

efficient as possible to process the huge amounts of data expected to pour through the system.

SKA's signal processing will require exceptionally high-speed computer systems that must meet budget, processing, and thermal requirements. Four micro-processing platforms capable of supporting signal processing are currently being developed and tested by the astronomy engineering community as potential solutions: general-purpose processors, a graphics processing unit, FPGAs, and an application-specific integrated circuit.

Cornwell says he spends a great deal of time thinking about the massive amounts of data that SKA will generate. “Processing that involves going from the data that's emitted from the correlator through to images—that's very complex processing, and for SKA 1 [the project's first phase] it requires a supercomputer running at about 100 petaflops,” he says. “I think that's going to be one of the real challenges of this project: to get our methods, our algorithms, and our software to work on that scale.”

EXOPLANET EXPLORATION

Last year, with the help of a basic signal processing technique, a team of Massachusetts Institute of Technology (MIT) researchers announced that they had discovered an Earth-sized exoplanet, Kepler 78b, a world that orbits around its host star in only 8.5 hours—one of the shortest orbital periods ever detected. The planet has an orbital radius only about

special **REPORTS** continued

three times the radius of the star. Such close proximity to its host results in an estimated surface temperature as high as 3,000 °K, or more than 5,000 °F. “Some people have taken to calling these really, really close-in Earth-sized planets ‘lava worlds,’ even though we don’t know what they’re made of, or what their surfaces look like,” says Josh Winn, an associate professor of physics at MIT (Figure 2) and a member of the team led by physics professor emeritus Saul Rappaport.

To discover Kepler 78b, the team pored through more than 150,000 stars monitored by the Kepler Telescope, a space observatory launched by NASA in 2009 to discover Earth-like planets orbiting other stars. The goal for the MIT researchers was to look for Earth-sized planets with very short orbital periods. To find such worlds, the team scrutinized light data from thousands of stars, looking for dips indicating that a planet may be periodically passing in front of a star.

Yet other types of periodic stellar phenomena can also affect light emission, such as a star eclipsing another star. To detect only signals specifically associated with actual planets, physics graduate student Roberto Sanchis-Ojeda searched through the set of periodic light curves

looking for frequent smaller dips in the data midway between the planetary transits. “We take kind of a shortcut,” Winn says. “We look for the planets that happen to be eclipsing their stars so that, as they go around, their orbit is lined up with the Earth just so, and as the exoplanet’s orbit takes it right in front of the star, it blocks a tiny amount of its light and we can register that dimming.”

Still, detecting tiny dips among tens of thousands of light curves is lengthy, painstaking work. To accelerate the process, the researchers turned to signal processing in the form of an FT search. “Signal processing is very much a part of what we do,” Winn says.

The standard algorithm for transit searching is the box least squares (BLS) algorithm, which generally offers the greatest efficiency for transits with a duration that is short in comparison to the orbital period. Yet BLS also presents some drawbacks. One critical problem is that the BLS spectrum includes peaks at multiples of the orbital period and at multiples of the orbital frequency, complicating attempts to determine the correct period. Winn notes that BLS spectrum computation is basically a time-domain method. “It is essentially a matched filter for the transit signal (an inverse boxcar function),” he explains. “A detection statistic is computed after searching a range of candidate orbital periods, transit phases, and transit depths.” The researchers also found that the standard BLS algorithm generates spurious signals at periods that are integer multiples of the Kepler sampling period of close to half an hour.

Winn credits Rappaport with suggesting the Fourier approach. “He was really the one who had the insight that we could get much further just by using the plain old FT as opposed to the very complicated wavelet-based matched filter,” Winn says. “He’s retired, but he’s spending his retirement finding planets with Kepler data.”

The spurious peaks often lead to significant noise background in searches for planets with periods less than half a day.

While a method exists to partially suppress the spurious peaks, the researchers felt that the introduction of an additional step would complicate the search. The team was also reluctant to follow in the footsteps of several other exoplanet research projects that scoured the Kepler database using a BLS algorithm.

Winn and his colleagues were able to take advantage of the fact that FTs can be computed so quickly that it was practical to repeat the search of the entire database many times while the code was being developed. Although the FT of a transit signal has power that is divided among several harmonics, the number of significant harmonics below the Nyquist limit declines as the orbital period is decreased. The FT is therefore quite sensitive to the shortest-period planets.

According to the researchers, the ratio of transit duration to period, or duty cycle, varies as $P^{-2/3}$ (where P is the planet’s orbital period) and is as large as 20% for ultra-short-period planets, in which case the efficacy of the FT search is nearly equivalent to that of the BLS. Additionally, it’s rather simple to detect a peak in the FT and its equally spaced harmonics, either by means of an automated algorithm or by eye. Meanwhile, the absence of any subharmonics is a useful and important property of a true planet transit as opposed to a background blended binary.

In retrospect, Winn is pleased that taking a seemingly counterintuitive approach led the researchers to an important discovery. “The nice thing about the FT is that it’s as simple as anything that you learn in your first signal processing class in college, and we’re able to compute them extremely quickly,” he says. “Even though it’s not what the orthodox procedure would be, it turned out to work really well because it was so fast and so simple, and we could really tune it to the specific problem.”

AUTHOR

John Edwards (jedwards@johndwardsmedia.com) is a technology writer based in the Phoenix, Arizona area.



[FIG2] Josh Winn, associate professor of physics at MIT, discovered an exoplanet with the help of a basic signal processing technique. (Photo courtesy of MIT.)

Ron Schneiderman

Health Alliance Boosts Influence in Standards Development

Despite barriers relating to regulation, patient acceptance, and privacy concerns, market researchers estimate the growth of the mobile health-care market at US\$9 billion in 2014. Looking ahead, analysts are projecting growth in the mHealth sector at a compound annual growth rate of nearly 40% over the next six years. Equally impressive, mHealth has the potential to dramatically reduce the cost of health care.

But the sector has become a moving target, with rapid changes in mobile device technology and technical standards with design cycles that are longer than most wireless products, mainly due to regulatory approval requirements. Then there's the market itself—it's becoming more consumer centric, intensifying competition among the market's incumbent players.

One of the most influential organizations in the field is the Continua Health Alliance, an international nonprofit organization enabling end-to-end, plug-and-play connectivity of personal health devices and services with more than 220 member companies, including medical device, telecom, health tech service, and health-care industry leaders, working to develop new standards in medical electronics and take advantage of existing standards. While not formally a standards organization itself, Continua also works to identify and resolve gaps in standards to ensure that mHealth devices are interoperable.

The alliance has been a major contributor to technical standards developed by the IEEE Standards Association (IEEE-SA), including the development of the IEEE 802.11 family of standards, and has

worked with the Wi-Fi Alliance to facilitate and promote the adoption of Wi-Fi technology in connected health applications. Since its approval as a formal standard, 802.11 has become the dominant wireless area network technology, while Bluetooth, ZigBee, and near-field communications (NFCs) continue to gain market share in mHealth products.

For this second in a series of Q&A features for *IEEE Signal Processing Magazine (SPM)*, we talked to Michael Kirwan (Figure 1), technical operations director of Continua, about its relationship with the IEEE-SA, its collaboration with other health organizations, and changes in its new design guidelines for mHealth original equipment manufacturers.

IEEE SPM: You recently signed an agreement to collaborate with other health industry organizations. What's that about?

Michael Kirwan: Continua recently partnered with the newly formed Personal Connected Health Alliance (PCHA). This is a collaboration with Continua, the mHealth Summit, and Healthcare Information and Management System Society (HIMSS) to establish a global nonprofit alliance representing the consumer voice in personal connected health. PCHA will promote personal connected health solutions featuring interoperable, plug-and-play devices and systems, such as mhealth tools, remote monitoring devices, and sensors. Each member organization brings its own perspective to the collaboration, but this will strengthen Continua's international expansion efforts. The Continua brand is unchanged. Our vision and mission remain the same, with the same processes, events, and working groups. We will continue to focus on standards.

We have also signed a strategic agreement with IEEE Standards to help



[FIG1] Michael Kirwan is the technical operations director of the Continua Health Alliance. (Photo courtesy of the Continua Health Alliance.)

accelerate and broaden the adoption of globally relevant standards-based technologies for the health-care arena. IEEE Standards developed the IEEE 11073 family of standards designed for the entire health-care continuum for personal health device communications. The collaboration follows the U.S. Food and Drug Administration (FDA) announcement in November 2013 that it recognized the importance of interoperability in standards and published what it called its "final guidance" for developers of mobile medical devices last year in September. The agency said it will oversee apps that function like medical devices, but it does not expect manufacturers to submit premarket review applications or to register and list their apps with the FDA. It also listed 25 standards that help support medical device interoperability, including 12 IEEE 11073 standards.

IEEE SPM: Will the PCHA have any influence on the development of IEEE 11073 standards updates?

Kirwan: Absolutely. Continua members are also members of the IEEE Standards working groups that developing

Digital Object Identifier 10.1109/MSP.2014.2315332

Date of publication: 13 June 2014

special **REPORTS** continued

these standards. Of course, other organizations are involved with the IEEE-SA, such as universities, that are not members of Continua.

IEEE SPM: *You publish Continua Design Guidelines every year to facilitate the interoperability and efficient use of smartphones and tablets for connected health. What can we expect in the newest version of the guidelines?*

Kirwan: Going forward, we're now working on what we refer to internally as Genome. This will be our 2015 version, and it will add additional device specialization from IEEE Standards, and additional functionality, along with improvements to the existing guidelines as well. The guidelines also include new initiatives, such as NFCs in smartphones, the adoption of a RESTful (RESTful, or "representational state transfer," is generally described as the underlying architecture for the Web. Focusing on data elements in its construction, it has been used to develop Web services) style architecture to better engage app developers, and SMS-based capability, which can wake up a device to receive data. Continua requires that anything in our guidelines matches up with IEEE standards.

The Continua Design Guidelines have been adopted by the International Telecommunications Union (ITU) and have been translated into six different languages. The ITU has given final approval of a new standard, Recommendation ITU-T H.810, that is now part of the Continua Design Guidelines. As a next step, Continua will submit testing specifications for ITU-T H.810 for approval by ITU-T's Study Group 16. This will allow devices to be tested for conformance to the standard.

The guidelines specifically focus on plug-and-play connectivity across hubs (a common connection point for devices in a network), local area networks, personal area networks, wide area network interfaces, and health records networks. Continua certification indicates that a mobile device can communicate simply and securely with any other Continua certified product across networks as well as with health records networks.

IEEE SPM: *Other than the IEEE Standards Association and ITU, do you work with any other organizations involved in standards development?*

Kirwan: One is the Bluetooth Special Interest Group (SIG). I work with them almost daily. I also work with the ZigBee Alliance, the NFC Forum, the USB group on occasion, and others.

IEEE SPM: *Who has access to the Continua Design Guidelines?*

Kirwan: It's free from Continua. And it's free to the ITU. All you have to do is tell us who you are and we'll send you a copy through a link over the Internet.

IEEE SPM: *Do you see any technology bottlenecks in the health-care industry?*

Kirwan: Regulation is often an issue. We have a regulatory work group, and we weren't getting enough guidance from the FDA, and then last year it came out with its "final guidance" for developers of mobile medical devices, giving IEEE standards recognition that its 11,073 standards are relevant to interoperability of medical devices, and how apps should be treated on mobile phones.

Another area we worked on for some time was the shift from an earlier version of Bluetooth that Continua had adopted, which was a health device profile standard by the Bluetooth SIG that was difficult for some companies to implement. The SIG has since switched from that to what is now Bluetooth Low Energy that Continua has adopted and included in its design guidelines. Everyone, including the IEEE, is now on board with the new [Bluetooth] standard, and companies are now designing their products to that standard. We're also working with Google directly on Android to try to get them to support Continua standards.

IEEE SPM: *What's the impact of "big data" technology on the health-care industry?*

Kirwan: Our job is to get the data. Without Continua, you're stuck in proprietary channels. You're not going to achieve big data that way. The way you achieve big data is by making your blood pressure cuff work with everything, and to go into every manufacturer's back-end

system, or in the cloud. You have to do that as a standard, and you can do that with Continua. Then, you can have multiple blood pressure cuffs, produced by multiple manufacturers, located around the world, sending data to multiple mobile devices.

IEEE SPM: *The Internet of Things and machine-to-machine (M2M) technologies are getting a lot of attention in the industry. Is sensor technology currently up to the task of meeting the requirements of mHealth, or so-called connected health, applications?*

Kirwan: We're working with the ITU on M2M. The ITU established a Focus Group on the M2M Service Layer early in January 2012 that would provide a cost-efficient platform, and could be easily deployed. Continua is also a member of oneM2M [a global organization launched in 2012 by seven international standards development organizations, the Association of Radio Industries and Business, the Telecommunications Technology Committee of Japan, the Alliance for Telecommunications Industry Solutions, the Telecommunications Industry Association of the United States, the China Communications Standards Association, the European Telecommunications Standards Institute, and the Telecommunications Technology Association of Korea], which is doing similar work and is probably a lot more interesting. oneM2M is expected to have its first [standards] release in July of this year. They're developing a new architecture to help everyone build their Internet of Things from apps to systems in a similar way. Continua is helping them create a model of what they should be developing in the future, which would eventually be turned into a formal standard.

IEEE SPM: *Is Continua focusing on any one area at the moment?*

Kirwan: In terms of standard development activity, the clinical and personal health devices groups are the busiest right now. But most of our focus in the last year

(continued on page 148)

[from the **GUEST EDITORS**]Joachim Ender, Moeness G. Amin,
Gianfranco Fornaro,
and Paul A. Rosen

Recent Advances in Radar Imaging

Radar imaging reaches back to the patent on synthetic aperture radar (SAR) by John Wiley in the year 1954. From the early days of SAR when imaging was performed using photographic film technology, to modern times where enormous images can be formed on a single computer in practically no time with exquisite accuracy and resolution, there have been tremendous advances in the field. These advances have been, to some degree, motivated by the increasing availability of high-quality SAR data from the ever-expanding fleet of international airborne and spaceborne SAR systems in both the civilian and military sector. In the civilian sector alone, the National Aeronautics and Space Administration's (NASA's) SEASAT in 1978, followed by the NASA shuttle imaging radars SIR-A, SIR-B, and SIR-C, initiated a remarkable development of international radar missions including Canada's RADARSAT mission, Japan's Earth Resources Satellite (JERS) and Advanced Land Observing Satellite (ALOS) missions, Europe's European Remote Sensing (ERS) and Environmental Satellite (ENVISAT), and NASA's Shuttle Radar Topography mission (SRTM), as well as Germany's TerraSAR-X satellite. These, in turn, have led to a new generation of missions with even greater sophistication in modes and operational characteristics. Airborne SAR test beds that offer even greater resolution and mode diversity often support the satellite programs. The multidecade time series of data these missions provide have inspired researchers to develop exciting new processing technologies for exploitation, which continue to evolve.

Digital Object Identifier 10.1109/MSP.2014.2312464

Date of publication: 13 June 2014

SAR systems are now capable of providing resolutions comparable to optical systems while operating in all weather and times, which are features of key importance for many applications. SAR data provide key information about the imaged area, unique and distinct from what optical systems can provide in that the SAR is sensitive to the electrical and roughness characteristics of the scene rather than its chemical properties. The ability to control the illumination source gives a range of diversity in observations—polarization, phase-time, and frequency dependence—enabling broad applications including classification and change detection, forestry, soil characterization, monitoring of areas subject to natural and anthropogenic hazard, and many others.

Air- and space-based sensors that have been realized span frequencies extending from very high frequency to the upper millimeter wave region, offering deep exploration of scattering phenomenology and insights into the nature of targets and surfaces. Extended SAR capabilities, such as the Shuttle Radar Topographic mission cross-track interferometer, the TanDEM-X satellite pair and the Constellation of Small Satellites for the Mediterranean Basin Observation (COSMO)/SKYMED constellation, have expanded applications of SAR in unique and important ways, including across/along track and repeat pass interferometry techniques for topographic mapping, velocity estimation of moving targets, and accurate deformation monitoring, as well as multiband operations and polarimetric exploitation: options that add to the almost incredible improvements in geolocating fine-resolution images through precision data processing. Today's SAR technology offers a cost-effective alternative to traditional techniques, capable of reaching accuracy and measurement

density that are starting to be comparable to lidar systems while retaining synoptic view and global coverage advantages.

This special issue of *IEEE Signal Processing Magazine (SPM)* provides an overview of recent developments in SAR imaging and delineates potential research avenues for further progress in this area. It covers the relevant topics of high-resolution and multistatic SAR imaging, SAR imaging of complex scenarios and buried targets, SAR interferometry, SAR tomography and polarimetric SAR, and multipath mitigation and exploitation in SAR. The intent is to provide readers with a breadth of topics in the theory and applications of SAR processing, capturing recent developments and highlighting new frontiers.

The first article by Ash et al. addresses the issue of overcoming limitations of traditional SAR imaging based on narrow-band/narrow angle acquisition. It provides an overview of the methods used for wide-angle SAR imaging and deals with problems related to anisotropic scattering and the deviation from point scattering assumptions and their effects on data interpretation and processing.

Çetin et al. provide an overview of recent research on SAR imaging for increased resolvability of point scatterers, reduced speckle, proper segmentation, and robustness to limitations in data quality and quantity.

The article by Fornaro et al. focuses on the developments of SAR interferometry, which has enabled the monitoring of ground deformations with applications to natural hazards as in revealing seismic and volcanic risks and landslides and underground excavation/withdrawal. It also addresses the developments of SAR tomography that turns interferometric into multidimensional (space-time) imaging methods.

(continued on page 158)

[Joshua N. Ash, Emre Ertin, Lee C. Potter, and Edmund G. Zelnio]

Wide-Angle Synthetic Aperture Radar Imaging

[Models and algorithms for anisotropic scattering]

Advances in radar hardware have enabled the sensing of ever-wider synthesized apertures. In this article, radar video—a sequence of radar images indexed on sub-aperture—is discussed as a natural, convenient, and revealing representation to capture wide-angle scattering behavior of complex objects. We review the inverse problem of recovering wide-angle scene reflectivity from synthetic aperture radar (SAR) measurements, survey signal processing approaches for its solution, and introduce a novel Bayesian estimation method. Examples from measured and simulated scattering data are presented to illustrate scattering behavior conveniently revealed by the SAR video framework.

INTRODUCTION

Radar performs echo-location using a band-pass signal by measuring time delays due to reflecting objects. This is illustrated in Figure 1, where the red curve shows the envelope of the echo. The echo provides a one-dimensional projection of the three-dimensional (3-D) scene; points along concentric spheres collapse into a single position in the measurement. The radar bandwidth provides timing accuracy, and hence gives range resolution. To form a spatial map of scene reflectivity, the scene is viewed from a diversity of viewing angles; this is accomplished by moving the transmitter, here colocated with the receiver, to synthesize an aperture

much larger than the antenna's physical size. Measurement positions along a notional synthetic aperture are depicted by dots in Figure 1. A small diversity of viewing angles can provide significant spatial resolution; for example, for a 3-cm wavelength, approximately 3° of azimuth suffices to achieve 1-ft resolution [1].

Technological advances in digital hardware, radio frequency signal generation, and navigation have facilitated the use of ever-larger synthetic apertures in airborne radars [2]–[5]. Wide-angle SAR may be defined as employing any synthesized aperture whose azimuthal angular extent exceeds the sector required for equal resolution in range and cross-range. That is, a wide-angle aperture has extent exceeding $2 \sin^{-1}(BW/(2f_c))$ radians, where

BW and f_c are the bandwidth and center frequency of the radar, in Hertz. However,

reflector geometry, shadowing, and coherent scintillation cause scattering behavior that can be strongly dependent on viewing angle. With the scattering dependent not only on space, but also on viewing angle, measurement over a large aperture invites the question, “What is a wide-angle radar image?” In this tutorial article, the viewpoint is that SAR video, a map of reflectivity as a function of both space and viewing angle, is a natural signal processing choice. An image product from SAR video is illustrated in Figure 2. The red circle on the left graphically depicts frequency-domain radar measurements on a polar grid where radius corresponds temporal frequency and angle corresponds to the azimuthal viewing angle. Simulated far-field echoes here are collected for a 360° circular aperture, 640-MHz bandwidth and

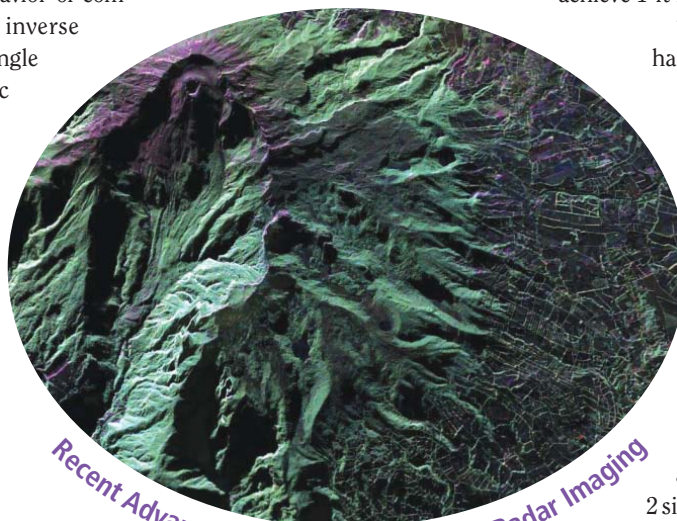
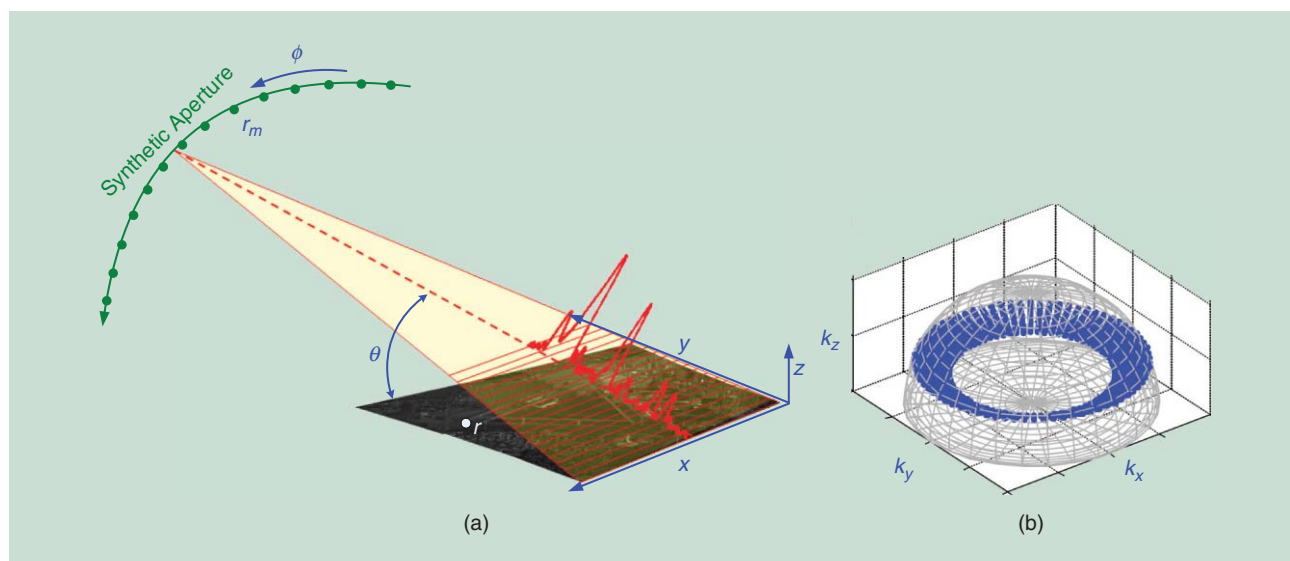


PHOTO COURTESY OF NASA

Recent Advances in Synthetic Aperture Radar Imaging

Digital Object Identifier 10.1109/MSP.2014.2311828

Date of publication: 13 June 2014



[FIG1] (a) A radar measures the Fourier transform of echoes observed from a given viewing angle. (b) The combination of viewing angles forms a synthetic aperture that determines the portion of k -space transduced by the measurements.

10-GHz center frequency [6]. Images are computed for a sequence of subapertures, possibly overlapping, to produce images of reflectivity, $\Psi(r, \phi)$ indexed on both spatial location, r , and azimuth angle, ϕ . [For reference, a mesh model of the reflecting object is given in Figure 3(a).]

A wide aperture greatly increases information about objects of unknown orientation [7]. Given the specular nature of radar returns from man-made objects, the wide-angle aperture captures more glints and yields a higher probability of capturing the most discriminating features. In addition, for reflectors that

persist across angle, a wider aperture provides improved spatial resolution [1]. For reflectors that do not persist, a wide aperture allows detection of the anisotropic behavior.

Table 1 lists the classes of signal processing approaches surveyed in this article for reconstruction of a sequence of aspect-dependent images, $\Psi(r, \phi)$. Across a wide aperture, scattering is aspect dependent, and the reconstruction of a single image therefore obscures the anisotropic behavior. We first survey the subaperture, or windowed, approach in which the wide aperture is divided into smaller subapertures on

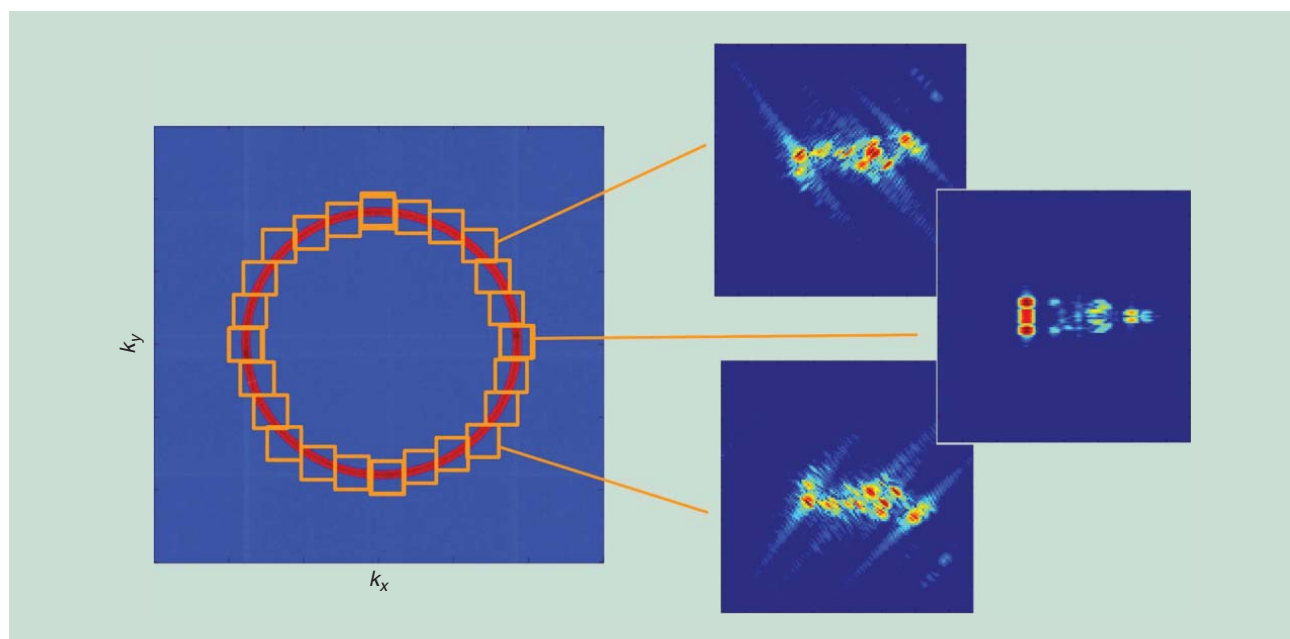


[FIG2] A coherent 360° two-dimensional image is an invertible baseband representation that retains all 3-D information, but poses significant storage, processing, and interpretation challenges. SAR video (three example 15 m × 15 m frames are extracted to the right) provides a compact real-time representation enabling postprocessing of wide-angle information.

which scattering is more nearly homogeneous; on each subaperture, a single subimage is formed. For subaperture methods, we review a recursive linear imaging procedure and survey several nonlinear techniques that have been proposed for sharpening the resolution of the individual subimages. We next survey three inversion approaches that jointly process the wide-aperture data to explicitly reconstruct scattering as a function of both space and viewing angle. Before proceeding to the survey, we provide an elementary statement of the image reconstruction problem. Following the survey, we discuss the benefits of SAR video and contrast the merits of the various approaches.

INVERSE SCATTERING

Traditional transmitters employ linear FM chirp waveforms for a constant envelope transmission; a receiver, after mixing and filtering, directly yields the in-phase and quadrature samples of the Fourier transform of the complex-baseband echo signal. Thus, far-field measurements can be indexed by the frequency and viewing angle, as illustrated in Figure 1.

[TABLE 1] A SURVEY OF ANISOTROPIC IMAGING PROCEDURES.

METHOD	EXAMPLE REFERENCES
SUBAPERTURE METHODS	
LINEAR: RECURSIVE BACKPROJECTION	[11]
NONLINEAR: FILTER BANKS	[12]–[15]
NONLINEAR: REGULARIZED LEAST-SQUARES	[17]–[20]
FULL-APERTURE METHODS	
PARAMETRIC MODELING	[21]–[25]
REGULARIZED LEAST-SQUARES	[26]–[27]
BAYESIAN	[29]

For decades, airborne radar systems have typically operated with a small diversity of wavelengths and viewing angles. Two consequences result for imaging [1], [8]. First, the point scattering assumption that reflectivity is constant across frequency and angle may be used with great success. Second, the small aperture allows for a plane-wave (far-field) assumption to hold across a large scene. Together, these approximations render the

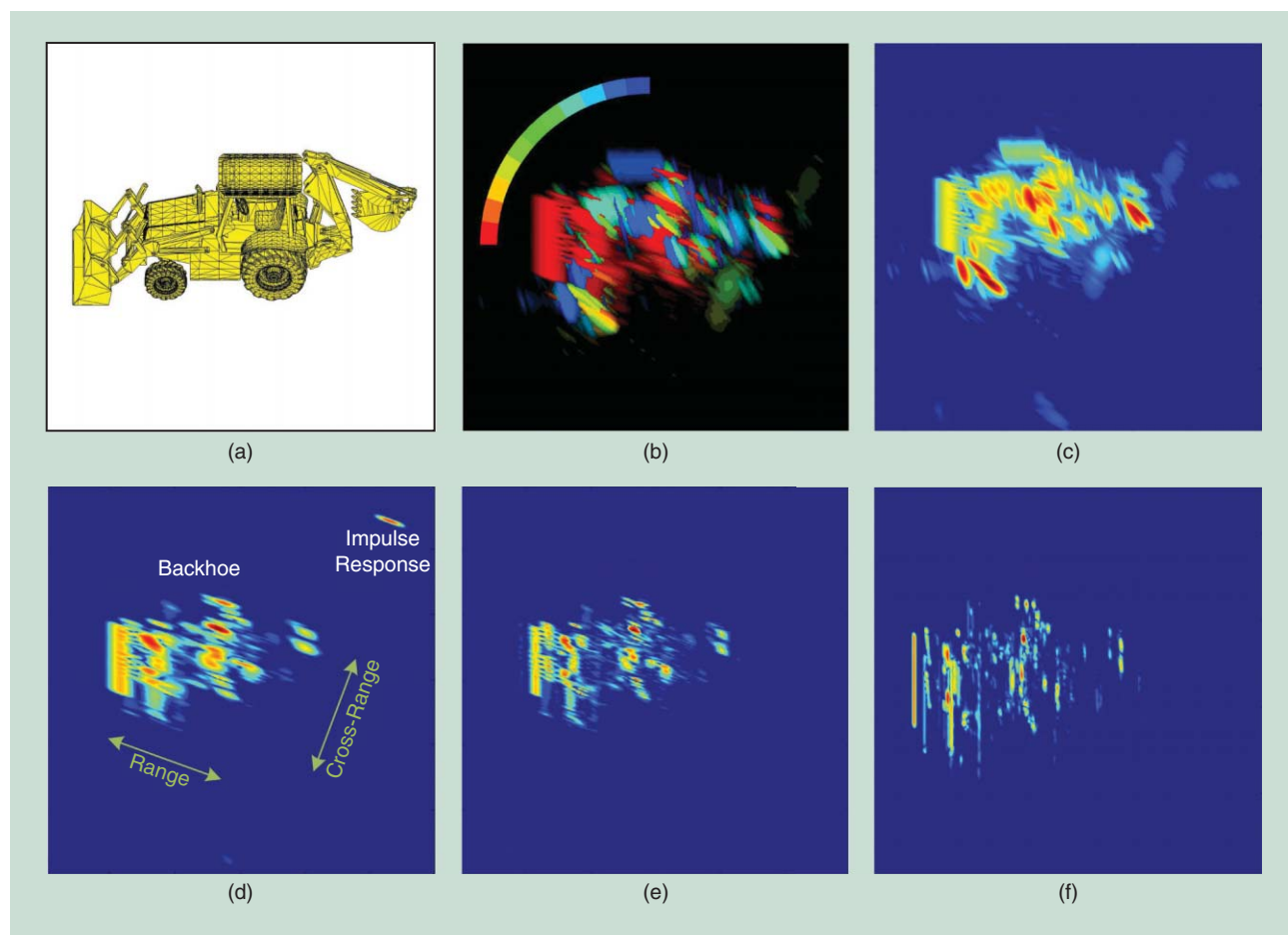


[FIG3] Subaperture X-band imaging of a backhoe with 600-MHz bandwidth. (a) A mesh model, (b) composite backprojection image color-coded to azimuth angle of peak response across 11 subapertures, (c) composite backprojection image from maximum amplitude across 11 subapertures, (d) backprojection image from a single 20° subaperture, (e) nonlinear imaging to deconvolve sidelobes from a single 20° subaperture, and (f) reference image from a single 20° subaperture and 4-GHz bandwidth. In (c)–(f), color encodes the top 40 dB of response amplitude.

measurements to be simply samples of the Fourier transform of the scene reflectivity; the rectangular coordinates in Figure 1, (k_x, k_y, k_z) , are these spatial frequencies. Thus, imaging via Fourier transformation results in an image that is bandlimited in spatial frequency. Backprojection with convolution [8] yields the same result, and backprojection alone serves to approximate an inverse operator by the adjoint operator. This adjoint operator is the matched filter for ideal point scattering.

Taking a closer look, electromagnetic scattering from a scene may be fully described as a function of spatial location, viewing geometry, frequency, and polarization. For monostatic data collection, the scattered electric field from an object can be described by a 2×2 polarimetric scattering matrix,

$$\Psi(\mathbf{r}, \mathbf{r}_m, f), \quad (1)$$

where $\mathbf{r} = (x, y, z)$ is the object location, $\mathbf{r}_m \in \mathbb{R}^3$ is the m th measurement location, and f is frequency. The measured fields are modeled by [1]

$$E(f, \mathbf{r}_m) = \int_r \frac{1}{\|\mathbf{r} - \mathbf{r}_m\|^4} \Psi(\mathbf{r}, \mathbf{r}_m, f) \times E_i \exp\left\{j2\pi f \frac{\|\mathbf{r}_m\| - \|\mathbf{r}_m - \mathbf{r}\|}{c/2}\right\} d\mathbf{r}. \quad (2)$$

The 2×1 complex-valued vector E_i is the incident field for a given polarization basis, and the two-way propagation time relative to the scene center, $\mathbf{r} = 0$, is $2(\|\mathbf{r}_m\| - \|\mathbf{r}_m - \mathbf{r}\|)/c$. In this linear (Born) model, only backscatter is modeled; any nonlinear interactions in actual scattering must be accounted for in the linear model by additional, spurious reflectors or “artifacts.”

Via traditional imaging, a two-dimensional or 3-D spatial representation is formed of the multivariable function Ψ . Consequently, some behaviors may be obscured. A linear aperture leaves unresolvable any displacement orthogonal to the slant plane containing the aperture and the scene center. Thus, for a linear aperture the viewing position may be parametrized by one angle, and location by two variables. In addition, with a narrowband assumption, the frequency variable is eliminated to arrive at scattering as a function of three real variables, $\Psi(x, y, \phi)$, where ϕ is the azimuth angle. Traditional imaging techniques further abandon the angle dependence [1], [8], yielding a function of two variables readily depicted as a two-dimensional map, $\Psi(x, y)$. Finally, a far-field plane-wave propagation assumption yields a linearization of the differential range, $\|\mathbf{r}_m\| - \|\mathbf{r}\|$, and

$$E(f, \phi) \approx \int_{x,y} \Psi(x, y) \times E_i \exp\left\{j2\pi f \cos\theta \frac{(x \cos\phi + y \sin\phi)}{c/2}\right\} dx dy. \quad (3)$$

The plane wave assumption yields the simplicity of Fourier processing for inversion of (3) but results in a predominantly quadratic phase error due to wavefront curvature; this error is limited by restricting the image scene size to be small relative to the standoff distance. For example, for a linear aperture subtending 30° , a 10-GHz center frequency, and a 15-km standoff

distance, the scene radius must be less than 28 m to limit quadratic phase error to $\pi/4$ radians. Backprojection imaging, and its fast variations [5], apply with or without the far-field approximation, while Fourier imaging requires the phase linearization provided by the approximation.

In contrast to a linear aperture, a curvilinear aperture can disambiguate reflector locations in three spatial dimensions [1]. A special case is circular SAR (CSAR), in which the aperture positions lie on a circle of constant altitude, and a wide-beam antenna persistently illuminates a scene within the projection of the circle onto the ground below. Multiple circular orbits can further diversify viewing geometry and improve the 3-D resolution, e.g., using interferometric approaches [9], [10]. Experimental demonstration of 3-D reconstructions, $\Psi(\mathbf{r})$, has been reported at X-band [2], VHF [4], and L-band [5]. For either linear or circular apertures, SAR video introduces an angle index, ϕ , to reconstruct $\Psi(\mathbf{r}, \phi)$. Examples below consider both linear and circular apertures.

SUBAPERTURE METHODS

We first survey the subaperture, or windowed, approach: the wide aperture is divided into smaller subapertures on which scattering is more nearly homogeneous. On each subaperture, a single subimage is formed. Nonlinear techniques have been proposed for deconvolving the sidelobes, or “sharpening,” of the individual subimages.

RECURSIVE BACKPROJECTION

A sequence of subaperture images may be linearly constructed by recursive implementation of backprojection imaging. The recursive approach offers computational advantage in memory and peak-processing requirements, versus a block-processing strategy. In traditional block processing, a set of echoes across a contiguous set of aperture positions are filtered, weighted, and then backprojected to an imaging surface to form a complex-valued map of reflectivity. Fast backprojection algorithms reduce computational load (e.g., [5]). An aperture weighting provides suppression of the image point spread function sidelobes due to the finite aperture, but at the cost of a modest increase in the mainlobe width. Traditional block-processing image formation computes an aperture-weighted backprojection image, $\widehat{\Psi}^{(t)}(\mathbf{r})$, at slow-time azimuth position t . The image is made using the synthetic aperture defined by the J most recent pulses and takes the form

$$\widehat{\Psi}^{(t)}(\mathbf{r}) = \sum_{j=0}^{t-1} w_j \mathcal{B}(\psi_{t-j}), \quad (4)$$

where ψ_t is the echo at aperture position t , \mathcal{B} is the filter-and-backproject operator, and w_j , $j = 0, \dots, J-1$, is an aperture weighting sequence, such as that provided by a Taylor or Hanning window. In SAR video applications requiring the production of a sequence of t -indexed images, the block-processing approach suffers from high memory and peak computation overhead, both proportional to the aperture size J .

In contrast, a recursive approach [11] to the computation (4) can offer nearly identical imagery with orders of magnitude reduction in memory and peak processing requirements,

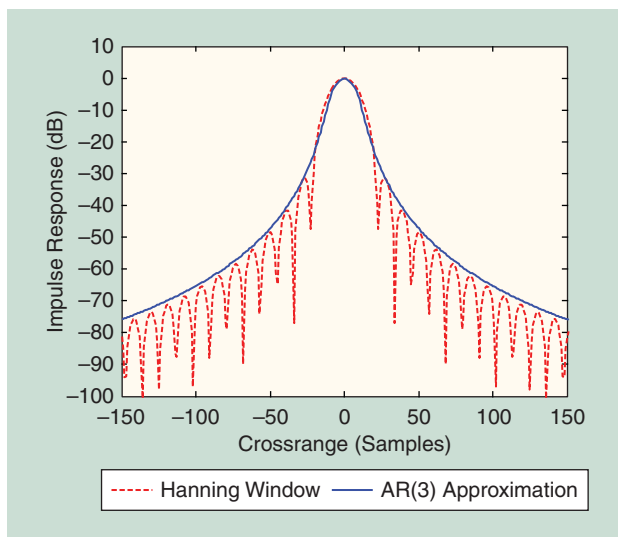


[FIG4] Recursive backprojection imaging enables orders of magnitude reduction in memory and peak computation for typical SAR video scenarios [11]. Here a third-order recursion well approximates a Hanning sequence for cross-range sidelobe control.

thereby enabling real-time SAR video imaging of large scenes. The recursion is given by

$$\hat{\Psi}^{(l)}(\mathbf{r}) = \sum_{m=1}^M \alpha_m \hat{\Psi}^{(l-m)}(\mathbf{r}) + \beta \mathcal{B}(\psi_t), \quad (5)$$

where $M \ll J$ is the recursion order, and $\{\alpha_m\}, \beta$ are constants controlling the effective weighting sequence. An example is provided in Figure 4 illustrating that a third-order recursion provides an excellent match to a Hanning window for aperture weighting. The recursive imaging provides SAR images at a frame rate equal to the pulse repetition frequency.

NONLINEAR RESOLUTION ENHANCEMENT

The processing of subapertures presents a tradeoff between spatial cross-range resolution and the blurring of scattering changes versus aspect angle. The same tradeoff is encountered, e.g., in the use of the short-time Fourier transform for time-series analysis. Nonlinear processing procedures have been applied in radar to enhance the resolution of a single subaperture image. The methods implicitly assume nearly isotropic reflectivity across the small subaperture and result in a spatially varying point spread function. We briefly survey two classes of such approaches: filter banks and regularized least-squares.

FILTER BANKS

The linear image formation techniques noted above can be viewed as fixed filter banks, where the image at location \mathbf{r} is a linear combination of the vector \mathbf{y} of data samples, $\hat{\Psi}(\mathbf{r}) = \mathbf{w}_r^H \mathbf{y}$. Nonlinear sharpening techniques used in SAR are largely adapted from the rich literature of spectrum estimation; see [12] for an expansive survey. For adaptive filter bank methods, the weight vector itself is a function of the data. The data adaptive approaches reduce both

speckle and sidelobes at the expense of the processing gain in the target-to-clutter ratio (TCR). Let \mathbf{a}_r denote the ideal, noiseless modeled response from location \mathbf{r} ; an isotropic point is the ubiquitous modeling choice. The minimum variance method (MVM) [12] seeks to minimize the expected energy, $\mathbb{E}\{\|\hat{\Psi}(\mathbf{r})\|^2\}$, subject to a unity gain constraint, $\mathbf{w}_r^H \mathbf{a}_r = 1$. The solution to the linearly constrained quadratic optimization yields

$$\mathbf{w}_r = \frac{\mathbf{R}^{-1} \mathbf{a}_r}{\mathbf{a}_r^H \mathbf{R}^{-1} \mathbf{a}_r}.$$

The covariance matrix, \mathbf{R} , is estimated as the sample covariance matrix computed from multiple overlapping data subapertures. Variations on the MVM approach include diagonal regularization of the covariance, $\mathbf{R} + \mu \mathbf{I}$, and a rank-1 modification [13]. The high-definition imaging (HDI) approach [14] modifies MVM to constrain the angle between \mathbf{w}_r and \mathbf{a}_r . Each of these MVM variations have a computational complexity that is cubic in the number of pixels.

Adaptive sidelobe reduction (ASR) [12] provides a computational complexity that is merely linear in the number of pixels; a single snapshot viewpoint is adopted, and, implicitly, a rank-1 covariance assumption. Data-adaptive weights are used to modify a matched-filter image via a spatially varying finite impulse response filter. The filter is constrained to be real valued, symmetric, have center tap equal to one, and to have all other taps yield sum of squares less than a prescribed constant. The constrained filter taps are then adapted to minimize the output energy. The approach is further simplified in spatially variant apodization (SVA), whereby the filtering is separable, uses only the two neighboring pixels in each direction, and imposes a coefficient positivity constraint. To suppress sidelobes, the SVA approach relies on the oscillatory structure of a separable sinc point response.

Other spectrum estimation approaches have been proposed, as well, such as the use of a smoothed Wigner-Ville distribution, rather than short-time Fourier transform, in cross-range [15].

REGULARIZED INVERSION

To enhance the resolution of a single subaperture image, sidelobes may be deconvolved via a regularized least-squares inversion of the linear, isotropic scattering model. Adopting Ψ as a vectorized representation of the discrete pixels in $\Psi(\mathbf{r})$, the inversion may be expressed

$$\hat{\Psi} = \min_{\Psi} \|\Psi\|_0 \quad \text{subject to} \quad \|\mathbf{A}\Psi - \mathbf{y}\|_2^2 \leq \epsilon, \quad (6)$$

where the ℓ_0 pseudo-norm $\|\cdot\|_0$ counts nonzero entries in a vector and expresses the preference for an image dominated by a few strong reflectors (or, more generally, sparse in some basis). Greedy methods, such as CLEAN and orthogonal matched pursuit (e.g., references in [10] and [16]) have been widely used and can solve this NP-hard problem with suitable restrictions on both the correlation in columns of \mathbf{A} and the sparsity of Ψ ; likewise, the ℓ_0 pseudo-norm can be relaxed to an ℓ_p quasi-norm, $\|\Psi\|_p = \{\sum_n |\Psi_n|^p\}^{1/p}$. Authors have used

$p = 1$, resulting in a convex problem, and also $0 < p < 1$ [17], [18] in the nonconvex formulation

$$\widehat{\Psi} = \min_{\Psi} \|A\Psi - y\|_2^2 + \mu \|\Psi\|_p. \quad (7)$$

A fixed-point iteration has appeared in the literature as a solution technique (e.g., [19] and [20]) for (6); and, a conjugate gradient (CG) procedure has been applied to (7) with good success [17]. Moreover, in the CG framework, the objective can be generalized from $\|\Psi\|_p$ to $\|D(|\Psi|)\|_p$ with a differentiable function D providing an edge-preserving region enhancement in the recovered imagery [17]. Lagrange multipliers, such as the μ in (7), are tunable algorithm parameters and may significantly impact resulting imagery. The use in radar imaging of greedy and optimization-based approaches for sparse linear inversion predates the theoretical underpinnings provided by compressive sensing [16]; however, the recent explosion of work in the area of compressive sensing has given rise to many good convex programming algorithms for numerical solution of (6) relaxed to $\|\Psi\|_p$ for $p = 1$.

SUBAPERTURE PROCESSING EXAMPLES

We next illustrate the application of subaperture methods, providing visualization of both aspect-dependent scattering and the ability of nonlinear processing to deconvolve sidelobes. For the examples, synthetic monostatic scattering data are generated for a backhoe model, illustrated in Figure 3(a), using a high-frequency computational electromagnetics code [6]. The center frequency is 10 GHz, and the bandwidth is 600 MHz unless otherwise noted. A linear aperture in the far field is used, with 45° depression angle at the center of the aperture.

In Figure 3(b) and (c), a 110° aperture is processed as a sequence of 11 overlapping subapertures, each of 20°. False color encodes the center azimuth angle of the subaperture at which the maximum amplitude occurs in (b), and in (c) encodes the maximum amplitude across the subapertures. Note that the noncoherent combination of subaperture images as in (c) can be interpreted as a generalized likelihood ratio test for a single reflector with 20° persistence and an unknown orientation aligned to one of the 11 subapertures.

Figure 3(d)–(f) illustrates nonlinear sidelobe deconvolution applied to a single 20° subaperture. The point spread function is displayed in the upper right-hand corner of (d) and reveals a finer resolution in cross-range than range, as expected. Also note that the orientation of the impulse response points towards the center of the 20° synthetic subaperture. Linear backprojection processing results in (d); at this orientation the glint due to the backhoe shovel appears prominently, seen at the far left. Deconvolution processing [17] of the coherent data, with $p = 0.7$ and $\mu = 0.1$ in (7), results in (e), yielding many features that are more clearly delineated than in (d). For comparison, a reference image is shown in (f); the reference is based on a large 4,000-MHz bandwidth, integration over the same 20° subaperture, and formed via backprojection as in (d), without deconvolution processing.

The choice of very large subapertures for nonlinear deconvolution of the point spread function (psf) offers no benefit; the

modeled psf implicit in the deconvolution algorithm can become increasingly mismatched to actual scattering as the subaperture is extended. Hence, the bias due to model mismatch can result in undesired imaging artifacts.

FULL-APERTURE METHODS

In contrast to the subaperture methods that presume nearly constant reflectivity versus azimuth angle across a small subaperture, the class of full-aperture methods models scattering as a function of both space and azimuth angle across the full aperture. By explicitly adopting azimuth angle as an independent variable, the dimensionality of the image object, $\Psi(r, \phi)$ grows, which therefore invites some form of regularization to recover the image from the sampled data. Here we survey three such approaches: parametric modeling, regularized linear inversion, and Bayesian estimation.

PARAMETRIC MODELING

Parametric modeling approaches explicitly posit a parametric model for the scattering behavior and compute a nonconvex least-squares fit. These approaches are computationally expensive, especially considering the need to estimate a model order. Representative examples of this approach include sinc behavior in aspect [21]–[23], and Gaussian aspect dependence [24]. A larger family of canonical scattering objects has likewise been employed [25].

As an example of the parametric model fitting approaches, Figure 5 shows a 3-D reconstruction comprising even bounce (red) and odd bounce (blue) reflectors with a sinc response in azimuth, as predicted by physical optics approximation to high-frequency scattering [23], [25]. The reconstruction is computed via nonlinear least-squares estimation from the Gotcha X-band airborne measurements [2] using eight circular apertures and copolarized data measurements. The extent of a sinc response in azimuth is inversely related to the length of the reflector given in the visualization. In (a), a model of the Ford Taurus wagon vehicle is superimposed on the estimated reflectors, and the 3-D backprojection image is displayed in (b).

REGULARIZED INVERSION

The regularized least-squares approach in (7) has been explicitly extended from $\Psi(r)$ to the anisotropic model, $\Psi(r, \phi)$. For example, in [26], a large dictionary of angle-dependent returns in the matrix A is managed by an iterative selection of a subset of columns. In [27], an angle-indexed image, $\widehat{\Psi}(x, y, \phi)$ is explicitly recovered using two regularization terms. The first is a total variation norm on the aspect dependence of pixel magnitudes, to promote correlation in scattering behavior versus viewing angle. The second is a q -norm on the scattering strength at a given spatial location, to promote sparse reflectors

$$\min_{\Psi(x,y,\phi)} \|A\Psi - y\|_2^2 + \lambda_1 \sum_{x,y} \sum_i \left| |\Psi(x, y, \phi_{i+1})| - |\Psi(x, y, \phi_i)| \right|^q + \lambda_2 \sum_{x,y} \left\{ \sum_i |\Psi(x, y, \phi_i)|^2 \right\}^q. \quad (8)$$

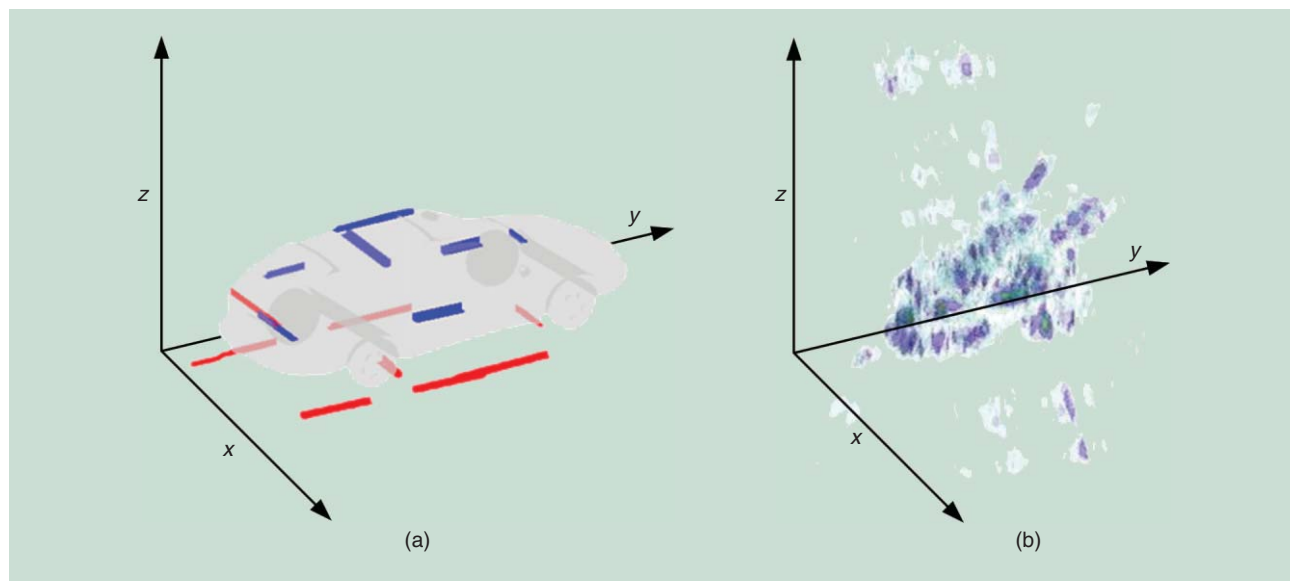


[FIG5] (a) A 3-D parametric modeling of wide-angle scattering data [2] as a sum of dihedrals (red) and flat plates (blue). Lengths of estimated reflectors are inferred from the anisotropy of the azimuthal responses. A facet model of the Ford Taurus wagon is superimposed on the estimated reflectors for visual comparison. (b) The SAR image from same measurements processed by 3-D backprojection.

BAYESIAN INVERSION

Here, we introduce an alternative wide-angle imaging technique that extends the regularized least-squares philosophy to a Bayesian estimator. The approach makes the modeling assumptions explicit, reports posterior confidence in inferred scattering behavior, and can provide automated tuning of algorithm parameters.

For wide-angle collections, the generation of azimuth-indexed SAR imagery has a natural interpretation as a state-space estimation problem within a dynamical system. In this context, a state vector $\Psi^{(t)} \in \mathbb{C}^N$ encodes the reflectivity at N spatial points of interest within the scene and when viewed from a particular azimuth angle ϕ_t , measured at time t . The state vector may be considered as a spatial image, and the collection $\{\Psi^{(1)}, \Psi^{(2)}, \dots, \Psi^{(T)}\}$ comprises a time-series of images capturing the azimuth-dependent scattering behavior that we wish to recover from radar measurements,

$$\mathbf{y}^{(t)} = \mathbf{F}^{(t)} \Psi^{(t)} + \boldsymbol{\epsilon}^{(t)}. \quad (9)$$

Here, $\mathbf{y}^{(t)} \in \mathbb{C}^M$, $t = 1, \dots, T$, denotes the k -space measurements obtained at time t , and $\mathbf{F}^{(t)}$ is the Fourier operator accounting for the radar bandwidth, sampling, and platform position at time t . It is assumed that the measurements are corrupted by additive noise, assumed to be zero-mean complex circular Gaussian, to be independent across time and space, and to have variance σ_ϵ^2 . This is denoted $\boldsymbol{\epsilon}^{(t)} \sim \mathcal{CN}(0, \sigma_\epsilon^2 \mathbf{I})$.

When the state dynamics governing the evolution of $\Psi^{(t)}$ are known, we may employ classical methods to generate filtered estimates of $\Psi^{(t)}$, based on linear measurements $\{\mathbf{y}^{(1)}, \dots, \mathbf{y}^{(t)}\}$, or smoothed estimates, based on measurements $\{\mathbf{y}^{(1)}, \dots, \mathbf{y}^{(T)}\}$. A thorough review of classical state-space estimation may be found, e.g., in [28] and references therein. However, for the

anisotropic SAR problem, recent results in large-scale Bayesian inference of sparse time series are more appropriate. This field is generally referred to as dynamic compressive sensing (DCS) within the compressive sensing literature [29]. In wide-angle scenarios, sparsity is not only important because radar backscatter is often spatially sparse, but also because anisotropic behavior implies sparsity in the azimuth dimension as well.

The DCS problem considers the estimation of a sparse time series $\{\Psi^{(t)}\}$ from linear measurements $\{\mathbf{y}^{(t)}\}$ and exploits two forms of structure. First, the sparsity pattern of the signal is expected to change slowly over time (azimuth), and second, the nonzero coefficients (reflector amplitudes) vary slowly with time, as prescribed by an a priori model [29]. Incorporating the dynamics of amplitude and sparsity evolution enables DCS algorithms to outperform “snapshot” approaches based on solving a sequence of standard compressive sensing problems over a set of subapertures. Further, DCS problems may be considered in a completely Bayesian setting where both the time-varying amplitudes and the supports are estimated with posterior uncertainty. As such, the Bayesian DCS approach to wide-angle imaging is distinct in two respects from SAR video formed by independent processing of overlapping subapertures. First, the azimuth-indexed state estimates utilize all available data (in the case of smoothing), as opposed to a limited integration window with size selected by the user. In the Bayesian setting, an a priori model for reflector persistence implicitly controls the effective azimuth extent attributed to a scattering location. Second, the Bayesian DCS approach produces a measure of confidence to accompany the sequence of azimuth-indexed images. Specifically, the approach generates an estimate of the posterior marginal distribution of reflectivity as a function of scattering location and azimuth look angle. Knowledge of this uncertainty

is useful for subsequent exploitation tasks, such as automated target recognition, that utilize the wide-angle measurements.

APPROXIMATE BELIEF PROPAGATION

In the context of wide-angle SAR imaging, we review in this section a Bayesian approach to DCS based on approximate message passing [29]. An auxiliary time series $\{s^{(1)}, s^{(2)}, \dots, s^{(T)}\}$ is introduced, where $s^{(t)} \in \{0, 1\}^N$ indicates the nonzero support at time t . That is, if the n th pixel of $\Psi^{(t)}$, $\Psi_n^{(t)}$, has nonzero amplitude, then $s_n^{(t)} = 1$, otherwise $s_n^{(t)} = 0$. A second time-varying random process $a^{(t)} \in \mathbb{C}^N$, $t = 1, \dots, T$, is introduced representing the amplitudes of the nonzero elements of $\Psi^{(t)}$. Combined, the sparsity $s^{(t)}$ and amplitudes $a^{(t)}$ fully characterize the reflectivity of the n th pixel at time- t as

$$\Psi_n^{(t)} = s_n^{(t)} a_n^{(t)}. \quad (10)$$

The support and amplitudes are both hidden vector-valued random processes that we wish to estimate from radar measurements. To impose the notions of sparsity and smoothness described above onto the model, the $\{s^{(t)}\}$, and $\{a^{(t)}\}$; processes are imbued with certain a priori dynamical structures.

The support structure is modeled as a first-order Markov chain where the value of $s_n^{(t)}$ only depends on its temporal ancestor $s_n^{(t-1)}$. Independent Markov chains are used for $n = 1, \dots, N$, although spatial correlation across n is possible. The Markov chains are fully defined by the initial probability that the n th pixel is nonzero $\lambda_1 \triangleq \text{prob}(s_n^{(1)} = 1)$ and the transition probabilities $\lambda_{1,0} \triangleq \text{prob}(s_n^{(t)} = 1 | s_n^{(t-1)} = 0)$ and $\lambda_{0,1} \triangleq \text{prob}(s_n^{(t)} = 0 | s_n^{(t-1)} = 1)$. The λ -probabilities fully control the sparsity assumptions in the model. For example, small values of $\lambda_{1,0}$, and large values of $\lambda_{0,1}$, favor short sequences of nonzero support. This would be appropriate to model specular reflectors with limited persistence [3], [9].

Smooth structure in the amplitude parameters is captured using a first-order Gauss–Markov model

$$a_n^{(t)} = \alpha a_n^{(t-1)} + \zeta_n^{(t)}, \quad (11)$$

where the scaling factor α and zero-mean Gaussian process noise $\zeta_n^{(t)} \sim \mathcal{CN}(0, \sigma_{\text{proc}}^2)$ control the temporal dynamics, with the initial state assumed to be Gaussian, $a_n^{(1)} \sim \mathcal{CN}(0, \sigma_{\text{init}}^2)$. Large values of $|\alpha|$, and small process variance σ_{proc}^2 , favor a slowly varying radar cross section (RCS) across azimuth look angle. Conversely, small $|\alpha|$ and large σ_{proc}^2 imply rapidly varying RCS across azimuth with little correlation between adjacent look angles. As with the support variables, independent scalar processes are assumed for $n = 1, \dots, N$.

The models for azimuth-dependent scattering dynamics combine with the radar measurement model (9) to form a complete dynamical model describing the posterior distribution of the state space variables

$$p(\{s^{(t)}\}, \{a^{(t)}\}, \{\Psi^{(t)}\} | \{y^{(t)}\}) \propto \prod_{t=1}^T p(y^{(t)} | \Psi^{(t)}) p(\Psi^{(t)} | s^{(t)}, a^{(t)}) p(s^{(t)} | s^{(t-1)}) p(a^{(t)} | a^{(t-1)}), \quad (12)$$

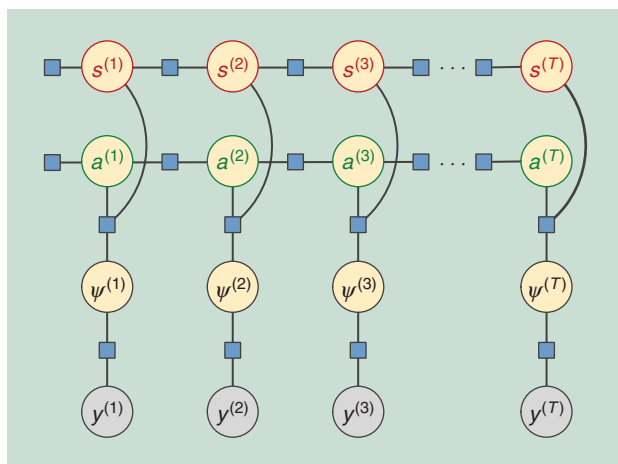


[FIG6] The factor graph model representing the Bayesian state-space interpretation of wide-angle SAR imaging includes two coupled Markov chains: a hidden Markov model governing the sparsity dynamics $\{s^{(t)}\}$, and a linear dynamical system governing amplitude dynamics $\{a^{(t)}\}$; both are coupled through the radar measurements $\{y^{(t)}\}$.

where $p(s^{(1)} | s^{(0)}) \triangleq p(s^{(1)})$ and $p(a^{(1)} | a^{(0)}) \triangleq p(a^{(1)})$ correspond to the initial prior distributions. The model (12) is illustrated graphically by the factor graph in Figure 6. In the graph, square nodes represent factors in the posterior distribution, and circles represent random variables, with shaded circles corresponding to observed random variables. From (9), the measurement factors are $p(y^{(t)} | \Psi^{(t)}) = \mathcal{CN}(y^{(t)}; F^{(t)} \Psi^{(t)}, \sigma_e^2 I)$, and from (10), $p(\Psi^{(t)} | s^{(t)}, a^{(t)}) = \delta(\Psi^{(t)} - s^{(t)} a^{(t)})$, where δ denotes the Dirac delta function applied element-wise.

Apparent in the factor graph is that the model describes a coupled dynamical system where the support variables form a hidden Markov model that is coupled to the linear dynamical system describing the amplitude process through the jointly dependent linear measurements $\{y^{(t)}\}$, governed by the radar system. Inference in coupled systems is generally difficult, and tackled, for example, by structured variational approximations. Alternatively, recent DCS work [29] leverages approximate message passing algorithms [30] and loopy belief propagation to efficiently generate approximate marginal state estimates for the exact system model, (12).

EXAMPLE

Figure 7 illustrates the results of applying the approximate message passing approach to measured circular SAR data of a Ford Taurus wagon, similar in orientation to the model shown in Figure 5. The measured SAR data comes from the X-band Gotcha data set [2] with 640 MHz of bandwidth. In (a), a backprojection image is illustrated utilizing the entire 360° in the circular collection. The vehicle is oriented such that its front corresponds to approximately 45° azimuth, and the passenger broadside is at approximately 315°. This wide-angle image displays scattering from all aspect angles, but does not reveal the anisotropic behavior of the constituent scatterers on the vehicle. In contrast, the two plots in (b) illustrate the azimuth-dependent posterior mean

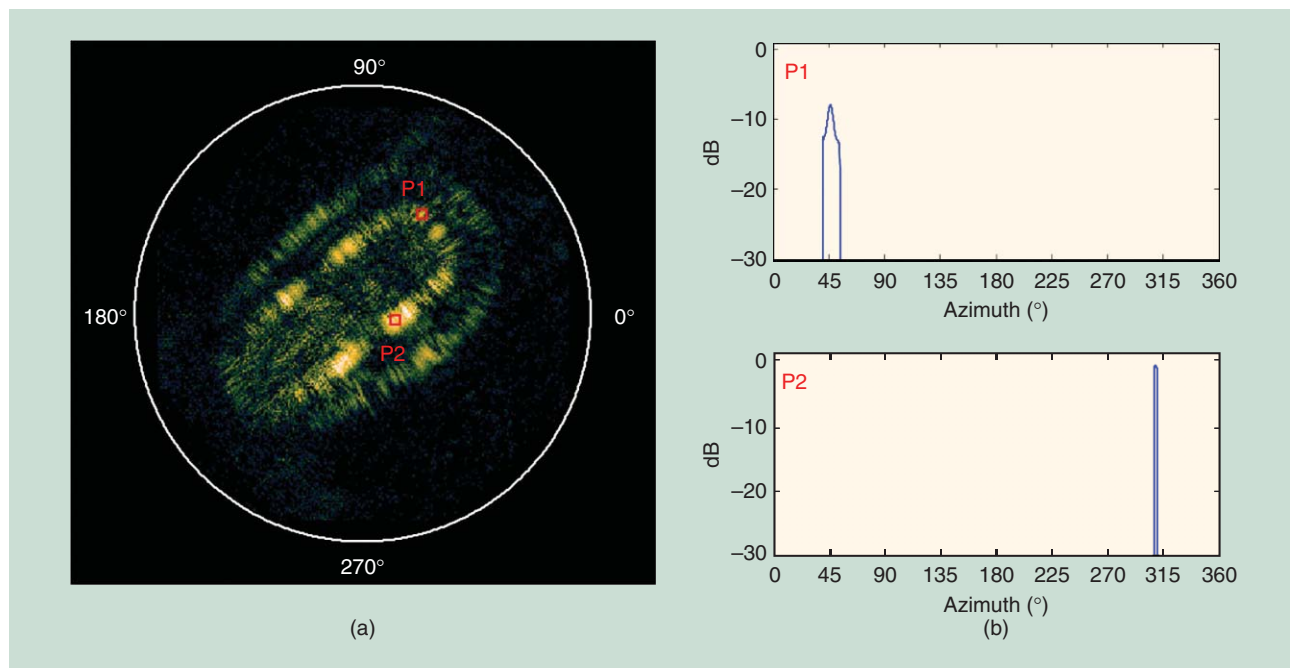


[FIG7] Bayesian state-space processing for wide-angle measured X-band data. (a) A traditional 360° backprojection image of a Ford Taurus wagon. (b) Dynamic compressive sensing reveals dominant scattering on the front of the vehicle (P1) at an azimuth angle of ~45° and from the passenger broadside of the vehicle (P2) at ~315°.

state estimates for two particular points on the vehicle. The state-space includes a uniform grid of spatial points covering the vehicle, although the figure only presents results for two locations: the first, P1, is from the front of the vehicle, and the second, P2, is from the passenger broadside.

The state-space estimates exhibit sparsity and low noise as expected. Further, the posterior state estimates correctly identify the dominant response directions: approximately 45° for the front of the vehicle (P1), and approximately 315° for the passenger broadside (P2). The P1 response also appears with lower amplitude, and broader, than P2. This is consistent with dihedral scattering approximations to vehicle sides [23], where the relatively longer broadside induces a larger RCS, but with shorter persistence, relative to the front of the vehicle.

DISCUSSION

WHY SAR VIDEO?

For wide-angle radar imaging, SAR video can provide maximum TCR and is a revealing format for analysis of scattering signatures.

First, for a signal detection application, SAR video can provide maximum TCR. Application of the radar range equation yields the TCR

$$\text{TCR} = \frac{\sigma T_{\text{ot}}}{\sigma_0 \delta T_{\text{oc}}}, \quad (13)$$

where σ is the target's radar cross section, σ_0 is the probabilistic clutter return power per unit area, and δ is the pixel area, given by the product of range and cross-range resolutions. The

variables T_{ot} and T_{oc} are the time (equivalently, aperture extent) on target and clutter, respectively. All other radar range equation terms, such as radiated power, antenna area, and energy spreading, cancel in the ratio. The TCR equation predicts the behavior shown in Figure 8 for a reflector with limited angular persistence. In the denominator of (13), an increase in the clutter integration time is offset by finer cross-range resolution; in the numerator, received power at a pixel increases with increasing integration aperture, until the reflector ceases to persist. For example, at 10 GHz a dihedral reflector 30 cm in length with base parallel to the xy plane has azimuth angular response that persists only 5°, as measured by the 6-dB beam width [25]. Thus, in SAR video, TCR is maximized for any subaperture integration angle greater than T_{ot} . Pixel amplitude histograms from measured Ku-band data illustrate the effect experimentally in Figure 8. Histograms are computed from clutter pixels and target pixels for coarse-resolution (30 cm) and fine-resolution (3.75 cm) images. The two histograms correspond to the two points highlighted on the TCR curve. The 8×8 reduction in pixel area results in $10 \log_{10} 64 = 18$ dB shift in the clutter histogram, as predicted by (13).

Second, for fine-scale analysis of target signatures, SAR video provides a revealing format for automated or human-aided interpretation of scattering physics, owing to several effects. For high-frequency radar, energy in a target signature is dominated by specular returns, which are highly directional. These dominant returns can obscure other scattering behaviors; a sequence of subaperture images serves to combat this dynamic range issue. Additionally, the number of strong

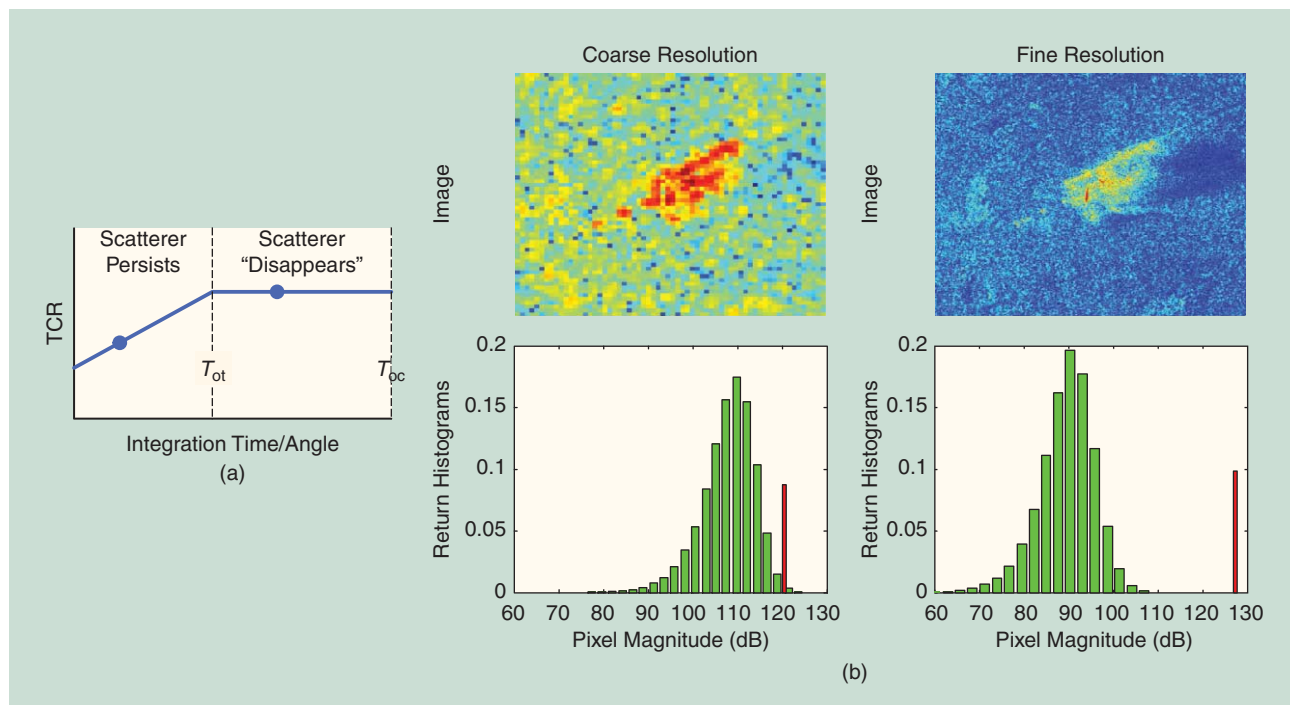


[FIG8] (a) Any subaperture integration angle exceeding the persistence of a reflector serves to maximize TCR. (b) Coarse- and fine-resolution images and corresponding return histograms display clutter (green) and target (red) distributions.

reflectors present in a single subaperture is less than across the full aperture, resulting in a more parsimonious, or more sparse, signature that is more amenable to nonlinear sharpening methods which deconvolve sidelobes. Moreover, the aperture index provides a simple data structure for using the anisotropic behavior of the scattering to improve object classification [7]. Thus, several physical behaviors provide rationale for the use of SAR video format in the signature analysis context.

MERITS

Of the imaging procedures outlined in Table 1, the recursive backprojection is simple, low complexity, linear, and robust to modeling assumptions. Further, pulse-by-pulse autofocus can be embedded using a closed-form procedure. The recursive backprojection procedure is well suited to wide-area coverage, and the analysis illustrated in Figure 8 informs proper choice of the subaperture extent. Several conclusions can be drawn for the subaperture nonlinear sharpening techniques. The model fitting and spectrum estimation techniques are computationally demanding, and therefore are only applicable for the processing of small regions of interest. In addition, the plane-wave assumption can limit the applicability of the spectrum estimation techniques. However, the nonlinear sharpening technique has been empirically demonstrated to provide a modest improvement in object classification due to resolution enhancement (e.g., see [10] and references therein).

The full-aperture procedures operate on the entire wide-aperture data record; consequently, they are inherently more computationally costly than the subaperture techniques and

offer less opportunity for efficient parallelization. The applicability of the full-aperture techniques is therefore limited to the processing of small regions of interest. The Bayesian approach avoids difficulties in both order selection for parametric techniques and Lagrange multiplier choice for regularized inversion.

CONCLUSIONS

Radio frequency scattering varies not only with spatial location, but also with viewing angle, polarization, and frequency. Technological advances have allowed for a more comprehensive measurement of this behavior. Interpretation of the measurements can be formulated as an inverse task to provide a rich characterization of scattering behavior across dimensions beyond simply two or three spatial coordinates, as depicted in traditional imagery. The signal processing tools surveyed in this article provide aspect-dependent characterization of scene reflectivity.

ACKNOWLEDGMENTS

This work was supported in part by the Defense Advanced Research Projects Agency under grant N66001-10-1-4090, by the Army Research Office under grant W911NF-11-1-0391, and by the Air Force Research Laboratory under award FA8650-07-D-1220.

AUTHORS

Joshua N. Ash (ash.48@osu.edu) received B.S. degrees in physics and electrical engineering in 1998 and the M.S.E.E. degree in 2003 from Washington University, St. Louis, Missouri. He received the Ph.D. degree in electrical and computer engineering from The Ohio State University, Columbus, in 2007. From

2000 to 2002, he was a technical staff member at Celox Networks in St. Louis, Missouri. He is currently a research scientist with the Institute of Sensing Systems at The Ohio State University. His research interests include statistical signal processing and machine learning, with applications in sensor networks, synthetic aperture radar, and hyperspectral imaging.

Emre Ertin (ertin.1@osu.edu) is a research assistant professor with the Department of Electrical and Computer Engineering at The Ohio State University. He received the B.S. degree in electrical engineering and physics from Bogazici University, Turkey, in 1992, the M.S. degree in telecommunication and signal processing from Imperial College, United Kingdom, in 1993, and the Ph.D. degree in electrical engineering from The Ohio State University in 1999. From 1999 to 2002 he was with the Core Technology Group at Battelle Memorial Institute. His current research interests are statistical signal processing, wireless sensor networks, radar signal processing, and mobile health.

Lee C. Potter (potter.36@osu.edu) received the B.E. degree from Vanderbilt University, Nashville, Tennessee, and the M.S. and Ph.D. degrees from the University of Illinois at Urbana-Champaign, all in electrical engineering. Since 1991, he has been with the Department of Electrical and Computer Engineering, The Ohio State University, Columbus, where he is also an investigator at the Davis Heart and Lung Research Institute. His research interests include statistical signal processing, inverse problems, detection, and estimation, with applications in radar and medical imaging. He received the Ohio State University College of Engineering MacQuigg Award for Outstanding Teaching.

Edmund G. Zelnio (edmund.zelnio@us.af.mil) graduated from Bradley University, Peoria, Illinois, in 1975 and has pursued doctoral studies at The Ohio State University in electromagnetics and at Wright State University in signal processing. During his 37-year career with the Air Force Research Laboratory (AFRL), Wright Patterson Air Force Base, Ohio, he has spent 35 years working in the area of automated exploitation of imaging sensors primarily addressing synthetic aperture radar. He is a former division chief and technical advisor of the Automatic Target Recognition Division of the Sensors Directorate in AFRL and serves in an advisory capacity to the Department of Defense and the intelligence community. He is currently the director of the Automatic Target Recognition Center in AFRL. He is the recipient of the 53rd Department of Defense Distinguished Civilian Service Award and is a fellow of the AFRL.

REFERENCES

[1] W. G. Carrara, R. S. Goodman, and R. M. Majewski, *Spotlight Synthetic Aperture Radar Signal Processing Algorithms*. Norwood, MA: Artech House, 1995.

[2] C. H. Casteel, Jr., L. A. Gorham, M. J. Minardi, S. M. Scarborough, K. D. Naidu, and U. K. Majumder, "A challenge problem for 2D/3D imaging of targets from a volumetric data set in an urban environment," in *Proc. SPIE, Algorithms for Synthetic Aperture Radar Imagery XIV*, 2007, vol. 6568, pp. 65680D-1–65680D-7.

[3] H. Oriot and H. Cantalloube, "Circular SAR imagery for urban remote sensing," in *Proc. 7th Int. European Conf. Synthetic Aperture Radar (EUSAR 2008)*, June, pp. 1–4.

[4] P. Frolind, A. Gustavsson, M. Lundberg, and L. M. H. Ulander, "Circular-aperture VHF-band synthetic aperture radar for detection of vehicles in forest concealment," *IEEE Trans. Geosci. Remote Sensing*, vol. 50, no. 4, pp. 1329–1339, Apr. 2012.

[5] O. Ponce, P. Prats-Iraola, M. Pinheiro, M. Rodriguez-Cassola, R. Scheiber, A. Reigber, and A. Moreira, "Fully polarimetric high-resolution 3-D imaging with circular SAR at L-band," *IEEE Trans. Geosci. Remote Sensing*, vol. 52, no. 6, pp. 3074–3090, June 2014.

[6] K. Naidu and L. Lin, "Data dome: Full k-space sampling data for high frequency radar research," in *Proc. SPIE, Algorithms for Synthetic Aperture Radar Imagery XI*, Orlando, FL, 2004, vol. 5427, pp. 200–207.

[7] K. E. Dungan and L. C. Potter, "Classifying vehicles in wide-angle radar using pyramid match hashing," *IEEE J. Select. Topics Signal Processing*, vol. 5, no. 3, pp. 577–591, 2011.

[8] D. C. Munson, Jr., J. D. O'Brien, and W. K. Jenkins, "A tomographic formulation of spotlight-mode synthetic aperture radar," *Proc. IEEE*, vol. 71, no. 8, pp. 917–925, 1983.

[9] Y. Lin, W. Hong, W. Tan, Y. Wang, and Y. Wu, "Interferometric circular SAR method for three-dimensional imaging," *IEEE Geosci. Remote Sensing Lett.*, vol. 8, no. 6, pp. 1026–1030, Nov. 2011.

[10] L. Potter, E. Ertin, J. Parker, and M. Cetin, "Sparsity and compressed sensing in radar imaging," *Proc. IEEE*, vol. 98, no. 6, pp. 1006–1020, 2010.

[11] R. Moses and J. Ash, "An autoregressive formulation for SAR backprojection imaging," *IEEE Trans. Aerosp. Electron. Syst.*, vol. 47, no. 4, pp. 2860–2873, 2011.

[12] S. R. DeGraaf, "SAR imaging via modern 2-D spectral estimation methods," *IEEE Trans. Image Processing*, vol. 7, no. 5, pp. 729–761, 1998.

[13] P. Stoica, H. Li, and J. Li, "A new derivation of the APES filter," *IEEE Signal Processing Lett.*, vol. 6, no. 8, pp. 205–206, Aug. 1999.

[14] G. R. Benitz, "High-definition vector imaging," *Lincoln Lab. J.*, vol. 10, no. 2, pp. 147–170, 1997.

[15] Y. Wu and D. C. Munson, Jr., "Wide angle ISAR passive imaging using smoothed pseudo Wigner-Ville distribution," in *Proc. 2001 IEEE Radar Conf.*, pp. 363–368.

[16] E. Candes and M. Wakin, "An introduction to compressive sampling," *IEEE Signal Processing Mag.*, vol. 25, no. 2, pp. 21–30, Mar. 2008.

[17] M. Çetin and W. C. Karl, "Feature-enhanced synthetic aperture radar image formation based on nonquadratic regularization," *IEEE Trans. Image Processing*, vol. 10, no. 4, pp. 623–631, Apr. 2001.

[18] R. Chartrand and V. Staneva, "Restricted isometry properties and nonconvex compressive sensing," *Inverse Problems*, vol. 24, no. 3, pp. 1–14, 2008.

[19] S. D. Cabrera and T. W. Parks, "Extrapolation and spectral estimation with iterative weighted norm modification," *IEEE Trans. Acoust., Speech, Signal Processing*, vol. 39, no. 4, pp. 842–851, 1991.

[20] A. E. Brito, S. D. Cabrera, and C. Villalobos, "Optimal sparse representation algorithms for harmonic retrieval," in *Proc. 35th Asilomar Conf. Signals, Systems and Computers*, 2001, vol. 2, pp. 1407–1411.

[21] Z.-S. Liu and J. Li, "Feature extraction of SAR targets consisting of trihedral and dihedral corner reflectors," *IEEE Radar, Sonar Navig.*, vol. 145, no. 3, pp. 161–172, 1998.

[22] M. J. Gerry, L. C. Potter, I. J. Gupta, and A. van der Merwe, "A parametric model for synthetic aperture radar measurements," *IEEE Trans. Antennas Propag.*, vol. 47, no. 7, pp. 1179–1188, 1999.

[23] E. Ertin, C. D. Austin, S. Sharma, R. L. Moses, and L. C. Potter, "GOTCHA experience report: Three-dimensional SAR imaging with complete circular apertures," in *Proc. SPIE, Algorithms for Synthetic Aperture Radar Imagery XIV*, 2007, vol. 6568, pp. 656802-1–656802-12.

[24] L. C. Trintinalia, R. Bhalla, and H. Ling, "Scattering center parameterization of wide-angle backscattered data using adaptive Gaussian representation," *IEEE Trans. Antennas Propag.*, vol. 45, no. 11, pp. 1664–1668, 1997.

[25] J. Jackson, B. Rigling, and R. Moses, "Canonical scattering feature models for 3D and bistatic SAR," *IEEE Trans. Aerosp. Electron. Syst.*, vol. 46, no. 2, pp. 525–541, 2010.

[26] K. R. Varshney, M. Çetin, J. W. Fisher III, and A. S. Willsky, "Sparse signal representation in structured dictionaries with application to synthetic aperture radar," *IEEE Trans. Signal Processing*, vol. 56, no. 8, pp. 3548–3561, 2008.

[27] I. Stojanovic, M. Çetin, and W. C. Karl, "Joint space aspect reconstruction of wide-angle SAR exploiting sparsity," in *Proc. SPIE, Algorithms for Synthetic Aperture Radar Imagery XV*, 2008, vol. 6970, pp. 697005-1–697005-12.

[28] M. S. Arulampalam, S. Maskell, N. Gordon, and T. Clapp, "A tutorial on particle filters for online nonlinear/nonGaussian Bayesian tracking," *IEEE Trans. Signal Processing*, vol. 50, no. 2, pp. 174–188, 2002.

[29] J. Ziniel and P. Schniter, "Dynamic compressive sensing of time-varying signals via approximate message passing," *IEEE Trans. Signal Processing*, vol. 61, no. 21, pp. 5270–5284, 2013.

[30] D. Donoho, A. Maleki, and A. Montanari, "Message passing algorithms for compressed sensing," *Proc. Natl. Acad. Sci.*, vol. 106, no. 45, pp. 18914–18919, 2009.

[Müjdat Çetin, Ivana Stojanović, N. Özben Önhon, Kush R. Varshney,
Sadeqh Samadi, W. Clem Karl, and Alan S. Willsky]

Sparsity-Driven Synthetic Aperture Radar Imaging

[Reconstruction, autofocusing, moving targets,
and compressed sensing]

This article presents a survey of recent research on sparsity-driven synthetic aperture radar (SAR) imaging. In particular, it reviews 1) the analysis and synthesis-based sparse signal representation formulations for SAR image formation

together with the associated imaging results, 2) sparsity-based methods for wide-angle SAR imaging and anisotropy characterization, 3) sparsity-based methods for joint imaging and autofocusing from data with phase errors, 4) techniques for exploiting sparsity for SAR imaging of scenes containing moving objects, and 5) recent work on compressed sensing (CS)-based analysis and design of SAR sensing missions.

INTRODUCTION

SAR imaging and sparse signal representation are well-established distinct lines of research. That said, sparsity has been of interest for SAR imaging implicitly over many years, and more explicitly within the last 15 years or so. In fact, a considerable fraction of recent developments for SAR imagery have been driven by moving from a purely Fourier transform type processing paradigm to one that couples physics-motivated sensing models with some form of sparsity-based priors. Ideas based on sparse signal representation, proposed by a number of research groups, have recently led to advanced image formation

methods offering a number of benefits for SAR, including increased resolvability of point scatterers, reduced speckle, easier-to-segment regions, and robustness to limitations in data quality and quantity.

Furthermore, the sparse signal representation perspective has provided inspiration for new ways

to think about and produce solutions for several important problems for SAR, which are also motivated by a number of emerging SAR data collection scenarios.

These problems include autofocusing, wide-angle imaging, interferometry, SAR tomography (TomoSAR), through-the-wall radar imaging, multiple-input, multiple-output (MIMO) radar imaging, passive radar imaging, and moving target imaging, among others. Finally, recent results on CS, built upon sparse signal representation, have generated considerable interest in radar waveform design as

well as analysis and design of radar sensing scenarios under data collection constraints. Pursuing this overall new line of inquiry on SAR imaging leads to the discovery of a variety of technical problems that fall outside the standard domain of sparse signal representation, but that involve issues of critical concern for SAR imaging. The result is a rich, new area of research that has already shown its promise but that also motivates interesting lines of inquiry for the future. In this article, we present an overview of the recent line of research pursued by several research groups on sparsity-driven SAR imaging. Our article shares some aspects of two recent survey papers [1], [2]. The first of these papers [1] provides a broad introduction to the use of CS in radar,



PHOTO COURTESY OF NASA

Digital Object Identifier 10.1109/MSP.2014.2312834

Date of publication: 13 June 2014

and considers three applications: pulse compression, radar imaging, and air space surveillance with antenna arrays. The second paper [2] provides an overview and examples of how central themes in sparsity and CS have been present in the array processing literature in general, and in radar imaging in particular, over many years. Our article complements these papers in several ways and presents a focused and up-to-date picture of sparsity-driven radar imaging. In particular, we provide a comprehensive coverage of recent use of sparsity in a variety of radar imaging scenarios, with a signal processing focus and perspective. Applications and connections covered include wide-angle imaging, autofocusing, moving target imaging, as well as CS.

ANALYSIS AND SYNTHESIS-BASED SPARSE RECONSTRUCTION FOR SAR

SAR imaging can be viewed as a linear inverse problem in which an unknown spatial reflectivity field is reconstructed from noisy measurements of waves backscattered from a scene. After certain steps of preprocessing of the radar returns, the resulting data can be related to the underlying reflectivity field through a discretized model of the following form, which essentially involves a spatial Fourier transform:

$$r(f_k, \theta_l) = \sum_{m=1}^M s(x_m, y_m) e^{-j \frac{4\pi f_k}{c} (x_m \cos \theta_l + y_m \sin \theta_l)} + n(f_k, \theta_l), \quad (1)$$

where c denotes the speed of light. We can stack the entire set of noisy phase history measurements $r(f_k, \theta_l)$, and the noise $n(f_k, \theta_l)$ at all available frequencies f_k , $k = 1, \dots, K$, and viewing angles θ_l , $l = 1, \dots, L$, as well as the reflectivity function or scattering response $s(x_m, y_m)$ at all spatial locations (x_m, y_m) , $m = 1, \dots, M$ (which include all the points containing the non-negligible scatterers), into vectors to obtain the following observation model:

$$\mathbf{r} = \mathbf{H}\mathbf{s} + \mathbf{n}, \quad (2)$$

where \mathbf{s} denotes the underlying, complex-valued reflectivity image and \mathbf{H} is the mathematical model of the observation process described by (1). While this model and the ideas described in this article can be used in the context of a variety of SAR operating modes, for basic SAR imaging we will mostly assume spotlight-mode operation for concreteness. Given limitations in the bandwidth of the measured data and in the diversity of look angles, as well as the inherently noisy nature of the measurement process, the inverse problem in (2) is ill posed. To generate a solution, implicit or explicit assumptions need to be made. Principled ways to incorporate such assumptions, in the form of constraints or prior information, include regularization and Bayesian estimation methods. Within this context, the information or constraint that the underlying reflectivity field admits a sparse representation has proved to be a very useful asset for SAR imaging. The simplest form of sparsity (or compressibility) to exploit would be a scene consisting of a small number of dominant scatterers (e.g.,

man-made metallic objects). Exploitation of this type of sparsity has led to superresolution imaging in SAR (see Figure 1) [56]. More generally, the scene could be sparse in a different domain, as we discuss in more detail below. The remainder of this section provides an overview of analysis and synthesis-based sparse signal representation methods applied to SAR imaging.

In an analysis model, sparsity is imposed on some transformation or features of the signal of interest, and, in this case, is often called *cosparsity*. Such an approach for SAR imaging was proposed in [3], where an estimate of \mathbf{s} is obtained by minimizing the following cost functional:

$$J(\mathbf{s}) = \|\mathbf{r} - \mathbf{H}\mathbf{s}\|_2^2 + \lambda_1 \|\mathbf{s}\|_p^p + \lambda_2 \|\nabla|\mathbf{s}|\|_p^p. \quad (3)$$

Here $\|\cdot\|_p$ denotes the ℓ_p -norm, ∇ is a discrete approximation to the two-dimensional (2-D) derivative operator (gradient), $|\mathbf{s}|$ denotes the vector of magnitudes of the complex-valued vector \mathbf{s} , and λ_1 and λ_2 are scalar parameters. For $p < 2$ we have promotion of sparsity, which gets weaker as we approach $p = 2$. The values used for p in sparsity-driven SAR imaging are around 1, so the second and third terms enforce sparsity. The relative contribution of these two terms are determined through the choice of the hyperparameters λ_1 and λ_2 . The second term indicates a preference for spatially sparse reflectivity fields. The third term enforces sparsity on the gradient of the reflectivity magnitudes, indicating a preference for piecewise smooth reflectivity magnitude fields. Such piecewise smoothness constraints have a long history in real-valued image restoration and reconstruction, under various names including edge-preserving regularization and total variation restoration. Within the context of SAR imaging, such smoothness is expected within homogenous natural terrain types and within some man-made structures. Even in homogeneous regions, the phases of the reflectivities in spatially neighboring pixels however are generally uncorrelated, hence no such smoothness is expected in phase. As a consequence, we need to impose sparsity on $\nabla|\mathbf{s}|$, and not on $\nabla\mathbf{s}$, as the latter would lead to smoothing of the real and imaginary parts of the reflectivity field, which may not lead to the desired smoothing effect on the magnitudes.

Another perspective on sparsity-driven SAR imaging is that it can be used to preserve and enhance features that might be used in decision making based on SAR images, such as automatic target recognition. With this perspective, the image formation approach of (3) was called *feature-enhanced imaging* in [3], with a dominant second term leading to *point-enhanced imaging* and a dominant third term leading to *region-enhanced imaging*. Point-enhanced imaging provides improved resolvability in sparse scenes, an example of which is provided in Figure 1. Region-enhanced imaging imposes sparsity on spatial gradients and leads to images with reduced speckle and easier to segment regions. Such improvements have partially been quantified in terms of feature extraction accuracy and object classification performance [4], [5].

Having to use a penalty on the magnitudes makes the optimization problem in (3) more challenging than its counterparts in real-valued sparse signal recovery problems. Efficient algorithms

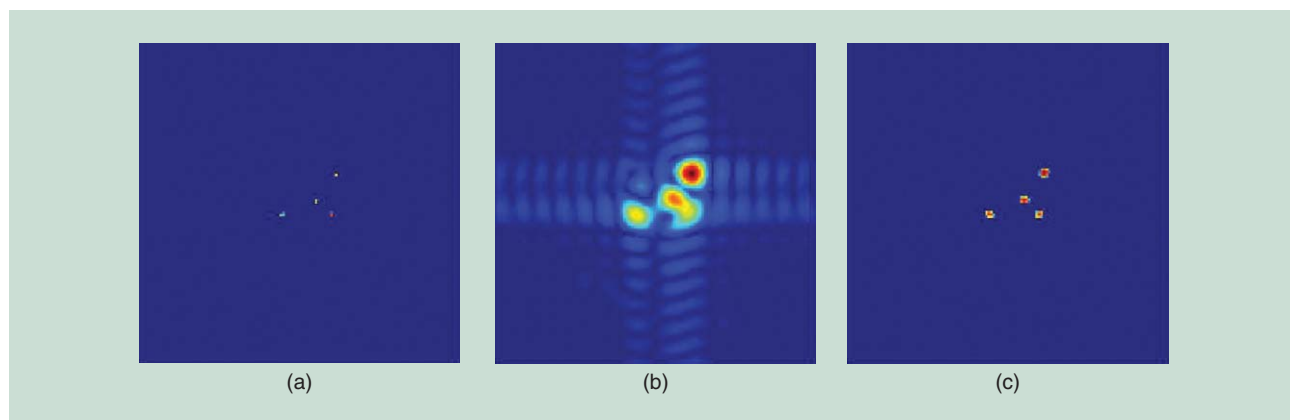


[FIG1] The reconstructions of the slicy target from the MSTAR data set [56]. (a) The reference image reconstructed from high-bandwidth data. (b) The conventional image reconstructed from limited-bandwidth data. (c) The sparsity-driven, point-enhanced image reconstructed from limited-bandwidth data.

matched to this problem structure have been developed [3]. These algorithms are based on half-quadratic regularization, and can be viewed as quasi-Newton methods with a specific Hessian update scheme. Another interpretation is that the overall nonquadratic problem is turned into a series of quadratic problems, each of which is efficiently solved in each iteration using conjugate gradients. The special case of point-enhanced imaging can be solved by a variety of algorithms developed for sparse signal representation. In [6], a fast and adaptive sequential basis selection strategy is employed for point-enhanced imaging. Rather than solving a basis pursuit type optimization problem for point-enhanced SAR imaging, an alternative is to use a greedy matching pursuit algorithm, as in [7] and [8]. While the development of computationally efficient algorithms matched to the problem structure has been and continues to be an important line of research, at the fundamental level, the cost of solving the optimization problems involved in sparsity-driven SAR imaging is significantly higher than conventional processing. Hence there is certainly a price to be paid for potential improvements obtained in image quality. We should also note that many cost functionals considered in sparsity-driven SAR imaging are nonconvex. Throughout the work surveyed in this article, local optimization algorithms aiming to find the local minima of such cost functionals are used.

Now let us turn to synthesis-based models for sparse representation. In a synthesis model, the formulation is based on representing the signal of interest in terms of a dictionary and imposing sparsity on the dictionary coefficients. Let us just focus on one appealing feature of a synthesis model in the context of SAR imaging. We note that (3) uses two different regularization terms, one imposing the spatial sparsity of the field, and the other its piecewise smoothness. (One could combine the two terms into a single terms using a “tall” operator carrying out both analysis operations.) These two terms are used together to handle cases in which one of these terms does not serve as a good enough constraint throughout the scene. However, (3) imposes these two potentially conflicting constraints jointly everywhere in the scene, leading to some degree of inconsistency with the stated objective. This issue may be handled in a more consistent manner

within a synthesis model. In particular, one can form an overcomplete dictionary consisting of atoms corresponding to the different types of features represented by the two constraints in (3). As the atoms can also exhibit spatial locality, one or the other type of feature can be “active” at a particular location in the scene, avoiding simultaneous use of potentially conflicting constraints. This could lead to a sparser representation for scenes exhibiting different types of features at different spatial locations. Based on these thoughts, a synthesis model for sparsity-driven SAR imaging has been proposed in [9]. As in (3), what admits sparse representation is the magnitude of the reflectivity field s . Hence we are interested in a representation of the form $|s| = D\alpha$, where D is an overcomplete dictionary with the coefficient vector α . Let us also write $s = \Phi |s|$, where Φ is a diagonal matrix, the i th diagonal element of which is $e^{j\gamma_i}$, with γ_i indicating the unknown phase of the i th scene element s_i . Based on this notation, we can rewrite the observation model as

$$\mathbf{r} = \mathbf{H}\mathbf{s} + \mathbf{n} = \mathbf{H}\Phi\mathbf{D}\boldsymbol{\alpha} + \mathbf{n}. \quad (4)$$

Letting ϕ be a vector consisting of the diagonal elements of Φ , we can write the following cost functional to be minimized for SAR imaging:

$$J(\boldsymbol{\alpha}, \phi) = \|\mathbf{r} - \mathbf{H}\Phi\mathbf{D}\boldsymbol{\alpha}\|_2^2 + \lambda \|\boldsymbol{\alpha}\|_p^p \quad \text{s.t.} \quad |\phi_i| = 1 \quad \forall i. \quad (5)$$

We note that the variables to be optimized involve the phase of the field, and the representation coefficients of its magnitude. This problem can be solved using the coordinate descent algorithm developed in [9]. Figure 2 contains a sample reconstruction using a wavelet transform-based dictionary based on TerraSAR-X data [57]. For examples of other dictionaries used in this framework, including ones that are better matched to the task of representing reflectivity magnitudes, see [9]. This approach provides the capability to preserve and enhance multiple distinct features on different spatial regions of the scene utilizing combinations of a variety of standard and custom-made signal dictionaries including contourlets, combination of spikes



[FIG2] Reconstructions of a scene based on TerraSAR-X data [57]. (a) A conventional image. (b) A synthesis-based sparsity-driven image reconstructed using a multiresolution wavelet dictionary.

(the canonical basis to represent strong point scatterers) and edges, as well as dictionaries of various geometric shapes matched to the expected scene structure. Furthermore, the synthesis-based approach can be used to combine a standard dictionary with a learning-based dictionary. For example, [10] combines spikes with a learned dictionary. The reconstructed SAR scene would then be a composite image that can be decomposed into multiple components represented by each dictionary, as illustrated in Figure 3.

While the sparsity-driven SAR imaging problem was formulated as a regularized optimization problem above, it could alternatively be viewed as a maximum a posteriori (MAP) estimation problem with a Bayesian perspective, in which the sparsity constraint turns into a heavy-tailed prior distribution for the features of interest. Continuing with the Bayesian perspective, one could also be interested in choosing other costs, leading to other estimators than MAP, or characterizing the posterior density rather than finding just a point estimate. There has been some exploration in this direction [11], [12]. There also exists some preliminary work on automatic regularization parameter selection for sparsity-driven SAR imaging [13].

Sparsity-driven SAR imaging has been extended to and applied in emerging sensing scenarios in which the sensing aperture or the data are limited or sparse in some sense (see the section “Compressed Sensing-Based Analysis and Design of SAR Sensing Missions”), as well as in multistatic active and passive radar [14] including MIMO architectures [15]. The benefits provided by sparsity-driven imaging are even greater in such non-conventional sensing scenarios. Sparsity-driven imaging has also been used for the problem of inverse SAR (ISAR) imaging of rotating targets [16], as well as for through-the-wall radar imaging [17]. It has also been extended to interferometric SAR [18] and SAR tomography (TomoSAR) [19] adding the elevation direction into the problem for 3-D imaging, as well as to four-dimensional (4-D) (differential, i.e., space-time) TomoSAR [20]. Sparsity-driven three-dimensional (3-D) image formation has also been used to initialize the process of geometric feature extraction from SAR data collected over arbitrary, monostatic or bistatic SAR apertures [21].

WIDE-ANGLE SAR IMAGING OF ANISOTROPIC SCATTERING

Wide-angle SAR, a SAR modality in which radar returns are collected over a large azimuth extent or long aperture, has become possible due to advances in navigation and avionics that permit aircraft to follow precise routes for long distances. In theory, the wider the aspect angle covered by the synthetic aperture is, the finer the resolution of images in the cross-range direction can be. However, there are two main issues that arise in wide-angle SAR image formation. First, the sampling pattern of the collected radar returns in the frequency domain takes on an arch shape. However, the conventional Fourier transform-based polar format algorithm [22] is predicated on the polar frequency sampling pattern being a good approximation to a rectangular sampling pattern, which is violated with wide-angle apertures. Violation of this assumption leads to an irregular point spread function and to artifacts in imagery formed by conventional processing.

The second issue, and the main point of discussion in this section, is that when objects are viewed from diverse aspect angles, they have different scattering behaviors, i.e., the scattering response is a function of the azimuth angle. Imagine an upright flat metal plate; it will reflect radar signals back to the receiver strongly when viewed straight on but weakly when viewed obliquely. Angle-dependent scattering, termed *angular anisotropy*, is only prominent with wide-angle apertures, not narrow-angle apertures, in which case it is a reasonable assumption that scattering amplitude is constant over the aperture. The failure to model anisotropy in conventional image formation algorithms results in an averaging of scattering response over angle, leading to inaccurate scattering estimates in the formed imagery. Moreover, as anisotropy of scatterers is not characterized, one misses the opportunity of using it as a feature for automatic target recognition and scene understanding.

The problems of detecting, estimating, and modeling aspect-dependent scattering behavior have recently been studied. Anisotropy characterization methods may be broadly categorized into those employing parameterizations for angle-dependent scattering in the phase history domain, multiaperture methods that operate in the image domain, and sparsity-driven nonparametric image formation and anisotropy characterization methods. Within the third category, techniques either apply sparse reconstruction methods described in the previous section independently on a set of (possibly overlapping) small subapertures [8], [23]–[25] or jointly process wide-aperture data by incorporating prior information on aspect-dependent scattering [26]–[28]. The independent processing methods have similarities with image domain multiaperture methods. In the remainder of this section, we describe one example formulation of a sparsity-driven subaperture approach and two formulations of joint processing: one analysis based and one synthesis based.

Let us consider the following discrete version of the measurement model with anisotropy:

$$r(f_k, \theta_l) = \sum_{m=1}^M s(x_m, y_m; \theta_l) e^{-j \frac{4\pi f_k}{c} (x_m \cos \theta_l + y_m \sin \theta_l)} + n(f_k, \theta_l), \quad (6)$$

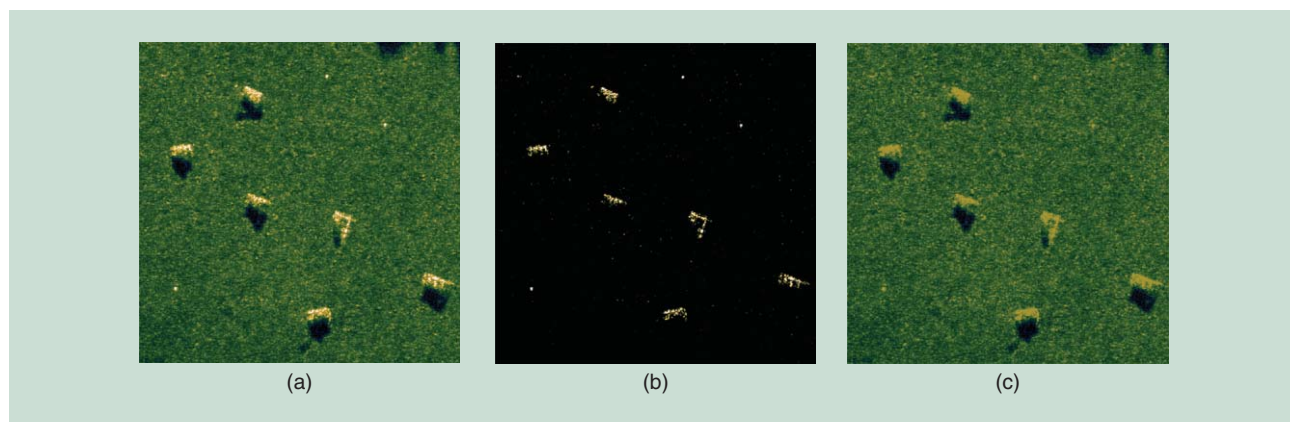


[FIG3] Reconstruction of a scene from the MSTAR data set [56] using a synthesis-based sparse representation approach combining the canonical (spike) dictionary with a learned dictionary. (a) A composite image containing six military vehicles and three corner reflectors. (b) A component consisting of strong scatterers represented by the spike dictionary. (c) A component represented by the learned dictionary. (Figure used with permission from [10].)

where $k = 1, \dots, K$, and $l = 1, \dots, L$. The difference from the previous section is the scattering response now being a function of the viewing angle $s(x_m, y_m; \theta_l)$. In the narrow-angle setting, the entire set of phase history measurements $r(f_k, \theta_l)$ is inverted to obtain the isotropic scattering response $s(x_m, y_m)$. For the wide-angle case, if we assume isotropic scattering within small ranges of azimuth angles, we can perform the inversion separately on intervals of θ to obtain I separate subaperture images $s_{\theta_i}(x_m, y_m)$ centered at angles θ_i , $i = 1, \dots, I$ [23]. The ranges of angle, which may overlap from one subaperture image to the next, lead to I linear systems of equations $\mathbf{r}_{\theta_i} = \mathbf{H}_{\theta_i} \mathbf{s}_{\theta_i} + \mathbf{n}_{\theta_i}$, where \mathbf{r}_{θ_i} represents the subset of phase history measurements corresponding to the subaperture centered at θ_i , \mathbf{H}_{θ_i} is the corresponding subset of forward operations, and \mathbf{s}_{θ_i} is the i th subaperture image we would like to find. Using methods described in earlier sections, one can reconstruct point-enhanced subaperture images by minimizing

$$J(\mathbf{s}_{\theta_i}) = \|\mathbf{r}_{\theta_i} - \mathbf{H}_{\theta_i} \mathbf{s}_{\theta_i}\|_2^2 + \lambda \|\mathbf{s}_{\theta_i}\|_p^p, \quad i = 1, \dots, I. \quad (7)$$

The resulting set of subaperture images can then be stacked and viewed as a 3-D volume in the two spatial dimensions and the angular dimension. Also, in a generalized likelihood ratio test fashion, a composite image can be formed by taking the maximum magnitude (over angles) at each pixel location [23], on which one might also use color coding to display dominant angular response directions of scatterers. Noncoherent combination of subaperture images is also studied in [24]. Motivated by a number of applications including foliage penetration (FOPEN) radar, this approach has also been shown to be effective on data with frequency-band omissions. The idea of independent processing of small subapertures described above has recently been applied in the context of 3-D circular SAR with little elevation diversity, where improved image quality is attributed to scattering center sparsity that is incorporated into the algorithms [5], [8], [25]. A sample 3-D imaging result from [25] is shown in Figure 4.

The forming of independent subaperture images fails to take prior information about the expected angular behavior of scatterers into account. In particular, point scatterers resulting from natural and man-made objects tend to have contiguous intervals of strong scattering response as a function of angle. Although each scatterer has limited persistence over the full wide-angle aperture, there exists a high correlation in magnitude response at closely spaced aspect angles within its persistence interval. Therefore, an improvement over independent reconstruction of subapertures is joint reconstruction of all subaperture images with an additional regularization term penalizing the ℓ_q -norm, $q \leq 1$, of the change in scattering magnitude at each spatial location across subaperture images [27]. The cost functional for such analysis-based joint (point-enhanced) processing is

$$J(\mathbf{s}_{\theta_1}, \dots, \mathbf{s}_{\theta_I}) = \sum_{i=1}^I \|\mathbf{r}_{\theta_i} - \mathbf{H}_{\theta_i} \mathbf{s}_{\theta_i}\|_2^2 + \lambda_1 \sum_{m=1}^M \left(\sum_{i=1}^I |s_{\theta_i}(x_m, y_m)| \right)^{p/2} + \lambda_2 \sum_{i=1}^{I-1} \|\mathbf{s}_{\theta_{i+1}} - \mathbf{s}_{\theta_i}\|_q^q, \quad (8)$$

where p is chosen to be around 1 to promote sparse solutions. The second term imposes spatial sparsity on the total scattering magnitude response collected over all aspect angles, whereas the third term enforces piecewise smoothness of the scattering magnitude in the angular dimension.

An alternative synthesis-based joint processing to take the prior information on contiguity of angular persistence into account constructs an overcomplete dictionary representation for the angular dimension with atoms that are zero over some aspect angles and positive-valued over contiguous ranges of aspect angles [26]. There are no subaperture images in this approach. Specifically, for a single spatial location, the anisotropic scattering function is expanded as

$$s(x_m, y_m; \theta_l) = \sum_{n=1}^N a_{m,n} b_n(\theta_l), \quad (9)$$

where the $a_{m,n}$ are coefficients and the $b_n(\theta_i)$ are atoms. For each spatial location, there is one atom for each possible angular persistence width within the wide-angle aperture and each possible center angle. With such a dictionary construction, the number of atoms per spatial location is quadratic in L , the number of aspect angles in the aperture. Substituting the dictionary expansion (9) into the anisotropic phase history expression (6), and stacking all data points into vector form yields an underdetermined system of linear equations of the form $\mathbf{r} = \Psi\mathbf{a}$, where \mathbf{a} is a vector of all coefficients in the problem. The overcomplete dictionary at each spatial location can represent all contiguous angular scattering functions with a single atom. Hence in addition to spatial sparsity, the anisotropic scattering at each pixel can, in principle, be sparsely represented as well. So the problem is solved using sparsity regularization by minimizing

$$J(\mathbf{a}) = \|\mathbf{r} - \Psi\mathbf{a}\|_2^2 + \lambda\|\mathbf{a}\|_p^p, \quad (10)$$

where p is chosen to be around 1. Because of the quadratic number of atoms in the number of aspect angles, it is not tractable to optimize (10) directly, however the nesting structure of the dictionary allows the optimization to be approximated using a greedy graph search procedure [26]. Another challenge posed by a very large dictionary is that the problem becomes more underdetermined and it becomes harder to guarantee perfect recovery. The atomic decomposition allows for a direct interpretation of the coefficients in terms of the persistence and center angle of scattering centers. This idea can be taken a step further by setting the dictionary atoms to be canonical scattering response magnitudes from typical object geometric configurations [28].

Image formation and anisotropy characterization from wide-aperture data collection using sparsity-driven approaches leads to improved results over conventional Fourier-based methods. We illustrate this point by showing results on a 110° aperture data set corresponding to a scene containing a backhoe loader [58]. Numerical quantifications of algorithm performance may be found in the respective papers [23], [26], and [27]. In this data set, the radar signals are generated using a high fidelity electromagnetic scattering code. Backhoe results from the conventional, independent point-enhanced subaperture, joint subaperture

reconstruction, and overcomplete dictionary algorithms are shown in Figure 5 (b)–(e), respectively. The image formed by conventional processing is quite unresolved and full of artifacts—it is difficult to even discern that the scene contains a backhoe. The backhoe is much more recognizable in the sparsity-driven results. Among the sparsity-driven approaches, joint processing gives finer resolution of the scattering behavior. The approaches we have described produce more than 2-D reflectivity images, in particular, these methods essentially reconstruct an angular scattering response at each pixel, leading to anisotropy characterization. This is demonstrated in Figure 6 for the analysis-based joint processing approach of [27]. The figure shows varying persistence of scattering as a function of angle in different parts of the backhoe. Such information could not be recovered by conventional image formation methods and could serve as an important feature for automatic target recognition and scene understanding.

IMAGING AND AUTOFOCUSING IN THE PRESENCE OF PHASE ERRORS

Phase errors in SAR phase history data arise due to errors in the estimation of the time required for the transmitted signal to propagate from the SAR platform to the scene and back. The most common causes of inaccuracies on the roundtrip propagation time are SAR platform position uncertainties and propagation induced errors due to atmospheric effects. The implication of such errors on conventional SAR imagery is the convolution of the image with a blurring kernel. Because of the defocusing effect of such errors, techniques developed for removing phase errors are called autofocus techniques. Existing well-known autofocus techniques commonly postprocess conventionally reconstructed defocused images to estimate the phase errors. One of these state-of-the-art techniques is mapdrift autofocus [29] which uses subaperture data to estimate the phase errors. Subaperture based techniques are suitable mostly for quadratic and slowly varying phase errors across the aperture. One of the most widely used autofocus techniques, phase gradient autofocus (PGA) [30], estimates phase errors using the data obtained by isolating several defocused targets via center-shifting and windowing operations. Another well-known approach for autofocus is based on the optimization of a sharpness metric. Commonly used metrics are entropy or square of the image intensity. A relatively new autofocus technique, multichannel autofocus, is based on a noniterative algorithm that finds the focused image in terms of a basis formed from the defocused image, relying on a condition on the image support to obtain a unique solution.

The SAR autofocus problem has recently been handled in the context of sparsity-driven imaging as well. In [31], phase error estimation is performed by comparing and aligning sparsity-driven images produced from a sequence of smaller coherent processing intervals, for which motion errors can be assumed to be tolerable. For sparse aperture ISAR imaging, [32] proposes first to remove the phase errors by a weighted eigenvector-based phase correction method and then to form the image by sparsity-driven imaging. The study in [33] demonstrates the effects of phase errors on sparsity-driven imaging and presents results

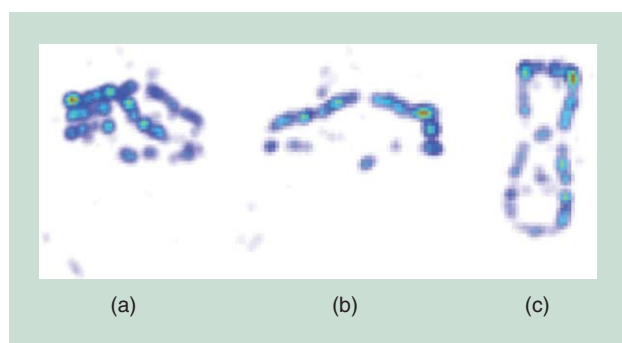


[FIG4] Sparsity-driven 3-D SAR imaging of a car. (a) Isometric view. (b) Side view. (c) Top view. (Figure used with permission from [25].)

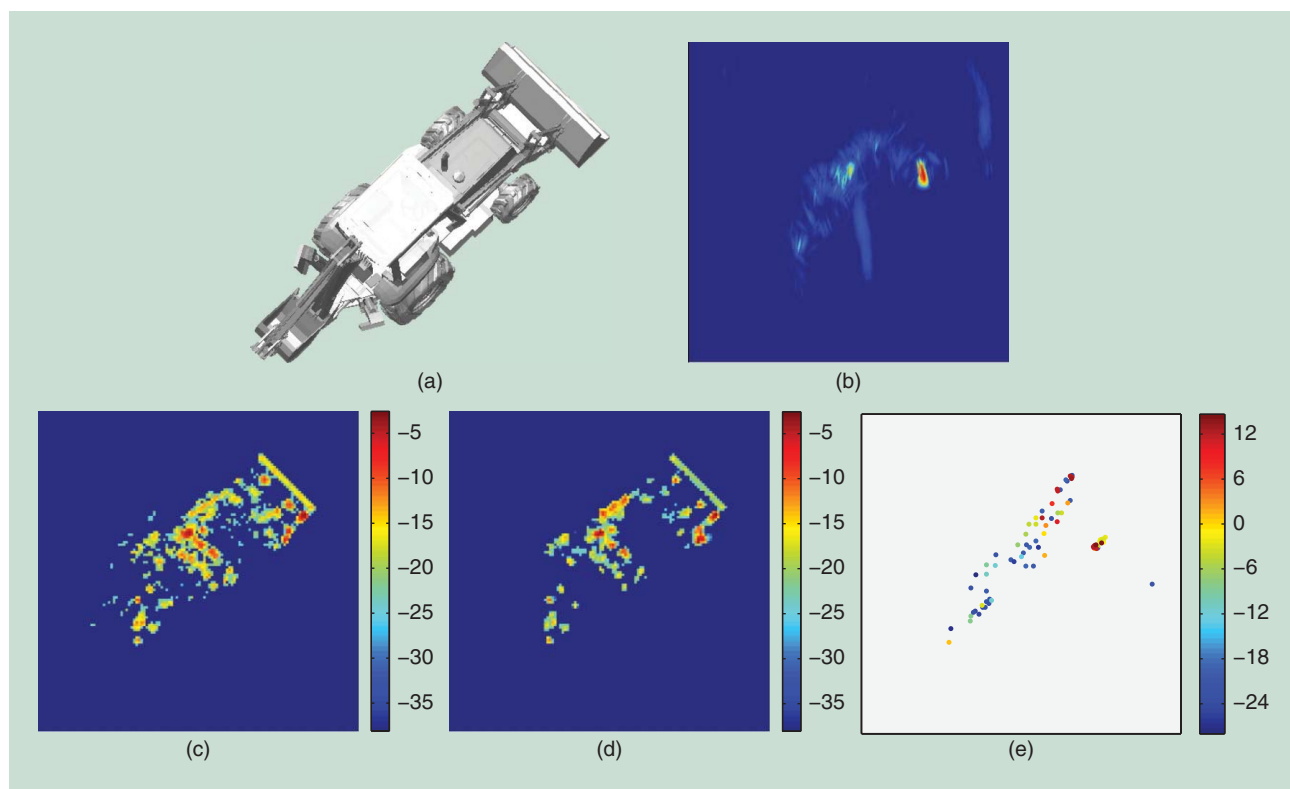


[FIG5] Wide-angle SAR imaging of a backhoe loader. (a) A CAD model. (b) Conventional reconstruction. (c) A composite independent subaperture image. (d) A composite joint subaperture image imposing piecewise smoothness in angular scattering. (e) A composite joint subaperture image based on an overcomplete dictionary for angular scattering. (Images used courtesy of [26] and [27].)

obtained by implementing PGA on sparsity-driven reconstructions. In these pieces of work, the process of sparsity-driven imaging and that of autofocusing are rather isolated.

Going one step further, one can perform autofocusing and imaging simultaneously in a sparsity-driven framework, which has been shown to produce promising results [5], [34]–[37]. As an example of such an approach, the sparsity-driven autofocus (SDA) method [34] for an isotropic scattering scenario is based on the following observation model in which phase errors are considered as model errors:

$$\mathbf{r} = \mathbf{H}(\epsilon)\mathbf{s} + \mathbf{n}. \tag{11}$$

Here, $\mathbf{H}(\epsilon)$ denotes the model matrix that takes the phase errors ϵ into account. Assuming spatial sparsity of the reflectivity field, the following cost functional is minimized over both the field and the phase errors using a coordinate descent approach:

$$J(\mathbf{S}, \epsilon) = \|\mathbf{r} - \mathbf{H}(\epsilon)\mathbf{s}\|_2^2 + \lambda\|\mathbf{s}\|_1. \tag{12}$$

Hence, SDA estimates the phase errors and performs sparsity-driven imaging jointly by solving this optimization problem. SDA has been used to compensate a variety of commonly encountered types of phase errors. A sample result on the backhoe data for a case involving randomly varying phase errors along the aperture

with a uniform distribution in $[-\pi, \pi]$, is displayed in Figure 7. Note that this is a wide-angle imaging scenario and SDA is applied on subapertures within the framework of the wide-angle imaging method of [23]. Figure 7(a) and (b) show the reconstructions obtained by conventional imaging, and direct application of sparsity-driven imaging without phase error compensation, respectively. The result of joint sparsity-driven imaging and phase error compensation through SDA is shown in Figure 7(c), which demonstrates the effectiveness of SDA in removing phase errors and reconstructing a high-quality image. The experimental analysis in [34] also shows how SDA provides improvements over existing autofocus methods.

More recently, [35] and [36] have used similar ideas to achieve autofocusing of undersampled SAR data. The method proposed in [35] is based on minimizing a constrained version of the cost functional in (12). Optimization is performed through a three-block relaxation approach by using an extra surrogate parameter for the field to guarantee convergence. In [36], motion compensation and image reconstruction are performed for SAR data obtained at a fraction of the Nyquist rate using reduced rate analog-to-digital converters. A total variation penalty on the field is incorporated into the optimization problem as well. In [37], the idea of joint sparsity-driven imaging and autofocusing is used for 3-D imaging based on undersampled linear array SAR data.

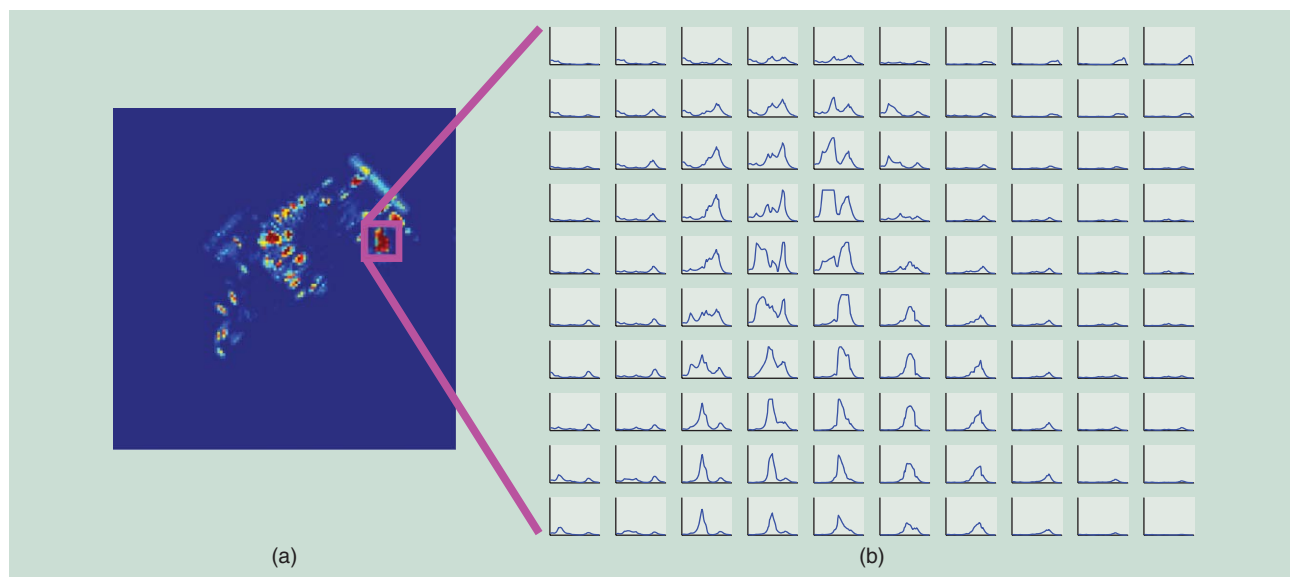


[FIG6] Anisotropy characterization for a subset of pixels in the backhoe loader using joint subaperture reconstruction imposing piecewise smoothness in angular scattering. The individual small plots in (b) have subaperture angle θ as the abscissa and the scattering magnitude $|s(\theta)|$ as the ordinate. They are arranged to match the pixel locations in (a).

MOVING TARGET IMAGING

Joint SAR imaging and ground moving target localization has proven to be an important but challenging task due to an inherent ambiguity in target geolocation and velocity. While the components of the received signal belonging to a particular stationary target have the same phase in successive radar returns, the phase of a moving target varies due to its varying range. Hence, to the conventional SAR imager working under the assumption that the scene is stationary during aperture synthesis, motion amounts to phase errors and results in defocusing and even displacement of moving target energy. On the other hand, if the SAR imager assumes a particular nonzero scene motion, the moving target with a matching velocity appears focused, while all stationary and velocity mismatched targets appear defocused.

A common approach for SAR moving target imaging is first to find the smeared imagery of moving targets in a conventionally formed image and then perform phase error estimation and compensation for the corresponding image parts. Space-time adaptive processing uses data obtained from multiple channels to suppress clutter and separate moving targets from the background. Velocity SAR exploits phase information from multiple receive antennas, whereas dual-speed SAR processes the data collected by a platform flying with two different speeds in the radar observation duration.

Sparsity-based methods have recently made their way into moving target SAR imaging. In [38]–[41], sparse representation techniques are used to search for a solution over an overcomplete dictionary that consists of atoms for several velocity-position combinations. The overcomplete dictionary approach amounts to linearizing the nonlinear problem of target scattering and motion estimation and subsequently to solving the problem as a larger, unified regularized inversion problem involving sparsity constraints. A sample multistatic imaging result from [38] is illustrated in Figure 8. When a scene consisting of a

stationary, a slowly moving, and a fast-moving target [shown in Figure 8(a) at time zero] is conventionally imaged under a zero-velocity assumption, the slowly moving target is defocused, while the fast-moving target disappears [Figure 8(b)]. The conventional reconstruction over a set of hypothesized velocities accurately localizes the moving targets, albeit with residual blur. Finally, Figure 8(d) shows that target features can be recovered by the sparsity-enforcing overcomplete dictionary approach [38]. In [40], a similar optimization problem to the one in [38] is solved after a clutter cancellation procedure is applied to the data.

Based on the observation that radar returns from a scene with motion can be viewed as data from a stationary scene, but with phase errors due to motion, a recently proposed idea is to view moving target imaging as a generalized, spatially variant autofocusing problem. The work in [42] does just that and extends the SDA framework, described in the previous section, to the problem of moving target imaging. Due to the spatially variant nature of the defocusing (due to the possibility of targets with different velocities at different locations), the number of unknowns is much greater than a basic autofocusing problem, making this a very ill-posed problem, requiring effective constraints for a successful solution. Based on this observation, [42] not only exploits the sparsity of the reflectivity field, but also imposes a constraint on the spatial sparsity of the phase errors based on the assumption that motion in the scene will be limited to a small number of spatial locations. The phase errors corresponding to all points in the scene, for all aperture positions are incorporated into the problem using the vector β , whose elements are in the form of $e^{j\epsilon} s$. The following cost functional is minimized jointly with respect to the field and the phase errors:

$$J(s, \beta) = \|r - H(\beta)s\|_2^2 + \lambda_1 \|s\|_1 + \lambda_2 \|\beta - \mathbf{1}\|_1 \quad s.t. \quad |\beta(i)| = 1 \quad \forall i. \quad (13)$$

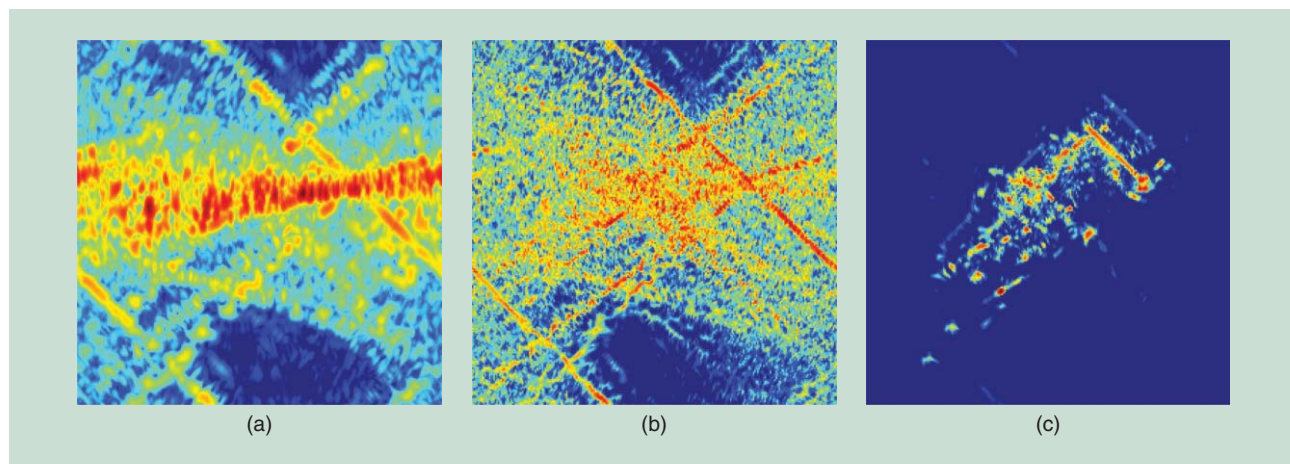


[FIG7] Imaging in the presence of phase errors uniformly distributed in $[-\pi, \pi]$. (a) Conventional imaging. (b) Sparsity-driven imaging without phase error compensation. (c) SDA.

Here, $\mathbf{1}$ is a vector of ones. Assuming that the number of moving points constitutes a small percentage of the total number of points in the scene, most of the ϵ values are zero, and subsequently most of the elements in the vector β are one. Therefore, this sparsity on the phase errors is incorporated into the problem formulation by using the regularization term $\|\beta - \mathbf{1}\|_1$. Results of an experiment on a synthetic scene containing two moving targets are shown in Figure 9. The six pointlike targets are stationary. To simulate the SAR returns from the two large targets moving with constant cross-range velocities, quadratic phase errors with a center to edge amplitude of π radians and 2.5π radians have been added to the data of these particular targets. These phase errors correspond to velocities of 2 m/s and 5 m/s, respectively, for the SAR system used in this experiment. Figure 9(a) and (b) show the results of conventional imaging and sparsity-driven imaging without phase error compensation, respectively. The result of sparsity-driven moving target imaging [42], displayed in Figure 9(c), shows the effectiveness of the method in removing the phase errors due to motion, as well as in producing an image that exhibits the qualities of sparsity-driven SAR imaging.

There exist several other pieces of recent work exploiting sparsity for moving target SAR imaging. The work in [39] concentrates on targets with micromotions that are mainly embodied with rotation and vibration. To enforce sparsity, generalized Gaussian and student-t prior models are considered, and the variational Bayes' approximation estimator is applied to the hierarchical Bayesian models involved in the problem. The paper [41] considers the problem of motion parameter estimation of moving targets with Doppler spectrum ambiguity and Doppler centroid frequency ambiguity encountered in SAR systems with low pulse repetition frequency, and presents a sparsity-based method that involves the use of the Radon transform to acquire unambiguous across-track velocities and range positions in the range profile domain. The paper [43] proposes an adaptive CS-based SAR system for dynamic sparse target scenes. The proposed system uses the recovered target scene information to detect if the scene has changed and optimizes the transmission waveform and sensing matrix accordingly. Finally, the paper [44] presents an approach that combines sparsity-driven radar imaging and change detection for detecting and localizing moving humans behind walls and inside enclosed structures.

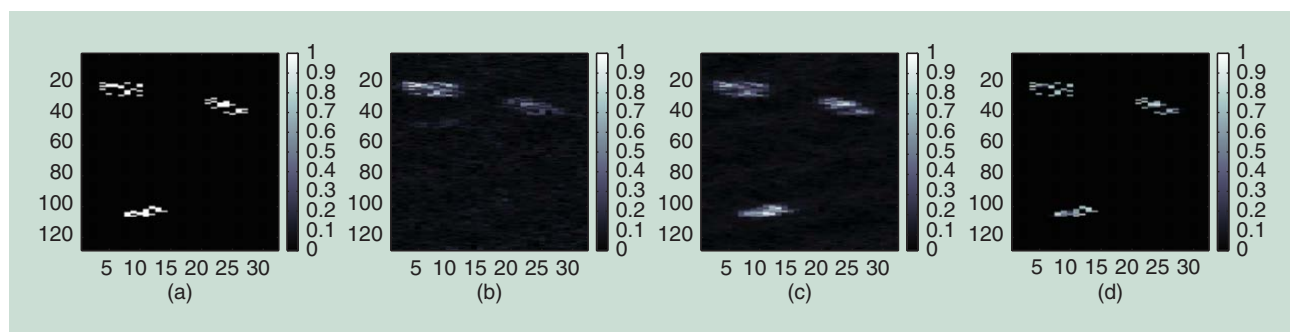


[FIG8] Multistatic moving target imaging. (a) A simulated ground truth scene at time $t = 0$. The upper left target is stationary, the upper right target moves slowly, and the bottom target moves at a faster velocity. (b) Conventional reconstruction when motion is ignored. (c) Conventional reconstruction over a set of velocity hypotheses. (d) Sparsity-enforcing overcomplete dictionary reconstruction. (Images used courtesy of [38].)

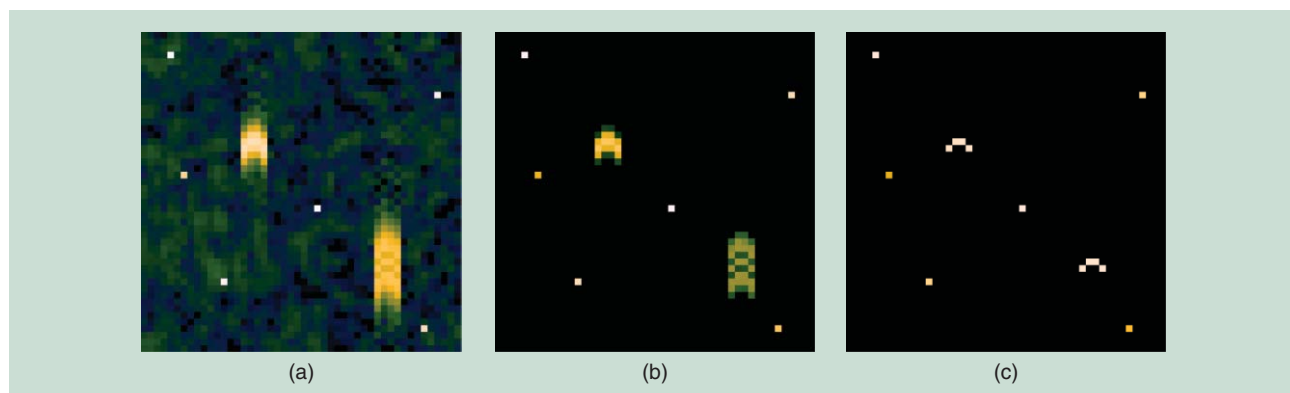


[FIG9] Imaging of a synthetic scene with moving targets. (a) Conventional imaging. (b) Sparsity-driven imaging assuming a stationary scene. (c) Joint sparsity-driven imaging and phase error correction.

COMPRESSED SENSING-BASED ANALYSIS AND DESIGN OF SAR SENSING MISSIONS

As discussed in previous sections, ideas based on sparse signal representation have led to advanced image formation methods that offer a number of benefits for SAR such as increased resolvability of point scatterers and reduced speckle, as well as robustness to limitations in data quality and quantity. Robustness to missing or undersampled data has recently become a particularly critical concern due to new mission requirements and sensor geometries that result in nondense and irregular sampling patterns in the SAR measurement space. Current radar systems are capable of accommodating multiple operational modes such as searching, tracking, and imaging on the same platform. Timeline constraints of a higher priority mode may require interrupts in SAR data collection and lead to gaps in the synthetic aperture. Likewise, jamming and interference from nearby transmitters may lead to frequency gaps in SAR data collection. Furthermore, multiplatform and passive sensing from transmitters of opportunity result in sparse sensing geometries and irregular sampling of the SAR measurement space. Such irregular and undersampled data scenarios motivate the application of CS [45] ideas and signal processing algorithms to SAR. Sparsity-driven methods described in previous sections serve as the main computational tool for inverting such limited data. In this section, we provide an overview of a subset of recent work on the use of CS theory and principles for analysis and design of monostatic and multistatic SAR sensing missions under various constraints on data collection.

CS seeks to acquire as few measurements as possible about an unknown signal, and given these measurements, reconstruct the signal either exactly or with provably small probability of error. Reconstruction methods used in CS involve sparsity-constrained, nonquadratic regularization ideas and algorithms similar to the ones discussed in previous sections. Based on CS theory, such methods can successfully recover the signal sampled well below the Nyquist rate provided that the signal has a sparse representation in some suitable domain and that its measurement process satisfies certain properties (such as incoherence [46]) with respect to the signal's sparsifying basis [45]. For example, signals sparse in the canonical basis (which is what we will assume in this section) can be

accurately reconstructed from measurements involving extremely few, but randomly chosen Fourier samples of a signal. Since both monostatic and multistatic SAR sensing can be viewed as obtaining samples of the spatial Fourier transform of the scattering field, these results open opportunities for reduced-data SAR sensing.

Random sampling of SAR data in 2-D Fourier space closely matches observation scenarios assumed in existing CS theory. While random subsampling can be primarily used to reduce on-board data storage requirements, it may not represent data limitations due to more structured interrupts and it may not enable reallocation of SAR sensing resources to other tasks. To enable such resource management and retasking, one could consider collecting returns of, e.g., a reduced number of transmitted waveforms by imposing randomness into the synthetic aperture [47], [48]. It would then be of interest to analyze and design sensing missions, i.e., practical data sampling configurations, based on the expected signal reconstruction quality and assess how well metrics appearing in CS theory (and that are defined by the measurement scenario) predict reconstruction performance from such limited data. Recent work on this question suggests CS principles may be used to analyze and guide the design of monostatic and multistatic SAR sensing missions under various constraints on data collection.

Here we provide highlights of such an analysis. One idea is to study sensitivity to data limitations and to the sampling patterns through mutual-coherence based metrics, which appear in CS theory. The mutual coherence of a measurement operator was proposed as a simple, but conservative measure of the ability of sparsity-enforcing reconstruction to accurately reconstruct a signal [46]. The mutual coherence of a complex-valued matrix \mathbf{H} , which in our case becomes the mutual coherence of a sensing configuration, is defined as

$$\mu(\mathbf{H}) = \max_{i \neq j} g_{ij}, \quad g_{ij} = \frac{|\langle \mathbf{h}_i, \mathbf{h}_j \rangle|}{\|\mathbf{h}_i\|_2 \|\mathbf{h}_j\|_2}, \quad i \neq j, \quad (14)$$

where \mathbf{h}_i is the i th column of the matrix \mathbf{H} , and the inner product is defined as $\langle \mathbf{h}_i, \mathbf{h}_j \rangle = \mathbf{h}_i^H \mathbf{h}_j$. The i th column vector \mathbf{h}_i can be viewed as a range-aspect “steering vector” of a sensing

geometry or the contribution of a scatterer at a specific spatial location to the received phase history data. The mutual coherence measures the worst case correlation between responses of two distinct scatterers at different spatial locations. The $t\%$ -average mutual coherence, $\mu_{t\%}$, has been proposed as a measure more closely related to the average reconstruction performance of sparsity-driven SAR reconstruction [47]

$$\mu_{t\%}(\mathbf{H}) = \frac{\sum_{i \neq j} g_{ij} \mathcal{I}_{ij}(t\%) }{\sum_{i \neq j} \mathcal{I}_{ij}(t\%)}, \mathcal{I}_{ij}(t\%) = \begin{cases} 1, & g_{ij} \in \mathcal{E}_{t\%} \\ 0, & \text{otherwise,} \end{cases} \quad (15)$$

where $\mathcal{E}_{t\%}$ denotes the set containing the largest $t\%$ column cross-correlations g_{ij} . Based on this definition, $\mu_{t\%}(\mathbf{H})$ measures the average cross-correlation value within the set of the $t\%$ most similar column pairs. A large value of $\mu_{t\%}(\mathbf{H})$ indicates that there are many similar pairs of columns of \mathbf{H} that can potentially confuse the reconstruction algorithm. This measure is more robust to outliers, which can unfairly dominate the mutual coherence. The $t\%$ -mutual coherence can be related to the cumulative coherence [49] that, in the CS literature, has been used to derive sparse signal recovery conditions with convex cost function relaxations. The cumulative coherence provides an upper bound on the $t\%$ -mutual coherence. Note that $\mu_{t\%}(\mathbf{H})$ can be computed for a sensing configuration before actual data collection. The question then is whether it can serve as a predictor of reconstruction quality of a sparse scene based on data to be collected through a particular configuration.

Figure 10 provides an example of the utility of $t\%$ -average mutual coherence on an urban scene from the publicly released Gotcha SAR data set [59]. Figure 10(a) shows the scatter plot of root-mean-square error (RMSE) of the reconstructions versus $\mu_{0.5\%}$ when the number of randomly missing aperture positions increases linearly up to 50%. Just for visualization, Figure 10(b) and (c) shows sample conventional and sparsity-driven reconstructions of the scene with 24% of the synthetic aperture missing. The result in Figure 10(a) indicates that configurations with sufficiently small values of the $t\%$ -average mutual coherence achieve high-quality reconstruction and that $\mu_{0.5\%}$ appears to be a good predictor of reconstruction quality. This is an easily computed parameter that can be utilized for real-time evaluation of sensing configurations and task planning of multimode radars. Although we have considered a simple monostatic scenario here for simplicity, the analysis in [47] suggests that such a CS-motivated metric can be useful in the analysis and design of multistatic sensing missions as well. In the multistatic case, CS and sparsity-driven reconstruction have the potential to allow for sensing with fewer transmitted probes and reduced acquisition time.

Another way CS theory has recently impacted SAR imaging is by motivating the design of new radar waveforms. New radar waveforms such as Alltop and pseudorandom sequences have been shown to lead to high-resolution imaging radar and reduced analog-to-digital conversion bandwidth [7], [50]. Compressive sensing through convolution using random noise-like transmitted waveforms followed by random time-domain subsampling and its application to SAR was discussed in [51]. These

waveforms result in incoherent radar sensing matrices and allow for accurate reconstruction of sparse target scenes. Multistatic and distributed radar waveform design for CS was discussed in [52]. CS for MIMO radars was addressed in scenarios involving uniform linear antenna array configurations [53], [54] and antennas randomly distributed over a small area [55].

SUMMARY AND DISCUSSION

We have presented an overview of recent lines of inquiry that lie at the intersection of two domains: sparse signal representation and SAR image formation. For basic SAR imaging, we have described image formation methods founded upon analysis and synthesis-based sparse signal representation ideas, and discussed how the complex-valued and potentially random-phase nature of SAR reflectivities have led to interesting optimization formulations different from those encountered in basic sparse signal representation problems. Motivated by emerging applications, including those involving sensing by unmanned aerial vehicles, we have considered the problem of wide-angle SAR imaging and described how exploitation of the sparsity of the scene and that of the angular scattering response can lead to effective imaging and anisotropy characterization. Then we have turned to the issue of phase errors, and described how exploitation of sparsity enables autofocusing in challenging conditions. We have pointed to

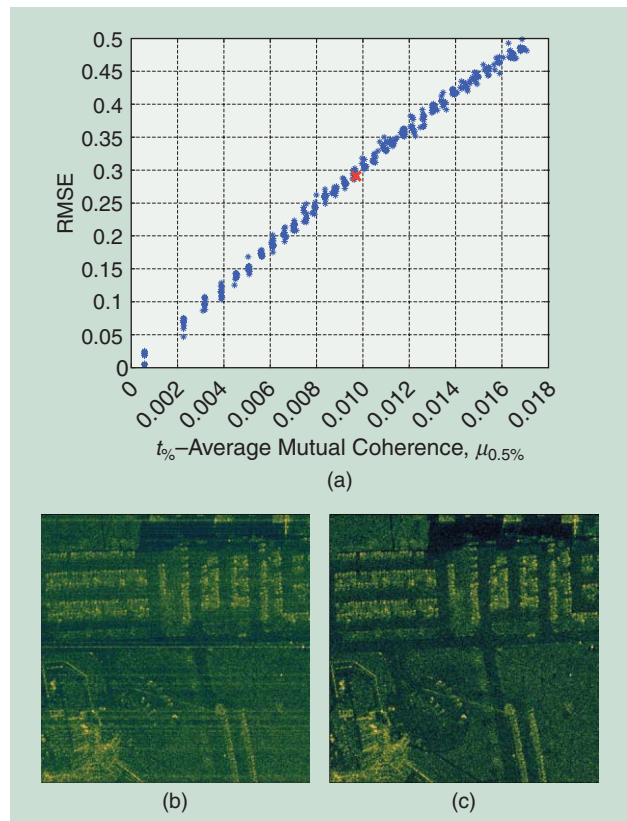


[FIG10] A compressed sensing-based analysis of sensing configurations. (a) RMSE versus $\mu_{0.5\%}$. (b) Conventional reconstruction, and (c) sparsity-driven reconstruction corresponding to the red point in (a) with 24% of missing data. (Images used courtesy of [47].)

recent pieces of work that attempt to use sparsity for the challenging problem of moving target SAR imaging. Finally, we have discussed how recent developments in CS theory have motivated not only the use of sparsity-driven methods for SAR imaging, but also the analysis and design of SAR sensing missions under physical, geometric, or temporal constraints on data collection.

The body of work on sparsity-driven SAR imaging we have covered here (and related pieces of work we were not able to cover due to space constraints), shows that sparsity can be a useful asset for SAR imaging especially in nonconventional data collection scenarios (e.g., when the data are sparse, irregular, limited) leading to severely underconstrained, ill-posed problems for image formation. Sparsity-driven imaging should not necessarily be viewed as a general-purpose approach that should replace more traditional SAR image formation methods completely. When used properly, it is a tool that can enable the radar engineer to extract interesting pieces of information from SAR data that is not possible through more conventional means. As any approach for solving an ill-posed problem, it relies on a certain type of assumption, which, in this particular case, is that the scene admits sparse representation in some domain. It performs very well on scenes that exhibit sparsity or compressibility, and enhances aspects of a particular scene that exhibit these characteristics. If the important characteristics of the scene and the sparse structure imposed through a particular dictionary are mismatched, we would obviously not expect the approach to produce improved imagery. This is why we expect “learning” to be an important theme in future work, as we describe below. Furthermore, when sparsity by itself is not sufficient to capture the rich information content of a scene, it might be possible to combine it with other types of priors each of which describes a component of a decomposed scene.

The research we have reviewed provides a principled basis and demonstrates how sparsity can be exploited in several contexts in SAR imaging. We believe we will witness wider utilization of sparsity-based methods in real SAR imaging applications over the upcoming years if several challenges are addressed and further research is carried out with a broader perspective. These challenges include reducing computational complexity, establishing stronger connections between imaging and decision-making, using effective machine-learning ideas to tune the notion of sparsity to a particular context, and going beyond sparsity to capture other forms of simple structures present in the data. Based on this perspective, we briefly describe four lines of research that we believe will enrich this problem domain and widen its applicability.

1) *Computational advances*. The first issue is computational complexity. While we might never expect sparsity-driven imaging to be as fast as simple Fourier transform-based imaging methods, more work is needed to develop exact and approximate algorithms that exploit the problem structure to produce faster solutions. One can think of several related research thrusts under this theme. First, given recent developments in convex optimization methods, it is of interest to adapt promising methods to particular SAR imaging problems to improve computational efficiency. As an example, augmented Lagrangian methods such as alternating direction

method of multipliers could be considered not only because of their fast convergence properties, but also due to their potential for distributed implementation leading to parallelization. This brings us to our next point, which is whether one could exploit parallel processing on graphics processing units (GPUs) for sparsity-driven SAR imaging. While there exist GPU implementations of sparse signal representation ideas used as postprocessing despeckling methods, effective GPU implementations of the solution of the inverse problem for imaging is more challenging. Finally, for sparsity-driven SAR imaging problems involving large dictionaries, it is of interest to develop approximate algorithms that intelligently search the solution space exploiting the problem structure to achieve fast and reasonably accurate solutions. Advances in computational tools would enable wider utilization of sparsity-driven SAR imaging methods especially in relatively large problems involving, e.g., 3-D imaging in the context of TomoSAR.

2) *Decision-directed imaging*. We envision two potential major lines of inquiry suggesting the establishment of closer connections between SAR imaging and machine learning. The one we describe here involves the interplay between SAR imaging and further decision making. As discussed in the body of this article, one of the early motivations for sparsity-driven SAR imaging has been the preservation and enhancement of features important for tasks such as automatic target recognition. While this line of thinking has produced images with, e.g., better preservation of scatterer locations or easier to segment regions, accomplishments have been limited in at least two ways: first, only very low-level features have been used, and second, this has been an “open-loop” process. It would be interesting to bring in higher-level information, such as object shapes, into the problem formulation. It would also be interesting to take a decision-directed perspective and use information fed back from the inference engine, such as partial information on classes of objects in the scene, while solving the image formation problem. Whether one could formulate a sparse representation perspective to incorporate such high-level statistical information is a question worthy of exploration.

3) *Closer connections to machine learning*. Another major line of inquiry we foresee involves close integration of machine-learning methods into sparsity-driven SAR imaging. We have already mentioned that sparsity-driven imaging can be formulated using a Bayesian perspective that involves priors on the reflectivity field and the parameters, and in which the imaging problem involves characterizing a posterior density. While there exists some work with this perspective, using machine learning methods to demonstrate the benefits offered by such a statistical perspective is of interest for the future. Another aspect in which we expect learning methods to play a more prominent role is the construction of the dictionaries used in sparse representation. While there has been some preliminary work on dictionary learning in the context of SAR imaging, significant benefits are yet to be demonstrated. Connecting this back to decision-directed processing, one might consider performing discriminative dictionary learning as well.

4) *Other forms of "simplicity."* The final area of research we anticipate is about exploiting other types of structures potentially exhibited by SAR data in addition to sparsity. In particular, a concrete potential line of work could involve the use of low-rank models. Recent theoretical work on low-rank models shares many aspects of earlier work on sparsity and CS: low-rank matrix recovery problems are posed as optimization problems, relaxed forms of which, involving nuclear norms of matrices, are solved efficiently. Temporal and spatial dependencies in SAR data may lead to successful use of low-rank models, in a variety of contexts including moving target imaging and wide-angle imaging, and could possibly involve decomposition of some of the signals into sparse and low-rank components as well.

Overall, sparsity-driven SAR imaging is an exciting topic of study for both radar imaging experts and statistical signal processing researchers. Due to its connections to interesting ongoing theoretical work on signal representation and CS, as well as due to its potential for real impact on existing and emerging applications, we expect that it will continue to be an active area of academic and engineering development in the near future.

AUTHORS

Müjdat Çetin (mcetin@sabanciuniv.edu) is an associate professor at Sabancı University, İstanbul, Turkey. He was the technical program cochair for the International Conference on Information Fusion in 2013 and for the International Conference on Pattern Recognition in 2010. He has received several awards including the 2013 IET Radar, Sonar, and Navigation Premium Award, the 2010 IEEE Signal Processing Society Best Paper Award, the 2007 Elsevier Signal Processing Journal Best Paper Award, and the 2008 Turkish Academy of Sciences Distinguished Young Scientist Award. He was an associate editor of *IEEE Signal Processing Letters* and *IEEE Transactions on Cybernetics* from 2012 to 2014. He is currently an associate editor of *IEEE Transactions on Image Processing*. His current research interests include image reconstruction and restoration, brain-computer interfaces, biomedical information processing, and image analysis.

Ivana Stojanović (ivana.z.stojanovic@gmail.com) received the Dipl.Ing. degree from the University of Belgrade, Serbia, in 1999 and the M.S. and Ph.D. degrees in electrical engineering from Boston University in 2007 and 2012, respectively. At Boston University, she worked on sparse signal reconstruction and compressed sensing application to synthetic aperture radar imaging and biomedical signal processing. She is currently a lead research engineer at HERE, a Nokia business developing 3-D maps. Previously, she held a senior research scientist position at Scientific Systems Company, where she worked on interrupted synthetic aperture radar. From 1999 to 2005, she held positions in Iospan Wireless and Intel working as a wireless systems engineer developing WiMax systems.

N. Özben Önhon (onhon@sabanciuniv.edu) received the B.S. degree in electronics and telecommunication engineering and the M.S. degree in telecommunication engineering from İstanbul Technical University, in 2003 and 2006, respectively. She received the Ph.D. degree in electronics engineering from Sabancı University in 2012. She is currently a faculty member at

Turkish-German University, İstanbul, Turkey. Her research interests are in the areas of signal and image processing.

Kush R. Varshney (krvarshn@us.ibm.com) received the B.S. degree in electrical and computer engineering with honors from Cornell University in 2004 and the S.M. and Ph.D. degrees, both in electrical engineering and computer science, from the Massachusetts Institute of Technology in 2006 and 2010, respectively. He is a research staff member in the Mathematical Sciences and Analytics Department at the IBM Thomas J. Watson Research Center. He received a Best Student Paper Travel Award at the 2009 International Conference on Information Fusion; the Best Paper Award at the 2013 IEEE International Conference on Service Operations and Logistics, and Informatics; and several IBM awards for contributions to business analytics projects. He is on the editorial board of *Digital Signal Processing* and a member of the IEEE Signal Processing Society Machine Learning for Signal Processing Technical Committee.

Sadegh Samadi (samadi@sutec.ac.ir) is a faculty member at the Department of Electrical and Electronics Engineering, Shiraz University of Technology, Iran. He received the Ph.D. degree from Shiraz University, Iran, in 2010. He received the 2013 IET Radar, Sonar, and Navigation Premium Award. His research interests lie within the broad field of statistical signal and image processing.

W. Clem Karl (wckarl@bu.edu) received the Ph.D. degree in electrical engineering and computer science from the Massachusetts Institute of Technology. He is a professor of electrical and computer engineering and biomedical engineering at Boston University. He is currently the editor-in-chief of *IEEE Transactions on Image Processing* and a member of the IEEE Signal Processing Society's Conference Board. He is a past member of the Society's Board of Governors and was the general chair of the 2009 IEEE International Symposium on Biomedical Imaging. His current research interests include statistical image processing, estimation, detection, and inverse problems, such as tomography.

Alan S. Willmsky (willsky@mit.edu) is the E.S. Webster professor of electrical engineering and computer science at the Massachusetts Institute of Technology and was a founder of Alphatech, Inc. Among his awards are the 1975 American Automatic Control Council Eckman Award, 1979 American Society of Civil Engineers Alfred Noble Prize, 1980 IEEE Browder Thompson Award, 2004 IEEE Donald Fink Prize Paper Award, Doctorat Honoris Causa from Université de Rennes, 2009 Technical Achievement and 2014 Society Awards from the IEEE Signal Processing Society. He is a member of the National Academy of Engineering and is a coauthor of *Signals and Systems*. His research interests are in the development and application of methods of estimation, machine learning, and statistical signal and image processing.

REFERENCES

- [1] J. Ender, "On compressive sensing applied to radar," *Signal Process.*, vol. 90, no. 5, pp. 1402–1414, May 2010.
- [2] L. C. Potter, E. Ertin, J. T. Parker, and M. Çetin, "Sparsity and compressed sensing in radar imaging," *Proc. IEEE*, vol. 98, no. 6, pp. 1006–1020, June 2010.
- [3] M. Çetin and W. C. Karl, "Feature-enhanced synthetic aperture radar image formation based on nonquadratic regularization," *IEEE Trans. Image Processing*, vol. 10, no. 4, pp. 623–631, Apr. 2001.

- [4] M. Çetin, W. C. Karl, and D. A. Castañón, "Feature enhancement and ATR performance using non-quadratic optimization-based SAR imaging," *IEEE Trans. Aerosp. Electron. Syst.*, vol. 39, no. 4, pp. 1375–1395, Oct. 2003.
- [5] S. I. Kelly, C. Du, G. Rilling, and M. E. Davies, "Advanced image formation and processing of partial synthetic aperture radar data," *IET Signal Process.*, vol. 6, no. 5, pp. 511–520, July 2012.
- [6] Z. Wang and W. Wang, "Fast and adaptive method for SAR superresolution imaging based on point scattering model and optimal basis selection," *IEEE Trans. Image Processing*, vol. 18, no. 7, pp. 1477–1486, July 2009.
- [7] R. Baraniuk and P. Steeghs, "Compressive radar imaging," in *Proc. IEEE Radar Conf.*, Waltham, MA, Apr. 2007, pp. 128–133.
- [8] M. Ferrara, J. A. Jackson, and C. Austin, "Enhancement of multi-pass 3D circular SAR images using sparse reconstruction techniques," in *Algorithms for Synthetic Aperture Radar Imagery XVI*, ser. Proc. SPIE, E. G. Zelnio and F. D. Garber, Eds., vol. 7337, Orlando, FL, Apr. 2009, p. 733702.
- [9] S. Samadi, M. Çetin, and M. A. Masnadi-Shirazi, "Sparse representation-based synthetic aperture radar imaging," *IET Radar, Sonar Navigat.*, vol. 5, no. 2, pp. 182–193, Feb. 2011.
- [10] I. Stojanović, "Sparse reconstruction in monostatic and multistatic SAR," Ph.D. dissertation, Dept. Electrical and Comput. Engin., Boston Univ., 2012.
- [11] L. C. Potter, P. Schniter, and J. Ziniel, "Sparse reconstruction for radar," in *Algorithms for Synthetic Aperture Radar Imagery XV*, ser. Proc. SPIE, E. G. Zelnio and F. D. Garber, Eds., vol. 6970, Orlando, FL, Mar. 2008, p. 697003.
- [12] G. Xu, M. Xing, L. Zhang, Y. Liu, and Y. Li, "Bayesian inverse synthetic aperture radar imaging," *IEEE Geosci. Remote Sensing Lett.*, vol. 8, no. 6, pp. 1150–1154, Nov. 2011.
- [13] O. Batu and M. Cetin, "Parameter selection in sparsity-driven SAR imaging," *IEEE Trans. Aerosp. Electron. Syst.*, vol. 47, no. 4, pp. 3040–3050, Oct. 2011.
- [14] M. Çetin and A. Lanterman, "Region-enhanced passive radar imaging," *IEE Proc. Radar, Sonar Navigat.*, vol. 152, no. 3, pp. 185–194, June 2005.
- [15] X. Tan, W. Roberts, J. Li, and P. Stoica, "Sparse learning via iterative minimization with application to MIMO radar imaging," *IEEE Trans. Signal Processing*, vol. 59, no. 3, pp. 1088–1101, Mar. 2011.
- [16] W. Rao, G. Li, X. Wang, and X.-G. Xia, "Adaptive sparse recovery by parametric weighted L_1 minimization for ISAR imaging of uniformly rotating targets," *IEEE J. Select. Topics Appl. Earth Observ. Remote Sensing*, vol. 6, no. 2, pp. 942–952, Apr. 2013.
- [17] M. G. Amin and F. Ahmad, "Compressive sensing for through-the-wall radar imaging," *J. Electron. Imag.*, vol. 22, no. 3, p. 030901, July 2013.
- [18] N. Ramakrishnan, E. Ertin, and R. Moses, "Enhancement of coupled multichannel images using sparsity constraints," *IEEE Trans. Image Processing*, vol. 19, no. 8, pp. 2115–2126, Aug. 2010.
- [19] A. Budillon, A. Evangelista, and G. Schirrinzi, "Three-dimensional SAR focusing from multipass signals using compressive sampling," *IEEE Trans. Geosci. Remote Sensing*, vol. 49, no. 1, pp. 488–499, Jan. 2011.
- [20] X. X. Zhu and R. Bamler, "Tomographic SAR inversion by L_1 -norm regularization—The compressive sensing approach," *IEEE Trans. Geosci. Remote Sensing*, vol. 48, no. 10, pp. 3839–3846, Oct. 2010.
- [21] J. Jackson and R. Moses, "Synthetic aperture radar 3D feature extraction for arbitrary flight paths," *IEEE Trans. Aerosp. Electron. Syst.*, vol. 48, no. 3, pp. 2065–2084, July 2012.
- [22] W. G. Carrara, R. M. Majewski, and R. S. Goodman, *Spotlight Synthetic Aperture Radar: Signal Processing Algorithms*. Norwood, MA: Artech House, 1995.
- [23] R. L. Moses, L. Potter, and M. Çetin, "Wide angle SAR imaging," in *Algorithms for Synthetic Aperture Radar Imagery XI*, ser. Proc. SPIE, E. G. Zelnio and F. D. Garber, Eds., vol. 5427, Orlando, FL, Apr. 2004, pp. 164–175.
- [24] A. Fasoula, H. Driessen, and P. van Genderen, "De-ghosting of tomographic images in a radar network with sparse angular sampling," in *Proc. European Radar Conf.*, Rome, Italy, Sept.–Oct. 2009, pp. 286–289.
- [25] C. D. Austin, E. Ertin, and R. L. Moses, "Sparse signal methods for 3-D radar imaging," *IEEE J. Select. Topics Signal Processing*, vol. 5, no. 3, pp. 408–423, June 2011.
- [26] K. R. Varshney, M. Çetin, J. W. Fisher III, and A. S. Willsky, "Sparse representation in structured dictionaries with application to synthetic aperture radar," *IEEE Trans. Signal Processing*, vol. 56, no. 8, pp. 3548–3561, Aug. 2008.
- [27] I. Stojanović, M. Çetin, and W. C. Karl, "Joint space aspect reconstruction of wide-angle SAR exploiting sparsity," in *Algorithms for Synthetic Aperture Radar Imagery XV*, ser. Proc. SPIE, E. G. Zelnio and F. D. Garber, Eds., vol. 6970, Orlando, FL, Mar. 2008, p. 697005.
- [28] G. B. Hammond and J. A. Jackson, "SAR canonical feature extraction using molecule dictionaries," in *Proc. IEEE Radar Conf.*, Ottawa, Canada, Apr.–May 2013.
- [29] T. C. Calloway and G. Donohoe, "Subaperture autofocus for synthetic aperture radar," *IEEE Trans. Aerosp. Electron. Syst.*, vol. 30, no. 2, pp. 617–621, Apr. 1994.
- [30] C. V. Jakowatz, D. E. Wahl, P. S. Eichel, D. C. Ghiglia, and P. A. Thompson, *Spotlight-Mode Synthetic Aperture Radar: A Signal Processing Approach*. Norwell, MA: Kluwer Academic, 1996.
- [31] J. H. G. Ender, "Autofocusing ISAR images via sparse representation," in *Proc. European Conf. Synthetic Aperture Radar*, Nuremberg, Germany, Apr. 2012, pp. 203–206.
- [32] J. Duan, L. Zhang, and M. Xing, "A weighted eigenvector autofocus method for sparse-aperture ISAR imaging," *EURASIP J. Adv. Signal Process.*, vol. 2013, p. 92, Apr. 2013.
- [33] T. Jihua and Z. Bingchen, "Motion compensation for compressive sensing SAR imaging with autofocus," in *Proc. IEEE Conf. Industrial Electronics and Applications (ICIEA)*, Beijing, China, June 2011, pp. 1564–1567.
- [34] N. O. Önhon and M. Çetin, "A sparsity-driven approach for joint SAR imaging and phase error correction," *IEEE Trans. Image Processing*, vol. 21, no. 4, pp. 2075–2088, Apr. 2012.
- [35] S. I. Kelly, M. Yaghoobi, and M. E. Davies, "Auto-focus for under-sampled synthetic aperture radar," in *Proc. Sensor Signal Processing for Defence (SSPD)*, London, Sept. 2012.
- [36] S. Uğur and O. Arıkan, "SAR image reconstruction and autofocus by compressed sensing," *Digital Signal Process.*, vol. 22, no. 6, pp. 923–932, Dec. 2012.
- [37] S.-J. Wei and X.-L. Zhang, "Sparse autofocus recovery for under-sampled linear array SAR 3-D imaging," *Prog. Electromagn. Res.*, vol. 140, pp. 43–62, 2013.
- [38] I. Stojanović and W. Karl, "Imaging of moving targets with multi-static SAR using an overcomplete dictionary," *IEEE J. Select. Topics Signal Processing*, vol. 4, no. 1, pp. 164–176, Feb. 2010.
- [39] S. Zhu, A. M. Djafari, H. Wang, B. Deng, X. Li, and J. Mao, "Parameter estimation for SAR micromotion target based on sparse signal representation," *EURASIP J. Adv. Signal Process.*, vol. 2012, p. 13, Jan. 2012.
- [40] A. S. Khwaja and J. Ma, "Applications of compressed sensing for SAR moving-target velocity estimation and image compression," *IEEE Trans. Instrum. Meas.*, vol. 60, no. 8, pp. 2848–2860, Aug. 2011.
- [41] Q. Wu, M. Xing, C. Qiu, B. Liu, Z. Bao, and T.-S. Yeo, "Motion parameter estimation in the SAR system with low PRF sampling," *IEEE Geosci. Remote Sensing Lett.*, vol. 7, no. 3, pp. 450–454, 2010.
- [42] N. Ö. Önhon and M. Çetin, "SAR moving target imaging in a sparsity-driven framework," in *Proc. SPIE Optics+Photonics, Wavelets and Sparsity XIV*, ser. Proc. SPIE, M. Papadakis, D. Van De Ville, and V. K. Goyal, Eds., 2011, vol. 8138, p. 813806.
- [43] J. Zhang, D. Zhu, and G. Zhang, "Adaptive compressed sensing radar oriented toward cognitive detection in dynamic sparse target scene," *IEEE Trans. Signal Processing*, vol. 60, no. 4, pp. 1718–1729, Apr. 2012.
- [44] F. Ahmad and M. Amin, "Through-the-wall human motion indication using sparsity-driven change detection," *IEEE Trans. Geosci. Remote Sensing*, vol. 51, no. 2, pp. 881–890, Feb. 2013.
- [45] D. L. Donoho, "Compressed sensing," *IEEE Trans. Inform. Theory*, vol. 52, no. 4, pp. 1289–1306, Apr. 2006.
- [46] D. L. Donoho and M. Elad, "Optimally sparse representation in general (nonorthogonal) dictionaries via ℓ_1 minimization," *Proc. Natl. Acad. Sci.*, vol. 100, no. 5, pp. 2197–2202, Mar. 2003.
- [47] I. Stojanović, M. Çetin, and W. C. Karl, "Compressed sensing of monostatic and multistatic SAR," *IEEE Geosci. Remote Sensing Lett.*, vol. 10, no. 6, pp. 1444–1448, June 2013.
- [48] V. Patel, G. Easley, D. Healy, and R. Chellappa, "Compressed synthetic aperture radar," *IEEE J. Select. Topics Signal Processing*, vol. 4, no. 2, pp. 244–254, Apr. 2010.
- [49] J. Tropp, "Just relax: Convex programming methods for identifying sparse signals in noise," *IEEE Trans. Inform. Theory*, vol. 52, no. 3, pp. 1030–1051, Mar. 2006.
- [50] M. Herman and T. Strohmer, "High-resolution radar via compressed sensing," *IEEE Trans. Signal Processing*, vol. 57, no. 6, pp. 2275–2284, June 2009.
- [51] J. Romberg, "Compressive sensing by random convolution," *SIAM J. Imag. Sci.*, vol. 2, no. 4, pp. 1098–1128, Oct. 2009.
- [52] N. Subotic, B. Thelen, K. Cooper, W. Buller, J. Parker, J. Browning, and H. Beyer, "Distributed RADAR waveform design based on compressive sensing considerations," in *Proc. IEEE Radar Conf.*, Rome, Italy, May 2008.
- [53] C. Chen and P. Vaidyanathan, "Compressed sensing in MIMO radar," in *Proc. Asilomar Conf. Signals, Systems and Computers*, Pacific Grove, CA, Oct. 2008, pp. 41–44.
- [54] T. Strohmer and B. Friedlander, "Compressed sensing for MIMO radar—Algorithms and performance," in *Proc. Asilomar Conf. Signals, Systems and Computers*, Pacific Grove, CA, Nov. 2009, pp. 464–468.
- [55] Y. Yu, A. Petropulu, and H. Poor, "MIMO radar using compressive sampling," *IEEE J. Select. Topics Signal Processing*, vol. 4, no. 1, pp. 146–163, Feb. 2010.
- [56] Air Force Research Laboratory, Sensor Data Management System, Moving and Stationary Target Acquisition and Recognition (MSTAR) data set. [Online]. Available: <https://www.sdms.af.mil/index.php?collection=mstar>
- [57] Astrium TerraSAR-X sample imagery. [Online]. Available: <http://www.astrium-geo.com/en/23-sample-imagery>
- [58] Air Force Research Laboratory, Sensor Data Management System, Civilian Vehicle Radar Data Domes. [Online]. Available: https://www.sdms.af.mil/index.php?collection=cv_dome
- [59] Air Force Research Laboratory, Sensor Data Management System, Gotcha Volumetric SAR data set. [Online]. Available: <https://www.sdms.af.mil/index.php?collection=gotcha>

Gianfranco Fornaro, Fabrizio Lombardini, Antonio Pauciuolo,
Diego Reale, and Federico Viviani

Tomographic Processing of Interferometric SAR Data

[Developments, applications, and future research perspectives]

Synthetic aperture radar (SAR) data processed with interferometric techniques are widely used today for environmental risk monitoring and security. SAR tomography techniques are a recent advance that provide improved three-dimensional (3-D)

reconstruction and long-term deformation monitoring capabilities. This article is meant to discuss the main developments achieved in the last few years in the SAR tomography framework, with particular reference to both urban and forest scenarios. An insight on classical multipass interferometric processing is also included to summarize the importance of the technology for natural hazards monitoring and to provide the basis for the description of SAR tomography.

INTRODUCTION

SAR synthesizes a large antenna along the movement direction to provide images at microwaves with resolutions comparable with those achieved with optical sensors but with the advantage of day–night and all-weather acquisition capabilities [1]. Interferometric SAR (InSAR) techniques exploit angular imaging diversity, offered by vertical spatial orbit, flight track, or antenna position offsets (spatial baselines), to reconstruct the scene topography: the technology is cost effective in terms of coverage/accuracy [2] and has been also used to map the Earth topography on a global scale [1]. The typical

satellite-enabled regular and systematic data acquisition plays a key role in applications to environmental risk monitoring and security. In particular, differential interferometry (DInSAR) can reveal Earth displacements to a subcentimeter accuracy and has been widely used for the analysis of large deformations, for instance,

associated with main earthquakes.

In the last decade, the development of algorithms [1], [3]–[5] able to process large stacks of multipass interferometric SAR images relevant to an area of interest has also allowed the monitoring of slow and long-term movements, for instance, of landslides and subsidence, e.g., due to mining and water/oil extraction. SAR tomography techniques are a recent advance that “turn” interferometric methods into

(multidimensional) imaging [6]–[11]. By exploiting acquisitions collected with multiple spatial base-

lines and temporal separation (temporal baselines), these techniques allow the implementation of a synthetic fine beam (radar) scanner along the vertical direction for full 3-D scene reconstruction [6]–[8], as well as for slow, long-term deformation monitoring in complex areas [9]–[11], i.e., four-dimensional (4-D) (3-D+time) imaging.

The 3-D imaging (focusing) enables the investigation of the scene scattering structure along the vertical direction, which is not possible with neither conventional two-dimensional (2-D) SAR imaging nor with InSAR. This is an important feature for applications where the scattering is distributed along the height, for instance, for application to forests and glaciers

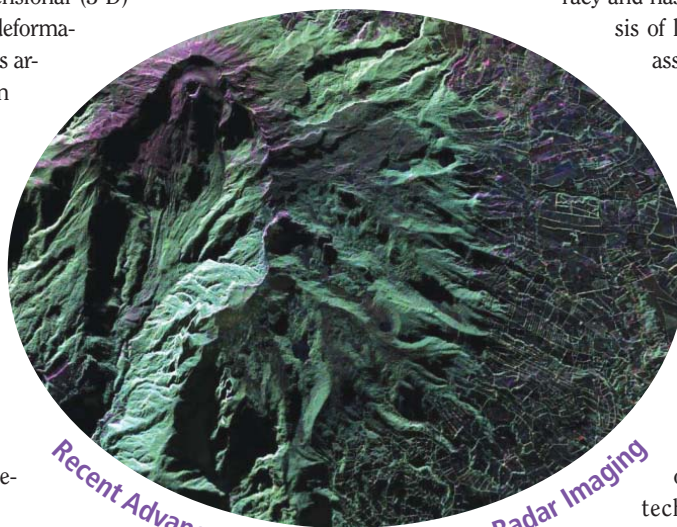


PHOTO COURTESY OF NASA

Recent Advances in Synthetic Aperture Radar Imaging

Digital Object Identifier 10.1109/MSP.2014.2312073

Date of publication: 13 June 2014

INSIGHTS ON SAR INTERFEROMETRY

SAR interferometry exploits at least two SAR images acquired with angular or time diversity to estimate the scene topography or the possible displacements of ground targets [2]. The key principle is the use of the phase difference between complex SAR images for the accurate measurement (to a subwavelength accuracy) of the radiation traveled path variation (path difference) in the two images. For images acquired simultaneously from multiple sensors or from multiantenna platforms (single-pass interferometry) observing the scene with slightly different incidence angles (across-track interferometry), such a measurement allows, on one hand, estimating the scatterer elevation s , i.e., the scene topography. On the other hand, when images are acquired through different passes (repeat-pass acquisitions) the path difference is used to measure possible displacements of the target even due to slow deformation with sub-cm accuracy (differential SAR interferometry, DInSAR).

We refer to (1), that in the hypothesis of high azimuth and range resolution, is the most general expression of the complex signal received at different antennas. Assuming the presence of a single scatterer at elevation s , the phase of the complex interference between a pair of acquisitions g_1 and g_2 is

$$\varphi = \arg[g_2^* g_1] = \frac{4\pi}{\lambda} \frac{b}{r} s + \frac{4\pi}{\lambda} d + \varphi_a + \varphi_\gamma + \varphi_w, \quad (S1)$$

wherein b is the orthogonal baseline difference between the acquisitions and d is the scatterer displacement. All remaining terms are error sources: φ_γ and φ_a are the backscattering phase change and the atmospheric phase delay (APD) variation between the two acquisitions, respectively, and φ_w is the phase contribution of the thermal noise.

On one side, simultaneous or quasi-simultaneous acquisitions (in the absence of fast target movements) makes both φ_a and d be zeroed: the system is able to measure, pixel by pixel, s , and therefore to generate accurate digital elevation models. On the opposite side, for $b \approx 0$, the systems is able to measure d provided that the associated component has a dynamic larger than φ_a (for instance, displacements associated with earthquakes). In the case of large b , an external digital elevation model (DEM) must be used to subtract (DInSAR) the term related to the topography thus reducing the variation of s . The possibilities mentioned above are feasible when φ_γ and φ_w do not overwhelm the useful signal component.

Effects of φ_w are "felt" generally in areas characterized by low backscattering; on the other hand, effects of φ_γ are, as speckle, independent on the target backscattering magnitude and relate to decorrelation, which originates from imaging

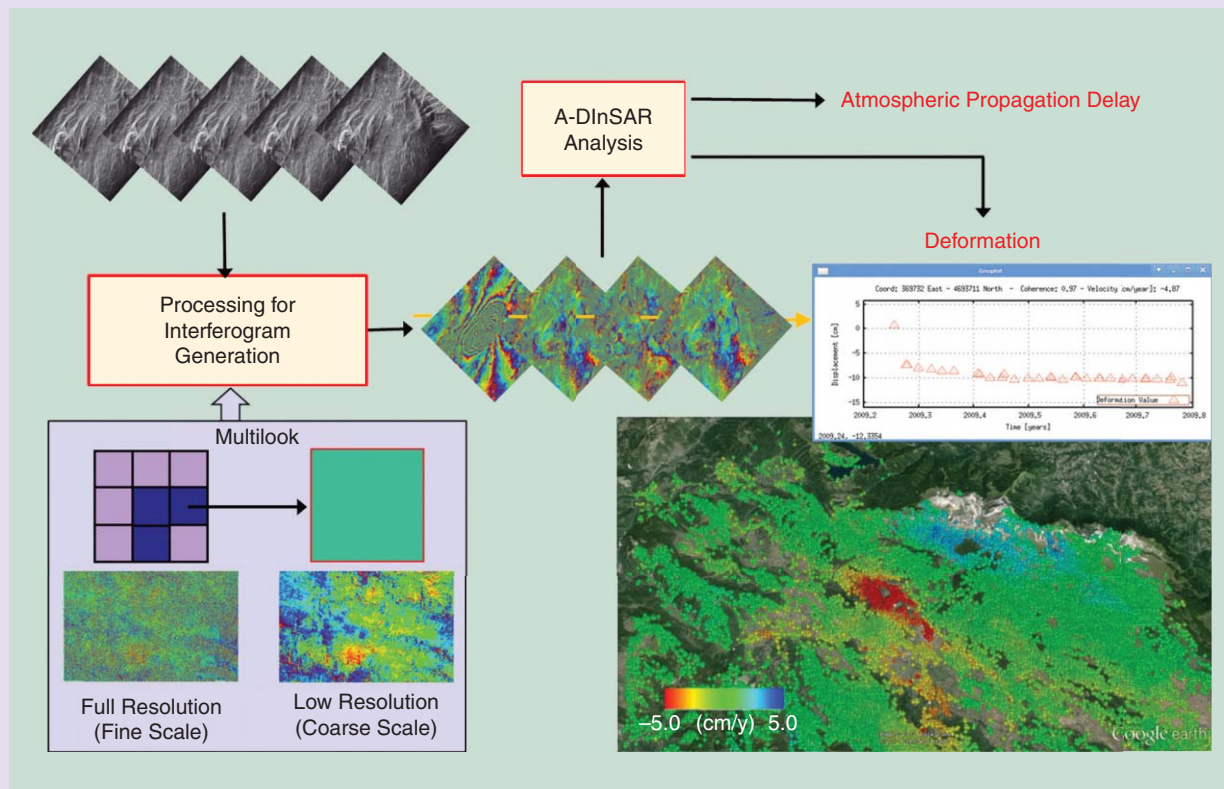
angular variations (even associated with small variation of the target incidence or aspect angles) or from temporal backscattering changes. In the former case, the phenomenon is referred to as angular decorrelation, whereas in the latter case it is referred to as temporal decorrelation. The image cross correlation index, specifically its amplitude (coherence), evaluated on a pixel-by-pixel basis through a suitable complex multilooking, provides a way to quantify the decorrelation and is used to discriminate between reliable and unreliable regions for interferometric processing [1], [2].

The APD shows, unfortunately, spatial correlation and cannot be mitigated, as thermal noise, via spatial multilooking. The only possibility to separate it from the deformation signal is provided by the use of multiple observations at different times: in such a case the APD can be estimated via advanced DInSAR (A-DInSAR) techniques and compensated essentially by exploiting its different temporal statistics (typically uncorrelated over the epochs). A-DInSAR techniques, which allow APD removal and measurement of deformation time series (Figure S1), are essentially divided in two classes: the DInSAR stacking techniques and the PSI, which rely on different assumptions about the ground scattering. DInSAR stacking methods, such as the small baseline subset [4] and the coherent point targets [5], assume the scattering to be spatially distributed over the resolution cell and are based on the exploitation of both only small baseline interferograms (hard baseline thresholding) and spatial coherent multilook to limit the effects of decorrelation (8); see Figure S1. They are tailored to the monitoring of wide areas, including rural areas with slow temporal correlation losses. On the other hand PSI, such as the PSInSAR [3], [28] assumes the presence of dominant scatterers (8) and uses all (i.e., also large) baselines to achieve high accuracy in the localization of targets for precise and accurate monitoring of man-made structures. Differently from SAR tomography, PSI methods are essentially phase model-based, i.e., do not use the amplitude information for estimating the target position and deformation parameters. Moreover, besides an early work on separation of double scatterers moving with the same velocity proposed in [29], precursor of the application of tomographic methods for layover solution over vertical buildings, they assume the presence of a single persistent scatterer per resolution cell.

Recently a new approach, SqueeSar, has been introduced [23]: it relies on the use of the data covariance matrix, estimated by spatial adaptive averaging (Figure S1) to implement a soft and adaptive baseline threshold aimed at handling both the distributed and the dominant scatterers model. A principle

(sensed by P- and L-band sensors [6]) which is of paramount importance in the climate change issues. With reference to forest applications it is worth noting that the European Space Agency is developing a dedicated satellite (BIOMASS Earth Explorer mission) operating at P-band. Multidimensional (MultiD) SAR imaging also benefits from the fine beam vertical scanning capabilities to investigate complex man-made scenes, such as urban areas and infrastructures, where perspective distortions

due to the radar imaging geometry frequently occur and lead to interference of the response of multiple scatterers relevant to different ground structures mapped in the same image pixel. This typical layover effect dramatically impairs urban areas and, in particular, data of high- and very high-resolution systems such as the recent X-band TerraSAR-X (TSX) and Cosmo-Skymed (CSK) missions, due to the spread of the effect over a large number of pixels.



[FIGS1] The multipass DInSAR processing scheme. Deformation measurements are separated by the APD by analyzing stacks of interferograms generated by multiple SAR observations. The multilook operation, which can be carried out adaptively, is used to trade off the scale of analysis (fine and coarse scale) and the mitigation of noise. The images on the right (deformation map and deformation time series) show an example of application of the technique to postseismic monitoring typically associated with main earthquakes.

of optimal coherent SAR data combination, for accurate multi-baseline interferometry exploiting also amplitude information for the reconstruction of the single scatterers heights and accounting for the distributed scattering, had been also first introduced; see modeling in [7] and introductory comments in [18], and references therein.

In all of the processing approaches, a critical step is the phase unwrapping (PhU) that must be handled to access the absolute phase measurements. The availability of a 2-D (typically sparse) spatial grid can be favorably exploited to perform PhU on spatially redundant networks. The latest-generation algorithms developed for multipass/multibaseline also exploits the redundancy of interferograms to improve the PhU step; see, e.g.,

[30] and other similar noncited (to limit the number of references in the article) recently published papers.

To show the importance of SAR interferometry for monitoring natural hazards, the images in the right part of Figure S1 are provided to show a sample of the DInSAR stacking product in the region of L'Aquila (Italy) hit by the 2009 Mw 6.2 earthquake: the colors of the map are associated with the deformation mean velocity evaluated only on the postseismic acquisitions, and the plotted time series shows the possibility to identify and monitor also postseismic effects that typically lead to an exponential decrease of the deformation over time. Results were obtained by processing 33 CSK images between April and October 2009.

By solving the layover problem, today SAR tomography techniques offer a unique tool [11]–[13] to carry out accurate 3-D reconstruction and long-term slow displacements monitoring of even single-built structures, which can be useful for security and long-term structural health-monitoring issues.

The article is meant to provide a concise overview of SAR interferometry and, together with the companion article [31] focused on the use of compressive sensing (CS), of the devel-

opments of SAR tomography. The experiments' results on real data are provided for both airborne and spaceborne SAR sensors to give a flavor of the application scenarios of the described techniques. Multiple polarization and polarimetric processing approaches have been also employed in the SAR tomography context, leading to polarimetric SAR tomography [14]–[16], however, this topic is outside the scope of this article.

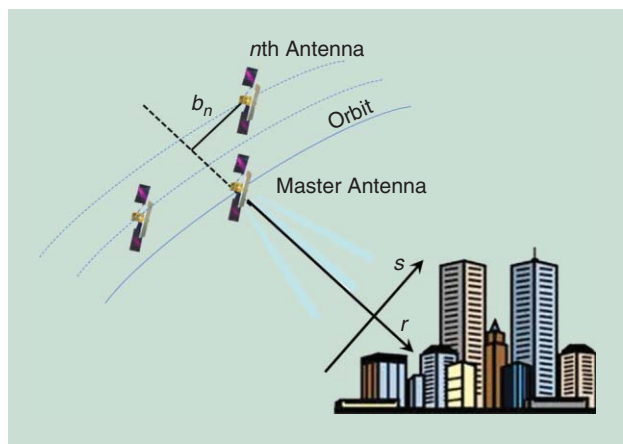


[FIG1] Tomographic SAR and reference geometry.

SIGNAL MODELS

The multiacquisition SAR geometry is depicted in Figure 1 in the slant range r -slant height (elevation) s plane, which is defined with respect to a reference ground plane and is orthogonal to the azimuth direction (x), this latter being coincident with the track of a reference master antenna. Assuming parallel antenna tracks (typically obtained by multiple passes with current satellite and airborne technologies), b_n in Figure 1 ($n = 0, \dots, N - 1$) is the orthogonal component of the baseline connecting the n th antenna to the master one.

For a generic n th acquisition (at time t_n), after the application of a standard azimuth-range (2-D) raw SAR focusing, the complex values g_n of each (x, r) image pixel is the superposition of multiple elementary backscattering contributions described by the distribution of the complex amplitude of the scattering $\gamma_n(s)$ along s (at t_n)

$$g_n = e^{j\varphi_a(n)} \int_{I_s} \gamma_n(s) e^{j\frac{4\pi}{\lambda} \frac{b_n s}{r}} e^{j\frac{4\pi}{\lambda} d(s, t_n)} ds + w_n, \quad (1)$$

where

- $e^{j\varphi_a(n)}$ is the term associated with the atmospheric phase delay variation caused by the propagation of the radiation in the atmosphere
- λ is the radar wavelength
- I_s is the scene extension in the slant height direction
- $d(s, t_n)$ is the deformation signal at epoch t_n (positive toward the sensor) affecting the generic scatterer at elevation s
- w_n is the noise term in the focused pixel accounting for thermal noise, which has a strong impact in low backscatter areas.

As anticipated in the introduction, the model we consider refers to the single polarization case.

In the following, we neglect the term φ_a by assuming that the atmospheric contribution is compensated through a preliminary standard multipass interferometric processing (data calibration) [10], as depicted in the left part of the tomographic processing block diagram in Figure 2. In “Insights on SAR Interferometry,” details are provided on the data

calibration step and, in general, on the main issues related to InSAR and DInSAR for application to digital elevation model generation and monitoring of surface deformation, which have significantly pushed the development of the SAR technology. The double-framework, i.e., interferometric and tomographic, description is fundamental to clarify that the latter (SAR tomography) must be considered as a tool that enhances the former (SAR interferometry) with reference to specific applications, e.g. urban areas, infrastructures, and forest.

With reference to (1), the particular case of simultaneous acquisitions implying the absence of temporal diversity, i.e., t_n fixed, or alternatively of the absence of any deformation (and temporal backscattering change), leads to the classical tomographic (3-D) framework

$$g_n = \int_{I_s} \gamma(s) e^{+j\frac{4\pi}{\lambda} \frac{b_n s}{r}} ds + w_n. \quad (2)$$

Equation (2) constitutes a Fourier transform (FT) operator. Two different equivalent visions can be considered depending on the choice of the transformation pairs:

$$\{s, \xi_n = -2b_n/(\lambda r)\} \quad \{b_n, f_s = 2s/(\lambda r)\}. \quad (3)$$

In a first vision, the sequence g_n is a (sampled) spatial spectrum, at frequencies ξ_n , of the (tomographic) scene, with $\gamma(s)$ being the (spatial) signal; this is the so-called wavenumber domain frame. Dually, in a second vision, the data sequence g_n is the spatial (baseline) sampled signal, while $\gamma(s)$ is a spatial spectrum (elevation scattering distribution) in the variable spatial frequencies f_s : this frame can be termed *spectral analysis*, or *SPECAN*, vision and is also used in array signal processing [direction of arrival (DOA) estimation] [7]. For this reason it is also referred to as *array processing-based vision*.

In the more general and frequent case of acquisitions carried out with multiple passes at time t_n , the deformation term cannot be neglected. By introducing the conjugate variable v having the dimensions of a velocity (m/s), the second exponential term in (1), related to motion of the scatterer at elevation s , can be expanded in Fourier harmonics with Fourier conjugate variables $\{v, \eta_n = -2t_n/\lambda\}$ as follows:

$$e^{j\frac{4\pi}{\lambda} d(s, t_n)} = \int_{I_v} h(s, v) e^{j2\pi v 2t_n/\lambda} dv, \quad (4)$$

where $h(s, v)$ plays in v the role of the spectrum of the motion-related signal for elevation s . Note that the decomposition in (4) is analogous to the quick-time Doppler spectrum used in surveillance radars, which can be expressed as a distribution of spectral velocities (“equivalent velocities”). This effect was exemplified for a jittered motion in [9]. It is also worth noting that, as happens for Doppler spectra, the spectral velocity variable v in the $h(s, v)$ distribution is not an instantaneous (deformation) velocity; the difference between the two velocities is exactly that associated with spectral and instantaneous frequencies in the common signal theory and frequency modulation

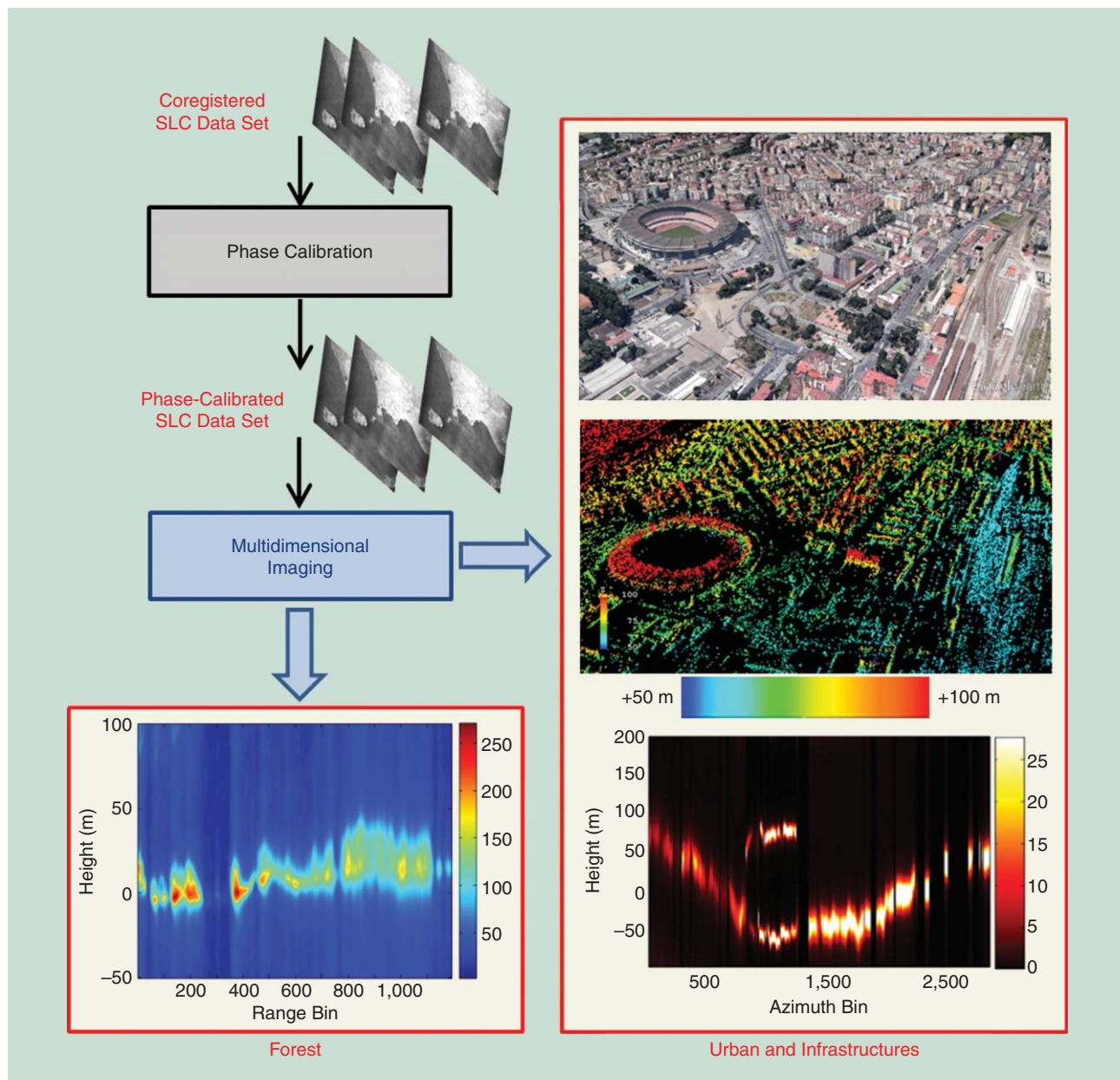


[FIG2] A scheme of the SAR tomography processing for forest and urban/infrastructures scenarios.

context. In particular, in the case of uniform deformation motion at a given s , where the motion-related signal in (4) is a pure complex sinusoid, the spectral velocity turns to be a single one (i.e., h is δ Dirac-shaped along v) and coincides with the constant velocity of the motion. On the other hand, the presence of a peak at a given spectral velocity \bar{v} corresponds to a scatterer motion with a deformation mean velocity of \bar{v} .

The substitution of (4) in (1) leads to

$$g_n = \iint_{s,v} \gamma_n(s,v) e^{j\frac{4\pi}{\lambda} \frac{b_n s}{r}} e^{j\frac{4\pi v t_n}{\lambda}} ds dv + w_n, \quad (5)$$

where $\gamma_n(s,v) = \gamma_n(s)h(s,v)$ is the backscattering distribution in the (s,v) plane.

Equation (5) describes what is known as differential-tomography (4-D) model [9]–[11]. It shows that a 2-D FT relation stands between the data g_n , which notably are typically irregularly sampled both in the baseline and temporal domains and the backscattering distribution. Similar to the 3-D case, a dual vision is possible by introducing, in addition to (3), the two following FT variables pairs:

$$\{v, \eta_n = -2t_n/\lambda\} \quad \{t_n, f_t = 2v/\lambda\}, \quad (6)$$

wherein, the use of the left variable pair leads to the wavenumber vision, whereas the use of the right variable pairs refer to the array processing vision.

Accordingly, (5), (3), and (6) show that, in the presence of deformations, the 3-D model in (2) is extended to the velocity domain and involves a 2-D FT in both elevation and velocity.

The (3-D/4-D) tomography problem consists of the estimation, in each image pixel, of the scene backscattering profile $\gamma(s)$, or of the backscattering distribution $\gamma(s, v)$, starting from the N samples g_n : it involves, in the most general case, the inversion of (5), that is a spectral analysis of the data.

Equation (5) represents the most general (4-D) imaging model. Nevertheless some important particularizations are useful to link to classical concepts, well known in the InSAR and DInSAR context, as well as for the developments of advanced 3-D/4-D imaging methods. In particular, to link to the classical persistent scatterers (PS) approach [3], a temporal invariant ($\gamma_n = \gamma$) and concentrated nature of the scattering is assumed. With reference to the application to urban areas and particularly with high frequency systems (for instance, C-band and X-band sensors), due to frequent occurrence of the layover, the backscattering profile can be in fact assumed to be composed by a finite number K of δ -Dirac functions in the (s, v) domain (line spectrum) centered in the different elevation/velocity scatterers phase centers (s_k, v_k) . Under this assumption $\gamma(s, v) = \sum_{k=0}^{K-1} \gamma_k \delta(s - s_k) \delta(v - v_k)$, where γ_k is the complex amplitude of the k th scatterer, and the 4-D model in (5) (including the 3-D case) reduces to

$$\mathbf{g} = \sqrt{N} \sum_{k=0}^{K-1} \mathbf{a}(s_k, v_k) \gamma_k + \mathbf{w}, \quad (7)$$

where $\mathbf{g} = [g_0, \dots, g_{N-1}]^T$ is the vector collecting, for each pixel, the measured complex data, $\mathbf{w} = [w_0, \dots, w_{N-1}]^T$ collects the noise contribution at each acquisition (T defines the transposition operator) and $\mathbf{a}(s, v)$ can be termed *steering vector*, as from the array processing area, and its elements are defined as $[\mathbf{a}(s, v)]_n = \exp[-j2\pi(\xi_n s + \eta_n v)] / \sqrt{N}$ for the generic elevation/velocity pair (s, v) . We refer to (7) as the *fully coherent* (concentrated, i.e., pointlike, and time invariant) *scattering model*.

In real cases, the scattering cannot be always assumed to be concentrated at discrete heights, thus leading to angular (spatial baseline) decorrelation; even more important, it cannot be considered invariant over the time (temporal decorrelation) [1][2]. We refer therefore to (5) and restore the dependence of the backscattering over time and suppose the scattering to be distributed over "small" elevation intervals $\Delta_{s,k}$ (compact scatterers) centered in s_k and moving with velocity v_k . In this case we have [7], [17]

$$\mathbf{g} = \sqrt{N} \sum_{k=0}^{K-1} \mathbf{a}(s_k, v_k) \odot \boldsymbol{\gamma}_k + \mathbf{w}, \quad (8)$$

where \odot denotes the Hadamard (element-by-element) product and $\boldsymbol{\gamma}_k = [\gamma_{k,0}, \dots, \gamma_{k,N-1}]^T$, with $\gamma_{k,n} = \int_{\Delta_{s,k}} \gamma_n(s) \exp[j2\pi\xi_n(s - s_k)] ds$, is a vector collecting the (angularly decorrelating and time-variant speckled) realizations of the k th scattering as seen at the N tracks. The decorrelation property of the scatterer, including compact time-invariant, concentrated time-variant, and more generally compact time-variant scattering will be statistically described through the correlation

matrix defined as $\mathbf{R}_{\gamma_k} = E[\boldsymbol{\gamma}_k \boldsymbol{\gamma}_k^H]$. The particular case in which $\mathbf{R}_{\gamma_k} = E[|\gamma_k|^2] \mathbf{1}_N \mathbf{1}_N^T$, where $\mathbf{1}_N$ is the N -dimensional unity vector and $E[|\gamma_k|^2]$ is the (possibly temporally averaged) scatterer powers, leads to the (statistical) equivalence between the speckled and time variant model in (8) and the pointlike model in (7) when γ_k are random variables. For this reason, we refer to the time-variant speckled model in (8) as the *partially coherent scattering model*.

MULTIDIMENSIONAL TOMOGRAPHY IMAGING METHODS

The 3-D and 4-D SAR imaging is achieved via inversion of (2) or (5), respectively. The acquisition geometry poses limitation on the imaging capabilities which can be overcome by the use of some specific techniques. The baseline distribution defines a reliable elevation span, i.e., the maximum extension in elevation direction to avoid heavy effects of aliasing. Assuming a uniform baseline distribution with an antenna separation of Δb , the unambiguous elevation interval is $\Delta_s = \lambda r / (2\Delta b)$: in the nonuniform case Δb is typically replaced by the average baseline separation. The Rayleigh elevation resolution of the system is $\delta_s = \lambda r / (2B)$, with B being the total baseline span. In the same way, an unambiguous velocity interval and a velocity resolution can be also defined as $\Delta_v = \lambda / (2\Delta t)$ and $\delta_v = \lambda / (2T)$, where Δt and T are the average temporal separation and total temporal span, respectively.

Several techniques can be used to implement the inversion that leads to the estimation of the backscattering distribution along s or in the elevation/velocity plane (s, v) . Each is characterized by a different tradeoff between simplicity, computational efficiency, sidelobes reductions, and super-resolution capability and may be well suited for specific applications. Nonparametric methods, i.e., beamforming (BF), singular value decomposition (SVD), and adaptive Capon BF, provide flexibility of application to scenarios with any elevation backscattering profile, in particular with distributed (speckled) scatterers, and including also the pointlike scattering case. However, for 3-D imaging of forest volumes, linear methods such as SVD and nonparametric Capon BF can be well suited for handling the case of irregular baselines. On the contrary, for application to 3-D/4-D urban imaging and monitoring areas characterized by layover, super-resolution methods for compact scatterers like, e.g., multiple signal classification (MUSIC) may be better suited but require a prior determination of the scattering order for each pixel. In any case, as better specified in the following section dedicated to detection issues, with reference to this application even the simple BF performs better than classical interferometric approaches, such as persistent scatterers interferometry (PSI).

BEAMFORMING

Referring to the 3-D model in (2), the backscattering profile $\gamma(s)$ can be estimated as follows:

$$\hat{\gamma}(s) = \sum_{n=0}^{N-1} g_n [a(s)]_n^* = \mathbf{a}^H(s) \mathbf{g}, \quad (9)$$

where $(\bullet)^*$ and $(\bullet)^H$ denotes the conjugation and Hermitian operators, respectively. This technique is also usually referred to as

(classical) BF in array processing or matched filter. Extension to the 4-D case of estimating $\gamma(s, v)$ is easily carried out by the use of the 2-D steering vectors $\mathbf{a}(s, v)$. Hereafter, we will refer to the generic 4-D inversion problem, assuming the 3-D focusing as a special case in which all dependences on v drop out ($v = 0$).

According to (9), BF corresponds to a rephase-and-sum array processing that forms a “beam” in the elevation/velocity directions. In practical applications, as baselines are far from being uniformly distributed, BF may give poor reconstruction performances in terms of sidelobes and leakage of the point spread function. Strategies alternative to plain BF have been adopted to improve the resolution below the inherent Rayleigh limit (superresolution) and the sidelobes suppression.

SINGULAR VALUE DECOMPOSITION

The discretization of the integral in (5) is now introduced with the assumption of a temporal invariant behavior, i.e., $\gamma_n = \gamma$. Letting $\boldsymbol{\gamma} = [\gamma(s_0, v_0), \dots, \gamma(s_{M-1}, v_{M-1})]^T$ be the vector that collects the $M = M_s \times M_v$ samples of $\gamma(s, v)$ at the discrete points, hereafter called *bins*, (s_m, v_m) , $m = 0, \dots, M-1$, belonging to the $M_s \times M_v$ elevation/velocity grid, we have that the FT operator in (5) can be rewritten in the discrete case as

$$\mathbf{g} = \mathbf{A}\boldsymbol{\gamma} + \mathbf{w}, \quad (10)$$

where $\mathbf{A} = [\mathbf{a}_0, \dots, \mathbf{a}_{M-1}]^T$ is the $N \times M$ system matrix collecting the steering vectors associated with each discretization bin synthetically defined as $\mathbf{a}_m = \mathbf{a}(s_m, v_m)$.

Particularly, with reference to the fully coherent model in (7), assuming the discretization grid to include the scatterer locations in the (s, v) -plane, the vector $\boldsymbol{\gamma}$ will be characterized by only K nonzero elements at the bins corresponding to the scatterers phase centers. The case in which $K \ll M$ leads to a sparsity nature of the unknown vector $\boldsymbol{\gamma}$, which is of interest, as explained in [31], for the use of CS approaches.

The use of the SVD of the operator \mathbf{A} in (10) allows regularizing the inversion by restricting the solution space and benefiting of the inclusion of very limited a priori information on the expected scene elevation extent. The regularization, obtained through the so-called truncated SVD, allows the avoidance of noise amplification and inversion instabilities, and hence generally provides a better sidelobe reduction as well as slight super-resolution than plain BF [8], [10].

CAPON SPECTRAL ESTIMATION

To counteract the increase of sidelobes even more, 3-D and 4-D SAR focusing has been successfully set in the adaptive spectral estimation/array BF framework, in particular employing the Capon method [7], [13], [18]. As a result, (elevation) superresolution adaptive tomography methods have been developed of non-parametric kind. The strong (elevation) spatial leakage associated with the irregular baselines is significantly reduced through the adaptive nulling, which interestingly results, jointly with a sensible reduction of the anomalous sidelobes, in some elevation superresolution capabilities beyond the Rayleigh limit. This also

allows dealing with system problems of limited baseline span or of very detailed layover/volumetric analysis needs. In the general 4-D case, the data-dependent processing is based on the multi-baseline array spatial/temporal (“hybrid”) correlation matrix of the data \mathbf{R}_g [7], which requires operation with multilook data (multiple observations of the array data vector) for its estimation. The multilook operation is coherent, as in SAR interferometry, and the looks are typically obtained from multiple adjacent pixels (multilook cell). In this context, the tomographic output is the average squared modulus of $\gamma(s, v)$, $P(s, v) = E\{|\gamma(s, v)|^2\}$, which is retrieved as follows:

$$\hat{P}(s, v) = (\mathbf{a}^H(s, v)\mathbf{R}_g^{-1}\mathbf{a}(s, v))^{-1}. \quad (11)$$

In the tomographic application of the Capon beamformer, the integration of diagonal loading methods is necessary to handle problems related to the possible nonpositive-definiteness of the correlation matrix and to generally improve the inversion robustness [9]. Today, 3-D Capon tomography is a standard tool to get image enhancements beyond the above linear methods, in particular being very suitable for analyses of volumetric scatterers and thus being commonly used for forest scenes [1], [14], [15], [19].

A typical result, which shows a demonstration of the Capon tomography [7] capability to well perform 3-D focusing on forest scenarios [19], is reported in the lower left plot in Figure 2. The figure reports a tomographic slice obtained by processing nine tracks of P-band data (HV polarization) acquired with DLR E-SAR airborne platform over a boreal region in Sweden, where light temporal decorrelation effects occur.

MUSIC

Model-based beamformers matched to line spatial spectra have been applied to SAR tomography to get further performance improvements for the (urban) pointlike scatterers scenarios, revealing good capabilities even for distributed scatterers, depending on the compactness degree, despite the model approximation [7]. In particular, the spatial correlation matrix-based MUSIC method relying on the subspace decomposition [7] has been validated both for urban/infrastructure [16], [20] and forest scenarios 3-D imaging [15], [19]. In the case of compact or pointlike scatterers and nonfull yet sensible time coherence, a 2-D MUSIC estimator can be used for the 4-D case as follows [19], [21]:

$$\hat{P}(s, v) = (\mathbf{a}^H(s, v)\mathbf{Q}\mathbf{Q}^H\mathbf{a}(s, v))^{-1}, \quad (12)$$

where \mathbf{Q} is the noise eigenvector matrix and $\hat{P}(s, v)$ is a pseudospectrum.

As an example, the plot in the lower right part of Figure 2 shows an automatic-order MUSIC [7] tomogram obtained with the X-band airborne three-antenna (single-pass) system AER-II (FGAN) data [22] acquired over Weitingen, Germany. The result has been obtained by integrating an information theoretic criterion [21] order selection method exploiting the eigenvalues [7],

[22] of R_g , with eigenvalue leakage stabilized by diagonal loading [9] into the MUSIC method. In particular, being the scene constituted by a bridge crossing a valley, practically the whole bridge portion is correctly imaged jointly with the layover valley.

A significant recent advancement has been the extension for single-look processing of the Capon and MUSIC [20]: this has allowed obtaining high superresolution and sidelobe cleaning capabilities at full horizontal resolution operation. The principle relies on knowledge-based baseline interpolation [20]. These resulting methods are intrinsically computationally light with respect to CS with a processing burden very close to plain linear focusing. A typical sample of the backscattering distribution in the (s, v) plane for an urban cell obtained with 4-D single-look BF and Capon processing of CSK data is reported in Figure 3. The Capon distribution, in (b), is apparently characterized by a sub-Rayleigh double scatterer (the height distance between the two scatterers is equal to 2.5 m), going beyond the manifest resolution limits of the classical BF method shown in (a). Moreover, the Capon sidelobes level is much better than the BF one. Validation on wide regions are presented in [21], and notably

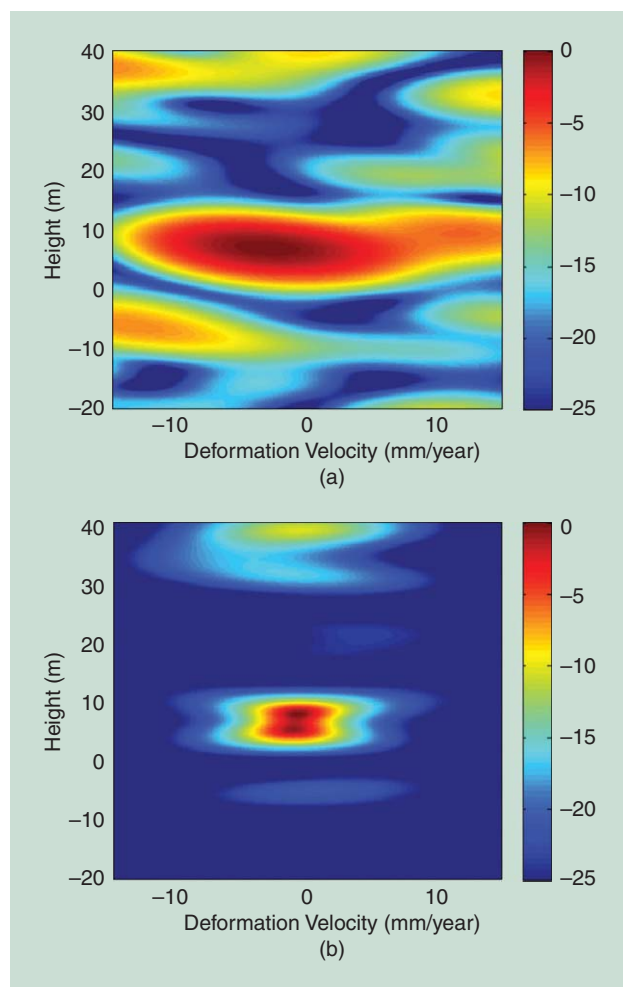


[FIG3] Four-dimensional backscattering distributions (decibels), satellite X-band CSK data: (a) BF and (b) Capon reconstructions, respectively.

the best height superresolution gain achieved is about seven times below the Rayleigh limit, the methods thus being an alternative to CS.

DETECTION OF CONCENTRATED SCATTERERS

The interpretation of the produced MultiD images requires the detection of typical pointlike scatterers where the retrieved information is reliable. Referring to the signal model in (7) with K scatterers, starting from the backscattering profile reconstructed through one of the above inversions, it is necessary to detect the generic k th scatterer in relative low signal-to-noise ratio conditions and estimate its parameters (s_k, v_k) . For the case of $K = 1$ (single scatterers) the detection problem consists in discriminating between the hypothesis \mathcal{H}_0 (absence of target) and \mathcal{H}_1 (presence of target). Under the typical Gaussian statistical modeling [2], [23], the generalized likelihood ratio test is [24]

$$\max_{(s,v)} \frac{|g^H a(s,v)|}{\|g\| \|a(s,v)\|} \underset{\mathcal{H}_0}{\overset{\mathcal{H}_1}{\geq}} T, \quad (13)$$

where T is the detection threshold, belonging to the $[0, 1]$ interval and set according to the desired level of false alarm. It is worth noting that, for single scatterers, the test statistic represents the highest peak of the normalized BF reconstruction and the argument of the maximization is the maximum likelihood estimation of the (s, v) position. Comparison of the performances of tomographic reconstruction in detecting single scatterers with the standard PSI technique [3], which is based on the use of only the phase information, i.e., by substituting g in (13) with its version obtained by considering only the phase of the elements, leads to the conclusion that the tomographic approach allows achieving significant increase of the detection probability for a fixed false alarm rate [24]. An extension to the case of $K = 2$ based on the sequential use of the detection scheme in (13) has been proposed in [25].

Results of the application of the detector in (13) on a data set of 28 CSK (3-m spatial resolution) acquisitions is shown in the middle image in the right column of Figure 2, representing the 3-D cloud of detected points over the area of the San Paolo stadium in Naples, Italy (colors are set according to the estimated height). The shapes of buildings are well recognizable: notice the comparison with the optical view of the same area taken from Google Earth, reported in the upper image in the same figure. Conversely, Figure 4 is relevant to the deformation mean velocity map estimated again through the detector in (13) on a data set of 29 CSK images over the city of Rome. In this case, the color of each point is associated with the estimated velocity. The area is affected by the presence of severe subsidence caused by consolidation of the alluvial sediments of the Tevere River and affecting the stability of buildings: it has been widely investigated with the SAR technology for geotechnical and structural reasons.

The literature provides a large number of contributions to the problem of detecting the presence of single and multiple scatterers in tomographic processing framework based also on

model order estimation strategies. As an example of application of the least square (LS) detector [13], [18], [20], 4-D single-look fitting fed by the Capon output in Figure 3(b) identifies a double scatterer, in agreement with the visual interpretation. Other 3-D/4-D extensive results of Capon-LS/MUSIC-LS detection are reported in [20] and [21] for CSK data.

CONCLUSIONS AND FUTURE RESEARCH

This work has given an overview of the main advances achieved over the last decade in the SAR interferometry/tomography areas. The basic concepts of multipass DInSAR and PSI have been summarized to provide indications about importance of such techniques for surface height mapping and monitoring in the natural risk and security areas as well as to perform the calibration steps necessary for describing the advances achieved by adopting an imaging view, i.e., SAR tomography (3-D SAR imaging) and differential SAR tomography (4-D SAR imaging) with reference to application to forest, urban, and infrastructure imaging and monitoring.

A general formulation that starts from a model also addressing the typical decorrelation problem has been introduced to provide the basis for future research accounting for target correlation properties [17], [19], and several imaging methods have been considered. Examples of results relevant to real cases for L- and P-band airborne data for application to forest imaging and latest-generation X-Band data for urban and infrastructure monitoring have been discussed, leaving to the existing litera-

ture validations that were also carried out on C-band medium-resolution data [8], [10], [13], [18], [20].

The existing SAR tomography literature also cover topics that have not been discussed due to article space limitations. This is the case of the extension of 4-D imaging to match specific nonuniform deformation motion models, e.g., of thermal building dilations associated with temperature (baseline) distribution, to get five-dimensional (4-D+temperature) single-look analyses [26], and parametric superresolution [21]. Besides, fertilization of the MultiD imaging area with Cramer-Rao bounding tools has been also given for tomographic system and mission planning; see [7] and [24]. The extension of 4-D SAR imaging for improved monitoring of thermal dilations has shown that a high correlation degree between (mainly temporal and temperature) baseline distributions may lead to detection ambiguity problems. In any case, an unnecessary increase in the dimensionality of the imaging reduces the scatterer detection performances.

Emerging research topics are related to the extension of SAR tomography to unstructured SAR tomographic and scattering decomposition methods based on principal component analysis for urban and rural area monitoring [27]. With reference to forest tomography, where nonconcentrated partially coherent scattering occurs, it is worth mentioning the possibility of exploiting 4-D imaging to obtain 3-D multipass volumetric tomographic imaging robustness to (long-term) temporal decorrelation, reducing the possible height blurring effects [19].

EMERGING RESEARCH TOPICS ARE RELATED TO THE EXTENSION OF SAR TOMOGRAPHY TO UNSTRUCTURED SAR TOMOGRAPHIC AND SCATTERING DECOMPOSITION METHODS BASED ON PRINCIPAL COMPONENT ANALYSIS.

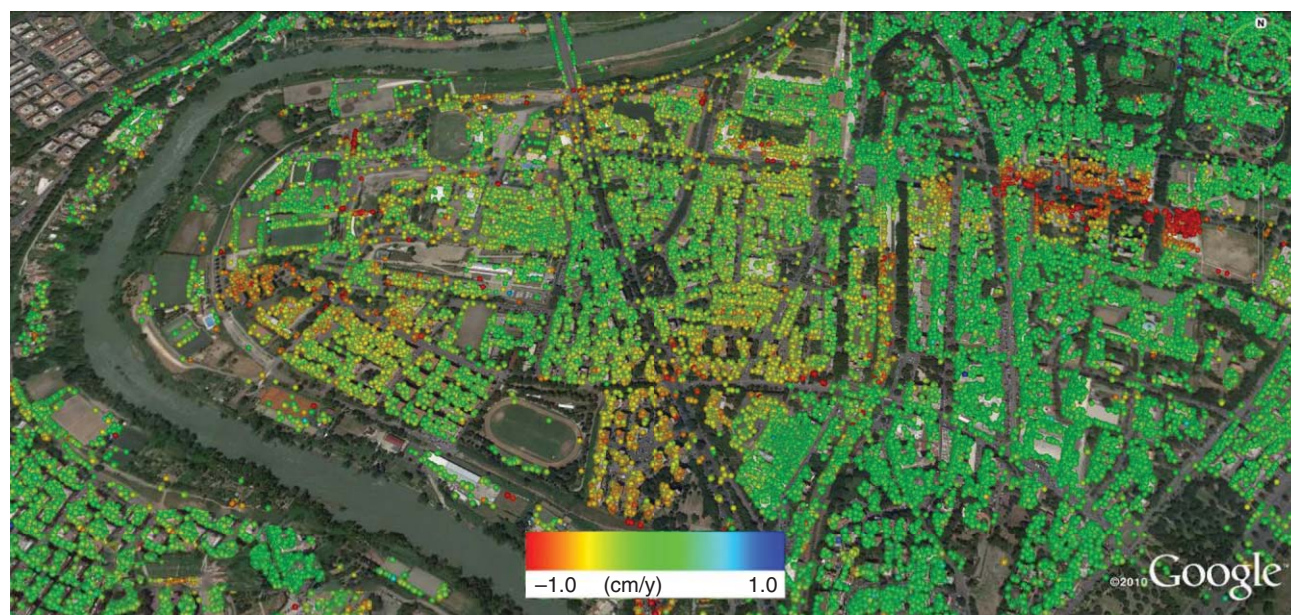


[FIG4] The deformation mean velocity of scatterers detected on the BF reconstruction on a data set of 29 CSK images over Rome. The subsidence due to consolidating alluvial-deposit close to the Tevere River is well recognizable. (Image courtesy of Google.)

ACKNOWLEDGMENTS

We wish to thank the Italian Space Agency (ASI) for providing the CSK Rome and Naples data set under the ASI AO Project ID2246 and the LAquila CSK data set under the emergency plan with the Italian Department of Civil Protection. We are also thankful to the anonymous reviewers for their valuable comments.

AUTHORS

Gianfranco Fornaro (fornaro.g@irea.cnr.it) received the M.D. degree in 1992 and the Ph.D. degree in 1997. He is a senior researcher of IREA-CNR and has achieved the full professor habilitation in 2013. He is an associate editor of *IEEE Geoscience and Remote Sensing Letters (GRSL)* and received the IEE Mountbatten Premium Award in 1997, the IEEE GRSL Best Paper Award, and the 2012 IEEE Transactions on Geoscience and Remote Sensing Mention for Best Reviewer.

Fabrizio Lombardini (f.lombardini@iet.unipi.it) received the M.D. degree in 1993 and the Ph.D. degree in 1997. He is a senior assistant professor at the Department of Information Engineering at the University of Pisa, Italy, and achieved the associate professor habilitation in 2013. He originated the differential synthetic aperture radar tomography framework and received the Best Remote Sensing Paper Award on this topic at the annual GTTI Meeting in 2009.

Antonio Pauciuolo (pauciuolo.a@irea.cnr.it) received the M.D. degree in 1998 and the Ph.D. degree in 2003. He is a researcher at IREA-CNR. His current research interests regard the field of statistical signal processing with emphasis on synthetic aperture radar processing and code division multiple access systems.

Diego Reale (reale.d@irea.cnr.it) received the M.D. degree in 2007 and the Ph.D. degree in 2011. He is a researcher at IREA-CNR. In 2011, he received an award at the IEEE Joint Urban Remote Sensing Event 2011 Student Competition Contest. In 2012, he received the 2011 IEEE Geoscience and Remote Sensing Letters Best Paper Award.

Federico Viviani (federico.viviani@for.unipi.it) received the M.D. degree in 2009. He was awarded the "Best Remote Sensing Thesis for the Year 2007" Prize from the IEEE Geoscience and Remote Sensing Society South Italy Chapter. He has been a research assistant and is now pursuing his Ph.D. degree at the University of Pisa/CNIT-RaSS, Italy, with attention to both urban and forest multidimensional synthetic aperture radar imaging.

REFERENCES

- [1] A. Moreira, P. Prats-Iraola, M. Younis, G. Krieger, I. Hajnsek, and K. P. Papathanassiou, "A tutorial on synthetic aperture radar," *IEEE Geosci. Remote Sens. Mag.*, vol. 1, no. 1, pp. 6–43, Mar. 2013.
- [2] P. A. Rosen, S. Hensley, I. R. Joughin, F. K. Li, S. N. Madsen, E. Rodriguez, and R. M. Goldstein, "Synthetic aperture radar interferometry," *Proc. IEEE*, vol. 88, no. 3, pp. 333–382, 2000.
- [3] A. Ferretti, C. Prati, and F. Rocca, "Permanent scatterers in SAR interferometry," *IEEE Trans. Geosci. Remote Sensing*, vol. 39, no. 1, pp. 8–20, Jan. 2001.
- [4] P. Berardino, G. Fornaro, R. Lanari, and E. Sansosti, "A new algorithm for surface deformation monitoring based on small baseline differential SAR interferograms," *IEEE Trans. Geosci. Remote Sensing*, vol. 40, pp. 2375–2383, Nov. 2002.
- [5] O. Mora, J. J. Mallorqui, and A. Broquetas, "Linear and nonlinear terrain deformation maps from a reduced set of interferometric SAR images," *IEEE Trans. Geosci. Remote Sensing*, vol. 41, no. 10, pp. 2243, 2253, 2003.

- [6] A. Reigber and A. Moreira, "First demonstration of airborne SAR tomography using multibaseline L-band data," *IEEE Trans. Geosci. Remote Sensing*, vol. 38, no. 5, pp. 2142–2152, 2000.
- [7] F. Gini, F. Lombardini, and M. Montanari, "Layover solution in multibaseline SAR interferometry," *IEEE Trans. Aerosp. Electron. Syst.*, vol. 38, no. 4, pp. 1344–1356, Oct. 2002.
- [8] G. Fornaro, F. Lombardini, and F. Serafino, "Three-dimensional multipass SAR focusing: Experiments with long-term spaceborne data," *IEEE Trans. Geosci. Remote Sensing*, vol. 43, no. 4, pp. 702–714, 2005.
- [9] F. Lombardini, "Differential tomography: A new framework for SAR Interferometry," *IEEE Trans. Geosci. Remote Sensing*, vol. 43, no. 1, pp. 37–44, 2005.
- [10] G. Fornaro, D. Reale, and F. Serafino, "Four-dimensional SAR imaging for height estimation and monitoring of single and double scatterers," *IEEE Trans. Geosci. Remote Sensing*, vol. 47, no. 1, pp. 224–237, Jan. 2009.
- [11] X. Zhu and R. Bamler, "Very high resolution spaceborne SAR tomography in urban environment," *IEEE Trans. Geosci. Remote Sensing*, vol. 48, no. 12, pp. 4296–4308, Dec. 2010.
- [12] D. Reale, G. Fornaro, A. Pauciuolo, X. Zhu, and R. Bamler, "Tomographic imaging and monitoring of buildings with very high resolution SAR Data," *IEEE Geosci. Remote Sensing Lett.*, vol. 8, no. 4, pp. 661–665, July 2011.
- [13] F. Lombardini and M. Pardini, "Superresolution differential tomography: Experiments on identification of multiple scatterers in spaceborne SAR data," *IEEE Trans. Geosci. Remote Sensing*, vol. 50, no. 4, pp. 1117–1129, 2012.
- [14] S. Tebaldini, "Single and multipolarimetric SAR tomography of forested areas: A parametric approach," *IEEE Trans. Geosci. Remote Sensing*, vol. 48, no. 5, pp. 2375–2387, 2010.
- [15] M. Nannini, R. Scheiber, and A. Moreira, "First 3D reconstructions of targets hidden beneath foliage by means of polarimetric SAR tomography," *IEEE Geosci. Remote Sensing Lett.*, vol. 47, no. 2, pp. 531–543, Feb. 2009.
- [16] S. Sauer, L. Ferro-Famil, A. Reigber, and E. Pottier, "Three-dimensional imaging and scattering mechanism estimation over urban scenes using dual-baseline polarimetric InSAR observations at L-band," *IEEE Trans. Geosci. Remote Sensing*, vol. 49, no. 11, pp. 4616–4629, Nov. 2011.
- [17] A. Pauciuolo, A. De Maio, S. Perna, D. Reale, and G. Fornaro, "Detection of partially coherent scatterers in multidimensional SAR tomography: A theoretical study," *IEEE Trans. Geosci. Remote Sensing*, to be published.
- [18] F. Lombardini, M. Pardini, G. Fornaro, F. Serafino, L. Verrazzani, and M. Costantini, "Linear and adaptive spaceborne three-dimensional SAR tomography: A comparison on real data," *IET Radar, Sonar Navigat.*, vol. 3, no. 4, pp. 424–436, 2009.
- [19] F. Lombardini and F. Cai, "Temporal decorrelation-robust SAR tomography," *IEEE Trans. Geosci. Remote Sensing*, vol. 52, no. 9, pp. 5412–5421, Sept. 2014.
- [20] F. Lombardini, F. Cai, and D. Pasculli, "Spaceborne 3-D SAR tomography for analyzing garbled urban scenarios: Single-look superresolution advances and experiments," *IEEE J. Select. Topics Appl. Earth Observ. Remote Sensing (JSTARS)*, vol. 6, no. 2, pp. 960–968, 2013.
- [21] F. Viviani, A. Pulella, and F. Lombardini, "Multidimensional tomography with new generation VHR SAR data for urban monitoring," in *Proc. 2013 IEEE Int. Geoscience Remote Sensing Symp. (IGARSS)*, 2013, pp. 81–84.
- [22] L. Roessing and J. Ender, "Advanced SAR interferometry techniques with AER-II," in *Proc. Int. Radar Symp.*, 1998, pp. 1261–1269.
- [23] A. Ferretti, A. Fumagalli, F. Novali, C. Prati, F. Rocca, and A. Rucci, "A new algorithm for processing interferometric data-stacks: SqueeSAR," *IEEE Trans. Geosci. Remote Sensing*, vol. 49, no. 9, pp. 3460–3470, 2011.
- [24] A. De Maio, G. Fornaro, and A. Pauciuolo, "Detection of single scatterers in multi-dimensional SAR imaging," *IEEE Trans. Geosci. Remote Sensing*, vol. 47, no. 7, pp. 2284–2297, July 2009.
- [25] A. Pauciuolo, D. Reale, A. De Maio, and G. Fornaro, "Detection of double scatterers in SAR tomography," *IEEE Trans. Geosci. Remote Sensing*, vol. 50, no. 9, pp. 3567–3586, Sept. 2012.
- [26] X. Zhu and R. Bamler, "Let's do the time warp: Multicomponent nonlinear motion estimation in differential SAR tomography," *IEEE Geosci. Remote Sensing Lett.*, vol. 8, no. 4, pp. 735–739, 2011.
- [27] G. Fornaro, A. Pauciuolo, D. Reale, and S. Verde, "SAR coherence tomography: A new approach for coherent analysis of urban areas," in *Proc. 2013 IEEE Int. Geoscience Remote Sensing Symp. (IGARSS)*, 2013, pp. 73–76.
- [28] O. Monserrat, M. Crosetto, M. Cuevas, and B. Crippa, "The thermal expansion component of persistent scatterer interferometry observations," *IEEE Geosci. Remote Sensing Lett.*, vol. 8, no. 5, pp. 864–868, 2011.
- [29] A. Ferretti, M. Bianchi, C. Prati, and F. Rocca, "Higher-order permanent scatterers analysis," *EURASIP J. Adv. Signal Process.*, vol. 2005, no. 20, pp. 3231–3242, Jan. 2005.
- [30] P. Agram and H. Zebker, "Edgelist phase unwrapping algorithm for time-series InSAR analysis," *J. Opt. Soc. Am. A*, vol. 27, no. 3, pp. 605–612, Mar. 2010.
- [31] X. Zhu and R. Bamler, "Superresolving SAR tomography for multidimensional imaging of urban areas," *IEEE Signal Process. Mag.*, vol. 31, no. 4, pp. 51–58, July 2014.

[Xiao Xiang Zhu and Richard Bamler]

Superresolving SAR Tomography for Multidimensional Imaging of Urban Areas

[Compressive sensing-based TomoSAR inversion]

Synthetic aperture radar (SAR) is capable of assessing the deformation of the ground and buildings in the order of centimeters and millimeters due to its coherent nature and short wavelengths. Spaceborne SAR systems are particularly suited for long-term monitoring of such dynamic processes. A single SAR image, however, only provides a two-dimensional (2-D) projection of the objects, which is in many cases noninjective (i.e., suffers from layover). To retrieve the real three-dimensional (3-D) localization and motion of scattering objects, advanced interferometric methods, like persistent scatterer interferometry (PSI) or SAR tomography (TomoSAR), are required, which exploit stacks of complex-valued SAR images with diversity in space and time [1]–[6]. Modern spaceborne SAR sensors like TerraSAR-X, TanDEM-X, and COSMO-SkyMed, provide data with very high spatial resolution (VHR) in the order of 1 m, which matches well with the scale of building features (typical

floor height and window size and distance). This motivated the further development of existing TomoSAR techniques for exploring the potentials of VHR SAR data for urban infrastructure mapping [6]–[8]. In the last decade, conventional spectral

estimation methods have been implemented for tomographic SAR imaging [3]–[6], [8]. However, for VHR urban monitoring, the following requirements should be met:

- Maintaining the meter azimuth-range resolution, i.e., avoiding multilooking
- Improving the elevation resolution, i.e., providing superresolution (SR)
- Achieving high 3-D localization accuracy even in the presence of unmodeled, non-Gaussian noise
- Retrieving nonlinear motion, e.g., due to seasonal thermal dilation [9].

Driven by these requirements, new algorithms have been invented in the last few years that take advantage of recent developments in signal processing such as sparse reconstruction and compressive sensing (CS) [10]–[12]. This article deals with CS-based TomoSAR inversion and is a follow-up to a companion TomoSAR article, also in this issue of *IEEE Signal Processing Magazine* [13].

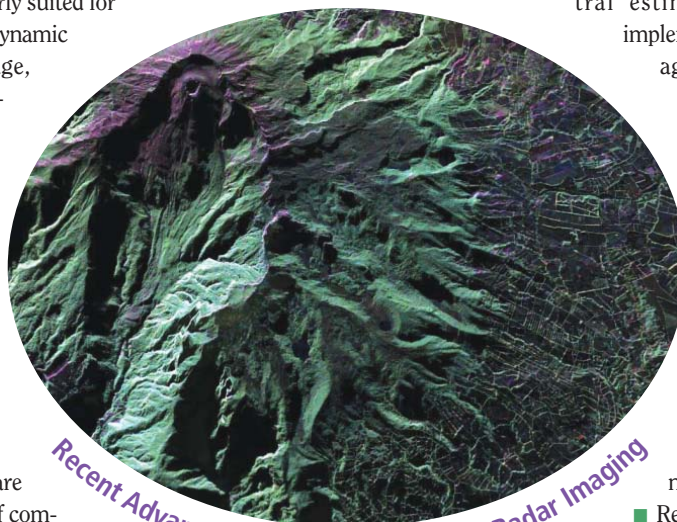


PHOTO COURTESY OF NASA

Digital Object Identifier 10.1109/MSP.2014.2312098
Date of publication: 13 June 2014

TomoSAR SYSTEM MODEL

Conventional SAR imaging provides a projection of the 3-D object reflectivity to the 2-D azimuth-range (x - r) plane. TomoSAR is a technique that allows resolving scatterer densities in the third native radar coordinate “elevation” (s), orthogonal to the azimuth-range plane. The term *tomography* is misleading since it suggests that a large range of angles is required like in computed axial tomography. TomoSAR uses only an extremely small angular diversity though. It rather extends the synthetic aperture principle—as employed in the azimuth direction—to the elevation direction $b \parallel s$ by combining multiple passes of the radar at slightly different orbit positions to establish a virtual array of antennas, as depicted in Figure 1. Typically, the elevation extent Δb of the antenna array, i.e., the maximum orbit spread, is about 250 m for TerraSAR-X and the distance to the scene 700 km, leading to an angular diversity as small as 0.02 degrees.

By stacking all the multiview coherent images and by performing the tomographic processing, s -profiles can be retrieved for every x - r pixel. These profiles can be continuous in the case of forest biomass imaging or may consist of only a few discrete responses, typically corresponding to scatterers located on the ground, façade, and roof, in the case of urban mapping. This article is devoted to the latter application, i.e., the result of tomographic retrieval is a point cloud.

Since the elevation antenna array is in the Fraunhofer far-field of the imaged objects, the complex value g_n of an azimuth-range pixel for the n th acquisition at aperture position b_n ($n = 1, \dots, N$) is a sample of the Fourier transform of the reflectivity profile $\gamma(s)$ along s

$$g_n = \int_{I_s} \gamma(s) \exp(-j2\pi\xi_n s) ds + w_n, \quad (1)$$

where geometric phase terms and atmospheric phase errors have been neglected, I_s represents the range of possible elevations, $\xi_n = -2b_n/(\lambda r)$ is the spatial (elevation) frequency depending on the (more or less random) elevation aperture position b_n , λ stands for the wavelength, and w_n is noise. Therefore, retrieval of the s -profile is a spectral estimation problem. The inherent (Rayleigh) elevation resolution ρ_s of the

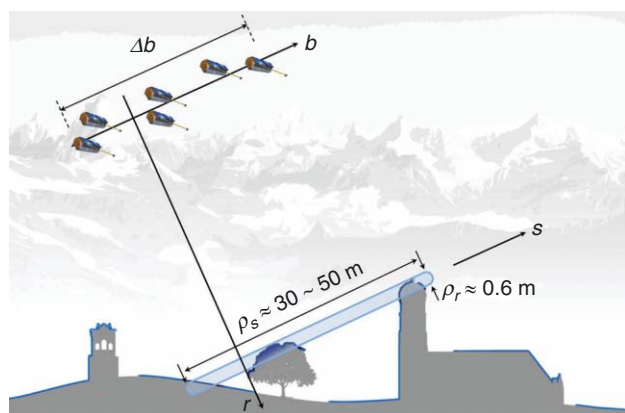


[FIG1] TomoSAR geometry and signal sparsity in the range-elevation (r - s) plane.

tomographic arrangement is related to the elevation aperture extent Δb

$$\rho_s = \frac{\lambda r}{2\Delta b}. \quad (2)$$

For the typical TerraSAR-X parameters given above, $\rho_s = 30\sim 50$ m.

EXTENSION TO MULTIMODAL DEFORMATION

For the spaceborne case, the multipass acquisitions used in tomographic reconstruction are taken over a time span of several weeks to years. Hence, the long-term motion of a scattering object during this time period must be considered or is even the signal of interest. The additional motion term leads to an extended version of the system model from (1)

$$g_n = \int_{I_s} \gamma(s) \exp(-j2\pi(\xi_n s + 2d(s, t_n)/\lambda)) ds + w_n, \quad (3)$$

where $d(s, t_n)$ is the line of sight (LOS) displacement as a function of elevation and time. The motion may be modeled as a linear combination of M basis functions $\tau_m(t_n)$

$$d(s, t_n) = \sum_{m=1}^M p_m(s) \tau_m(t_n), \quad (4)$$

where $p_m(s)$ is the corresponding motion coefficient to be estimated. The choice of the basis functions depends on the underlying physical motion processes. For example, long-term geodynamic processes may lead to a linear, accelerating, or decelerating motion; instantaneous geodynamic events, like earthquakes, result in a stepwise motion; thermal expansion causes a motion correlated to temperature, etc.

To convert (3) into a convenient Fourier transform, we warp the acquisition time axis for each motion basis function $\tau_m(\cdot)$ according to $\eta_{m,n} = 2\tau_m(t_n)/\lambda$. Then (3) can be rewritten as an $(M+1)$ -dimensional Fourier transform of $\gamma(s)\delta(p_1 - p_1(s), \dots, p_M - p_M(s))$ which is an M -dimensional linear δ -manifold (line, plane, or hyperplane) in the $(M+1)$ -dimensional elevation-motion parameter space [9]:

$$g_n = \int_{I_{pM}} \dots \int_{I_{p1}} \int_{I_s} \gamma(s) \delta(p_1 - p_1(s), \dots, p_M - p_M(s)) \exp(-j2\pi(\xi_n s + \eta_{1,n} p_1 + \dots + \eta_{M,n} p_M)) ds dp_1 \dots dp_M + w_n, \quad (5)$$

where I_{pm} stands for the maximum support of motion parameter $p_m(s)$. The ideal δ -manifold may broaden up a bit if the real motion does not follow our motion model. With this system model, the elevation profile and motion parameter retrieval boils down to an $(M+1)$ -dimensional spectral estimation problem. In the following, for the sake of simplicity of the equations, we refer to one-dimensional (1-D) spectral estimation, i.e., the 3-D reconstruction case. Any motion term can be considered by adding another dimension. For the same reason we make no explicit distinction between “TomoSAR” and “differential TomoSAR.”

Discretizing the elevation profile in (1) [or the M -dimensional $s-p_1 - \dots - p_M$ space in (5)] leads to this standard linear system equation

$$\mathbf{g} = \mathbf{A} \boldsymbol{\gamma} + \mathbf{w}, \quad (6)$$

where \mathbf{g} is the measurement vector of length N , \mathbf{A} is an $N \times L$ irregular Fourier matrix composed of the so-called steering vectors, $\boldsymbol{\gamma}$ is the reflectivity profile uniformly sampled in elevation at s_l ($l = 1, \dots, L$), and \mathbf{w} is noise. The profile $\boldsymbol{\gamma}$ to be reconstructed is often sampled much more densely than suggested by the elevation resolution ρ_s to allow SR. As a consequence, $L \gg N$ and (6) is severely underdetermined. An appropriate SR regularization is required for obtaining an unambiguous and robust estimate of $\boldsymbol{\gamma}$.

SPARSITY AND THE CITY

The tomographic imaging configuration for urban scenes of Figure 1 illustrates the following:

- Short-wavelength microwaves are scattered at surfaces and to a limited extent in vegetation volumes. The vegetation responses tend to decorrelate over time and mostly contribute to noise rather than to the useful signal. Hence, our object to be retrieved is more or less a 2-D surface in 3-D space, or, for every azimuth position, a 1-D line in the 2-D range-elevation plane. The object is zero elsewhere in space; it is sparse.
- The tomographic 3-D resolution element (the blue-shaded elongated area in Figure 1) is highly anisotropic, if the elevation aperture size, i.e., the maximum orbit spread Δb , is limited as it is with modern satellite systems. For TerraSAR-X, the azimuth and range resolutions are in the range of 0.5~1 m, while $\rho_s = 30\sim 50$ m. Therefore, SR in elevation is desirable; otherwise layover cannot be resolved in the lower parts of buildings.

As mentioned previously, SR, i.e., oversampling of $\boldsymbol{\gamma}$, is equivalent to setting up an underdetermined equation system that requires either regularization or parametric estimators. The standard L_2 norm regularizer leads to the conventional linear maximum a posteriori (MAP) estimator

$$\hat{\boldsymbol{\gamma}}_{\text{MAP}} = (\mathbf{A}^T \mathbf{C}_{\text{ww}}^{-1} \mathbf{A} + \mathbf{C}_{\boldsymbol{\gamma}\boldsymbol{\gamma}}^{-1})^{-1} \mathbf{A}^T \mathbf{C}_{\text{ww}}^{-1} \mathbf{g}, \quad (7)$$

where \mathbf{C}_{ww} and $\mathbf{C}_{\boldsymbol{\gamma}\boldsymbol{\gamma}}$ are the covariance matrices of noise and prior, respectively. The truncated SVD method described in [5] and [13] falls into the same class. These solutions are not able to achieve significant SR, however. Several nonlinear or parametric estimators known from spectral analysis are presented in the companion article [13] in this issue. Instead, we use the mentioned sparsity property and the CS framework.

Object sparsity could be exploited in several ways. A brute-force approach would attempt to reconstruct the line segments representing the surfaces, visible to the SAR (bold in Figure 1), in the 2-D range-elevation plane for every azimuth position. However, in the case of an anisotropic resolution element like the one in Figure 1, we only need SR in the elevation direction. The intersections of such an elongated resolution element with

the ground, the façade, and the roof of a building have an extent much smaller than ρ_s . Hence, the elevation profiles to be reconstructed for every azimuth-range pixel can be considered as consisting of a few δ -functions, i.e., as sparse. The sparsity property can be used as a strong prior for regularizing the underdetermined inverse problem.

THE COMPRESSIVE SENSING-BASED SLIMMER ALGORITHM

Using the concept of CS for TomoSAR has been proposed by [10] and first demonstrated by the authors in [11]. We developed the SLIMMER algorithm (pronounced “slimmer”). The acronym stands for the three processing steps: 1) scale-down by L_1 norm minimization, 2) model order selection, and 3) parameter estimation reconstruction. Considering that the elevation profile is sparse, we may assume that among the infinitely many solutions of the underdetermined system equation, the sparsest solution, i.e., the solution having the minimum L_0 norm $\|\boldsymbol{\gamma}\|_0$ (number of nonzero elements), is assumed to be the most probable one. The solution could be found by parametric nonlinear least squares (NLS) estimates of increasing number of scatterers combined with model order selection. However, this optimization task is NP-hard, it requires a combinatorial search of all possible scatterer positions. CS theory [14], [15] tells us that under certain constraints, the L_0 norm may be replaced by the (convex) L_1 norm. Since the measurements are contaminated with noise, the L_1 norm is preferably jointly minimized with the classical residual data term (log-likelihood)

$$\hat{\boldsymbol{\gamma}} = \arg \min_{\boldsymbol{\gamma}} \{ \|\mathbf{g} - \mathbf{A}\boldsymbol{\gamma}\|_2^2 + \lambda_K \|\boldsymbol{\gamma}\|_1 \}. \quad (8)$$

Equation (8) gives the sparsest estimate of $\boldsymbol{\gamma}$ if the mapping matrix \mathbf{A} fulfills the restricted isometry (RIP) and incoherence properties [15]. However, for TomoSAR, RIP and incoherence are violated for several reasons. First, the mapping matrix \mathbf{A} is predetermined by the measurement system (the elevation aperture sampling pattern) and may not be optimum. Second, oversampling the elevation profile $\boldsymbol{\gamma}$ renders \mathbf{A} overcomplete, reduces RIP, and increases coherence. Nevertheless, the L_2 - L_1 norm minimization step shrinks \mathbf{A} dramatically [16] and gives a first sparse estimate of $\boldsymbol{\gamma}$. This estimate, though, may still contain outliers and, hence, the sparsity K (i.e., the number of discrete scatterers, typically $K = 0\sim 3$) is often overestimated.

As the second algorithm step, model order selection is used to clean the $\boldsymbol{\gamma}$ estimate of spurious, nonsignificant scatterers and to finally obtain the most likely number \hat{K} of scatterers along elevation. The model complexity can be described by the number of parameters that is proportional to the number of scatterers K . Let $\boldsymbol{\Theta}(K)$ be the vector of the unknown amplitudes, phases, and elevations for all the K scatterers. The goodness-of-model-fit can be described by the likelihood $p(\mathbf{g} | \boldsymbol{\Theta}(K), K)$. A more complex model always fits the observations better, hence, for the purpose of selecting the most probable model, its complexity must be penalized to avoid overfitting of the data. The general form of penalized likelihood criteria is

$$\hat{K} = \arg \min_K \{-2 \ln p(\mathbf{g} | \hat{\boldsymbol{\theta}}(K), K) + 2C(K)\}, \quad (9)$$

where $C(K)$ is a complexity penalty, e.g., the Bayesian information criterion (BIC) [17], the Akaike information criterion (AIC) [18], or the minimum description length (MDL) [19]. Note that those penalty terms are proportional to K , i.e., $C(K) \propto \|\boldsymbol{\gamma}\|_0$ and (9) is an L_2 - L_0 norm minimization, but with known and few K candidate elevation positions, and hence can be easily solved.

As a last refinement, a much slimmer mapping matrix $\mathbf{A}(\hat{\mathbf{s}})$, i.e., the $N \times \hat{K}$ matrix with $A_{n,k}(\hat{\mathbf{s}}) = \exp(-j2\pi\xi_n\hat{s}_k)$, is built up, where \hat{s}_k is the estimated elevation value of the k th scatterer. The final complex-valued reflectivity $\boldsymbol{\gamma}(\hat{\mathbf{s}})$ for the \hat{K} scatterers is obtained by solving the following overdetermined linear system equation:

$$\mathbf{g} = \mathbf{A}(\hat{\mathbf{s}})\boldsymbol{\gamma}(\hat{\mathbf{s}}) + \mathbf{w}', \quad (10)$$

where \mathbf{w}' combines the measurement noise and the model error, i.e., the deviation from sparsity or unmodeled motion-induced phase terms. The complex amplitudes of the \hat{K} discrete scatterers are finally found by the classical least-squares solution

$$\hat{\boldsymbol{\gamma}}(\hat{\mathbf{s}}) = (\mathbf{A}(\hat{\mathbf{s}})^H \mathbf{A}(\hat{\mathbf{s}}))^{-1} \mathbf{A}(\hat{\mathbf{s}})^H \mathbf{g}. \quad (11)$$

This last (debiasing) step is performed because (8) is known to slightly underestimate the magnitudes of $\boldsymbol{\gamma}$ [20]. Although amplitude fidelity is not the main purpose of TomoSAR, (11) renders SLIMMER a generic unbiased CS algorithm. Since the main step of SLIMMER is the L_2 - L_1 norm minimization known from CS, the analysis and the results in the following sections apply similarly to other CS-based TomoSAR algorithms.

BY MAKING USE OF SPARSITY, THE SLIMMER ALGORITHM CAN ACHIEVE SUBSTANTIAL SUPERRESOLUTION IN ELEVATION WHILE MAINTAINING THE FULL AZIMUTH-RANGE RESOLUTION.

SUPERRESOLUTION FACTOR: THEORY, SIMULATIONS, AND REAL DATA EXAMPLES

By making use of object sparsity, the SLIMMER algorithm can achieve substantial SR in elevation while maintaining the full azimuth-range resolution. A simulation example may demonstrate SR with SLIMMER. Since multiple scatterers inside an azimuth-range pixel at different elevation positions most likely occur in high-rise urban areas, we simulated a situation with two scatterers inside a pixel: one point scatterer at the building façade and another rough surface reflection

from the ground with an elevation distance of 0.4 of the Rayleigh resolution unit under an SNR of 10 dB and a number of acquisitions $N = 30$, i.e., $N \times SNR \approx 25$ dB. Figure 2 compares the reconstructed reflectivity profiles along the elevation direction using the linear MAP estimator and SLIMMER. The MAP estimator is subject to the Rayleigh resolution limit and is not able to separate the two closely spaced scatterers while SLIMMER easily separates them.

The example also shows that nonlinear (and semiparametric) spectral estimators like SLIMMER yield reconstructions with much sharper “point responses” than traditional nonparametric ones. However, the nice shape of the responses tells us neither their location accuracy nor the ability of the algorithm to resolve two close scatterers. To study the SR power of such algorithms, let us define the (elevation) resolution as the *minimum distance* ρ_{p_D} between two δ -functions (point scatterers) that are separable at a prespecified probability of detection P_D . Note that we investigate the detection rate in the SR regime, while in the companion article [13] the detection rates in the non-SR regime have been studied. ρ_{p_D} depends on the amplitude ratio of the scatterers, their phase difference, and (asymptotically) on

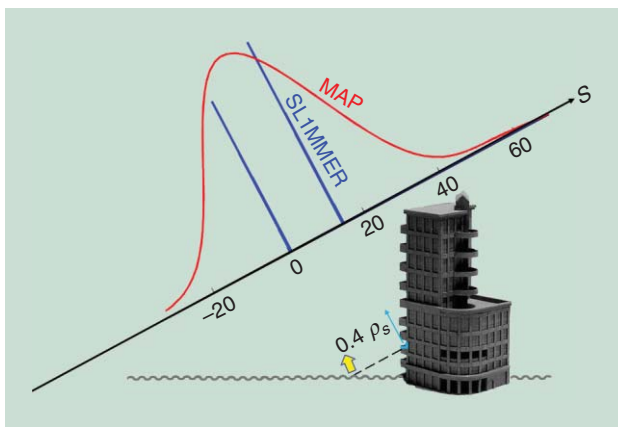


[FIG2] A demonstration of SR: reflectivity profiles along elevation direction reconstructed by the classical MAP estimator and by SLIMMER. The elevation distance between the layovered double scatterers is 0.4 of the Rayleigh resolution unit. In this example, $N = 30$ and $SNR = 10$ dB.

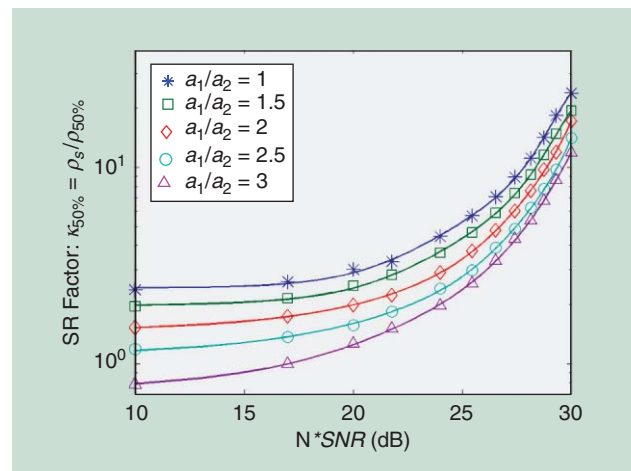


[FIG3] The fundamental bound of SR: SR factor of the SLIMMER algorithm averaged over $\Delta\varphi$ as a function of $N \times SNR$ for different amplitude ratios a_1/a_2 of two close scatterers [21].

the product $N \times SNR$. We define the *SR factor* κ_{P_D} as an improvement factor relative to the Rayleigh resolution ρ_s

$$\kappa_{P_D} = \frac{\rho_s}{\rho_{P_D}}. \tag{12}$$

It depends on the required detection rate P_D and is larger than unity for SR. Figure 3 shows the SR power of SLIMMER for $P_D = 50\%$ as a function of $N \times SNR$ for different amplitude ratios. These curves have been found by Monte Carlo simulations [21]. For each realization the phase differences $\Delta\varphi$ of the two scatterers were chosen randomly from $[0, 2\pi]$ as it is the case in real scattering scenarios. In [21] it was shown that these SR factors are close to those of NLS estimation, which is theoretically the best, and hence establish a kind of fundamental bound. For interested readers, the SR of CS-based algorithms is shown to significantly outperform multiple signal classification (MUSIC) in [22]. For other moderately superresolving estimators, like Capon, see [13] and the references therein. In the interesting parameter range of TomoSAR, i.e., $N = 10 \sim 100$ and $SNR = 0 \sim 10$ dB (which applies for the majority of pixels of urban scenes) the achievable SR factor is in the order of 1.5~25.

CRAMÉR–RAO LOWER BOUND FOR SINGLE AND DOUBLE SCATTERER POSITIONING ACCURACY

Assuming two scatterers at elevation positions s_1 and s_2 with amplitudes a_1 and a_2 and phases φ_1 and φ_2 have been detected, we are now interested in how accurately their positions can be estimated. To find the Cramér–Rao lower bound

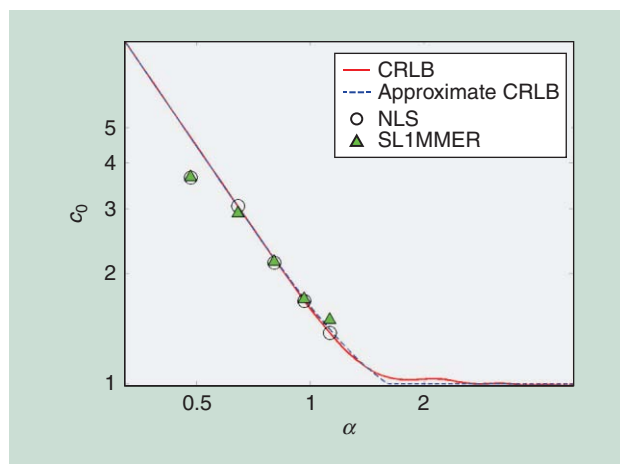


[FIG4] A location estimation error factor of two scatterers from (15) and (16) as a function of their normalized distance α CRLB, approximation of CRLB from (16), and experimental results from NLS and SL1MMER [21].

(CRLB) of the elevation estimation error, the Fisher information matrix \mathbf{J} is constructed from the derivatives of the log-likelihood function $\ln p(\mathbf{g}|\boldsymbol{\theta})$, where the parameter vector $\boldsymbol{\theta} = [a_1, \varphi_1, s_1, a_2, \varphi_2, s_2]^T$. We obtain the CRLB matrix by $\mathbf{P}_{\text{CRLB}} = \mathbf{J}^{-1}$, from which the elements $P_{\text{CRLB},3,3} = \sigma_{s_1}^2$ and $P_{\text{CRLB},6,6} = \sigma_{s_2}^2$ are the ones of interest, i.e., the CRLBs of the location estimation errors for the two scatterers. Since the analytic inversion of \mathbf{J} leads to a complicated and lengthy expression, it is

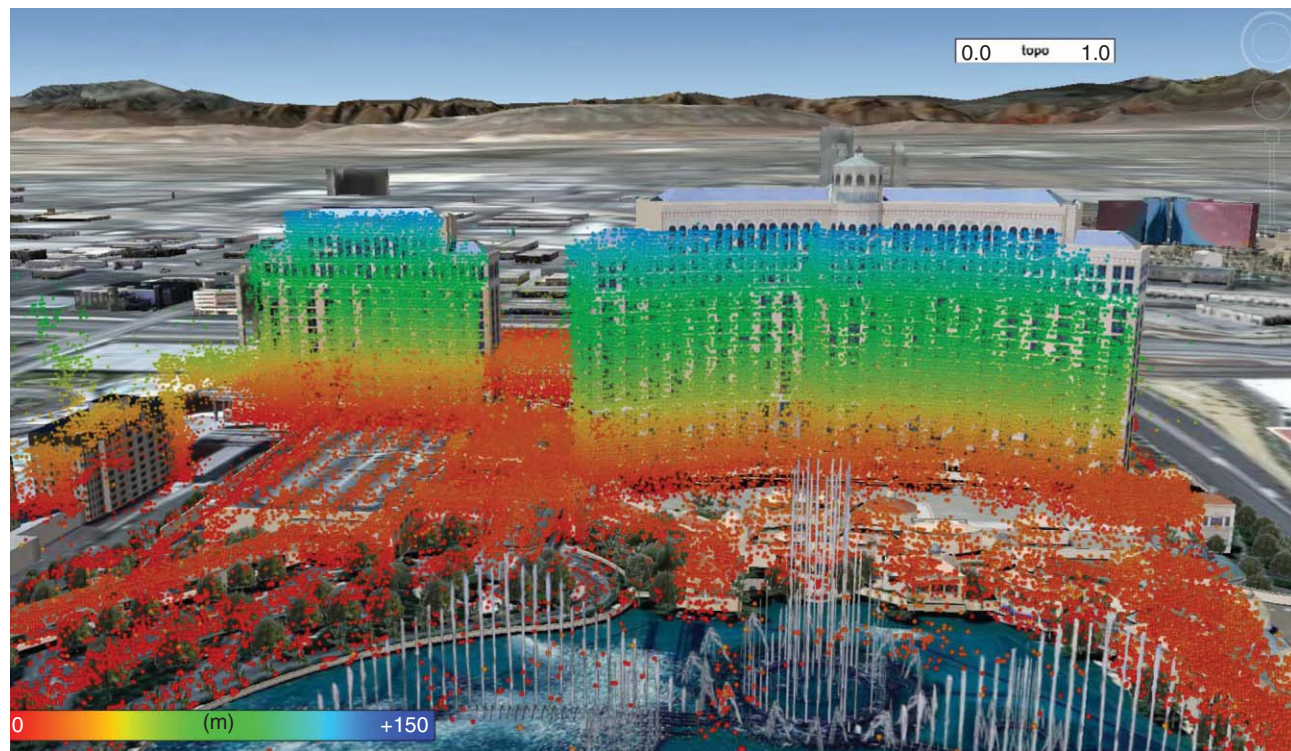


[FIG5] The 3-D view of buildings visualized in Google Earth reconstructed by SL1MMER using a stack of 25 TerraSAR-X images (color represents height). (Figure used with permission from DLR.)

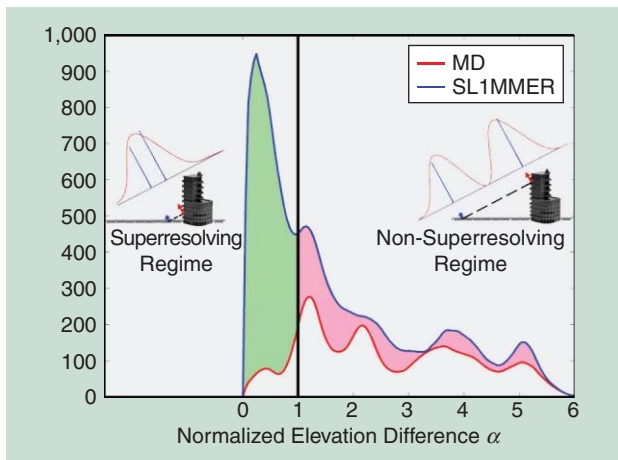


[FIG6] Histogram of the distance between the detected double scatterers using MAP (red) and SL1MMER (blue). (Figure used with permission from [23].)

more convenient to retrieve the relevant elements of \mathbf{P}_{CRLB} by solving the inversion numerically. For the sequel, we split the elevation estimation error standard deviation into two contributions [21]

$$\sigma_{s_q} = c_0 \cdot \sigma_{s_q,0}, \tag{13}$$

where

$$\sigma_{s_q,0} = \frac{\lambda r}{4\pi\sqrt{2} \cdot \sqrt{N \cdot \text{SNR}_q} \cdot \sigma_b} \tag{14}$$

is the CRLB of the elevation estimates of the q th scatterer ($q = 1$ or 2) in the absence of the other one. σ_b is the standard deviation of the elevation aperture antenna positions b_n . For

uniformly distributed aperture sampling (randomly or equidistantly spaced) $\sigma_b = \Delta b / \sqrt{12}$ and $\sigma_{s_q,0} \approx 0.39 / \sqrt{N \cdot \text{SNR}_q} \cdot \rho_s$. In the parameter range of TomoSAR, $\sigma_{s_q,0}$ is in the order of 1/100 to 1/10 of the Rayleigh resolution unit ρ_s . The more interesting term is c_0 , the interference correction factor for closely spaced scatterers. It is asymptotically independent of SNR and N and can be shown to be approximately (see [21] and the references therein)

$$c_0 = \max \left\{ \sqrt{\frac{40\alpha^{-2}(1-\alpha/3)}{9-6(3-2\alpha)\cos(2\Delta\phi)+(3-2\alpha)^2}}, 1 \right\}, \tag{15}$$

where $\alpha = \delta_s / \rho_s$ is the distance between the two scatterers, normalized to the Rayleigh resolution unit. Obviously, c_0 depends strongly on the phase difference $\Delta\phi$. Since for TomoSAR $\Delta\phi$ is totally random and depends on the unknown geometric configuration, we integrate c_0^2 over $\Delta\phi$. The resulting CRLB for the interference correction factor is plotted in Figure 4 as a function of the normalized distance α together with a convenient approximation [21]

$$c_0 = \frac{\sigma_s}{\sigma_{s_q,0}} \approx \max \left\{ \sqrt{2.57(\alpha^{-1.5} - 0.11)^2 + 0.62}, 1 \right\}. \tag{16}$$

The location estimation error is $\sigma_{s_q,0}$, i.e., $c_0 = 1$, as long as the two scatterers are far apart but increases at a rate of $\alpha^{-1.5}$ once the scatterers are closer than about 1.6 times the Rayleigh resolution unit.

Figure 4 also compares the CRLB with the results from NLS (solution with the L_0 norm prior) and SLIMMER. These have been obtained by simulations with randomly distributed phase differences. The elevation estimation accuracy of the CS-based algorithm SLIMMER approaches the CRLB and is almost identical to NLS, i.e., both algorithms are efficient.

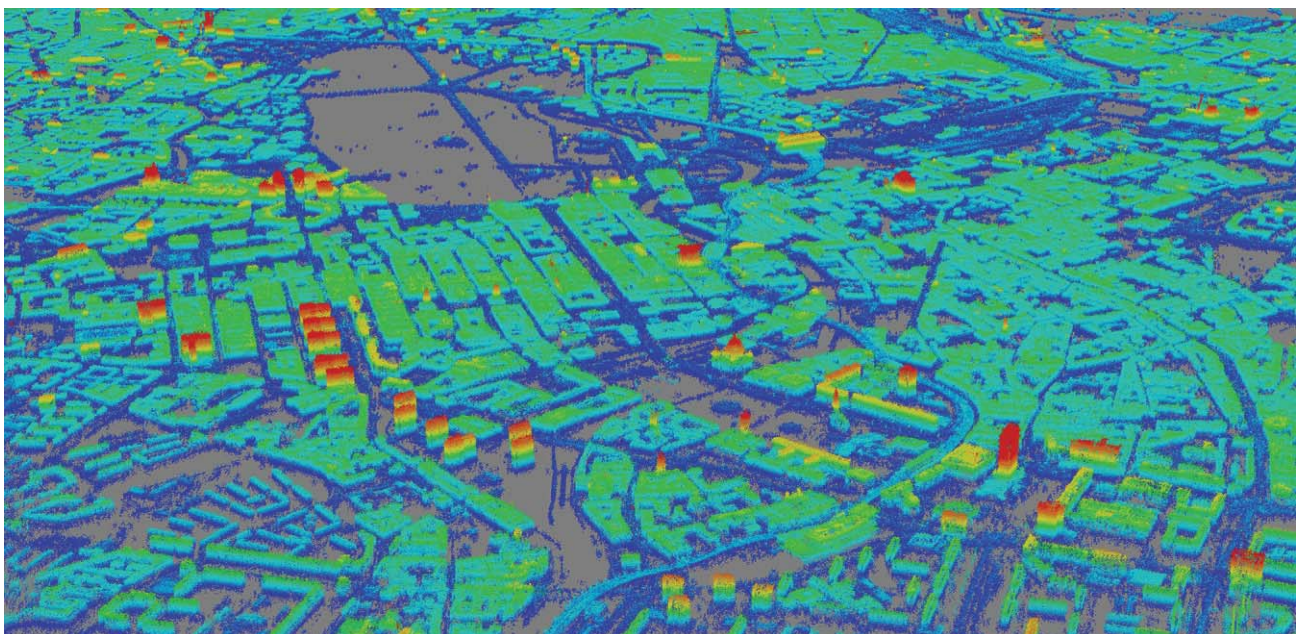


[FIG7] The fusion of two point clouds generated from TerraSAR-X data stacks of ascending and descending orbits. The color represents height. Grey areas are temporally decorrelated objects, e.g., vegetation or water.

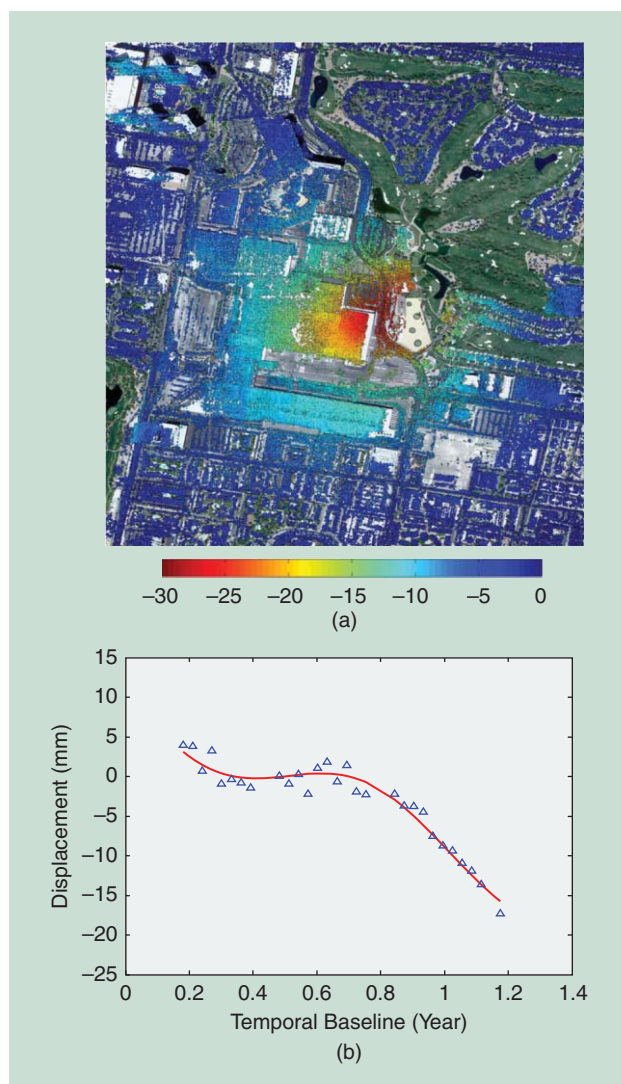


[FIG8] (a) TomoSAR deformation estimates of an area around the Las Vegas Convention Center: linear deformation velocity (unit: mm/y). (b) Phase (= deformation) history of one of the scatterers on the roof of the center building.

EXAMPLES WITH VHR TerraSAR-X DATA

TomoSAR with VHR X-band data can achieve point densities in the order of 600,000~1,000,000/km², which are much higher than with PSI (40,000~100,000 PS/km²) where only pixels containing single or dominant scatterer are considered. As a consequence, detailed monitoring of even single buildings and in general of infrastructure as well as cultural heritage is possible. In the following, we demonstrate practical use of TomoSAR with TerraSAR-X data.

Figure 5 presents a 3-D view of the Bellagio Hotel complex in downtown Las Vegas, Nevada visualized in Google Earth and reconstructed by SLIMMER using a stack of 25 TerraSAR-X images.

To demonstrate the effect of the SR power of SLIMMER on real data, Figure 6 shows the histogram of the elevation distance between detected double scatterers using MAP (red) and SLIMMER

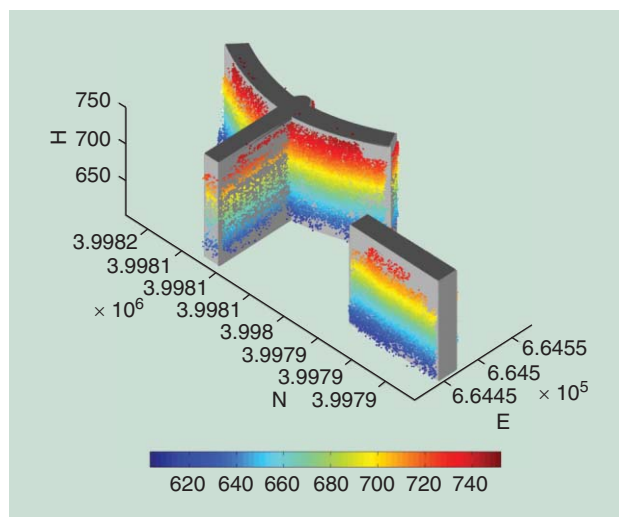


[FIG9] From TomoSAR point clouds to objects: reconstructed building façades of the Bellagio hotel complex in Las Vegas [25]. The point cloud is overlaid on the facade model, color corresponds to height.

(blue) over the Bellagio Hotel area. It is not surprising that the number of double scatterers detected by SLIMMER is much higher than those detected by MAP and most of them lie in the SR regime $\alpha < 1$ (green area). For an urban scene like this typically 30~40% of the scatterers detected by SLIMMER are double scatterers compared to 10~20% detected by linear estimators.

Due to the side-looking geometry of SAR, a single stack of SAR images only provides information on one side of a building (see the bold surface segments in Figure 1). For comprehensive urban structure monitoring, a shadow-free point cloud is desirable. It requires fusion of the TomoSAR results of multiple stacks from opposite view angles. This is a nontrivial task, since all the scatterer locations detected from TomoSAR are relative to a reference point and it is usually not possible to identify the same object as a reference for all the view angles [24]. Figure 7 presents the fusion result from two stacks, one from ascending orbit (94 acquisitions) and one from descending orbit (79 acquisitions), over the city of Berlin, Germany. The scene contains about 40 million detected scatterers each of which also contains its own deformation history. Small structures like the Victory Column, i.e., the statue at the center of the park can be easily identified.

Figure 8 shows an example of multicomponent motion estimation. Since July 2009, an area in the city of Las Vegas is undergoing a pronounced subsidence centered at the Convention Center. Together with the thermal dilation-induced seasonal motion of the metallic building structure, the selected area is characterized by a two-component nonlinear motion as shown in the phase history. Here, we chose the motion basis functions as a sine-function with a period of one year for seasonal motion and a linear function for subsidence. The estimated linear deformation velocity in mm/year is shown in Figure 8(a), while (b) shows the LOS motion of one of the scatterers on the roof of the Convention Center. The two-component motion is evident.

BUILDING RECONSTRUCTION FROM TomoSAR POINT CLOUDS

The point clouds from VHR TomoSAR can reach a density comparable to lidar. These tomographic point clouds can be potentially used for building facade reconstruction in urban environment from space with some special considerations such as the side-looking geometry, anisotropic estimation accuracy, and decorrelation. Yet to provide a high-quality spatiotemporal four-dimensional (4-D) city model, object reconstruction from these TomoSAR point clouds is an emergent topic. A 3-D view of the reconstructed facades over the Bellagio Hotel complex in Las Vegas (see Figure 5) using point clouds retrieved from stacks from both ascending and descending orbits, is exemplified in Figure 9.

CONCLUDING REMARKS

With reference to the current status of VHR spaceborne tomographic SAR inversion presented in this article, the following conclusions can be drawn:

- VHR tomographic SAR inversion is able to reconstruct the shape and motion of individual buildings and entire city areas.
- SR is crucial and possible, e.g., using CS, for VHR tomographic SAR inversion for urban infrastructure.
- The motion or deformation of buildings is often nonlinear (periodic, accelerating, stepwise, etc.). Multicomponent nonlinear motion of multiple scatterers can be separated.
- The 4-D point clouds retrieved by VHR TomoSAR has a point density comparable to LiDAR and can be potentially used for dynamic city model reconstruction.

AUTHORS

Xiao Xiang Zhu (xiao.zhu@dlr.de) is a scientist with the Remote Sensing Technology Institute at the German Aerospace Center (DLR), where she is the head of the synthetic aperture radar (SAR) Signal Analysis Team and with the Technische Universität München. Her main research interests are signal processing, including innovative algorithms such as compressive sensing, sparse reconstruction with applications in Earth observation, including SAR, and optical and hyperspectral remote sensing. She received the IEEE International Geoscience and Remote Sensing Symposium Best Paper Award in 2010, the Dimitri N. Chorofas Foundation Research Award in 2011, and the IEEE Geoscience and Remote Sensing Society Letters Best Paper Award in 2012.

Richard Bamler (richard.bamler@dlr.de) is the director of the Remote Sensing Technology Institute at the German Aerospace Center. Since 2003 he has also held a full professorship at the Technische Universität München. His team and his institute work on synthetic aperture radar (SAR), optical remote sensing, computer vision, atmospheric sounding, and laboratory spectrometry. They develop and have developed operational processors for Earth observation missions such as SIR-C/X-SAR, SRTM, TerraSAR-X, TanDEM-X, ERS-2/GOME, ENVISAT/SCIAMACHY, MetOp/GOME-2, Sentinel 5p, and EnMAP. His research interests are in

algorithms for optimum information extraction from remote sensing data with emphasis on SAR.

REFERENCES

- [1] A. Reigber and A. Moreira, "First demonstration of airborne SAR tomography using multibaseline L-band data," *IEEE Trans. Geosci. Remote Sensing*, vol. 38, no. 5, pp. 2142–2152, 2000.
- [2] F. Gini, F. Lombardini, and M. Montanari, "Layover solution in multibaseline SAR interferometry," *IEEE TAES*, vol. 38, no. 4, pp. 1344–1356, 2002.
- [3] G. Fornaro, F. Lombardini, and F. Serafino, "Three-dimensional multipass SAR focusing: experiments with long-term spaceborne data," *IEEE Trans. Geosci. Remote Sensing*, vol. 43, no. 4, pp. 702–714, 2005.
- [4] F. Lombardini, "Differential tomography: A new framework for SAR interferometry," in *Proc. IGARSS*, Toulouse, France, 2003, pp. 1206–1208.
- [5] G. Fornaro, D. Reale, and F. Serafino, "Four-dimensional SAR imaging for height estimation and monitoring of single and double scatterers," *IEEE Trans. Geosci. Remote Sensing*, vol. 47, no. 1, pp. 224–237, 2009.
- [6] X. Zhu and R. Bamler, "Very high resolution spaceborne SAR tomography in urban environment," *IEEE Trans. Geosci. Remote Sensing*, vol. 48, no. 12, pp. 4296–4308, 2010.
- [7] R. Bamler, M. Eineder, N. Adam, X. Zhu, and S. Gernhardt, "Interferometric potential of high resolution spaceborne SAR," *Photogrammetrie Fernerkundung Geoinformation* 5/2009, 2009, pp. 407–419.
- [8] D. Reale, G. Fornaro, A. Pauciuolo, X. Zhu, and R. Bamler, "Tomographic imaging and monitoring of buildings with very high resolution SAR data," *IEEE Geosci. Remote Sensing Lett.*, vol. 8, no. 4, pp. 661–665, 2012.
- [9] X. Zhu and R. Bamler, "Let's do the time warp: Multi-component nonlinear motion estimation in differential SAR tomography," *IEEE Geosci. Remote Sensing Lett.*, vol. 8, no. 4, pp. 735–739, 2012.
- [10] A. Budillon, A. Evangelista, and G. Schirrinzi, "SAR tomography from sparse samples," in *Proc. IEEE Int. Geoscience Remote Sensing Symp. (IGARSS)*, Cape Town, Africa, 2009, pp. 865–868.
- [11] X. Zhu and R. Bamler, "Very high resolution SAR tomography via compressive sensing," in *Proc. FRINGE Workshop*, Frascati, Italy, 2009, pp. 1–7.
- [12] X. Zhu and R. Bamler, "Tomographic SAR inversion by L1 norm regularization – The compressive sensing approach," *IEEE Trans. Geosci. Remote Sensing*, vol. 48, no. 10, pp. 3839–3846, 2010.
- [13] G. Fornaro, F. Lombardini, A. Pauciuolo, D. Reale, and F. Viviani, "Tomographic processing of interferometric SAR data," *IEEE Signal Processing Mag.*, vol. 31, no. 4, pp. 41–50, July 2014.
- [14] E. Candès, "Compressive sampling," in *Proc. Int. Congr. Mathematics*, Madrid, 2006, vol. 3, pp. 1433–1452, 2006.
- [15] R. Baraniuk, "Compressive sensing," *IEEE Signal Processing Mag.*, vol. 24, no. 4, pp. 118–126, 2007.
- [16] X. Zhu, "Very high resolution tomographic SAR inversion for urban infrastructure monitoring—A sparse and nonlinear tour," Ph.D. thesis, Deutsche Geodätische Kommission, Reihe C, Nr. 666, Verlag der Bayerischen Akademie der Wissenschaften, 2011.
- [17] K. P. Burnham and D. R. Anderson, "Multimodel inference: Understanding AIC and BIC in model selection," *Sociol. Methods Res.*, vol. 33, no. 2, pp. 261–304, 2004.
- [18] G. Schwarz, "Estimating the dimension of a model," *Ann. Stat.*, vol. 6, no. 2, pp. 239–472, 1978.
- [19] J. Rissanen, "Modelling by shortest data description," *Automatica*, vol. 14, no. 5, pp. 465–471, 1978.
- [20] S. J. Wright, R. D. Nowak, and M. At Figueiredo, "Sparse reconstruction by separable approximation," *IEEE Trans. Signal Processing*, vol. 57, no. 7, pp. 2479–2493, 2009.
- [21] X. Zhu and R. Bamler, "Super-resolution power and robustness of compressive sensing for spectral estimation with application to spaceborne tomographic SAR," *IEEE Trans. Geosci. Remote Sensing*, vol. 50, no. 1, pp. 247–258, 2012.
- [22] P. Khomchuk, I. Bilik, and D. P. Kasilingam, "Compressive sensing-based SAR tomography," in *Proc. IEEE Radar Conf.*, Arlington, TX, 2010, pp. 354–358.
- [23] X. Zhu and R. Bamler, "Demonstration of super-resolution for tomographic SAR imaging in urban environment," *IEEE Trans. Geosci. Remote Sensing*, vol. 50, no. 8, pp. 3150–3157, 2012.
- [24] Y. Wang, X. Zhu, Y. Shi, and R. Bamler, "Operational TomoSAR processing using multitrack TerraSAR-X high resolution spotlight data stacks," in *Proc. IEEE Int. Geoscience Remote Sensing Symp. (IGARSS)*, Munich, Germany, 2012, pp. 7047–7050.
- [25] X. Zhu and M. Shahzad, "Façade reconstruction using multi-view spaceborne TomoSAR point clouds," *IEEE Trans. Geosci. Remote Sensing*, vol. 52, no. 6, pp. 3541–3552, 2014.

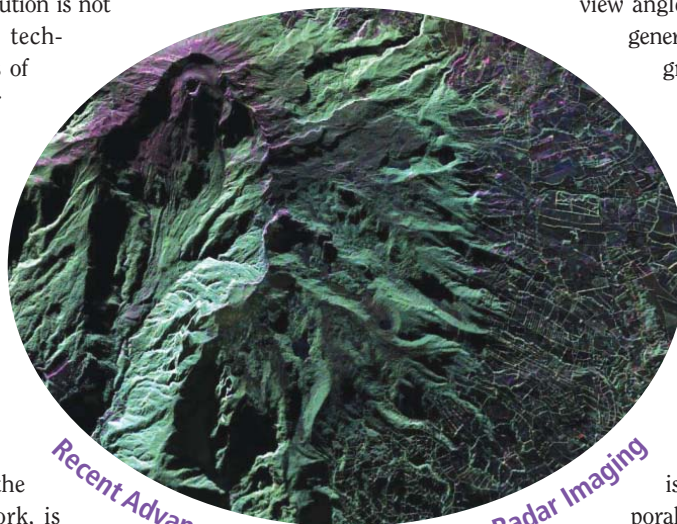


[Fabio Baselice, Giampaolo Ferraioli, Vito Pascazio, and Gilda Schirinzi]

Contextual Information-Based Multichannel Synthetic Aperture Radar Interferometry

[Addressing DEM reconstruction using contextual information]

Interferometric synthetic aperture radar (InSAR) systems are capable of providing an estimate of the digital elevation model (DEM) of the imaged ground scene. This is usually done by means of a phase unwrapping (PU) operation. In the absence of additional regularity constraints, PU is an ill-posed problem, because the solution is not unique. Multichannel (MCh) techniques, using stacks of images of the same scene, can be used for restoring the solution uniqueness and reducing the effect of phase noise. Moreover, statistical techniques exploiting the contextual information contained in the data can provide satisfactory results. In this article, an overview of the main MCh statistical DEM reconstruction methods, developed both in the classical and in the Bayesian estimation framework, is presented. In particular, the effectiveness of the exploitation of contextual statistical models is shown by means of numerical experiments on simulated and real data sets.



Recent Advances in Synthetic Aperture Radar Imaging

PHOTO COURTESY OF NASA

INTRODUCTION

Today, InSAR systems are widely used and represent an effective tool for geoscience and topographic mapping of the earth's surface. InSAR systems typically make use of two complex SAR images of the same scene, acquired with slightly different view angles, from which it is possible to generate the so-called phase interferogram, given by the wrapped difference of the two image phases. The phase interferogram is linked through a known (nonlinear) relation to the height profile of the observed scene [1], [2], usually also denoted as DEM. Phase interferograms suffer from two main problems: they are wrapped in the interval $]-\pi, \pi]$, and are corrupted by noise, which is related to the spatial and temporal decorrelation between the two acquisitions and, in general, cannot be neglected. The DEM reconstruction is, then, performed by means of a PU operation, which allows the phase reconstruction in the interval $]-\infty, \infty[$ starting from the wrapped phase values [1]. Since there is an infinite number of height profiles that can be mapped in the same interferogram [2], PU is an ill-posed problem unless proper regularity constraints are imposed. This problem has been widely studied in many

Digital Object Identifier 10.1109/MSP.2014.2312282

Date of publication: 13 June 2014

other application fields, such as radio astronomy [3] and magnetic resonance imaging [4].

A constraint that is commonly adopted to regularize the PU problem, restoring the solution uniqueness, consists of imposing that the absolute values of the unwrapped phase jumps between adjacent pixels are less than π . This constraint is satisfied in the case of height profiles without strong discontinuities and high slopes, and for small baseline values [2].

One of the first techniques proposed for InSAR dates back more than 25 years ago [5]. Since then, many other PU algorithms have been developed.

Most PU traditional techniques can be classified as either path-following methods or minimum norm methods. A good review is provided in [6]. A significant and more recent extension of the path-following methods is based on constrained optimization of network flows [7]. However, even the best PU method, based on a single interferogram, will fail for steep mountainous or urban areas due to the solution ambiguity and presence of noise.

The solution uniqueness can be recovered, without imposing any constraint on the height profile, by using MCh techniques [8]–[13], which exploit the availability of more than two images (i.e., more than one interferogram) obtained using multibaseline or multifrequency interferometric acquisitions. They have shown to be more robust compared to the ones based on a single interferogram, and, besides solving the problem of the multiplicity of the solution, they provide improved accuracy and can be applied to a larger class of height profiles. The time series of SAR images are also useful for reducing noise in topographic applications or measuring time-varying surface deformations [2] in the differential interferometric configuration (DInSAR).

A boost to the development of MCh InSAR techniques has been also given by the recent launch of very high-resolution (VHR) SAR system constellations (e.g., TerraSAR-X, COSMO-SkyMed), providing a huge amount of interferometric data acquired with small revisiting times.

Most of the MCh DEM reconstruction methods are based on statistical estimation techniques. Initially, methods based on maximum likelihood (ML) estimators have been proposed [11], [12], [14]. Such techniques, by exploiting the statistical distribution of the interferometric phase noise, are able to effectively combine the MCh data to estimate the height of a pixel independently from the ones surrounding. Achievable performances depend significantly on the number of images, the operating frequency, the baselines, and coherence values of each interferogram [15]. Reliable and accurate reconstructions require a large number of channels, especially in the presence of low coherence areas.

To increase the performance of DEM reconstructions, especially in the presence of a small number of channels, contextual information can be considered. Instead of working pixel-wise, this approach requires the simultaneous processing of pixel clusters by exploiting relationships existing between the nearby pixels (also called a *neighborhood*).

Contextual information methods can be grouped into two classes: methods imposing deterministic constraints between

the nearby pixel, and methods adopting statistical constraints between nearby pixels.

As far as deterministic constraints are concerned, pixels are jointly processed in clusters, in which some geometrical relations are imposed [16]. In the case of statistical constraints based methods, instead, pixels are modeled considering their a priori joint statistical distribution [17]–[22].

The joint use of MCh data and contextual information noticeably improves DEM reconstruction accuracy. In particular, MCh information allows solving the solution ambiguity problem, while the exploitation of neighboring pixel constraints allows reducing the reconstruction noise.

In [16], an MCh PU method using a deterministic constraint was proposed. The constraint imposes that a pixel and its neighboring ones are belonging to the same local plane, whose parameters are estimated by a local cluster of data using an ML approach.

Later, statistical constraints have been explained. Bayesian approaches, such as the maximum a posteriori (MAP), taking into account the a priori statistical distributions for the two-dimensional (2-D) height profiles together with MCh data, have been introduced in [19].

The joint use of MCh data and contextual information can be particularly useful in the absence of coherent stable reflecting structures on the ground, as, for instance, permanent scatterers [2], and in the presence of high decorrelation. These techniques are particularly helpful when the fiducial points density is not sufficient to guarantee good results, even if algorithms properly developed to find networks of stable points are applied [23]. In this case, contextual MCh techniques can allow high-quality reconstructions also for distributed and progressively decorrelating targets.

A deep and quantitative analysis on the best reconstruction accuracy that can be achieved by both ML- and MAP-based approaches is reported in [15]. The obtained results are very interesting. It shows that while ML techniques exhibit an accuracy that weakly depends on the height slope and strongly depends on the baselines choice, the MAP technique exhibits an accuracy that strongly depends on the height slope and weakly depends on the baselines choice, thus relaxing the requirements on the baseline values, thus allowing a larger flexibility in their choice.

Within this article, an overview of the statistical methods, developed in both the classical and Bayesian estimation framework for solving the MCh InSAR PU problem for DEM generation is presented, stressing the usefulness of the contextual information and drawing evolutions and new scenarios of PU approaches for the future.

MULTICHANNEL SYSTEMS AND CONTEXTUAL INFORMATION

An InSAR MCh system exploits different interferograms related to the same observed scene acquired with a diversity, i.e., by using different channels. Two typologies of diversity are commonly adopted: multifrequency and multibaseline configurations. In multifrequency systems, multiple acquisition are obtained by observing the scene from the same position but using different working frequencies (or wavelengths λ), or by partitioning the SAR signal

spectrum in subbands [16], [24]. Multibaseline systems consist of observing the scene with the same frequency from at least three slightly different positions (i.e., at least two different orthogonal baselines B_{\perp}). The multibaseline geometry is shown in Figure 1 in the case of two baselines: $B_{\perp 1}$ and $B_{\perp 2}$.

Considering K different channels, the acquired interferometric phase signal for the pixel s is related to the ground height via the following equation:

$$\phi_k(s) = \langle \alpha_k h(s) + w_k(s) \rangle_{2\pi}, \quad k = 1, \dots, K, \quad s = 1, \dots, S, \quad (1)$$

where S is the number of image pixels, k is the channel index, w is the interferometric phase noise, $\langle \cdot \rangle_{2\pi}$ represents the “modulo- 2π ” operation, and α_k is a coefficient that takes into account the multifrequency or multibaseline diversity. In particular, α_k is given by

$$\alpha_k = \frac{4\pi d_k}{R_0 \sin \theta}, \quad (2)$$

where d_k is equal to B_{\perp}/λ_k in case of multifrequency systems, or to $B_{\perp k}/\lambda$ in the case of multibaseline systems, θ is the view angle, and R_0 is the distance between the master antenna and the center of the scene. The DEM reconstruction problem, in an MCh framework, consists of estimating the height values $h(s)$ by properly combining the K channels measured wrapped phases at position s , i.e., the vector $\Phi(s) = [\phi_1(s) \phi_2(s) \dots \phi_K(s)]^T$.

As previously mentioned, MCh approaches are useful in removing the problem of solution multiplicity; however, they could not guarantee optimal performances in DEM estimation. To improve the reconstruction accuracy and regularize the solution, contextual information has proven to be helpful.

The choice of the quantity (how many?) and the quality (which one?) of the baselines affects the final performance of the DEM estimation: the larger the number of baselines, and the more different (from each other) the baseline values, the better the expected estimation performance. Unfortunately, it is often difficult to be able to collect SAR data relevant to several baselines of required length. In the repeat pass system configuration, this circumstance would imply several days or, worse, weeks of data acquisition. Such a situation has a twofold undesired effect: very long acquisition time and lower coherence values due to the increasing of the temporal decorrelation (the positive effect due to the acquisition of several baselines can be thwarted for the presence of larger phase noise).

For this reason, it is very interesting and useful, from a practical point of view, to use a limited number of baselines, without impairing the performance of the method. It can be realized with the application of an external regularization rule, i.e., the introduction of constraints on the height profile to be reconstructed through contextual information, as opposed to a pixel-based approach. Such an approach is closer to human perception and presents strong relations with computer vision, image analysis, and pattern recognition.

DEM reconstruction capabilities can dramatically be improved if contextual information is exploited. Contextual information exploits the connections between adjacent pixel behaviors across

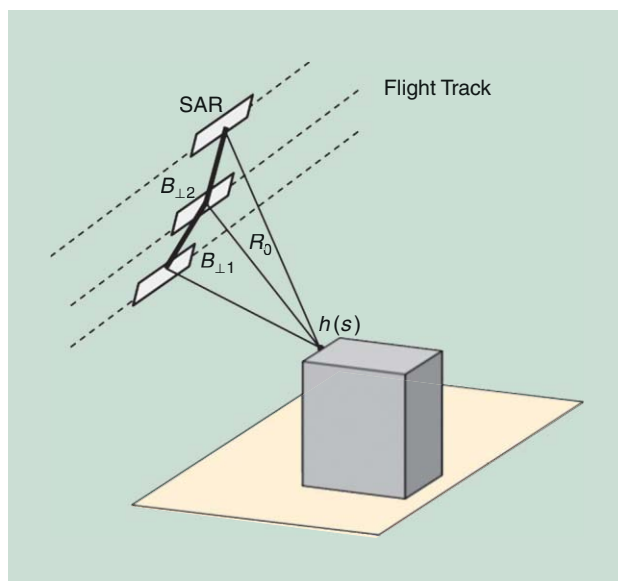


[FIG1] Two-baselines ($B_{\perp 1}$ and $B_{\perp 2}$) InSAR system geometry for the estimation of height $h(s)$.

the considered scene. It is likely that, especially in natural scenarios, the height relevant to a pixel is strictly related to its surrounding pixels, particularly its neighborhood. The exploitation of the contextual information provides a regularization that derives from the natural properties of the imaged scene, instead from an external rule imposition. In our case, being the unknown image representative of the height of an observed scene, strong contextual pixel information is very likely to be.

Two main classes of contextual information can be identified: deterministic and stochastic. Within the first class, an interesting approach is the so-called local planes technique [16]. The method consists of estimating the profile values at a given position starting from the wrapped phase values in the same position and in a “cluster” of neighboring positions. The assumption is that the height of a pixel, and consequently its interferometric phase value, is linearly related to its neighborhood. The characteristic parameters of a plane, linearly approximating the height profile in correspondence of the position of the pixel of the cluster, are estimated. In practice, planes in a three-dimensional (3-D) space can approximate the DEM locally. As an example, considering a pixel s , a squared neighboring system \mathcal{N}_s , constituted by $N = 9$ positions, has been considered in Figure 2. The height behavior of the pixels of the cluster can be approximated and modeled as a plane (the grey plane of Figure 2).

A second contextual information-based approach consists of modeling the interpixel dependencies of the neighboring system \mathcal{N}_s in a stochastic way, instead of a deterministic one, through an a priori joint probability density function (pdf). In such a way, the statistical distribution similarities of adjacent pixels can be taken into account, assigning different probabilities to different pixel configurations.

In this framework, the Markov random field (MRF) theory has proved to be a powerful and effective tool for modeling images, taking into account the contextual pixel information [17]. In the MRF

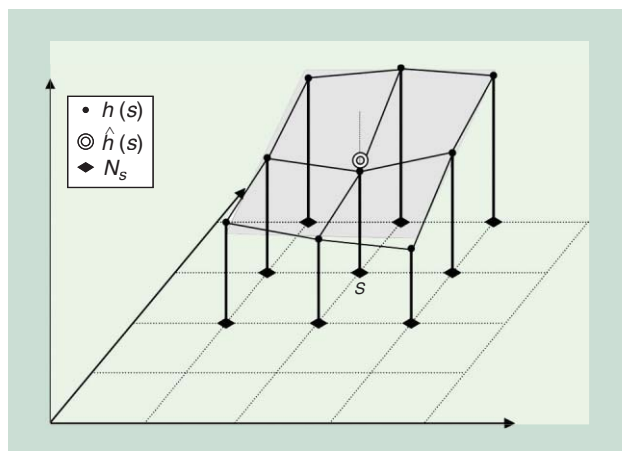


[FIG2] The plane (grey) approximating the true profile for position s in the grid, for a neighboring system consisting of $N = 9$ positions: \blacklozenge represents the neighborhood N_s of pixel s , \bullet represents the true height values, and \odot represents the height value approximated by the plane.

framework, the local Gaussian MRF (LGMRF) model described in [19] adapts well to describe natural scenarios. By properly tuning the locally defined model parameters related to the statistical correlation between neighboring pixels, an LGMRF can be adapted to any imaged scene, even in the presence of high slopes or strong height discontinuities. This peculiarity leads to a general model, well suited to represent a wide class of height profiles.

MULTICHANNEL PHASE UNWRAPPING FOR DIGITAL ELEVATION MODEL GENERATION

Within this section, MCh PU techniques for DEM generation are presented. By exploiting the statistical distribution of data, such techniques are able to effectively combine the MCh-available data.

In the following, three techniques developed in the statistical estimation framework will be presented and discussed: the ML approach, which does not exploit any constraints between neighboring pixels; ML with local planes (MLLP), which exploits deterministic constraints between neighboring pixels; and MAP approach, which exploits statistical constraints between neighboring pixels.

MAXIMUM LIKELIHOOD

Let us consider the height value $h(s)$ of an image as deterministic parameters. The ML solution consists of finding the unknown $h(s)$ maximizing the likelihood function $f(\phi_k(s); h(s))$. Starting from the interferometric phase noise statistical distribution [25] and taking into account the phase-height relation of (1), the likelihood

function in case of a single interferogram for the k th channel is shown in (3) at the box at the bottom of the page, where $\gamma_k(s)$ is the coherence of the k th channel, i.e., the complex correlation coefficient between the two SAR images that produce the k th interferogram, at position s . Its value is related to different aspects, such as phase noise and ground scene changes that occurred during the temporal interval between the two acquisitions [1].

The likelihood function (3) is periodic with period $T_k = 2\pi/\alpha_k$, and so it exhibits an infinite number of global maxima (see the dotted line of Figure 3), leading to ambiguous solutions.

The ambiguity can be solved considering additional MCh phase measures $\phi_k(s), (k = 1, \dots, K)$. Considering K independent phase measures, the MCh likelihood function can be defined as

$$F_{MCh}(\Phi(s); h(s)) = \prod_{k=1}^K f(\phi_k(s); h(s)). \tag{4}$$

The multiplication of K single channel likelihood functions with different periods (effect of different baselines and/or working frequencies) avoids multiple global maxima that occur in single channel likelihood function, at least in the range of interest for $h(s)$. This effect is shown in Figure 3 (continuous line).

The assumed independence between interferometric phases is strictly related to the choice of the interferograms. In case of multifrequency systems, the independence can be easily satisfied by exploiting nonoverlapped bands [16]. This hypothesis is not always verified in case of multibaseline. An interesting study on the multibaseline configuration, in case the interferograms are not statistically independent, can be found in [26] for the dual baseline case. In [26], it is shown that assuming the two interferograms to be independent, does not significantly affect the results, even if they are statistically dependent. The independence hypothesis can become more critical in the case of more than two baselines. In any case, it has to be pointed out that a closed-form expression of the joint pdf of the interferometric phases is not available for more than two baselines. Then, its approximate expression, obtained by using the independency assumption, is always adopted. The effect of this approximation on the DEM reconstruction accuracy is an important point that merits further investigations.

The MCh ML solution of the PU problem is

$$\begin{aligned} \hat{h}(s)_{ML} &= \arg \max_h F_{MCh}(\Phi(s); h(s)) \\ &= \arg \max_h \prod_{k=1}^K f(\phi_k(s); h(s)). \end{aligned} \tag{5}$$

The position of the global maximum of F_{MCh} represents the estimated height. Several global optimization procedures can be applied for solving the nonlinear maximization in (5). It must be pointed out that, for each fixed pixel, the maximization in (5) has to be performed respect to a scalar

$$\begin{aligned} f(\phi_k(s); h(s)) &= \frac{1}{2\pi} \frac{1 - |\gamma_k(s)|^2}{1 - |\gamma_k(s)|^2 \cos^2(\phi_k(s) - \alpha_k h(s))} \\ &\times \left\{ 1 + \frac{|\gamma_k(s)| \cos(\phi_k(s) - \alpha_k h(s)) \cos^{-1}[-|\gamma_k(s)| \cos(\phi_k(s) - \alpha_k h(s))]}{[1 - |\gamma_k(s)|^2 \cos^2(\phi_k(s) - \alpha_k h(s))]^{1/2}} \right\} \end{aligned} \tag{3}$$

unknown parameter, so that numerical complexity is not critical and parallel and efficient numerical techniques can be easily implemented.

MAXIMUM LIKELIHOOD WITH LOCAL PLANES

As described in the previous section, ML works pixel-wise, treating the height estimation of each pixel independently from the surrounding ones. Better performance can surely be achieved if some constraints based on contextual information are introduced. In particular, within this section, the joint exploitation of the ML approach with the deterministic contextual information provided by local planes, reported in the section “Multichannel Systems and Contextual Information,” is presented.

Let us consider a “cluster” of neighbors of the pixel s , called \mathcal{N}_s , formed by the pixel itself, and by $N - 1$ neighboring pixels. The considered contextual information consists of approximating the height surface in the cluster \mathcal{N}_s by a plane. The height $z(n)$ of each pixel belonging to \mathcal{N}_s can be approximated by the equation [16]

$$z(n) = a(s) \Delta\alpha + b(s) \Delta\beta + c(s), \quad n \in \mathcal{N}_s, \quad (6)$$

where only the case of a perfect vertical plane is excluded. Note that $\Delta\alpha$ and $\Delta\beta$ of (6) represent the ground range and the azimuth sampling steps, respectively.

In place of estimating the height values for each pixel independently from the others as performed by the ML method, the parameters $a(s)$, $b(s)$, and $c(s)$ of the plane best approximating in the ML sense the true height profile of the pixel belonging to \mathcal{N}_s are sought. Thus, for each pixel, a vector of three unknown parameters $\mathbf{x}_s = [a(s) \ b(s) \ c(s)]^T$ has to be estimated by exploiting $N \times K$ wrapped phase values $\{\Phi^T(n), n \in \mathcal{N}_s\}$, where $\Phi(n)$ are the measured wrapped phase K -element vectors defined in (4).

The MLLP solution for the $h(s)$ reconstruction is achieved via a two-step procedure. The first step consists of estimating the unknown parameter vector \mathbf{x}_s by computing

$$\begin{aligned} \hat{\mathbf{x}}_s &= \underset{\mathbf{x}}{\operatorname{argmax}} \prod_{n \in \mathcal{N}_s} F_{\text{MCh}}(\Phi(n) | \mathbf{x}_s) \\ &= \underset{\mathbf{x}}{\operatorname{argmax}} \prod_{n \in \mathcal{N}_s} \prod_{k=1}^K f(\phi_k(n) | \mathbf{x}_s). \end{aligned} \quad (7)$$

The likelihood term $f(\phi_k(n) | \mathbf{x}_s)$ is derived from (3) by considering the neighborhood cluster $n \in \mathcal{N}_s$ instead of a single pixel s , and instead of the height $h(n)$ the local plane $z(n)$ that depends on the unknown parameter vector \mathbf{x}_s . Once $\hat{\mathbf{x}}_s$ is estimated, the height of the pixel is assumed as the “central” point s of the estimated plane.

Considering Figure 2, the height of the central pixel (referred to as \bullet) is approximated by the central point of the plane (referred to as \odot), computed by exploiting the $N \times K$ ($N = 9$) wrapped phase measures. This led to an improvement of the ratio between the number of independent measures and the number of unknowns, compared to the ML.

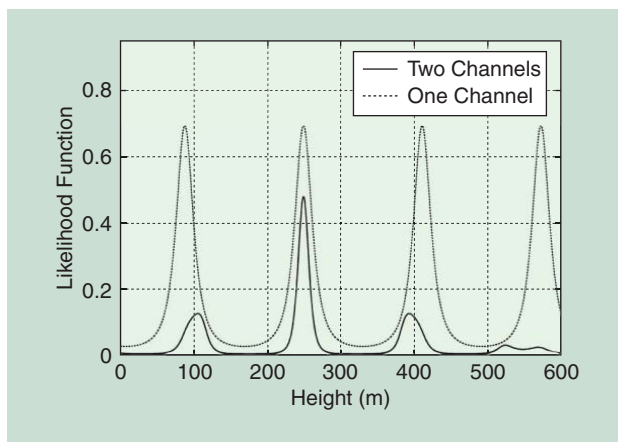


[FIG3] Single channel (dotted line) and multichannel (continuous line) likelihood functions.

In this case, the maximization in (7) has to be performed pixel-wise with respect to a vector of three unknown parameters, exploiting a number of data that depends on the neighborhood. Also in this case, the numerical complexity is not critical, and parallel and efficient numerical techniques can be easily implemented.

MAXIMUM A POSTERIORI

The contextual information can also be exploited in a statistical framework, i.e., modeling the behavior of a pixel to its neighborhood by considering the statistical distribution of the unknown image. This distribution is usually defined in such a way to assign high probability to particular pixel configurations. An effective tool to statistically describe and model the unknown height profile, able to take into account the contextual information between neighboring pixels, is provided by MRF theory.

According to the Hammersley–Clifford theorem [17], an MRF can be analytically expressed by a Gibbs distribution. The type of Gibbs distribution, or equivalently of the MRF, can be chosen according to the characteristics of the image. As already stated, a general model that well fits in case of a wide class of height profiles is the local Gaussian MRF (LGMRF), whose expression is [19]

$$g_H(h; \boldsymbol{\sigma}) = \frac{1}{Z(\boldsymbol{\sigma})} \exp \left\{ - \sum_{s=1}^S \sum_{n \in \mathcal{N}_s} \left[\frac{(h(s) - h(n))^2}{2\sigma_{s,n}^2} \right] \right\}, \quad (8)$$

where $\sigma_{s,n}$ are the so-called hyperparameters, $\boldsymbol{\sigma}$ is the hyperparameter vector collecting all $\sigma_{s,n}$ values, and $Z(\boldsymbol{\sigma})$ is the so-called partition function. In this framework, the unknown image $\mathbf{h} = [h(1) \ h(2) \ \dots \ h(s)]^T$ is considered as a sample of a random vector \mathbf{H} with an a priori Gibbs distribution.

The hyperparameter values, which are locally defined, are related to the height spatial variation between adjacent pixels. The hyperparameter $\sigma_{s,n}$, in fact, can be seen as an indicator of the spatial correlation of the neighboring pixels. A high value of $\sigma_{s,n}$ means that the probability that two neighboring pixels s and n have different height values is high. On the contrary, a low value of $\sigma_{s,n}$ implies that the probability that $h(s)$ and $h(n)$ are different is small. By changing the hyperparameter values, the LGMRF model can be adapted to describe the image local nature.

Exploiting the LGMRF model for the a priori statistical description of the unknown \mathbf{h} , and following Bayes' rule, the MAP solution for the height reconstruction is provided by the value that maximizes the logarithm of the a posteriori distribution

$$\begin{aligned} \hat{\mathbf{h}}_{\text{MAP}} &= \arg \max_{\mathbf{h}} \ln \left\{ \prod_{s=1}^N F_{\text{MCh}}(\Phi(s)|h(s)) \right\} g_H(\mathbf{h}, \hat{\sigma}) \\ &= \arg \min_{\mathbf{h}} \left\{ - \sum_{s=1}^S \ln F_{\text{MCh}}(\Phi(s)|h(s)) \right. \\ &\quad \left. + \sum_{s=1}^S \sum_{n \in N_s} \left[\frac{(h(s) - h(n))^2}{2\hat{\sigma}_{s,n}^2} \right] \right\}. \end{aligned} \quad (9)$$

The a posteriori distribution of (9) is obtained as the product of the MCh likelihood function of (4) and the a priori distribution of (8).

Clearly, the hyperparameters as they appear in (9) are not a priori known and have to be estimated from the available data, the measured phase interferograms $\mathbf{y} = [\Phi^T(1) \ \Phi^T(2) \ \dots \ \Phi^T(S)]^T$ defined in (4).

An efficient and effective way to estimate the hyperparameters from the available noisy data is provided by the expectation-maximization (EM) algorithm [17]. The expression of the hyperparameter estimation update at the $(l+1)$ th step of the EM algorithm with respect to pixel s is

$$\hat{\sigma}_s^2(l+1) = E \left[\frac{1}{9} \sum_{n \in N_s} [h(s) - h(n)]^2 \mid \mathbf{y}, \hat{\sigma}_s(l) \right]. \quad (10)$$

The conditional expectation $E[\cdot]$ of the unknown \mathbf{h} given the observed data \mathbf{y} and the current estimation $\hat{\sigma}_s(l)$ is performed. To compute the expectation over \mathbf{h} , samples of this random vector at the l th iteration are mandatory. The sampling is iteratively performed starting from the a posteriori distribution of \mathbf{h} using the Metropolis algorithm. The local estimation of hyperparameters is very powerful, because it allows the localization of the flat regions and the discontinuities of the image.

Once the hyperparameters have been estimated for all the pixels, $\sigma_{s,n}$ is set to be $\hat{\sigma}_{s,n} = (\hat{\sigma}_s + \hat{\sigma}_n)/2$. More details on hyperparameter estimation can be found in [19].

The height samples generated during the hyperparameter estimation procedure can be used to initialize the search of the solution of (9). Therefore it is possible to carry out the optimization step using a semideterministic solution: the iterated conditional modes (ICM) algorithm is appropriate for this purpose. For a deeper analysis on the numerical implementation of the algorithms required by both hyperparameter estimation and optimization steps (i.e., Metropolis algorithm and ICM) refer to [17].

The computational burden can be, differently from the previous cases, critical for large size images. Anyway, alternative more efficient optimization schemes can be adopted (see the next section).

NEW TRENDS

Besides the previously presented MCh algorithm, some new techniques developed in the contextual information framework have been recently proposed.

An improvement of the MAP approach, called *multichannel phase unwrapping + total variation*, has been presented in [27]. Such an algorithm is able to overcome some limitations of MAP approach regarding computational time and robustness to local optima in the optimization process. In particular, the new technique is able to provide the global optimum for the considered energy function within a short time exploiting the graph-cut-based optimization tools. Its main drawback regards the memory occupation, which is excessive in the case of large images.

Recently, an evolution of multichannel phase unwrapping + total variation, specifically thought for 3-D reconstruction of urban areas using VHR images, able to exploit the additional information provided by the amplitude of SAR data, has been introduced [28]. The amplitude data plays a double role: it helps both phase regularization and PU steps. In particular, amplitude data are useful for preserving height discontinuities and smoothing noise in homogeneous areas. The method is also able to correctly handle MCh InSAR data corrupted by atmospheric artifacts and phase offsets, which is mandatory for a correct 3-D mapping.

Within the Bayesian estimation framework, interesting algorithms for PU that exploit the extended Kalman filter (EKF) have been proposed. The usefulness of the EKF for joint PU and noise reduction has been first demonstrated in [29] and recently adapted to work with MCh interferometric stacks, achieving interesting reconstruction improvements [30]. The EKF is a two-step technique for nonlinear fixed interval smoothing, performing simultaneously PU, noise reduction, and data fusion by a proper state space model design. Since it does not require an accurate numerical maximization of nonconvex objective functions, it can achieve high computational efficiency while maintaining the benefits of statistical Bayesian approaches. Its main drawback is related to the application of a monodimensional filter to a 2-D domain problem, which implies that, at the present, some empirical coefficients have to be set.

EXPERIMENTS

To evaluate the performances of the described MCh PU algorithms, three case studies are considered. In particular, a simulated data set has been generated to quantitatively evaluate the unwrapping performances of the different approaches, and two real data sets (acquired by ENVISAT and COSMO-SkyMed sensors) have been considered to validate results on real images.

SIMULATED DATA

A simulated data set has been generated using the profile shown in Figure 4(a). Five noisy interferograms with orthogonal baselines of [237.72 255.90 322.60 399.92 544.81] m have been simulated. The working frequency has been set to 5.3 GHz while R_0 , the distance between the sensor and the center of the scene, has been set to 700 km. The coherence for the whole scene has been simulated according to the rule $\gamma_k = \gamma_0 (1 - (B_{\perp k}) / (B_{\perp \max}))$, where $B_{\perp \max}$ is a constant related to the critical baseline, and set equal to 1,000 m.

The interferogram related to the smallest baseline is shown in Figure 4(b). The DEM has been estimated by applying ML, MLLP, and MAP, the results of which are reported in Figure 4(c)–(e),

respectively. The reconstruction error progressively reduces from ML to MLLP solution (i.e., when deterministic contextual information is exploited) and from MLLP to MAP result (i.e., when statistical contextual information is considered).

To quantitatively evaluate the performances of the considered approaches with respect to stack characteristics, estimations have been performed varying both coherence value γ_0 and number of channels K . As an index of reconstruction accuracy, the normalized root mean square error defined as

$$\varepsilon_h = \sqrt{\frac{\|\hat{\mathbf{h}} - \mathbf{h}\|^2}{\|\mathbf{h}\|^2}}, \quad (11)$$

has been computed and reported in Figure 5. In (11) \mathbf{h} is the vector collecting the true height values, $\hat{\mathbf{h}}$ is the vector collecting the estimated values, and $\|\cdot\|^2$ is the quadratic norm. Results confirm what is expected: MAP overcomes MLLP and MLLP overcomes the ML solution. It is evident how the contextual information can greatly improve the accuracy of the estimated DEM, in particular in the case of stochastic relation between nearby pixels.

REAL DATA SET

The considered algorithms have been tested on two real data sets. The first image stack has been acquired by the ENVISAT

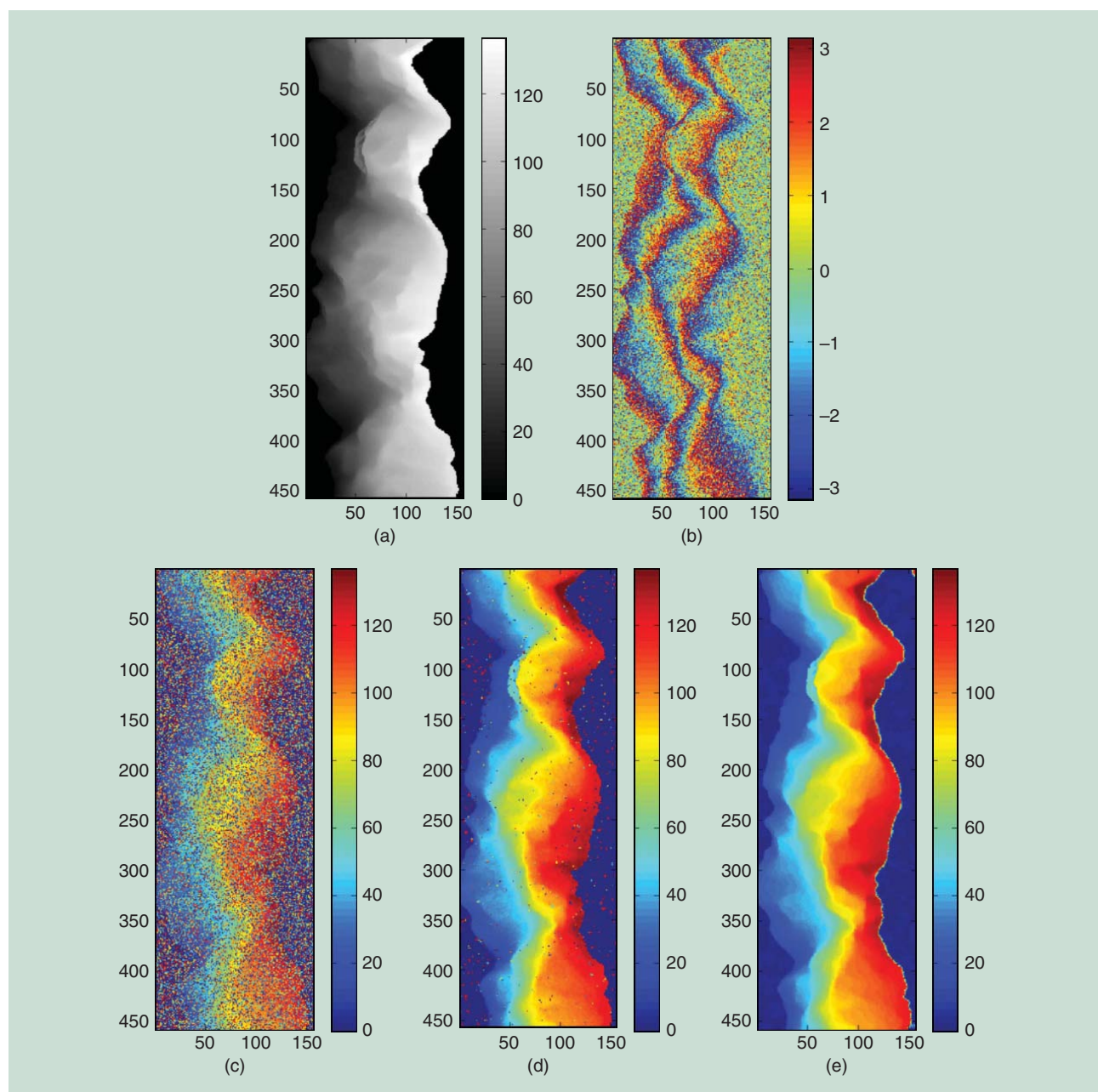


[FIG4] A simulated data set. (a) The height profile and (b) smallest baseline interferogram. The coherence has been set to 0.85. (c) The DEM reconstruction with ML, (d) MLLP, and (e) MAP approaches. On the axes, the pixel indices are reported.

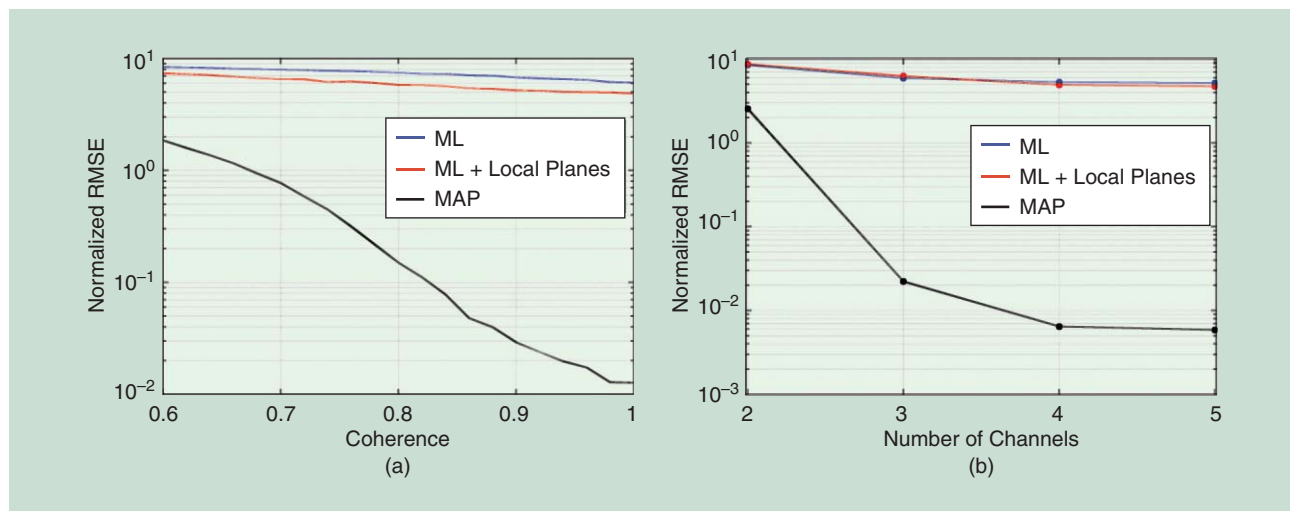


[FIG5] The normalized root mean square error of considered MCh PU techniques with respect to (a) the coherence value γ_0 and (b) number of channels K .

sensor and refers to a natural scenario, a mountain in the region of Las Vegas, Nevada (United States). Acquisition parameters are the same of the simulated data set. Before applying MCh PU algorithms, the flat earth component has been removed, and phase offsets have been compensated. To better appreciate the accuracy of the obtained results, the SRTM DEM has been subtracted to the reconstructed profiles. These residual components—ML, MLLP, and MAP—are reported in Figure 6(a)–(c), respectively. The obtained results confirm the outcome of the simulated data. The MAP solution

outperforms MLLP and ML, both in terms of restoration and reconstructed details. It provides a reliable and realistic reconstruction, as it is evident in the 3-D projection of the computed DEM [Figure 6(d)].

The second data set is composed by 30 COSMO-SkyMED sensor images acquired in the urban area of Nola, Italy. This data set has been chosen to test the algorithms on a different scenario, compared to the Las Vegas one: data are acquired in X-band, instead of C-band, and are related to an urban area which, differently from a natural scenario, is characterized by

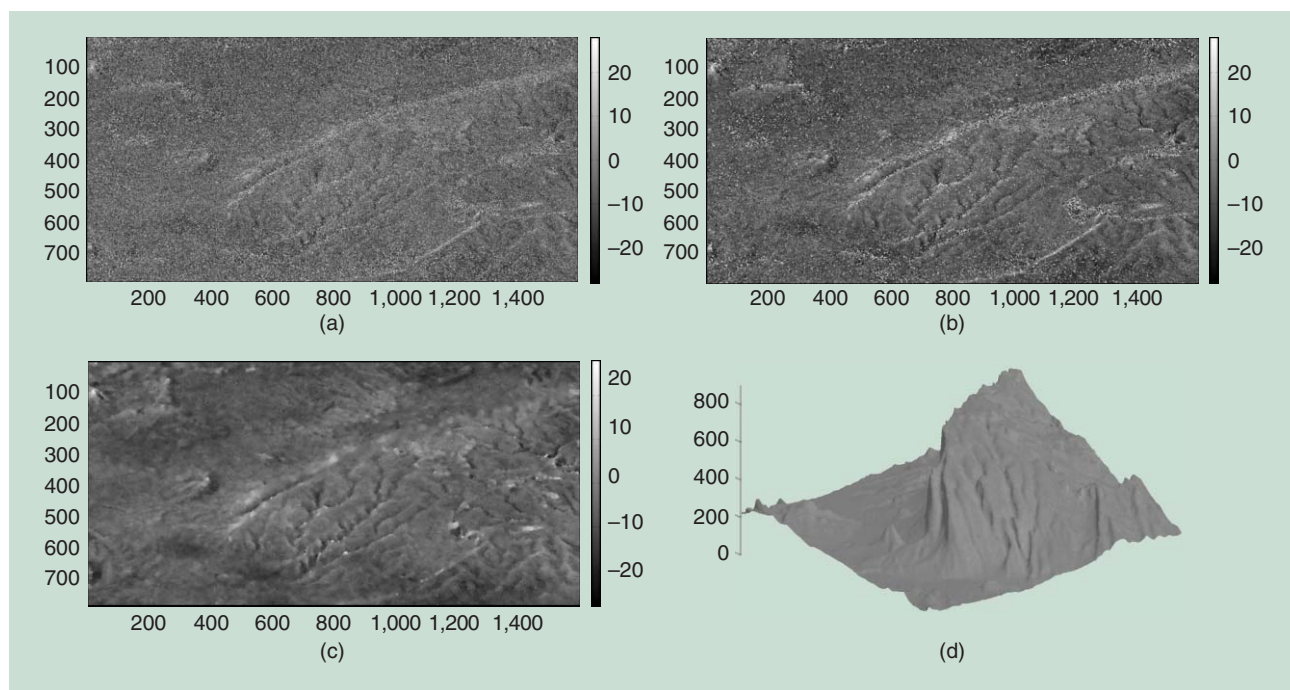


[FIG6] The results on the Las Vegas site—ENVISAT data: (a) ML, (b) MLLP, and (c) MAP residual reconstructions, and (d) 3-D projection of MAP solution. On the axes, the pixel indices are reported.

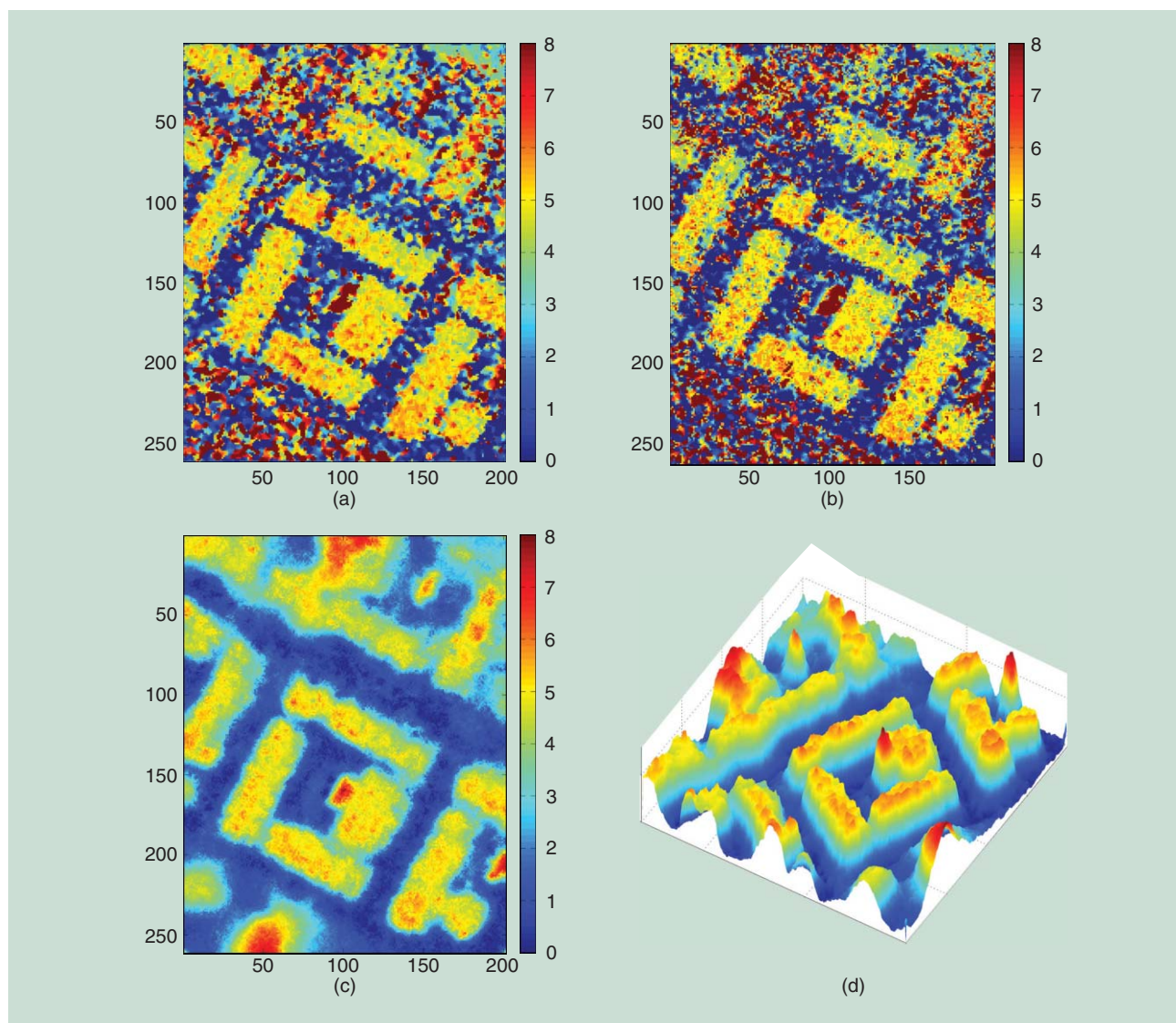


[FIG7] The results on the Nola site–COSMO–SkyMED data: (a) ML, (b) MLLP, and (c) MAP solutions, and (d) the MAP 3-D projection. On the axes, the pixel indices are reported.

sharp discontinuities due to the presence of man-made structures. Results of the considered approaches are reported in Figure 7: (a) ML, (b) MLLP, and (c) MAP. Even in this scenario, contextual information, in particular the stochastic one (MAP solution) is able to sensibly improve the performances of the DEM generation. To appreciate the high accuracy and reliability of the MAP solution, its 3-D projection is presented in Figure 7(d).

CONCLUSIONS

The role of the contextual information in the MCh InSAR PU problem has been discussed. The exploitation of interdependency between nearby pixels has been shown to be effective in regularizing the solution and in providing high-accuracy DEM. To assess the positive effect of contextual methods, three different MCh PU techniques have been investigated:

ML, MLLP, and MAP. The first methodology, the ML, makes no use of any contextual information, the second one, the MLLP describes the pixel neighborhood dependency using a deterministic model, while MAP exploits a stochastic relation between nearby pixels. The obtained results show that contextual information can substantially improve the DEM reconstruction performances, particularly in the case of stochastic models. This improvement has been quantitatively evaluated on a simulated data set and validated on two different real data scenarios.

ACKNOWLEDGMENTS

This work was supported in part by the Italian Space Agency within project ID2246 “Development of Imaging and Monitoring Methodologies Based on the Use of COSMO–SkyMed SAR Data” under contract I/065/09/0.

AUTHORS

Fabio Baselice (fabio.baselice@uniparthenope.it) received the B.S. and M.S. degrees in telecommunication engineering and the Ph.D. degree in information engineering from the Università di Napoli "Parthenope" in 2004, 2007, and 2010, respectively. He was a visiting student at Telecom ParisTech, France, and at the University of Antwerp, Belgium. He previously worked as a post-doctoral researcher with the Italian Consortium of Telecommunications (CNIT) and the Università di Napoli "Parthenope." He is the author of more than 35 scientific papers. His research interests are in statistical signal processing, synthetic aperture radar interferometry, and magnetic resonance imaging.

Giampaolo Ferraioli (giampaolo.ferraioli@uniparthenope.it) received the B.S. and M.S. degrees (summa cum laude) and Ph.D. degree in telecommunication engineering from the Università di Napoli "Parthenope" in 2003, 2005, and 2008, respectively. Currently, he is an assistant professor at the Università di Napoli "Parthenope." He is the author of more than 40 scientific papers published in international journals and conference proceedings. His main research interests are in statistical signal and image processing, synthetic aperture radar, and magnetic resonance imaging. He won the IEEE 2009 Best European Ph.D. Thesis in Remote Sensing Prize, sponsored by the IEEE Geoscience and Remote Sensing Society.

Vito Pascazio (vito.pascazio@uniparthenope.it) graduated summa cum laude in 1986 from the Università di Bari with the M.S. degree in electronic engineering and received the Ph.D. degree in 1990 from the Università di Napoli Federico II. In 1990, he joined the Università di Napoli Parthenope, where he is a full professor of telecommunications and the chair of the Department of Engineering. He is the director of the National Laboratory of Multimedia Communications of the Italian Consortium of Telecommunications. He is the general cochair of the 2015 IEEE International Geoscience and Remote Sensing Symposium. His main scientific interests are in the fields of remote sensing, and statistical estimation, with emphasis on image processing and the reconstruction of microwave images. He has published more than 150 technical papers. He is a Senior Member of the IEEE.

Gilda Schirinzi (gilda.schirinzi@uniparthenope.it) graduated with the M.S. degree in electronic engineering in 1983 from the Università di Napoli "Federico II" (Italy). In the same year she joined the Electronic Engineering Department as a research fellow. In 1988, she joined the Istituto di Ricerca per l'Elettromagnetismo e i Componenti Elettronici of the Italian National Council of Researches. She became an associate professor of telecommunications at the University of Cassino (Italy) in 1998, and, in 2005, she became a full professor. She has been with the Università di Napoli "Parthenope" since 2008. Her main scientific interests are in the field of image and signal processing, with particular reference to synthetic aperture radar systems and microwave remote sensing.

REFERENCES

[1] R. Bamler and P. Hartl, "Synthetic aperture radar interferometry," *Inv. Probl.*, vol. 14, no. 4, pp. R1–R54, 1998.

[2] G. Fornaro and V. Pascazio, *SAR Interferometry and Tomography: Theory and Applications* (Vol. 2: Academic Press Library in Signal Processing). Amsterdam, the Netherlands: Elsevier, 2013.

[3] A. R. Thompson, J. M. Moran, and G. W. Swenson, *Interferometry and Synthesis in Radio Astronomy*. New York: Wiley Interscience, 1986.

[4] A. K. Funai, J. A. Fessler, D. T. B. Yeo, V. T. Olafsson, and D. C. Noll, "Regularized field map estimation in MRI," *IEEE Trans. Med. Imag.*, vol. 27, no. 10, pp. 1484–1494, 2008.

[5] R. M. Goldstein, H. A. Zebker, and C. L. Werner, "Satellite radar interferometry: Two-dimensional phase unwrapping," *Radio Sci.*, vol. 23, no. 4, pp. 713–720, 1988.

[6] H. A. Zebker and Y. Lu, "Phase unwrapping algorithms for radar interferometry: Residue-cut, least-squares, and synthesis algorithms," *J. Opt. Soc. Am.*, vol. 15, no. 3, pp. 586–598, 1998.

[7] M. Costantini, "A novel phase unwrapping method based on network programming," *IEEE Trans. Geosci. Remote Sensing*, vol. 36, no. 3, pp. 813–821, 1999.

[8] F. Li and R. Goldstein, "Studies of multibaseline spaceborne interferometric synthetic aperture radars," *IEEE Trans. Geosci. Remote Sensing*, vol. 28, no. 1, pp. 88–97, 1990.

[9] F. Lombardini, "Optimum absolute phase retrieval in three-element SAR interferometry," *Electron. Lett.*, vol. 34, no. 5, pp. 1522–1524, 1998.

[10] A. Ferretti, C. Prati, and F. Rocca, "Multibaseline phase unwrapping for InSAR topography estimation," *Il Nuovo Cimento*, vol. 24, no. 1, pp. 159–176, 2001.

[11] M. Eineder and N. Adam, "A maximum-likelihood estimator to simultaneously unwrap, geocode, and fuse SAR interferograms from different viewing geometries into one digital elevation model," *Appl. Numer. Math.*, vol. 43, no. 4, pp. 359–373, 2002.

[12] G. Fornaro, A. Monti Guarnieri, A. Pauciuolo, and F. De-Zan, "Maximum likelihood multibaseline SAR interferometry," *IEEE Proc. Radar, Sonar Navig.*, vol. 153, no. 3, pp. 279–288, 2006.

[13] F. Gini and F. Lombardini, "Multibaseline cross-track SAR interferometry: A signal processing perspective," *IEEE Aerosp. Electron. Syst. Mag.*, vol. 20, no. 8, pp. 71–93, Aug. 2005.

[14] V. Pascazio and G. Schirinzi, "Estimation of terrain elevation by multifrequency interferometric wide band SAR data," *IEEE Signal Processing Lett.*, vol. 8, no. 1, pp. 7–9, 2001.

[15] G. Ferraiuolo, F. Meglio, V. Pascazio, and G. Schirinzi, "DEM reconstruction accuracy in multichannel SAR interferometry," *IEEE Trans. Geosci. Remote Sensing*, vol. 47, no. 1, pp. 191–201, 2009.

[16] V. Pascazio and G. Schirinzi, "Multifrequency InSAR height reconstruction through maximum likelihood estimation of local planes parameters," *IEEE Trans. Image Processing*, vol. 11, no. 12, pp. 1478–1489, 2002.

[17] S. Z. Li, *Markov Random Field Modeling in Image Analysis*. New York: Springer-Verlag, 2009.

[18] J. Dias and J. Leita, "The π algorithm: A method for interferometric image reconstruction in SAR/SAS," *IEEE Trans. Image Processing*, vol. 11, no. 4, pp. 408–422, 2002.

[19] G. Ferraiuolo, V. Pascazio, and G. Schirinzi, "Maximum a posteriori estimation of height profiles in InSAR imaging," *IEEE Geosci. Remote Sensing Lett.*, vol. 1, no. 2, pp. 66–70, 2004.

[20] G. Nico, G. Palubinskas, and M. Datcu, "Bayesian approaches to phase unwrapping: Theoretical study," *IEEE Trans. Signal Processing*, vol. 48, no. 9, pp. 2545–2556, 2000.

[21] R. Chen, W. Yu, R. Wang, G. Liu, and Y. Shao, "Integrated denoising and unwrapping of InSAR phase based on Markov random fields," *IEEE Trans. Geosci. Remote Sensing*, vol. 51, no. 8, pp. 4473–4485, 2013.

[22] G. Ferraiuolo and G. Poggi, "A Bayesian filtering technique for SAR interferometric phase fields," *IEEE Trans. Image Processing*, vol. 13, no. 10, pp. 1368–1378, 2004.

[23] F. Rocca, "Modeling interferogram stacks," *IEEE Trans. Geosci. Remote Sensing*, vol. 45, no. 10, pp. 3289–3299, 2007.

[24] R. Bamler and M. Eineder, "Split band interferometry versus absolute ranging with wideband SAR systems," in *Proc. 2004 IEEE Int. Geoscience Remote Sensing Symp. (IGARSS)*, vol. 2, pp. 980–984.

[25] D. Just and R. Bamler, "Phase statistics of interferograms with applications to synthetic aperture radar," *Appl. Opt.*, vol. 33, no. 20, pp. 4361–4367, 1994.

[26] M. Lucido, F. Meglio, V. Pascazio, and G. Schirinzi, "Closed-form evaluation of the second-order statistical distribution of the interferometric phases in dual-baseline SAR systems," *IEEE Trans. Signal Processing*, vol. 58, no. 3, pp. 1698–1707, 2010.

[27] G. Ferraioli, A. Shabou, F. Tupin, and V. Pascazio, "Multichannel phase unwrapping with graph-cuts," *IEEE Geosci. Remote Sensing Lett.*, vol. 6, no. 3, pp. 562–566, 2009.

[28] A. Shabou, F. Baselice, and G. Ferraioli, "Urban digital elevation model reconstruction using very high resolution multichannel InSAR data," *IEEE Trans. Geosci. Remote Sensing*, vol. 50, no. 11, pp. 4748–4758, 2012.

[29] O. Loffeld, H. Nies, S. Knedlik, and Y. Wang, "Phase unwrapping for SAR interferometry—A data fusion approach by Kalman filtering," *IEEE Trans. Geosci. Remote Sensing*, vol. 46, no. 1, pp. 47–58, 2008.

[30] D. Chirico and G. Schirinzi, "Multichannel interferometric SAR phase unwrapping using extended Kalman smoother," *Int. J. Microwave Wireless Technol.*, vol. 5, no. 3, pp. 429–436, 2013.



[Charles-Alban Deledalle, Loïc Denis, Giovanni Poggi, Florence Tupin, and Luisa Verdoliva]

Exploiting Patch Similarity for SAR Image Processing

[The nonlocal paradigm]

Most current synthetic aperture radar (SAR) systems offer high-resolution images featuring polarimetric, interferometric, multifrequency, multiangle, or multitime information. SAR images, however, suffer

from strong fluctuations due to the speckle phenomenon inherent to coherent imagery. Hence, all derived parameters display strong signal-dependent variance, preventing the full exploitation of such a wealth of information. Even with the abundance of despeckling techniques proposed over the last three decades, there is still a pressing need for new methods that can handle this variety of SAR products and efficiently eliminate speckle without sacrificing the spatial resolution.

Recently, patch-based filtering has emerged as a highly successful concept in image processing. By exploiting the redundancy between similar patches, it succeeds in suppressing most of the noise with good preservation of texture and thin structures. Extensions of patch-based methods to speckle reduction and joint exploitation of multichannel SAR images (interferometric, polarimetric, or PolInSAR data) have led to the best denoising performance in radar imaging to date. We give a comprehensive survey of patch-based nonlocal filtering of SAR images, focusing on the two main ingredients of the methods: measuring patch similarity and estimating the parameters of interest from a collection of similar patches.

Digital Object Identifier 10.1109/MSP.2014.2311305

Date of publication: 13 June 2014

INTRODUCTION

Current SAR systems share two common characteristics: they provide a wealth of information thanks to polarimetric, wavelength, or angle diversity, and they offer very high spatial resolutions that give access to the shape of man-made structures. In radar images, however, parameters of interest, like interferometric phase, coherence, polarimetric properties, or radiometry, are not directly accessible but must be estimated from unreliable data. It is essential that the estimation procedure be robust to the strong fluctuations in the measurements due to speckle without trading off the spatial resolution.

The simplest way to reduce speckle noise is to average pixels in a rectangular window around the target pixel, so-called spatial multilooking.

Although speckle is itself a signal of possible interest, in the context of despeckling it is an undesired component, and hence customarily referred to as *noise* with a slight abuse of terminology [1]. This process, already present in the first European Remote Sensing (ERS) satellite images and still widely used for interferometric or polarimetric data, leads to a uniform reduction of speckle in homogeneous areas, with a residual variance inversely proportional to the number of pixels averaged. However, by potentially mixing different signals, it also impairs such important signal features as region edges, man-made structures, and fine textures. The point is that multilooking is just a basic nonadaptive form of parameter estimation: to remove speckle without degrading fine features, local image content must be taken into account.

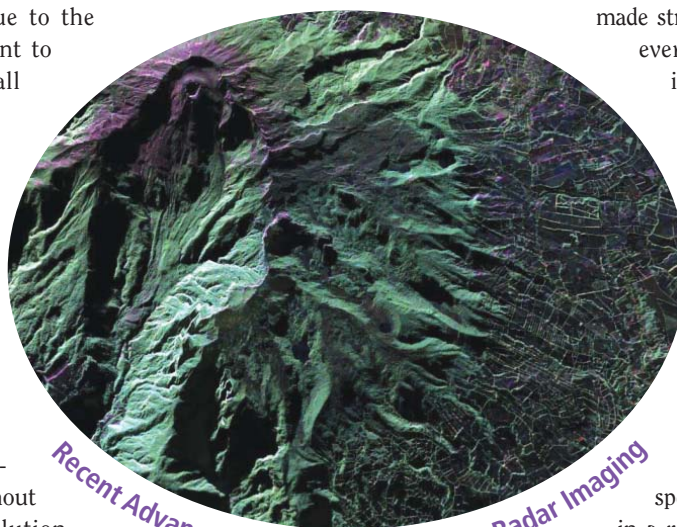


PHOTO COURTESY OF NASA

The design of efficient despeckling filters is a long-standing problem that has been the object of intense research since the advent of SAR technology [2], with the first contributions dating back to the 1980s [3]. However, research activity has accelerated significantly in recent years, reflecting both the success of SAR remote sensing in general and the lack of satisfactory methods for resolution-preserving speckle reduction. Some of the most successful methods proposed in the recent past for locally adaptive estimation are based on image models that enforce strong regularity constraints, either in the original domain (e.g., Markov random fields [4]), or in some transform domain (e.g., wavelet-based sparse representations [5]).

Very recently, patches, i.e., small rectangular image regions (typically squares of size between 3×3 and 11×11 pixels), have emerged as a powerful representation on which to build rich and flexible statistical models of natural images. Patches capture richer neighborhood configurations than first-order Markov random fields and are better localized than wavelets. Patch-based models do not enforce the solution to belong to a restricted class of signals, such as signals with bounded variations or with sparse

transform coefficients. They exploit the self-similarity, typical of natural scenes, and look for similar patches not just in the immediate neighborhood of the target pixel but in an extended search area. Unlike a local method like [6] that considers only connected pixels, far apart pixels can be combined, thereby justifying the widespread nonlocal appellation. The evolution from explicit image models to the concept of patch redundancy corresponds to a true methodological

shift in image processing. In particular, recent denoising methods most often rely on the notion of a patch.

Interestingly, the concept of nonlocal filtering originally emerged in image processing after the pioneering work of Lee [7] for SAR despeckling. However, it was only with the development of patch-based methods, following the seminal work [8] in the 2000s, and the definition of highly discriminative patch-based similarity measures, that nonlocal filtering could be successfully applied to the low-SNR speckle-corrupted SAR images. The paradigm of patch-based nonlocal estimation is particularly interesting for SAR image processing given the poor fit of classical models to SAR scenes, characterized by many very strong punctual targets and high-contrast structures that are poorly modeled with piece-wise constants or wavelets.

The potential of this new paradigm for SAR imaging has quickly been recognized, with more than 30 papers published since 2009 that describe patch-based methods applied to SAR, including most state-of-the-art despeckling techniques [9]–[11]. In addition, nonlocal patch-based methods are very flexible and can readily be extended to different SAR modalities [12]–[14].

This article reviews the underlying ideas and principles of nonlocal estimation methods proposed in SAR imaging. We consider despeckling as a familiar and important case study, but we also address the more general point of view of parameter estimation, looking ahead at extensions to more challenging SAR modalities and estimation problems. Before diving into the core of patch-based methods, we begin by describing the classical speckle model in SAR imaging and the major families of estimation methods that have emerged over the last three decades.

A SHORT OVERVIEW OF SAR DESPECKLING

Depending on the modality, SAR systems can record up to six channels of complex valued signals (see “SAR Imaging Modalities”). All of these signals present highly varying fluctuations because SAR is a coherent imaging system (see “Speckle Fluctuations in Radar Images”). The simplest way to reduce these fluctuations and estimate the values of the physical parameters is to average several independent samples from the data. This operation, called *multilooking*, was applied in various forms from the very beginning of the SAR era. However, such simple averaging that applies equally to every region of the image, regardless of the local heterogeneity, strongly degrades the spatial resolution.

IT IS ESSENTIAL THAT THE ESTIMATION PROCEDURE BE ROBUST TO THE STRONG FLUCTUATIONS IN THE MEASUREMENTS DUE TO SPECKLE WITHOUT TRADING OFF THE SPATIAL RESOLUTION.

SAR IMAGING MODALITIES

SAR systems are based on the emission of an electromagnetic wave that is then backscattered by the ground level features and finally recorded by the receiving antenna. Several modalities are used in SAR imaging (see [15] for a comprehensive survey):

- **Amplitude:** The simplest configuration provides, after SAR synthesis, an image of scattering coefficients \mathbf{k} that are complex values with a magnitude (i.e., amplitude) that is representative of the radar cross-section. The square magnitude (i.e., intensity) is also often considered.

- **Polarimetric:** The use of different polarizations at emission and reception of the radar wave provides a deeper insight into the backscattering mechanisms inside the resolution cell. The scattering vector \mathbf{k} is formed by the complex values corresponding to each combination of emission/reception polarizations. Usually, horizontal (H) and vertical (V) polarizations are used for emission and reception providing the scattering vector $\mathbf{k} = [z_{HH}, z_{HV}, z_{VH}, z_{VV}]^t$ (or, by reciprocity, $\mathbf{k} = [z_{HH}, z_{HV}, z_{VV}]^t$). This modality (PolSAR) is widely used to study vegetation growing or urban areas.

- **Interferometric:** The combination of two backscattered signals, \mathbf{k}_1 and \mathbf{k}_2 , measured by two close configurations of the acquisition systems can yield elevation information or ground displacement maps. In interferometric configurations, a composite signal \mathbf{k} can be defined by the concatenation of the two received signals $\mathbf{k} = [\mathbf{k}_1^t, \mathbf{k}_2^t]^t$. These can be single (InSAR) or multipolarization (PolInSAR) signals.

SPECKLE FLUCTUATIONS IN RADAR IMAGES

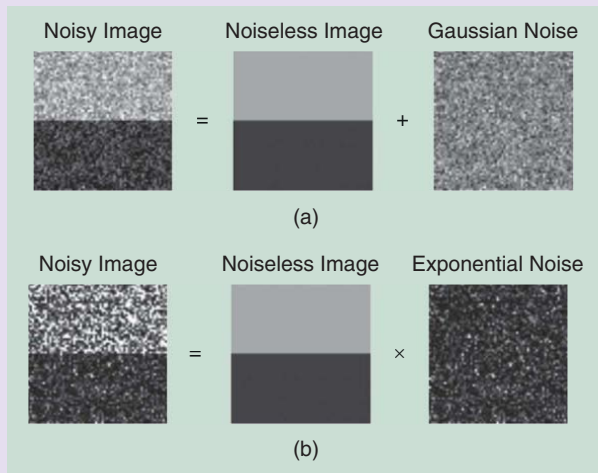
Coherent signals like SAR data present strong fluctuations. The waves backscattered by elementary scatterers inside each resolution cell are not “in phase” but arbitrarily “out-of-phase,” which results in constructive and destructive interferences. In a SAR intensity image, fluctuations due to speckle follow a heavy-tail distribution (large deviations occur often) and are signal dependent (standard deviation is proportional to the radiometry), which departs from the usual additive Gaussian noise model (Figure S1).

Measured SAR intensity $I > 0$ in untextured areas deviates from the radiometry $R > 0$ according to an exponential distribution:

$$p(I|R) = \frac{1}{R} \exp\left(-\frac{I}{R}\right). \tag{S1}$$

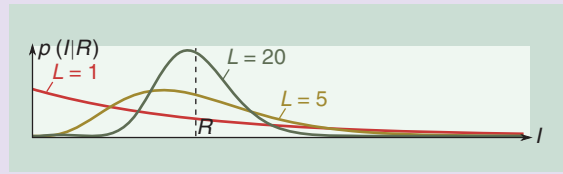
Multilook SAR images, obtained by averaging L intensity images, follow a gamma distribution (Figure S2):

$$p(I|R) = \left(\frac{L}{R}\right)^L \frac{I^{L-1}}{\Gamma(L)} \exp\left(-\frac{LI}{R}\right). \tag{S2}$$



[FIGS1] (a) Additive white Gaussian noise versus (b) multiplicative speckle noise.

Improved approaches have long been proposed to enhance this basic estimation method by better taking into account the image information. Many efforts have been devoted to the case of amplitude images, corresponding to the modulus of single polarization data. Most of these “filtering” methods are described in a review paper [2] and very recent tutorial [1]. The first attempts were derived according to estimation theory: Lee [3] proposed a minimum mean square error (MMSE) estimator in the class of linear filters, while Lopes et al. [16] considered the maximum a posteriori estimator. Both works used a statistical model limited to local distributions, and it is worth noting that these two filters were popular because of the clever analysis of the local context, using window splitting, or edge and target detection [16]. The idea of selecting the most relevant samples in the window has been further developed in [6] and is the main motivation of patch-based approaches. The following generation of filtering approaches introduced stronger priors to guide the solution.



[FIGS2] Gamma distributions for three different number looks L .

In the more general case of a K -dimensional scattering vector as encountered in polarimetric and interferometric modalities $\mathbf{k} = [z_1, \dots, z_K]^t$, the observed complex vector \mathbf{k} follows a K -dimensional circular complex Gaussian distribution under Goodman’s fully developed speckle model (valid for untextured areas with physically homogeneous and rough surfaces)

$$p(\mathbf{k}|\Sigma) = \frac{1}{\pi^K |\Sigma|} \exp(-\mathbf{k}^\dagger \Sigma^{-1} \mathbf{k}), \tag{S3}$$

where $\Sigma = \mathbb{E}\{\mathbf{k}\mathbf{k}^\dagger\}$ is a $K \times K$ complex covariance matrix characteristic of the imaged surface, \mathbb{E} is the expectation, and † the Hermitian transpose. Some radar images are not available in the form of scattering vectors, but rather as empirical covariance matrices

$$\mathbf{C} = \frac{1}{L} \sum_{i=1}^L \mathbf{k}_i \mathbf{k}_i^\dagger, \tag{S4}$$

where the sum is carried over several scattering vectors for each pixel. In the case of amplitude images, \mathbf{k} is a scalar and \mathbf{C} corresponds to an L -looks intensity image. The empirical covariance \mathbf{C} follows a Wishart distribution given by

$$p(\mathbf{C}|\Sigma, L) = \frac{L^K |\mathbf{C}|^{L-K}}{\Gamma_K(L) |\Sigma|^L} \exp(-L \text{Tr}(\Sigma^{-1} \mathbf{C})), \tag{S5}$$

where $\text{Tr}(\cdot)$ is the matrix trace. The equivalent number of looks L acts as the shape parameter of the Wishart distribution.

The first family includes Markovian and variational approaches, which impose smoothness or regularity constraints on the solution through a suitable prior model. These approaches usually lead to minimizing an energy function composed of two terms. The first term reflects the data distribution and is related to statistical models of speckle (see “Speckle Fluctuations in Radar Images”). Due to the heavy tail of the distributions of speckle-corrupted images, classical least-squares data fitting must be replaced by a more relevant criterion derived from speckle distributions. The second term relies on some prior on the solution. Although regularization models such as gradient sparsity have been investigated [4], they do not fit well SAR signal properties. The Markovian formalism can be easily extended to deal with different SAR modalities like interferometric data. However, the specific nature of SAR signals is poorly captured by simple models and more complex ones lead to very hard optimization problems.

The second large family of approaches is based on wavelet transforms. Thanks to their spatially localized and multiresolution basis functions, wavelets yield sparse yet accurate representations of natural images in the transform domain. Sharp discontinuities and pointlike features, so common in SAR images, are well described by a small number of basis functions, just like the large homogeneous regions between them. This compact representation was quickly recognized as a powerful tool for denoising. In fact, while the signal is projected on a relatively small number of large wavelet coefficients, the white noise remains white after the transform, and hence evenly distributed on all coefficients. Signal and noise can be, therefore, efficiently separated by means of an appropriate nonlinear processing, such as hard/soft thresholding or more sophisticated shrinkages. The encouraging results provided by early SAR despeckling techniques spawned an intense research to overcome the shortfalls of soft/hard thresholding. A popular approach considered wavelet shrinkage as a Bayesian estimation problem, possibly expressed after application of a homomorphic transform to reduce speckle to an independent additive perturbation. The major problem in this context becomes the modeling of signal and noise by suitable distributions, and a number of parametric models have indeed been proposed [5], [17]. Further improvements come from joint modeling of wavelet coefficients in and across subbands, like in [18]. Despite its potential, the wavelet transform cannot deal by itself with the high heterogeneity of SAR scenes. A number of spatially adaptive techniques were therefore proposed, based on some prior classification of the image, typically in homogeneous, heterogeneous (e.g., textures), and highly heterogeneous (e.g., point targets) regions, to tune filtering parameters or strategies to the different regions [19].

The approaches reviewed above generally try to estimate the signal at a certain pixel from the noisy observations at pixels close to it. However, with plenty of data to estimate the signal, i.e., the observations over the whole image, why restrict attention only to a small neighborhood of the target? The obvious answer is that not all image pixels carry valuable information on the target, and only close pixels are used because they are expected to be more similar to it, and hence, better estimators. The above consideration makes clear that the image denoising problem may be performed in two separate steps: 1) selecting good predictors, which carry useful information on the target, and then 2) using them to perform the actual estimate. Lacking any other hints, spatial closeness is taken

as a surrogate of signal similarity relying heavily on the fact that natural images are predominantly low-pass. Needless to say, sophisticated filters go much beyond a simple distance-based weighting of contributions, but this basic criterion remains a founding paradigm of local filters.

The patch-based nonlocal approach avoids the potentially dangerous identification between closeness and similarity and goes back to the original problem, trying to identify the pixels more similar to the target, irrespective (to a certain extent) of their spatial distance from it. In the next section, we explore in more depth the fundamental steps involved in nonlocal SAR despeckling and review the current state of the art.

NONLOCAL APPROACHES: EXPLOITING PATCH REDUNDANCY

At the core of the nonlocal approach stands the selection of suitable predictors based on their similarity with the target. This idea began to gain some popularity with the bilateral filter, proposed for additive white Gaussian noise (AWGN) denoising, with predictor weights depending not only on their spatial distance from the target, but also on their similarity with it, measured by the difference between observed values. Despite its simplicity, this filter gave a surprisingly good denoising performance, reducing the annoying edge-smearing phenomenon. However, the pixel-wise estimation of similarity was very rough and happened to reinforce observed values affected by strong noise, justifying the need for the spatial-distance term. The fundamental step toward nonlocal filtering was then the introduction, in nonlocal means (NL-means) [8], of a reliable patch-wise measure of similarity. When a relatively large patch is taken into account, it is very unlikely that pixels characterized by a signal much different from the target be accepted as good predictors. Thanks to the improved reliability, predictors can be weighted based only on similarity, with no reference to spatial information. Unlike local filters, nonlocal ones do not impose any specific structure (connectivity, shape) or smoothness, but only exploit that patches recur more or less frequently, a self-similarity property common to most images. Recurring patches are easily found in smooth regions, but just as well around region boundaries, textures, artificial structures, etc., as shown in Figure 1. Hence, for most patches, several other patches can be found with similar content. This form of stationarity in the space of patches is central to nonlocal approaches.

Nonlocal estimation methods generally follow a three-step scheme, summarized in Figure 2 with many possible variations at each step and, possibly, preprocessing steps and/or iterative refinement of results by repeated nonlocal estimations. The first step identifies similar patches (patch size is generally set from 3×3 to 11×11 pixels). It must reliably find, within an extended search window (typically 21×21 to 39×39), patches that are close to the reference central patch. Once several patches have been selected (from a few tens to all the hundreds of patches within the search window), they are assigned relative weights. The second step combines patches, according to their weights, to form an estimate of either the central pixel, the central patch, or all selected patches. The estimates computed from

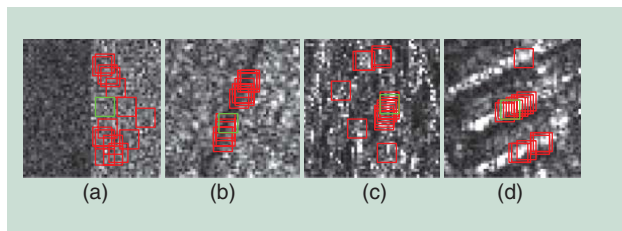


[FIG1] Typical fragments of SAR images (51×51 pixels): (a) homogeneous region, (b) line, (c) texture, and (d) structure. For each target patch (green) several similar 8×8 patches (red) are easily found in the same fragment.

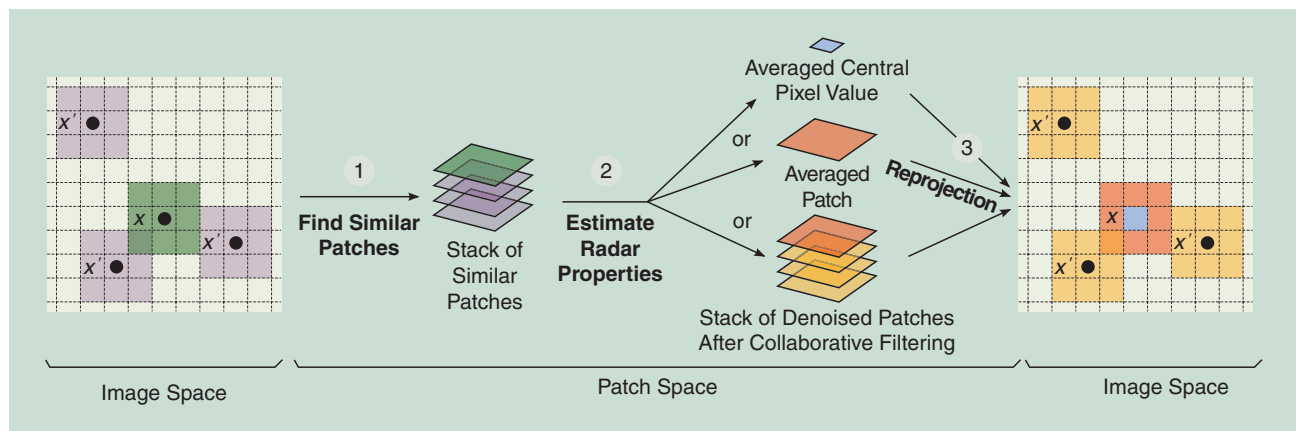


[FIG2] Nonlocal estimation in action: processing at pixel x .

all possible reference patches are then merged in a last step to produce the final image.

We now illustrate these steps for the special case of NL-means [8], indicating by $v(x)$ and $\underline{v}(x)$, respectively, the value at pixel x , and the image patch centered on x in the observed image. In NL-means, each pixel x' in a large search area around the target pixel x is considered and a similarity measure $\Delta(x, x')$ is computed by comparing the two patches centered on x and x' . Under AWGN, the sum of squared differences is a natural criterion to evaluate similarity

$$\Delta(x, x') = \|\underline{v}(x') - \underline{v}(x)\|^2. \quad (1)$$

This measure is used to compute the weight for each predictor pixel x' , with large weights associated with similar patches and negligible weights with dissimilar ones. An exponential kernel is used to this end

$$w(x, x') = \exp(-\Delta(x, x')/h), \quad (2)$$

with the bandwidth parameter h governing the weight distribution. Finally, the target pixel x is estimated through the weighted average of all pixels within the search area

$$\hat{u}^{\text{NL}}(x) = \frac{\sum_{x'} w(x, x') v(x')}{\sum_{x'} w(x, x')}, \quad (3)$$

where \hat{u} denotes an estimate of the unknown signal value u .

In the NL-means, therefore, only one estimate is obtained for each pixel x , which corresponds to the top branch depicted in Figure 2. Generalizations provide several estimates for each pixel that must be properly combined in the last step.

The NL-means filter and its numerous variants are known to perform well under AWGN. However, the extension to SAR imaging, and in particular to speckle, is by no means trivial, and has been the object of several recent papers. One has to understand the foundation of such filters, and provide a flexible formulation suitable for different modalities and models of noise. In the following, we focus on the main concepts that have been proposed in SAR imaging, and try to provide some insight into the problems that emerge when noise departs from the Gaussian distribution,

and possible solutions to them. The key point of all these extensions is the consideration of the specific distributions of radar data.

STEP 1: DEFINING PATCH SIMILARITIES

The first step of nonlocal estimation methods is the identification of similar patches through a (dis)similarity criterion $\Delta(x, x')$. This criterion quantifies, in a principled manner, by how much the unknown patches $\underline{u}(x)$ and $\underline{u}(x')$ differ. Based on the similarity to the reference patch at x , predictor patches at x' can be either soft-assigned or hard-assigned to the set of similar patches. In the case of soft-assignment, a weight reflecting the level of similarity is associated to each patch within the search area, otherwise the most similar patches are included and used to perform the prediction.

Under AWGN, (1) is a natural criterion to evaluate similarity between two patches. Fluctuations created by speckle are multiplicative and non-Gaussian; see "Speckle Fluctuations in Radar Images." Specific criteria must be derived for the comparison of patches in SAR imaging.

The similarity between two patches is generally defined as the sum of the similarity δ of each pair of corresponding pixels in the two noisy patches: $\Delta(x, x') = \sum_{\tau} \delta(v(x + \tau), v(x' + \tau))$. To improve the discrimination power of the similarity criterion, several authors suggest using a pre-estimate \tilde{u} computed either over the whole patch [20], obtained after a first iteration [11] or at the previous iteration [9] of the nonlocal method. The similarity then takes the form $\Delta(x, x') = \sum_{\tau} \delta(\tilde{u}(x + \tau), \tilde{u}(x' + \tau))$. Described next are possible approaches to derive the pixel-wise similarity δ .

DETECTION APPROACH

Dissimilarity can be defined based on the detection of the difference between the underlying values u_1 and u_2 [21]. This detection problem can be formulated as an hypothesis test where the null hypothesis corresponds to no difference ($H_0: u_1 = u_2 = u_{12}$) and the alternative one to a difference ($H_1: u_1 \neq u_2$). Among several criteria considered in [21], the generalized likelihood ratio (GLR) is shown to perform best and fulfill several invariance properties

$$\delta^{\text{GLR}}(v_1, v_2) = -\log \frac{\sup_{u_{12}} [p(v_1 | u_{12}) p(v_2 | u_{12})]}{\sup_{u_1} [p(v_1 | u_1)] \sup_{u_2} [p(v_2 | u_2)]}. \quad (4)$$

Criteria specific to SAR imaging can be derived from (4) by using the statistical speckle models recalled in “Speckle Fluctuations in Radar Images.” Both single channel (intensity) and multichannel (polarimetric and/or interferometric) configurations lead to a criterion defined as the log of the ratio between arithmetic and geometric means [22]

$$\delta^{\text{GLR}}(C_1, C_2) = 2L \log \frac{\frac{1}{2} |C_1 + C_2|}{\sqrt{|C_1| \cdot |C_2|}}, \quad (5)$$

where C may represent either the L -looks intensity (single-channel images) or the L -looks empirical covariance matrices (multi-channel images). This is a natural criterion to compare patches corrupted by a multiplicative noise such as speckle since the criterion is invariant to a multiplicative change of contrast. It has been successfully used in nonlocal filtering of intensity, interferometric, and polarimetric SAR images [12], [14]. Detection-based criteria using similar expressions are also at the heart of [9], [13], [23], and [24].

INFORMATION APPROACH

In line with the detection approach, the authors of [9] and [20] consider a similar hypothesis test involving pre-estimates of the parameters. Good criteria to perform such a hypothesis test are provided by the h - ϕ divergences where h and ϕ refer to pre-defined functions. The h - ϕ divergences measure the quantity of information shared by the distributions parametrized by \tilde{u}_1 and \tilde{u}_2 : they evaluate the proportion of samples from one distribution that can be explained by the other. Specific choices of h and ϕ lead for instance to the Hellinger divergence or the Kullback–Leibler divergence. Again, taking into account specific SAR distributions provides well-founded criteria. The symmetrical version of Kullback–Leibler divergence (sKL) gives, in the case of Wishart-distributed empirical covariance matrices,

$$\delta^{\text{sKL}}(\tilde{\Sigma}_1, \tilde{\Sigma}_2) = L \text{Tr}(\tilde{\Sigma}_1^{-1} \tilde{\Sigma}_2 + \tilde{\Sigma}_2^{-1} \tilde{\Sigma}_1) + \text{const.}, \quad (6)$$

again involving ratios, as customary in SAR imagery.

GEOMETRIC APPROACH

The similarity can be defined by deriving a metric suitable to the specificities of SAR data. D’Hondt et al. [25] suggest using Hermitian semidefinite positive matrices and propose a metric connected to geodesic and Riemannian distances

$$\delta^{\text{Geo}}(\tilde{\Sigma}_1, \tilde{\Sigma}_2) = \|\log(\tilde{\Sigma}_2^{-1/2} \tilde{\Sigma}_1 \tilde{\Sigma}_2^{-1/2})\|_F^2, \quad (7)$$

where \log is the matrix logarithm and $\|\cdot\|_F$ the Froebenius norm. This similarity offers some interesting invariance properties. In the case of intensity images with pre-estimated

radiometry \tilde{R} , this criterion boils down to $(\log(\tilde{R}_2) - \log(\tilde{R}_1))^2$, which is the square distance between observations after applying a homomorphic transform on the pre-estimates. It has been shown in the framework of detection theory that criteria based on variance-stabilization (such as the log transform in SAR) enjoy good properties [21]. It is interesting to see that such a criterion can be derived using different interpretations (a geometric founding or a statistical reasoning).

ESTIMATION APPROACH

Lee et al. [26] have shown that the estimation of radar properties may suffer from a systematic bias arising from the procedure that detects similar noisy values (hard-assignment). For SAR intensity images, they suggest using a preselection rule of the form $I_2 \in [R_1 \zeta, R_1 \zeta']$ —called *sigma range*—for which the preselected samples I_2 do not introduce bias in the subsequent estimation when the radiometry is identical ($R_1 = R_2$). Values of ζ and ζ' are computed by an iterative method, while the unknown R_1 is replaced by a pre-estimate \tilde{R}_1 called a *priori mean* [10], [26]. By rather considering a preselection rule of the form $\delta(I_1, I_2) \leq \gamma$, numerical integrations over I_1 and I_2 show that the subsequent estimation is unbiased as soon as the rule can be rewritten as $I_2 \in [I_1/\zeta, I_1 \zeta]$. Detection rules such as GLR (5) verify this property.

Some of the estimators used in the second step of nonlocal estimation methods use the similarity $\Delta(x, x')$ to weight the importance of the patch $v(x')$ (i.e., soft-assignment). The similarity $\Delta(x, x')$ is mapped into a weight $w(x, x')$ using a function termed *kernel*. Many different kernels have been proposed in the literature, from simple thresholding $w(x, x') = \mathbb{1}[\Delta(x, x') < h]$, exponential kernels as in (2), to more sophisticated ones [14], [20], [24]. The shape of the kernel (e.g., smooth, discontinuous, or trapezoidal) changes the contributions of patches that may correspond to false detections and thus controls the bias/variance tradeoff. In [14] and [20], suitable kernels have been defined to guarantee the same bias/variance tradeoff, irrespective of the modality, the noise statistic, or the patch size.

STEP 2: ESTIMATION OF RADAR PROPERTIES

After the selection of a stack of patches and/or computation of relative weights during the first step of the nonlocal estimation method, these patches are combined in a second step to form an estimate of the radar properties. This combination can be a simple (weighted) averaging as in the NL-means, or a more evolved estimator.

In SAR imaging, observations v may denote a collection of intensities I , amplitudes \sqrt{I} or log-transformed values $\log(I)$, a vector of noisy coefficients in a transformed domain (discrete cosine transform, Fourier, wavelets, etc.), a collection of scattering vectors k or of empirical covariance matrices C . The associated collection of parameters of interest u , are generally the radiometry R or covariance matrix Σ . The estimation step computes radar parameters from the collection of observations v and/or pre-estimations \tilde{u} gathered during the first step. The most common estimators for patch-based denoising of SAR images are:

■ **SME/WSME:** NL-means and many of its successors combine similar patches into a weighted average [weighted sample mean estimator (WSME)], where the weights are derived from the similarities; see (3). By using weights, the estimation relies more heavily on samples that are more similar (thus, more reliable), which reduces bias. Compared to an estimation based solely on a collection of patches detected as highly similar (i.e., by hard-assignment), the variance can also be reduced by considering a larger number of samples. The sample mean estimator corresponds to the conditional expectation $\mathbb{E}[v | u]$. This expectation may not directly be equal to the parameter of interest u , but require a debiasing step. A notable example is the case of (weighted) averaging of log-transformed SAR images. The estimation of covariance matrices from empirical ones can be performed by WSME [12], [14], [20], [24], [25]

$$\hat{\Sigma}^{\text{WSME}}(x) = \frac{\sum_{x'} w(x, x') C(x')}{\sum_{x'} w(x, x')} \quad (8)$$

with $w(x, x')$ the weight depending on the similarity $\Delta(x, x')$ between patches extracted at pixel locations x and x' .

■ **MLE/WMLE:** The sample mean is not a correct estimator of some parameters, e.g., the amplitude \sqrt{I} . The sample mean should then be replaced by an estimator adjusted to the specific noise distribution of the observations, such as the maximum likelihood estimator. Similarly to the WSME, sample weights can be introduced in the estimation method. Maximum likelihood can be generalized into the weighted maximum likelihood estimator (WMLE) [9]:

$$\hat{u}^{\text{WMLE}}(x) = \arg \max_u \sum_{x'} w(x, x') \log p[v(x') | u]. \quad (9)$$

WMLE leads to (8) for Wishart-distributed covariance matrices, but improvements are obtained for matrices with particular structures as in interferometric SAR imaging [13].

■ **MMSE:** Kervrann et al. proposed a method called Bayesian NL-means [27] that estimates the parameters u as a linear combination of pre-estimated patches \tilde{u} , with weights defined by the likelihood of each pre-estimated patch with respect to the observation v :

$$\hat{u}^{\text{MMSE}}(x) \approx \frac{\sum_{x'} p[v(x) | \tilde{u}(x')] \tilde{u}(x')}{\sum_{x'} p[v(x') | \tilde{u}(x')]} \quad (10)$$

This estimator can be interpreted as an approximation of the MMSE error estimator, i.e., the posterior mean. Pre-estimates are usually obtained thanks to a two-step or iterative prefiltering [10]. Since the pre-estimation step provides only a coarse estimation \tilde{u} of the patches u , a smoothing parameter is introduced to reduce the selectivity of the likelihood function and thus avoid weighting too much patches that are very close to the observation [27].

■ **LMMSE:** The linear MMSE (LMMSE) error estimator has long been used in SAR imaging [26]. This estimator restricts the form of the solution to linear transforms of v , which is most efficient when noise and signal are well

separated. In SAR-BM3D [11], the LMMSE is computed after an undecimated discrete wavelet transform (UDWT) is applied to the stack of similar patches. Expectation and variance of observations and parameters can be obtained from band-wise statistics and later refined using prefiltered patches after a first restoration has been performed.

The family of homomorphic approaches transform the multiplicative noise into an additive one by taking the logarithm of the observed intensity/amplitude. Several papers have derived nonlocal estimators in this sense, e.g., [28], where an “adjust mean” step is used to deal correctly with the bias arising from the Gaussian assumption (i.e., debiasing step described for SME). Note that estimators that process directly SAR data (i.e., without log-transforms) are often preferable since the debiasing step is then unnecessary.

STEP 3: REPROJECTION TO IMAGE SPACE

The second step of nonlocal methods provides estimates either for a single pixel (pixel-wise estimation), for a single patch (patch-wise estimation), or for the whole stack of patches (stack-wise estimation). The first option corresponds to basic NL means, already described above, so let us focus on the other two strategies.

The difference in patch-wise filtering is that all pixels in the patch, not just the central one, are estimated at once. Since each pixel is estimated several times, a suitable aggregation phase is necessary to combine all such estimates. In particular, we need to define a reprojection function, $g(\cdot)$, to get an estimate in the pixel domain: $\hat{u}(x) = g(\hat{u}_1(x), \dots, \hat{u}_K(x))$. What is more important, these estimates refer to different patches, with different reliability levels, an information that can be exploited to improve results. The reprojection can be performed through a weighted average of the K estimators:

$$\hat{u}(x) = \sum_{k=1}^K \alpha_k \hat{u}_k(x). \quad (11)$$

The simplest form of aggregation is to consider uniform weights α_k , as done in the block-wise NL-means [8]. Another strategy is to set the weight associated with each estimate as inversely proportional to its variance [29].

To illustrate why patch-wise estimation improves performance, let us consider the special case of a pixel near the boundary between two homogeneous regions. Since the patch centered on it is strongly heterogeneous, most other patches of the search area, coming from homogeneous regions on either side of the boundary, are markedly dissimilar from it, and contribute very little to the average. The estimate, thus, involves only a small effective number of predictors, those along the edge, which results in a high variance. As a result, a visible “halo” of residual noise is observed near the edges, a phenomenon well-known in NL-means, also referred to as the rare patch effect. The target pixel, however, belongs to a large number of patches, not just the patch centered on it, many of them drawn from the homogeneous region to which the pixel belongs. In patch-wise reprojection, all of these patches are included in the average reducing the

OVERVIEW OF NONLOCAL ESTIMATION METHODS IN SAR IMAGING

Nonlocal estimation methods perform the three steps depicted in Figure 2. A great variety of methods dedicated to SAR images have been proposed over the last few years. These methods follow different paths to implement each of the three steps:

1) similar patches identification (choice of the similarity criterion)

2) estimation of radar properties (choice of the estimator)
3) reprojection of estimates onto the image space (choice of the domain).

Table S1 is an overview of some of the main methods devoted to SAR imaging.

[TABLE S1] MAIN PATCH-BASED METHODS FOR SPECKLE REDUCTION IN SAR IMAGES.

METHOD (OLDEST FIRST)	DOMAIN	ESTIMATOR	SAR MODALITY	SELF-SIMILARITY DOMAIN	SIMILARITY CRITERION	SCHEME
PPB/NL-INSAR [9], [13]	PIXEL-WISE	WMLE	SAR (ANY L) / INSAR ($L = 1$)	PATCH-WISE	DETECTION + INFORMATION	ITERATIVE
	<i>ORIGINALITY:</i> ITERATIVELY REFINES THE WEIGHTS BY COMPARING PATCHES OF PREVIOUS ESTIMATES AND PATCHES OF THE NOISY IMAGE.					
PRETEST NLN [12]	PIXEL-WISE	WSME	POLSAR ($L \geq 3$)	PATCH-WISE	DETECTION	ONE STEP
	<i>ORIGINALITY:</i> DIRECT EXTENSION OF [8] WITH A SELECTION BASED ON A GLR (REFERRED TO AS <i>PRETEST STEP</i>).					
BAYESIAN NLN [10]	PIXEL-WISE	MMSE	SAR (ANY L)	PATCH-WISE	ESTIMATION	ONE STEP
	<i>ORIGINALITY:</i> PRIOR PATCHES ARE EXTRACTED IN A MULTILOKED IMAGE. A SIGMA-RANGE PRESELECTION IS USED AND DARKER PIXELS ARE DISCARDED.					
SAR-BM3D [11]	STACKWISE	LMSE	SAR (ANY L)	PATCH-WISE	DETECTION + INFORMATION	TWO STEPS
	<i>ORIGINALITY:</i> WORKS ON THE UDWT OF STACKS: FIRST STEP USES STATISTICS OF EACH SUBBAND; SECOND ONE USES STATISTICS PROVIDED BY THE FIRST ITERATION.					
BILATERAL NLN [25]	PIXEL-WISE	WSME	POLSAR (ANY L)	PIXEL-WISE	GEOMETRIC	ITERATIVE
	<i>ORIGINALITY:</i> IMAGES ARE MULTILOKED, THEN ITERATIVELY UPDATED BY NONLOCAL AVERAGING BASED ON GEOMETRICAL COMPARISON OF PIXEL VALUES (NO PATCH).					
STOCHASTIC NLN [20]	PIXEL-WISE	WSME	POLSAR (NON- STATIONNARY L)	STATSWISE	INFORMATION	ONE STEP
	<i>ORIGINALITY:</i> LETS L VARY IN THE IMAGE. PATCH SIMILARITY IS BASED ON THE DIVERGENCE BETWEEN MLE ESTIMATES OF Σ AND L WITHIN THE PATCH.					
DISCRIMINATIVE NLN [24]	PIXEL-WISE	WSME	POLSAR	PATCH-WISE	DETECTION	ITERATIVE
	<i>ORIGINALITY:</i> ITERATIVELY REFINES WEIGHTS BASED ON THE RATIO OF DIAGONAL ELEMENTS OF EMPIRICAL COVARIANCE MATRICES AND THE SPAN OF THE PREVIOUS ITERATE.					
NL-SAR [14]	PIXEL-WISE	WMLE	(POL)(IN)SAR (ANY L)	PATCH-WISE	DETECTION	ADAPTIVE
	<i>ORIGINALITY:</i> FULLY AUTOMATIC: PATCH SIZES, SEARCH WINDOWS AND PREFILTERING STRENGTHS ARE SPATIALLY TUNED TO PROVIDE IMPROVED RESULTS.					

estimate variance, especially if suitable weights are used to take into account the reliability of each contribution.

Let us now consider the third strategy, with stack-wise filtering. The first difference with regard to patch-wise filtering is that now all patches collected in the stack are collaboratively filtered before reprojecting them to their original position. The major improvement is that the stack is filtered in three dimensions, i.e., not only along the stack but also in the spatial domain. In BM3D [29] and, with necessary adjustments to the SAR domain, in SAR-BM3D [11], the whole stack, formed by just a limited number of similar patches, is wavelet transformed, Wiener filtered, and back transformed. By so doing, strong spatial structures are emphasized through filtering while random noise is efficiently suppressed. As a matter of fact, these techniques exhibit significant improvements especially in highly structured areas (edges, point reflectors,

textures). The efficiency of collaborative filtering comes from the full exploitation of the redundancy of information in a stack of similar patches.

In “Overview of Nonlocal Estimation Methods in SAR Imaging,” we compare nine recent patch-based techniques in relation to each of the three steps previously described. Needless to say, performance depends on the setting of several parameters, like patch size and search area size, which should be related to image resolution, smoothing strength, and balance between original and pre-estimated data. In most of the nonlocal approaches these parameters are set by hand. Few works have considered semisupervised setting or automatic setting with spatial adaptation [14].

Some sample experimental results that confirm the potential of nonlocal methods are presented in Figure 3 for an amplitude



[FIG3] (a) The single-look TerraSAR-X image of Barcelona and (b) the radiometry estimated by the nonlocal method [11]. Images are $511 \times 1,043$ pixels with a spatial resolution of 2.5 m. (Images used with permission of Infoterra GmbH.)

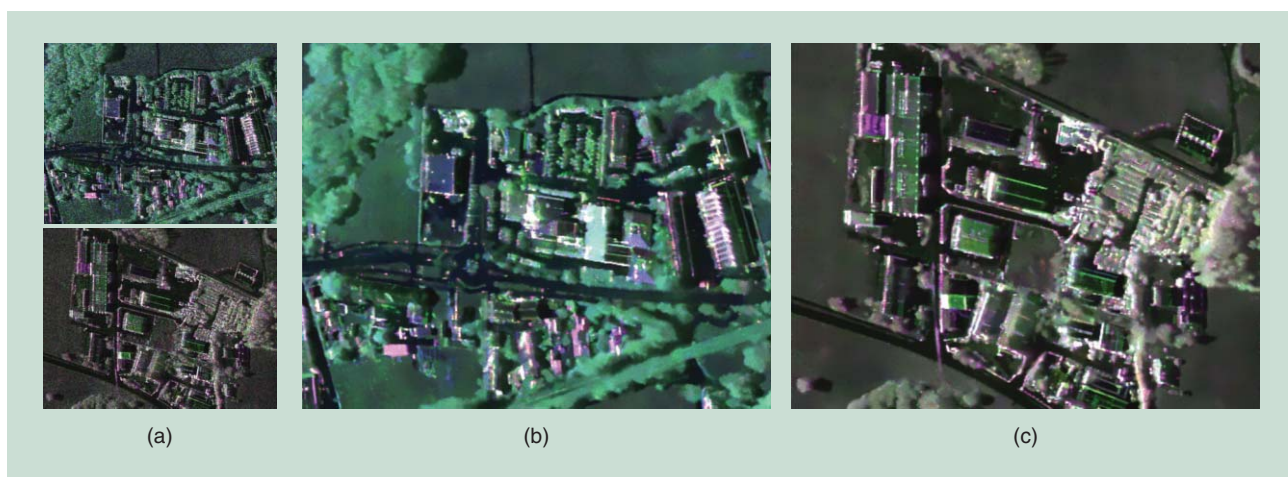


[FIG4] (a) Two PolSAR images of the area of Kaufbeuren, Germany, sensed by F-SAR, single-look, X-band (top) and S-band (bottom) (image courtesy DLR). In (b) and (c), estimated polarimetric signatures using the nonlocal patch-based method (images used with permission from [14]). Images are 400×512 pixels with a spatial resolution of 0.5 m.

image with SAR-BM3D [11] and in Figure 4 for a polarimetric data with NL-SAR [14]. Visual inspection shows the performance of the approach in reducing strong fluctuations while preserving important features like targets and lines. Note that no systematic artefacts should be observed with these approaches unless the parameters are not set properly (e.g., no consideration of oversampled data). A rigorous performance evaluation of nonlocal despeckling techniques is beyond the scope of this article. Some frameworks for SAR despeckling evaluation and comparison are proposed in [1] and [30].

OPEN ISSUES AND FUTURE TRENDS

Patch-based approaches provide the best performance to date for speckle reduction in SAR intensity images [30] and polarimetric or interferometric SAR images [14]. Beyond speckle suppression, they improve parameter estimation, drastically enhancing radar measures. Therefore, they can be expected to have a strong impact, in the near future, on major applications of radar imaging, improving the biomass estimation with polarimetric-interferometric data; increasing the spatial resolution in

urban monitoring with radar tomography; enabling more reliable phase unwrapping methods for interferometric SAR.

As a by-product of patch-based speckle reduction methods, several similar criteria especially suited for SAR imaging have been established. These criteria are central to many applications: for classification and indexing using patch clustering; for change detection; for movement monitoring by patch tracking.

Patch-based methods are at their beginning and many open issues have yet to be solved. The speckle model considered so far (simple complex Gaussian) is known to inaccurately describe very high-resolution images or textured areas. The introduction of more accurate models (e.g., Weibull, Fisher, or generalized gamma distributions for amplitude, and corresponding matrix-variate polarimetric distributions) raises questions about the increased complexity of estimators and the possible loss of robustness with the increase of degrees of freedom. Another limit is the geometric deformations appearing on SAR images with elevated objects. Such deformations should be considered to perform joint restoration of images taken from multiple incidence angles.

ACKNOWLEDGMENTS

This work has been supported in part by the following grants: ANR DEFI 09-EMER-008-01, ANR-11-IDEX-0007, ANR-11-LABX-0063, and project MIUR-PRIN 2012 "Very High Spatial and Spectral Resolution Remote Sensing: A Novel Integrated Data Analysis System."

AUTHORS

Charles-Alban Deledalle (charles-alban.deledalle@math.u-bordeaux1.fr) received the Ph.D. degree from Telecom ParisTech, France, in 2011. In 2011–2012, he was a postdoctoral fellow at the Université Paris Dauphine, France. He is currently a Centre National de la Recherche Scientifique researcher associate at the Institut de Mathématiques de Bordeaux, France. His research interests include image restoration, inverse problems, and parameter selection.

Loïc Denis (loic.denis@univ-st-etienne.fr) received the Ph.D. degree from the Université de Saint-Etienne in 2006. He is currently an assistant professor at Telecom St. Etienne. His main research interests are in image restoration and reconstruction with applications in remote sensing, optical metrology, biomedical imaging, and astronomy.

Giovanni Poggi (poggi@unina.it) received the laurea degree in electronic engineering from the University Federico II of Naples, Italy, in 1988. He is currently a professor of telecommunications with the same institution. His research is on statistical image processing, including compression, restoration, and segmentation of remote-sensing images, both optical and synthetic aperture radar, and digital forensics.

Florence Tupin (Florence.Tupin@telecom-paristech.fr) received the engineering and Ph.D. degrees in signal and image processing from Ecole Nationale Supérieure des Télécommunications, Paris, France, in 1994 and 1997, respectively. Since 2009 she has been a professor of image processing at Telecom ParisTech. Her main research interests are image analysis and interpretation for remote sensing applications, in particular with synthetic aperture radar.

Luisa Verdoliva (verdoliv@unina.it) received the laurea degree in telecommunication engineering and the Ph.D. degree in information engineering from the University Federico II of Naples, Italy, in 1998 and 2002, respectively. She is currently an assistant professor of telecommunications with the same institution. Her research is on image processing, in particular compression and restoration of remote-sensing images, both optical and synthetic aperture radar, and digital forensics.

REFERENCES

- [1] F. Argenti, A. Lapini, L. Alparone, and T. Bianchi, "A tutorial on speckle reduction in synthetic aperture radar images," *IEEE Geosci. Remote Sens. Mag.*, vol. 1, pp. 6–35, Sept. 2013.
- [2] R. Touzi, "A review of speckle filtering in the context of estimation theory," *IEEE Trans. Geosci. Remote Sensing*, vol. 40, no. 11, pp. 2392–2404, 2002.
- [3] J. S. Lee, "Digital image enhancement and noise filtering by use of local statistics," *IEEE Trans. Pattern Anal. Mach. Intell.*, vol. 2, no. 2, pp. 165–168, 1980.
- [4] L. Denis, F. Tupin, J. Darbon, and M. Sigelle, "Joint regularization of phase and amplitude of In SAR data: Application to 3D reconstruction," *IEEE Trans. Geosci. Remote Sensing*, vol. 47, no. 11, pp. 3774–3785, 2009.

- [5] A. Achim, P. Tsakalides, and A. Bezerianos, "SAR image denoising via Bayesian wavelet shrinkage based on heavy-tailed modeling," *IEEE Trans. Geosci. Remote Sensing*, vol. 41, no. 8, pp. 1773–1784, 2003.

- [6] G. Vasile, E. Trounev, and J. Lee, "Intensity-driven adaptive-neighborhood technique for polarimetric and interferometric SAR parameters estimation," *IEEE Trans. Geosci. Remote Sensing*, vol. 44, no. 6, pp. 1609–1621, 2006.

- [7] J. S. Lee, "Digital image smoothing and the sigma filter," *Comput. Vis. Graph. Image Process.*, vol. 24, no. 2, pp. 255–269, 1983.

- [8] A. Buades, B. Coll, and J. M. Morel, "A review of image denoising algorithms, with a new one," *Multiscale Modell. Simul.*, vol. 4, no. 2, pp. 490–530, 2005.

- [9] C.-A. Deledalle, L. Denis, and F. Tupin, "Iterative weighted maximum likelihood denoising with probabilistic patch-based weights," *IEEE Trans. Image Processing*, vol. 18, no. 12, pp. 2661–2672, 2009.

- [10] H. Zhong, Y. Li, and L. Jiao, "SAR image despeckling using Bayesian nonlocal means filter with sigma preselection," *IEEE Geosci. Remote Sensing Lett.*, vol. 8, no. 4, pp. 809–813, 2011.

- [11] S. Parrilli, M. Poderico, C. V. Angelino, and L. Verdoliva, "A nonlocal SAR image denoising algorithm based on LLMSE wavelet shrinkage," *IEEE Trans. Geosci. Remote Sensing*, vol. 50, no. 2, pp. 606–616, 2012.

- [12] J. Chen, Y. Chen, W. An, Y. Cui, and J. Yang, "Nonlocal filtering for polarimetric SAR data: A pretest approach," *IEEE Trans. Geosci. Remote Sensing*, vol. 49, no. 5, pp. 1744–1754, 2011.

- [13] C.-A. Deledalle, L. Denis, and F. Tupin, "NL-InSAR: Nonlocal interferogram estimation," *IEEE Trans. Geosci. Remote Sensing*, vol. 49, no. 4, pp. 1441–1452, 2011.

- [14] C.-A. Deledalle, L. Denis, F. Tupin, A. Reigbers, and M. Jäger, "NL-SAR: A unified non-local framework for resolution-preserving (Pol)(In)SAR denoising." Preprint HAL – hal-00844118, 2013. [Online]. Available: <http://hal.archives-ouvertes.fr/hal-00844118>

- [15] A. Moreira, P. Prats-Iraola, M. Younis, G. Krieger, I. Hajnsek, and K. Papathanassiou, "A tutorial on synthetic aperture radar," *IEEE Geosci. Remote Sens. Mag.*, vol. 1, no. 1, pp. 6–43, 2013.

- [16] A. Lopes, R. Touzi, and E. Nezry, "Adaptive speckle filters and scene heterogeneity," *IEEE Trans. Geosci. Remote Sensing*, vol. 28, no. 6, pp. 992–1000, 1990.

- [17] F. Argenti, T. Bianchi, and L. Alparone, "Multiresolution MAP despeckling of SAR images based on locally adaptive generalized Gaussian PDF modeling," *IEEE Trans. Image Processing*, vol. 15, no. 11, pp. 3385–3399, 2006.

- [18] H. Xie, L. E. Pierce, and F. T. Ulaby, "SAR speckle reduction using wavelet denoising and Markov random field modeling," *IEEE Trans. Geosci. Remote Sensing*, vol. 40, no. 10, pp. 2196–2212, Jan. 2002.

- [19] S. Foucher, G. B. Béné, and J. M. Boucher, "Multiscale MAP filtering of SAR images," *IEEE Trans. Image Processing*, vol. 10, no. 1, pp. 49–60, Jan. 2001.

- [20] L. Torres, S. J. S. Sant'Anna, C. da Costa Freitas, and A. C. Frery, "Speckle reduction in polarimetric SAR imagery with stochastic distances and nonlocal means," *Pattern Recognit.*, vol. 47, no. 1, pp. 141–157, Jan. 2014. [Online]. Available: <http://dx.doi.org/10.1016/j.patcog.2013.04.001>

- [21] C. Deledalle, L. Denis, and F. Tupin, "How to compare noisy patches? Patch similarity beyond Gaussian noise," *Int. J. Comput. Vis.*, vol. 99, no. 1, pp. 86–102, 2012.

- [22] K. Conradsen, A. A. Nielsen, J. Schou, and H. Skriver, "A test statistic in the complex Wishart distribution and its application to change detection in polarimetric SAR data," *IEEE Trans. Geosci. Remote Sensing*, vol. 41, no. 1, pp. 4–19, 2003.

- [23] G. Poggi, F. Sica, L. Verdoliva, G. Fornaro, D. Reale, and S. Verde, "Non-local methods for filtering interferometric SAR datasets," in *Proc. TyWRRS: From Earth Observation to Homeland Security*, 2012, pp. 136–139.

- [24] G. Liu and H. Zhong, "Nonlocal means filter for polarimetric SAR data despeckling based on discriminative similarity measure," *IEEE Geosci. Remote Sensing Lett.*, vol. 11, no. 2, pp. 514–518, 2014.

- [25] O. D'Hondt, S. Guillaso, and O. Hellwich, "Iterative bilateral filtering of polarimetric SAR data," vol. 6, no. 3, pp. 1628–1639, 2013.

- [26] J.-S. Lee, J.-H. Wen, T. L. Ainsworth, K.-S. Chen, and A. J. Chen, "Improved sigma filter for speckle filtering of SAR imagery," *IEEE Trans. Geosci. Remote Sensing*, vol. 47, no. 1, pp. 202–213, 2009.

- [27] C. Kervrann, J. Boulanger, and P. Coupé, "Bayesian non-local means filter, image redundancy and adaptive dictionaries for noise removal," in *Scale Space and Variational Methods in Computer Vision*. New York: Springer, 2007, pp. 520–532.

- [28] M. Makitalo, A. Foi, D. Fevrale, and V. Lukin, "Denoising of single-look SAR images based on variance stabilization and nonlocal filters," in *Int. Conf. Mathematical Methods in Electromagnetic Theory*. Piscataway, NJ: IEEE, 2010.

- [29] K. Dabov, A. Foi, V. Katkovnik, and K. Egiazarian, "Image denoising by sparse 3-D transform-domain collaborative filtering," *IEEE Trans. Image Processing*, vol. 16, no. 8, 2007.

- [30] G. Di Martino, M. Poderico, G. Poggi, D. Riccio, and L. Verdoliva, "Benchmarking framework for SAR despeckling," *IEEE Trans. Geosci. Remote Sensing*, vol. 52, no. 3, 2014.

[Si-Wei Chen, Yong-Zhen Li, Xue-Song Wang, Shun-Ping Xiao, and Motoyuki Sato]

Modeling and Interpretation of Scattering Mechanisms in Polarimetric Synthetic Aperture Radar

[Advances and perspectives]

Polarimetric target decomposition is a powerful technique to interpret scattering mechanisms in polarimetric synthetic aperture radar (PolSAR) data. Eigenvalue-eigenvector-based and model-based methods are two main categories within the incoherent

decomposition techniques. Eigenvalue-eigenvector-based decomposition becomes relatively mature since it has a clearer mathematical background and has only one decomposition solution. In contrast, model-based decompositions can obtain different decomposition solutions in terms of various scattering models. Meanwhile, conventional methods with models or assumptions that do not fit the observations may induce deficiencies. Thereby, the development of effective model-based decompositions has received considerable attention and many advances have been reported. This article aims to provide a review for these notable advances, mainly including the incorporation of orientation compensation processing, nonnegative eigenvalue constraint, generalized scattering models, complete information utilization, full-parameter inversion schemes, and fusion of polarimetry and interferometry. Airborne

Pi-SAR data sets are used for demonstration. Besides, natural disaster damage evaluation using model-based decomposition is carried out based on advanced land-observing satellite/phased array type L-band synthetic aperture radar (ALOS/PALSAR) data. Finally, further development perspectives are presented and discussed.

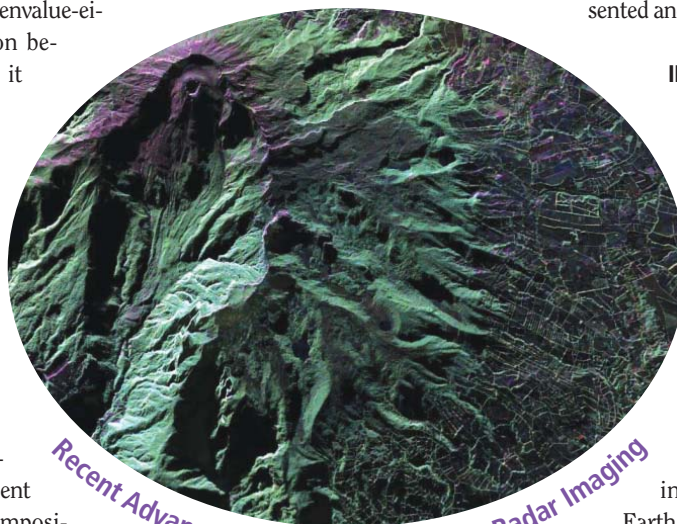


PHOTO COURTESY OF NASA

INTRODUCTION

Microwave remote sensing has been rapidly developing over the past few decades with progresses in hardware systems, signal processing techniques, and interpretation theories. Microwave remote sensors, which can work day and night and are nearly unaffected by weather and atmospheric conditions, play an increasingly important role for Earth and other planet monitoring in both global and regional scales. PolSAR is one of the mainstream imaging systems in microwave remote sensing. It can obtain fully polarimetric information by transmitting and receiving microwaves with specific polarization states [1]–[3]. Fully polarimetric information is sensitive to scattering mechanisms related to target responses during a back-scattering procedure. Full polarization acquisition can enhance the radar capability in scattering mechanism understanding and target parameters (e.g., material, shape, and orientation) retrieval. In this vein, many current airborne and spaceborne synthetic aperture

Digital Object Identifier 10.1109/MSP.2014.2312099

Date of publication: 13 June 2014

radar (SAR) systems are equipped with a full-polarization mode. A number of PolSAR data sets have been acquired by these systems especially the routinely operated spaceborne systems such as on-orbit Radarsat-2 and TerraSAR, the retired ALOS/PALSAR, etc. [1]. These valuable data sets greatly stimulate the studies in both theory and application. Scattering mechanism understanding is a bridge between the collected data and real applications.

Generally, scattering mechanisms are determined by a set of factors such as radar frequency, radar bandwidth, illumination direction, and target dielectric/geometric properties. Although the basic theory of radar polarimetry has been well established [1]–[3], scattering mechanism modeling and interpretation are still ongoing. How to effectively extract robust and useful information from collected data is still challenging.

In past decades, many scientists and researchers have been involved in this field to interpret the scattering mechanisms present in PolSAR data [1]–[4]. Polarimetric target decomposition theorems [5], originated from Huynen's work in the 1970s [6], became one of the most powerful and the most popularly used techniques. With this technique, a measured polarimetric matrix can be decomposed into a summation of several canonical scattering mechanisms. Thereby, the dominant scattering mechanism can be determined and physical parameters can be retrieved. A number of successful applications, such as land-cover classification and target detection [1], [4], soil moisture estimation [2], [7], forest study [1], [3], ocean study [1], agriculture study [1], glacier study [8], and natural disaster study [9]. Since the measured scattering matrix is commonly affected by speckle phenomenon [1], incoherent analysis using the second-order statistics such as the coherency/covariance matrix is mostly used. Incoherent decompositions can be divided into two categories: eigenvalue-eigenvector-based decomposition [1], [3], [5] and model-based decomposition [10], [11]. Eigenvalue-eigenvector-based decomposition becomes relatively mature since it has clearer mathematical background and has only one decomposition solution. Polarimetric entropy, mean alpha angle $\bar{\alpha}$, and polarimetric anisotropy are the most popular parameters derived from this technique and are widely used for scattering mechanism understanding [1], [3], [5]. In contrast, with various combination of scattering models, model-based decompositions can obtain different decomposition solutions. Meanwhile, conventional model-based decompositions with models or assumptions that do not fit the observations may induce deficiencies, such as the appearances of negative powers for scattering mechanisms, overestimations of volume scattering, scattering mechanism ambiguities, etc. Thereby, the development of effective model-based decompositions has received considerable attention [12]. The Freeman–Durden decomposition [10] is the pioneer of incoherent model-based decompositions. Thereafter, to enhance the scattering mechanism interpretation performance, many notable advances have been achieved, including orientation compensation strategy [13]–[15]; nonnegative eigenvalue constraint

PolSAR IS ONE OF THE MAINSTREAM IMAGING SYSTEMS IN MICROWAVE REMOTE SENSING.

[16]–[18]; generalized scattering models [7], [19]–[26]; complete information utilization [18], [23], [26], [27]; full-parameter inversion technique [20], [21], [26]; and polarimetric-interferometric decomposition [21], [24], [25].

In 1996, Cloude and Pottier published an excellent review for target decomposition theorems [5]. Reference [12] also provides a short overview. Based on these papers, this article will investigate all these recent advances, present a brief summary, and discuss the perspectives for future developments.

BASICS OF SCATTERING MECHANISM MODELING

REPRESENTATION OF PolSAR DATA

For PolSAR, the acquired full polarimetric information can be expressed in the form of the scattering matrix, as

$$S = \begin{bmatrix} S_{HH} & S_{HV} \\ S_{VH} & S_{VV} \end{bmatrix}, \quad (1)$$

where S_{HV} is the backscattered return from vertical transmitting and horizontal receiving polarization.

Subject to the reciprocity condition ($S_{HV} = S_{VH}$), the Pauli scattering vector is $k_P = (1/\sqrt{2})[S_{HH} + S_{VV} \quad S_{HH} - S_{VV} \quad 2S_{HV}]^T$. When rotated with angle θ around the radar line of sight (LOS), it becomes [1]

$$k_P(\theta) = R_3(\theta)k_P = \begin{bmatrix} 1 & 0 & 0 \\ 0 & \cos 2\theta & \sin 2\theta \\ 0 & -\sin 2\theta & \cos 2\theta \end{bmatrix} k_P. \quad (2)$$

The coherency matrix T without rotation is

$$T = \langle k_P k_P^H \rangle = \begin{bmatrix} T_{11} & T_{12} & T_{13} \\ T_{21} & T_{22} & T_{23} \\ T_{31} & T_{32} & T_{33} \end{bmatrix}, \quad (3)$$

where $\langle \rangle$ denotes the sample average, and k_P^H is the conjugate transpose of k_P . T_{ij} is the (i, j) entry of T .

The coherency matrix T with rotation angle θ is [1]

$$T(\theta) = k_P(\theta) k_P^H(\theta) = R_3(\theta) T R_3^H(\theta). \quad (4)$$

BASIC SCATTERING MODELS

The general principle of incoherent model-based decomposition is to decompose a polarimetric matrix into a summation of a set of basic scattering models. Using the coherency matrix as an example, basic scattering models include volume scattering T_{vol} , double-bounce scattering T_{dbl} , odd-bounce scattering T_{odd} , and helix scattering T_{hel} . In practice, volume scattering can represent the scattering mechanism from areas with a number of elemental scatterers inside, such as vegetation canopy and ice. Double-bounce scattering indicates dihedral

corner reflection formed by ground-wall structures and ground-trunk interactions. Odd-bounce scattering can describe both single-bounce scattering from rough surfaces such as grass area and ocean, and triple-bounce scattering from ground-wall-ground and ground-trunk-ground structures. Helix scattering fits the reflection asymmetry condition valid in heterogeneous areas, such as complicated shape targets and built-up areas. Decomposition framework can be presented as

$$T = f_v T_{\text{vol}} + f_d T_{\text{dbl}} + f_s T_{\text{odd}} + f_c T_{\text{hel}} + \dots, \quad (5)$$

where f_v , f_d , f_s , and f_c are model coefficients.

The number of model components is tunable for certain decomposition. With the determination of the power of each component, scattering mechanisms can be understood and applications can be explored thereafter.

VOLUME SCATTERING MODEL

Volume scattering is usually modeled by a cloud of elemental scatterers with some orientation defined by an angle θ . The coherency matrix for volume scattering is obtained by the integration with a probability density function (PDF) $p(\theta)$, and can be generally expressed as

$$T_{\text{vol}} = \int_0^{2\pi} T(\theta) p(\theta) d\theta = \begin{bmatrix} a & d & e \\ d^* & b & f \\ e^* & f^* & c \end{bmatrix}. \quad (6)$$

For randomly oriented thin dipoles, if the PDF is assumed to be uniform ($p(\theta) = 1/2\pi$) [10], the corresponding model is

$$T_{\text{vol1}} = \frac{1}{4} \begin{bmatrix} 2 & 0 & 0 \\ 0 & 1 & 0 \\ 0 & 0 & 1 \end{bmatrix}. \quad (7)$$

With another PDF ($p(\theta) = 1/2\sin\theta$) proposed in [11], two models can be obtained using horizontal and vertical dipoles

$$T_{\text{vol2}} = \frac{1}{30} \begin{bmatrix} 15 & 5 & 0 \\ 5 & 7 & 0 \\ 0 & 0 & 8 \end{bmatrix} \text{ and } T_{\text{vol3}} = \frac{1}{30} \begin{bmatrix} 15 & -5 & 0 \\ -5 & 7 & 0 \\ 0 & 0 & 8 \end{bmatrix}. \quad (8)$$

DOUBLE-BOUNCE SCATTERING MODEL

The double-bounce scattering is basically modeled by scattering from a dihedral corner reflector, such as ground-wall structures and ground-trunk interactions, where the reflector surfaces can be made of different dielectric materials. The corresponding coherency matrix [1] is

$$T_{\text{dbl}} = \begin{bmatrix} |\alpha|^2 & \alpha & 0 \\ \alpha^* & 1 & 0 \\ 0 & 0 & 0 \end{bmatrix}, \quad (9)$$

where α is complex valued and $|\alpha| < 1$ [1].

ODD-BOUNCE SCATTERING MODEL

The odd-bounce scattering is represented by a Bragg surface scattering model for slightly rough surfaces for which the depolarization effect and the cross-polarization component is negligible. The corresponding coherency matrix [1] is

$$T_{\text{odd}} = \begin{bmatrix} 1 & \beta^* & 0 \\ \beta & |\beta|^2 & 0 \\ 0 & 0 & 0 \end{bmatrix}, \quad (10)$$

where $|\beta| < 1$ and β is real valued from most natural surfaces [1].

HELIX SCATTERING MODEL

The roll-invariant helix scattering component was proposed in [11] to fit the reflection asymmetry condition, such as in built-up areas. The corresponding coherency matrix is

$$T_{\text{hel}} = \frac{1}{2} \begin{bmatrix} 0 & 0 & 0 \\ 0 & 1 & \pm j \\ 0 & \mp j & 1 \end{bmatrix}. \quad (11)$$

CONVENTIONAL THREE- AND FOUR-COMPONENT DECOMPOSITIONS

The Freeman–Durden decomposition [10] is the first three-component incoherent model-based decomposition with the formulation as

$$T = f_v T_{\text{vol}} + f_d T_{\text{dbl}} + f_s T_{\text{odd}}. \quad (12)$$

The Freeman–Durden decomposition assumes the reflection symmetry condition for which the cross-correlation between copolarization and cross-polarization are always zero ($T_{13} = 0$ and $T_{23} = 0$). In this way, there are five known observables (T_{11} , T_{22} , T_{33} , and complex valued T_{12}) with six unknown model parameters f_v , f_d , f_s , β , and complex-valued α to be determined. From the adopted models (7), (9), and (10), only the volume scattering contributes to the cross-polarization term T_{33} . Thereby, the volume model coefficient f_v can be determined at first and its contribution is subtracted

$$T_{\text{remainder}} = T - f_v T_{\text{vol}} = f_d T_{\text{dbl}} + f_s T_{\text{odd}}. \quad (13)$$

Based on the sign of $\text{Re}(\langle S_{\text{HH}} S_{\text{VV}}^* \rangle)$, the dominance of double- or odd-bounce scattering in the remainder matrix $T_{\text{remainder}}$ can be determined. If $\text{Re}(\langle S_{\text{HH}} S_{\text{VV}}^* \rangle)$ is positive, parameter α of model (9) is fixed as -1 , otherwise parameter β of model (10) is fixed as 1 . In this vein, all the model parameters can be determined.

The Yamaguchi decomposition [11] includes helix scattering model to remove the reflection symmetry assumption since it is not always valid for various land covers

$$T = f_v T_{\text{vol}} + f_d T_{\text{dbl}} + f_s T_{\text{odd}} + f_c T_{\text{hel}}. \quad (14)$$

Another improvement is the extension of volume scattering modeling. For instance, a PDF for elemental scatterer orientation

and another two volume scattering models are introduced, shown in (8). The most suitable volume model is determined by the ratio of copolarization terms. Since only helix scattering contribute to $\text{Im}[T_{23}]$, its model coefficient f_c is determined and its contribution is subtracted with the highest priority. The inversion strategy then follows the Freeman–Durden decomposition procedure.

**THE GENERAL PRINCIPLE OF
INCOHERENT MODEL-BASED
DECOMPOSITION IS TO DECOMPOSE
A POLARIMETRIC MATRIX INTO A
SUMMATION OF A SET OF BASIC
SCATTERING MODELS.**

EXISTING PROBLEMS

Freeman–Durden and Yamaguchi decompositions are the pioneer model-based decomposition techniques. They are popularly used due to the easy physical interpretation of the scene they provide, together with their simplicity, computational efficiency, and relatively good performance. However, some issues exist too. The first is the occurrence of negative powers for double- or odd-bounce scattering after the subtraction of volume or helix scattering components. Although scattering powers can be forced to be zero or positive, these decomposition results are physically incorrect. Intrinsically, it means the scattering models do not fit the observations. The second is that double- and odd-bounce scattering components are modeled with zero cross-polarization terms. In a real situation, the depolarization effect and polarization state rotation from terrain slopes and oriented buildings can induce significant cross-polarization power. Therefore, especially oriented man-made structures and hills are usually misjudged as volume scattering dominant, which produces serious scattering mechanism ambiguity. The volume scattering models $T_{\text{vol}1}$, $T_{\text{vol}2}$, and $T_{\text{vol}3}$ from (7)–(8) all have constant model parameters. Therefore, using (6), the volume scattering contribution is fully determined by these constants and the cross-polarization term

$$P_v = (a + b + c)f_v = \left(1 + \frac{a+b}{c}\right)T_{33} = F_v T_{33}. \quad (15)$$

The dynamic range is limited and the volume scattering contribution is easily overestimated. Moreover, for parameter inversion, the implicit assumption of model priority is included, since the observations are used to satisfy helix and volume components first. In addition, conventional methods do not use the full information of a coherency matrix for modeling. For example, all models (7), (9), and (10) used in the Freeman–Durden decomposition [10] do not account for elements T_{13} and T_{23} , while elements T_{13} and $\text{Re}[T_{23}]$ are not utilized in the Yamaguchi decomposition [11].

RECENT ADVANCES IN MODEL-BASED DECOMPOSITION

This section reviews recent advances in model-based decomposition and the key features are summarized in Table 1.

ORIENTATION COMPENSATION PROCESSING

Polarimetric responses of the same target with different orientations can be quite different due to the rotation of polarization state. This phenomenon causes ambiguity for scattering mechanism discrimination. Orientation compensation [1], [14], also

named *deorientation processing* [6], can mitigate this orientation dependence effect by polarimetric matrix rotation around radar LOS until the cross-polarization term is minimized.

Orientation compensation was incorporated into model-based decomposition [13]–[15]. The general orientation compensation effect is to minimize the cross-polarization term T_{33} . From (15), the decomposed volume scattering power is consistently reduced.

Therefore, orientation compensation can partially cure the overestimation of volume scattering power and the occurrence of negative powers. Besides, it is possible to compensate the target orientation effect on the perpendicular plane to the radar LOS using this technique. However, since there is an intersection angle between the rotation plane of oriented buildings or terrain slopes and the perpendicular plane, complete orientation compensation cannot be achieved only using this technique, which deserves further efforts.

NONNEGATIVE EIGENVALUE CONSTRAINT

The appearance of negative power due to the subtraction of the scattering component is an important issue of conventional methods. Van Zyl et al. [16] recognized this fact and proposed the nonnegative eigenvalue decomposition to theoretically avoid the occurrence of nonphysical negative power. Using three-component decomposition as an example, they introduced the nonnegative eigenvalue constraint (NNEC) during the subtraction of the volume scattering component. The core idea is to guarantee the eigenvalues of remainder matrix $T_{\text{remainder}}$ are nonnegative. Then, the subtraction processing will not produce negative power. Using NNEC, the maximum volume model coefficient can be determined

$$T_{\text{remainder}} = T - f_v^{\text{max}} T_{\text{vol}}. \quad (16)$$

Therefore, when $f_v \leq f_v^{\text{max}}$ is satisfied, the negative power can be avoided. With the reflection symmetry condition, the analytical expression of f_v^{max} is derived in [16]. More recently, its analytical expression is extended to the nonreflection symmetry condition using the principle minor theory [17]. The optimal determination of f_v is still open. In [3], a generalized Freeman–Durden decomposition is established and the appearance of negative powers is theoretically avoided using both the eigenvalue technique and the orthogonality of double- and odd-bounce scattering models. Furthermore, with certain conditions, the idea of NNEC is generalized and volume model coefficient f_v can be uniquely determined [18].

OTHER VOLUME SCATTERING MODELS

To better fit the elemental scatterer orientation and to extend the dynamic range of volume scattering model, other PDFs have been utilized [21]–[23]. The von Mises distribution has been used in [21] to characterize a vegetation canopy. The n th

[TABLE 1] A SUMMARY OF TYPICAL MODEL-BASED DECOMPOSITIONS.

METHODS	INFORMATION UTILIZATION	NEGATIVE POWER	MODEL INVERSION PRIORITY	COMPUTATION EFFICIENCY	NOTABLE REMARKS
FREEMAN-DURDEN DECOMP. [10]	T_{13} , T_{23} UNACCOUNTED	YES	VOLUME>DOUBLE-/ ODD-BOUNCE	HIGH	BASIC SCATTERING MODELS
FREEMAN II DECOMP. [19]	T_{13} , T_{23} UNACCOUNTED	YES	VOLUME>DOUBLE/ ODD-BOUNCE	HIGH	VOLUME SCATTERING MODEL IS FITTED BY A SHAPE PARAMETER
YAMAGUCHI DECOMP. [11]	T_{13} , $RE[T_{23}]$ UNACCOUNTED	YES	HELIX>VOLUME> DOUBLE-/ ODD-BOUNCE	HIGH	INTRODUCE THE FOURTH HELIX COMPONENT AND TWO MORE VOLUME SCATTERING MODELS
YAMAGUCHI (FREEMAN-DURDEN) DECOMP. + ORIENTATION COMPENSATION [13]–[15]	T_{13} (T_{13} , $IM[T_{23}]$) UNACCOUNTED	YES	HELIX>VOLUME> DOUBLE-/ ODD-BOUNCE	HIGH	INCORPORATE THE ORIENTATION COMPENSATION TO MINIMIZE T_{33} AND ELIMINATE $RE[T_{23}]$
GENERALIZED FREEMAN-DURDEN DECOMP. [3]	T_{13} , T_{23} UNACCOUNTED	NO	VOLUME>DOUBLE-/ ODD-BOUNCE	HIGH	HYBRID FREEMAN-DURDEN/EIGENVALUE TECHNIQUE
VAN ZYL ET AL. DECOMP. [16]	T_{13} , $IM[T_{23}]$ UNACCOUNTED	NO	VOLUME>DOUBLE-/ ODD-BOUNCE	HIGH	INCORPORATE THE NNEC TO THEORETICALLY AVOID THE NEGATIVE POWER
GULAB ET AL. DECOMP. [27]	FULL POLARIMETRIC INFORMATION	YES	HELIX>VOLUME> DOUBLE-/ ODD-BOUNCE	HIGH	DOUBLE UNITARY ROTATION PROCESSING
CUI ET AL. DECOMP. [18]	FULL POLARIMETRIC INFORMATION	NO	VOLUME>DOUBLE-/ ODD-BOUNCE	HIGH	HYBRID DECOMPOSITION USING BOTH SCATTERING MODELS AND EIGENDECOMPOSITION
LEE ET AL. DECOMP. [23]	T_{13} , $IM[T_{23}]$ UNACCOUNTED	VERY LIMITED	VOLUME>DOUBLE-/ ODD-BOUNCE	HIGH	GENERALIZED DOUBLE- AND ODD-BOUNCE OR VOLUME SCATTERING MODELS
ARRI ET AL. DECOMP. [20], [22]	T_{13} UNACCOUNTED OR FULL POLARIMETRIC INFORMATION	NO	PARTIAL PRIORITY, SIMULTANEOUSLY INVERSION	LOW	GENERALIZED VOLUME SCATTERING MODELS, FULL-PARAMETER INVERSION
CHEN ET AL. DECOMP. [26]	FULL POLARIMETRIC INFORMATION	NO	NO PRIORITY, SIMULTANEOUSLY INVERSION	LOW	GENERALIZED DOUBLE- AND ODD-BOUNCE MODELS, FULL-PARAMETER INVERSION
NEUMANN ET AL. DECOMP. [21]	POLARIMETRIC AND INTERFEROMETRIC INFORMATION	NO	NO PRIORITY, SIMULTANEOUSLY INVERSION	LOW	GENERALIZED MODELS ESPECIALLY FOR VEGETATIONS, FULL-PARAMETER INVERSION
DAVID BALLESTER-BERMAN ET AL. DECOMP. [24]	POLARIMETRIC AND INTERFEROMETRIC INFORMATION	NO	VOLUME>DOUBLE-/ ODD-BOUNCE	LOW	OBTAIN THE POWER AND LOCATION OF EACH SCATTERING MECHANISM AT THE VERTICAL DIMENSION OF THE SCENE
POLARIMETRIC-INTERFEROMETRIC DECOMP. [25]	POLARIMETRIC AND INTERFEROMETRIC INFORMATION	NO	VOLUME>DOUBLE/ ODD-BOUNCE	HIGH	USING POLARIMETRIC AND INTERFEROMETRIC INFORMATION TO FIT VOLUME SCATTERING

power cosine-squared distribution, including two parameters of the mean orientation angle and the randomness indicator, was developed in [22]. Meanwhile, generalized volume scattering models generated from arbitrary-shaped elemental scatterers instead of the thin dipole assumption were also proposed [22]. Besides, a family of models based on the multilook phase difference distributions, which are better suited to characterize orientation angle distributions, was proposed [23].

In addition, empirical volume scattering models have also been proposed as another alternative. An empirical model with shape parameter ρ was introduced to particularly fit randomly oriented prolate spheroidal and elliptical scatterers in [19] (notated as the Freeman II decomposition). Since polarimetric SAR interferometry (PolInSAR) coherence has a close relationship to forest structures [3], [28], volume scattering can be modeled from it and an adaptive volume scattering model was proposed [25] using PolInSAR coherence to be functioned as

the shape parameter. Identity matrix with the highest entropy was also proposed to fit volume scattering [13].

GENERALIZED DOUBLE- AND ODD-BOUNCE SCATTERING MODELS

In conventional methodologies, the double- and odd-bounce scattering mechanisms are assumed not to contribute to the cross-polarization term. However, in real situations, terrain slopes in the along-track direction and/or oriented buildings rotate the polarization basis of the scattering matrix, which will induce significant cross-polarization power [1], [2], [16]. Since the conventional models do not fit these situations, the scattering mechanism ambiguity is serious. Recently, several papers addressed this issue for more generalized double- and odd-bounce scattering modeling [7], [23], [26]. In [7], the Bragg surface model has been extended as the advanced X-Bragg model to fit the cross-polarization term induced by the depolarization effect. In [23], incoherent double- or

odd-bounce scattering models have been incorporated. Recently, in [26], double- and odd-bounce scattering models are generalized to fit the cross-polarization and off-diagonal terms, by separating their independent orientation angles θ_{dbl} and θ_{odd} .

COMPLETE INFORMATION UTILIZATION

A coherency matrix contains nine real values (three real-valued quantities and three complex-valued quantities). Each of them has specific physical meaning. If scattering mechanisms are well modeled, each element of a coherency matrix should be fitted. The three-component Freeman–Durden decomposition [10] accounts for five of these parameters. The Yamaguchi decomposition [11] introduced the fourth component and accounts for six parameters. With the orientation compensation [14], $\text{Re}[T_{23}] = 0$ is achieved and nine elements are reduced to eight. Thereby, there remains three and two unaccounted parameters in Freeman–Durden and Yamaguchi decompositions, respectively. The details of many current model-based decompositions are summarized in Table 1.

How to model the scattering mechanisms using complete information is a major motivation, and three representative approaches were presented in [18], [26], and [27]. A further modified Yamaguchi decomposition was reported [27] and accounts for all parameters based on special double unitary transformations. In [26], a general decomposition framework was proposed to utilize all elements of a coherency matrix. All model parameters are optimally obtained using the full-parameter inversion technique. A hybrid decomposition using full information was established [18]. It generalized the van Zyl et al. decomposition [16] to uniquely determine volume scattering contribution from the scattering model while using the eigendecomposition to determine the double- and odd-bounce scattering contributions.

FULL-PARAMETER INVERSION STRATEGY

Model parameters inversion is carried out at a certain order under some specific conditions for majority of the established model-based decompositions. For conventional Freeman–Durden and Yamaguchi decompositions, the volume scattering and helix scattering solely contributes to cross-polarization term T_{33} and $\text{Im}[T_{23}]$, respectively. Therefore, their contributions are subtracted from the total measured data at first. Double- and odd-bounce scattering contributions are calculated in turn from the remainder matrix thereafter with a branch condition. This strategy is the main weakness and may overestimate volume scattering contribution, induce negative power, etc. In addition, it also implies that the volume and helix scattering components share the higher priority. Especially in mixed scenes, such a priority assumption seems unreasonable.

Generalized decomposition frameworks and full-parameter inversion techniques have been proposed [20], [26] to obtain all

the unknown parameters simultaneously using linear or nonlinear optimization algorithms. Basically, the decomposition framework is generalized as

$$T = f_v T_{vol} + f_d T_{dbl} + f_s T_{odd} + f_c T_{hel} + \dots + f_r T_{residual}. \quad (17)$$

Suitable scattering models that guarantee parameter inversion as a determined problem can be included into (17). $T_{residual}$ is regarded as the residual induced by speckle, noise, and unmodeled contributions to the data. The residual matrix $T_{residual}$ can measure how well those models fit the observations. Therefore, for model inversion, the optimization criterion is to minimize the residual. The optimization adopted in [20] and [26] is

$$\min : \|T_{residual}\|_2, \quad (18)$$

where $\|T_{residual}\|_2$ is the L2-norm of $T_{residual}$.

Minimization (18) can be solved by a nonlinear least squares optimization, as adopted in [26]. Full-parameter inversion can obtain all model parameters optimally and simultaneously while avoiding the model priority assumption and negative power issue. Note that nonlinear optimization takes more computation time and may obtain only local minimal of $\|T_{residual}\|_2$, which needs further studies.

THE COMPLEMENTARY INFORMATION BETWEEN POLARIMETRY AND INTERFEROMETRY HAS BEEN DEMONSTRATED TO BE VERY PROMISING FOR MANY APPLICATIONS, SUCH AS FOREST CHARACTERIZATION AND LAND-COVER CLASSIFICATION.

POLARIMETRIC-INTERFEROMETRIC DECOMPOSITION

PolInSAR, which is a combination of PolSAR and interferometric SAR, has been well established [3], [28]. This combination allows understanding different scattering mechanisms located at different heights. The complementary information (e.g., PolInSAR coherence) between polarimetry and interferometry has been demonstrated to be very promising for many applications, such as forest characterization and land-cover classification [1], [3]. PolInSAR studies contain two main aspects. The first is the development of innovative imaging techniques especially for the vertical profile or the three-dimension reconstruction of targets using single- or multibaseline PolInSAR data. The second is the physical parameters (e.g., forest height, biomass) inversion, which also covers a wide scope. Each of these important topics and recent advances deserves separate papers to discuss in depth. In the second aspect, there is a small branch utilizing the concept of model-based decomposition and the framework of (5). Only this technique branch, mainly including three reported methods [21], [24], [25], will be introduced in this section. The main purpose of these methods is to incorporate interferometric information in scattering mechanism modeling. With extra information to conventional polarimetric decomposition framework, decomposition performance can be enhanced. In [21], scattering modeling especially in vegetation areas has been intensively studied and a set of volume scattering models using single- or multibaseline PolInSAR data has been established.

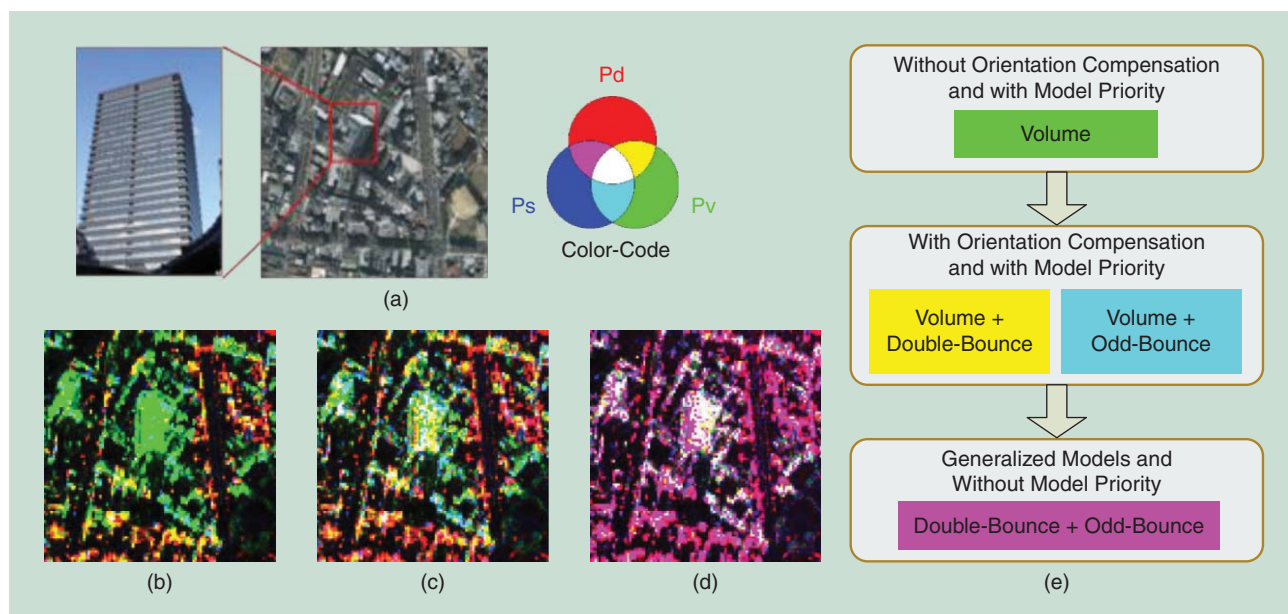


[FIG1] A demonstration with Pi-SAR PolSAR data. (a) A Google Earth optical image and a photo for the tall building, (b) and (c) Freeman–Durden decomposition without and with orientation compensation [10], [14], (d) Chen et al. decomposition [26] without orientation compensation. The decomposition images are colored by P_d (red), P_v (green), and P_s (blue). (e) Decomposition performance comparison over oriented buildings.

Detailed geophysical parameters describing the vegetation layers can be derived. In [24], the concept of the Freeman–Durden decomposition has been extended to PolInSAR polarimetric-interferometric correlation matrix by adding the interferometric responses of each scattering mechanism. Thereby, both the power and location of each scattering mechanism can be determined. In [25], an adaptive polarimetric-interferometric model-based decomposition has been developed using PolInSAR coherence. Demonstrations with real PolInSAR data validated its performance especially for oriented building characterization. These are the first attempts to fuse the polarimetric and interferometric information for scattering mechanism modeling. More efforts are needed for further study.

EXPERIMENTAL DEMONSTRATION AND INVESTIGATION

DEMONSTRATION WITH AIRBORNE Pi-SAR DATA

This example demonstrates the effects of model priority issue, orientation compensation, generalized models, and full parameter inversion scheme. Airborne Pi-SAR X-band PolSAR data covering an urban region from the downtown of Sendai, Japan, is used. The optical image and a photo for the tall building are shown in Figure 1(a). The representative three-component Freeman–Durden decomposition without and with orientation compensation [10], [14] and the recently developed Chen et al. decomposition [26] are used for comparison. The Chen et al. decomposition [26] uses the generalized double- and odd-bounce scattering models fitting the cross-polarization term and off-diagonal terms of a coherency matrix. To guarantee that the model inversion is a determined problem, a lookup table

including representative volume scattering models with constant parameters is formed. Suitable volume scattering model and optimal model parameters are determined using the full-parameter inversion technique (18). Decomposition results are shown in Figure 1(b)–(d), respectively. For Freeman–Durden decomposition, volume scattering contribution is first determined and subtracted. This processing implies the model priority assumption and volume scattering contribution always exist for any target. In Figure 1, without orientation compensation, the oriented tall building is obviously judged as dominant volume scattering, which is usually exhibited by vegetated areas. Thereby, scattering mechanism ambiguity occurs. With orientation compensation, the cross-polarization term is minimized and the volume scattering contribution is reduced. As can be seen in Figure 1(c), volume scattering contribution is greatly decreased. In reality, oriented buildings also induce significant cross-polarization term. Since conventional double- and odd-bounce models (9) and (10) do not account for it, and due to the model priority issue, the volume scattering contributions over these man-made targets are still overestimated. By that

[TABLE 2] DOMINANT SCATTERING POWER CONTRIBUTION (%) FOR THE SELECTED BUILDING.

	P_d	P_v	P_s
FREEMAN–DURDEN DECOMPOSITION [10]	2	94	4
FREEMAN–DURDEN DECOMPOSITION WITH ORIENTATION COMPENSATION [14]	30	45	25
CHEN ET AL. DECOMPOSITION [26]	46	13	41

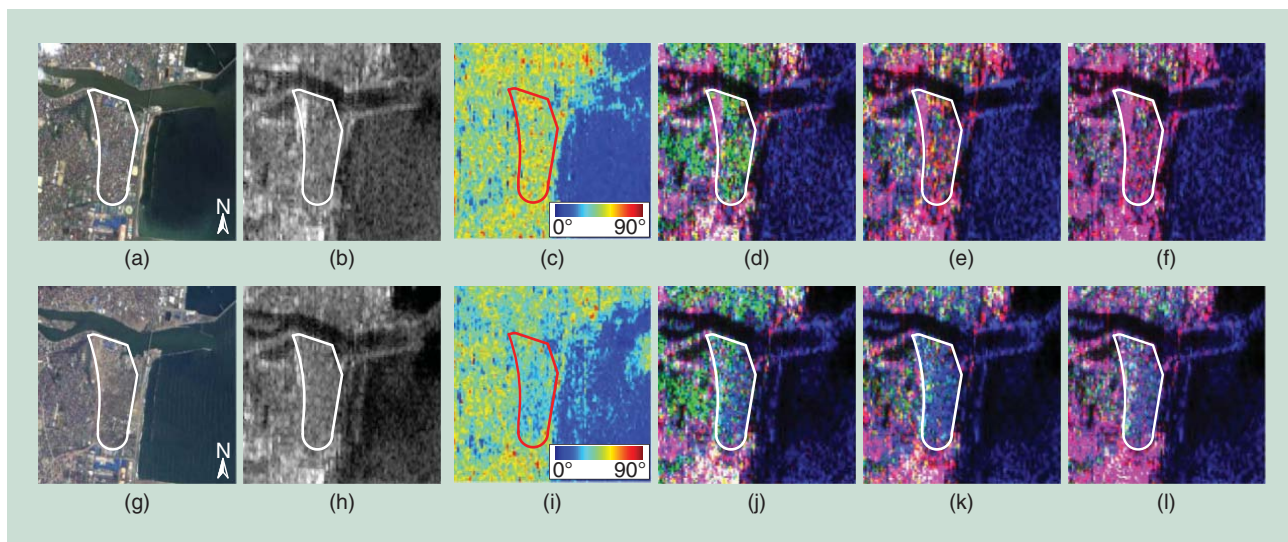


[FIG2] (a)–(f) Before- and (g)–(l) after-tsunami ALOS data and decomposition results. (a) and (g) show the ALOS optical image, (b) and (h) illustrate HH polarization amplitude data, (c) and (i) are the mean alpha angle parameter derived from Cloude–Pottier decomposition [1], [5], (d) and (j) show the Yamaguchi decomposition without orientation compensation [11], (e) and (k) show the Yamaguchi decomposition with orientation compensation [15], and (f)–(l) shows the Chen et al. decomposition [26] without orientation compensation. The decomposition images are colored by P_d (red), P_v (green), and P_s (blue).

means, comparable volume scattering and double- or odd-bounce scattering contributions coexist for these oriented buildings, which appear yellow or cyan in the RGB composite image in Figure 1(c). In comparison, the generalized models fit the cross-polarization terms while the full-parameter inversion technique avoids the negative power and model priority assumption. The general decomposition can successfully identify these buildings as man-made structures. In Figure 1(d), these buildings show purple since both double- and odd-bounce scattering mechanisms are dominant. For the tall building shown in Figure 1(a), quantitative examination is also carried out and summarized in Table 2. Compared to the original Freeman–Durden decomposition [10], with orientation compensation, dominant volume scattering obviously reduces from 94% to 45%, while the percentages of the dominant double- and odd-bounce scattering increase from 2% to 30% and 4% to 25%, respectively. Even still, volume scattering contribution is still overestimated and this building will be misjudged as dominant volume scattering. In comparison, dominant volume scattering further reduces to 13%, while dominant double- and odd-bounce scattering increase up to 46% and 41%. This building can be successfully discriminated as a man-made structure, which validates the efficiency of the advances.

APPLICATION FOR NATURAL DISASTER EVALUATION

The occurrence of observed natural disasters, such as earthquakes and tsunamis, appears to have increased in recent decades [9]. With the advantages of a large imaging scene, revisiting capability,

and multitemporal data archives, spaceborne SAR sensors play an extremely important role for natural disaster evaluation. The following demonstration uses the spaceborne ALOS data over the seriously damaged city of Ishinomaki, induced by the Eastern Japan great earthquake and tsunami that happened 11 March 2011. The after-tsunami optical and PolSAR data sets were acquired on 8 April 2011, while the latest before-tsunami data sets were acquired on 21 November 2010. Optical images are shown in Figure 2(a) and (g). The Pacific Ocean is located to the right of the images. Buildings in the region, highlighted by the line, were almost completely flushed away leaving a relatively rough surface. Besides, the orientations of these buildings are inclined to the sensor flight pass.

From scattering interpretation theory, this built-up area should response dominant double-bounce scattering induced by the ground-wall structures before the damage. However, after the tsunami, most of these buildings were swept away

and the ground-wall structures were dramatically decreased. Therefore, this seriously damaged area should be obviously changed into dominant odd-bounce (surface) scattering. As a comparison, the amplitudes of HH polarization are shown in Figure 2(b) and (h). Visually, single polarization is less sensitive to the changes of target structures, compared with fully polarimetric features. Meanwhile, mean alpha angle $\bar{\alpha}$, which is the primary parameter for scattering mechanism indication in the Cloude–Pottier decomposition [1], [5], is derived and shown in Figure 2(c) and (i). For before-tsunami cases, $\bar{\alpha} \rightarrow 90^\circ$ and indicates double-bounce scattering, while $\bar{\alpha} \rightarrow 0^\circ$ and indicates surface scattering for after-tsunami cases. Therefore, the $\bar{\alpha}$

SPACEBORNE SAR SENSORS PLAY AN EXTREMELY IMPORTANT ROLE FOR NATURAL DISASTER EVALUATION.

parameter can potentially discriminate damaged buildings. The Yamaguchi decomposition without and with orientation compensation [11], [15] and the Chen et al. decomposition [26] are also used for demonstration, shown in Figure 2(d)–(f) for before-tsunami cases and Figure 2(j)–(l) for after-tsunami cases, respectively. After the tsunami, the damaged area is correctly judged as dominant odd-bounce scattering (blue) indicating a rough surface from all three methods. However, for before-tsunami cases, the overestimation of volume scattering is significant without orientation compensation and this built-up area is falsely determined as dominant volume scattering (green), shown in Figure 2(d). In comparison, the other two approaches can successfully identify them as man-made structures that exhibit dominant double-bounce scattering (red). These polarimetric features are more stable during repeated data collects. The reduction of dominant double-bounce scattering amount has been verified to have a linear relationship with the amount of damaged ground-wall structures and has been utilized for quantitative evaluation of urban damage [9].

DISCUSSIONS AND PERSPECTIVES

PolSAR DATA PREPROCESSING ISSUE

There are two main aspects in PolSAR data preprocessing. The first is the data calibration. Generally, the acquired PolSAR data is affected by the channel imbalance and cross-talk effects that distort the polarization purity [2], [3]. Polarimetric calibration should be implemented at first for further processing. The aforementioned polarimetric target decompositions are all based on well-calibrated data. For low-frequency band (e.g., P-, L-band) spaceborne systems, the Faraday rotation effect induced by the ionosphere should also be compensated beforehand. Propagation distortions including Faraday rotation effect in model-based decomposition have been investigated in [3].

The second aspect is speckle reduction. Speckle phenomenon is an intrinsic property for coherent imaging system of PolSAR [1]. The existence of speckle phenomenon makes information extraction more difficult. Speckle reduction is also a preprocessing step for PolSAR data utilization. Suitable speckle filter should significantly reduce speckle phenomenon while preserving image details [1].

RADAR FREQUENCY ISSUE

Target backscattering properties usually vary with the illumination frequency due to its physical characteristics, especially the geometric features (e.g., size, shape, and structure) with respect to the radar wavelength. Meanwhile, low frequencies such as P- and L-band usually have a penetration depth into forest/vegetation canopies, deserts, dry bare soil areas, etc. Intrinsically, incident microwaves with different wavelengths

interact with different parts of a complex target or medium and the polarimetric responses may differ accordingly. Thereby, scattering mechanisms of a same target strongly

depend on the observation frequency and so are the interpretation results from model-based decomposition. For example, the scattering mechanism from vegetations may totally differ at the P- and X-band. In addition, the scattering models presented in the sections “Basics of Scattering Mechanism Modeling” and “Recent Advances in Model-Based Decom-

position” have their theoretical assumptions that should be well satisfied before utilization.

HIGH SPATIAL RESOLUTION ISSUE

With the advances in SAR imaging systems, fine-resolution data in the order of decimeter and centimeter can be available. At such resolutions, scatterers may be very limited. Some of the current modeling schemes should be updated. For example, modeling volume scattering by a cloud of oriented elemental scatterers should be reconsidered. Besides, note that incoherent polarimetric decomposition with sample average of measured data may blur image detail, while coherent polarimetric decomposition with scattering matrix (1) have only five freedoms for modeling. Thereby, how to fit these fine-resolution data provides challenges to scattering mechanism modeling and interpretation. In another aspect, more detailed information such as opening or closing a window may be sensed with high spatial resolution systems. Suitable decomposition techniques are highly expected for these situations.

PERFORMANCE EVALUATION ISSUE

A number of advanced model-based decompositions have been reported. They raise urgent questions: how to judge whether one proposed scattering model is reasonable or superior and how to fairly evaluate the performance? Actually, there is no standard answer. From the literature and according to our studies, the used evaluation criterion are summarized and discussed:

- 1) *Reflection symmetry assumption.* This assumption is mainly satisfied in vegetated areas with relatively flat topography. More generalized decomposition should also account for the reflection asymmetry condition.
- 2) *Information utilization.* The number of the used quantities of a polarimetric matrix is a good measure to evaluate a model-based decomposition proposal. Complete information utilization will be a mainstream concept for future development.
- 3) *Negative power occurrence.* This is an important issue since the decomposition results are nonphysical. Intrinsically, it indicates that the scattering models do not fit the observations.
- 4) *Scattering mechanism discrimination.* This is one key criterion to evaluate the performance of model-based decomposition. The majority of recent advances are also motivated to

SINCE THE SCATTERING MECHANISM CLOSELY RELATES TO LOCAL INCIDENCE ANGLE AND TARGET ORIENTATION, USING MULTILOOKING DIRECTION DATA SETS IS ANOTHER PROMISING TECHNIQUE.

overcome the scattering mechanism ambiguity between forests and oriented buildings.

5) *Model priority assumption*. For mixed land covers, there is no proper reason to assign the model priority. If the volume scattering component is determined at first, each scatterer will have volume scattering contribution. For oriented buildings, this contribution is not negligible. Generally, it is more reasonable to consider each scattering model share the equivalent priority.

6) *Computation efficiency*. Computation time and implementation complexity are considered in real applications. Basically, computationally effective methods are preferred.

These criteria can be the basics for model-based decomposition performance evaluation and comparison. Table 1 provides a summary of these criteria for typical model-based decompositions. Note that it is not reasonable to claim one proposed decomposition is always superior to others. In practice, how to choose the most suitable decomposition is also data oriented and application oriented.

FURTHER GENERALIZED MODELING

One difficulty in further development of model-based decomposition is how to balance model generalizations and model parameters inversion. A coherency matrix, providing nine inputs, allows at most nine unknown parameters for scattering mechanism modeling. There are several potential ways for future exploration. The first is still based on polarimetric data and segments the land cover beforehand. Specifically generalized scattering models are established for different terrains using more freedom in the modeling. For example, for pure built-up areas with dominant double-bounce scattering, ocean and grass areas with dominant odd-bounce scattering, more generalized double- and odd-bounce models can be founded accordingly. The core idea is that it may not be necessary to keep three or four scattering components for known land covers, and more detailed information can be extracted thereafter. The second method is to develop more generalized scattering models that do not reduce the scattering components by fusing additional data sets. The polarimetric-interferometric decomposition [21], [24], [25] is one attempt. Since the scattering mechanism closely relates to local incidence angle and target orientation, using multilooking-direction data sets is another promising technique. Furthermore, a combination of the aforementioned techniques may also be investigated in further studies.

CONCLUSIONS

Recent advances in scattering modeling and model-based decomposition theorem were reviewed. The notable achievements include orientation compensation processing, nonnegative eigenvalue constraint, generalized scattering models, complete information utilization, full-parameter inversion strategy, and the polarimetric-interferometric decomposition scheme. These advances contribute to make scattering models more adaptive, better fit observations and guarantee physically meaningful decomposition solutions. The key features of these

advances have been summarized. Performance evaluation and further development perspectives were also discussed. One promising way is to fuse multiple data to better model scattering mechanisms, such as the polarimetric-interferometric modeling attempts. Besides, with the progress in PolSAR sensors, imaging modes (e.g., bistatic, hybrid-polarization and multi-incident-angle modes) and application requirements, the development of specific scattering mechanism interpretation techniques, multiangular decomposition [29], and compact/hybrid decomposition [30] techniques are also highly preferred.

ACKNOWLEDGMENTS

We would like to thank the National Institute of Information and Communications Technology, Japan, and the Japan Aerospace Exploration Agency for providing the PolSAR data. We also deeply thank the editors and anonymous reviewers for their careful proofreading and constructive suggestions. This work was supported in part by the National Natural Science Foundation of China under grant 41301490.

AUTHORS

Si-Wei Chen (chenswnudt@163.com) received the Ph.D. degree (with honors) from the Graduate School of Environmental Studies, Tohoku University, Sendai, Japan, in 2012. He is an assistant professor at the State Key Laboratory of Complex Electromagnetic Environment Effects on Electronics and Information System, National University of Defense Technology. His research interests include radar polarimetry, polarimetric synthetic aperture radar, polarimetric synthetic aperture radar interferometry, and natural disaster study. He is a recipient of the 2011 Young Researcher Award from the IEEE Geoscience and Remote Sensing Society–Japan Chapter, the 2013 Dean Prize from the Graduate School of Environmental Studies, Tohoku University, and the Best Poster Award at the 2013 IET International Radar Conference. He was granted a Tohoku University president fellowship (2011–2012). He is a coinvestigator of the European Space Agency Earth Observation Campaign and ALOS data.

Yong-Zhen Li (e0061@sina.com) received the B.E. and Ph.D. degrees (with honors) from the School of Electronic Science and Engineering, National University of Defense Technology, Changsha, China, in 1999 and 2004, respectively. He is currently an associate professor at the National University of Defense Technology. His research interests include radar polarimetry, synthetic aperture radar, signal processing, and target recognition.

Xue-Song Wang (wxs1019@vip.sina.com) received the B.E. and Ph.D. degrees (with honors) from the School of Electronic Science and Engineering, National University of Defense Technology, Changsha, China, in 1994 and 1999, respectively. He is currently a professor at the National University of Defense Technology, and he has been the dean of the College of Science, since 2013. His current research interests include radar polarimetry, synthetic aperture radar, signal processing, and

target recognition. He is a senior member of the Chinese Institute of Electronics.

Shun-Ping Xiao (spxiao@gmail.com) received the B.E. and Ph.D. degrees (with honors) in electronic engineering from the National University of Defense Technology, Hunan, China, in 1986 and 1995, respectively. He is currently a professor with the National University of Defense Technology, and he has been the director of the State Key Laboratory of Complex Electromagnetic Environment Effects on Electronics and Information System, Changsha, China, since 2012. His current research interests include radar polarimetry, synthetic aperture radar, signal processing, and target recognition. He is a senior member of the Chinese Institute of Electronics.

Motoyuki Sato (sato@cneas.tohoku.ac.jp) has been a professor at Tohoku University since 1997 and a distinguished professor of Tohoku University since 2007. He was the director of the Center for Northeast Asian Studies, Tohoku University (2009–2013). His current interests include transient electromagnetics and antennas, radar polarimetry, ground penetrating radar (GPR), borehole radar, electromagnetic induction sensing, and interferometric and polarimetric synthetic aperture radar. He has conducted the development of the GPR sensor Advanced Landmine Indication System for humanitarian demining. He is a visiting professor at Jilin University, China, Delft University of Technology, The Netherlands, and the Mongolian University of Science and Technology. He is a member of the IEEE Geoscience and Remote Sensing Society (GRSS) Administrative Committee (2006–present), where he is responsible for specialty symposia and Asian issues. He was the chair of the IEEE GRSS Japan Chapter (2006–2007). He served as the general chair of the 2011 IEEE International Geoscience and Remote Sensing Symposium. He is a Fellow of the IEEE.

REFERENCES

- [1] J. S. Lee and E. Pottier, *Polarimetric Radar Imaging: From Basics to Applications*. Boca Raton, FL: CRC Press, 2009.
- [2] J. J. van Zyl and Y. Kim, *Synthetic Aperture Radar Polarimetry*. Hoboken, NJ: Wiley, 2011.
- [3] S. R. Cloude, *Polarisation Application in Remote Sensing*. New York: Oxford Univ. Press, 2010.
- [4] W. M. Boerner, "Recent advances in extra-wide-band polarimetry, interferometry and polarimetric interferometry in synthetic aperture remote sensing and its applications," *Proc. Inst. Elect. Eng.-Radar, Sonar Navig.*, vol. 150, no. 3, pp. 113–124, June 2003.
- [5] S. R. Cloude and E. Pottier, "A review of target decomposition theorems in radar polarimetry," *IEEE Trans. Geosci. Remote Sensing*, vol. 34, pp. 498–518, Mar. 1996.
- [6] J. R. Huynen, "Phenomenological theory of radar targets," Ph.D. thesis, Dept. Electr. Eng., Math. Comput. Sci., Technical Univ., Delft, The Netherlands, 1970.
- [7] I. Hajnsek, T. Jagdhuber, H. Schcon, and K. P. Papathanassiou, "Potential of estimating soil moisture under vegetation cover by means of PolSAR," *IEEE Trans. Geosci. Remote Sensing*, vol. 47, pp. 442–454, Feb. 2009.
- [8] J. J. Sharma, I. Hajnsek, K. P. Papathanassiou, and A. Moreira, "Polarimetric decomposition over glacier ice using long-wavelength airborne PolSAR," *IEEE Trans. Geosci. Remote Sensing*, vol. 49, pp. 519–535, Jan. 2011.
- [9] S. W. Chen and M. Sato, "Tsunami damage investigation of built-up areas using multi-temporal spaceborne full polarimetric SAR images," *IEEE Trans. Geosci. Remote Sensing*, vol. 51, no. 4, pp. 1985–1997, Apr. 2013.
- [10] A. Freeman and S. L. Durden, "A three-component scattering model for polarimetric SAR data," *IEEE Trans. Geosci. Remote Sensing*, vol. 36, pp. 963–973, May 1998.
- [11] Y. Yamaguchi, T. Moriyama, M. Ishido, and H. Yamada, "Four-component scattering model for polarimetric SAR image decomposition," *IEEE Trans. Geosci. Remote Sensing*, vol. 43, pp. 1699–1706, Aug. 2005.
- [12] J. S. Lee, T. L. Ainsworth, and Y. Wang, "Recent advances in scattering model-based decompositions: An overview," in *Proc. IEEE Int. Geoscience Remote Sensing Symp.*, Vancouver, Canada, July 2011, pp. 9–12.
- [13] W. T. An, Y. Cui, and J. Yang, "Three-component model-based decomposition for polarimetric SAR data," *IEEE Trans. Geosci. Remote Sensing*, vol. 48, pp. 2732–2739, June 2010.
- [14] J. S. Lee and T. L. Ainsworth, "The effect of orientation angle compensation on coherency matrix and polarimetric target decompositions," *IEEE Trans. Geosci. Remote Sensing*, vol. 49, pp. 53–64, Jan. 2011.
- [15] Y. Yamaguchi, A. Sato, W. M. Boerner, R. Sato, and H. Yamada, "Four-component scattering power decomposition with rotation of coherency matrix," *IEEE Trans. Geosci. Remote Sensing*, vol. 49, pp. 2251–2258, June 2011.
- [16] J. J. Van Zyl, M. Arii, and Y. Kim, "Model-based decomposition of polarimetric SAR covariance matrices constrained for nonnegative eigenvalues," *IEEE Trans. Geosci. Remote Sensing*, vol. 49, pp. 3452–3459, Sept. 2011.
- [17] S. Kusano, K. Takahashi, and M. Sato, "Volume scattering power constraint based on the principal minors of the coherency matrix," *IEEE Geosci. Remote Sensing Lett.*, vol. 11, no. 1, pp. 361–365, Jan. 2014.
- [18] Y. Cui, Y. Yamaguchi, J. Yang, H. Kobayashi, S. E. Park, and G. Singh, "On complete model-based decomposition of polarimetric SAR coherency matrix data," *IEEE Trans. Geosci. Remote Sensing*, vol. 52, no. 4, pp. 1991–2001, Apr. 2014.
- [19] A. Freeman, "Fitting a two-component scattering model to polarimetric SAR data from forests," *IEEE Trans. Geosci. Remote Sensing*, vol. 45, pp. 2583–2592, Aug. 2007.
- [20] M. Arii, J. J. van Zyl, and Y. Kim, "Adaptive model-based decomposition of polarimetric SAR covariance matrices," *IEEE Trans. Geosci. Remote Sensing*, vol. 49, pp. 1104–1113, Mar. 2011.
- [21] M. Neumann, L. Ferro-Famil, and A. Reigber, "Estimation of forest structure, ground, and canopy layer characteristics from multibaseline polarimetric interferometric SAR data," *IEEE Trans. Geosci. Remote Sensing*, vol. 48, no. 3, pp. 1086–1104, Mar. 2010.
- [22] M. Arii, J. J. van Zyl, and Y. Kim, "A general characterization for polarimetric scattering from vegetation canopies," *IEEE Trans. Geosci. Remote Sensing*, vol. 48, pp. 3349–3357, Sept. 2010.
- [23] J. S. Lee, T. L. Ainsworth, and Y. Wang, "Generalized polarimetric model-based decompositions using incoherent scattering models," *IEEE Trans. Geosci. Remote Sensing*, vol. 52, no. 5, pp. 2474–2491, May 2014.
- [24] J. D. Ballester-Berman and J. M. Lopez-Sanchez, "Applying the Freeman-Durden decomposition concept to polarimetric SAR interferometry," *IEEE Trans. Geosci. Remote Sensing*, vol. 48, no. 1, pp. 466–479, Jan. 2010.
- [25] S. W. Chen, X. S. Wang, Y. Z. Li, and M. Sato, "Adaptive model-based polarimetric decomposition using PolInSAR coherence," *IEEE Trans. Geosci. Remote Sensing*, vol. 52, no. 3, pp. 1705–1718, Mar. 2014.
- [26] S. W. Chen, X. S. Wang, S. P. Xiao, and M. Sato, "General polarimetric model-based decomposition for coherency matrix," *IEEE Trans. Geosci. Remote Sensing*, vol. 52, no. 3, pp. 1843–1855, Mar. 2014.
- [27] G. Singh, Y. Yamaguchi, and S.-E. Park, "General four-component scattering power decomposition with unitary transformation of coherency matrix," *IEEE Trans. Geosci. Remote Sensing*, vol. 51, no. 5, pp. 3014–3022, May 2013.
- [28] S. R. Cloude and K. P. Papathanassiou, "Polarimetric SAR interferometry," *IEEE Trans. Geosci. Remote Sensing*, vol. 36, no. 5, pp. 1551–1565, Sept. 1998.
- [29] T. Jagdhuber, I. Hajnsek, A. Bronstert, and K. P. Papathanassiou, "Soil moisture estimation under low vegetation cover using a multi-angular polarimetric decomposition," *IEEE Trans. Geosci. Remote Sensing*, vol. 36, no. 4, pp. 2201–2215, Apr. 2013.
- [30] S. R. Cloude, D. G. Goodenough, and H. Chen, "Compact decomposition theory," *IEEE Geosci. Remote Sensing Lett.*, vol. 9, no. 1, pp. 28–32, Jan. 2012.



[Raffaele Solimene, Ilaria Catapano, Gianluca Gennarelli, Antonio Cuccaro,
Angela Dell'Aversano, and Francesco Soldovieri]

SAR Imaging Algorithms and Some Unconventional Applications

[A unified mathematical overview]

This article deals with two significant aspects related to synthetic aperture radar imaging (SAR-I) of relevant theoretical and applicative interest. The first objective regards the analysis of the most-used SAR-I approaches under the

unified mathematical framework provided by the Porter–Bojarski integral equation. The second objective is to provide an updated overview on how SAR-I research is generalizing previous algorithms to deal with unconventional scenarios.

INTRODUCTION

SAR-I was originally introduced with regard to a scenario where the investigated scene is probed by a satellite platform-based synthetic aperture radar (SAR). Now, the corresponding imaging algorithms have crossed the boundaries of satellite imaging so that SAR-I refers to more general radar imaging contexts that encompass real (not synthetic) arrays, near-zone configurations, and layered (more in general lossy) scenarios. Therefore, SAR-I algorithms are relevant to many applicative scenarios, ranging from monitoring and nondestructive diagnostics to border surveillance, security, and crisis management. Accordingly, a large body of methods has populated the specialized literature; see, e.g., [1] and [2].

Digital Object Identifier 10.1109/MSP.2014.2311271

Date of publication: 13 June 2014

The need to link/compare these imaging methods arises quite naturally, and few works attempting to address such a comparative analysis have been presented in the literature [3]. In [4], the

classical matched filtered approach is reinterpreted as a particular case of some seismic migration; a similar analysis has been presented in [5], where the version of SAR-I given in [6] was compared to the frequency-wave-

number (F-K) migration.

From a different point of view, Bamler showed in [7] that the wavenumber SAR focusing is related to the classical Range–Doppler method without explicitly invoking the wave equation. The relationship

between the Kirchhoff migration and the seismic method is instead well known [2]. However, most of the aforementioned works compared only a couple of methods and a more comprehensive study is still missing.

Accordingly, the first objective of this article is to provide a unified and rigorous mathematical framework for several SAR-I approaches. To this end, we consider the traditional SAR-I scenario, i.e., the scattered field is collected under a multimonostatic measurement configuration (i.e., the transmitter and receiver are colocated) in a free-space scenario and the scattering phenomenon is assumed to be scalar. Despite SAR-I traditionally dealing with two-dimensional (2-D) scene approximations (e.g., slant plane imaging or 2-D sliced approach), here the case of three-dimensional (3-D) scene is considered. This is



PHOTO COURTESY OF NASA

Recent Advances in Synthetic Aperture Radar Imaging

because full 3-D SAR-I algorithms are being developed due to the possibility to exploit multipass data [8] or are already routinely used when data are measured on a scanning surface [9].

It is shown that the formal mathematical root of SAR-I is the Porter–Bojarski integral equation derived in the framework of generalized holography [10]. Accordingly, different SAR-I imaging methods can be reinterpreted on the basis of this equation, depending on the adopted approximations and the data spaces. These algorithms are here addressed as *migration algorithms*. A second class of SAR-I is explicitly founded on linear models of the electromagnetic scattering and is known as *inverse filtering*. Both the class of methods will be discussed and compared.

The necessity to achieve imaging in complex scenarios is gaining increasing interest due to new applicative fields such as security and monitoring applications, rescue assessment, and border surveillance. As applicative cases, through-the-wall imaging (TWI), imaging in urban canyons, and underground tunnel detection are of timely interest [11]–[13]. Therefore, the second objective of this article is to provide a quick view on how SAR-I can be generalized to face unconventional scenarios. In particular, the focus will be on inverse scattering methods as they offer the remarkable advantage that, even in presence of different and complex scenarios, the inversion procedure holds the same once the relevant Green’s function has been evaluated.

THE SCATTERING EQUATIONS

Consider a volume D probed by an incident field $\varphi_i(\underline{r}, \underline{r}_o, \omega)$ provided by a source, for simplicity assumed to be pointlike, located at \underline{r}_o [see Figure 1(a)]. Accordingly, due to the interaction between the incident field and the target in D , a scattered field $\varphi_s(\underline{r}, \underline{r}_o, \omega)$ arises so that the total field is given by $\varphi(\underline{r}, \underline{r}_o, \omega) = \varphi_i(\underline{r}, \underline{r}_o, \omega) + \varphi_s(\underline{r}, \underline{r}_o, \omega)$. In the following, the case of electromagnetically penetrable scatterers is addressed, but similar arguments can be developed also for not penetrable scatterers. Accordingly, the scattered field satisfies the nonhomogeneous Helmholtz equation

$$\nabla^2 \varphi_s(\underline{r}, \underline{r}_o, \omega) + k^2 \varphi_s(\underline{r}, \underline{r}_o, \omega) = -k^2 \chi(\underline{r}) \varphi(\underline{r}, \underline{r}_o, \omega), \quad (1)$$

where k is the wavenumber and $\chi(\underline{r})$ is the so-called contrast function, which accounts for the relative difference between the dielectric permittivity of the target and the one of the background medium; $k^2 \chi(\underline{r}) \varphi(\underline{r}, \underline{r}_o, \omega)$ is the current induced inside the target due to the incident field. The inverse scattering problem amounts to retrieve the target (represented by the contrast function $\chi(\underline{r})$) from scattered field data. As the induced current depends upon the total field (and hence on the scatterer itself) such an inverse problem is nonlinear. A number of methods have been devised to tackle the nonlinearity, and they cast the inversion as a nonlinear optimization [14], which suffers from local minima (false solutions) and convergence problems. Moreover, the nonlinear inverse methods generally require a high computational burden and accurate knowledge of the background scenario, which impair their applicability in most practical cases. The problem is drastically simplified by adopting approximate scattering models. In particular, for the case of penetrable scatterers, the Born approximation allows for linearization of the problem by approximating $\varphi(\underline{r}, \underline{r}_o, \omega)$ with $\varphi_i(\underline{r}, \underline{r}_o, \omega)$ inside the scatterer [15]. The Born approximation generally poses severe limitations on the class of scatterers (weak targets) when a quantitative reconstruction is required. Fortunately, inversion schemes based on linear models are very suitable to achieve scatterer localization and morphological information (i.e., size and shape) [11]–[13]. Turning to consider (1), under the Born approximation, the scattered field can be expressed as

$$\varphi_s(\underline{r}, \underline{r}_o, \omega) = -k^2 \iiint_D G(\underline{r}, \underline{r}', \omega) \chi(\underline{r}') \varphi_i(\underline{r}', \underline{r}_o, \omega) d\underline{r}'. \quad (2)$$

Note that the electromagnetic properties of the scatterer have been assumed not dependent on the frequency (nondispersive scatterer). This allows the exploitation of data collected at different frequencies but, on the other side, this is not the most general case that occurs. In any case, the scatterer’s frequency dependence can be often considered negligible over the work frequency bandwidth. By making explicit the Green’s function and the incident field in (2) for the free space and for the observation point coinciding with the source position \underline{r}_o , we have

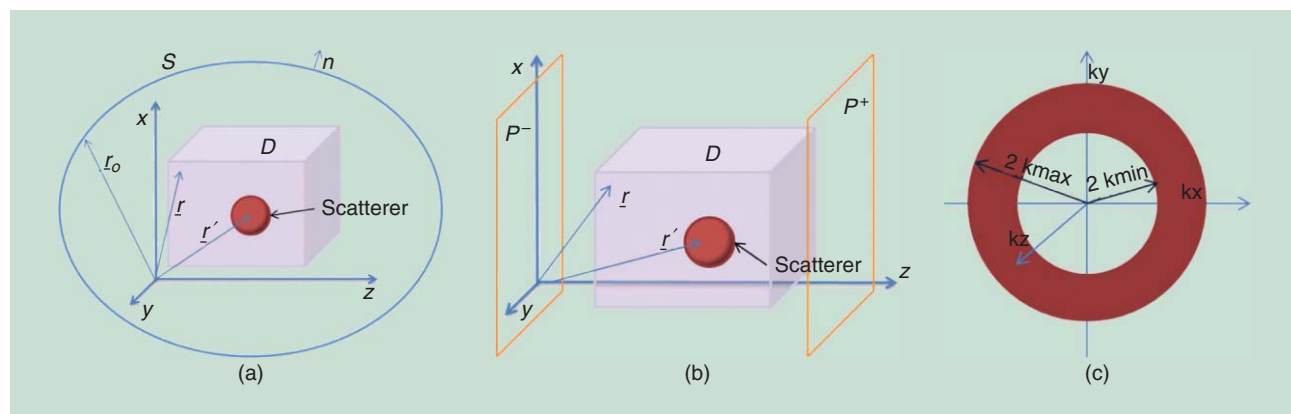


[FIG1] (a) The scattering configuration, (b) aspect limited configuration, and (c) spatial spectral domain.

$$\varphi_s(\underline{r}_o, \omega) = -\frac{k^2 I(\omega)}{4\pi} \iint_D \frac{\exp(-2jk|\underline{r}_o - \underline{r}|)}{4\pi|\underline{r}_o - \underline{r}|^2} \chi(\underline{r}) d\underline{r}, \quad (3)$$

where $I(\omega)$ is the transmitted signal Fourier spectrum. Therefore, $\chi(\underline{r})$ can be retrieved by inverting the linear integral equation (3). The SAR-I based on the inversion of (3) are addressed as the inverse filtering methods.

Under ideal conditions (no noise and sampling effects), the scattering operator in (3) is injective and so, in principle, the contrast reconstruction can be obtained with “unlimited” resolution. However, the scattering operator in (3) is compact [16] and uncertainties are always present. Therefore, to obtain stable reconstructions, a tradeoff between resolution and stability must be always established.

As suggested in [15], starting from (3) and by considering $\tilde{\varphi}_s(\underline{r}_o, \omega) = \partial/\partial k [4\pi\varphi_s(\underline{r}_o, \omega)/jk^2 I(\omega)]$ as data, the following relationship can be established:

$$\begin{aligned} \iint_S \tilde{\varphi}_s(\underline{r}_o, \omega) \frac{\partial}{\partial n} G^*(\underline{r}, \underline{r}_o, \omega) - G^*(\underline{r}, \underline{r}_o, \omega) \frac{\partial}{\partial n} \tilde{\varphi}_s(\underline{r}_o, \omega) dS \\ = 2j \iint_D G_{\text{im}}(\underline{r}, \underline{r}') \omega \chi(\underline{r}') d\underline{r}', \quad (4) \end{aligned}$$

where $G(\underline{r}, \underline{r}_o, \omega)$ and $G_{\text{im}}(\underline{r}_o, \underline{r}, \omega)$, are the Green's function corresponding to real and imaginary parts of the quantity $2k$, respectively; S is a closed measurement surface surrounding D , and $\partial/\partial n$ is the derivative along the outward normal. The obtained equation is the Porter–Bojarski equation, which represents the foundation of generalized holography and establishes in a rigorous way the link between the backpropagated field and the scatterer. It is also interesting to outline that the time-domain version of (4) is equivalent to the widely used time-reversal imaging [17]. Differently from (3), (4) readily permits an estimate of $\chi(\underline{r})$ from the scattered field (and its normal derivative). However, for a finite frequency bandwidth, only a spatial band-limited version of $\chi(\underline{r})$ can be retrieved, with Fourier transform supported over the spherical shell $2k_{\min} \leq \eta \leq 2k_{\max}$, k_{\min} and k_{\max} , being the wavenumbers corresponding the minimum and maximum work frequencies, respectively, and η is the radial coordinate in the Fourier k -space [see Figure 1(c)]. This can be explained by noting that the volume integral in (4) is a spatial convolution whose kernel, $G_{\text{im}}(\underline{r}_o, \underline{r}, \omega)$, at a single frequency has a spatial Fourier transform supported on the Ewald's sphere of radius $2k$. It is interesting to note that the limit on the achievable resolution due to the aforementioned filtering [at variance of what happens while inverting (3)] is intrinsic of the method as no noise, uncertainties, and sampling effects have been considered in its derivation.

It must be stressed that full-view data (i.e., over a closed surface containing the scattering scene) have been considered while deriving (3) and (4). In most practical cases, data can be gathered only over a part of S and often under a reflection mode configuration. Therefore, it is necessary to address how (4) changes for aspect limited configurations. To this end, S can be deformed into two planes so that $S = P_- \cup P_+$ (say P_- and P_+ are orthogonal to the z -axis) and the scattering volume is now

the spatial region enclosed between these planes [see Figure 1(b)]. For a reflection mode configuration, data are collected only over P_- (or P_+). Accordingly, the surface integral in (4) particularizes as

$$\begin{aligned} - \iint_{P_-} 2\tilde{\varphi}_s(\underline{r}_o, \omega) \frac{\partial}{\partial z} G^*(\underline{r}, \underline{r}_o, \omega) dP_- \\ = \iint_{P_+} 2G^*(\underline{r}, \underline{r}_o, \omega) \frac{\partial}{\partial z} \tilde{\varphi}_s(\underline{r}_o, \omega) dP_+. \quad (5) \end{aligned}$$

Some clarifications are in order. First, the surface integration restricted over a plane requires knowing only the field or its normal derivative [15]. Second, it can be shown that it is possible to retrieve only the spatial spectrum of $\chi(\underline{r})$ belonging to the Ewald's sphere part with $k_z \leq 0$. Finally, when the measurement aperture Σ is a subset of P_- , the spatial filtering is even more severe and dictated by the aperture size [18].

SAR-I

In this section, most of the SAR-I approaches are reviewed and reinterpreted under a unified framework provided by (3) and (4).

MIGRATION

In view of the assumed linearity for the scattering phenomenon, the reconstruction performances of the imaging algorithms can be provided by analysing the point spread function (i.e., the reconstruction of a pointlike scatterer). Accordingly, consider a pointlike scatterer located in the object space at $\underline{r} = (x, y, z)$, and denote as \underline{r}_o the observation point belonging to the measurement aperture Σ (a subset of the plane $z = z_o$) and let $i(t)$ be the transmitted signal. The corresponding backscattered field is given by

$$\varphi_s(\underline{r}_o, t) = i\left(t - 2\frac{|\underline{r}_o - \underline{r}|}{c}\right), \quad (6)$$

where amplitude factor due to the propagation spreading has been neglected and $i(t)$ is a short duration pulse or the pulse after range compression has occurred. Actually, due to the finite directivity of the antennas, a point scatterer appears as a diffraction hyperboloid whose apex is located at $(x, y, 2z/c)$. The aim of migration is to compensate such a spreading by refocusing each segment of the hyperbola to its apex.

The first method to accomplish such a task is a graphical method, which dates back to the work of Hogendoorn [19]. Basically, for each measurement point, a semisphere centered on the source-receiver position and of radius equal to the travel-time times half the wave speed is drawn; then, the scatterer's location is identified as the point where all the semispheres intersect. This graphical method is known as *wave interference migration* [20]. A different way to implement the same imaging concept is through the so-called diffraction summation [20]. In this method, the object space is divided in pixels and for each of them a diffraction hyperboloid is constructed in the data space. Then, the reconstruction at each pixel is obtained by summing up contributions where the synthetic hyperboloid intersects data. Formally, the reconstruction is provided by $R(\underline{r})$ (corresponding to the migrated data)

$$R(\underline{r}) = \int_{\Sigma} \int_T \varphi_S(\underline{r}_O, t) \delta\left(t - \frac{2}{c} |\underline{r} - \underline{r}_O|\right) d\Sigma dt, \quad (7)$$

where T is the time interval during which data are collected. After Fourier transforming with respect to the time, (7) can be recast (apart an unessential factor) as

$$R(\underline{r}) = \int_{\Sigma} \int_{\Omega_k} \varphi_S(\underline{r}_O, k) \exp(j2k |\underline{r} - \underline{r}_O|) d\Sigma dk, \quad (8)$$

Ω_k being the frequency band in the k domain. Equation (8) points out the equivalence between the diffraction summation and the range migration technique [9] as well as to the SAR focusing technique [21]. The spatial convolution in (8) can be conveniently computed in the spatial Fourier domain so that

$$R(\underline{r}) = \int_{\Omega_{k_x-k_y}} \int_{\Omega} f(k_x, k_y, k) \varphi_S(k_x, k_y, k) \exp[-j(k_x x + k_y y)] \exp[jk_z(z - z_O)] dk_x dk_y dk, \quad (9)$$

where $\Omega_{k_x-k_y}$ is the selected frequency band in the spatial spectral plane (k_x, k_y) , $k_z = \sqrt{4k^2 - k_x^2 - k_y^2}$; $f(k_x, k_y, k)$ is a slowly varying amplitude factor arising by performing the Fourier transform of the exponential kernel $\exp(j2k\sqrt{x^2 + z^2})$ thanks to the stationary phase method. Finally, (9) can be recast as a 3-D Fourier transform as

$$R(\underline{r}) = \int_{\Omega} \frac{k_z f(k_x, k_y, k_z)}{\sqrt{k_x^2 + k_y^2 + k_z^2}} \varphi_S(k_x, k_y, k_z) \exp[-j(k_x x + k_y y)] \exp[jk_z(z - z_O)] dk_x dk_y dk_z. \quad (10)$$

Equation (10) has the computational advantage that it can be efficiently computed by FFT for each point in the object space but also requires data to be interpolated and resampled according to a rectangular grid in the k space [22]. It can be noted that, unless the amplitude factor, (10) is identical to the SAR-I algorithm presented in [6] and also very similar to the F-K migration as outlined in [5].

A more rigorous derivation follows the wave equation along with to the so-called exploding source model, which holds for both penetrable and nonpenetrable targets. Accordingly, the scattered field is thought as being radiated by a source at time $t = 0$ embedded within a medium characterized by a half the wave speed. Therefore, by accounting for only up-traveling (i.e., toward the measurement aperture) waves and by enforcing the boundary condition over the measurement aperture at $z = z_O$, the field can be backpropagated in the object space as

$$R(\underline{r}) = \int_{\Omega_{k_x-k_y}} \int_{\Omega} \varphi_S(k_x, k_y, \omega) \exp[-j(k_x x + k_y y)] \exp[jk_z(z - z_O)] dk_x dk_y d\omega. \quad (11)$$

This is the so-called F-K migration and (11) can be readily recast in spatial domain as

$$R(\underline{r}) = \int_{\Sigma} \int_{\Omega} \varphi_S(\underline{r}_O, \omega) \frac{\partial}{\partial z} G^*(\underline{r}, \underline{r}_O, \omega) d\Sigma d\omega. \quad (12)$$

Migration in (12) is known as the *Rayleigh–Sommerfeld holography* and its time domain is the well-known Kirchhoff migration [2]. Equation (12) has been obtained by requiring fewer approximations with respect to the previous methods; in fact, the amplitude spreading term has not been ignored and the stationary phase method has not been employed. Therefore, it can be considered as the mathematical rationale supporting the intuitive discussion under which previous migration schemes have been developed. However, (12) suffers of an implicit contradiction: while the field is backpropagated as a solution of a homogeneous wave equation, the exploding source assumes it is being radiated by a localized source. Differently, these issues are completely avoided in (5), and therefore, the Porter–Bojarski equation can be considered as a rigorous mathematical foundation for the migration algorithms. Nonetheless, migration algorithms succeed in the localization of the discontinuities and the estimation of the geometry of the targets, since all previous methods led to a correct phase compensation. This is apparent by comparing the point spread function returned by (12)

$$\text{psf}(\underline{r}, \underline{r}') = \left| \int_{\Sigma} \int_{\Omega} k^2 \frac{\exp(-2jk |\underline{r}_O - \underline{r}'|)}{|\underline{r}_O - \underline{r}'|^2} \frac{\partial}{\partial z} \left[\frac{\exp(2jk |\underline{r} - \underline{r}_O|)}{|\underline{r} - \underline{r}_O|} \right] d\Sigma d\omega \right|, \quad (13)$$

and (5)

$$\text{psf}(\underline{r}, \underline{r}') = \left| \int_{\Sigma} \int_{\Omega} \frac{\exp(-2jk |\underline{r}_O - \underline{r}'|)}{|\underline{r}_O - \underline{r}'|} \frac{\partial}{\partial z} \left[\frac{\exp(2jk |\underline{r} - \underline{r}_O|)}{|\underline{r} - \underline{r}_O|} \right] d\Sigma d\omega \right|. \quad (14)$$

The difference between (13) and (14) resides only in amplitude factors $|\underline{r}_O - \underline{r}'|$, which become relevant only for near zone configuration, and in the k^2 term that basically acts as a high-pass filter [5].

INVERSE FILTERING

Inverse filtering algorithms aim at reconstructing $\chi(\underline{r})$ by solving (2). A simple way to address such a task is to Fourier transform the kernel function [20] and the resulting inversion scheme is referred to as *diffraction tomography*. More generally, the reconstruction problem can be cast as the inversion of the linear scalar operator (2). Rewriting such an equation in operator notation

$$A: \chi \rightarrow \varphi_S, \quad (15)$$

where χ and φ_S are assumed to belong to suitable functional sets possibly according to a priori information about the unknown. To accommodate the effect of uncertainties and noise on data, usually the data space is assumed to be the Hilbert space of square integrable functions. This choice is also quite common for the unknown space, when no a priori information is available. The solution is then stated as

$$\tilde{\chi} = \inf\{\|A\chi - \varphi_S\|^2\}. \quad (16)$$

Since the operator A is compact, (16) cannot have a solution, or if the solution exists it does not depend continuously on data, so the inverse problem is ill posed [16]. The lack of stability of solution can be restored by adopting a regularizing inversion scheme such as the Tikhonov method. This regularization scheme exploits a priori information about the unknown [16] and casts the inversion problem as a constrained optimization problem

$$\tilde{\chi}_\alpha = \inf \{ \|A\chi - \varphi_s\|^2 + \alpha \|B\varphi_s\|^2 \}. \quad (17)$$

Here B is a suitable constraint (smoothing) operator and α is the regularization parameter; a popular choice is $B = I$, which constrains the energy of solution. Important questions are the existence of the solution and its convergence (to the generalized solution) as the regularization parameter and the noise tend to zero. On this topic, there is a large body of literature, and the reader can find an excellent basic review in [16]. It is clear that the key question is the choice of the regularization parameter, which actually establishes the tradeoff between stability and smoothing of the solution. Different methods exist to select the regularization parameter. These methods can explicitly exploit the knowledge of the noise level, as the Morozov discrepancy principle, or not such as the generalized cross validation [16]. Another very popular method is the so-called L-curve, which estimates the regularization parameter in correspondence of the knee exhibited by the trajectory described by the solution in the discrepancy-norm of the solution plane as α varies [23]. However, the Tikhonov method as well as the regularization schemes based on (17) are particular cases of windowing regularization, i.e.,

$$\tilde{\chi}_\alpha = \sum_{n=0}^{\infty} W_{n,\alpha} \frac{\langle \varphi_s, v_n \rangle}{\sigma_n} u_n, \quad (18)$$

where $W_{n,\alpha}$ filtering window and $\{v_n, u_n, \sigma_n\}$ is the singular system of the scattering operator A . In inverse scattering problems, the relevant operator kernel is an analytic function of exponential type (far from its singularities) and this entails, for most situations, that the singular values have a nearly steplike behavior. Accordingly, the choice of $W_{n,\alpha}$ is simplified as it can be set equal to $W_{n,\alpha} = \{1: n \leq N_T, 0: n > N_T\}$, where N_T (the number of degrees of freedom) is the truncation index chosen around the knee exhibited by the singular values [24]. This regularization method is addressed as truncated singular value decomposition (TSVD) [16].

We end this section by making a comparison between the migration and inverse filtering methods. By looking at (8), it can be easily understood that migration basically performs the inversion by resorting to the adjoint of the scattering operator. This allows at obtaining a stable reconstruction, but even in absence of noise there is an intrinsic limitation on achievable resolution.

Finally, in the framework of inverse filtering, a new paradigm based on compressive sampling [25] has gained recent attention. The approach is of relevant interest when the scattering scene is sparse with respect to a suitable representation dictionary (roughly saying, if the target occupies a small fraction of the area to be imaged). In this case, the imaging problem is formulated as in (17), but the regularization term is based on the L_1 norm.

Details on why such a kind of inverse filtering allows obtaining highly resolved reconstructions with sparse set of data is left to the pertinent literature. Here, we just mention the Baraniuk's article [26] where an intuitive geometrical interpretation is provided in terms of the "shape" of the hyperspheres in L_1 . Of course, also for this scheme, the choice of the regularization parameter α is crucial, since it dictates the degree of sparsity at which the scene is reconstructed.

SOME UNCONVENTIONAL APPLICATIONS

Many operational contexts require image scatterers embedded in complex obscuring and multipath environments (see Figure 2) [11]–[13], as in ground penetrating radar (GPR) and TWI surveys. In these cases, the first main difficulty regards the clutter arising from the obscuring medium, which can overwhelm the desired target response, especially for lossy background and/or when targets are close to the air/soil interface or wall. In most cases, using classical preprocessing procedures, such as time-gating and background removal solves the problem. The problem is more challenging when the target response overlaps to the background returns. In this case, more sophisticated methods have to be employed [27].

The second difficulty regards the inaccurate knowledge of the electromagnetic properties of the embedding medium, which leads to defocused and delocalized reconstructions. Accordingly, a large body of research has been dedicated to the estimation of medium properties before/while imaging (e.g., see [27]).

Assuming that previous issues have been solved, we now focus on the reconstruction capabilities of model-based inversion methods, particularly on the inverse filtering and the migration (inversion by using the adjoint of the operator). These imaging approaches are formulated by taking into account the Green's function pertinent to the reference scenario under test. Accordingly, even though inverse filtering generally are computationally more challenging, they provide procedures more flexible and adaptable to a larger class of scenarios. The last consideration also includes measurement set-up where data are taken over a nonplanar aperture and possibly nonuniformly.

The first applicative example concerns the reconstruction of a dielectric target hidden in a dry soil, whose average dielectric permittivity has been estimated to be 4.5, while its electric conductivity has been fixed equal to 1 ms/m. The target is a sphere having diameter 6.5 cm and hidden 7.5 cm below the air–soil interface within a 100 cm \times 70 cm \times 45 cm wood tank; see Figure 3(a). The data have been collected on a 24 cm \times 24 cm square grid with a 4-cm measurement step along both the x and y axis by means of a K2-RIS GPR system (produced by IDS Corporation) equipped with a single polarization 2-GHz antenna. The GPR traces have been gathered in a 16-ns time window. The measured data have been preprocessed by means of the background removal filtering procedure to remove the direct antenna coupling and the backscattered field due to the air–soil interface. Then they have been transformed into the frequency domain and processed by means of Born approximation-based imaging approaches and the adjoint-based inversion procedure. A

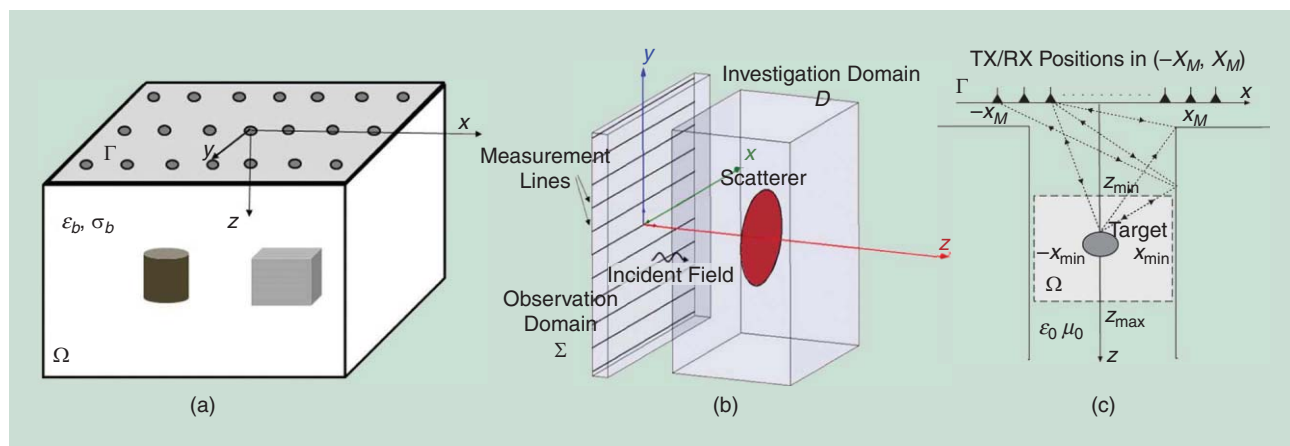


[FIG2] A schematic view for (a) GPR imaging, (b) TWI imaging, and (c) urban street canyon SAR-I.

frequency range [1.1; 1.8] GHz has been selected and evenly sampled with a frequency step of 70 MHz (11 frequencies).

The obtained results are given in Figure 3(b)–(d), which show the constant depth slices of the reconstructed contrast function as normalized to its maximum value. These results have been obtained by assuming a half space as a reference scenario and assess the utility of a full 3-D wave propagation model. In particular, by comparing the results in Figure 3(b)–(d), we can state that the full 3-D Born approximation imaging approach provides cleaner images, from which the target's shape and size can be estimated. Conversely, the migration-based reconstruction of Figure 3(c) is most sensitive to the soil inhomogeneity, and it is affected by several ghosts appearing in the upper part of the investigation domain. Finally, the most common pseudo-3-D algorithm, which produces 3-D images by interpolating 2-D reconstructions, does not allow for an accurate reconstruction of the geometrical features of the target. The results in Figure 3(b) and (d) have been obtained by fixing the TSVD threshold in such a way to filter out all those singular values that are 30 dB below the maximum.

Inverse filtering approaches are suitable also for SAR-I in complex urban environments. In this framework, building walls obscuration and attenuation reduce the ability to detect targets, and most notably the electromagnetic signal propagation undergoes multipath effects. This usually produces artefacts (ghosts) so increasing the number of false alarms. A possible strategy to overcome this last problem is to mitigate multipath returns. In this frame, frequency dependence of scattering properties of target and multipath structure cannot be ignored and a multipath separation requires large operational bandwidth.

However, when the target and the radar are not in the line of sight, the only possibility to retrieve information about its presence is thanks to multipath exploitation. Multipath exploitation is an emerging field of research in the framework of SAR-I for urban sensing applications [12], [28]. The main focus is on the development of multipath models leading to correct and easily interpretable SAR images free from multipath ghosts. Furthermore, as shown in [12] and [28], a correct modeling and exploitation of the multipath provides additional information that may potentially improve imaging performance in terms of resolution limits.

We will discuss a novel and interesting application that helps us to elucidate these concepts [12]. Specifically, we are concerned with the problem of imaging strong scattering targets located in an urban canyon. In particular, we consider the 2-D scenario in Figure 4(a), which, though simple, accounts for all the relevant ingredients to highlight the necessity of a correct model-based approach for imaging targets in a complex multiscattering environment. The scene is probed by a ground-based SAR standing in close proximity of the canyon entrance. Due to the peculiar geometry, at each measurement point the received echo from the target is the superposition of various multipath contributions (e.g., direct path, single reflection path, diffraction path, etc.). It must be stressed that, depending on the system constraints in terms of operating bandwidth and/or aperture size, these multipath returns may be or not well separated in time.

A linear scattering model is applicable under Kirchhoff's approximation; however, as a noncanonical geometry is involved, no closed-form analytical expressions for the Green's function are readily available. A possible answer may be to compute approximate expressions for instance by ray optics models. Alternatively, one must necessarily resort to numerical techniques which are quite flexible and therefore applicable in several contexts. In particular, the finite difference time domain (FDTD) method represents a good candidate.

Some representative results for a perfectly cylindrical target with radius 0.1 m and centered at the point (0, 1.3) m are reported in Figure 4, along with the scattering layout [Figure 4(a)]. A UWB electromagnetic pulse having the shape of a Ricker wavelet with central frequency of 1,600 MHz is radiated by each antenna, whereas the working frequency range is [1, 2] GHz discretized at a 50-MHz step. The SAR array is composed by 11 line sources with a spacing of 0.1 m placed in correspondence of the canyon entrance. The frequency domain scattered field data have been inverted by applying the TSVD inversion scheme with a truncation index selected in such a way to filter out the singular values lower than -20 dB with respect to the maximum one.

As can be seen in Figure 4(b), when the image is obtained by inverting the actual data by means of the free-space Green's function, some artefacts, due to multipath, arise in the image

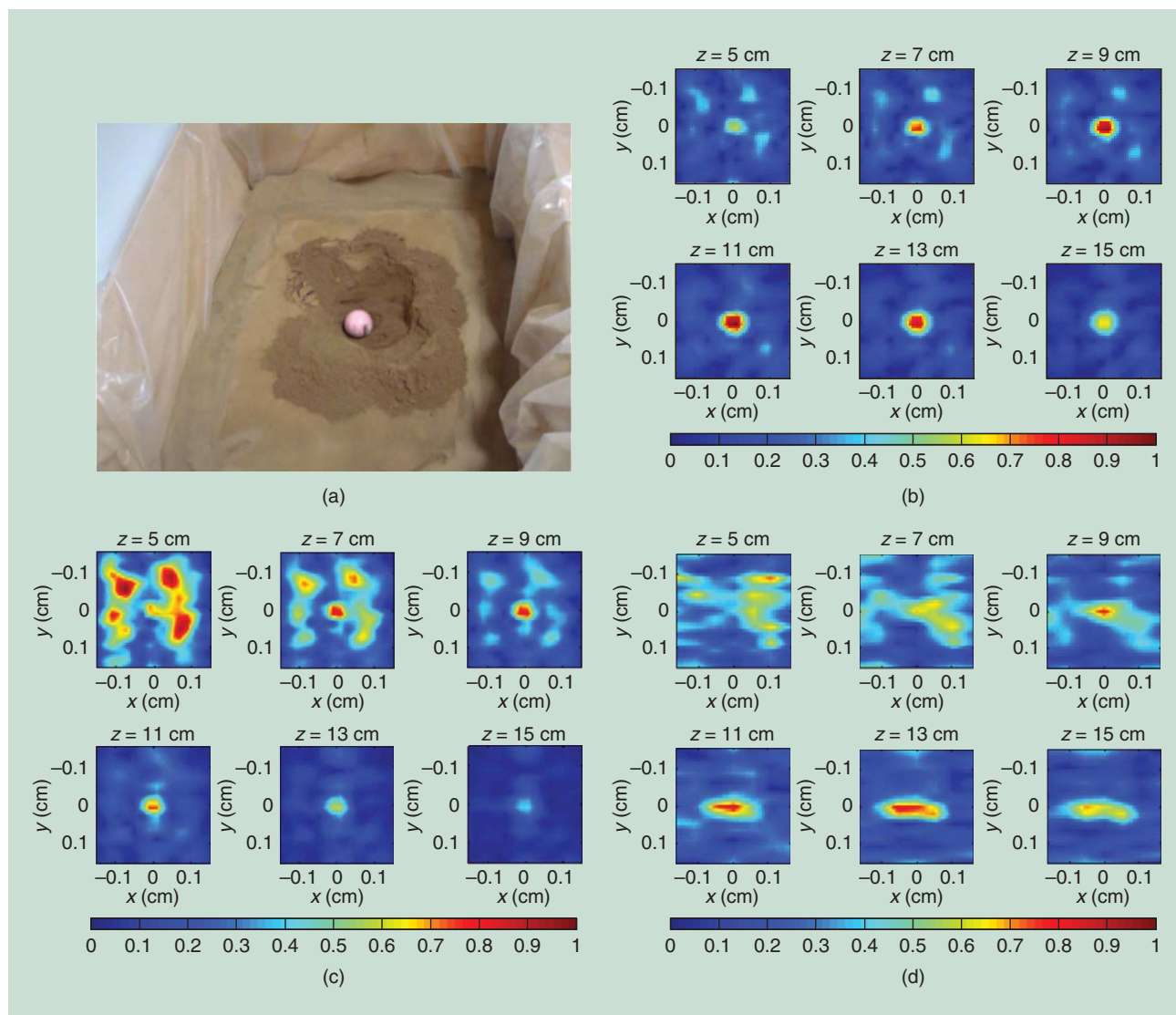


[FIG3] A GPR imaging example. (a) An experimental setup, (b) depth slices of the full 3-D TSVD reconstruction, (c) depth slices of the full 3-D migration (reconstruction by the adjoint of the operator), and (d) depth slices of the pseudo-3-D TSVD reconstruction.

so to impair the localization of the real target. On the other hand, when the correct Green's function (computed by FDTD) is adopted, the true target is well localized and the multipath ghosts are completely suppressed [see Figure 4(c)].

As a term of comparison, we report in Figure 4(d) the tomographic reconstruction achievable with the adjoint inversion and the reconstruction performance are worse compared to the inverse filtering solution. Finally, by comparing the urban canyon reconstruction in Figure 4(c) to that attainable in a free-space scenario [see Figure 4(e)] with the same array configuration, it can be seen that the image relevant to the canyon scenario highlights a larger portion of the upper scatterer's contour. This peculiar feature is a direct consequence of multipath exploitation that, in the specific example, is mainly related to the specular reflections from the building walls. From the physical perspective, this fact can be interpreted by considering that the rays emitted by the source, reflected from the walls and reaching the target can be seen as originated by

“virtual sources” falling outside the array. In other words, the target is “viewed” under a wider angle. As a result, once taken into account in the forward model, the multipath improves the image resolution in crossrange. Further details on the resolution enhancement due to multipath exploitation can be found in [12].

Finally, as further examples of unconventional measurement configurations, significant attention has been recently devoted to the development of hardware and data processing solutions for the multistatic SAR-I both for satellite imaging [29] and in [30] for high-resolution imaging for short-range applications.

CONCLUDING DISCUSSION

In this article, a quick overview of several SAR-I algorithms has been presented. The discussion mainly focused on establishing the rigorous mathematical framework upon which such imaging algorithms are founded. It has been shown that SAR-I algorithms can be classified in inverse filtering and migration methods. The

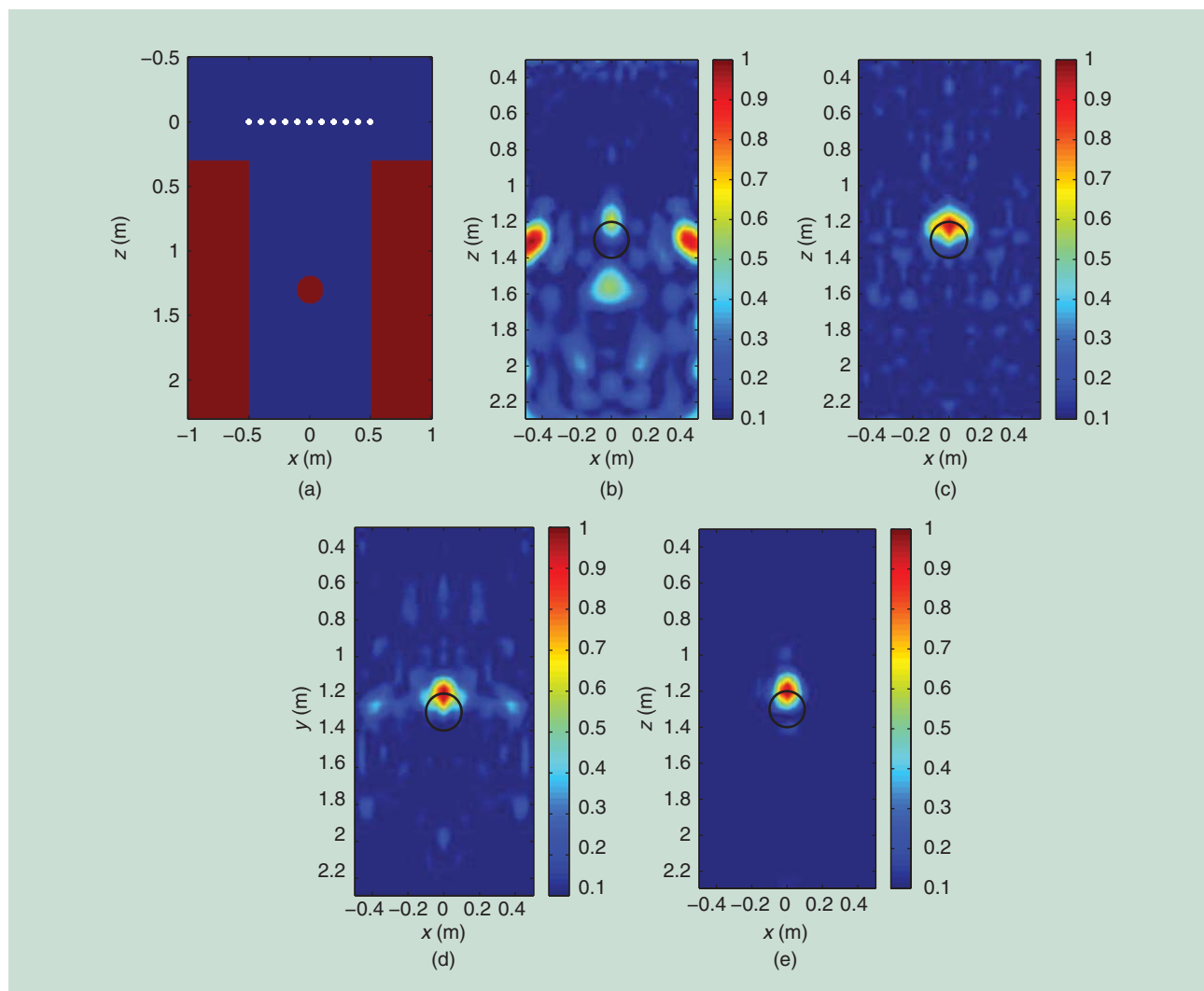


[FIG4] Urban canyon SAR imaging: (a) scattering layout, (b) reconstruction with TSVD and free-space Green's function, (c) reconstruction with TSVD and urban canyon Green's function, (d) reconstruction with adjoint inversion and urban canyon Green's function, and (e) reconstruction with TSVD obtained with the same array configuration in a free-space scenario.

first are methods that achieve imaging by inverting the linearized scattering operator. Migration, instead, basically achieves imaging by compensating the scattering phase by properly adopting a spatially varying filter. Interestingly, it has been shown that the generalized holography coming from the Porter–Bojarski equation is the more rigorous migration scheme. In fact, the generalized holography provides an explicit relationship between the migrated field and the target and does not rely on the homogeneous wave equation and the exploding source model. Nonetheless, all migration schemes provide similar results because they compensate the scattering phase in the same way.

A comparison between migration and inverse filtering has been briefly addressed as well. Basically, as migration performs the inversion by approximating the inverse operator by the adjoint of the scattering operator, the achievable resolution is intrinsically limited. However, the inverse scattering problem is ill posed and noise and uncertainties are always present.

As shown by representative examples based on synthetic and experimental data, migration generally provides worse imaging performance compared to the inverse filtering; however, inverse filtering is usually more computationally demanding.

AUTHORS

Raffaele Solimene (raffaele.solimene@unina2.it) received the laurea degree (summa cum laude) in 1999 and the Ph.D. degree in 2003 in electronic engineering, both from the Seconda Università di Napoli (SUN), Aversa, Italy. In 2002, he became an assistant professor at the Faculty of Engineering of the University Mediterranea of Reggio Calabria, Italy. Since 2006, he has been with the Dipartimento di Ingegneria Industriale e dell'Informazione at SUN. His research activities focus on nondestructive subsurface investigations, through-the-wall imaging, and breast cancer detection. On these topics, he coauthored more than 150 scientific works.

Ilaria Catapano (catapano.i@irea.cnr.it) is a level-three research scientist at the Institute for Electromagnetic Sensing of the Environment, National Research Council of Italy (IREA-CNR). She received the Ph.D. degree in electric and information engineering from the University of Cassino, Italy, in 2006. In 2003, she started her research activity at IREA-CNR. Her scientific interest mainly concerns noninvasive electromagnetic diagnostics, the development and performance assessment of microwave imaging approaches, and subsurface radar systems. She received the 2004 G. Barzilai Award by the Italian Electromagnetic Society, was one of the Young Scientist Awardees at the 2008 XXIX Union Radio-Scientifique Internationale General Assembly, served as an adjunct professor at the Mediterranean University, Reggio Calabria, Italy (2010), and was an invited lecturer at São Paulo University, Brazil (2013).

Gianluca Gennarelli (gennarelli.g@irea.cnr.it) received the M.S. degree (summa cum laude) in electronic engineering and the Ph.D. degree in information engineering from the University of Salerno, Italy, in 2006 and 2010, respectively. He held a postdoctoral fellowship at the University of Salerno from April 2010 to December 2011. Since January 2012, he has been a research fellow with IREA-CNR, Napoli, Italy. His interests cover theoretical and applied electromagnetic research topics such as microwave sensors, electromagnetic inverse scattering problems for nondestructive subsurface investigations, through-the-wall imaging, diffraction problems, near-field far-field transformation techniques, and electromagnetic simulation.

Antonio Cuccaro (antonio.cuccaro@unina2.it) received the laurea degree (summa cum laude) in electronic engineering from the Seconda Università di Napoli, Aversa (SUN), Italy, in 2012. Since then he joined the research group in applied electromagnetic fields of SUN as a Ph.D. student in electronic engineer. His main fields of interest are through-the-wall imaging applications and biomedical imaging.

Angela Dell'Aversano (angela.dellaversano@unina2.it) received the laurea degree (summa cum laude) in electronic engineering from the Seconda Università di Napoli (SUN), Aversa, Italy, in 2012. Since then she joined the SUN research group in applied electromagnetic fields as a Ph.D. student in electronic engineering, and she is currently working on her Ph.D. thesis. Her main research interests include inverse scattering problems and microwave imaging.

Francesco Soldovieri (soldovieri.f@irea.cnr.it) received the Ph.D. degree in electronic engineering from the University of Naples "Federico II," Naples, Italy, in 1996. Since 2006, he has been a senior researcher at IREA-CNR. He was the general chair of the 2007 International Workshop on Advanced Ground Penetrating Radar (GPR) and cochair of the 2010 International Conference on GPR. He is an associate editor of *IEEE Geoscience and Remote Sensing Letters*. He was awarded the 1999 Honorable Mention for the H.A. Wheeler Applications Prize Paper Award of the IEEE Antennas and Propagation Society. His main scientific interests include electromagnetic diagnostics, inverse scattering, GPR applications, antenna diagnostics and characterization, and security applications. He is a Member of the IEEE.

REFERENCES

- [1] D. C. Munson and R. L. Visentin, "A signal processing view of strip-mapping synthetic aperture radar," *IEEE Trans. Acoust., Speech, Signal Process.*, vol. 37, no. 12, pp. 2131–2147, 1989.
- [2] W. A. Schneider, "Integral formulation for migration in two and three dimensions," *Geophysics*, vol. 43, no. 1, pp. 49–76, 1978.
- [3] J. van der Kruk, "Three-dimensional imaging of multicomponent ground-penetrating radar data" Ph.D. dissertation, Dept. Appl. Earth Sci., Delft Univ. Technology, The Netherlands, 2001.
- [4] C. Cafforio, C. Prati, and F. Rocca, "SAR data focusing using seismic migration techniques," *IEEE Trans. Aerosp. Electron. Syst.*, vol. 27, no. 2, pp. 194–207, 1991.
- [5] G. Gilmore, I. Jeffrey, and J. Lo Vetri, "Derivation and comparison of SAR and frequency-wavenumber migration within a common inverse scalar wave problem formulation," *IEEE Trans. Geosci. Remote Sensing*, vol. 44, no. 16, pp. 1454–1461, 2006.
- [6] M. Soumekh, *Synthetic Aperture Radar Signal Processing with MATLAB Algorithms*. New York: Wiley, 1999.
- [7] R. Bamler, "A comparison of range-Doppler and wavenumber domain SAR focusing algorithms," *IEEE Trans. Geosci. Remote Sensing*, vol. 30, no. 4, pp. 706–713, 1992.
- [8] G. Fornaro, F. Lombardini, and F. Serafino, "Three-dimensional multipass SAR focusing: Experiments with long-term spaceborne data," *IEEE Trans. Geosci. Remote Sensing*, vol. 43, no. 4, pp. 702–714, 2005.
- [9] J. M. Lopez-Sanchez and J. Fortuny-Guasch, "3-D radar imaging using range migration techniques," *IEEE Trans. Antennas Propag.*, vol. 48, no. 5, pp. 728–737, 2000.
- [10] R. P. Porter and A. J. Devaney, "Holography and the inverse source problem," *J. Opt. Soc. Am.*, vol. 72, no. 3, pp. 327–330, 1982.
- [11] M. G. Amin, *Through-the-Wall Radar Imaging*. Boca Raton, FL: CRC Press, 2011.
- [12] G. Gennarelli, and F. Soldovieri, "A linear inverse scattering algorithm for radar imaging in multipath environments," *IEEE Geosci. Remote Sensing Lett.*, vol. 10, no. 5, pp. 1085–1089, 2013.
- [13] L. Lo Monte, D. Erricolo, F. Soldovieri, and M. C. Wicks, "Radio frequency tomography for tunnel detection," *IEEE Trans. Geosci. Remote Sensing*, vol. 48, no. 3, pp. 1128–1137, 2010.
- [14] W. C. Chew, *Waves and Fields in Inhomogeneous Media*. Piscataway, NJ: IEEE, 1995.
- [15] K. J. Langenberg, "Applied inverse problems for acoustic, electromagnetic and elastic wave scattering," in *Basic Methods for Tomography and Inverse Problems*, P. C. Sabatier, Ed. Bristol: Hilger, 1987, pp. 127–467.
- [16] M. Bertero, "Linear inverse and ill-posed problems," *Adv. Electron. Electron. Phys.*, vol. 45, pp. 1–120, 1989.
- [17] D. Cassereau and M. Fink, "Time-reversal of ultrasonic fields—Part III: Theory of the closed time-reversal cavity," *IEEE Trans. Ultrason. Ferroelectr., Freq. Control*, vol. 39, no. 5, pp. 579–592, 1992.
- [18] V. T. Vu, T. K. Sjogren, M. I. Pettersson, and H. Hellesten, "An impulse response function for evaluation of UWB SAR imaging," *IEEE Trans. Signal Processing*, vol. 58, no. 7, pp. 3927–3932, 2010.
- [19] J. G. Hagedoorn, "A process of seismic reflection interpretation," *Geophys. Prosp.*, vol. 2, no. 2, pp. 85–127, 1954.
- [20] J. Gazdag and P. Sguzzer, "Migration of seismic data," *Proc. IEEE*, vol. 72, no. 10, pp. 1302–1315, 1984.
- [21] R. Markelein, K. Mayer, R. Hannemann, T. Krylow, K. Balasubramanian, K. J. Langenberg, and V. Schmitz, "Linear and nonlinear algorithms applied in non-destructive evaluation," *Inv. Probl.*, vol. 18, pp. 1733–1757, Nov. 2002.
- [22] R. H. Stolt, "Migration by Fourier transform," *Geophysics*, vol. 43, no. 1, pp. 23–48, 1978.
- [23] P. C. Hansen, J. Nagy, and D. P. O'Leary, *Deblurring Images: Matrices, Spectra and Filtering*. New York: SIAM, 2008.
- [24] R. Solimene, M. Maisto, and R. Pierri, "Role of diversity on the singular values of linear scattering operators: The case of strip objects," *J. Opt. Soc. Am. A*, vol. 30, no. 11, pp. 2266–2272, 2013.
- [25] D. L. Donoho, "Compressed sensing," *IEEE Trans. Inform. Theory*, vol. 52, no. 4, pp. 1289–1306, 2006.
- [26] R. G. Baraniuk, "Compressive sensing [Lecture Notes]," *IEEE Signal Processing Mag.*, vol. 24, no. 4, pp. 118–121, 2007.
- [27] H. Jol, *Ground Penetrating Radar Theory and Applications*, 1st ed. Amsterdam, The Netherlands: Elsevier Science, 2008.
- [28] P. Setlur, M. Amin, and F. Ahmad, "Multipath model and exploitation in through-the-wall and urban radar sensing," *IEEE Trans. Geosci. Remote Sensing*, vol. 49, no. 10, pp. 4021–4034, 2011.
- [29] D. Cerutti-Maori and J. Ender, "Performance analysis of multistatic configurations for spaceborne GMTI based on the auxiliary beam approach," *IEE Proc. Radar, Sonar Navigat.*, no. 2, pp. 96–103, 2006.
- [30] X. Zhuge, A. G. Yarovoy, T. Savelyev, and L. Ligthart, "Modified Kirchhoff migration for UWB MIMO array-based radar imaging," *IEEE Trans. Geosci. Remote Sensing*, vol. 48, no. 6, pp. 2692–2703, 2010.



Robert Kedzierawski, Jean-Marc Le Caillec, and Witold Czarnecki

The Time-Reversal Technique for SAR Focusing of Buried Targets

[Theoretical improvements and practical limitations]

This tutorial-style article presents the novel concept of time-reversal-based airborne ground penetrating radar (TR-AGPR) and its application for soil imaging and gives a brief description of the time-reversal

synthetic aperture radar SAR (TR-SAR) focusing algorithm. The intent of this article is to answer the question as to whether the time-reversal-based algorithm is a feasible technique for SAR focusing of a buried target (structure).

INTRODUCTION

Synthetic aperture radar (SAR) [1], [2] is one of the most important engineering inventions of the last century. High-resolution images are commonly used over a wide range of applications. With a varied number of modes and purposes, the SAR system provides comprehensive imaging capabilities in microwave frequency range at different altitudes (airborne or spaceborne systems), on a large scale (depending on the footprint size), and in different frequency bands. Furthermore, electromagnetic (EM) waves have the ability to penetrate into the soil, be scattered on its inhomogeneities, and travel toward the initial source location in the form of backscattered waves. On the other hand, a radar system designed for nondestructive subsurface soil imaging,

referred to as *ground penetrating radar (GPR)* [3], more often uses the SAR technique for high-resolution imaging of the sub-surface soil structure. A GPR system mostly operates as

an ultra-wideband (UWB) [4] system in a low-frequency range [very high frequency (VHF)/ultrahigh frequency (UHF), and P-band and L-band of frequency] and has a limited

area of imaging, thus significantly reducing the ability to image complex and vast buried structures to local-scale applications. The area of the GPR imaging process depends on three factors: 1) the width of footprint over the surface (antenna pattern, height, and incident angle), 2) the effective penetration depth of soil, and 3) the antenna displacement.

SAR and GPR imaging processes exhibit similarities. For instance, both imaging processes have a common feature, i.e., they are formed as a result of antenna movement above the surface at a constant height. Although having many differences, similarities between the two imaging processes led to the idea that it is possible to model and develop a concept of airborne GPR (AGPR), i.e., a radar system combining the advantages and essential features of the two well-known SAR/GPR techniques and operating over a large scale.

Some early attempts at this concept have been already performed in the Shuttle Imaging Radar-B mission: for instance, with the shuttle over a desert [5], [6] or glacier [7]. Due to natural environmental conditions, the structures of a desert and

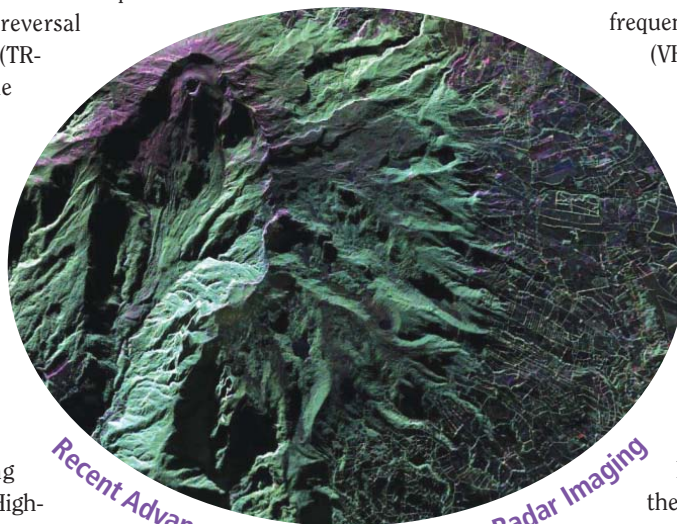


PHOTO COURTESY OF NASA

Digital Object Identifier 10.1109/MSP.2014.2311165

Date of publication: 13 June 2014

glacier are strongly similar to a homogeneous structure (dry sand or ice) with almost constant EM parameters in the observed area. Hence, the propagation medium can be approximated as two homogeneous half-spaces, i.e., free space and a material medium. A similar homogeneous approach of the soil structure, with constant values of permittivity ϵ and conductivity σ , was used in discussions, analysis, and numerical simulations [8]–[10]. Unfortunately, such a homogeneous approximation of the soil structure does not correspond to the vast majority of lands, which are a mixture of different soil types, arranged in horizontal-layered structures with varied texture and parameters inside a single layer. Due to the inhomogeneous nature of the soil, the backscattered signal derived from multireflections of the EM waveform transmitted through the soil is disrupted by dispersion and loss effects. This leads to energy dissipation and pulse distortion strongly affecting the output of the matched filtering and significantly degrading the spatial resolution. Detailed analysis of the low-frequency SAR focusing problems was carried out in [11]. The most important problem is the strong defocusing of the backscattered signal in range (depth) dimension, which does not allow one to fully benefit from the SAR processing. The primary step to take advantage of the SAR processing should be the neutralization (or compression) of the defocusing effects in depth dimension. On the other hand, the time-reversal (TR) [12]–[15] technique is used to exploit multipath propagation in rich scattering media and to provide significant detection gain. For instance, experiments in the microwave frequency range 4–6 GHz with single antenna were described and performed in [15]. Overall, the TR is incorporated with the wide range of remote sensing applications to improve their imaging and detection efficiency [16]. Its applications in the SAR were described, e.g. for target focusing and removing ghost images [17], [18], as well as for change detection [19]. Furthermore, the TR were used for beamforming imaging [20] and source localization in changing media [21]. In addition, the TR were applied in the GPR for the focusing algorithm [22] and for TR-based range estimation [23].

The expansion of the functionality of the side-looking airborne radar (SLAR) with a new method of scanning along a modern signal focusing algorithm, based on the TR approach, may result in novel and uncommon capabilities for high-resolution imaging of soil structure over a large scale and in many areas. A validation of the TR focusing algorithm would provide new broad-area imaging capabilities that would be usable in many fields, such as soil-resource mapping, environmental protection, and military surveillance and recognition. Before focusing on a general TR-AGPR concept, the modeling of the soil texture and the EM parameters are introduced to fully understand the complex nature of soil as a material medium, and TR principles are presented.

SOIL MODELING

PHYSICAL MODEL

In general, modeling of the EM parameter of the soil is limited to estimating the permittivity ϵ and the conductivity σ . The permeability μ is assumed to be free space. Estimation of the

relative complex dielectric constant ϵ_r is performed by a pedotransfer function [24], [25] based on the soil texture and moisture profile. In [26], it is shown that the geological database is a valuable source of information about the soil texture, its inhomogeneous and layered nature.

The soil typological unit (STU), from the geological database Soil Profile Analytical Database For Europe (SPADE)/2, contains averaged information about soil texture of the selected volume of ground, is organized as a column vector defined in depth dimension, and presents information, e.g., about the percentage of clay c_t , percentage of silt s_t , percentage of sand s_d , and bulk density ρ_b . Relative amounts of clay, silt, and sand determine the soil class. The fundamental method for classifying the soil types has been illustrated by the U.S. Department of Agriculture in the form of triangle, based on the relationships between percentages of different sizes of particles. The 12 classes of unequal areas are distinguishable, ranging from homogeneous (sand, silt, clay) to highly mixed (loam) [25].

The theory of pedotransfer function assumes the estimation of the immeasurable (or difficulty measurable) parameters from one or more measurable ones, i.e., estimation of ϵ_r based on soil texture (c_t, s_t, s_d, ρ_b) and soil moisture profile m_v . The ϵ_r of soil mixture can be expressed as

$$\epsilon_r = \epsilon'_r - j\epsilon''_r, \quad (1)$$

where the real part ϵ'_r is the dielectric constant of an equivalent lossless material, and the imaginary part ϵ''_r is the dielectric loss factor. Using the pedotransfer function proposed in [24], the real and imaginary part of (1) can be expressed as

$$\epsilon'_r = 1.15 \left[1 + \frac{\rho_b}{\rho_s} (\epsilon_s^\alpha - 1) + m_v^{\beta'} \epsilon'_{\omega} - m_v \right]^{\frac{1}{\alpha}} - 0.68, \quad (2)$$

$$\epsilon''_r = [m_v^{\beta''} \epsilon''_{\omega}]^{\frac{1}{\alpha}}, \quad (3)$$

respectively. Variables in (2) and (3) mean m_v is soil moisture profile; ρ_b is bulk density of soil mixture; $\rho_s = 2.66 \text{ g/cm}^3$ is characteristic bulk density of soil mixture; ϵ_s is the dielectric constant of the soil solids and is given by $\epsilon_s = (1.01 + 0.44\rho_s)^2 - 0.062$; $\alpha = 0.65$ is the empirical coefficient; β' and β'' are empirical coefficients dependent on soil texture (i.e., c_t and s_d); and ϵ'_{ω} and ϵ''_{ω} are mainly frequency-dependent parameters, and less texture-and-moisture dependent [24]–[26]. The frequency dependence of ϵ_r is one of the most important issues for UWB signals. According to (2) and (3), the soil mixture shows a dispersion nature and variations of both parts of ϵ_r are not monotonic [26]. Moreover, (2) and (3) indicate a strong dependence of permittivity from the soil moisture profile m_v . Referring to [26], the permittivity changes can be described as a process whose amplitude is similar to the soil moisture profile m_v and is modulated by the soil texture, implying the influence of s_d and c_t into β' and β'' [see [26, eqs. (13) and (14)]. Figure 1 shows an example of geological and EM modeling of the soil layered structure based on data from SPADE/2 and the pedotransfer function. Originally, soil typological unit (STU)

HU360084 was composed of three classes of soil (horizons), starting from the top:

- sandy clay loam (0, -0.96) m
- sand (-0.96, -1.38) m
- sandy clay (-1.38, -2.5) m.

Other classes of soil were artificially added in this STU profile to get more complex geological structures. Figure 1(a) presents the soil's geological structure estimated on the basis of STU HU360084 to a depth of $Z_N = 2.5$ m; the thickness of the each planar layer L_n equals $d_n = 5$ mm. Thus, it results in structure of $N = 500$ layers each with different geological structures and a planar interface between consecutive layers (L_n, L_{n+1}). In realistic conditions, several man-made objects (or structures) can be buried at different depths, locations, and inclinations to the surface, e.g., pipelines, underground storage tanks, cables, rocks, archaeological remains,

mines, unexploded ordinances, and others. For the sake of simplicity, a bare and flat soil surface is assumed, thus avoiding taking into account the surface shape (roughness) and vegetation in the back-scattered signal simulation.

Referring to the modeling process presented in [26], the equivalent absolute value of the $|\epsilon_r|$ is presented in Figure 1(b), for single frequency $f = 480$ MHz. Although three main horizons of soil geological texture [see Figure 1(a)], due to the nonmonotonic changes of the moisture profile m_v , the volume of $|\epsilon_r|$ presented on Figure 1(b) consists of four ranges of similar dielectric constant values, from the top:

- (0, -0.96) m
- (-0.96, -1.38) m
- (-1.38, -1.59) m
- (-1.59, -2.5) m.

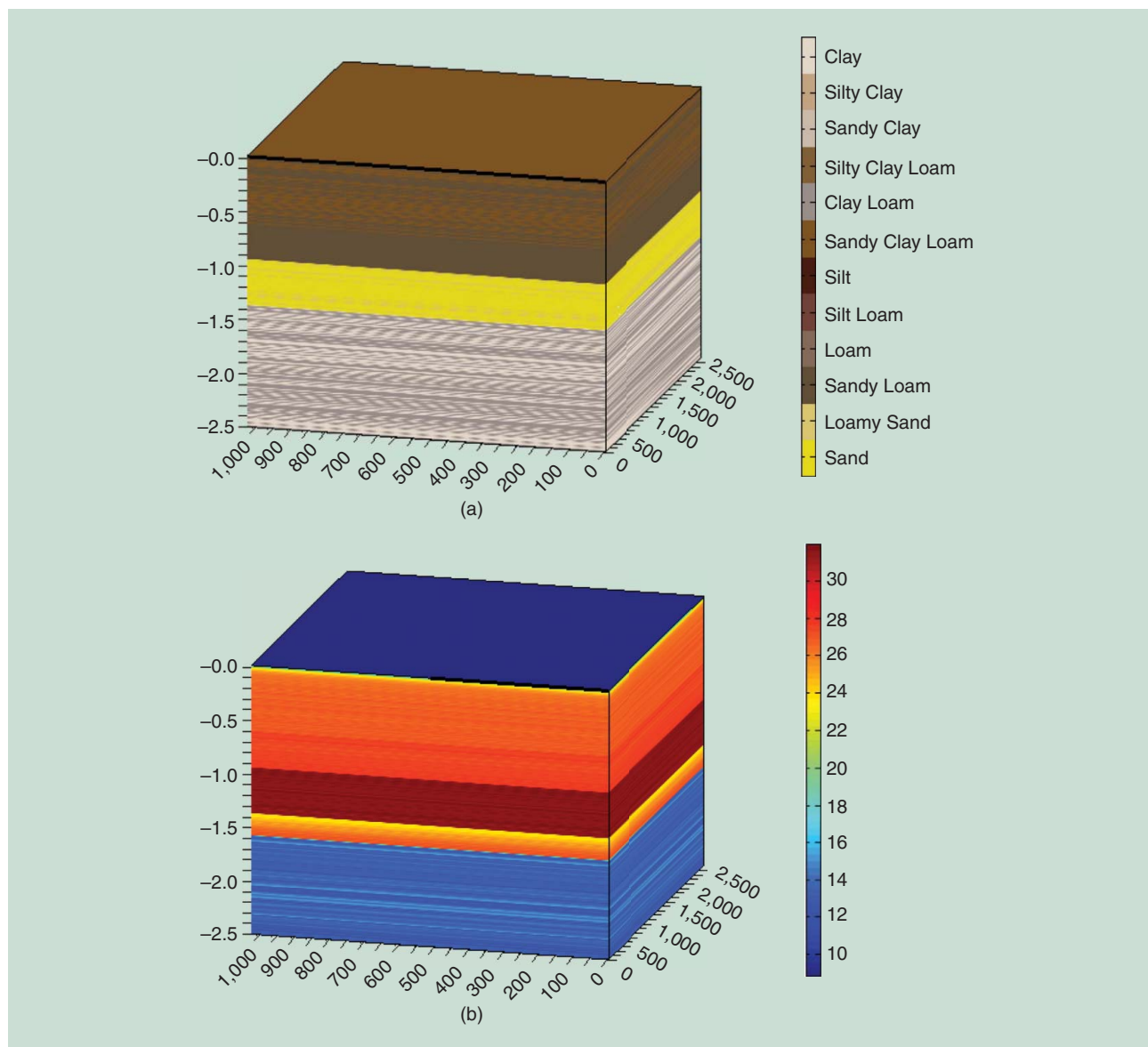


[FIG1] An example of a horizontal-layered soil structure: (a) geological and (b) relevant absolute value of complex relative dielectric constant $|\epsilon_r|$.

Inner range values differ slightly, the largest differences of the $|\varepsilon_r|$ occur at the interfaces between ranges, due to the water exchange processes. Various hydrological properties of the individual soil layers cause the nonmonotonic progress of water percolation into and evaporation from soil structure. A complex nature of the m_v (with respect to its shape and variation over time and spatial coordinates) forces to it numerical calculation [11], [26], for instance, based on the Richards' equations [27] and the soil hydraulic parameters [25].

BACKSCATTERED SIGNAL

Theoretically, in a rich scattering medium, the target response of a point scatterer consists of a direct amplitude-scaled echo and multipath echoes from the surrounding scatterers. On the other hand, the target response $s_r(t)$ in an AGPR consists of a strong backscattered echo derived from surface reflection and a weak cumulative echo from soil structure. The strong backscattered echo comes from the boundary between the sensor half-space and soil half-space. Furthermore, the weak echo from soil structure contains direct amplitude-scaled and distorted echo from point scatterers, and superposition of every indirect multipath reflections from the point scatterers and an infinite number of multipath reflections from soil inhomogeneities. Therefore, the target response $s_r(t)$ can be generally expressed as

$$s_r(t) = \underbrace{\sigma_r s_t(t - \tau_d)}_{\text{surface reflection}} + \underbrace{\sum_{i=1}^{\infty} h_i(t) * s_t(t - \tau_d - t_i)}_{\text{internal multireflections}}, \quad (4)$$

where σ_r is surface reflection coefficient, $s_t(t)$ is transmitted radar signal, τ_d is the two-way time delay between radar and surface, $h_i(t)$ is impulse response of i th propagation path inside the soil, t_i is propagation time of i th path, and $*$ denotes time convolution. The first term in (4), representing surface reflection, strongly disturbs a weak cumulative echo derived from internal multireflections in the soil structure and should be processed as clutter. Furthermore, even a slight difference of EM parameters (e.g., ε_r) between two consecutive layers (l_n, l_{n+1}) causes energy reflection proportionally to the reflection coefficient [3]. Permittivity $\varepsilon_{r,n}$ affects the propagation time through the layer l_n , thus in consequence, the change of $\varepsilon_{r,n}$ affects the propagation time t_i of the i th path (passing by the layer l_n). Considering the downward and upward traveling of the UWB pulse only through a small number of dispersive layers L in the structure presented in Figure 1(b), where $L \ll N$, with N of considered layers (see the section "Physical Model"), the backscattered pulse distortion becomes nonnegligible. In addition, L decreases when the bandwidth of UWB pulse increases.

The main task of source separation methods is the extraction of weak cumulative echoes occurring on the strong surface reflection background. This operation is similar to the ground reflection removal (GRR) used in the GPR imaging process and is aimed at the separation of strong terrain returns, which dominate in backscattered signal and shade weak echoes from the entire soil structure and not only from the upper shallow layers. In conventional GPR, the separation of surface reflection is

performed, for example, by the blind source separation [28], compressive sensing [29], or the simple averaging-and-subtraction methods. The perpendicular location of the antenna directly above the ground surface reduces the footprint and allows one to process ground returns as point reflection assigned only to antenna coordinates, which simplifies processing. Unfortunately, there are a number of theoretical and practical issues related with the use of source separation methods in AGPR. First, the use of an airborne platform considerably increases the level of the ground returns caused by a significant expansion of the observed surface (a broader footprint on the surface in comparison to the vehicle-mounted GPR). Second, a nonperpendicular observation angle results in the spread of ground returns across time in the range from near slant range R_{sn} to far slant range R_{sf} . Therefore, a weak cumulative echo from soil structure derived from the slant range $R_{s,r}$ occurs on the background of the superposition of every ground return within the footprint. Additionally, the incident angle affects both the level of ground returns and the backscattered echo from buried targets, similarly as in conventional GPR. The complexity of source separation issues is only briefly highlighted in this article, however, the investigation of source separation techniques and their applicability is outside the scope of this article and will be addressed in future works.

TIME-REVERSAL

HYPOTHESIS

The TR technique [12]–[16] exploits the reversibility (reciprocity) of the propagation medium, which means that a field and its time symmetric form can both propagate in this medium. Using the TR operator $\mathcal{T}[\]$ [14], the "reversible" form of four vectorial fields describing EM waves \vec{E} , \vec{H} , \vec{D} , and \vec{B} are expressed as follows:

$$\begin{aligned} \mathcal{T}[\vec{E}(\vec{r}, t)] &= \vec{E}(\vec{r}, -t), & \mathcal{T}[\vec{D}(\vec{r}, t)] &= \vec{D}(\vec{r}, -t), \\ \mathcal{T}[\vec{H}(\vec{r}, t)] &= -\vec{H}(\vec{r}, -t), & \mathcal{T}[\vec{B}(\vec{r}, t)] &= -\vec{B}(\vec{r}, -t). \end{aligned} \quad (5)$$

The TR invariance of the following wave equation in nondispersive and lossless media

$$\nabla^2 \vec{E}(\vec{r}, t) - \mu(\vec{r}) \varepsilon(\vec{r}) \frac{\partial^2}{\partial t^2} \vec{E}(\vec{r}, t) = 0 \quad (6)$$

indicates that vector electric field $\vec{E}(\vec{r}, t)$ and its time-reversed version $\mathcal{T}[\vec{E}(\vec{r}, t)]$ are solutions of the same wave equation (6). However, loss and dispersive media are naturally present in the environment, e.g., a soil mixture with all its natural belongings and man-made objects. The basic idea of the TR is to re-emit the received pulse to alleviate these loss effects. A nonzero value of the conductivity $\sigma(\vec{r})$ and dependence of medium permittivity from frequency $\varepsilon(\vec{r}, \omega) = \mathcal{F}^{-1}[\varepsilon(\vec{r}, \omega)]$ leads to the wave equation

$$\nabla^2 \vec{E}(\vec{r}, t) - \mu(\vec{r}) \frac{\partial^2}{\partial t^2} (\varepsilon(\vec{r}, t) * \vec{E}(\vec{r}, t)) - \mu(\vec{r}) \sigma(\vec{r}) \frac{\partial}{\partial t} \vec{E}(\vec{r}, t) = 0. \quad (7)$$

The comparison of (6) and (7) shows the presence of the additional term with first derivation of the $\vec{E}(\vec{r}, t)$ in our case. Thus, the conventional TR operator cannot be directly applied into

loss media. In addition, the attenuation in dispersive media affecting each frequency component of $\bar{E}(\vec{r}, t)$ depends on the medium properties, for instance, the conductivity [compare (6) and (7)]. Without taking theoretical considerations into account [30], we describe the influence of dispersion and irregular attenuation on the (ultra-)wideband signal, e.g., on the common radar linear frequency modulated (LFM) pulse.

■ *Dispersion:* In a dispersive medium, each wave component has a different phase velocity. Depending on the dispersion characteristic of the medium, when higher frequency components travel faster than the lower frequency components, then the duration time of up-chirp decreases while for down-chirp it increases, and reversely. Thus, the LFM pulse (whether up- or down-chirp) traveling through the dispersive medium does not maintain a constant value. Therefore, the once-changed shape can be retrieved with a fairly high accuracy after retransmission through the same medium but with reversed internal frequency changes (down- or up-chirp).

■ *Irregular attenuation:* The frequency-dependent attenuation separately affects the amplitude of each frequency component of the LFM pulse. Depending on the attenuation properties of the medium, the amplitude of the LFM characteristic spectrum can change to any other shape. The attenuation characteristic in the frequency domain can be obtained based on the comparison between the initial spectrum and the attenuated signal spectrum. Nevertheless, a priori knowledge about attenuation properties (for instance, based on the physical soil model, as shown in the section “Soil Modeling”) can be used to selectively amplify the attenuated frequency components to reach the desired shape. Thus, based on the attenuation characteristics obtained in a first transmission with initial LFM pulse, in retransmission each frequency component can be selectively overamplified to ensure the shape of the reattenuated spectrum similar to the characteristic spectrum of the LFM pulse.

Taking both effects into account, it can be assumed that the mirrored (time-reversed) retransmission of the once irregularly attenuated and dispersed signal through the same medium, with selective amplification of each frequency components, allows restoration of the initial pulse with very high precision. This hypothesis assumes a unchanging medium as well as the same location of the transmitter and receiver in the initial transmission and the secondary retransmission.

FOCUSING ALGORITHM

As shown in [12]–[16], TR measurement is organized as two successive and implicitly linked probings, where a single probing is composed of its own signal transmission and registration. Thus, TR measurement can be simply represented as two pairs of signals: the first pair of $[s_t^f(t), s_r^f(t)]$ representing the transmitted $s_t^f(t)$ and recorded $s_r^f(t)$ signal in forward probing, and the second pair of $[s_t^{tr}(t), s_r^{tr}(t)]$ representing the transmitted $s_t^{tr}(t)$ and recorded $s_r^{tr}(t)$ signals in TR probing. As follows from the TR assumptions, $s_t^{tr}(t)$, depends on $s_r^f(t)$, i.e., $s_t^{tr}(t) = \mathcal{F}^{-1}[K_a S_r^f(\omega)]$, where K_a is an energy normalization factor, $S_r^f(\omega) = \mathcal{F}[s_r^f(t)]$, $\mathcal{F}[\]$ is the Fourier transform, and *

denotes conjugation. This time-frequency dependence between $s_t^{tr}(t)$ and $s_r^f(t)$ results from the TR assumptions and is aimed at retracing the signal propagation path and coherent energy refocusing phenomenon. Hence, the two remaining signals, i.e., $s_t^f(t)$ and $s_r^{tr}(t)$, represent an input and an output of TR measurement. The first, $s_t^f(t)$, is a well-known radar waveform. The second, $s_r^{tr}(t)$, is supposed to represent the temporal and spatial refocused energy. While the signal is emitted with pulses centered on the carrier frequency, the (re)focusing algorithm consists of matched filtering performed in the baseband frequency range on $s_r^{tr}(t)$ and with $s_t^f(t)$ as a reference signal for providing a high resolution and maximizing signal-to-noise ratio (SNR).

TR-BASED AGPR CONCEPT

Within the soil geological structure as well as the consequences on the backscattered signal presented in the section “Soil Modeling” and the focusing hypothesis and algorithm described in the section “Time-Reversal,” we describe the TR-AGPR system designed for imaging of an optically invisible soil structure. From the geometrical point of view, the TR-AGPR configuration is identical to the SLAR configuration. The key difference lies in the different purposes of observation. Classical SAR systems are devoted to imaging the terrain surface, and a typical high-resolution SAR image represents only a reflectivity of the terrain surface. On the contrary, TR-AGPR intends to image the optically invisible soil structure located under the surface and process typical backscattered terrain returns as clutter. Figure 2 presents an adequate geometry of a TR-AGPR system (in SLAR, strip-mode SAR) with an example location of buried objects in the soil.

An AGPR mission, similar to SAR missions, is performed at a height H with the platform velocity v_p . The antenna beam, with azimuth θ_{az} and elevation θ_{el} beamwidth, is oriented at an angle θ_{in} . TR-AGPR systems, during an acquisition along the synthetic aperture line L_{sar} , observe swath about width W_L meters and length dependent on the duration of the TR-SAR acquisition. The near slant range to swath is R_{sn} and the far slant range is R_{sf} . The soil structure, presented in Figure 2, contains three types of usual objects located at typical depths for each. Antipersonnel mines are placed just below the surface, pipelines are usually located down to several meters, and stones (or rocks) may occur at every depth. Such objects have their own dielectric constants, defined by the material from which they are made (for instance, see [3, Table 2.1]).

TR-BASED METHOD OF SCANNING

As shown in Figure 2, from the geometrical point of view, the conventional SLAR and TR-AGPR configurations are similar. The difference lies in the way of pulse transmission and signal processing. Unlike traditional SARs, as stated in the section “Focusing Algorithm,” TR-AGPR has two signal transmissions. First, a chirplike radar signal, of duration T_s and total energy E_s , is transmitted. Backscattered returns are recorded in time window T_w . Then, after source separation (see the section “Backscattered Signal”), TR operation and energy normalization, a new radar signal is transmitted and backscattered

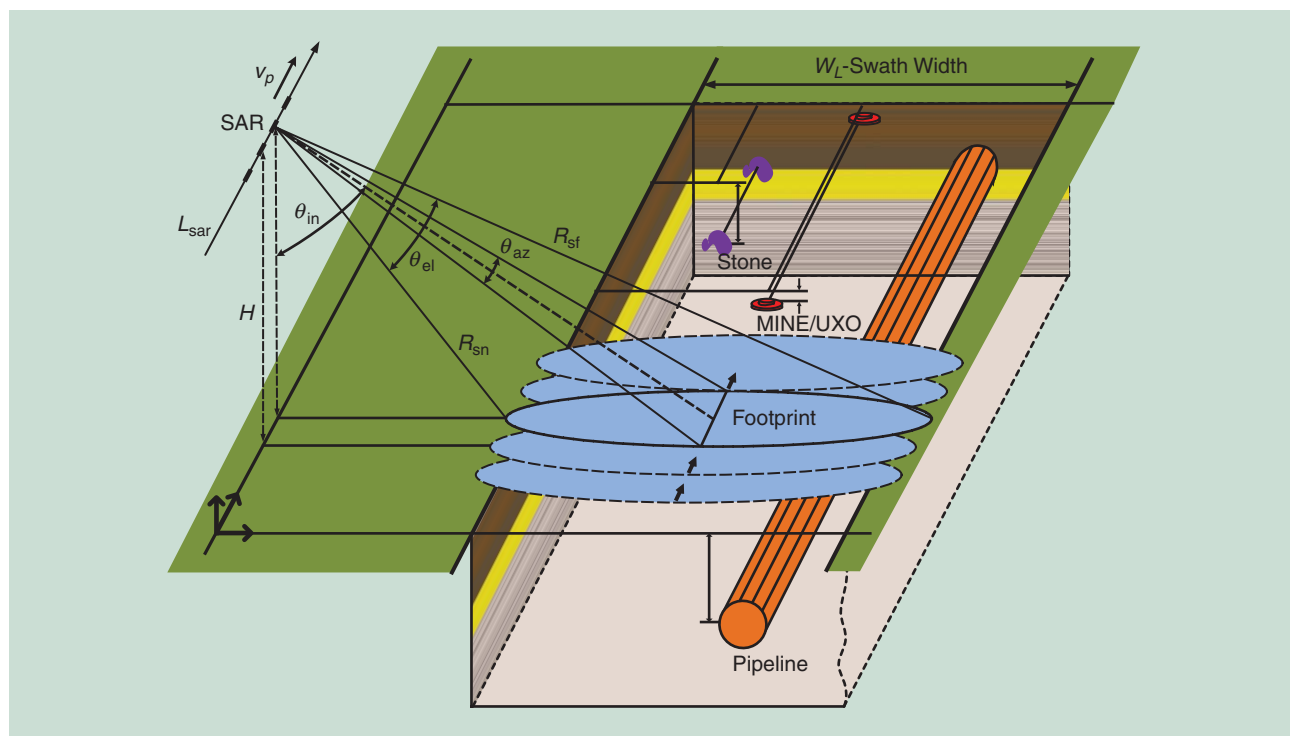


[FIG2] The TR-AGPR configuration with three man-made objects buried at different depths and locations.

returns are recorded. In other words, three separate steps can be distinguished at a given position along the L_{sar} , specifically, forward probing, TR operation, and TR probing. Figure 3 presents a possible time-schedule of system functionality at a particular position along the synthetic aperture. Naturally, other schedules of TR scanning can be assumed.

FORWARD PROBING

In the usual transmission of SAR systems, backscattered signals are recorded in time t_w between T_{sn} and T_{sf} , corresponding to the near and far slant range, R_{sn} and R_{sf} , respectively

$$T_{sn} \leq t_w \leq T_{sf} \Rightarrow \frac{2H}{c \cos(\theta_{in} - \frac{\theta_{el}}{2})} \leq t_w \leq \frac{2H}{c \cos(\theta_{in} + \frac{\theta_{el}}{2})} + T_s, \tag{8}$$

where c is speed of the light and term T_s is added to fully record whole returns from the far slant range. Therefore, the time period T_w , intended for the terrain returns registration is $T_w = T_{sf} - T_{sn}$. However, the time period T_w can be too short for registration of the sufficient amount of backscattered energy derived from internal reflections inside the soil on its inhomogeneities, as well as from the buried objects (structures). In fact, as outlined in the section “Soil Modeling,” variations of the relative complex dielectric constant ϵ_r result in changes of wave propagation velocity v_s in soil, which is locally in layer l_n given by $v_{s,n} = c/\sqrt{\epsilon_{r,n}}$. In consequence, variation of v_s affects the effective depth of propagation. Moreover, we have to consider what effective depth of penetration it is possible to achieve and what effective depth of penetration is desirable from the mission

point of view. For mine detection, small penetration depths are sufficient (to tens of centimeters), but for pipeline monitoring, higher depths are required (to several meters). Therefore, the upper time limit for returns registration in (8) should be increased by the term representing the sufficient penetration time T_{sp} , so (8) is now changed

$$T_{sn} \leq t_w \leq T_{sf} \Rightarrow \frac{2H}{c \cos(\theta_{in} - \frac{\theta_{el}}{2})} \leq t_w \leq \frac{2H}{c \cos(\theta_{in} + \frac{\theta_{el}}{2})} + T_s + T_{sp}. \tag{9}$$

The value of T_{sp} should be selected according to the AGPR application and a priori information about the type of soil, as seen in the section “Physical Model.” An appropriate choice of time window T_w and its location at the time axis is one of several issues in proper selection.

TR OPERATION

This step is the formation of a new radar waveform based on the backscattered signal recorded in the previous step. All tasks in this step consist only of signal processing in the base band frequency range. The effective duration of this step T_{OP} is dependent on the hardware performance of the radar unit and the efficiency of signal processing algorithms. TR operation is equivalent to a mirror operation, i.e., last in, first out, and performed in the time window T_w . In the frequency domain, this operation corresponds to the spectrum conjugation. The Fourier transform of time-reversed signal $S_t^{tr}(\omega)$ equals

$$S_t^{tr}(\omega) = K_a S_r^*(\omega), \tag{10}$$

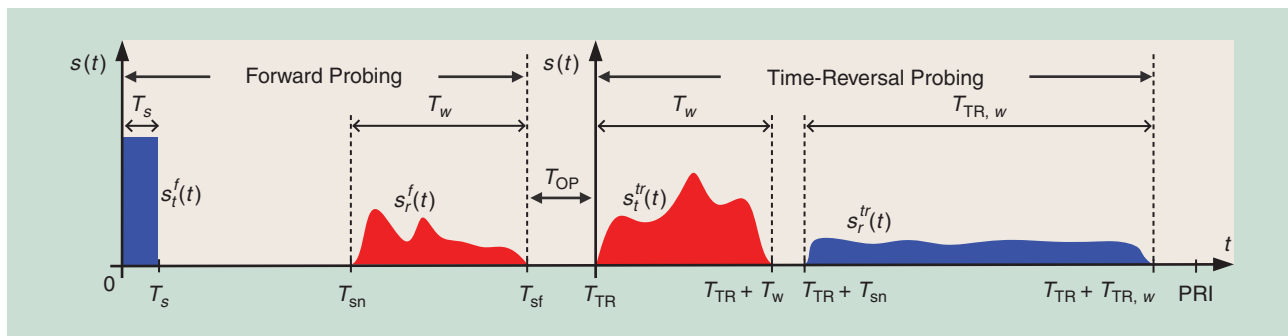


[FIG3] The schedule of TR acquisition at a given position along the synthetic aperture line.

where $S_t^f(\omega) = \mathcal{F}[s_t^f(t)]$ and K_a is the energy normalization factor (see the section “Focusing Algorithm”). Energy normalization (EN) provides compensation for energy losses and keeps average energy at a constant level [15]. The normalization factor K_a is given by

$$K_a = \sqrt{\frac{E_s}{E_w}}, \quad (11)$$

where E_s is the total energy of the transmitted radar signal and E_w is the total backscattered energy from soil structure. It should be noted that E_s is calculated during T_s and E_w during T_w , respectively, where $T_w \gg T_s$. However, (11) expresses a normalization coefficient, which is valid only in the medium where the attenuation does not depend on the frequency, i.e., in a non-dispersive medium. In such a medium, EN can be performed as a compensation of average energy.

TR PROBING

This key step starts at T_{TR} (see Figure 3) and consists of retransmission and backscattered returns registration. The duration of the signal transmitted in TR probing is equal to T_w . Additionally, $T_{sn} \gg T_w$ has to be satisfied to prevent signals overlapping and uncertainty of returns registration. Due to $T_w \gg T_s$, the radar blind zone for TR probing is greater than for forward probing. In this acquisition, the time period $T_{TR,w}$ intended for backscattered returns registration is considerably longer than T_w .

DIFFERENCES, LIMITATIONS, AND EXCEPTIONS

The extended measurement times at individual positions along synthetic aperture, more than twice that of the conventional SAR, due to $T_{sf} \leq (T_{sn} + T_{TR,w})$, decrease the value of pulse repetition frequency (PRF). For the TR-AGPR, the mission value of PRF is considerably lower than PRF in conventional SAR missions. A decreasing PRF value causes less precise reconstruction of the azimuth reference signal, and thus, deterioration of the azimuth resolution. Proper selection of PRF is the important issue in the TR-AGPR system, in particular, to perform the accurate synthesis of the antenna along the radar track.

The scheme of TR-AGPR acquisition with TR operation, presented in the section “TR-Based Method of Scanning,” differs considerably from a typical scheme of TR measurements [15]–[16] in one field. Specifically, the conventional TR scheme assumes the

performance of additional (initial) probing of the clutter channel as a measure of clutter response only, i.e., when the target is absent. In the case of TR-AGPR, the presence of objects in the soil is difficult to identify due to their invisibility and buried nature. However, an additional flight and preacquisition over terrain, with the drawback of increasing the cost of the AGPR mission, may provide useful information about backscattered terrain returns, which are identified as clutter [see (4)]. Afterward, based on the properly developed source separation methods, the weak cumulative echoes derived from internal multireflection can be separated from clutter, time-reserved, and energy normalized, and used in TR probing. Unfortunately, as shown in the section “Backscattered Signal,” the use of source separation methods in AGPR requires additional and intensified investigations due to the complexity of this issue.

Moreover, the TR experiment, in the original form, specifies the location of the transmitter and receiver on opposite sides of the scattering environment. Such a configuration is not appropriate for GPR measurements due to natural impracticality. During the last few years, several configurations of the TR experiment (various transmitter–receiver configurations) were used: monostatic pulse-echo [18], [19] or bistatic pulse-echo [20], [23]. With regard to the AGPR mission configuration (i.e., one antenna for signal transmission and backscattered echo registration), the TR experiment with the use of an airborne platform can be carried out only in the monostatic pulse-echo configuration.

Further, as stated in the section “Focusing Algorithm,” the TR hypothesis assumes the invariant medium and the same position of the transmitter and receiver in the initial transmission and the secondary retransmission. The condition of invariant medium is valid since the TR-AGPR acquisition along L_{sar} takes up to several seconds, and thus, the geological and hydrological parameters impacting the value of complex relative dielectric constant [(1)–(3)] are constant. Unfortunately, since the radar is in motion, at the altitude H , the second condition is not satisfied. However, proper selection of PRF and consideration the fact that $H \gg h$, where h is the depth determined by the purpose of the mission, allow for presumption that radar motion at H slightly affect the (re)focusing effect. Generally, since the reference signal used in matched filtering is the pulse sent in the initial probing, the (re)focusing effect depends only on “the quality of restoration” of the initial pulse in TR probing. As shown in

[21], minor perturbations in probing position, relative to the inhomogeneous medium, have few effects on TR focusing.

Beyond the lack of strict clutter probing, the main idea of the TR approach for AGPR remains the same (as presented in the section “Time-Reversal”). Due to complex scattering phenomena in soil structure, TR should coherently cover and exploit the original multipath propagation to provide a temporal and spatial energy refocusing effect.

TR-AGPR SIMULATION SETUP

The TR-AGPR simulations were performed on the basis of (relatively) a simple ray tracing method, with three point scatterers S_1 , S_2 , S_3 located in the soil structure, each at a different horizon [see Figure 1(a)]. The coordinates, i.e., (depth, along-track, across-track) m, are (0.625, 127, 1,746) m, (1.25, 255, 1844) m, and (1.875, 383, 1945) m for the first S_1 , second S_2 , and third S_3 scatterer, respectively. Soil structure and AGPR geometry configuration were chosen as depicted in Figure 2 in the section “Physical Model.” For the AGPR mission, the SLAR configuration with the following parameters were assumed: $H = 3,500$ m, $v_p = 100$ ms⁻¹, PRF = 200 Hz, $\alpha_{in} = 35^\circ$, and TE polarization. As a radar signal, the up-chirp LFM pulse of $f_c = 430$ MHz, $B = 200$ MHz, and $\tau = 1.2$ μ s were used

$$s_f^f(t) = \cos(2\pi f_c t + \pi \gamma t^2) \quad -\frac{\tau}{2} \leq t \leq \frac{\tau}{2}, \quad (12)$$

where γ is the chirp rate. The SAR simulation was performed along 1,024 positions on the synthetic aperture line leading to a synthetic aperture length $L_s = 512$ m.

To simplify the backscattered signal simulation and processing, the ground reflections are not included; only backscattered signals from buried targets are taken into account. As stated in the section “Physical Model,” the total number of distinguishable layers in the selected STU profile is equal $N = 500$, each with a different value of the complex relative dielectric constant. The number of layers L_t taken into account in the simulation depends on the depth of the scatterer and is equal to 125, 250, and 375 for the first S_1 , second S_2 , and third S_3 scatterer, respectively. The different travel paths are modeled based on Snell’s law, starting from the radar location, through the entry point to the soil and relevant number of layers L_t , to the scatterer location (refer to [11] for a detailed description of the simulation). Moreover, pulse instantaneous frequency lies in the range of 330–530 MHz, i.e., in a frequency range where the imaginary part of the relative complex dielectric constant ϵ_r varies the most; see (1)–(3) and refer to [26].

REFOCUSING PHENOMENON

Figure 4 separately presents normalized output of the matched filtering for the three-point scatterers located inside the soil (see the section “TR-AGPR Simulation Setup”), for the scatterer S_1 in (a), S_2 in (b), and S_3 in (c). On these plots, dashed (blue) lines represent the output of matched filtering after forward probing [$s_f^f(t)$, $s_{r,S_i}^f(t)$], dotted (red) lines represent the output of matched filtering after TR probing [$s_{t,S_i}^{tr}(t)$, $s_{r,S_i}^{tr}(t)$], and solid (black) lines represent the output of cross-matched filtering [$s_f^f(t)$, $s_{r,S_i}^{tr}(t)$], respectively.

■ **Forward probing:** For each point scatterer, the effective time duration of backscattered echo $s_{r,S_i}^f(t)$ is proportionally shorter than the duration of radar (up-chirp) pulse $s_f^f(t)$, as seen in the section “Focusing Algorithm.” For up-chirp LFM, pulse dispersion caused a contraction of the backscattered echo. A cumulative nature of dispersion and attenuation makes echoes from deeper targets more deformed, the higher frequency components are more damped throughout the frequency band. Thus, the outputs of matched filtering are proportionally defocused, broader and (negatively) shifted from expected position at time axis; compare the dashed lines in Figure 4(a)–(c). The ghost targets appear, comparing the side-lobe level (SLL), faintly visible for S_1 in Figure 4(a), and clearly for S_2 in Figure 4(b) and S_3 in Figure 4(c).

■ **TR probing:** (As previously stated, this is a processing between input $s_{t,S_i}^{tr}(t)$ and output $s_{r,S_i}^{tr}(t)$ of TR probing treated as a separate measurement in a dispersive and loss medium.) TR (mirrored or down-chirp) and energy normalized retransmission of the backscattered echo through the same loss medium resulted in reattenuation, due to the constant attenuation factor for each frequency component of the LFM pulse, regardless of the internal frequency change inside the pulse. The level of ghost targets (i.e., the increasing of side lobes) is higher than for forward probing; compare the SLL between dotted and dashed lines in Figure 4(a)–(c). Nevertheless, the reversed mode of internal frequency changes inside the pulse induces a lengthening of the backscattered echo (see the section “Focusing Algorithm”). For each point scatterer, the effective time duration of backscattered echo $s_{r,S_i}^{tr}(t)$ is longer than the duration of the radar waveform $s_{t,S_i}^{tr}(t)$ and is almost equal to the time duration of $s_f^f(t)$. Furthermore, the energy normalization ensures an almost uniform level of $s_{r,S_i}^{tr}(t)$. Thus, outputs of matched filtering are still defocused and significantly broader. However, now they are reversely (positively) shifted, and moreover, centered at the expected location for each scatterer; compare the dotted plots in Figure 4(a)–(c).

■ **Cross-matched filtering:** Despite the strong frequency-dependent attenuation and dispersive characteristic of the soil, the results of cross-matched filtering are correctly focused. Retransmission of the time-reversed signal inversely restores the dispersion effects in backscattered echo and overstated energy normalization (selective overamplification) has neutralized attenuation in TR probing. Regardless of the scatterer location, the main lobes have the same width as the expected resolution. Furthermore, the value of (SLL) is slightly different between them, but oscillates around the theoretical value.

Performed simulations are based on an assumption about the time invariability of the $\epsilon_r(1)$ in individual layer l_n . Such an assumption is correct, when taking into account that conventional TR-SAR acquisition along synthetic aperture L_{sar} can take approximately a few seconds.

TR-BASED SAR PROCESSING

Figure 4 presents the refocusing effects in the fast time domain (in range/depth dimension). Data collected along the synthetic

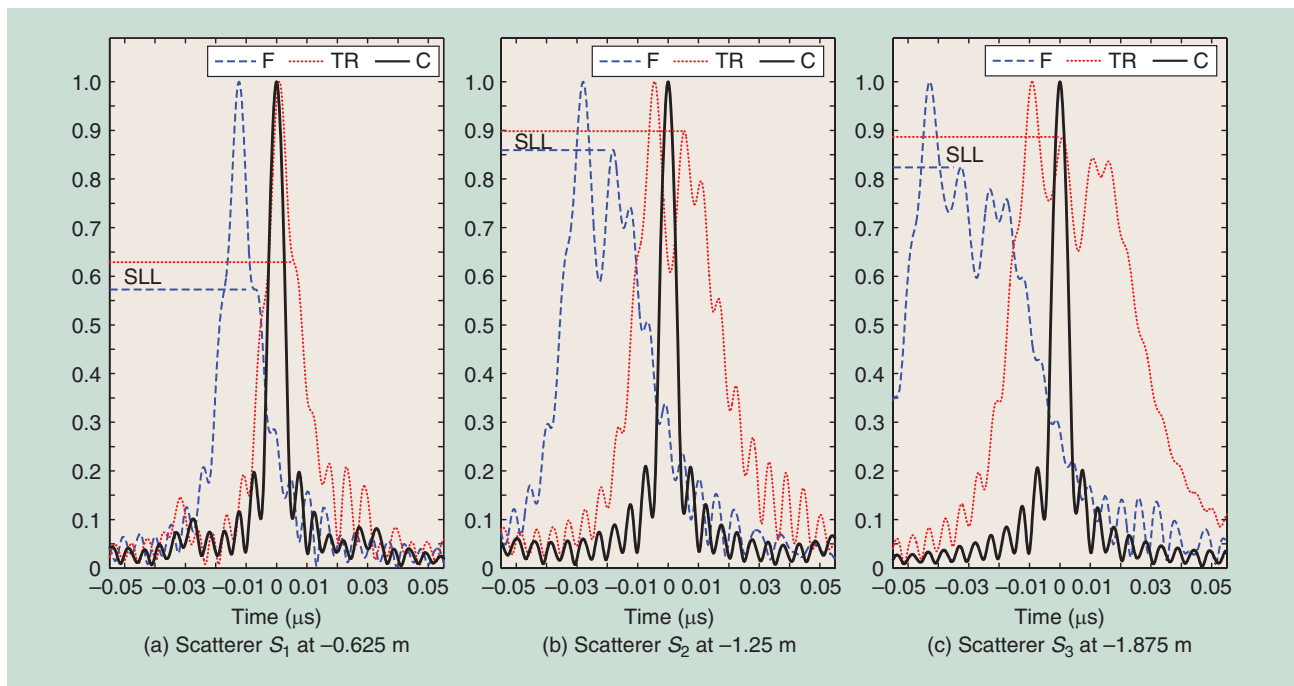


[FIG4] The normalized output of matched filtering for three point scatterers (S_1 , S_2 , S_3) after (a) forward probing (dashed lines), (b) TR probing (dotted lines), and (c) cross-matched filtering (solid lines).

aperture L_{sar} , similarly to conventional SAR acquisition, have a migration effect resulting from changes in the relative distances between platform position and target location. Based on the range compression results, only compression in azimuth has to be additionally performed. The azimuthal compression factor K_a is given by $K_a = 2v_p^2 f_c / R_s c$ [11], where v_p is platform velocity, f_c is carrier frequency, R_s is slant range to range cell, and c is the speed of the light. Azimuth reference function $a_{ref}(u, r)$, defined in slow time u and range r , is expressed as

$$a_{ref}(u, r) = \exp\left(j \frac{2\pi}{\lambda_c} \frac{v_p^2 (u - u_0)^2}{R_s(r)}\right), \quad (13)$$

and is created based on TR-AGPR parameters.

Using the fast convolution theory for azimuth compression, the data presented in Figure 5 has been obtained. Correction of range migration (RMC) was intentionally skipped to focus only on azimuth compression. Hence, the scatterers have a curved glow. Both TR-SAR images obtained after forward probing [Figure 5(a)] and TR probing [Figure 5(b)] have low azimuth resolution decreasing with depth. Results of azimuth compression are strongly distorted and targets are unresolved. In addition, ghost targets caused by energy dissipation and pulse distortion appear in the both SAR images. Various object depths result in different amplitudes and levels of distortion in the backscattered echo. Thus, the results of SAR processing are proportionally deformed. For forward probing, [see Figure 5(a)], despite the absence of focal in depth and azimuth, S_1 has the strongest echo of the three scatterers, S_2 has slightly weaker echo and S_3 is almost invisible. For TR probing, overstated energy normalization causes the opposite effect in SAR image; see Figure 5(b). Now, the

dominant echo from S_3 significantly blurring the remaining weak echoes from S_1 and S_2 , also the accumulation of ghost targets is highly visible for S_3 . The clearly visible width of the curved tail along synthetic aperture L_{sar} indicates the level of defocusing and distortion of backscattered echo. Figure 5(c) is much better focused, both in range and azimuth dimension. All targets are clearly resolved with nearly the same amplitude, despite the lack of the RMC (the curved tail along synthetic aperture L_{sar} is still present, but now is uniformly thin and identical for all scatterers). Due to the partial propagation in inhomogeneous soil structure scatterers are shifted (delayed) in range domain, proportionally to depth location. The range shift (delay) results from smaller and irregular velocity of EM wave propagation through the soil layered structure. The deeper targets have greater displacement than shallow targets.

CONCLUSIONS AND CHALLENGES

Conventional SAR systems, based on surface returns, process the backscattered energy as only reflected from terrain, and thus, omit the ability of the EM waves to penetrate through soil, scatter inside its inhomogeneous structure, and travel upward to the surface. Nevertheless, registration and processing of the backscattered waves derived from the internal multipath propagation and multireflection are a key aspect of remote sensing imaging of the ground. Thus, AGPR, unlike SAR, have to exploit the internal complex scattering phenomenon to provide range/depth focal of the backscattered energy and for high-resolution imaging of the soil structure.

As presented in this tutorial, configuration of the TR-AGPR acquisition involves a number of different nature issues and

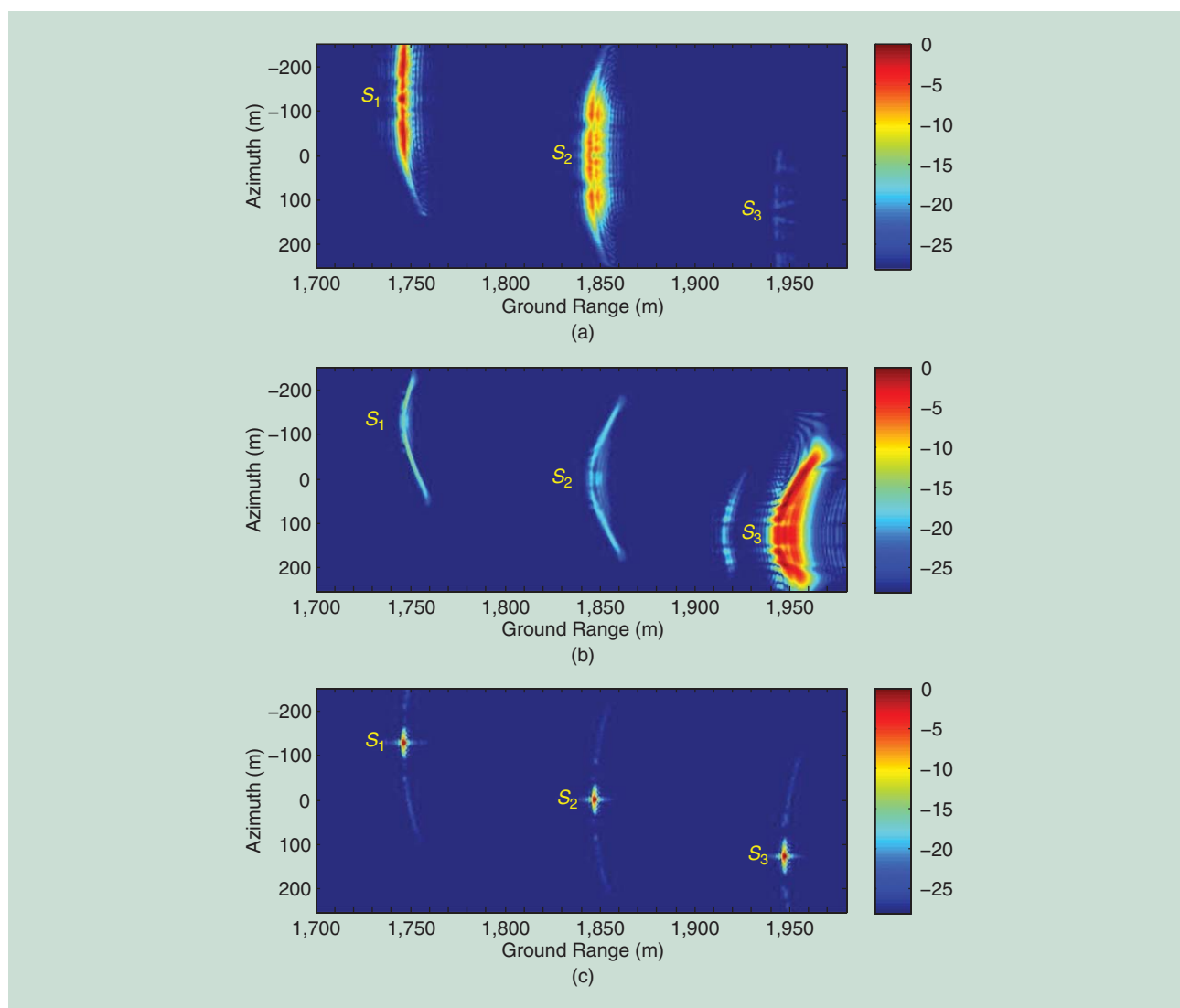


[FIG5] The result of SAR processing after (a) forward probing, (b) TR probing, and (c) cross-matched filtering (all in decibel scale).

limitations. First, the inhomogeneous nature of the soil (see the section “Physical Model”) affects both the EM parameters, and consequently, the time-frequency form of an incident signal propagating through it, scattering on its inhomogeneities and traveling upward in the form of backscattered waves. Backscattered returns consist of many deformed, amplitude-scale, and phase-shifted replicas of the transmitted signal (see the section “Backscattered Signal”). Second, knowing that the effectiveness of wave penetration depends on the incident angle (Snell’s law), the parameters of the TR-AGPR acquisition along L_{sar} have to be well aligned to one another. The acquisition settings (e.g., altitude, platform velocity, incident angle, elevation and azimuth beamwidth, and pulse repetition frequency) and radar configuration (e.g., frequency band, signal bandwidth, internal modulation, and signal power) affect the backscattered returns, for instance, by the implied impact of footprint dimensions, both on the surface clutter level and on the returns registration periods T_w and $T_{TR,w}$ (see the section “TR-Based Method of

Scanning”). Moreover, as presented in the section “Differences, Limitations, and Exceptions,” decreases of PRF negatively affects the performance of image synthesis. Third, adaptation of the TR technique into measurement schedule, besides increasing the acquisition time at a given position along L_{sar} , forces the creation of new signal processing algorithms aimed at source separation (see the section “Backscattered Signal”), at an estimation of selective attenuation characteristics of the soil as well as at TR-SAR processing.

Beyond these limitations, as shown in the section “Refocusing Phenomenon,” the TR approach for SAR focusing of buried targets, under certain conditions, can provide an energy refocusing phenomenon, and thus, significantly improve range resolution (Figure 4) and increase detection gain over the conventional approach. Additionally, assuming that shape of the radar waveform can have an important effect on the object detection in a dispersion and loss medium, the TR technique can provide a method for adaptation of the radar waveform to the medium. The

synthesis along L_{sar} results in a high-resolution TR-AGPR image of the soil subsurface structure (Figure 5), that similar to a conventional SAR image, represents only a reflectivity of buried objects located in the soil. Furthermore, properly devised and successfully validated algorithms for TR-AGPR are the basis for new challenges facing high-resolution and large-scale soil imaging. For example, application of the interferometry aimed at creating a digital soil model, similar to the digital terrain model.

In summary, proper defining of all issues related to TR-AGPR open up many areas for high-resolution and large-scale imaging of optically invisible soil structure.

ACKNOWLEDGMENTS

We would like to acknowledge the anonymous reviewers for helpful remarks and suggestions, as well as thank the European Commissions Joint Research Center (The Institute for Environment and Sustainability) for providing the SPADE/2v11: The Soil Profile Analytical Database for Europe Version 1.1.

AUTHORS

Robert Kedzierawski (robert.kedzierawski@wat.edu.pl) received the M.S. (Eng.) degree in electronics and telecommunications in 2010 from the Military University of Technology (MUT), Warsaw, Poland. He began his Ph.D. study at MUT in cooperation with the École Nationale Supérieure des Télécommunications de Bretagne, Brest, France, in 2010. Currently, he is a research and teaching assistant at MUT. His research interests are in radar signal processing, ground penetrating radar, and software-defined radar systems. He is a Student Member of the IEEE.

Jean-Marc Le Caillec (jm.lecaillec@telecom-bretagne.eu) obtained the degree of engineer in telecommunications in 1992 from the École Nationale Supérieure des Télécommunications de Bretagne. He received the Ph.D. degree in mathematics and signal processing from the University of Rennes I in 1992. From 1997 to 1999, he worked for Thomson AirSys (now Thales AirSys) on unsupervised radar management. In 1999 he joined the ENST Bretagne, where he is currently a professor. His main research interests are statistics, nonlinear system modeling, mathematics, and signal processing for applications in remote sensing. He is a Senior Member of the IEEE.

Witold Czarnecki (witold.czarnecki@wat.edu.pl) received the M.S. and Ph.D. degrees in signal processing and telecommunication from the Warsaw University of Technology (WUT) in 1967 and 1972, respectively, and the D.S. degree from the Military University of Technology (MUT) in 2010. He was an assistant professor in the Institute of Telecommunications of the WUT and is currently a professor in the Institute of Radioelectronics at MUT. He specializes in radar signal simulation and processing. Currently, his scientific interest is focused on synthetic aperture radar and ground penetrating radar techniques.

REFERENCES

[1] K. Tomiyasu, "Tutorial review of synthetic-aperture radar (SAR) with applications to imaging of the ocean surface," *Proc. IEEE*, vol. 66, no. 5, pp. 563–583, May 1998.
 [2] J. C. Curlander and R. N. McDonough, *Synthetic Aperture Radar: Systems and Signal Processing*. New York: Wiley-Interscience, 1991.

[3] H. M. Jol, *Ground Penetrating Radar: Theory and Applications*. Amsterdam, The Netherlands: Elsevier Science, 2009.
 [4] J. Taylor, *Ultra-wideband Radar: Applications and Design*. Boca Raton, FL: CRC Press, 2012.
 [5] G. L. Berlin, M. A. Tarabzouni, A. H. Al-Nazer, K. M. Sheikho, and R. W. Larson, "SIR-B subsurface imaging of a sand-buried landscape: Al Labbah Plateau, Saudi Arabia," *IEEE Trans. Geosci. Remote Sensing*, vol. 24, no. 4, pp. 595–602, July 1986.
 [6] G. G. Schaber, J. F. McCauley, C. S. Breed, and G. R. Olhoeft, "Shuttle imaging radar: Physical controls on signal penetration and subsurface scattering in the Eastern Sahara," *IEEE Trans. Geosci. Remote Sensing*, vol. 24, no. 4, pp. 603–623, July 1986.
 [7] J. J. Legarsky, S. P. Gogineni, and T. L. Akins, "Focused synthetic aperture radar processing of ice-sounder data collected over the Greenland ice sheet," *IEEE Trans. Geosci. Remote Sensing*, vol. 39, no. 10, pp. 2109–2117, Oct. 2001.
 [8] W. Zhai, Y. Zhang, and X. Zhang, "SAR imaging simulation for subsurface target detection," in *Proc. 7th Int. Symp. Antennas, Propagation, EM Theory (ISAPE'97)*, Guilin, China, Oct. 2006, pp. 1–5.
 [9] S. Liu and Y. Feng, "Airborne GPR: Advances and numerical simulation," in *Proc. 2011 IEEE Int. Geoscience Remote Sensing Symp. (IGARSS)*, Vancouver, BC, Canada, July 2011, pp. 3390–3340.
 [10] L. Fu, S. Liu, and L. Liu, "Numerical simulations and analysis for airborne ground penetrating radar," in *Proc. 14th Int. Conf. Ground Penetrating Radar (GPR)*, Shanghai, China, June 2012, pp. 200–203.
 [11] J.-M. Le Caillec, S. Redada, C. Sintes, B. Solaiman, and M. Benslama, "Focusing problems of a buried point scatterer using a low frequency SAR," *IEEE Trans. Aerosp. Electron. Syst.*, vol. 47, no. 1, pp. 438–453, Jan. 2011.
 [12] M. Fink, "Time reversal of ultrasonic yields – Part I: Basic principles," *IEEE Trans. Ultrason. Ferroelectr. Freq. Control*, vol. 39, no. 5, pp. 555–567, Sept. 1992.
 [13] F. Wu, J.-L. Thomas, and M. Fink, "Time reversal of ultrasonic yields—Part II: Experimental results," *IEEE Trans. Ultrason. Ferroelectr. Freq. Control*, vol. 39, no. 5, pp. 567–578, Sept. 1992.
 [14] J. de Rosny, G. Lerosee, and M. Fink, "Theory of electromagnetic time-reversal mirrors," *IEEE Trans. Antennas Propag.*, vol. 58, no. 10, pp. 3139–3149, Oct. 2010.
 [15] J. F. M. Moura and Y. Jin, "Detection by time reversal: Single antenna," *IEEE Trans. Signal Processing*, vol. 55, no. 1, pp. 187–201, Jan. 2007.
 [16] M. E. Yavuz and F. L. Teixeira, "Ultra-wideband microwave sensing and imaging using time-reversal techniques: A review," *Remote Sens.*, vol. 9, pp. 466–495, Sept. 2009.
 [17] Y. Jin and J. F. M. Moura, "TR-SAR: Time reversal target focusing in spotlight SAR," in *Proc. 2007 IEEE Int. Conf. Acoustics, Speech, Signal Processing (ICASSP)*, Honolulu, HI, Apr. 2007, pp. II–957–II–960.
 [18] Y. Jin, J. F. M. Moura, N. O'Donoghue, M. T. Mulford, and A. A. Samuel, "Time reversal synthetic aperture radar imaging in multipath," in *Proc. 41st Annu. Asilomar Conf. Signals, Systems, Computers (Asilomar '07)*, Pacific Grove, CA, Nov. 2007, pp. 1812–1816.
 [19] N. O'Donoghue, J. F. M. Moura, and Y. Jin, "Signal-domain registration for change detection in time-reversal SAR," in *Proc. 42nd Annu. Asilomar Conf. Signals, Systems, Computers (Asilomar '08)*, Pacific Grove, CA, Nov. 2008, pp. 505–509.
 [20] J. F. M. Moura and Y. Jin, "Time reversal imaging by adaptive interference canceling," *IEEE Trans. Signal Processing*, vol. 56, no. 1, pp. 233–247, Jan. 2008.
 [21] D. Liu, S. Vasudevan, J. Krolik, G. Bal, and L. Carin, "Electromagnetic time-reversal source localization in changing media: Experiment and analysis," *IEEE Trans. Antennas Propag.*, vol. 55, no. 2, pp. 344–354, Feb. 2007.
 [22] A. Crespi, I. Aliferis, M. J. Yedlin, C. Pichot, and J.-Y. Dauvignac, "Investigation of time-reversal processing for surface-penetrating radar detection in a multiple-target configuration," in *Proc. 5th European Radar Conf. (EuRAD)*, Amsterdam, The Netherlands, Oct. 2008, pp. 144–147.
 [23] F. Foroozan and A. Asif, "Time-reversal ground-penetrating radar: Range estimation with Cramér–Rao lower bounds," *IEEE Trans. Geosci. Remote Sensing*, vol. 48, no. 10, pp. 3698–3708, Oct. 2010.
 [24] N. R. Peplinski, F. T. Ulaby, and M. C. Dobson, "Dielectric properties of soils in the 0.3–1.3 GHz range," *IEEE Trans. Aerosp. Electron. Syst.*, vol. 33, no. 3, pp. 803–807, May 1995.
 [25] B. J. Cosby, G. M. Hornberger, R. B. Clapp, and T. R. Ginn, "A statistical exploration of the relationships of soil moisture characteristics to the physical properties of soil," *Water Resource Research*, vol. 20, no. 6, pp. 682–690, June 1984.
 [26] R. Kedzierawski, J.-M. Le Caillec, W. Czarnecki, and M. Pasternak, "Subsurface soil modeling based on geological database for simulation of electromagnetic wave propagation," in *Proc. 13th Int. Radar Symp. (IRS)*, Warsaw, Poland, May 2012, pp. 441–445.
 [27] L. A. Richards, "Capillary conduction of liquids through porous medium," *J. Appl. Phys.*, vol. 1, no. 5, pp. 318–333, June 1931.
 [28] M. Tria, M. Benidir, and E. Chaumette, "Application of the time-frequency-based blind source separation to an instantaneous mixture of secondary radar source," *Int. J. Comput. Inform. Eng.*, vol. 2, no. 8, pp. 539–544, 2008.
 [29] M. A. C. Tuncer and A. C. Gurbus, "Ground reflection removal in compressive sensing ground penetrating radar," *IEEE Geosci. Remote Sensing Lett.*, vol. 9, no. 1, pp. 23–27, Jan. 2012.
 [30] K. Zhang and D. Li, *Electromagnetic Theory for Microwaves and Optoelectronics*. Berlin: Springer-Verlag, 2008.



[Michael Leigsnering, Moeness G. Amin, Fauzia Ahmad, and Abdelhak M. Zoubir]

Multipath Exploitation and Suppression for SAR Imaging of Building Interiors

[An overview of recent advances]

Multipath that involves target scattering is an important phenomenon in synthetic aperture radar (SAR). It is highly pronounced in imaging of building interiors due to the presence of walls, ceilings, and floors surrounding the targets of interest. Multipath attributed to targets is a special type of clutter, which can be either suppressed or exploited. The latter has been the subject of many recent works in the area of SAR imaging and has led to tangible improvements in target detection and localization. In this article, we consider state-of-the-art multipath suppression and exploitation approaches, present their corresponding analytical models, and highlight their respective requirements, assumptions, and offerings. Both conventional and compressive sensing-based approaches are discussed, where the latter assumes the presence of a few behind-the-wall targets.

INTRODUCTION

In recent years, radar imaging of building interiors has gained much interest due to the rising and ubiquitous use in civilian, security, and defense applications [1]–[3]. Typically, there is no

visual access to the scene, and optical, ultrasound, or thermal imaging is not effective. In this case, sensing is performed by the electromagnetic (EM) modality and has allowed the emergence of the area of through-the-wall radar imaging (TWRI).

Indoor targets and interior building layout are detected and characterized from a stand-off distance. The radar systems may be ground based or airborne and assume different modes of operations and system parameters. One mode, which is consistent with many sensing objectives, is SAR. TWRI using SAR is the only viable choice when two-dimensional (2-D) physical apertures required to achieve the desired resolution are logistically difficult or impossible. We restrict the discussions to SAR imaging of stationary targets. Moving targets pose a whole set of different challenges, exceeding the scope of this article.

SAR imaging could be impaired by the many scatterers present in a typical indoor scene. In addition to the shortest path to the target and back to the receiver, the transmitted wave may travel on indirect paths due to secondary reflections arising from interior walls, floor, and ceiling. This leads to rich multipath associated with the targets, which, depending on the scattering environment, can have different adverse effects on the image quality and interpretation. The energy in the multipath returns may accumulate at locations where no physical targets reside, thus creating “ghosts.” With increased specular and diffuse

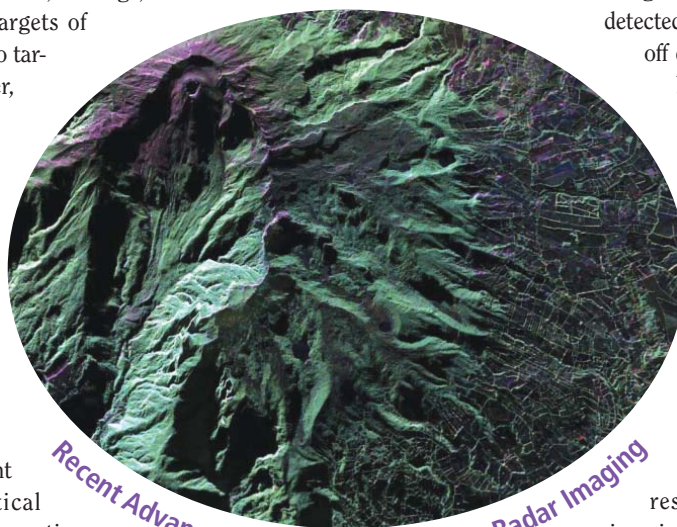


PHOTO COURTESY OF NASA

Digital Object Identifier 10.1109/MSP.2014.2312203

Date of publication: 13 June 2014

scatterings, the stationary scene can become very cluttered, masking the true targets and disabling their detection. The significance of multipath and ghost targets in imaging of building interiors has been shown in various works. Dogaru and Le [3] showed the ghost phenomenon using extensive numerical EM simulations. Others examined the same, using measurements in a lab setup [4], [5]. The radar community also acknowledged multipath as a significant problem on a special industry day [6].

Since multipath exists and is often observed, it must be described and accounted for, using accurate analytical models, and properly addressed in imaging techniques. Broadly, there are two paradigms to deal with indirect propagation: multipath suppression and multipath exploitation. The key idea of the former is to characterize the multipath returns and mitigate their effects on image formation [7]–[16]. Different properties of direct and indirect radar returns can be used to distinguish between the two arrivals and attenuate, if not remove, the indirect returns. These methods are generally straightforward to apply. However, they do not make use of the energy and target information contained in the multipath returns. The second method, reminiscent of the RAKE receiver in wireless communications [17], aims at exploiting the multipath and using it for imaging enhancements [4], [5], [18]–[24]. By properly modeling the indirect propagation paths, whether they are resolvable or not, their energy can be captured and attributed to their respective targets, allowing an increase in target to clutter and noise ratios, and thus culminating in an enhanced image. Further, areas in the shadow region of highly attenuative targets, which cannot be illuminated by the radar directly, can be imaged by utilizing multipath. Although multipath exploitation has potential and tangible benefits, it often requires prior information or is computationally demanding.

SIGNAL MODEL

A forward scattering model should be developed for multipath to be properly exploited or mitigated. This requires determining the scattered field from the targets inside the building. If the building layout and imaging geometry is known, this problem can be exactly solved by using Maxwell's equations [25]. However, there are two issues that render this approach impractical. First, solving a full wave model is computationally demanding and may require vast resources. Second, inferring the positions of the scatterers from the scattered field requires solving an inverse problem. Since the forward problem is nonlinear due to the influence of the scatterers on the surrounding field, the inverse problem is even more challenging and, for practical purposes, impossible to solve. To overcome these difficulties, various linear approximations of the forward scattering model, such as the Born approximation, Kirchoff approximation, and geometric optics (GO), have been introduced, all of which yield tractable solutions to the inverse problem [1], [26], [27]. More specifically, the Born approximation makes the weak scatterer assumption, i.e., the electrical parameters of the scatterers do not differ much from that of the background medium. As such, the total field inside the target is approximated by the incident field [26]. The Kirchoff or physical optics (PO) approximation assumes perfectly conducting targets,

and the interaction with the incident field takes place only on the surface of the targets [27]. For both Born and PO approximations, the background medium, which is the building enclosure in the problem at hand, is described by the Green's function that depicts the impulse response of the wave equation. The GO or ray-tracing approach uses local plane wave assumption or "ray of light" to model the propagation of the wave [1]. Since the latter is the simplest and most commonly used approximation in TWRI, we focus on ray tracing for describing the signal model.

BASIC SIGNAL MODEL

Consider an N -element monostatic linear array of transceivers. Either all of the array elements can be physically present or a single transceiver can be moved to different locations to synthesize the intended aperture. For the synthetic aperture, we assume the stop-and-go approximation for the movement pattern, i.e., the transceiver remains stationary while it transmits and receives at a particular array position and then moves to the next location. The model may be extended to a bistatic or multiple-input, multiple-output (MIMO) SAR scenario, where the transmitter(s) and receiver(s) move along different trajectories. However, this is not treated here for the sake of simplicity.

The linear array is located along the x -axis parallel to an exterior wall of thickness d , with its element locations denoted by $u_n, n = 0, \dots, N-1$. At the n th array element location, a modulated wideband pulse $\Re\{s(t) \exp(j2\pi f_c t)\}$ is transmitted, where t is the fast time, $s(t)$ is the pulse in the complex baseband, and f_c is the carrier frequency. For a scene of P stationary point targets behind the wall at positions (x_p, z_p) , the n th element receives the baseband signal $y_n(t)$, given by

$$y_n(t) = \sum_{p=0}^{P-1} \sigma_p s(t - \tau_{pn}) \exp(-j2\pi f_c \tau_{pn}) + v_n(t), \quad (1)$$

where σ_p is the deterministic complex reflectivity of the p th target, and τ_{pn} is the two-way propagation delay between the n th transceiver and the p th target. We consider additive receiver noise $v_n(t)$, which is typically assumed to be an independent and identically distributed complex circular Gaussian process. For through-the-wall propagation, τ_{pn} comprises the components corresponding to traveling distances before, through, and after the wall [1]. Note that the received signal is a superposition of the individual direct target returns only. Target interactions with other targets and the surrounding environment are ignored in this model. However, in indoor scenarios, such interactions are both pronounced and measurable and give rise to multipath propagation.

MULTIPATH PROPAGATION MODEL

We broadly categorize multipath returns as follows:

- *Interior wall/floor/ceiling multipath:* These involve indirect paths with secondary specular reflections at a large smooth surface.
- *Wall ringing multipath:* This type involves signals that undergo multiple reflections within the exterior wall in transit to/from the targets.

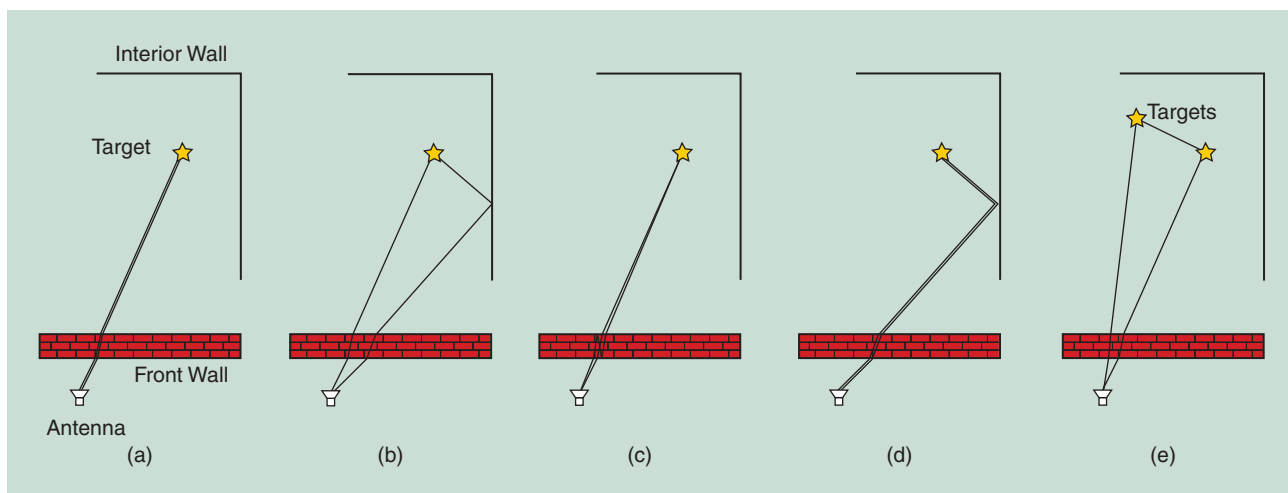


[FIG1] Various cases for multipath in indoor scenes. (a) Direct propagation, (b) one secondary reflection at an interior wall, (c) multiple reflections inside the front wall, (d) two secondary reflections at an interior wall, and (e) target-to-target multipath.

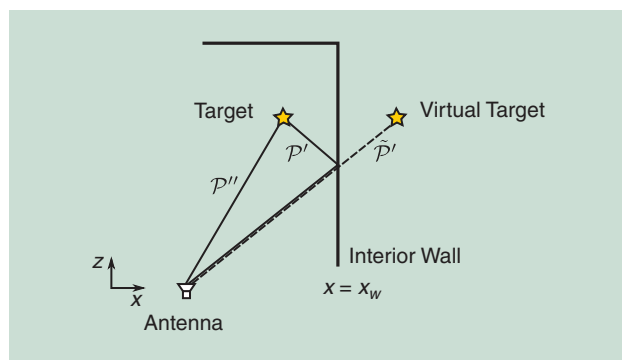


[FIG2] Multipath propagation via reflection at an interior wall. (Figure used with permission from [19].)

■ *Target-to-target interaction:* This includes paths where the wave interacts with more than one diffusely scattering targets. The interior wall/floor/ceiling multipath returns can be further subdivided into the following classes:

- *First-order multipath:* This involves one secondary reflection either on the transmit or receive path.
- *Second-order multipath:* This involves two secondary reflections during the round-trip path.
- *Higher-order multipath:* This includes multipath returns involving three or more secondary reflections during the round-trip path.

Figure 1 shows examples of various multipath propagation cases. As the signal weakens at each secondary reflection, the higher-order multipath returns can usually be neglected.

Considering a maximum of R possible propagation paths for each target–transceiver combination, including the direct path and excluding target-to-target interactions, we can extend the n th received signal model in (1) as

$$y_n(t) = \sum_{r=0}^{R-1} \sum_{p=0}^{P-1} \sigma_p^{(r)} s(t - \tau_{pn}^{(r)}) \exp(-j2\pi f_c \tau_{pn}^{(r)}) + v_n(t), \quad (2)$$

where $\tau_{pn}^{(r)}$ is the round-trip propagation delay between the n th transceiver and the p th target along the r th path, and $\sigma_p^{(r)}$ is the complex reflectivity of the p th target when observed through the r th path. Let $r = 0$ correspond to the direct path and the remaining $R - 1$ be the multipath returns. The various propagation delays can be readily calculated using GO considerations [5]. The number paths R is a deterministic parameter that depends on the number and type of scattering walls, which are assumed to be known a priori.

For illustration, Figure 2 depicts an example of an interior wall multipath. The associated propagation delay may be determined by considering the equivalent two-way path to the corresponding virtual target. Target-to-target interactions can be included in the multipath model of (2) by assuming additional double bounce paths between pairs of diffusely scattering targets. Note that, in this case, the associated propagation delays not only depend on the distances between the transceivers and the targets, but also on the separation between the targets themselves.

IMAGE FORMATION AND THE EFFECTS OF MULTIPATH

Having developed the forward scattering model, we now proceed with the inverse problem of determining the locations of the P point targets. The conventional approach is delay-and-sum beamforming or backprojection, which does not account for multipath propagation. As the number of targets is usually unknown a priori, the target space is discretized into a rectangular grid of P pixels. Hence, P is the deterministic total number of possible target positions, which is determined by the dimensions of the area being imaged and the system resolution. A nonexistent target is simply represented by a pixel with zero reflectivity. An estimate of the image is obtained as [1]

$$I(p) = \frac{1}{N} \sum_{n=0}^{N-1} y_n(t) * s(-t) \Big|_{t=\tau_{pn}^{(0)}}, p = 0, \dots, P-1, \quad (3)$$

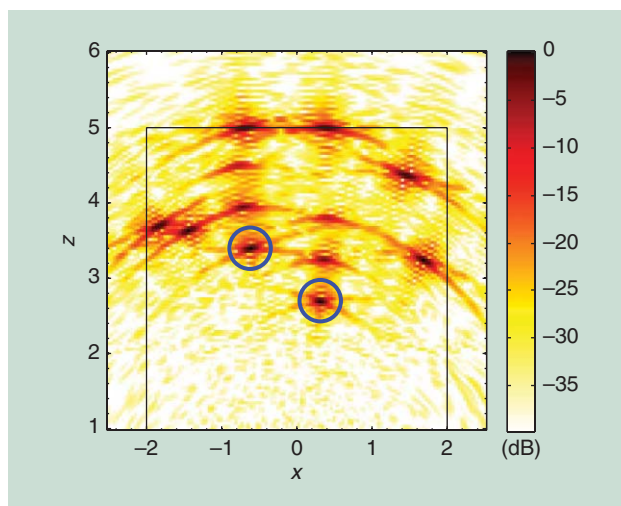


[FIG3] A beamformed image of a two-target scene showing five ghost targets associated with each target ($R = 6$ propagation paths per target).

which employs matched filtering of the n th received signal, followed by sampling the output at the delay corresponding to direct propagation to the current pixel, and finally, coherently summing the results corresponding to all N array locations.

If multipath returns are present in the received signals, the image formation process results in ghost targets, i.e., the energy in the multipath returns is focused at locations where no physical targets exist. Figure 3 shows the image of a scene consisting of two point targets inside a room, which was obtained by applying beamforming to data simulated using (2). In addition to the direct returns, only first-order interior wall multipath and two wall ringing multipath returns per target were assumed to be present in the measurements. We observe that the multipath via reflections at interior walls causes ghosts within the room, whereas the wall ringing multipath creates equally spaced

copies of the target response in the downrange direction. The ghosts cause the scene image to be highly cluttered, rendering interpretation difficult and challenging.

MULTIPATH SUPPRESSION

Having described the multipath model and the cluttering effects of multipath propagation, we revert back to multipath suppression and exploitation. The objective of multipath suppression is to mitigate the effects of indirect propagation on the quality of the reconstructed scene image. A variety of multipath suppression methods have been devised [7]–[14], which can either act directly on the raw data measurements or are implemented as a postprocessing step for the SAR image. These methods require the targets and ghosts/multipath returns to be well resolved and can achieve ghost suppression without any prior knowledge of the scene.

A SUPPRESSION USING GHOST PROPERTIES IN SAR IMAGES

We first describe methods applicable to suppression of ghosts in SAR images resulting from target-to-target interactions. Considering two targets separated by a distance 2δ , the received signal at the n th transceiver location would consist of three components: the two direct returns with respective round-trip propagation delays $\tau_{1n}^{(0)}$ and $\tau_{2n}^{(0)}$, and a double scattering return involving the two targets with a round-trip propagation delay of $\tau_n^{(1)} = (\tau_{1n}^{(0)} + \tau_{2n}^{(0)})/(2) + (2\delta)/(c)$, where c is the speed of light in free space. Since the conventional SAR image formation method, described in the section “Image Formation and the Effects of Multipath,” is based on direct returns of single target scatterings, the additional delay associated with the double scattering multipath results in a ghost located at a farther range than the two targets, as shown in Figure 4(a).

Ghosts in SAR images resulting from target-to-target interactions have very specific characteristics, which can be exploited to distinguish them from real targets. These characteristics stem

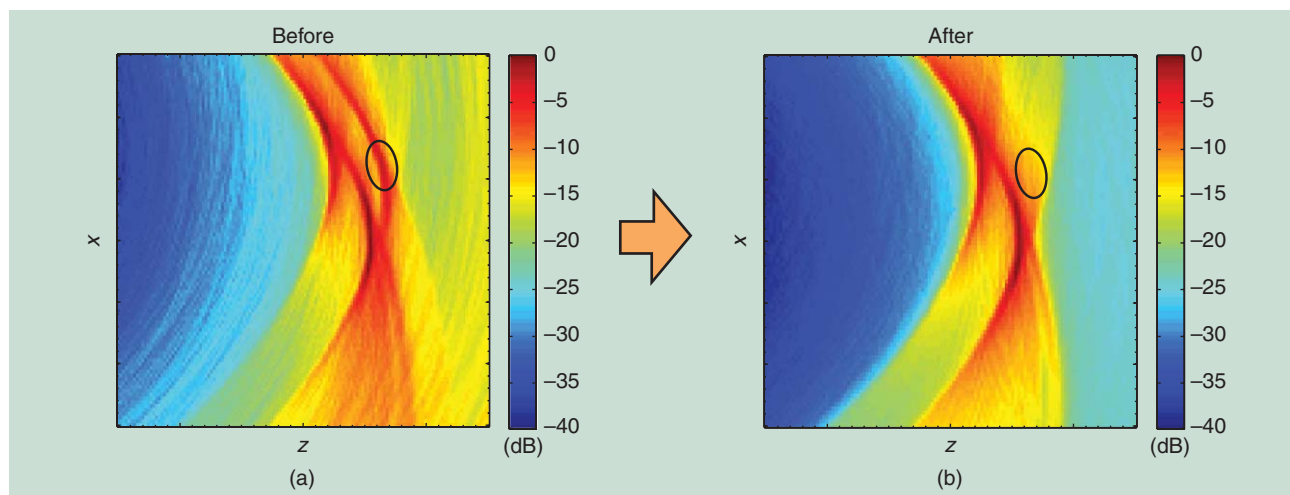


[FIG4] The multipath suppression using the HMM-based approach [8]. The ghost at the highlighted position in (a) has been suppressed in (b). (Figure adapted from [8] and used with permission.)

from the changes in the associated double scattering geometry with aspect angle as viewed by the imaging system [7].

Most targets exhibit aspect dependent scattering. However, unlike the targets, the ghost intensity takes on high values only over a portion of the synthetic aperture (see Figure 5), implying a smaller effective aperture for imaging of ghosts. This causes a wider point spread function in crossrange for the ghosts as compared to a real target, and subsequently lower crossrange resolution. Second, the phase characteristics of the ghost differ across the SAR aperture, leading to changes in the ghost location when observed through different smaller subapertures. This same characteristic causes the ghosts to be defocused when employing the full aperture. To reveal the ghost characteristics in SAR images, the full aperture is typically split into small subapertures for separate imaging. The above ghost characteristics across the subaperture images are effectively used for its suppression.

A simple technique for using the variation of the ghost intensity across the subaperture images was proposed in [7]. For each “candidate” target, the variance of the intensity is calculated across the subaperture images. Candidates with high variance are identified as ghosts and are attenuated or suppressed to obtain a ghost-free image. A more sophisticated technique models the intensity variations to distinguish between the targets and the ghosts based on their aspect dependency [8]. However, the target intensity is also a function of its orientation, which is typically unknown. As such, the intensity variation across the various subaperture images can be modeled by a hidden Markov model (HMM), where the hidden states are the possible target orientations. The output of the HMM is the intensity profile $\rho \in \mathbb{R}^M$ of a certain image pixel, where M is the number of subapertures. Training data from known targets is used to estimate the state-transition probabilities, the probability of observing a certain intensity in a given state, and the initial state probabilities. Thus, a specific HMM can be built for each considered target type. For notational brevity, we consider only one target type, denoted by T_1 .

In the testing phase, subaperture images are created from the full aperture image using directional filters. The p th image pixel has a corresponding intensity profile ρ_p , which may or

may not be generated by the T_1 target. The trained HMM is used to evaluate the likelihood that the observed intensity profile is generated by the given target. The likelihood is given by

$$P(\rho_p | T_1) = \sum_{\text{all } q} P(\rho_p | q, T_1) P(q | T_1), \quad (4)$$

where $P(\rho_p | q, T_1)$ is the probability that ρ_p was generated by state sequence q given target T_1 , $P(q | T_1)$ is the probability that state sequence q occurs given target T_1 , and the summation is carried out over all possible state sequences q . If the pixel corresponds to the target, the likelihood should be high, whereas the value should be low if it corresponds to a multipath ghost. The pixel in the ghost-mitigated image is obtained by multiplying the original full aperture image pixel with the obtained likelihood value

$$I(p)^{\text{mitigated}} = P(\rho_p | T_1) I(p).$$

Hence, only targets that fit the considered model with a high likelihood are retained and the ghosts are suppressed. The performance of the approach is illustrated in Figure 4. The ghost is strongly visible in the original image. However, it has been suppressed by about 15 dB in the processed image.

A different class of algorithms exploits the differences in the phase history of the subaperture images [9]. As explained above, the ghost targets exhibit a different phase history when viewed from different aspect angles, which depends on the distance 2δ between the two scattering centers. This is exploited for a SAR image reconstruction scheme that generates a separate image for each assumed δ . The true scatterer positions are then contained in the direct path image with $\delta = 0$. This approach can be combined with a scheme that exploits the drift of ghost targets with aspect angle [10]. Drifting and nondrifting target candidates are separated using the Fourier transform of a subaperture image pair. Nondrifting targets are retained, whereas drifting targets are suppressed. An issue with the described approach is that the phase changes have to be observed over a large number of aspect angles. Hence, a large aperture and antennas with a large azimuth beamwidth are required. This may work against the power constraints of the transmit chain.

One way to overcome the large synthetic aperture constraint is to exploit the nonlinearity in the phase delays of the ghosts directly in the raw data [11]. Under far-field assumptions, real targets exhibit a linear phase shift when viewed from a shifted aperture. In contrast, the ghosts have an additional nonlinear term in the phase history, which can be exploited to cancel multipath returns and obtain a ghost-free image.

All of the aforementioned methods have been mainly developed under the assumption of far-field conditions, which are mostly applicable to airborne platforms. For ground-based systems, the building resides usually in the near-field, and may be observed from different sides. This gives rise to another approach for ghost suppression in TWRI [12]. An image is generated for each vantage point used to interrogate the building

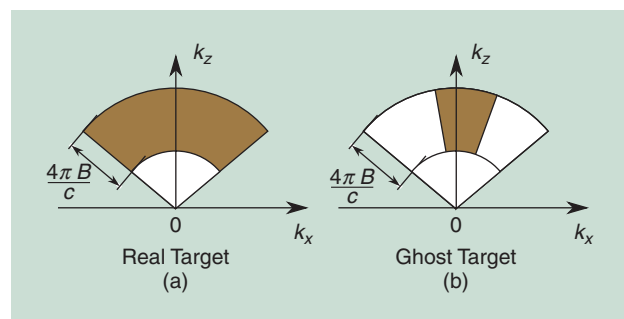


[FIG5] The support angle of SAR echoes in the wavenumber domain. Compared to the real target in (a), the ghost target in (b) exhibits a narrower support. (Figure adapted from [7] and used with permission.)

interior. After image registration, the primary reflections, i.e., the true targets, stay at the same location in all images. However, multipath returns place ghosts at different locations, since the multipath reflection geometry changes with the vantage point. Thus, multiplicative fusion of the registered images retains the overlapping true targets and mitigates the nonoverlapping ghosts. This approach is conceptually similar to [9] and [10]. However, the drifts are much larger as the vantage points have a large separation. We note that, as the secondary specular reflection geometry is a function of the vantage point or aspect angle, the drift-based methods described previously are also applicable to specular multipath cases.

OTHER METHODS FOR MULTIPATH SUPPRESSION

In this section, we briefly discuss multipath suppression methods that do not fit in the aforementioned class of algorithms. One possibility is a colocated MIMO-based approach [13]. In MIMO radar imaging, orthogonal waveforms are transmitted from a transmit array and the scene reflections are received, using a receive array. Exploiting the orthogonality of the transmitted waveforms, the returns can be associated with the respective transmitter. From the propagation model, we know that the angle of departure (AOD) equals the angle of arrival (AOA) for the direct path. However, in the multipath propagation case, particularly so for specular multipath, the transmit and receive paths are different and, consequently, the AOA is different from the AOD. This effect can be exploited by using spatial filtering on the transmit and receive signals. By retaining only the signal components with equal AOA and AOD, the multipath returns can be filtered out. Polarimetric features of the secondary reflections have also been exploited for multipath suppression [14]. Double scattering of the wave may change the polarization characteristics, which can be used to differentiate between targets and ghosts. Finally, even an optimized imaging geometry may help reduce ghosting [15]. If the secondary scatterer is known, the SAR trajectory can be adjusted such that very little energy is contained in the multipath returns.

For extended targets modeled by a number of scattering centers, ghosts can appear on or in the vicinity of the back wall due to target obstructing incident waves from reaching the back walls. This presents a vacuum in the image along the back wall or, if change detection is applied, it creates ghosts, which could be stronger than targets. In this case, ghost mitigation can proceed utilizing the respective interrelated geometry of target and ghosts. Extended targets tend, in general, to produce blurred ghosts beyond those created by point target model.

MULTIPATH EXPLOITATION

Multipath suppression discards the energy contained in the multipath returns to reduce their adverse effects on the image. Since multipath returns ultimately originate from the target, it is prudent to utilize the energy and information contained in such indirect target returns. Proper exploitation of the multipath returns has been shown to lead to higher signal-to-clutter ratio (SCR), higher crossrange resolution, and extended imaging regions.

However, all these imaging enhancements usually come at a price. Multipath exploitation schemes either require prior knowledge of the scattering environment or incur higher computational costs. In the sequel, we categorize multipath exploitation methods according to their multipath resolution requirements.

EXPLOITATION REQUIRING RESOLVED MULTIPATH

For resolved multipath, the radar returns are well separated in fast time and form the target images and their ghosts. This category includes shadow region imaging in indoor settings [18], where information of hidden areas of spatially extended targets, which are not in the line-of-sight of the radar, is obtained by exploiting target-to-target interactions. The proposed multipath exploitation is a two-step procedure. First, a conventional SAR image $I(\cdot)$ is obtained using the radar returns. The scattering centers observed in the conventional SAR image are treated as new sources for the double scattered multipath returns. That is, the scattering centers act as new transmitters that can illuminate the shadow region of the targets. Next, a modified SAR algorithm is employed that assumes double-scattering propagation to obtain an image $I^{\text{double}}(\cdot)$ as

$$I^{\text{double}}(p) = \sum_{p=0}^{P-1} \sum_{n=0}^{N-1} I(p') (y_n(t) * s(-t) |_{t=\tau_{pp'n}}) F(p, p', n), p = 0, \dots, P-1, \quad (5)$$

where $\tau_{pp'n}$ is the round-trip path between the transceiver, the first scattering center at (x_p, z_p) , and the second scattering point at $(x_{p'}, z_{p'})$. The weighting function $F(p, p', n)$ discards an ellipsoidal region surrounding the line-of-sight between the n th antenna location and the p' th first scattering center to reduce the introduction of ghosts at implausible locations [see Figure 6(a)]. Finally, the two images are normalized and superimposed to obtain a composite image, which depicts significantly enhanced visible regions of the targets. For illustration, Figure 6(b) and (c) also show the images $I(\cdot)$ and $I^{\text{double}}(\cdot)$ for a scene containing three targets of circular and rectangular shapes. Clearly, the conventional SAR image has difficulty in imaging the sides of the rectangular target, whereas the modified SAR algorithm can reconstruct the rectangular sides of the target. The main advantage of this algorithm is an extension of the visible target region without the need of prior knowledge of the scene distribution or the surrounding environment.

Following a similar idea, the work in [5] proposed a ghost-mapping approach, wherein the ghosts in the conventional SAR image, resulting from interior wall multipath, are mapped back onto the respective targets to obtain a ghost-free image with improved SCR. Complete knowledge of the room geometry is assumed, especially the locations of the interior walls. Using this prior knowledge, for any target position, the location of the associated ghosts (one for each interior wall) can be predicted. The exploitation scheme works as follows. Using conventional image formation, an image of the scene containing both real targets and ghosts is obtained. Next, for every image pixel (and

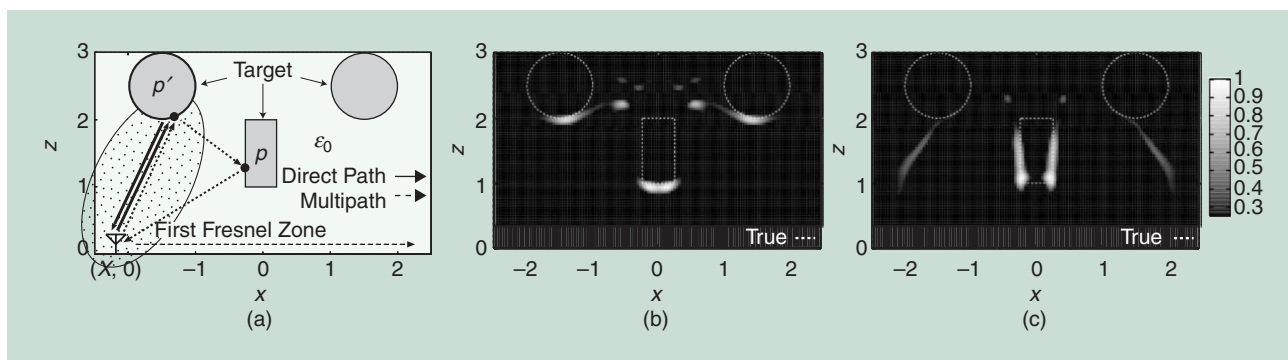


[FIG6] (a) Propagation paths of single- and double-scattered waves. (b) The conventional SAR image. (c) The double scattering image. (Figure adapted from [18] and used with permission.)

possible target location), the energy of the associated ghosts is mapped back onto the target's site. This is achieved by a 2-D convolution with a space-varying kernel $H(p,r)$ that uses the information of the ghost locations

$$I^{\text{mapping}}(p) = \sum_{r=0}^{R-1} |I(p) * H(p,r)|. \quad (6)$$

The weighting and shape of the kernel $H(p,r)$ is chosen such that the full energy of the ghosts is utilized to boost the amplitude of the real target. At the same time, the ghosts are suppressed. Finally, a composite ghost-free image with improved SCR is obtained by a pixel-by-pixel multiplication of the two images. Figure 7 illustrates the result of the multipath exploitation scheme using real data from a scene consisting of a single reflector located between front and back walls. The conventional SAR image in Figure 7(a) shows both the target and the ghost due to multipath, originating from the back wall. The ghost is clearly suppressed in the composite image in Figure 7(b) obtained using the exploitation scheme.

EXPLOITATION WITH UNRESOLVED MULTIPATH

The previously described exploitation methods fail if the multipath returns are not resolvable because they would lead to overlapping targets and ghosts in the conventional SAR image. Such situations may arise when system constraints permit use of limited bandwidth and/or aperture, and in the presence of non-homogeneous front walls. However, using proper modeling of the multipath returns, the additional energy and information therein may still be exploited to obtain an improved scene reconstruction.

If prior knowledge of the surrounding environment is available, i.e., the location and dielectric properties of the walls, a linear inverse scattering scheme based on the PO model may be employed for exploiting multipath from walls and other specular reflectors [20]. Using Kirchhoff's approximation, a linearized scattering equation can be obtained as

$$E_s(u_n, k_0) = \iint_{\Omega} E_i(u_n, x, z, k_0) G(u_n, x, z, k_0) \sigma(x, z) dx dz, \quad (7)$$

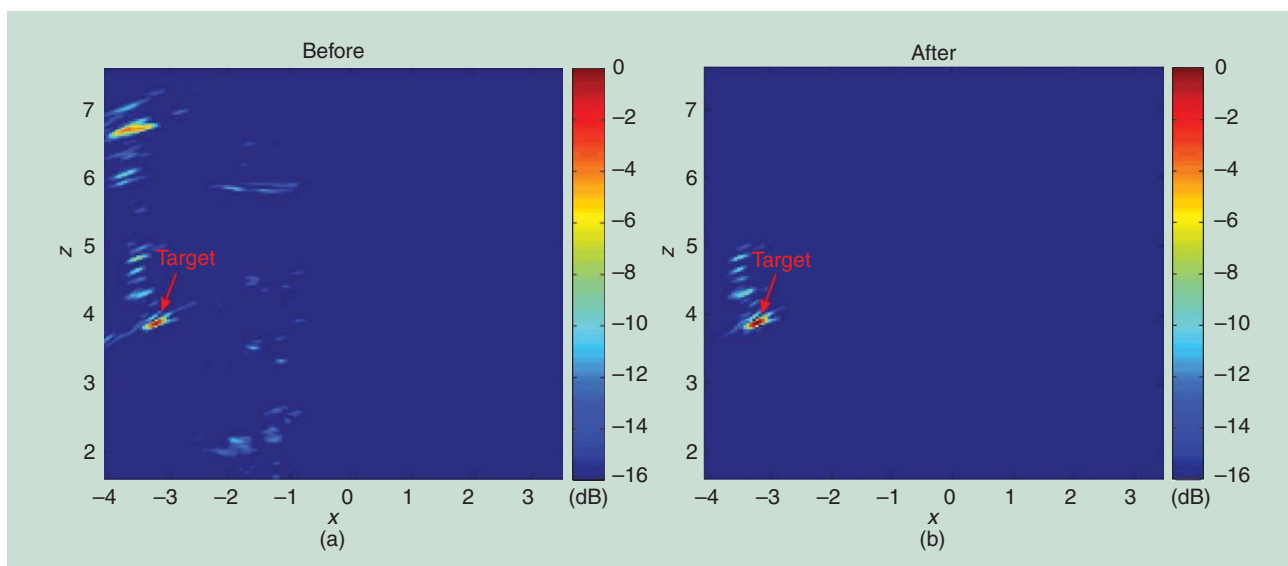


[FIG7] A backprojected image using the (a) conventional- and (b) multipath exploitation-based image formation approaches. (Figure adapted from [5] and used with permission.)

where $E_s(u_n, k_0)$ is the scattered field measured at the n th antenna location, k_0 is the wave number in free space, $E_i(\cdot)$ is the incident field, $G(\cdot)$ is Green's function for the relevant background medium, $\sigma(x, z)$ is the unknown target distribution, and Ω describes the spatial region being interrogated. With prior knowledge of the background scattering environment, Green's function can be calculated analytically or numerically. The incident field can be obtained by the known emitted field of the transmitter and the reflection/refraction properties of the front wall. Discretizing the region of interest Ω , a finite-dimensional equivalent representation of (7) is obtained as

$$E_s = A_{\text{linscat}} \sigma, \quad (8)$$

where E_s is the vectorized measured scattered field, A_{linscat} represents the discretized linear operator in (7), and σ is the discretized and vectorized scattering space. An estimate of σ can be achieved by finding the singular value decomposition of A_{linscat} and inverting only the dominant singular values [20], [27]. Other inversion methods may employ a sparsifying regularization, as in [21]. Sparse reconstruction-based multipath exploitation approaches are described in more detail in the section "Multipath Exploitation/Suppression in Sparse Reconstructions."

A similar method has been proposed to deal with multipath resulting from periodically structured front walls, e.g., cinder-block walls [4]. The propagation through the front wall is modeled analytically and is exploited in the image formation step to utilize the additional beams that are directed toward the target by the Floquet modes of the front wall.

Time-reversal methods [22]–[24] may also be applied to exploit multipath propagation in indoor imaging. The efficiency of this approach was first demonstrated by Fink [28], using acoustic waves and first applied to multipath environments in SAR by Sarabandi et al. [22]. Time-reversal is a two-step procedure. In the first step, the pulse is transmitted into the background scene and reflections are received by an array. This is done to obtain information of the scattering scenario without the target of interest. In the second step, a time reversed received signal is transmitted at the receive array into the scene containing the target of interest. In this way, the transmitted energy is focused at the original transmitter location. By using this scheme, the information of the scattering environment can be used to improve the effective array aperture. It should be noted that if the scattering environment is known a priori, the first transmit receive cycle can be executed via a simulation, thereby overcoming the otherwise limiting constraint of background scene access.

MULTIPATH EXPLOITATION/SUPPRESSION IN SPARSE RECONSTRUCTIONS

Sparse signal representation has been used successfully for solving SAR image formation problems in a variety of applications [29]. This framework is based on the observation that typical underlying scenes usually exhibit sparsity in terms of certain features, such as scene reflectivity.

Sparse representation was first employed for imaging of building interiors in [30]. As only a few targets usually reside in the room, the complex amplitude of the image can be sparsely represented. The measurement model, motivated by the ray-tracing formulation of (1), is given by

$$y = A \sigma, \quad (9)$$

where y is the stacked vector representing the measurements from all N array element locations, σ is the sparse vectorized image of the scene, and the matrix A is the dictionary of the radar responses under the assumed single-scattering-based point-target model. The scene image can be reconstructed using the basis pursuit denoising (BPDN) as follows:

$$\hat{\sigma} = \min_{\sigma} \frac{1}{2} \|A\sigma - y\|_2^2 + \lambda \|\sigma\|_1, \quad (10)$$

where λ is a regularization parameter which provides a tradeoff between fidelity to measurements and noise tolerance. BPDN is a regularized least-squares solution that favors sparse results. Other reconstruction methods use greedy approaches to build the solution iteratively. Optionally, a downsampling of the measurements in (9) can be done to reduce the amount of data. However, special care has to be taken to ensure incoherence of the sampling matrix and the dictionary to guarantee reliable recovery.

The sparse reconstruction approach for indoor images has been extended to exploit both the interior wall and wall ringing multipath returns in [19] under the assumption of prior knowledge of building layout. Using a discretized version of the ray-tracing signal model in (2) and assuming knowledge of the building layout, the measurement vector y can be expressed as a superposition of individual linear models for each of the R propagation paths

$$y = A^{(0)} \sigma^{(0)} + A^{(1)} \sigma^{(1)} + \dots + A^{(R-1)} \sigma^{(R-1)}, \quad (11)$$

where $\sigma^{(r)}$ is the vectorized image of the scene corresponding to the r th path and $A^{(r)}$ is the dictionary that embodies the GO propagation model for the r th path. Next, a stacked signal model is formed

$$y = \tilde{A} \tilde{\sigma}, \quad (12)$$

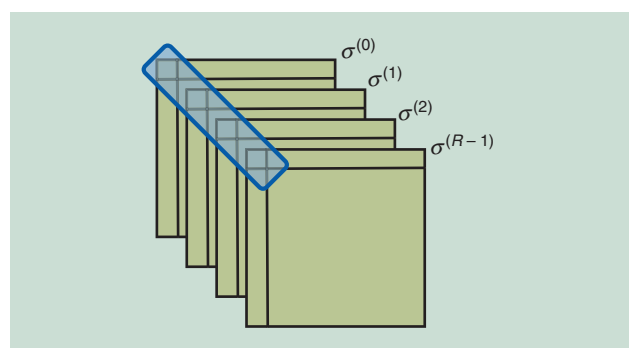


[FIG8] The group sparse structure for the subimages.

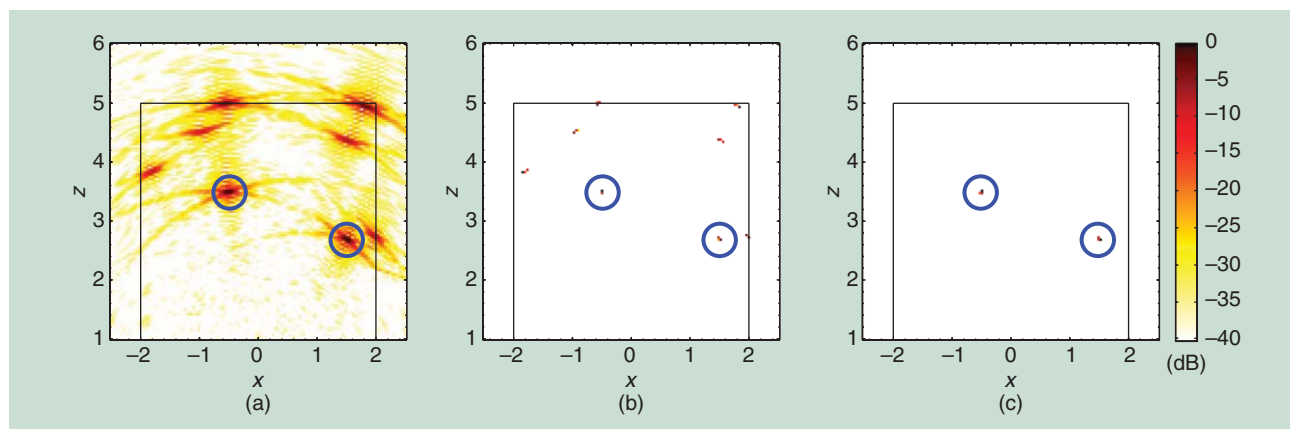


[FIG9] Backprojected image using the (a) full data, along with (b) conventional- and (c) multipath exploitation-based sparse reconstruction results. The sparse reconstruction used undersampled data, specifically, one-fourth of the array elements and one-eighth of the frequencies. (Figure adapted and used with permission from [31].)

with a combined dictionary $\tilde{A} = [A^{(0)} A^{(1)} \dots A^{(R-1)}]$ and stacked image vectors $\tilde{\sigma} = [(\sigma^{(0)})^T (\sigma^{(1)})^T \dots (\sigma^{(R-1)})^T]^T$.

The vector $\tilde{\sigma}$ can be estimated by exploiting the common support property of the R sparse images. This property stems from the fact that the images $\sigma^{(0)}, \dots, \sigma^{(R-1)}$ describe the same underlying scene. That is, if a certain element in, e.g., $\sigma^{(0)}$ has a nonzero value, the corresponding elements in the other images should be also nonzero.

This means that corresponding pixels in the image vectors should be grouped, as shown in Figure 8, necessitating a group sparse reconstruction approach

$$\hat{\tilde{\sigma}} = \arg \min_{\tilde{\sigma}} \frac{1}{2} \|\mathbf{y} - \tilde{A}\tilde{\sigma}\|_2^2 + \lambda \|\tilde{\sigma}\|_{2,1}, \quad (13)$$

where

$$\begin{aligned} \|\tilde{\sigma}\|_{2,1} &= \sum_{p=0}^{P-1} \|[\sigma_p^{(0)}, \sigma_p^{(1)}, \dots, \sigma_p^{(R-1)}]^T\|_2 \\ &= \sum_{p=0}^{P-1} \sqrt{\sum_{r=0}^{R-1} \sigma_p^{(r)} (\sigma_p^{(r)})^*}. \end{aligned} \quad (14)$$

The mixed-norm term in the regularizer ensures the group structure in the sparse reconstruction result. Finally, the reconstruction results for the individual paths are combined noncoherently to obtain an overall image with suppressed ghost targets and improved SCR; see Figure 9. Data undersampling can precede the sparse reconstruction in this approach as well.

An alternate approach for sparsity-based scene reconstruction in the presence of multipath has been proposed in [16]. The authors assume a convolutive model for multipath, wherein the echo waveform at each receiver is modeled as the superposition of the direct impulse response and the multipath impulse response for P targets convolved with the transmitted pulse waveform s

$$\mathbf{y}_p = \sum_{p=0}^{P-1} s * (\mathbf{g}_p + \mathbf{d}_p * \mathbf{g}_p). \quad (15)$$

The direct impulse response \mathbf{g}_p is assumed to be a single spike and stronger than the indirect returns. The multipath impulse response is the convolution of the direct impulse response \mathbf{g}_p with a sparse delay vector \mathbf{d}_p . The multipath delays for a particular target are assumed constant across the receivers. Using the above model, an iterative greedy sparse reconstruction approach is proposed by the authors to estimate the unknown impulse responses \mathbf{g}_p and delay vectors \mathbf{d}_p . The estimated direct impulse responses are then used to form a ghost-free image. The method performs well, especially in the case of wall ringing multipath. The advantage of this approach lies in the fact that no prior knowledge is needed. However, the additional energy in the multipath returns is suppressed rather than exploited for image formation.

CONCLUSIONS

We have considered the problem of imaging building interiors using SAR. The emerging TWRI technology has experienced a rising interest over the last decade due to its numerous civil and military applications. We have presented an overview of different approaches to deal with multipath in indoor radar imaging scenarios. Multipath mitigation and exploitation are key to obtaining reliable information when many and/or strong secondary scatterers are present in the scene of interest. We have provided a balanced and complete account of existing methods and discussed their respective advantages and disadvantages. Both conventional beamforming and compressive sensing-based methods have been presented, where the latter assume the underlying scene to be sparse. We bridged analysis with supporting simulation and experimental examples.

AUTHORS

Michael Leigsnering (leigsnering@spg.tu-darmstadt.de) received the Dipl.-Ing. degree in electrical engineering and information technology (summa cum laude) from Technische Universität Darmstadt in 2010. He is currently working toward his Ph.D. degree in the Signal Processing Group, Institute of Telecommunications, Technische Universität Darmstadt. His research interest lies in array

signal processing with a focus on through-the-wall radar imaging, compressive sensing, and multipath phenomena. He was a visiting research associate at the Center for Advanced Communications, Villanova University, Pennsylvania, in 2012 and 2013.

Moeness G. Amin (moeness.amin@villanova.edu) received the Ph.D. degree in 1984 from the University of Colorado, Boulder. He has been on the faculty of the Department of Electrical and Computer Engineering at Villanova University since 1985, where he is now a professor and the director of the Center for Advanced Communications. He is a Fellow of the IEEE, the International Society for Optical Engineering, and the Institute of Engineering and Technology. He received the IEEE Third Millennium Medal and the EURASIP Individual Technical Achievement Award. He was a Distinguished Lecturer of the IEEE Signal Processing Society. He has over 600 publications in the field of signal and array processing, including radar imaging. He is a recipient of eight Best Paper Awards. He serves on the editorial boards of *IEEE Signal Processing Magazine* and EURASIP's journal, *Signal Processing*.

Fauzia Ahmad (fauzia.ahmad@villanova.edu) received the M.S. and Ph.D. degrees in electrical engineering, both from the University of Pennsylvania, Philadelphia, in 1996 and 1997, respectively. Since 2002, she has been with the Center for Advanced Communications, Villanova University, Pennsylvania, where she is a research professor and the director of the Radar Imaging Lab. She has over 130 publications in the areas of radar imaging, radar signal processing, compressive sensing, array signal processing, waveform design and diversity, ultrasound imaging, and over-the-horizon radar. She is a Senior Member of the IEEE and the International Society for Optical Engineering (SPIE). She serves on the editorial boards of *IET Radar, Sonar, & Navigation* and the SPIE/IS&T *Journal of Electronic Imaging*.

Abdelhak M. Zoubir (zoubir@spg.tu-darmstadt.de) received his Dr.-Ing. degree from Ruhr-Universität Bochum, Germany. He was with Queensland University of Technology, Australia, from 1992 to 1998. He then joined Curtin University of Technology, Australia, as a professor of telecommunications and was interim head of the School of Electrical and Computer Engineering from 2001 to 2003. Since 2003, he has been a professor of signal processing at Technische Universität Darmstadt, Germany. He is an IEEE Distinguished Lecturer (Class of 2010–2011), past chair of the IEEE Signal Processing Society's Signal Processing Theory and Methods Technical Committee, and the current editor-in-chief of *IEEE Signal Processing Magazine*. His research interest lies in statistical methods for signal processing applied to telecommunications, radar, sonar, car engine monitoring, and biomedicine. He has published over 300 papers in these areas. He is a Fellow of the IEEE.

REFERENCES

- [1] M. Amin and F. Ahmad, "Wideband synthetic aperture beamforming for through-the-wall imaging [lecture notes]," *IEEE Signal Processing Mag.*, vol. 25, no. 4, pp. 110–113, July 2008.
- [2] M. Amin, Ed., *Through-the-Wall Radar Imaging*. Boca Raton, FL: CRC Press, 2010.
- [3] T. Dogaru and C. Le, "SAR images of rooms and buildings based on FDTD computer models," *IEEE Trans. Geosci. Remote Sensing*, vol. 47, no. 5, pp. 1388–1401, May 2009.

- [4] R. Burkholder, "Electromagnetic models for exploiting multi-path propagation in through-wall radar imaging," in *Proc. Int. Conf. Electromagnetics in Advanced Applications*, Torino, Italy, Sept. 2009, pp. 572–575.
- [5] P. Setlur, M. Amin, and F. Ahmad, "Multipath model and exploitation in through-the-wall and urban radar sensing," *IEEE Trans. Geosci. Remote Sensing*, vol. 49, no. 10, pp. 4021–4034, Oct. 2011.
- [6] E. J. Baranoski, *Multipath Exploitation Radar Industry Day*. Herndon, VA: DARPA, 2007.
- [7] W. Liang, H. Xiaotao, Z. Zhimin, and S. Qian, "Research on UWB SAR image formation with suppressing multipath ghosts," in *Proc. CIE Int. Conf. Radar*, Shanghai, China, Oct. 2006, pp. 1–3.
- [8] Q. Tan and Y. Song, "A new method for multipath interference suppression in through-the-wall UWB radar imaging," in *Proc. Int. Conf. Advanced Computer Control (ICACC)*, Shenyang, China, Mar. 2010, vol. 5, pp. 535–540.
- [9] D. Garren, "SAR image formation uncorrupted by multiple-bounce artifacts," in *Proc. IEEE Radar Conf.*, Long Beach, USA, Apr. 2002, pp. 338–343.
- [10] D. Obuchon, D. Garren, J. S. Goldstein, R. Greene, and J. North, "Drift inversion estimation of multipath ghosts in SAR image reconstruction," in *Proc. IEEE Radar Conf.*, Philadelphia, PA, Apr. 2004, pp. 556–558.
- [11] J. DeLaurentis, "Multipath synthetic aperture radar imaging," *IET Radar, Sonar Navig.*, vol. 5, no. 5, pp. 561–572, June 2011.
- [12] F. Ahmad and M. Amin, "Multi-location wideband synthetic aperture imaging for urban sensing applications," *J. Franklin Inst.*, vol. 345, no. 6, pp. 618–639, Sept. 2008.
- [13] L. Li and J. Krolik, "Vehicular MIMO SAR imaging in multipath environments," in *Proc. IEEE Radar Conf.*, Kansas City, USA, May 2011, pp. 989–994.
- [14] D. B. André, R. D. Hill, and C. P. Moate, "Multipath simulation and removal from SAR imagery," in *Proc. SPIE 6970, Algorithms for Synthetic Aperture Radar Imagery XV*, Apr. 2008, p. 69700M.
- [15] A. O. Knapkog, "Moving targets and multipath in sar images of harbour scenes," in *Proc. European Conf. Synthetic Aperture Radar (EUSAR)*, Nuremberg, Germany, Apr. 2012, pp. 547–550.
- [16] H. Mansour and D. Liu, "Blind multi-path elimination by sparse inversion in through-the-wall-imaging," in *Proc. IEEE Int. Workshop Computational Advances Multi-Sensor Adaptive Processing (CAMSAP)*, Saint Martin, Dec. 2013, pp. 256–259.
- [17] R. Price and P. Green, "A communication technique for multipath channels," *Proc. IRE*, vol. 46, no. 3, pp. 555–570, Mar. 1958.
- [18] S. Kidera, T. Sakamoto, and T. Sato, "Extended imaging algorithm based on aperture synthesis with double-scattered waves for UWB radars," *IEEE Trans. Geosci. Remote Sensing*, vol. 49, no. 12, pp. 5128–5139, Dec. 2011.
- [19] M. Leigsnering, F. Ahmad, M. Amin, and A. Zoubir, "Multipath exploitation in through-the-wall radar imaging using sparse reconstruction," *IEEE Trans. Aerosp. Electron. Syst.*, to be published.
- [20] G. Gennarelli and F. Soldovieri, "A linear inverse scattering algorithm for radar imaging in multipath environments," *IEEE Geosci. Remote Sensing Lett.*, vol. 10, no. 5, pp. 1085–1089, Sept. 2013.
- [21] G. Gennarelli, I. Catapano, and F. Soldovieri, "RF/microwave imaging of sparse targets in urban areas," *IEEE Antennas Wireless Propag. Lett.*, vol. 12, pp. 643–646, May 2013.
- [22] K. Sarabandi, I. Koh, and M. Casciato, "Demonstration of time reversal methods in a multi-path environment," in *Proc. IEEE Antennas Propagation Society Int. Symp.*, Monterey, USA, June 2004, Vol. 4, pp. 4436–4439.
- [23] J. M. F. Moura and Y. Jin, "Time reversal imaging by adaptive interference canceling," *IEEE Trans. Signal Processing*, vol. 56, no. 1, pp. 233–247, Jan. 2008.
- [24] W. Zheng, Z. Zhao, and Z.-P. Nie, "Application of TRM in the UWB through wall radar," *Prog. Electromagn. Res.*, vol. 87, pp. 279–296, 2008.
- [25] K. J. Langenberg, M. Brandfaß, K. Mayer, T. Kreutter, A. Brüll, P. Fellingner, and D. Huo, "Principles of microwave imaging and inverse scattering," *EARSel Adv. Remote Sens.*, vol. 2, no. 1, pp. 163–186, 1993.
- [26] F. Soldovieri and R. Solimene, "Through-wall imaging via a linear inverse scattering algorithm," *IEEE Geosci. Remote Sensing Lett.*, vol. 4, no. 4, pp. 513–517, 2007.
- [27] R. Solimene, F. Soldovieri, G. Prisco, and R. Pierri, "Three-dimensional through-wall imaging under ambiguous wall parameters," *IEEE Trans. Geosci. Remote Sensing*, vol. 47, no. 5, pp. 1310–1317, Mar. 2009.
- [28] M. Fink, "Time-reversal mirrors," *J. Phys. D*, vol. 26, no. 9, p. 1333, 1993.
- [29] L. Potter, E. Ertin, J. Parker, and M. Cetin, "Sparsity and compressed sensing in radar imaging," *Proc. IEEE*, vol. 98, no. 6, pp. 1006–1020, June 2010.
- [30] Y.-S. Yoon and M. Amin, "Compressed sensing technique for high-resolution radar imaging," in *Proc. SPIE Signal Processing, Sensor Fusion, Target Recognition XVII*, Orlando, FL, Mar. 2008, vol. 6968, no. 1, p. 69681A.
- [31] M. Leigsnering, F. Ahmad, M. Amin, and A. Zoubir, "Compressive sensing based specular multipath exploitation for through-the-wall radar imaging," in *Proc. IEEE Int. Conf. Acoustics, Speech, and Signal Processing (ICASSP)*, Vancouver, Canada, May 2013, pp. 6004–6008.

[Dimitris G. Manolakis, Steven E. Golowich, and Robert S. DiPietro]



Long-Wave Infrared Hyperspectral Remote Sensing of Chemical Clouds

[A focus on signal processing approaches]

Many military and civilian applications depend on the ability to remotely sense chemical agent (CA) clouds, from detecting small but lethal concentrations of chemical warfare agents (CWAs) to mapping plumes in the aftermath of natural disasters. Hyperspectral imaging sensors, in the long-wave infrared (IR) (LWIR) part of the spectrum, are particularly well suited for these gas-sensing tasks. Their wide fields of view allow many square kilometers to be imaged almost simultaneously, and their high spectral resolutions often allow the detection of chemical clouds even when they are optically thin (or nearly transparent).

In this review article, we focus on the signal processing approaches necessary to achieve the three main tasks of gas-phase remote sensing: detection of a plume, identification of its constituent gases, and quantification of the amounts present. We start with a tutorial introduction to the radiance phenomenology that drives the models on which exploitation algorithms are based. Next, we identify the fundamental aspects of the data-exploitation problem, develop algorithms that can successfully exploit data from many different sensors, and discuss the many challenges that remain open to the signal processing community. We present results using real hyperspectral data sets whenever possible.

INTRODUCTION

Spectroscopy, the study of the interaction between matter and radiated energy, originated with the study of visible light dispersed according to wavelength by a prism. IR spectroscopy is based on measurement of radiation, absorbed or emitted by a sample, as a function of the

Digital Object Identifier 10.1109/MSP.2013.2294804

Date of publication: 13 June 2014



IMAGE LICENSED BY INGRAM PUBLISHING



WIKIMEDIA COMMONS

wavelength in the IR region of the electromagnetic spectrum (0.75–14 μm). Hyperspectral sensors are essentially spectrometers that measure the distribution of radiation in the IR region using a large number (typically more than 100) of contiguous narrow spectral bands [1].

Some sensors measure the spectrum of the entire scene in their field of view. Such single-pixel sensors can be used to collect multiple spectra by scanning a region to build an image or by staring at the same point to obtain a time-series of spectra. In contrast, hyperspectral imaging sensors divide the field of view into a rectangular grid of pixels and almost simultaneously measure the spectrum of each pixel. As a result, they produce a data cube with two spatial dimensions and one spectral dimension. Hyperspectral sensors can be deployed on satellites, unmanned aerial vehicles, and ground-based platforms (see Figure 1). The choice of a specific platform, however, imposes crucial constraints on the design and performance of the sensor.

Standoff detection of chemical clouds is necessary when physical separation is required for convenience or to put people and assets outside the zone of severe risk. An important class of standoff sensors for chemical clouds is based on the principles of passive IR spectroscopy. Such sensors use passive imaging spectroscopy in the LWIR atmospheric window (8–14 μm). For passive IR detectors, sunlight and the earth's thermal emission provide the illuminating source. In the LWIR region, thermal emission from the ground is far stronger than reflected sunlight. Thus, LWIR spectroscopy provides day and night capability for remote chemical detection applications. The LWIR region is also well suited for gas-sensing applications because:

- A wide range of chemical compounds have unique identifying spectral signatures in the LWIR region. This is illustrated in Figure 2, which shows the spectral signature of ammonia.
- The atmosphere is relatively transparent within the LWIR window. This is also illustrated in Figure 2, which shows the atmospheric transmittance as a function of wavelength.

The objective of a standoff sensor is to determine the presence of a chemical cloud in its field of view and provide information for its identification and quantification. From a signal processing point of view, the goal is to develop algorithms to detect, identify, and quantify chemical gases using mathematical methodologies that address the physics of the problem, operational environment, characteristics of the sensor hardware, and user requirements.



[FIG1] Standoff hyperspectral sensors can be deployed on satellites, unmanned aerial vehicles, and ground-based platforms.

[TABLE1] OPERATIONAL AND SIGNAL PROCESSING ALGORITHM OBJECTIVES OF AN AUTOMATED STANDOFF CHEMICAL GAS-DETECTION SYSTEM.**OPERATIONAL OBJECTIVES**

IS AN AGENT CLOUD PRESENT?
WHICH AGENT?
HOW MUCH MATERIAL WAS RELEASED?
WHERE IS THE CLOUD HEADED?

ALGORITHMIC OBJECTIVES

DETECT CHEMICAL CLOUD
IDENTIFY CHEMICAL FROM LIBRARY
ESTIMATE CLOUD SHAPE AND STRENGTH OF CHEMICAL
TRACK CHEMICAL CLOUD

When IR radiation passes through a chemical cloud, its spectral composition is modified by the transmittance of the cloud, which in turn depends on the spectral signature of the gas. All practical data exploitation algorithms exploit the differences between radiation reaching the sensor directly or through the cloud.

When there is no plume in the sensor's field of view, the observed signal consists of detector noise and the radiation from the surrounding background, which is called *background clutter* or simply *clutter*. The presence of unwanted detector noise and background clutter complicates the sensing of chemical clouds. Noise, which can usually be reduced by better sensor design, sets the limit for performance. Background clutter can often be reduced by appropriate signal processing to reach, at best, noise-limited performance.

The basic operational objectives of a chemical-cloud detection system are summarized in Table 1. Figure 3 shows the fundamental signal processing operations required to address

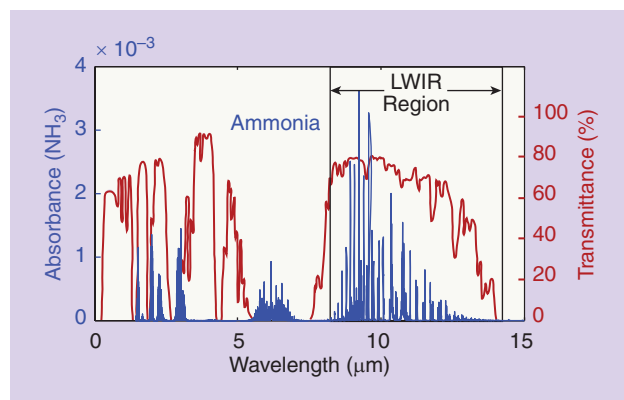


[FIG2] A wide range of chemical compounds, such as ammonia, have unique identifying spectral signatures in the LWIR region (8–13 μm). The atmospheric transmittance function shows the presence of an atmospheric window in the LWIR from 8 to 13 μm .

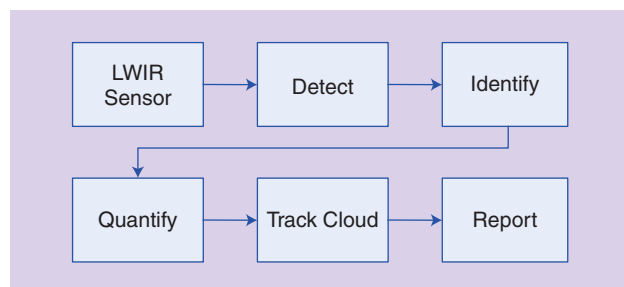


[FIG3] The fundamental signal processing functions of an automated standoff chemical cloud detection system.

the operational objectives in an automated fashion. Although many of these operations can be addressed by existing signal processing techniques, the complex interactions between the properties of the plume, atmosphere, and background pose challenges that are unique to the LWIR problem. In particular, the relative temperatures

of these three components, and variations thereof, can have a profound impact on the at-sensor radiance, while the nonlinear nature of the interactions can be both a help and a hindrance to inference algorithms. Understanding and appreciating such challenges is necessary to properly apply existing tools and develop new algorithms that enable the next generation of applications, such as real-time operation, exploitation of a greater variety of sensor geometries, and tomographic plume reconstruction.

APPLICATIONS

The list of applications of standoff hyperspectral imaging for chemical gas sensing is long and growing. Here, we provide a sampling of some of the major ways in which this technology is employed.

ENVIRONMENTAL MONITORING

Many gaseous pollutants, as emitted by industrial and other sources, exhibit strong LWIR signatures that lend themselves well to passive monitoring [2]. This option has many advantages over in situ monitoring, most prominently the ability to survey wide areas rapidly and remotely, eliminating the need for site access. Such monitoring may be carried out either with a ground-based sensor with a horizontal viewing geometry or from an aircraft passing over the scene under study.

A comprehensive study of the down-looking airborne scenario was carried out in [3] and [4], in which effluent gases from industrial emission stacks were imaged with the Aerospace Spatially Enhanced Broadband Array Spectrograph System (SEBASS) sensor [5]. A study [6] by the Environmental Protection Agency (EPA), using the University of Hawaii's Airborne Hyperspectral Imager (AHI) sensor [7], demonstrated the detection and identification of a number of hazardous emissions from petrochemical plants and other facilities. The side-looking geometry, with the ground-based Scanning IR Gas Imaging System (SIGIS) sensor [8], [9], was used in [10] to map the dispersion of a sulfur dioxide plume emitted from an oil-fired power plant under various atmospheric conditions. Similar side-looking geometries were employed in [11] and [12] using the Telops FIRST and Hyper-Cam sensors [13].

EMERGENCY RESPONSE

Natural and man-made disasters can result in the release of hazardous chemical vapors into the atmosphere. In such situations, the rapid assessment of the types and quantities of such plumes is crucial for the protection of both first responders and local residents. The EPA has been operating an always-on-call airborne system for this purpose for the past decade [14], [15]. The system employs two imagers that operate in the midwave IR (MWIR) and

LWIR atmospheric windows; a multispectral scanner for plume detection over wide areas, and a cued hyperspectral spectrometer to measure high-spectral resolution radiances from specific plume locations. These latter spectra are used for gas identification and quantification. A special-purpose spectral library tailored for this application has been developed [16]. The system has been flown operationally on many missions in response to accidents, fires, and natural disasters, including Hurricanes Katrina and Rita [17]. A ground-based system has been developed for similar purposes by the Hamburg University of Technology [18].

CHEMICAL WARFARE THREAT MITIGATION

The remote detection of CWAs and toxic industrial chemicals is of great importance for the protection of both civilian and military personnel and has been studied for more than 30 years. A great variety of deployment scenarios exist, including stationary ground-based sensors for the protection of fixed targets, ground vehicle deployments for mobile reconnaissance, and airborne missions to cover wide areas. The goals of such sensors are to detect possible threats, identify any constituent gases as belonging to a library of known agents, quantify the amount of gas present, and dynamically map the location of the plume, all with sufficiently low latency to allow responsive action to be taken. Wide-area sensors may also be used to locate CWA production facilities by the detection of fugitive emissions. Some of the sensors that have been developed to address these threats are described in the section “Imaging Spectrometers.”

EARTH SCIENCE

The applications of remote imaging spectrometry in the earth and planetary sciences are vast in scope, and we mention just two directions enabled by recent advances in LWIR imaging technology.

The monitoring of volcanic emissions is important for public health and environmental studies as they can have substantial effects on local and global atmospheric chemistry. The use of hyperspectral imagers for this purpose has been demonstrated with the AHI sensor flying over the Kilauea volcano [19] and by the SIGIS ground-based system viewing the Popocatepetl volcano [20].

Another promise of imaging spectrometry is the mapping of surface mineral composition. This area is most developed in the visible and near-IR/short-wave IR (VNIR/SWIR) window, in which the spectral signatures are dominated by electronic processes. The LWIR regime, by contrast, provides sensitivity to vibrational processes, and some minerals, mainly silicates and carbonates, have characteristic features in this range. Most work in this area has used multispectral radiometers, e.g., the orbital Advanced Spaceborne Thermal Emission and Reflection Radiometer (ASTER) sensor [21], but increased spectral resolution offers the possibility of much finer mineral classification. The SEBASS sensor has been successfully used to explore these applications [22], [23].

IMAGING SPECTROMETERS

The fundamental function of a hyperspectral imaging sensor, also known as an *imaging spectrometer*, is to measure the spectrum

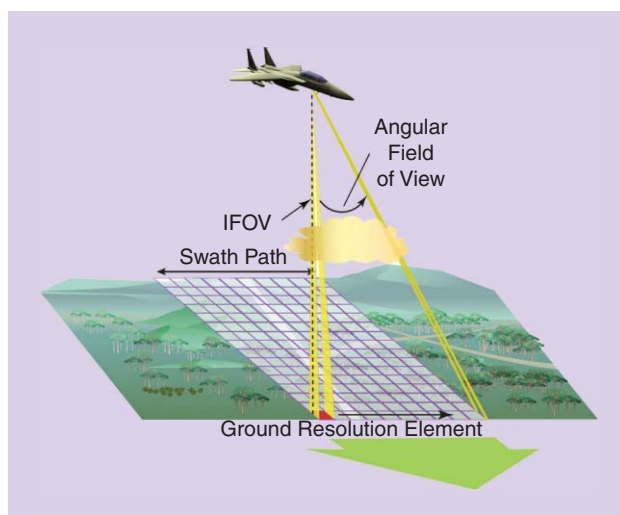


[FIG4] An illustration of basic ideas for a whisk broom hyperspectral remote sensing system.

of each picture element in the field of view of the sensor. Therefore, at least in principle, hyperspectral sensors consist of an optical system, an image scanning mechanism, and a spectrometer.

The optical system collects the radiation originating from some ground surface area and focuses the intercepted rays onto the surface of a detector element as shown in Figure 4. The area of the detector projected through the system's optics onto the earth's surface coincides with the ground resolution element.

The solid angle, through which radiation originating from the ground is accepted by the optical system and reaches the detector, is called the detector's *instantaneous field of view (IFOV)*. The IFOV is determined by the focal length of the optical system and the size of the detector. Because the IFOV subtends an area of the terrain equal to the ground resolution element, the combined detector–optics system functions as a spatial sampler with sampling area $\Delta x \times \Delta y$. Typically, the ground resolution element is square and the quantity $\Delta x = \Delta y$ is known as *ground-sample distance*.

At any instant of time, the sensor sees the energy within its IFOV. The sensor stares at a ground resolution element and collects photons for a time interval known as *residence* or *dwell time*. The energy measured within the IFOV is a weighted average of the energy reflected or emitted from all materials within this circular area. Because averaging is done by integration, the dwell time is also known as *integration time*. The weighting function, which is known as the *point spread function (PSF)* of the sensor, extends beyond the area of a ground resolution element. In practical systems, the PSF accounts for optical, motion, and detector-size effects. Each ground resolution element is mapped onto one pixel of the image created by proper scanning of the surface by the sensor.

In a whisk broom system, the optical system, with the help of a rotating mirror and the forward motion of the sensor platform, scans the surface to collect a two-dimensional (2-D) grid of pixels. The angular field of view is that portion of the mirror sweep,

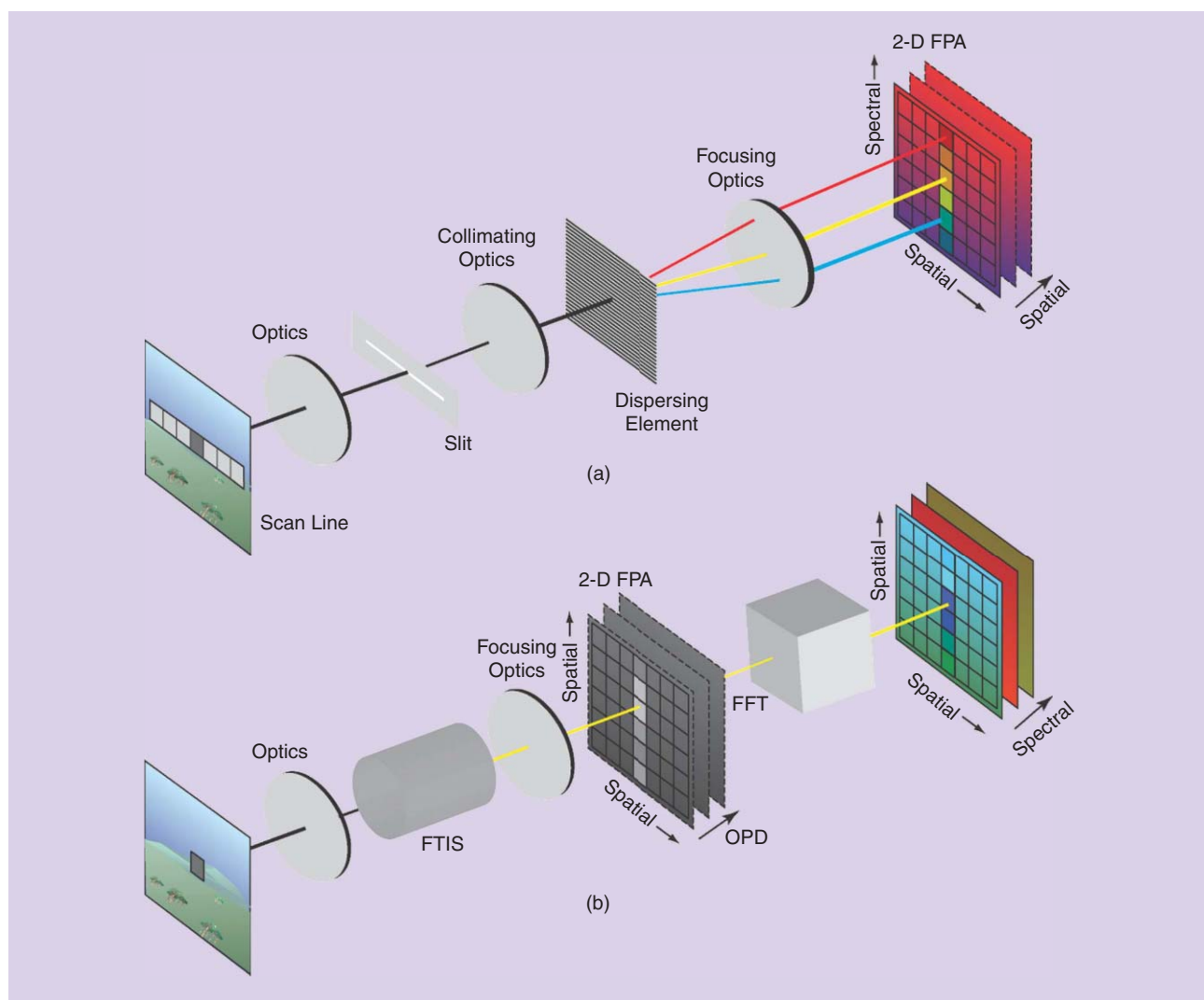


[FIG5] Types of imaging spectrometers. (a) A “push broom type” imaging spectrometer using a dispersive element. The spectra of all pixels in the scan line are measured simultaneously. (b) “Step-stare” FTIS. The interferogram of all pixels in the field of view is computed simultaneously for each optical path difference (OPD). The image cube is the Fourier transform of the interferogram cube along the spectral dimension.

measured in degrees, that is recorded as a scan line. The angular field of view and the altitude of the sensor determine the ground swath, which is the width of the terrain strip represented by the image. The radiance within the IFOV is passed onto a spectrometer that measures the spectrum of the pixel.

In a push broom system, there is a dedicated column of spectral detector elements for each cross-track pixel in the scene, which increases the dwell time (time-on-pixel) to the interval required to move one IFOV along the flight direction. The result is usually more accurate measurements because there is no moving mirror and the detector has more time to collect radiation from the ground resolution element. A step-stare Fourier-transform imaging spectrometer (FTIS) simultaneously measures the spectra of each pixel in a 2-D array of pixels, which itself may or may not be scanned.

For aircraft or spaceborne instruments like the ones illustrated in Figure 4, the motion of the platform usually provides

one of the scanning directions. Yet, for fixed site operation (such as tripod or mast-mounted instruments), either an FTIS must be employed or a scanning mechanism must be provided to build the required spatial dimensions. Measuring the spectrum of each ground resolution element requires a spectrometer. There are three types of imaging spectrometers.

In prism spectrometers, the light passing through the prism is refracted over an area as a function of wavelength. Spectral sampling is achieved by detectors placed at proper locations to collect the components from a given spectral band and measure their radiance.

In grating spectrometers, the discontinuities on the grating surface redirect the incident radiation at an angle dependent on the wavelength. Because frequencies ($\nu = c/\lambda$) of integer multiple of each other are redirected in the same direction, it is necessary to use order-sorting filters to choose only the radiation of the frequency of interest.

In Fourier transform spectrometers, the incident radiation is split into two beams whose optical paths are varied differentially and recombined to allow interference. Fourier transform spectroscopy consists of two processes: the first, experimental, is the measurement of an autocorrelation function called the interferogram using a Michelson interferometer; the second, mathematical, is the computation of the spectrum from the interferogram. Spectral resolution is determined by the length of the measured interferogram.

Prism and grating spectrometers [see Figure 5(a)] measure the spectrum directly in the frequency domain. In contrast, Fourier transform spectrometers [see Figure 5(b)] measure the spectrum indirectly by computing the Fourier transform of the physically measured interferogram. However, every spectrometer is characterized by its spectral resolution and the spanned spectral range. Spectral sampling is specified by the center wavelength and the width of each band (bandwidth or spectral resolution). The number of bands and their locations in the spectrum, expressed as wavelengths or frequencies specify the spectral response of the sensor.

The ground-based SEBASS (GBSS) [24] is a prism-based push broom imaging spectrometer with an IFOV of 1.1 mrad per pixel and spectral range of 7.8–13.4 μm . The focal plane array (FPA) is 128×128 and measures the spectrum of 128 pixels in 128 spectral bands. The entrance slit is aligned vertically and a large servo motor is used to do azimuth scanning.

The Telops FIRST imaging spectrometer [13] is a step-stare Michelson interferometer with spectral range of 8–12 μm , variable spectral resolution of 0.25–150 cm^{-1} , and optimum resolution 4 cm^{-1} . The sensor uses a 320×256 pixel FPA with an IFOV of 0.35 mrad.

The Joint Services Lightweight Standoff Chemical Agent Detector (JSLSCAD) [25] uses a 2-D scanning Michelson interferometer with a single detector element and a 1.5° IFOV. JSLSCAD, which has a spectral range of 7–14 μm , operates in a search mode with a spectral resolution of 16 cm^{-1} and an interrogation mode with a spectral resolution of 4 cm^{-1} .

Imaging spectrometers take indirect measurements of physical parameters in the sense that the output digital numbers are proportional to the incoming photon energy but they are not measured in any physically meaningful unit. The process of converting digital numbers into at-sensor spectral radiance is known as *radiometric calibration*. Conversion of at-sensor radiance to emissivity, which is a more complicated process, is discussed in the section “Signals, Distortions, and Clutter.”

AT-SENSOR RADIANCE SIGNAL MODELS

In this section, we explain the physical basis for gas detection with passive LWIR sensors. The radiance reaching the detector can often be modeled well using radiative transfer theory with three parallel atmospheric layers orthogonal to the line of sight of the sensor. The first layer extends from behind the plume to the background, the second layer is the plume itself, and the third layer is the atmosphere between the plume and the sensor. Each layer attenuates the radiation that passes through it and

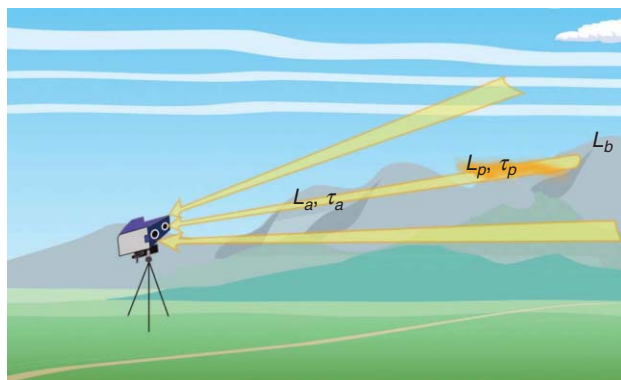


[FIG6] A pictorial representation of a three-layer side-looking radiative transfer signal model for standoff CA detection. L_a , τ_a , and L_p , τ_p are the path radiance and transmittance of the atmosphere and plume layers, respectively, and L_b is the background radiance.

emits radiation on the basis of its own content and temperature. This is illustrated in Figure 6 for a standoff sensor with a horizontal line of sight.

Several simplifying assumptions are made to arrive at expressions for the at-sensor radiance in the presence and absence of the chemical plume.

- The atmosphere and plume are assumed free of aerosols and particulate matter so that scattering may be neglected throughout.
- The plume and atmosphere are each assumed to be homogeneous in both temperature and composition.

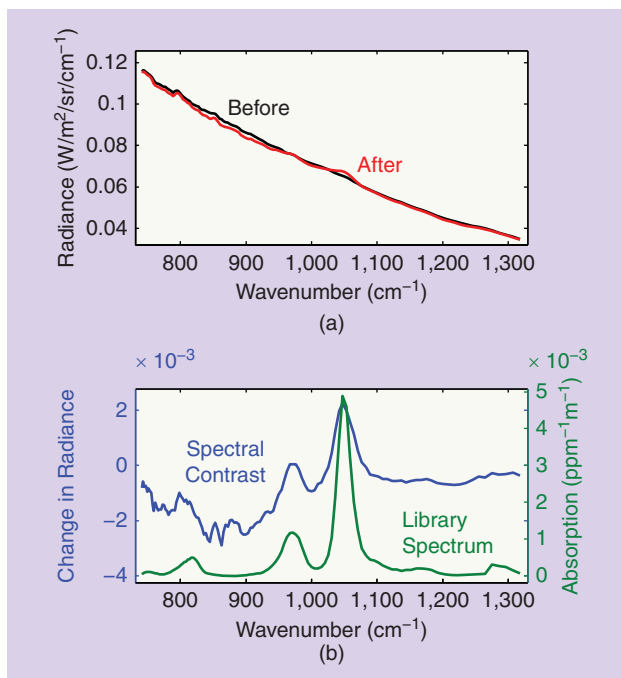


[FIG7] (a) The radiance spectra of the same pixel before and after the appearance of a TEP plume. (b) Plots of radiance spectral contrast $L_{on}(\lambda) - L_{off}(\lambda)$ and the absorption-coefficient library spectrum of TEP. (Notice the different units used for radiance and absorption.)

- The thickness of the plume layer and the distance between the plume and background are assumed to be small so that atmospheric transmittance can be neglected in those layers.
- Reflections off the background of both plume and downwelling atmospheric radiance are neglected.

Under these assumptions, the at-sensor radiance in the absence of plume, as a function of wavelength, is given by radiative transfer theory [26] to be

$$L_{\text{off}}(\lambda) = L_a(\lambda) + \tau_a(\lambda)L_b(\lambda), \quad (1)$$

where $L_a(\lambda)$ represents atmospheric path radiance and the second term is the contribution of background radiance $L_b(\lambda)$ modulated by the atmospheric transmittance $\tau_a(\lambda)$.

The presence of a plume has two effects: it absorbs part of the radiation emitted by the background, and it emits its own radiation. The resulting radiance is subsequently attenuated by transmission through the atmosphere and is given by

$$L_{\text{on}}(\lambda) = L_a(\lambda) + \tau_a(\lambda)\tau_p(\lambda)L_b(\lambda) + \tau_a(\lambda)[1 - \tau_p(\lambda)]B(\lambda, T_p), \quad (2)$$

where $\tau_p(\lambda)$ is the plume transmittance, T_p is its temperature, and $B(\lambda, T_p)$ is the Planck function, which describes the radiation emitted by a black body at the plume's temperature. Referring to Figure 6, we have used Kirchhoff's law [27] to write $L_p(\lambda) = [1 - \tau_p(\lambda)]B(\lambda, T_p)$. In (2), the three terms represent the at-sensor radiance due to the atmosphere, the background radiance as modulated by the plume and atmosphere, and the plume radiance as modulated by the atmosphere.

The spectral transmittance function, $\tau_p(\lambda)$, of a plume with N_G gas species can be modeled using Beer's law [27]

$$\tau_p(\lambda) = \exp\left[-\sum_{m=1}^{N_G} \gamma_m \alpha_m(\lambda)\right]. \quad (3)$$

The function $\alpha_m(\lambda)$, which is known as the *absorption coefficient spectrum*, is unique for each gaseous chemical and can be used as a spectral fingerprint. The quantity γ_m , which is called the *concentration pathlength*, is the product of two terms: the length along the sensor boresight that represents the depth of the cloud, and the average concentration along that path. Figure 7 shows examples of spectra with and without plume. The spectral contrast $L_{\text{on}}(\lambda) - L_{\text{off}}(\lambda)$ is shown on the same plot with the absorption coefficient spectrum $\alpha_m(\lambda)$ of triethyl phosphate (TEP), which is the released CA. Notice how the presence of the CA modifies the radiance spectrum of the background; this is precisely the information used by data exploitation algorithms to detect and identify CAs.

In preparation for the discussion of signal processing algorithms in the following sections, we present a mathematically equivalent form of the radiance equation that isolates the spectral contrast. Combining (1) with (2), we find after some algebra

$$L_{\text{on}}(\lambda) = \tau_a(\lambda)(1 - \tau_p(\lambda))(B(\lambda, T_p) - L_b(\lambda)) + L_{\text{off}}(\lambda). \quad (4)$$

This form expresses the effect of a plume as a contrast between the on- and off-plume radiance. Also, it highlights the physical requirements for plume detection: each of the terms in the product on the right-hand side of (4) must be nonzero. Because of their importance, we enumerate these plume visibility conditions as

- 1) $\tau_a(\lambda) > 0$ (atmosphere not opaque)
- 2) $\tau_p(\lambda) < 1$ (plume not transparent)
- 3) $B(\lambda, T_p) - L_b(\lambda) \neq 0$ (nonzero contrast between plume black body and background radiance).

In particular, plume detection is possible only if there is contrast between the plume black body and background radiance for at least some spectral channels.

The on-plume at-sensor radiance as a nonlinear function of parameters that characterize the plume, atmosphere, and background is represented in (4). For some tasks, this equation is of direct utility. Still, there are many situations in which simplifying assumptions are both valid and advantageous in terms of algorithmic complexity and intuition. We describe three approximations that, under a wide range of situations, lead to a powerful linear signal model.

Many applications call for maximum sensitivity to very weak plumes. In the optically thin plume approximation, Beer's law (3) is linearized by using the first term of its Taylor expansion. The flat background emissivity approximation exploits the fact that many background emissivity functions $\epsilon_b(\lambda)$ lack sharp spectral features, unlike most chemical plumes, leading to the approximation $\epsilon_b(\lambda) \simeq 1$. When $\Delta T = T_p - T_b$ is small in magnitude, typically less than 5 K, the linear Planck function approximation holds, in which the Planck function is linearized in the thermal contrast term. Furthermore, the wavelength dependence of this difference is weak over the LWIR window.

Taking into consideration all three approximations, the at-sensor radiance signal model (4) becomes

$$L_{\text{on}}(\lambda) = \sum_{m=1}^{N_G} (C_B \Delta T \gamma_m) \tau_a(\lambda) \alpha_m(\lambda) + L_{\text{off}}(\lambda), \quad (5)$$

where C_B is a constant independent of wavelength and temperature. This signal-plus-clutter model provides the basis for most detection, identification, and quantification algorithms used in practical applications.

The expression (5) represents the radiance present at the sensor input. The measurements of radiance that are output by the sensor contain the effects of the detector spectral response function $R_F(\lambda)$, along with noise $n(\lambda)$ introduced by the sensor. If $\tilde{L}(\lambda)$ denotes the measured radiance in a spectral channel centered at λ we have

$$\tilde{L}_{\text{on}}(\lambda) = L_{\text{on}}(\lambda) * R_F(\lambda) + n(\lambda), \quad (6)$$

where the convolution operator $*$ is defined by

$$L_{\text{on}}(\lambda) * R_F(\lambda) \triangleq \int_{-\infty}^{\infty} L_{\text{on}}(\nu) R_F(\lambda - \nu) d\nu. \quad (7)$$

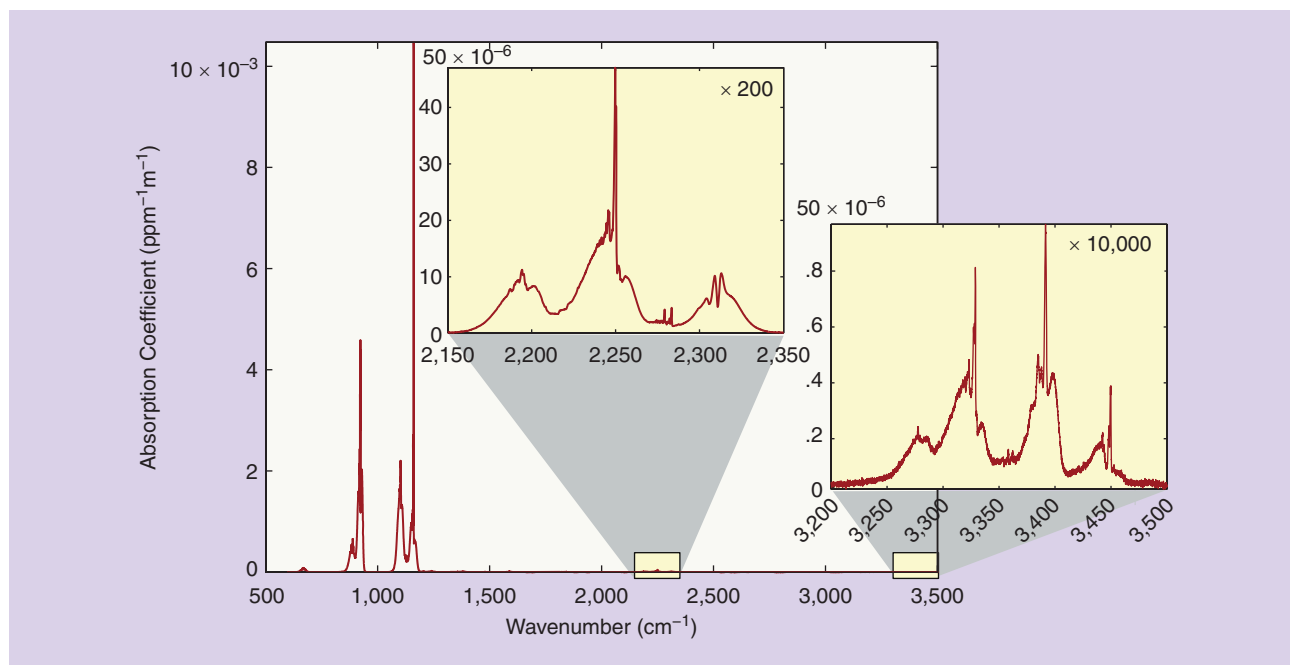


[FIG8] The library spectrum corresponding to freon-12 at 25 °C. The two insets contain the first and second overtones of the fundamental vibrational bands, appearing between 838–1,227 cm⁻¹. Note the large dynamic range of the spectral data and, in this case, a signal-to-noise (root mean square) of over one million.

We stress that sensor measured radiances are always affected by sensor noise and other artifacts.

Suppose next that the sensor measures radiance at p spectral bands centered at wavenumbers λ_k , $1 \leq k \leq p$. If we sample (6) at $\lambda = \lambda_k$, we obtain

$$x_k = \sum_{m=1}^{N_C} g_m s_{mk} + v_k, \quad k = 1, 2, \dots, p, \quad (8)$$

where

$$x_k \triangleq \bar{L}_{on}(\lambda_k), \quad (9a)$$

$$g_m \triangleq C_B \Delta T \gamma_m, \quad (9b)$$

$$s_{mk} \triangleq \{[\tau_a(\lambda) \alpha_m(\lambda)] * R_F(\lambda)\} |_{\lambda=\lambda_k}, \quad (9c)$$

and

$$v_k \triangleq \{L_{off}(\lambda) * R_F(\lambda)\} |_{\lambda=\lambda_k} + n(\lambda_k) \quad (9d)$$

are, respectively, the measured radiance, chemical contrast, at-sensor gas signature, and background clutter plus noise. Therefore, the principal relationship for the analysis of radiance data can be written in a concise matrix form as

$$x = \sum_{m=1}^{N_C} g_m s_m + v \triangleq Sg + v. \quad (10)$$

According to this model, the radiance spectrum of a plume pixel is a linear mixture of the at-sensor gas signatures superimposed upon the radiance spectrum of the background. In practice, it is usually assumed that chemical mixtures are made up of three or fewer gas species: $N_C \leq 3$.

SIGNALS, DISTORTIONS, AND CLUTTER

The at-sensor radiance model illustrates that the fundamental exploitation problem is to detect a known signal after modification by the surrounding environment and corruption by clutter and noise. This requires the mathematical representation of signal and clutter and understanding the effects of atmospheric transmission and temperature upon the observed data.

GAS SPECTRAL LIBRARIES

For ground-level remote sensing of chemical plumes, the absorbance spectra of chemicals of interest are needed at atmospheric pressure and temperatures close to typical surface values. The preferred approach for obtaining these spectra is to use experimentally measured spectra from a quality-assured reference database. Two such databases are publicly available, one maintained by the National Institute of Science and Technology (NIST) [28] and the other by the Pacific Northwest National Laboratory (PNNL) [29].

Both databases were developed with a view toward ground-level remote sensing applications and therefore use samples prepared at relevant pressure and temperatures. Both cover a spectral range that contains the LWIR atmospheric window, with similar spectral resolutions of about $\Delta\nu = 0.1 \text{ cm}^{-1}$ wavenumbers, consistent with the limiting values allowed by pressure broadening at one atmosphere. The gas species included differ in scope, although there is enough overlap to allow validating comparisons. The emphasis of the NIST database is greenhouse gases, the U.S. EPA hazardous air pollutants and freons, while that of the PNNL set is reactive compounds, industrial pollutants, and the Department of

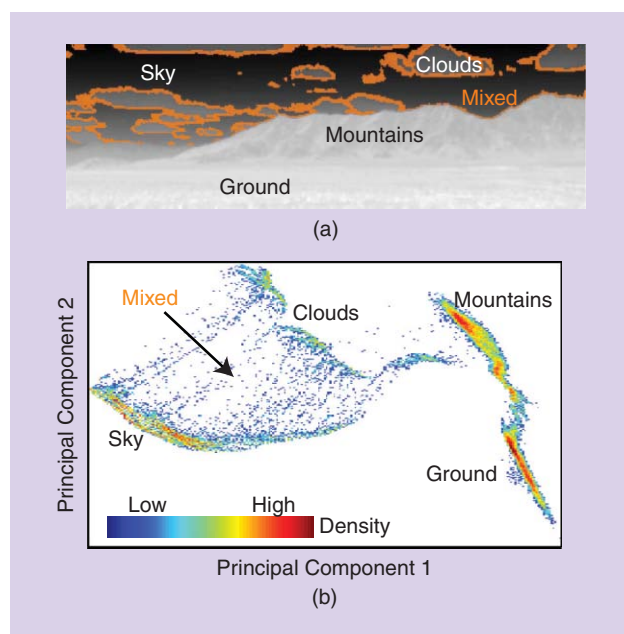


[FIG9] (a) The average spectral radiance for every pixel of a 128-spectral band LWIR data cube collected using the aerospace GBSS sensor. (b) A density scatterplot (a 2-D histogram) in the first two principal components of the LWIR cube shown in (a).

Energy fossil and nuclear fuel remediation species. The two groups deliberately chose different methods of sample preparation to allow meaningful cross-laboratory comparisons on common molecules. The interlaboratory comparison of 12 common species showed a root-mean-square deviation of less than 2% for integrated band densities, including small systematic errors in measurement [30]. In practical applications, these errors are ignored; they are insignificant when compared to the overwhelming effects introduced by non-Gaussian and nonstationary background clutter. A typical PNNL library spectrum is shown in Figure 8.

ATMOSPHERIC COMPENSATION AND TEMPERATURE-EMISSION SEPARATION

The radiance signal due to the plume is modulated by those of the atmosphere and background before arriving at the sensor, as demonstrated by (2). To extract the plume signal, both of these effects must be suppressed, which is one of the central problems of the remote sensing of chemical plumes, as we discuss in the sections “Background Clutter” and “Detection Algorithms.” Atmospheric compensation techniques can sometimes be used to approximately remove the path radiance and the transmittance of the atmosphere from the signal.

Many assumptions are required to render the compensation task feasible. All existing algorithms depend on the atmospheric properties remaining constant over the entire image, which effectively limits applicability to the down-looking geometry. The in-scene atmospheric compensation (ISAC) algorithm [31] further assumes that many pixels in the scene are well approximated as blackbodies and that there is temperature variability

within these pixels. In the LWIR regime, surface materials that radiate as blackbodies include water, vegetation, and very rough mineral surfaces in which many reflections occur. After such pixels are identified, the temperature variation may be exploited to recover the atmosphere parameters. The autonomous atmospheric compensation (AAC) algorithm [32] is a model-based alternative to ISAC. It assumes that the spatial variability of the atmospheric transmittance is primarily due to water vapor, with the other atmospheric constituents approximated by standard atmospheric profiles. A radiative transfer code is used to relate the atmospheric parameters to the observed radiances. There are several other approaches in the literature that refine and extend these two.

In gas-detection applications, the properties of the background are treated as nuisance parameters, and the objective is suppression of the background signal to observe that of the plume. However, there are many applications, such as mineral studies and hard target detection, in which study of the background properties is the goal. Radiance measured from the earth’s surface in the thermal IR region consists of emissivity and temperature information. Variations in emissivity relate to the chemistry and texture of materials at the surface. Temperature variations, which are an order of magnitude larger than emissivity variations, may obscure emissivity changes among pixels of the same or different clusters. Therefore, meaningful background modeling requires temperature-emissivity separation (TES). A fundamental difficulty is that p spectral band measurements alone cannot be used to unambiguously determine p spectral emissivities and a temperature [33]. This ambiguity is a serious problem for hard target detection applications, where association of emissivity spectra to physical materials is crucial. TES algorithms use prior information or ancillary measurements to obtain unique parameter recovery. A highly developed optimization algorithm for this task is automatic retrieval of temperature and emissivity using spectral smoothness (ARTEMISS) [34], [35], which exploits the relative smoothness of the background emissivity as compared to the sharp spectral features commonly present in gas signatures. ARTEMISS is still under active validation.

BACKGROUND CLUTTER

Real-world hyperspectral imaging scenes are made up of several spectrally distinct physical constituents. But, because of the limited spatial resolution of the sensor, a given pixel in the scene may be composed of a single pure constituent (or end member) or it may contain a mixture of two or more constituents. Figure 9(a) shows the average radiance at every pixel for a LWIR hyperspectral data cube collected with the aerospace GBSS sensor. Figure 9(b) shows a density scatterplot (2-D histogram) in the first two principal components [36] accounting for 99% of the overall data variance. The four significant clusters correspond to pixels associated with sky, clouds, mountain, and ground surfaces, respectively. These clusters comprise physically similar pixels that exhibit a certain amount of random variation about a nominal mean value due to changes in physical composition,

temperature, atmospheric transmission, and sensor noise. There is a set of pixels between the sky and cloud clusters that correspond to the borderline between the sky and clouds. A plausible explanation is that the radiance spectra of these pixels are obtained from the mixing of sky and cloud spectra.

Two classes of hyperspectral background clutter models that are widely used in gas detection, identification, and quantification applications are density mixture models and linear subspace models.

DENSITY MIXTURE MODELS

Inspection of several density scatterplots, like the one in Figure 9, suggests that LWIR radiance data cubes can be modeled as a mixture of unimodal densities, i.e.,

$$f(x) = \sum_{k=1}^{N_c} \pi_k f_k(x), \quad \pi_k \geq 0, \quad \sum_{k=1}^{N_c} \pi_k = 1, \quad (11)$$

where x is the spectral vector, $f(x)$ is the probability density function (pdf) describing the entire data cube, π_k is the a priori probability of the k th class, $f_k(x)$ the pdf of the k th class, and N_c is the number of classes. This model is used to develop performance-prediction models [37].

In most applications, we model each class by a multivariate normal distribution

$$f(x) = \frac{1}{(2\pi)^{\frac{p}{2}} |C|^{\frac{1}{2}}} \exp\left[-\frac{1}{2}(x-m)^T C^{-1}(x-m)\right], \quad (12)$$

where m is a $p \times 1$ vector with entries $m_i = E(x_i)$ and C is a $p \times p$ covariance matrix with entries $c_{ij} = \text{Cov}(x_i, x_j)$. The expression $x \sim N_p(m, C)$ denotes a random vector x with pdf given by (12).

In practice, the mean vector and covariance matrix are determined using the maximum likelihood estimators

$$\hat{m} = \frac{1}{N} \sum_{i=1}^N x_i, \quad (13)$$

$$\hat{C} = \frac{1}{N} \sum_{i=1}^N (x_i - \hat{m})(x_i - \hat{m})^T. \quad (14)$$

C is typically nonsingular in practice because noise is present and the number of pixels greatly exceeds the number of bands. The random vector

$$z = C^{-1/2}(x-m), \quad (15)$$

where $C^{-1/2}$ is the square root of C^{-1} , has the spherical distribution $N_p(0, I)$. The Mahalanobis square distance

$$\Delta^2 = (x-m)^T C^{-1}(x-m) = z^T z \sim \chi_p^2 \quad (16)$$

follows a central chi-square distribution. This distribution is used to assess deviations from normality in hyperspectral imaging data. The pdf of x has elliptical contours centered at m , whereas the pdf of z has spherical contours centered at the origin. For this reason, the operation (15) is called *whitening* or *spherizing*.

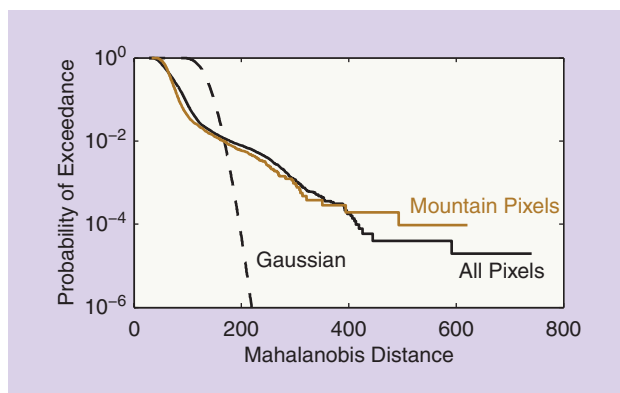


[FIG10] The empirical probability of exceedance for a GBSS data cube. The dashed line represents a theoretical exceedance curve for a Gaussian distribution, which underestimates tail heaviness even for individual classes (e.g., the mountain class).

Normal distribution models provide mathematical tractability but often are inconsistent with empirical hyperspectral imaging data [38]. This is demonstrated in Figure 10, which shows probability of exceedance distributions of Mahalanobis square distance for the GBSS data in Figure 9(a) and the theoretical multivariate normal distribution. These results clearly indicate that LWIR backgrounds exhibit tails heavier than those predicted by a multivariate normal distribution.

The class of elliptically contoured distributions [39] has been an attractive generalization of the multivariate normal distribution. It contains many distributions, which, in general, have heavier tails than the normal and provide a better model for the tails of hyperspectral data. One important application of elliptical distributions with heavy tails is in investigating the robustness of decision and estimation procedures based on the normal distribution.

A random vector x has an elliptical distribution with location vector m and scale positive-definite matrix C_0 , if its density takes the form

$$f(x) = c_p |C_0|^{-1/2} g[(x-m)^T C_0^{-1}(x-m)], \quad (17)$$

where the function g is typically known as the *density generator*. For a vector x distributed according to (17), we use the notation $EC_p(m, C_0; g)$ or simply $EC_p(m, C_0)$. When $m = 0$ and $C_0 = I$, we obtain the spherical family of densities. For the multivariate normal distribution $N_p(m, C)$, we have $g(u) = \exp(-u/2)$, $c_p = (2\pi)^{-p/2}$, and $C_0 = C$. This class of symmetric distributions includes the normal, Student's t , Cauchy, and logistic distributions, among others [39].

Many natural hyperspectral backgrounds in the reflective spectral region (400–2,500 nm) can be accurately modeled using mixtures of elliptically contoured multivariate t -distributions [40]. The development of models for LWIR hyperspectral backgrounds is more challenging because of complications resulting from temperature-emissivity coupling. In practice, modeling LWIR backgrounds as multivariate t mixtures often leads to underestimated false-alarm rates [41].

LINEAR SUBSPACE MODELS

These models assume that each spectrum can be expressed as

$$\mathbf{x} = \sum_{k=1}^{N_B} c_k \mathbf{b}_k + \mathbf{e} \triangleq \mathbf{B}\mathbf{c} + \mathbf{e}, \quad (18)$$

where $\{\mathbf{b}_1, \dots, \mathbf{b}_{N_B}\}$, $N_B \leq p$, is a fixed set of linearly independent vectors (which are not necessarily orthogonal), \mathbf{e} is an approximation error, and the values of the coefficients c_k vary from pixel to pixel.

The most practical ways to determine the basis vectors \mathbf{b}_k from the radiance data cube are automated clustering techniques and end member extraction algorithms. Nevertheless, the application of both approaches to thermal hyperspectral data can be quite challenging [3], [42]. The difficulties are due to the radiance fluctuations that are induced by those of the background temperature, which varies over the scene, and possibly within individual pixels. This source of variability is absent in the VNIR/SWIR band, in which radiance is almost completely due to reflected light.

For gas-detection applications, it is sufficient to represent the background subspace using any basis equivalent to $\{\mathbf{b}_1, \dots, \mathbf{b}_{N_B}\}$. For convenience, we use the orthogonal basis obtained from the singular value decomposition (SVD) of the $p \times N$ data matrix X^T with columns the spectra x_1, \dots, x_N , i.e.,

$$X^T = U\Sigma W^T = \sum_{k=1}^r \tilde{\sigma}_k \mathbf{u}_k \mathbf{w}_k^T, \quad (19)$$

where r is the rank of X and $\tilde{\sigma}_k$ its singular values. We note that \mathbf{u}_k are the eigenvectors of the unscaled correlation matrix $X^T X$. If we retain only the first $N_B < r$ dominant terms of (19), we obtain an approximation \hat{X} of X , which is optimum in the sense of least squares error. The resulting total squared error is given by the sum of squares of the dropped singular values.

The subspace matrix \mathbf{B} is constructed from the N_B most significant left singular vectors \mathbf{u}_k . We point out that the columns of \mathbf{B} do not have any physical meaning. Yet, this is not a problem for detection applications as long as the subspace model provides a good approximation of the background.

An affine representation can be obtained by centering the spectra x_i about their mean vector and computing the SVD of

the centered data matrix. This is equivalent to forming \mathbf{B} using the dominant eigenvectors of the estimated covariance matrix. This subspace is centered at the mean background spectrum. When the approximations of the linear signal model (5) hold with high accuracy, the spectral mean plays no essential role and the affine representation is appropriate. When higher-order corrections to the radiance model are taken into account, the subspace representation may be preferred [43], [44].

APPLICATION REQUIREMENTS AND PERFORMANCE METRICS

Although different applications often have different specific needs, they share some key tasks and associated performance metrics. Figure 11 illustrates the use of a hyperspectral imaging sensor in a typical standoff chemical sensing application. From a user's perspective, the performance of a sensor system (sensor and exploitation algorithms) is specified by metrics that are specific to the application. Yet, many chemical sensor systems are characterized by four key parameters: sensitivity, probability of detection, false-alarm rate, and response time [45]. The performance of a sensor system depends upon the sensor, environmental conditions, and signal exploitation algorithms.

Sensitivity, which is also known as *detection limit*, is defined by the lowest concentration of a CA that can be detected with high confidence and is typically specified in units of particles per million [ppm] or mass per unit air volume (particles/liter or mg/m^3). Sensitivity may also be a measure of a system's ability to discriminate between small differences in the concentration of an agent. Hence, a sensitive detector gives a large change in signal intensity for a small change in concentration. A meaningful quantitative definition of detection limit depends upon a quantitative definition of confidence. Furthermore, sensitivity is not directly applicable to LWIR monitoring systems because a minimum concentration does not exist; the optical path length of the cloud must be taken into account. These issues are further discussed in the section "Quantification Algorithms."

The sensor response time is defined as the time interval between the arrival of the target agent concentration and the sensor detection declaration [45]. Clearly, in detect-to-warn applications, the response time must be less than the time necessary to take protective actions.

An alarm or hit from a detection algorithm does not necessarily mean that a CA is present. If the hit is the correct response to the presence of a CA, we have a detection (true positive). False alarms occur if a detector responds when a CA is not present (false positive). When a detector fails to respond to a CA that is present, we have a missed detection (false negative). For some applications, missed detections are more problematic than false alarms because the failure to produce an alarm may lead to dangerous situations. There is typically a tradeoff between probability of detection and probability of false alarm (or false-alarm rate). This tradeoff is captured by the receiver operating characteristic (ROC) curves, which

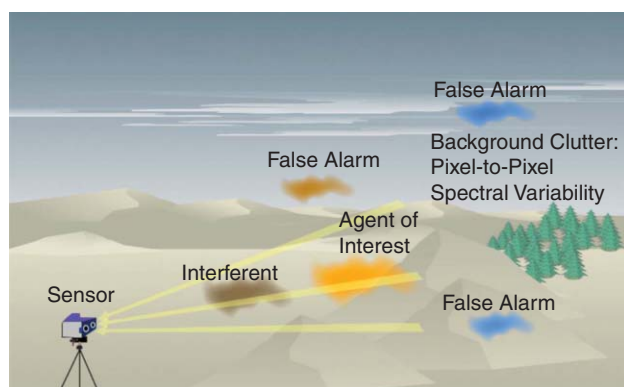


[FIG11] Detection, identification, and quantification are significantly hindered by environmental conditions, benign particulates, and background variability.

show the probability of detection as a function of probability of false alarm. We stress that detection performance, quantified by an ROC curve, depends on the combined effect of concentration, path length, agent spectral signature, noise, and background clutter. Thus, it is meaningless to specify sensitivity without reference to a specific ROC curve because different concentrations correspond to different ROC curves.

False alarms are usually observed when the targeted compound is in the presence of an interferent, which may be a chemical molecularly similar to a CA or a substance containing elements that are also present in CAs. In the context of CA sensing, an interferent is defined as any material present in the environment that retards and/or inhibits a detector's ability to accurately detect the agent or agents for which it is programmed, or causes a detector to false alarm or malfunction [45]. However, from a signal processing perspective, only clouds along the sensor line of sight act as interferents (see Figure 11). False alarms may also be due to background clutter, defined as a physical environmental condition that may adversely affect the performance of the detection system. In our context, clutter refers to the pixel-to-pixel spectral variability caused by differences in material composition and temperature over the scene.

The ability of a detection algorithm to deal with false alarms is affected by its selectivity. Selectivity is the ability of a detection algorithm to respond only to the targeted chemicals in the field of view. A selective detector must be able to separate targeted compounds, over a broad range of concentrations, from any other substances that may be present. Selectivity is related to the topics of signature mismatch (see the section "Detection Algorithms") and CA identification (see the section "Identification Algorithms").

Every detector has limited selectivity, which depends upon the detection algorithm, spectral resolution, and background clutter. Therefore, to distinguish true CA threats from false alarms, further processing of the spectroscopic measurements obtained by the sensor and/or additional active sensor measurements are required. Typically, the detection algorithm is followed by discrimination and identification algorithms. A discrimination algorithm assigns the alarm to one of a number of predetermined CA classes or to a false-alarm class. If each class, except for the false alarm class, consists of a single CA, we have a CA identification problem. The statistical variability of background clutter and the presence of sensor noise make inevitable the design and evaluation of CA detection, identification, and quantification algorithms using statistical techniques. These techniques are the subject of the next three sections.

DETECTION ALGORITHMS

In this section, we use the optically thin plume approximation to derive optimum algorithms for chemical plume detection. Despite their simplicity, these algorithms provide acceptable performance for many practical applications and provide the benchmark for chemical detection systems.

THEORETICAL DEVELOPMENT

The simplest and most practical algorithms for chemical gas detection use the linear signal model

$$\mathbf{x} = \mathbf{S}\mathbf{g} + \mathbf{v}, \quad \mathbf{v} \sim N(\mathbf{m}_b, \mathbf{C}_b) \quad (20)$$

developed in the section "At-Sensor Radiance Signal Models," assuming normally distributed clutter. If we assume that \mathbf{S} , \mathbf{m}_b , and \mathbf{C}_b are known, the maximum likelihood estimate of \mathbf{g} is the weighted-least-squares solution

$$\hat{\mathbf{g}} = (\mathbf{S}^T \mathbf{C}_b^{-1} \mathbf{S})^{-1} \mathbf{S}^T \mathbf{C}_b^{-1} \mathbf{x}. \quad (21)$$

Because $\hat{\mathbf{g}}$ is unbiased only when $E(\mathbf{x}) = 0$, we routinely remove \mathbf{m}_b from the observations. This yields the mean-centered signal model

$$\mathbf{x} = \mathbf{S}\mathbf{g} + \mathbf{v}, \quad \mathbf{v} \sim N(0, \mathbf{C}_b). \quad (22)$$

To avoid proliferation of notation, unless otherwise stated, we continue using the symbol \mathbf{x} to denote the demeaned vector $\mathbf{x} - \mathbf{m}_b$.

The competing hypotheses for gas detection are

$$H_0: \mathbf{g} = \mathbf{0} \quad (\text{Plume absent}), \quad (23a)$$

$$H_1: \mathbf{g} \neq \mathbf{0} \quad (\text{Plume present}). \quad (23b)$$

Using the generalized likelihood ratio test (GLRT) approach [46], we obtain the matched filter (MF) detector

$$T_{\text{MF}}(\mathbf{x}) = \mathbf{x}^T \mathbf{C}_b^{-1} \mathbf{S} (\mathbf{S}^T \mathbf{C}_b^{-1} \mathbf{S})^{-1} \mathbf{S}^T \mathbf{C}_b^{-1} \mathbf{x}. \quad (24)$$

If we assume that the clutter covariance matrix is given by $\sigma_b^2 \mathbf{C}_b$, where σ_b^2 is an unknown constant, the GLRT leads to the normalized MF (NMF) detector

$$T_{\text{NMF}}(\mathbf{x}) = \frac{T_{\text{MF}}(\mathbf{x})}{\mathbf{x}^T \mathbf{C}_b^{-1} \mathbf{x}}. \quad (25)$$

The NMF detector is also known as the *adaptive cosine or coherence estimator algorithm* [47].

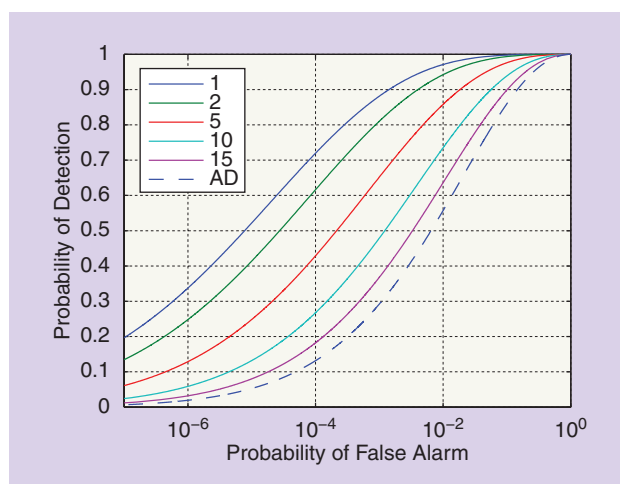


[FIG12] The performance of the MF with $N_G = 1, 2, 5, 10, 15$ chemicals. The sensor has $p = 20$ spectral channels and the SCR is $D = 20$. As the number of chemicals in \mathbf{S} increases, the MF's performance approaches the anomaly detector's performance. Equality occurs when the number of signatures in \mathbf{S} reaches the number of spectral channels.

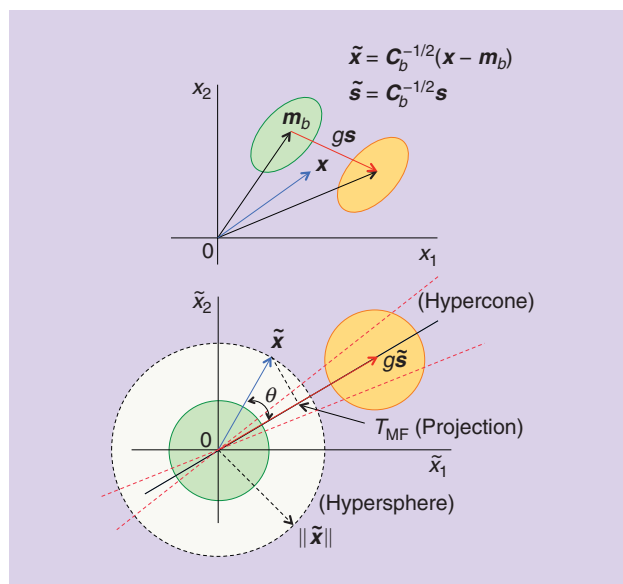


[FIG13] A geometric interpretation of the MF, NMF, and AD algorithms in whitened space.

The MF and NMF for $N_G = 1$ are given by

$$T_{MF}(x) = \frac{(x^T C_b^{-1} s)^2}{s^T C_b^{-1} s}, \tag{26}$$

$$T_{NMF}(x) = \frac{(s^T C_b^{-1} x)^2}{(s^T C_b^{-1} s)(x^T C_b^{-1} x)}, \tag{27}$$

because the matrix S is reduced to a single vector s .

If the number of gases is equal to the number of spectral bands ($N_G = p$) and S has full rank, we have

$$T_{AD}(x) = x^T C_b^{-1} x, \tag{28}$$

i.e., the MF becomes an anomaly detector (AD) algorithm.

The detector distributions under each hypothesis are

$$T_{AD}(x) \sim \chi_p^2(\mu D), \tag{29a}$$

$$T_{MF}(x) \sim \sigma_b^2 \chi_{N_G}^2(\mu D), \tag{29b}$$

$$T_{NMF}(x) \sim \beta_{N_G/2, (p-N_G)/2}(\mu D), \tag{29c}$$

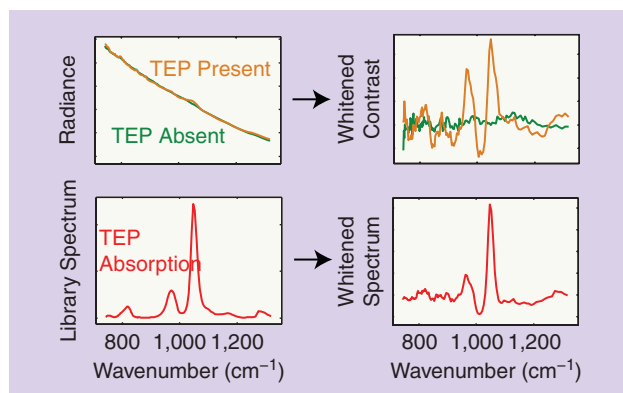


[FIG14] An illustration of background-clutter-based whitening operation on at-sensor radiance and a library spectrum.

where $\mu = 0$ under H_0 , $\mu = 1$ under H_1 , and

$$D = (Sg)^T (\sigma_b^2 C_b)^{-1} (Sg) \tag{30}$$

is the signal-to-clutter ratio (SCR). Using these distributions, we can determine detection performance using ROC curves. Inspection of the ROC curves in Figure 12 shows that the performance of the MF deteriorates with increasing N_G and reaches the performance of AD for $N_G = p$. Thus, in practice, it is preferable to use a separate detector for each chemical than to use one subspace detector that includes all chemicals.

To understand the meaning of single-gas AD, MF, and NMF, we use the whitening transformation

$$\tilde{x} = C_b^{-1/2} x \quad \text{and} \quad \tilde{s} = C_b^{-1/2} s \tag{31}$$

to express these detectors in the whitened space

$$T_{AD}(x) = \tilde{x}^T \tilde{x} = \|\tilde{x}\|^2, \tag{32}$$

$$T_{MF}(\tilde{x}) = \frac{(\tilde{s}^T \tilde{x})^2}{\tilde{s}^T \tilde{s}} = \left[\frac{(\tilde{s}^T \tilde{x})}{\sqrt{\tilde{s}^T \tilde{s}}} \right]^2 = T_{MF}^2(x), \tag{33}$$

$$T_{NMF}(\tilde{x}) = \frac{(\tilde{s}^T \tilde{x})^2}{(\tilde{s}^T \tilde{s})(\tilde{x}^T \tilde{x})} = \cos^2 \theta. \tag{34}$$

Inspection of the whitened space in Figure 13 shows that for each whitened observation vector: 1) the AD uses only its length (the AD is omnidirectional because it does not use the target signature); 2) the MF uses the length of its projection along the whitened signature; and 3) the NMF uses its angle with the whitened signature. The effectiveness of the whitening operation is further illustrated in Figure 14.

The MF maximizes the output SCR, i.e., it provides the maximum separation between the output distributions. The NMF is scale invariant and it is robust to clutter distributions with heavy tails.

The application of MF and NMF detectors requires estimation and inversion of the background covariance matrix C_b . But, in practice, C_b is often ill conditioned and its small eigenvalues and corresponding eigenvectors are difficult to estimate and hard to compute accurately. There are many ways to deal with this problem. We produce numerically stable and more robust detectors by eliminating the smaller eigenvalues through averaging and loading. Thus, we approximate C_b by

$$\tilde{C}_b = \sum_{k=1}^d \lambda_k q_k q_k^T + \alpha \sum_{k=d+1}^p q_k q_k^T + \delta I, \tag{35}$$

where $\alpha = (\lambda_{d+1} + \dots + \lambda_p)/(p-d)$ and $\delta \geq 0$. The inverse covariance matrix can be shown to be [48], [49]

$$\tilde{C}_b^{-1} = \frac{1}{\alpha + \delta} \left(I - \sum_{k=1}^d \frac{\lambda_k - \alpha}{\lambda_k + \delta} q_k q_k^T \right). \tag{36}$$

This expression shows that the inverse covariance matrix is built from the first d dominant eigenvectors.

Another approach to chemical detection assumes that background clutter can be represented by the subspace model (18), where $e \sim N(0, \sigma_b^2 I)$. Then, the signal model (22) becomes

$$x = Sg + Bc + e, \quad e \sim N(0, \sigma_b^2 I). \quad (37)$$

The GLRT approach for (2) with known σ_b^2 gives [50]

$$T_1(x) = x^T P_b^\perp x - x^T P_{tb}^\perp x, \quad (38)$$

where P_b^\perp and P_{tb}^\perp are orthogonal projection matrices

$$P_b^\perp = I - B(B^T B)^{-1} B^T, \quad (39)$$

$$P_{tb}^\perp = I - A(A^T A)^{-1} A^T, \quad A = [S \ B]. \quad (40)$$

If σ_b^2 is unknown, the GLRT yields

$$T_2(x) = \frac{x^T P_b^\perp x}{x^T P_{tb}^\perp x} = \frac{\|P_b^\perp x\|^2}{\|P_{tb}^\perp x\|^2}. \quad (41)$$

We note that $\|P_b^\perp x\|$ and $\|P_{tb}^\perp x\|$ are distances from the background and target-background subspaces, respectively. Note that (38) and (41) use the difference or ratio of lengths of the same vectors (see Figure 15). The performance of subspace detectors depends upon the SCR given by

$$D_0 = (Sg)^T P_b^\perp (Sg) / \sigma_b^2. \quad (42)$$

Finally, we note that if λ_k are much larger than α and δ , (36) yields $C_b^{-1} \propto P_b^\perp$ because b_k and q_k span the same space. Therefore, $y_{MF} \propto s^T P_b^\perp x$, which reveals a relationship between full-covariance and subspace detectors [49].

PRACTICAL CONSIDERATIONS

The most relevant metric by which to judge a detector is the ROC curve, as discussed in the section “Application Requirements and Performance Metrics,” but we can gain a great deal of insight by also considering the SCR, defined in (30). While the SCR, as a single summary statistic, cannot encode all of the information in the ROC curve in any but the simplest of models, it generally does correctly track the trends in the area-under-ROC (AUROC) statistic for optically thin gases, and it is far more amenable to analysis [51], [52]. The SCR can give misleading results for optically thick plumes, due to the importance of nonlinear effects in this case. We note that most of the analytic results for SCR apply directly only to the MF (26), but similar conclusions are generally found to hold experimentally for the NMF (27).

The detectors that we have discussed require estimates of the at-sensor gas signature matrix S along with the background mean and covariance m_b and C_b . Recalling (9c), the first of these requires knowledge of the atmospheric transmittance as well as the gas spectral signature; the other two must be obtained from background training data. Estimation error in any of these quantities will adversely affect the detector, in some cases, substantially.

There will always be some degree of signature mismatch between the estimated at-sensor gas signature and that

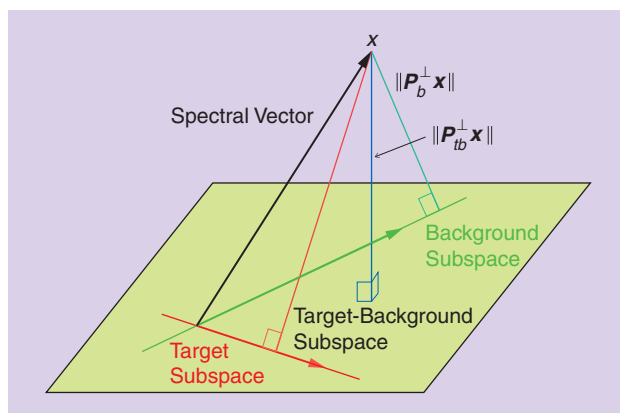


[FIG15] A geometric interpretation of subspace detectors.

present in the scene. A small part of this discrepancy is due to minor differences in sample composition and conditions (pressure and temperature) of the gas signature measured in the lab as compared to that in the field, and sensor calibration error. More significantly, the observed signature varies with concentration path length according to Beer’s law (3), a minor effect for optically thin gases but a major effect for thick gases. Still more importantly, the atmospheric transmittance modulates the gas signature in (9c), and must be estimated, either from ancillary measurements, substitution of a standard profile, or through an in-scene compensation algorithm as discussed in the section “Atmospheric Compensation and Temperature-Emissivity Separation.” If the gas spectral features overlap those of the local atmosphere, substantial uncertainties in the at-sensor signatures will exist. Also, for slant-path imaging geometries $\tau_a(\lambda)$ will vary throughout the scene, further complicating matters.

The most serious issue involving the estimation of m_b and C_b is the possibility that some of the pixels used as background training data contain the plume signal, which we refer to as contamination of the background estimates. Contamination is primarily an issue through its effect on the covariance. It is well known that such contamination does not affect the MF detector statistic in the absence of signature mismatch, but we have seen that some amount of mismatch is inevitable. The MF SCR can be computed analytically in the case that the plume is uncorrelated with the background and the gas signature is constant over the plume and is given by [53]

$$SCR = \frac{SCR_o \cos^2 C_b(s, s_o)}{1 + \left(2 + \frac{\sigma_a^2}{a^2} SCR_o\right) \left(\frac{\sigma_a^2}{a^2} SCR_o\right) \sin^2 C_b(s, s_o)}, \quad (43)$$

where SCR_o is the SCR under optimal conditions, σ_a^2 is the variance of the plume strength over all training pixels, a is the plume strength in the pixel under test, and the trigonometric functions are defined according to the Mahalanobis inner product [see (34)]. This expression makes apparent the facts that covariance contamination does not cause SCR loss

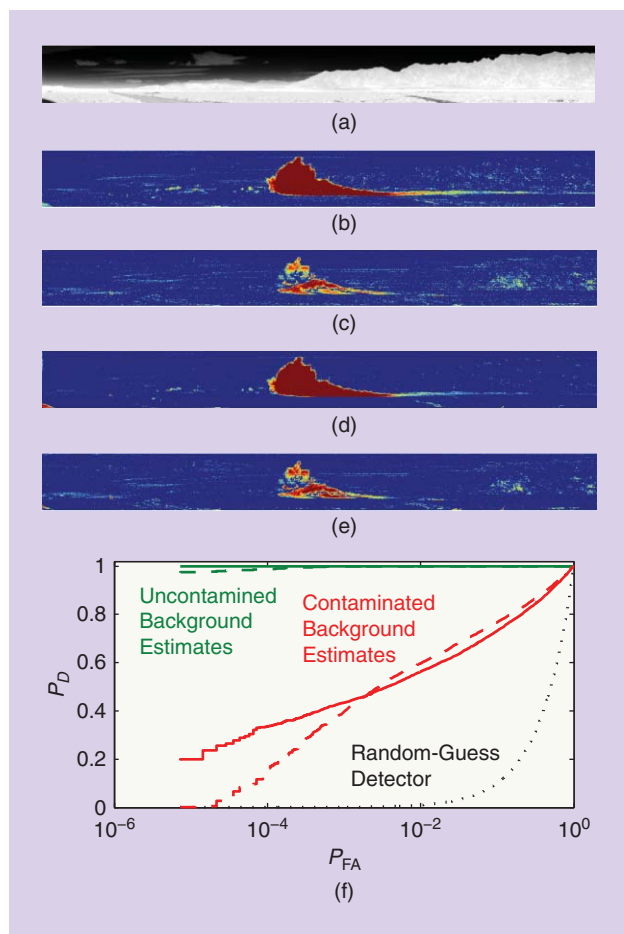


[FIG16] Detection images and receiver operator characteristics for a gas plume imaged by the aerospace GBSS sensor illustrating the necessity of computing background statistics using plume-free training data. Each detection image is normalized by background response (0–30 dB color scale). The solid ROC curves correspond to the NMF, the dashed ROC curves to the MF. (a) Broadband image, (b) NMF map (contaminated background estimate), (c) NMF map (uncontaminated background estimate), (d) MF map (uncontaminated background estimate), (e) MF map (contaminated background estimate), and (f) ROC curves derived from (b)–(e).

without signature mismatch (i.e., $s = s_0$), and that without covariance corruption ($\sigma_a = 0$), a small amount of signature mismatch causes only minor SCR loss. However, the combination of the two can cause substantial loss due to the quadratic dependence on SCR_0 in the denominator. In Figure 16, we illustrate this phenomenon with a data cube collected by the aerospace GBSS sensor containing a plume detection. The detection result is substantially improved when the plume is removed from the training data used for covariance estimation.

Another view of the contamination problem may be obtained by decomposing the SCR as a sum of projections onto the background’s principal components. When only a single gas is present, (30) can be written as

$$SCR = \frac{g^2}{\sigma_b^2} \sum_k \frac{(q_k^T s)^2}{\lambda_k}, \quad (44)$$

where λ_k and q_k are the eigenvectors and eigenvalues of C_b . Figure 17 shows this decomposition for a GBSS cube containing a plume. The vast majority of the variation in the image is contained in the first few eigenvectors (blue line, computed using plume-free training data), illustrating that principal-component-based dimensionality reduction using only a few components would preserve the background pixels of this cube almost perfectly. Nonetheless, the SCR in these components (green line) is very small, showing that such a dimensionality reduction would retain almost no information about the plume. By contrast, very high SCR values are seen at many principal components corresponding to much higher index eigenvalues. These are the plume signal components that are visible to detection algorithms. The inset images show projections of the cube onto individual principal components. The first (largest) component shows the background clearly but not the plume; the plume becomes visible in many of the higher-order components. The red line shows the SCR decomposition on the principal components of the plume-contaminated covariance matrix. Very little of the signal remains, which demonstrates that the amount of signature mismatch present was sufficient to almost completely obliterate the signal. This result underlines the necessity of mitigating plume contamination of background training data during detection processing.

There are two main strategies for dealing with the contamination problem. The first, plume-free background estimation, is to remove as much of the plume as possible from the covariance training data with a two-pass detection process [3]. The second is to introduce robust detectors [52], [54], [55]. The intuition behind this approach is that nearby signatures may be rendered effectively identical by sacrificing some of the discriminating ability of the detector. As it is the combination of mismatch and plume contamination that causes loss, small differences between the observed and assumed gas signatures are thus rendered benign. A robust MF $y = h^T x$ may be defined as the solution to the optimization problem

$$\min_h h^T C_b h \quad \text{subject to} \quad h^T s \geq 1 \quad (45)$$

for all signatures s in the hypersphere $\|s - s_0\|^2 \leq \epsilon^2$. The value of ϵ determines the selectivity of the detector. Several solutions to (45) have been proposed in the literature [56]; they all lead to some kind of diagonal loading. An interesting solution in [55] provides a direct link between ϵ and the diagonal loading factor ζ in $C_b + \zeta^2 I$. The resulting MFs are robust to signal mismatch and covariance contamination in exchange for a higher false-alarm rate. An alternate form of regularization is provided by dominant mode rejection [57]; both forms are included in the expression (36) for the inverse covariance.

There are many additional factors that affect the performance of practical detectors. The sample size of the covariance training set may be an issue with low-spatial-resolution (usually scanning) spectrometers, although it is not generally a problem with imaging spectrometers containing tens of thousands of pixels or more. Chemical plumes may be widely distributed spatially over a scene, with variations in plume strength,

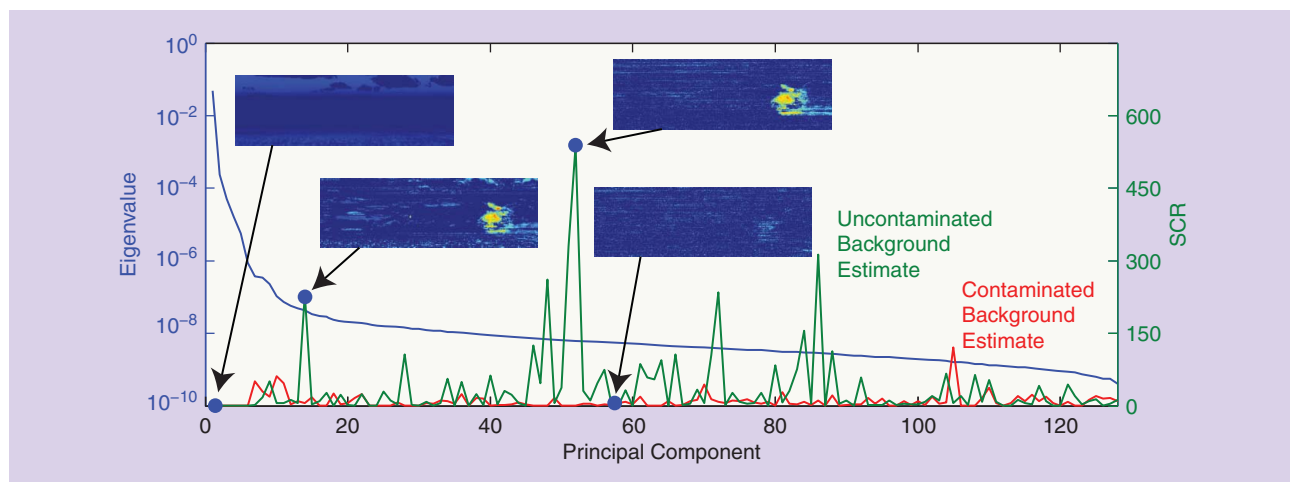


[FIG17] A signal-to-clutter illustration. As shown by the green and red curves, the SCR is significantly reduced when background estimates are contaminated with signal. We can also see that significant signal-to-clutter contributions come from seemingly insignificant principal components. Principal-component-based dimensionality reduction retains energy but reduces detectability.

temperature, and background characteristics over the spatial envelope of the plume. A spatially extended plume may be correlated with the background when the statistics of the latter are spatially nonstationary. This plume-background correlation, in conjunction with signature mismatch and covariance contamination, can cause additional performance loss [51], [58].

The detectors we have discussed operate on a pixel-by-pixel basis, but often detection of the entire plume is desired. In this case, spatial processing can be performed to integrate the decisions of nearby pixels, for example via binary integration [59], and segment the scene into plume-present and plume-absent regions. When false alarms are spatially unstructured, this procedure boosts the probability of detection and drives down the probability of false alarm. Further ROC gains can be obtained by integrating across frames of a time series of hyperspectral images, resulting in an event detector.

IDENTIFICATION ALGORITHMS

The task of determining the constituent gases of a detected plume is known as *identification*. Mathematically, this problem can be formulated as one of selecting variables in a linear model with correlated predictors, or model selection. There is an abundance of classical and recent statistical techniques dealing with this problem. Before delving into this subject, we will discuss the necessity of an identification step following the detector in a signal processing chain.

DETECTION VERSUS IDENTIFICATION

We observed in Figure 12 that ROC performance drops when multiple gases are included in a single detector, implying that a bank of detectors, with a separate detector for each kind of gas, should be employed instead. The question immediately arises as to how best to process the results of such a filter bank. An example that illustrates the problem is given in Figure 18, which shows the detection statistics at the output of a NMF filter bank for a TEP release observed by the aerospace GBSS

hyperspectral imaging sensor. We note that the TEP-tuned NMF shows the maximum response; on the other hand, the diethyl ethyl phosphonate (DEEP)-tuned filter shows a significant response, and some response is visible with the tributyl phosphate (TBP)-tuned filter. Another view of these results is afforded in Figure 19 by plotting the fraction of pixels that exceed a given threshold, for each detector, for sequences of cubes taken before and after the plume release. From the pre-release exceedance plots, we observe that an optimal detection threshold is approximately 0.4; however, using this threshold, DEEP would incorrectly be declared as present in the scene.

Ideally, our signal processing chain would not only detect this TEP release but also reliably inform us if TEP is the only gas present and, if not, what combination of gases is present. The detection algorithms that we discussed in the section “Detection Algorithms” do not address this latter task—they do not give any information as to whether simultaneous TEP and DEEP detections means that both gases are present or only one of them. They also do not indicate, in the latter case, whether the stronger NMF filter score corresponds to the gas that is present. It is also possible for false alarms to occur in pixels in which no gas from the detector bank is present at all; this can happen for a variety of reasons. Identification algorithms are designed to address all of these issues.

MODEL SELECTION

We recall from (22) that under the linear signal model, the observed radiance may be written as

$$x = Sg + v = S_1g_1 + S_2g_2 + v, \quad (46)$$

where we have decomposed the gas signatures in the matrix S into two subsets. The goal of model selection algorithms is to determine the subset of gases S_1 that are present in the scene along with their amounts g_1 , with the amounts of the remaining library gases set to $g_2 = 0$.

The most straightforward way to choose a subset of gases is to try every combination of gases in the CA library, and to

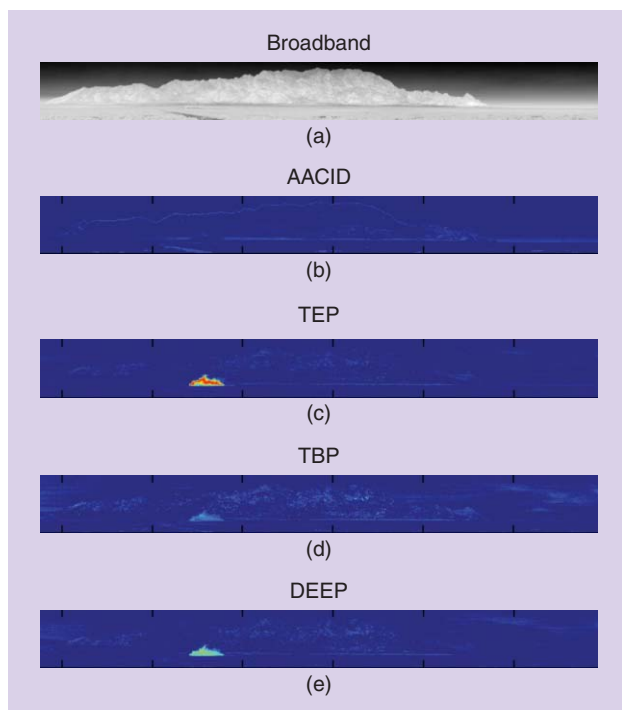


[FIG18] NMF images for various chemical signatures (0–1 color scale). TEP was released and imaged using the aerospace GBSS sensor; the other three chemicals are not present in the scene. (a) Broadband image, (b) acetic acid (AACID) signature, (c) TEP signature, (d) TBP signature, and (e) DEEP signature.

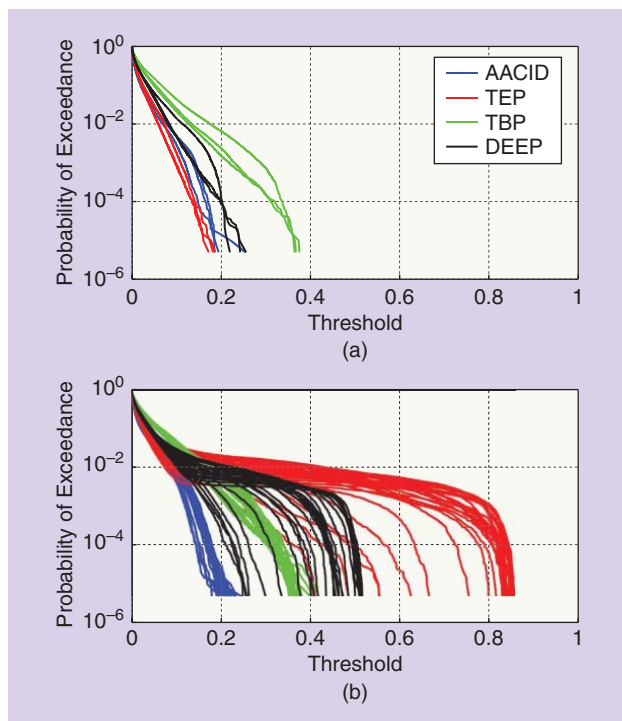


[FIG19] The probability of exceedance curves for a sequence of data cubes from the TEP release of Figure 18: (a) before and (b) after TEP's release. The color of each curve corresponds to the signature used by the NMF algorithm; different curves of the same color correspond to different cubes.

compare the results according to some criterion. This approach is known as all possible regressions (APRs) and is feasible when the library is small, and/or there is a prior belief that the number of gases present is small. When neither of these conditions hold, the combinatorics become prohibitive and other approaches must be used. A popular technique in this latter case is stepwise regression, in which individual gases are added and deleted in a stepwise fashion. There are also Bayesian approaches to this problem.

The primary difficulty in model selection is in comparing models of different complexity, i.e., different numbers of gases present. Even in the special case of searching for a single library gas, as may happen in a CWA detection system, we still must compare the single-gas models with the background-only model, to eliminate the possibility of a false alarm from the detector. A model that is a strict superset of another will always exhibit a superior fit to the data, because of its additional flexibility. Therefore, any useful measure of goodness of fit must account for this flexibility. The partial F -test is one solution [46], [50], [60]. It tests whether the benefit in goodness of fit of added term(s) is greater than that due to chance alone. Referring to (46), this approach tests the hypotheses

$$H_0 : g_2 = 0, \tag{47}$$

$$H_1 : g_2 \neq 0. \tag{48}$$

If $S(\hat{g})$ and $S(\hat{g}_1)$ are the sum of squared errors for the full model (under H_1) and the reduced model (under H_0), the H_0 hypothesis can be tested using the F -test

$$F(x) = \frac{q_2}{p-q} \frac{S(\hat{g}_1) - S(\hat{g})}{S(\hat{g})} \sim F_{q_2, p-q}(\delta), \tag{49}$$

where $F_{q_2, p-q}(\delta)$ is a noncentral F -distribution with a noncentrality parameter

$$\delta = \frac{1}{\sigma_v^2} (S_2 g_2)^T P_{S_1}^\perp (S_2 g_2). \tag{50}$$

Under H_0 , $F(x)$ follows a central F -distribution $F_{q_2, p-q}$. Therefore, if $F(x) > F_{q_2, p-q}^\alpha$, we reject H_0 with $100(1 - \alpha)$ percent confidence. The test (49) measures the contribution of gases S_2 , given that the other gases S_1 are already in the model. The derivation of the distribution of the F -test can be found in [46] and [60].

The partial F -test applies to nested models and is therefore a useful criterion for the stepwise regression approach. In this strategy, we begin with the background-only model. At each stage of the algorithm, we test for the addition of each gas in the library that is not already present, choosing that with the largest F statistic above a threshold (forward selection). We then test whether the elimination of any single gas in the model is significant (backward elimination). The procedure is repeated until no further variables are added.

While it may appear that the thresholds employed for the F -test are directly related to the probability of choosing the correct model, the situation is actually more complicated. The use of multiple tests, all based on the same data, to arrive

at a final model results in correlations that change the distribution of the outcome. Therefore, thresholds must be chosen empirically. For the same reason, the naive use of standard inferences based on the result of the test, such as confidence intervals, is generally incorrect.

Other model selection criteria may be applied to the gas identification problem, including the adjusted R^2 , Mallows's C_p , the Akaike information criterion, and the Bayesian information criterion (BIC). Instead of selecting a single model, as is done in APR and stepwise regression, Bayesian methods assign a posterior probability to each model, given the observed radiance. In general, the calculation of the posteriors requires time-consuming numerical methods such as Monte Carlo Markov chain [61], but approximate forms of BIC greatly simplify the computation [62]. Existing comparisons do not identify any one technique as clearly superior to the others [63]. More development of these methods will be necessary to explore the wide variety of deployment scenarios, as well as to study the many sources of model mismatch, as discussed in the section "Practical Considerations."

FALSE-ALARM MITIGATION

In most applications, the goal of a CA detection system is to flag the presence of one or more of a list of agents in a signature library. The output of the variable selection step of the section "Model Selection" is a subset of gases that were selected to best represent the observed radiance, along with estimates of their strengths. The gases that are chosen are those that are most significant by the criteria of the variable selection algorithm, but it is not necessarily the case that the selected gases are present in the scene. A false alarm is defined as a gas that is identified as present in the scene, when in fact it is not. False alarms can be due to a number of factors, such as a gas or other interferent present in the scene but not included in the CA library, atypical background radiance or other phenomenological fluctuation in the data, or excessive sensor noise, due either to random variation or sensor malfunction. In the first case, the interferent may have signature indistinguishable from that of the real gas at the resolution of the sensor. There is little that can be done in this case, but other sources of false alarms can potentially be eliminated by false-alarm mitigation (FAM) algorithms.

The root cause of a false alarm is that the observed radiance fits the class of models spanned by the CA library well enough that the presence of one or more gases is considered significant by the detection and identification algorithms, when the gas is not present. Nevertheless, this determination does not imply that the fit is good on an absolute scale. The goal of FAM algorithms is to test the absolute goodness-of-fit of a selected model to decide between an actual detection and a false alarm. There are many ways in which a lack of fit may manifest itself; hence, it is useful to have several measures of lack of fit, which may be combined to arrive at a final determination. Most such tests are based on various decompositions of the residuals; a variety of methods are discussed in [64] and similar texts. An additional degree of freedom that is available with imaging spectrometers

is the use of spatial information to pool the information contained in nearby pixels.

The application of FAM techniques based on goodness-of-fit statistics in practice can be challenging. A major reason is that many sources of potential model mismatch exist even when the scene contains only library gases. As we have seen in the sections "At-Sensor Radiance Signal Models" and "Detection Algorithms," the linear model (10) is only an approximate representation of the observed radiance. Many effects can influence the goodness of fit, including the presence of uncompensated atmospheric modulation, the nonlinear dependence of the gas signature on both the gas concentration and background radiance, and sensor calibration. These effects may interact in complicated ways. Some may be ameliorated with additional algorithms; e.g., when the scene and deployment geometry support atmospheric compensation (see the section "Atmospheric Compensation and Temperature-Emissivity Separation"), most of the atmospheric modulation may be removed. Nonlinear models (see the section "Quantification Algorithms") may be employed to correct for these sources of mismatch, but the additional complexity of these algorithms may conflict with other system requirements, such as real-time operation. In any case, some residual model mismatch will always be present, and the challenge in FAM is to distinguish between mismatch due to false alarms and that due to other sources. It is apparent that this area is in need of significant further development.

QUANTIFICATION ALGORITHMS

After a chemical plume has been detected, and its identity established, it is often necessary to establish the amount of gas present, which is known as *quantification*. The central parameter in chemical plume quantification is the mean concentration–path length (CL) product. When combined with information about the sensor and scene geometry, such as field of view and distance to the plume, estimates of CL may be used to obtain estimates of absolute gas quantity in each pixel of a scene. For some applications, this ancillary information may be available for single scenes from an individual sensor. Alternatively, when the plume is viewed

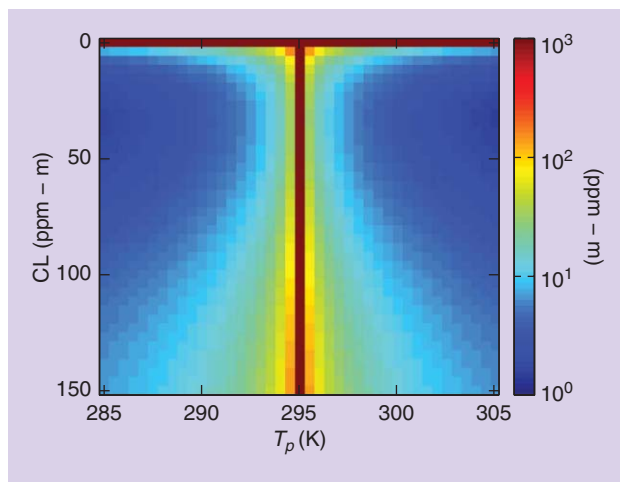


[FIG20] Cramer-Rao lower bounds on $\sqrt{\text{Var}(\hat{\gamma})}$ for SF_6 with a black body background at 295 K.

		Dispersion Mechanism			
		Explosive Release	Fugitive Emissions	Stack Emissions	Disaster Release
Enabling Phenomenology	Plume-Air Equilibrium				
	Plume Thickness				
	Spatially Varying Background				
	Spectrally Structured Background				
	Preferred Algorithms	SB	GLSF	SB, OLS (Adapted to Geometry)	SB, OLS

Favorable
 Mixed
 Unfavorable

[FIG21] The availability of enabling phenomenological effects (rows) for a variety of plume dispersion mechanisms (columns).

from more than one aspect with multiple sensors, tomographic reconstruction algorithms may enable unique plume quantification from CL estimates. Additionally, CL plays a large role as the key nonlinear parameter in the radiance signal model, through Beer's law. This nonlinear dependence is important when optically thick plumes are observed, and indeed in these cases CL estimation can play a role in identification as well as quantification.

PHYSICAL MECHANISMS

Before reviewing specific CL estimation algorithms, we describe the challenges posed by plume phenomenology and the various physical mechanisms that enable the algorithms to arrive at estimates. We begin by framing the task as a nonlinear optimization problem. In a scene containing a plume, we observe on-plume and off-plume pixels, with radiances modeled by (2) and (1), and we hope to recover estimates of

[TABLE2] A SUMMARY OF EXISTING CL ESTIMATION ALGORITHMS.

ALGORITHM	RADIANCE APPROXIMATION	
	PLUME TRANSMITTANCE	BACKGROUND CONTRAST
ELS, GLS [43]	LINEAR	LINEAR
ELSI, GLSI, GLSF [43]	LINEAR	ITERATIVE
OLS [3]	LINEAR	CONSTANT
SPATIAL OLS [3]	LINEAR	CONSTANT
OBS [66]	LINEAR	LINEAR
OBS [67]	TAYLOR SERIES	LINEAR
NLS [9]	EXPONENTIAL	ITERATIVE
NLS [12]	EXPONENTIAL	CONSTANT
SB [68]	EXPONENTIAL	ITERATIVE
BAYESIAN MAP [61], [69]	EXPONENTIAL	ITERATIVE
BAYESIAN MCMC [61]	EXPONENTIAL	ITERATIVE

the CL parameters $\{\gamma_i\}_{i=1}^{N_C}$ in Beer's law (3), with nuisance parameters T_p , L_a , $L_b(\lambda)$, and $\tau_a(\lambda)$. The observed radiances are corrupted by measurement noise. To isolate the fundamental drivers of the problem, we note that, as described in the section "Atmospheric Compensation and Temperature-Emissivity Separation," the atmospheric radiance $L_a(\lambda)$ and transmittance $\tau_a(\lambda)$ may in principle be estimated from the off-plume pixels $L_{off}(\lambda)$, reducing the number of nuisance parameters. We see that the primary challenge of CL estimation is to separate the contributions of the plume from those of the background.

To illustrate some of the difficulties of and prospects for CL estimation, it is helpful to compute the Cramer-Rao (CR) bounds for unbiased estimates of CL. Such bounds allow us to probe the limits of performance that are imposed by various physical mechanisms, without being tied to any particular algorithm. In [65], these bounds were computed under a variety of assumptions. Here, we will focus on a single example that illustrates a number of key points about the problem. We assume a single gas, sulfur hexafluoride, is present, and the atmospheric parameters are known exactly. The noise is taken to be Gaussian, independent across pixels, with a typical covariance from an experimentally measured cube. We work with the limiting case of the flat background approximation, so the background radiance is completely characterized by its temperature.

In Figure 20, the CR lower bound on the standard deviation of the estimator $\hat{\gamma}$ for the CL parameter is plotted against the plume temperature and CL, with fixed background temperature. Several important points can be inferred from this figure. First, the bounds diverge in two limits, those of a thin plume, and zero plume-background temperature contrast. This behavior is a result of nonidentifiability of the model. In the case of the thin plume, an explanation is given by (5), in which we observe that the CL parameter appears as a term in the product $C_B \Delta T \gamma$. Therefore, γ cannot be estimated independently from ΔT , so the only way that γ may be independently estimated is with extrinsic knowledge of T_p . The case of zero plume-background temperature contrast violates one of the plume visibility conditions given after (4). When this condition is violated the plume is completely invisible to the sensor. We note that the nonidentifiability is only strictly true for pure black body backgrounds, but when the flat background approximation is reasonable, the CR bounds will still be very large when the temperature contrast is small.

At a fixed value of plume temperature, distinct from that of the background, we observe that the CR bound for $\hat{\gamma}$ drops sharply as CL increases from zero. This behavior suggests that the non-linear dependence on γ resulting from an optically thick plume can be exploited, as we will see below. However, when the plume starts to become opaque, little background radiance reaches the sensor, the plume spectral signature is washed out into that of a black body at the plume temperature, and differences in plume strength are no longer visible. The CR bound therefore increases at very large values of CL.

In addition to exploiting the nonlinearity of Beer's law, there are other ways to determine the plume CL. If the plume is in

thermal equilibrium with the surrounding atmosphere, its temperature may be recovered from an atmospheric compensation algorithm [31]. If the background temperature or spectrum varies spatially across the image, some spatial resolution may be sacrificed in favor of estimating CL [3]. Finally, spectral structure in the background that overlaps that of the plume can render the model identifiable [65].

The physical mechanisms that enable CL estimation may each be present to a greater or lesser degree in a given scene, depending on the source of the gaseous plume. In Figure 21, we tabulate which phenomena may be available for exploitation for a number of common plume sources, including: explosive, referring to a sudden release caused by an explosive device; fugitive, meaning a slow, inadvertent release; stack, emissions from an industrial stack, and disaster, corresponding to a release caused by a man-made or natural disaster, such as a hurricane. For example, an explosive release would, at least initially, entail a large temperature differential between the plume and surrounding atmosphere. Such would not be the case for slow, fugitive emissions leaking from a chemical production facility. Therefore, algorithms that assume that the plume and ambient atmosphere share the same temperature would not be applicable in the former case, but would in the latter. The algorithms referred to in Figure 21 are described in the section “Algorithms.”

ALGORITHMS

Existing algorithms for gas quantification may be broadly classified according to the approximations made in the plume transmittance and plume-background thermal contrast terms in (4), as summarized in Table 2. Those that depend on a linearization of Beer's law are appropriate for optically thin plumes, while those that exploit the full nonlinear form can accommodate thick plumes. Each of these classes can be further subdivided by the treatment of the background radiance in the thermal contrast term, which may be approximated by a constant vector, a linear expansion in some basis, or an iteratively updated linear model. A variety of statistical techniques have been employed, many of which were compared in [44].

A class of algorithms was proposed in [43] for the case of a thin plume assumed to be in thermal equilibrium with the atmosphere. The temperature, mean transmittance, and upwelling radiance of the atmosphere are assumed known, as would be estimated from an atmospheric compensation algorithm or ancillary measurements. The algorithms are based on different variants of statistical linear models, including extended least squares (ELS) and generalized least squares (GLS), and iterative versions (ELSI, GLSI, and GLSF). Related techniques that allow the plume temperature to differ from that of the atmosphere were proposed in [3] and [66], based on ordinary least squares (OLS) and orthogonal background suppression (OBS), respectively.

A number of authors employ algorithms that exploit the nonlinearity in Beer's law to estimate CL, which in principle avoids the need for ancillary temperature estimates. The

approach taken in [67] is to expand Beer's law (3) in a series expansion, retaining terms beyond the linear one. The coefficients of the powers of the gas signature are obtained via a bank of projection filters. The CL parameter is obtained as a ratio of such coefficients.

The series expansion of Beer's law may be avoided by the use of nonlinear least-squares (NLS) techniques, as is done in [9] and [12]. This approach is in principle quite general, as it can be applied to the full radiance model (2). Still, special cases can lead to simplifications and improved performance of the algorithms. The algorithms in [9] are specific to the case of plume and atmosphere in thermal equilibrium, with their common temperature known from some ancillary measurement. By contrast, [12] treats the case of stack plumes, in which the gas and atmosphere are generally not in thermal equilibrium. The side-looking geometry particular to the case of stack emissions may be exploited by the choice of pixels on the chimney and in the clear sky close to, but outside of, the plume. The chimney pixels, which are assumed to have gray body emissivity, may be used to estimate the atmospheric transmittance between the plume and sensor. The clear sky pixels are used to directly estimate the background radiance, obviating the need for a statistical treatment. With knowledge of these parameters, the plume CL may be recovered.

An alternate approach for optically thick plumes is given by the selected band (SB) algorithm [68], which exploits the fact that the off-plume radiance in an on-plume pixel may be estimated from the bands in which the gas absorption is nearly zero. It is then possible to directly compute the difference between the on- and off-plume radiances and solve for the plume strength from Beer's law, assuming the atmospheric parameters are known. The CL retrieval may be performed in a single spectral band, which leads to efficiency improvements. This procedure works well for gases with narrow spectral features that are nearly transparent in many spectral bands, and has been generalized to an iterative version that accommodates a wide variety of gas signatures.

Bayesian approaches are taken by [69] and [61], which both start with the full nonlinear radiance model (2) and a low-dimensional subspace model for background emissivity. Both place Bayesian priors on the parameters, and compute the maximum a posteriori parameter values. In addition, [61] explores the full posterior distribution obtained by Markov chain Monte Carlo (MCMC). They present an example, with simulated data, to argue that estimates of the posterior distribution are particularly useful to handle the case of multiple gas species.

The previous algorithms for CL estimation all operate on a single pixel. An approach introduced in [3], which we refer to as Spatial OLS, exploits the spatial as well as spectral structure of a scene and enables CL estimation even in the flat background, thin plume limit with no extrinsic knowledge of the plume temperature. The crucial ingredient that must be present in the image is spatial variation of the background radiance, which is manifested as spatial variation of background temperature in the flat background limit. An essential assumption of this approach is that the spatial structure of the plume varies slowly compared to that of the background.

SUMMARY AND CHALLENGES

Rapid advancements in sensor and computer technology have led to a growing list of standoff LWIR hyperspectral gas-detection applications for different deployment scenarios. The effective sensing of chemical clouds requires the joint exploitation of signal processing algorithms, imaging-spectrometer characteristics, and thermal-radiance phenomenology. The underlying signal models serve as an indispensable guide to both the development of practical detection, identification, and quantification algorithms and the evaluation of their performance limits.

Detection algorithms based on MF theory are effective for optically thin plumes when the covariance matrix used for their implementation is not contaminated by the plume, i.e., it is plume-free. The development of effective algorithms for plume-free background estimation is a major practical challenge. Experimental results show that the NMF performs better than the MF detector. However, the performance of both algorithms deteriorates as plumes become optically thick. Although the detection of optically thick plumes is not a major obstacle, the identification of such plumes is still a challenge.

The gas identification problem may be framed as the statistical problem of selecting an optimal subset of a large number of variables in a linear or nonlinear model. Variable selection has deep connections to classical and modern variable selection techniques in regression models, Bayesian model averaging, and compressive sensing. The related problem of mitigating the effects of false alarms due to interferences or background anomalies involves assessing the goodness of fit of the resulting models. Both of these problems become dramatically more demanding as the number of gases in the library, and those potentially present in the plume, increase. Furthermore, these algorithms are sensitive to subtle nonlinear interactions in the plume radiance, rendering application of standard techniques challenging. New ideas will be needed for further progress in these areas.

Quantifying the amount of chemical vapor that is present is a poorly conditioned problem and quantification algorithms must therefore rely on application-specific physical effects. Some existing algorithms exploit nonlinearity among the radiance parameters, while others use spatial degrees of freedom or specific assumptions about elements of the scene. Important aspects of this area are in need of further development, e.g., the quantification of plumes not in thermal equilibrium with the surrounding atmosphere.

Although remote chemical plume sensing is already a widely deployed and successful technology, we are still some distance from the goal of fully autonomous, reliable, real-time systems. New developments in signal processing algorithms, properly informed by radiance phenomenology and statistical theory, will be needed to fully exploit this rapidly developing technology.

ACKNOWLEDGMENTS

This work was sponsored by the Defense Threat Reduction Agency under Air Force Contract FA8721-05-C-0002. Opinions, interpretations, conclusions, and recommendations are those of the authors and not necessarily endorsed by the United States Government.

AUTHORS

Dimitris G. Manolakis (dmanolakis@ll.mit.edu) received his B.S. degree in physics and his Ph.D. degree in electrical engineering from the University of Athens, Greece. He is currently a senior staff member at the Massachusetts Institute of Technology (MIT) Lincoln Laboratory in Lexington. Previously, he was a principal member of the research staff at Riverside Research Institute. He taught at the University of Athens, Northeastern University, Boston College, and Worcester Polytechnic Institute, and he is a coauthor of the textbooks *Digital Signal Processing: Principles, Algorithms, and Applications* (Prentice Hall, 2006, 4th ed.), *Statistical and Adaptive Signal Processing* (Artech House, 2005), and *Applied Digital Signal Processing* (Cambridge University Press, 2011). His research experience and interests include digital signal processing, adaptive filtering, array processing, pattern recognition, remote sensing, and radar systems.

Steven E. Golowich (golowich@ll.mit.edu) received his Ph.D. degree in physics from Harvard University and his A.B. degree in physics and mathematics from Cornell University. He is a technical staff member at the MIT Lincoln Laboratory, where his research interests include statistical signal processing, hyperspectral imaging, synthetic aperture radar, and structured light. Previously, he was a member of technical staff at the Bell Labs Mathematical Sciences Research Center and taught at Princeton University. He received the American Statistical Association Outstanding Application Award and the Wilcoxon Prize.

Robert S. DiPietro (rdipietro@jhu.edu) received his B.S. degree in applied physics and his M.S. degree in electrical engineering from Northeastern University, and he is currently pursuing a Ph.D. degree in computer science at Johns Hopkins University. He was an associate staff member at the MIT Lincoln Laboratory working on the detection of materials and CWAs in hyperspectral imagery. His research interests include detection theory, computer vision, and machine learning.

REFERENCES

- [1] R. A. Schowengerdt, *Remote Sensing: Models and Methods for Image Processing*. San Diego, CA: Elsevier, 2007.
- [2] T. Visser, "Infrared spectroscopy in environmental analysis," *Encyclopedia of Analytical Chemistry*, pp. 1–22, 2000.
- [3] S. J. Young, "Detection and quantification of gases in industrial-stack plumes using thermal-infrared hyperspectral imaging," *Aerosp. Rep. ATR-2002 (8407)*, vol. 1, 2002.
- [4] S. J. Young, "Remote sensing of CO₂ in industrial-stack plumes using thermal infrared hyperspectral imaging," *Aerosp. Rep. ATR-2003 (8407)-3*, vol. 1, 2003.
- [5] J. A. Hackwell, "LWIR/MWIR imaging hyperspectral sensor for airborne and ground-based remote sensing," in *Proc. SPIE*, Denver, CO, 1996, pp. 102–107.
- [6] D. J. Williams, B. L. Feldman, T. J. Williams, D. Pilant, P. G. Lucey, L. D. Worthy, A. M. Larar, M. Suzuki, and Q. Tong, "Detection and identification of toxic air pollutants using airborne LWIR hyperspectral imaging," in *Proc. SPIE Multi-spectral and Hyperspectral Remote Sensing Instruments and Applications II*, vol. 5655. Honolulu, HI, Jan. 2005, pp. 134–141.
- [7] P. G. Lucey, "Three years of operation of AHI: The University of Hawaii's airborne hyperspectral imager," in *Proc. SPIE*, Orlando, FL, 2001, pp. 112–120.
- [8] R. Harig and G. Matz, "Toxic cloud imaging by infrared spectrometry: A scanning FTIR system for identification and visualization," *Field Anal. Chem. Technol.*, vol. 5, no. 1–2, pp. 75–90, 2001.
- [9] R. Harig, G. Matz, and P. Rusch, "Scanning infrared remote sensing system for identification, visualization, and quantification of airborne pollutants," in *Proc. SPIE*, vol. 4574, 2002, pp. 83–94.
- [10] M. Grutter, R. Basaldud, E. Flores, and R. Harig, "Optical remote sensing for characterizing the spatial distribution of stack emissions," in *Proc. Advanced Environmental Monitoring*, 2008, pp. 107–118.

- [11] L. Sagiv, S. Rotman, and D. Blumberg, "Detection and identification of effluent gases by long wave infrared (LWIR) hyperspectral images," in *Proc. IEEE 25th Convention of Electrical and Electronics Engineers in Israel*, 2008, pp. 413–417.
- [12] P. Tremblay, S. Savary, M. Rolland, A. Villemaire, M. Chamberland, V. Farley, L. Brault, J. Giroux, J.-L. Allard, E. Dupuis, and T. Padia, "Standoff gas identification and quantification from turbulent stack plumes with an imaging Fourier-transform spectrometer," in *Proc. SPIE Advanced Environmental, Chemical, and Biological Sensing Technologies VII*, T. Vo-Dinh, R. A. Lieberman, and G. Gauglitz, Eds., vol. 7673. Orlando, FL, Apr. 2010, pp. 76 730H–12.
- [13] V. Farley, A. Vallieres, M. Chamberland, A. Villemaire, and J.-F. Legault, "Performance of the FIRST: A long-wave infrared hyperspectral imaging sensor," in *Proc. SPIE*, Stockholm, Sweden, 2006, pp. 63 980T–63 980T–11.
- [14] M. J. Thomas, P. E. Lewis, R. T. Kroutil, R. J. Combs, G. W. Small, R. W. Zywicki, D. L. Stageberg, C. T. Chaffin, Jr., and T. L. Marshall, "Infrared detection and analysis of vapor plumes using an airborne sensor," in *Proc. SPIE*, vol. 4725, 2002, p. 47.
- [15] R. Kroutil, P. Lewis, M. Thomas, T. Curry, D. Miller, R. Combs, and A. Cummings, "Emergency response chemical detection using passive infrared spectroscopy," in *SPIE Newsroom*, pp. 1–3, 2006.
- [16] M. J. Thomas, "Rationale and methodology for generating an airborne emergency response spectral reference library," in *Proc. SPIE*, San Diego, CA, 2003, pp. 222–229.
- [17] P. Lewis, M. Thomas, R. Kroutil, R. Combs, A. Cummings, D. Miller, T. Curry, and S. Shen, "Airborne mapping of chemical plumes in the aftermath of hurricanes Katrina and Rita," in *Proc. SPIE*, vol. 62331X–I–II, 2006.
- [18] R. Harig, G. Matz, P. Rusch, H. H. Gerhard, J. H. Gerhard, and V. Schlabs, "New scanning infrared gas imaging system (SIGIS 2) for emergency response forces," in *Proc. SPIE*, vol. 5995, 2005, pp. 174–181.
- [19] A. G. Mares, "LWIR spectral measurements of volcanic sulfur dioxide plumes," in *Proc. SPIE*, Orlando, FL, 2004, pp. 266–272.
- [20] M. Grutter, R. Basaldua, C. Rivera, R. Harig, W. Junkerman, E. Caetano, and H. Delgado-Granados, "SO₂ emissions from popocatepetl volcano: Emission rates and plume imaging using optical remote sensing techniques," *Atmos. Chem. Phys.*, vol. 8, no. 22, pp. 6655–6663, Nov. 2008.
- [21] Y. Yamaguchi, A. B. Kahle, H. Tsu, T. Kawakami, and M. Pniel, "Overview of advanced spaceborne thermal emission and reflection radiometer (ASTER)," *IEEE Trans. Geosci. Remote Sens.*, vol. 36, no. 4, pp. 1062–1071, 2002.
- [22] L. Kirkland, K. Herr, E. Keim, P. Adams, J. Salisbury, J. Hackwell, and A. Treiman, "First use of an airborne thermal infrared hyperspectral scanner for compositional mapping," *Remote Sens. Environ.*, vol. 80, no. 3, pp. 447–459, June 2002.
- [23] R. G. Vaughan, W. M. Calvin, and J. V. Taraniuk, "SEBASS hyperspectral thermal infrared data: Surface emissivity measurement and mineral mapping," *Remote Sens. Environ.*, vol. 85, no. 1, pp. 48–63, 2003.
- [24] J. A. Hackwell, D. W. Warren, R. P. Bongiovanni, S. J. Hansel, T. L. Hayhurst, D. J. Mabry, M. G. Stivjee, and J. W. Skinner, "LWIR/MWIR imaging hyperspectral sensor for airborne and ground-based remote sensing," in *Proc. SPIE*, 1996, pp. 102–107.
- [25] B. Hammond and M. Popa, "Overview of the joint services lightweight standoff chemical agent detector (JSLSCAD)," in *Proc. SPIE*, 2005, pp. 86–95.
- [26] R. M. Goody and Y. L. Yung, *Atmospheric Radiation: Theoretical Basis*. New York: Oxford Univ. Press, 1995.
- [27] G. E. Thomas and K. Stamnes, *Radiative Transfer in the Atmosphere and Ocean*. Cambridge, U.K.: Cambridge Univ. Press, 2002.
- [28] P. M. Chu, F. R. Guenther, G. C. Rhoderick, and W. J. Lafferty, "The NIST quantitative infrared database," *J. Res. Natl. Inst. Standards Technol.*, vol. 104, no. 1, pp. 59–81, 1999.
- [29] S. W. Sharpe, T. J. Johnson, R. L. Sams, P. M. Chu, G. C. Rhoderick, and P. A. Johnson, "Gas-phase databases for quantitative infrared spectroscopy," *Appl. Spectrosc.*, vol. 58, no. 12, pp. 1452–1461, 2004.
- [30] S. W. Sharpe, T. J. Johnson, R. L. Sams, P. M. Chu, G. C. Rhoderick, and P. A. Johnson, "Gas-phase databases for quantitative infrared spectroscopy," *Appl. Spectrosc.*, vol. 58, no. 12, pp. 1452–1461, Dec. 2004.
- [31] S. J. Young, B. R. Johnson, and J. A. Hackwell, "An in-scene method for atmospheric compensation of thermal hyperspectral data," *J. Geophys. Res. Atmos.*, vol. 107, no. D24, p. 4774, 2002.
- [32] D. Gu, A. R. Gillespie, A. B. Kahle, and F. D. Palluconi, "Autonomous atmospheric compensation (AAC) of high resolution hyperspectral thermal infrared remote-sensing imagery," *IEEE Trans. Geosci. Remote Sens.*, vol. 38, no. 6, pp. 2557–2570, 2000.
- [33] V. J. Realmuto, "Separating the effects of temperature and emissivity: Emissivity spectrum normalization," in *Proc. 2nd TMS Workshop*, 1990, pp. 90–55.
- [34] C. Borel, "Surface emissivity and temperature retrieval for a hyperspectral sensor," in *Geoscience and Remote Sensing Symp. Proc.*, vol. 1, July 1998, pp. 546–549.
- [35] C. Borel, "Error analysis for a temperature and emissivity retrieval algorithm for hyperspectral imaging data," *Int. J. Remote Sens.*, vol. 29, no. 17, pp. 5029–5045, 2008.
- [36] R. A. Johnson and D. W. Wichern, *Applied Multivariate Statistical Analysis*, 6th ed. Englewood Cliffs, New Jersey: Prentice Hall, 2007.
- [37] E. Truslow, D. Manolakis, M. Pieper, T. Cooley, M. Brueggeman, and S. Lipson, "Performance prediction of matched filter and ACE hyperspectral target detectors," *IEEE J. Select. Topics Signal Processing*, to be published.
- [38] D. Marden and D. Manolakis, "Modeling hyperspectral imaging data using elliptically contoured distributions," in *Proc. SPIE Algorithms and Technologies for Multispectral, Hyperspectral, and Ultraspectral Imagery IX*, S. S. Shen and P. E. Lewis, Eds. Orlando, FL, 2003.
- [39] K. T. Fang, S. Kotz, and K. W. Ng, *Symmetric Multivariate and Related Distributions*. New York: Chapman & Hall, 1990.
- [40] D. Manolakis, M. Rossacci, D. Zhang, J. Cipar, R. Lockwood, T. Cooley, and J. Jacobson, "Statistical characterization of hyperspectral background clutter in the reflective spectral region," *Appl. Opt.*, vol. 47, no. 28, pp. F96–F106, 2008.
- [41] R. S. DiPietro, E. Truslow, D. G. Manolakis, S. E. Golowich, and R. B. Lockwood, "False-alarm characterization in hyperspectral gas-detection applications," in *Proc. SPIE*, 2012, pp. 85 150I–85 150I–11.
- [42] A. R. Gillespie, "Spectral mixture analysis of multispectral thermal infrared images," *Remote Sens. Environ.*, vol. 42, no. 2, pp. 137–145, 1992.
- [43] N. B. Gallagher, B. M. Wise, and D. M. Sheen, "Estimation of trace vapor concentration-pathlength in plumes for remote sensing applications from hyperspectral images," *Anal. Chim. Acta*, vol. 490, no. 1–2, pp. 139–152, 2003.
- [44] S. Niu, S. E. Golowich, and D. G. Manolakis, "Algorithms for remote quantification of chemical plumes: A comparative study," in *Proc. SPIE*, vol. 8390, 2012, p. 83902I.
- [45] J. Carrano, "Chemical and biological sensor standards study," Defence Advanced Research Projects Agency, Washington, DC, Tech. Rep., ADA458370, 2004.
- [46] S. M. Kay, *Fundamentals of Statistical Signal Processing*. Englewood Cliffs, New Jersey: Prentice Hall, 1998.
- [47] S. Kraut, L. Scharf, and L. T. McWhorter, "Adaptive subspace detectors," *IEEE Trans. Signal Processing*, vol. 49, no. 1, pp. 1–16, Jan. 2001.
- [48] H. Cox and R. Pitre, "Robust DMR and multi-rate adaptive beamforming," in *Proc. Signals, Systems & Computers*, vol. 1, Nov. 1997, pp. 920–924.
- [49] D. Manolakis, R. Lockwood, T. Cooley, and J. Jacobson, "Hyperspectral detection algorithms: Use covariances or subspaces?" in *Proc. SPIE*, vol. 7457, 2009, pp. 745702I–8.
- [50] D. Manolakis, C. Siracusa, and G. Shaw, "Hyperspectral subpixel target detection using the linear mixing model," *IEEE Trans. Geosci. Remote Sens.*, vol. 39, no. 7, pp. 1392–1409, July 2001.
- [51] J. Theiler and B. Foy, "Effect of signal contamination in matched-filter detection of the signal on a cluttered background," *IEEE Geosci. Remote Sens. Lett.*, vol. 3, no. 1, pp. 98–102, 2006.
- [52] S. Niu, S. E. Golowich, V. K. Ingle, and D. G. Manolakis, "Implications and mitigation of model mismatch and covariance contamination for hyperspectral chemical agent detection," *Opt. Eng.*, vol. 52, no. 2, pp. 026 202–026 202, Feb. 2013.
- [53] H. Cox, "Resolving power and sensitivity to mismatch of optimum array processors," *J. Acoust. Soc. Am.*, vol. 54, no. 3, pp. 771–785, 1973.
- [54] H. Cox, R. Zeskind, and M. Owen, "Robust adaptive beamforming," *IEEE Trans. Acoust., Speech Signal Processing*, vol. 35, no. 10, pp. 1365–1376, 1987.
- [55] J. Li, P. Stoica, and Z. Wang, "On robust Capon beamforming and diagonal loading," *IEEE Trans. Signal Processing*, vol. 51, no. 7, pp. 1702–1715, July 2003.
- [56] R. Lorenz and S. Boyd, "Robust minimum variance beamforming," *IEEE Trans. Signal Processing*, vol. 53, no. 5, pp. 1684–1696, May 2005.
- [57] D. Manolakis, R. Lockwood, T. Cooley, and J. Jacobson, "Is there a best hyperspectral detection algorithm?" in *Proc. SPIE Defense, Security, and Sensing*, vol. 7334, no. 1, 2009, p. 733402.
- [58] J. Theiler, B. R. Foy, and A. M. Fraser, "Nonlinear signal contamination effects for gaseous plume detection in hyperspectral imagery," in *Proc. SPIE*, vol. 6233, 2006, pp. 623310–1–12.
- [59] M. A. Richards, *Fundamentals of Radar Signal Processing*, 1st ed. New York: McGraw-Hill, June 2005.
- [60] R. R. Hocking, *Methods and Applications of Linear Models*. New York: Wiley, 1996.
- [61] P. Heasler, C. Posse, J. Hylden, and K. Anderson, "Nonlinear Bayesian algorithms for gas plume detection and estimation from hyper-spectral thermal image data," *Sensors*, vol. 7, no. 6, pp. 905–920, 2007.
- [62] A. E. Raftery, D. Madigan, and J. A. Hoeting, "Bayesian model averaging for linear regression models," *J. Am. Stat. Assoc.*, vol. 92, no. 437, pp. 179–191, Mar. 1997.
- [63] T. Burr, H. Fry, B. Mcvey, E. Sander, J. Cavanaugh, and A. Neath, "Performance of variable selection methods in regression using variations of the bayesian information criterion," *Commun. Stat. Simul. Computat.*, vol. 37, no. 3, pp. 507–520, 2008.
- [64] G. A. F. Seber and A. J. Lee, *Linear Regression Analysis*. Hoboken, NJ: Wiley, Jan. 2012.
- [65] S. E. Golowich and D. G. Manolakis, "Cramer-Rao bounds for long-wave infrared gaseous plume quantification," *Opt. Eng.*, vol. 53, no. 2, p. 021109, 2014.
- [66] A. Hayden, E. Niple, and B. Boyce, "Determination of trace-gas amounts in plumes by the use of orthogonal digital filtering of thermal-emission spectra," *Appl. Opt.*, vol. 35, no. 16, pp. 2802–2809, 1996.
- [67] A. Hayden and R. Noll, "Remote trace gas quantification using thermal IR spectroscopy and digital filtering based on principal components of background scene clutter," in *Proc. SPIE*, vol. 3071, 1997, pp. 158–168.
- [68] S. Niu, S. E. Golowich, V. K. Ingle, and D. G. Manolakis, "Hyperspectral chemical plume quantification via background radiance estimation," in *Proc. SPIE*, vol. 8743, May 2013, p. 874,316.
- [69] C. M. Gittins, "Detection and characterization of chemical vapor fugitive emissions by nonlinear optimal estimation: Theory and simulation," *Appl. Opt.*, vol. 48, no. 23, pp. 4545–4561, 2009.

[lecture NOTES]

Emil Björnson, Mats Bengtsson,
and Björn Ottersten

Optimal Multiuser Transmit Beamforming: A Difficult Problem with a Simple Solution Structure

Transmit beamforming is a versatile technique for signal transmission from an array of N antennas to one or multiple users [1]. In wireless communications, the goal is to increase the signal power at the intended user and reduce interference to nonintended users. A high signal power is achieved by transmitting the same data signal from all antennas but with different amplitudes and phases, such that the signal components add coherently at the user. Low interference is accomplished by making the signal components add destructively at nonintended users. This corresponds mathematically to designing beamforming vectors (that describe the amplitudes and phases) to have large inner products with the vectors describing the intended channels and small inner products with nonintended user channels.

If there is line-of-sight (LoS) between the transmitter and receiver, beamforming can be seen as forming a signal beam towards the receiver; see Figure 1. Beamforming can also be applied in non-LoS scenarios, if the multipath channel is known, by making the multipath components add coherently or destructively.

Since transmit beamforming focuses the signal energy at certain places, less energy arrives at other places. This allows for so-called space-division multiple access (SDMA), where K spatially separated users are served simultaneously. One beamforming vector is assigned to each user and can be matched to its channel. Unfortunately, the finite number of transmit antennas only provides a limited amount of spatial directivity, which means that there are

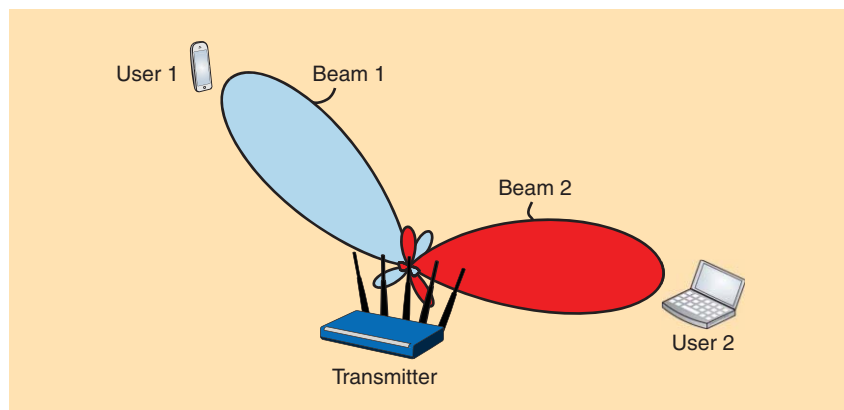


[FIG1] A visualization of transmit beamforming in an LoS scenario. The beamforming is adapted to the location of the intended user, such that a main-lobe with a strong signal power is achieved towards this user while the sidelobes that cause interference to other nonintended users are weak.

energy leakages between the users that act as interference.

While it is fairly easy to design a beamforming vector that maximizes the signal power at the intended user, it is difficult to strike a perfect balance between maximizing the signal power and minimizing the interference leakage. In fact, the optimization of multiuser transmit beamforming is generally a nondeterministic polynomial-time (NP)-hard problem [2]. Nevertheless, this lecture note shows that the optimal transmit beamforming has a simple structure with very intuitive properties and interpretations. This structure provides a theoretical foundation for practical low-complexity beamforming schemes.

RELEVANCE

Adaptive transmit beamforming is key to increased spectral and energy efficiency in next-generation wireless networks, which are expected to include very large antenna arrays [3]. In light of the difficulty to compute the optimal multiuser transmit beamforming, there is a plethora of

heuristic schemes. Although each scheme might be optimal in some special case and can be tweaked to fit other cases, these heuristic schemes generally do not provide sufficient degrees of freedom to ever achieve the optimal performance. The main purpose of this lecture note is to provide a structure of optimal linear transmit beamforming, with a sufficient number of design parameters to not lose optimality. This simple structure provides many insights and is easily extended to take various design constraints of practical cellular networks into account.

PREREQUISITES

The readers require basic knowledge in linear algebra, communication theory, and convex optimization.

PROBLEM (P1): POWER MINIMIZATION WITH SINR CONSTRAINTS

We consider a downlink channel where a base station (BS) equipped with N antennas communicates with K single-antenna

Digital Object Identifier 10.1109/MSP.2014.2312183

Date of publication: 13 June 2014

users using SDMA. The data signal to user k is denoted $s_k \in \mathbb{C}$ and is normalized to unit power, while the vector $\mathbf{h}_k \in \mathbb{C}^{N \times 1}$ describes the corresponding channel. The K different data signals are separated spatially using the linear beamforming vectors $\mathbf{w}_1, \dots, \mathbf{w}_K \in \mathbb{C}^{N \times 1}$, where \mathbf{w}_k is associated with user k . The normalized version ($\mathbf{w}_k / \|\mathbf{w}_k\|$) is called the beamforming direction and points out a direction in the N -dimensional vector space—note that it only corresponds to a physical direction in LoS scenarios. The squared norm $\|\mathbf{w}_k\|^2$ is the power allocated for transmission to user k . We model the received signal $r_k \in \mathbb{C}$ at user k as

$$r_k = \mathbf{h}_k^H \left(\sum_{i=1}^K \mathbf{w}_i s_i \right) + n_k, \quad (1)$$

where n_k is additive receiver noise with zero mean and variance σ^2 . Consequently, the signal-to-interference-and-noise ratio (SINR) at user k is

$$\begin{aligned} \text{SINR}_k &= \frac{|\mathbf{h}_k^H \mathbf{w}_k|^2}{\sum_{i \neq k} |\mathbf{h}_k^H \mathbf{w}_i|^2 + \sigma^2} \\ &= \frac{\frac{1}{\sigma^2} |\mathbf{h}_k^H \mathbf{w}_k|^2}{\sum_{i \neq k} \frac{1}{\sigma^2} |\mathbf{h}_k^H \mathbf{w}_i|^2 + 1}. \end{aligned} \quad (2)$$

We use the latter, noise-normalized expression in this lecture note since it emphasizes the impact of the noise.

The transmit beamforming can be optimized to maximize some performance utility metric, which is generally a function of the SINRs. The main goal of this lecture note is to analyze a general formulation of such a problem, defined later as Problem (P2), and to derive the structure of the optimal beamforming. As a preparation toward this goal, we first solve the relatively simple power minimization problem

$$\begin{aligned} &\underset{\mathbf{w}_1, \dots, \mathbf{w}_K}{\text{minimize}} && \sum_{k=1}^K \|\mathbf{w}_k\|^2 \\ &\text{subject to} && \text{SINR}_k \geq \gamma_k. \end{aligned} \quad (\text{P1})$$

The parameters $\gamma_1, \dots, \gamma_K$ are the SINRs that each user shall achieve at the optimum of (P1), using as little transmit power as possible. The γ -parameters can, for example, describe the SINRs required for achieving certain data rates.

The values of the γ -parameters are constant in (P1) and clearly impact the optimal beamforming solution, but we will see later that the solution structure is always the same.

SOLUTION TO PROBLEM (P1)

The first step toward solving (P1) is to reformulate it as a convex problem. The cost function $\sum_{k=1}^K \|\mathbf{w}_k\|^2$ is clearly a convex function of the beamforming vectors. To extract the hidden convexity of the SINR constraints, $\text{SINR}_k \geq \gamma_k$, we make use of a trick from [4]. We note that the absolute values in the SINRs in (2) make \mathbf{w}_k and $e^{j\theta_k} \mathbf{w}_k$ completely equivalent for any common phase rotation $\theta_k \in \mathbb{R}$. Without loss of optimality, we exploit this phase ambiguity to rotate the phase such that the inner product $\mathbf{h}_k^H \mathbf{w}_k$ is real valued and positive. This implies that $\sqrt{|\mathbf{h}_k^H \mathbf{w}_k|^2} = \mathbf{h}_k^H \mathbf{w}_k \geq 0$. By letting $\Re(\cdot)$ denoting the real part, the constraint $\text{SINR}_k \geq \gamma_k$ can be rewritten as

$$\begin{aligned} \frac{1}{\gamma_k \sigma^2} |\mathbf{h}_k^H \mathbf{w}_k|^2 &\geq \sum_{i \neq k} \frac{1}{\sigma^2} |\mathbf{h}_k^H \mathbf{w}_i|^2 + 1 \\ &\Leftrightarrow \frac{1}{\sqrt{\gamma_k \sigma^2}} \Re(\mathbf{h}_k^H \mathbf{w}_k) \\ &\geq \sqrt{\sum_{i \neq k} \frac{1}{\sigma^2} |\mathbf{h}_k^H \mathbf{w}_i|^2 + 1}. \end{aligned} \quad (3)$$

The reformulated SINR constraint in (3) is a second-order cone constraint, which is a convex type of constraint [4]–[6], and it is easy to show that Slater’s constraint qualification is fulfilled [7]. Hence, optimization theory provides many important properties for the reformulated convex problem; in particular, strong duality and that the Karush–Kuhn–Tucker (KKT) conditions are necessary and sufficient for the optimal solution. It is shown in [6, Appendix A] (by a simple parameter change) that these properties also hold for the original problem (P1), although (P1) is not convex. The strong duality and KKT conditions for (P1) play a key role in this lecture note. To show this, we define the Lagrangian function of (P1) as

$$\begin{aligned} \mathcal{L}(\mathbf{w}_1, \dots, \mathbf{w}_K, \lambda_1, \dots, \lambda_K) &= \sum_{k=1}^K \|\mathbf{w}_k\|^2 + \sum_{k=1}^K \lambda_k \left(\sum_{i \neq k} \frac{1}{\sigma^2} |\mathbf{h}_k^H \mathbf{w}_i|^2 \right. \\ &\quad \left. + 1 - \frac{1}{\gamma_k \sigma^2} |\mathbf{h}_k^H \mathbf{w}_k|^2 \right), \end{aligned} \quad (4)$$

where $\lambda_k \geq 0$ is the Lagrange multiplier associated with the k th SINR constraint. The dual function is $\min_{\mathbf{w}_1, \dots, \mathbf{w}_K} \mathcal{L} = \sum_{k=1}^K \lambda_k$ and the strong duality implies that it equals the total power $\sum_{k=1}^K \|\mathbf{w}_k\|^2$ at the optimal solution, which we utilize later. To solve (P1), we now exploit the stationarity KKT conditions, which say that $\partial \mathcal{L} / \partial \mathbf{w}_k = 0$, for $k = 1, \dots, K$, at the optimal solution. This implies

$$\mathbf{w}_k + \sum_{i \neq k} \frac{\lambda_i}{\sigma^2} \mathbf{h}_i \mathbf{h}_i^H \mathbf{w}_k - \frac{\lambda_k}{\gamma_k \sigma^2} \mathbf{h}_k \mathbf{h}_k^H \mathbf{w}_k = 0 \quad (5)$$

$$\begin{aligned} &\Leftrightarrow \left(\mathbf{I}_N + \sum_{i=1}^K \frac{\lambda_i}{\sigma^2} \mathbf{h}_i \mathbf{h}_i^H \right) \mathbf{w}_k \\ &= \frac{\lambda_k}{\sigma^2} \left(1 + \frac{1}{\gamma_k} \right) \mathbf{h}_k \mathbf{h}_k^H \mathbf{w}_k \end{aligned} \quad (6)$$

$$\begin{aligned} &\Leftrightarrow \mathbf{w}_k = \left(\mathbf{I}_N + \sum_{i=1}^K \frac{\lambda_i}{\sigma^2} \mathbf{h}_i \mathbf{h}_i^H \right)^{-1} \mathbf{h}_k \\ &\quad \times \underbrace{\frac{\lambda_k}{\sigma^2} \left(1 + \frac{1}{\gamma_k} \right) \mathbf{h}_k^H \mathbf{w}_k}_{= \text{scalar}} \end{aligned} \quad (7)$$

where \mathbf{I}_N denotes the $N \times N$ identity matrix. The expression (6) is achieved from (5) by adding the term $(\lambda_k / \sigma^2) \times \mathbf{h}_k \mathbf{h}_k^H \mathbf{w}_k$ to both sides and (7) is obtained by multiplying with an inverse. Since $(\lambda_k / \sigma^2) (1 + 1/\gamma_k) \mathbf{h}_k^H \mathbf{w}_k$ is a scalar, (7) shows that the optimal \mathbf{w}_k must be parallel to $(\mathbf{I}_N + \sum_{i=1}^K (\lambda_i / \sigma^2) \mathbf{h}_i \mathbf{h}_i^H)^{-1} \mathbf{h}_k$. In other words, the optimal beamforming vectors $\mathbf{w}_1^*, \dots, \mathbf{w}_K^*$ are

$$\begin{aligned} \mathbf{w}_k^* &= \underbrace{\sqrt{p_k}}_{= \text{beamforming power}} \underbrace{\left(\left(\mathbf{I}_N + \sum_{i=1}^K \frac{\lambda_i}{\sigma^2} \mathbf{h}_i \mathbf{h}_i^H \right)^{-1} \mathbf{h}_k \right)}_{= \tilde{\mathbf{w}}_k^* = \text{beamforming direction}} \\ &\text{for } k = 1, \dots, K, \end{aligned} \quad (8)$$

where p_k denotes the beamforming power and $\tilde{\mathbf{w}}_k^*$ denotes the unit-norm beamforming direction for user k . The K unknown beamforming powers are computed by noting that the SINR constraints (3) hold with equality at the optimal solution. This implies $(1/\gamma_k) \times p_k |\mathbf{h}_k^H \tilde{\mathbf{w}}_k^*|^2 - \sum_{i \neq k} p_i |\mathbf{h}_k^H \tilde{\mathbf{w}}_i^*|^2 = \sigma^2$ for $k = 1, \dots, K$. Since we know the beamforming directions, we have K linear equations and obtain the K powers as

lecture NOTES continued

$$\begin{bmatrix} p_1 \\ \vdots \\ p_K \end{bmatrix} = \mathbf{M}^{-1} \begin{bmatrix} \sigma^2 \\ \vdots \\ \sigma^2 \end{bmatrix},$$

where

$$[\mathbf{M}]_{ij} = \begin{cases} \frac{1}{\gamma_i} |\mathbf{h}_i^H \tilde{\mathbf{w}}_i^*|^2, & i = j, \\ -|\mathbf{h}_i^H \tilde{\mathbf{w}}_j^*|^2, & i \neq j, \end{cases} \quad (9)$$

and $[\mathbf{M}]_{ij}$ denotes the (i, j) th element of the matrix $\mathbf{M} \in \mathbb{R}^{K \times K}$.

By combining (8) and (9), we obtain the structure of optimal beamforming as a function of the Lagrange multipliers $\lambda_1, \dots, \lambda_K$. Finding these multipliers is outside the scope of this lecture note, for reasons that will be clear in the next section. However, we note that the Lagrange multipliers can be computed by convex optimization [4] or from the fixed-point equations $\lambda_k = \sigma^2 / \left((1 + (1/\gamma_k)) \mathbf{h}_k^H (\mathbf{I}_N + \sum_{i=1}^K (\lambda_i/\sigma^2) \mathbf{h}_i \mathbf{h}_i^H)^{-1} \mathbf{h}_k \right)$ for all k [5], [6].

PROBLEM (P2): GENERAL TRANSMIT BEAMFORMING OPTIMIZATION

The main goal of this lecture note is to analyze a very general transmit beamforming optimization problem. We want to maximize some arbitrary utility function $f(\text{SINR}_1, \dots, \text{SINR}_K)$ that is strictly increasing in the SINR of each user, while the total transmit power is limited by P . This is stated mathematically as

$$\begin{aligned} & \underset{\mathbf{w}_1, \dots, \mathbf{w}_K}{\text{maximize}} && f(\text{SINR}_1, \dots, \text{SINR}_K) \\ & \text{subject to} && \sum_{k=1}^K \|\mathbf{w}_k\|^2 \leq P. \quad (\text{P2}) \end{aligned}$$

Despite the conciseness of (P2), it is generally very hard to solve [7]. Indeed, [2] proves that it is NP-hard for many common utility functions; for example, the sum rate $f(\text{SINR}_1, \dots, \text{SINR}_K) = \sum_{k=1}^K \log_2(1 + \text{SINR}_k)$. Nevertheless, we will show that the structure of the optimal solution to (P2) is easily obtained.

SOLUTION STRUCTURE TO PROBLEM (P2)

Suppose for the moment that we know the SINR values $\text{SINR}_1^*, \dots, \text{SINR}_K^*$ that are achieved by the optimal solution to (P2). What would happen if we set $\gamma_k = \text{SINR}_k^*$, for $k = 1, \dots, K$, and solve (P1) for these particular γ -parameters? The answer is that the beamforming vectors that solve

(P1) will now also solve (P2) [7]. This is understood as follows: (P1) finds beamforming vectors that achieve the SINR values $\text{SINR}_1^*, \dots, \text{SINR}_K^*$. The solution to (P1) must satisfy the total power constraint in (P2), because (P1) gives the beamforming that achieves the given SINRs using the minimal amount of power. Since the beamforming vectors from (P1) are feasible for (P2) and achieves the optimal SINR values, they are an optimal solution to (P2) as well.

We can, of course, not know $\text{SINR}_1^*, \dots, \text{SINR}_K^*$ unless we actually solve (P2). In fact, the difference between the relatively easy (P1) and the difficult (P2) is that the SINRs are predefined in (P1) while we need to find the optimal SINR values (along with the beamforming vectors) in (P2). The connection between the two problem implies, however, that the optimal beamforming for (P2) is

$$\mathbf{w}_k^* = \sqrt{p_k} \frac{\left(\mathbf{I}_N + \sum_{i=1}^K \frac{\lambda_i}{\sigma^2} \mathbf{h}_i \mathbf{h}_i^H \right)^{-1} \mathbf{h}_k}{\left\| \left(\mathbf{I}_N + \sum_{i=1}^K \frac{\lambda_i}{\sigma^2} \mathbf{h}_i \mathbf{h}_i^H \right)^{-1} \mathbf{h}_k \right\|} \quad \text{for } k = 1, \dots, K \quad (10)$$

for some positive parameters $\lambda_1, \dots, \lambda_K$. The strong duality property of (P1) implies $\sum_{i=1}^K \lambda_i = P$, since P is the optimal cost function in (P1) and $\sum_{i=1}^K \lambda_i$ is the dual function. Finding the optimal parameter values in this range is equivalent to solving (P2), thus it is as hard as solving the original problem. However, the importance of (10) is that it provides a simple structure for the optimal beamforming.

Since the matrix inverse in (10) is the same for all users, the matrix $\mathbf{W}^* = [\mathbf{w}_1^* \dots \mathbf{w}_K^*] \in \mathbb{C}^{N \times K}$ with the optimal beamforming vectors can be written in a compact form. To this end, we note that $\sum_{i=1}^K (\lambda_i/\sigma^2) \mathbf{h}_i \mathbf{h}_i^H = (1/\sigma^2) \mathbf{H} \mathbf{\Lambda} \mathbf{H}^H$ where $\mathbf{H} = [\mathbf{h}_1 \dots \mathbf{h}_K] \in \mathbb{C}^{N \times K}$ contains the channels and $\mathbf{\Lambda} = \text{diag}(\lambda_1, \dots, \lambda_K)$ is a diagonal matrix with the λ -parameters. By gathering the power allocation in a matrix \mathbf{P} , we obtain

$$\mathbf{W}^* = \left(\mathbf{I}_N + \frac{1}{\sigma^2} \mathbf{H} \mathbf{\Lambda} \mathbf{H}^H \right)^{-1} \mathbf{H} \mathbf{P}^{\frac{1}{2}}, \quad (11)$$

where $\mathbf{P} = \text{diag}(p_1/\|\mathbf{I}_N + (1/\sigma^2) \mathbf{H} \mathbf{\Lambda} \mathbf{H}^H\|^{-1} \times \mathbf{h}_1\|^2, \dots, p_K/\|\mathbf{I}_N + (1/\sigma^2) \mathbf{H} \mathbf{\Lambda} \mathbf{H}^H\|^{-1} \times \mathbf{h}_K\|^2)$

and $(\cdot)^{1/2}$ denotes the matrix square root. In the next section we study the structure of (10) and (11) and gain some insights.

INTUITION BEHIND THE OPTIMAL STRUCTURE

The optimal beamforming direction in (10) consists of two main parts: 1) the channel vector \mathbf{h}_k between the BS and the intended user k ; and 2) the matrix $(\mathbf{I}_N + \sum_{i=1}^K (\lambda_i/\sigma^2) \mathbf{h}_i \mathbf{h}_i^H)^{-1}$. Beamforming in the same direction as the channel (i.e., $\tilde{\mathbf{w}}_k^{(\text{MRT})} = \mathbf{h}_k / \|\mathbf{h}_k\|$) is known as *maximum ratio transmission* (MRT) or matched filtering [8]. This selection maximizes the received signal power $p_k |\mathbf{h}_k^H \tilde{\mathbf{w}}_k|^2$ at the intended user, because

$$\underset{\tilde{\mathbf{w}}_k: \|\tilde{\mathbf{w}}_k\|^2=1}{\text{argmax}} |\mathbf{h}_k^H \tilde{\mathbf{w}}_k|^2 = \frac{\mathbf{h}_k}{\|\mathbf{h}_k\|} \quad (12)$$

due to the Cauchy–Schwarz inequality. This is the optimal beamforming direction for $K = 1$, but not when there are multiple users because the interuser interference is unaccounted for in MRT. This is basically what the multiplication of \mathbf{h}_k with $(\mathbf{I}_N + \sum_{i=1}^K (\lambda_i/\sigma^2) \mathbf{h}_i \mathbf{h}_i^H)^{-1}$ (before normalization) takes care of; it rotates MRT to reduce the interference that is caused in the co-user directions $\mathbf{h}_1, \dots, \mathbf{h}_{k-1}, \mathbf{h}_{k+1}, \dots, \mathbf{h}_K$. This interpretation is illustrated in Figure 2, where the optimal beamforming lies somewhere in between MRT and the vector that is orthogonal to all co-user channels. The optimal beamforming direction depends ultimately on the utility function $f(\cdot, \dots, \cdot)$. However, the parameter $\lambda_i \geq 0$ can be seen as the priority of user i , where a larger value means that other users' beamforming vectors will be more orthogonal to \mathbf{h}_i .

ASYMPTOTIC PROPERTIES

Next, we study the asymptotic beamforming properties. In the low signal-to-noise ratio (SNR) case, represented by $\sigma^2 \rightarrow \infty$, the system is noise-limited and the beamforming matrix in (11) converges to

$$\mathbf{W}_{\sigma^2 \rightarrow \infty}^* = (\mathbf{I}_N + 0)^{-1} \mathbf{H} \mathbf{P}_{\sigma^2 \rightarrow \infty}^{\frac{1}{2}} = \mathbf{H} \mathbf{P}_{\sigma^2 \rightarrow \infty}^{\frac{1}{2}}, \quad (13)$$

where the matrix inverse vanishes and $\mathbf{P}_{\sigma^2 \rightarrow \infty}$ denotes the asymptotic power allocation. This implies that \mathbf{w}_k^* is a

scaled version of the channel vector \mathbf{h}_k , which is equivalent to MRT.

At high SNRs, given by $\sigma^2 \rightarrow 0$, the system is interference-limited. We focus on the case $N \geq K$ with at least one spatial degree-of-freedom per user—this is the meaningful operating regime for SDMA. To avoid singularity in the inverse when σ^2 is small, we use the identity $(\mathbf{I} + \mathbf{A}\mathbf{B})^{-1}\mathbf{A} = \mathbf{A}(\mathbf{I} + \mathbf{B}\mathbf{A})^{-1}$ and rewrite (11) as $\mathbf{W}^* = \mathbf{H}(\sigma^2\mathbf{I}_K + \mathbf{\Lambda}\mathbf{H}^H\mathbf{H})^{-1}\tilde{\mathbf{P}}^{1/2}$, where $\tilde{\mathbf{P}} = \text{diag}(p_1/\|(\sigma^2\mathbf{I}_K + \mathbf{\Lambda}\mathbf{H}^H\mathbf{H})^{-1}\mathbf{h}_1\|^2, \dots, p_K/\|(\sigma^2\mathbf{I}_K + \mathbf{\Lambda}\mathbf{H}^H\mathbf{H})^{-1}\mathbf{h}_K\|^2)$ denotes the corresponding rewritten power allocation matrix. It now follows that

$$\begin{aligned} \mathbf{W}_{\sigma^2 \rightarrow 0}^* &= \mathbf{H}(\mathbf{0}\mathbf{I}_K + \mathbf{\Lambda}\mathbf{H}^H\mathbf{H})^{-1}\tilde{\mathbf{P}}_{\sigma^2 \rightarrow 0} \\ &= \mathbf{H}(\mathbf{H}^H\mathbf{H})^{-1}\mathbf{\Lambda}^{-1}\tilde{\mathbf{P}}_{\sigma^2 \rightarrow 0}, \end{aligned} \quad (14)$$

where the term $\sigma^2\mathbf{I}_K$ vanishes when $\sigma^2 \rightarrow 0$ and $\tilde{\mathbf{P}}_{\sigma^2 \rightarrow 0}$ denotes the asymptotic power allocation. This solution is known as *channel inversion* or *zero-forcing beamforming* (ZFBF) [9], because it contains the pseudoinverse $\mathbf{H}(\mathbf{H}^H\mathbf{H})^{-1}$ of the channel matrix \mathbf{H}^H . Hence, $\mathbf{H}^H\mathbf{W}_{\sigma^2 \rightarrow 0}^* = \mathbf{\Lambda}^{-1}\tilde{\mathbf{P}}_{\sigma^2 \rightarrow 0}$ is a diagonal matrix. Since the off-diagonal elements are of the form $\mathbf{h}_i^H\mathbf{w}_k^* = 0$ for $i \neq k$, this beamforming causes zero interuser interference by projecting \mathbf{h}_k onto the subspace that is orthogonal to the co-user channels.

The asymptotic properties are intuitive if we look at the SINR in (2). The noise dominates over the interference at low SNRs, thus we should use MRT to maximize the signal power without caring about interference. On the contrary, the interference dominates over the noise at high SNRs, thus we should use ZFBF to remove it. We recall from Figure 2 that MRT and ZFBF are also the two extremes from a geometric perspective and the optimal beamforming at arbitrary SNR balance between these extremes.

Another asymptotic regime has received much attention: the use of very large arrays where the number of antennas, N , goes to infinity in the performance analysis [3]. A key motivation is that the squared channel norms ($\|\mathbf{h}_k\|^2$) are proportional to N , while the cross-products ($|\mathbf{h}_i^H\mathbf{h}_k|$ for $i \neq k$) increase more slowly with N (the exact scaling depends on the channel models). Hence,

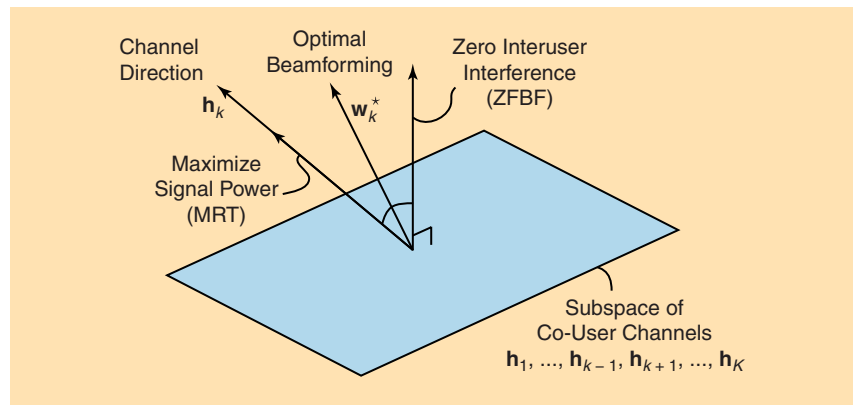


[FIG2] The optimal beamforming \mathbf{w}_k^* is based on the channel direction \mathbf{h}_k but rotated to balance between high signal power and being orthogonal to the co-user channels.

the user channels become orthogonal as $N \rightarrow \infty$, which reduces interference and allows for less transmit power. Observe that $\sigma^2\mathbf{I}_K + \mathbf{\Lambda}\mathbf{H}^H\mathbf{H} \approx \mathbf{\Lambda}\mathbf{H}^H\mathbf{H}$ for large N , since only the elements of $\mathbf{H}^H\mathbf{H}$ grow with N . Similar to (14), one can then prove that ZFBF is asymptotically optimal. MRT performs relatively well in this regime due to the asymptotic channel orthogonality, but will *not* reach the same performance as ZFBF [3, Table 1].

RELATIONSHIP TO RECEIVE BEAMFORMING

There are striking similarities between transmit beamforming in the downlink and receive beamforming in the uplink, but also fundamental differences. To describe these, we consider the uplink scenario where the same K users are transmitting to the same BS. The received signal $\mathbf{r} \in \mathbb{C}^{N \times 1}$ at the BS is $\mathbf{r} = \sum_{i=1}^K \mathbf{h}_i s_i + \mathbf{n}$, where user k transmits the data signal s_k using the uplink transmit power q_k . The receiver noise \mathbf{n} has zero mean and the covariance matrix $\sigma^2\mathbf{I}_N$. The uplink SINR for the signal from user k is

$$\text{SINR}_k^{\text{uplink}} = \frac{\frac{q_k}{\sigma^2} |\mathbf{h}_k^H \mathbf{v}_k|^2}{\sum_{i \neq k} \frac{q_i}{\sigma^2} |\mathbf{h}_i^H \mathbf{v}_k|^2 + \mathbf{v}_k^H \mathbf{I}_N \mathbf{v}_k}, \quad (15)$$

where $\mathbf{v}_k \in \mathbb{C}^{N \times 1}$ is the unit-norm receive beamforming vector used by the BS to spatially discriminate the signal sent by user k from the interfering signals. The uplink SINR in (15) is similar to the downlink SINR in (2), but the noise term is scaled by

$\|\mathbf{v}_k\|^2$ and the indices are swapped in the interference term: $|\mathbf{h}_k^H \mathbf{w}_i|^2$ in the downlink is replaced by $q_i |\mathbf{h}_i^H \mathbf{v}_k|^2$ in the uplink. The latter is because downlink interference originates from the beamforming vectors of other users, while uplink interference arrives through the channels from other users. This tiny difference has a fundamental impact on the optimization, because the uplink SINR of user k only contains its own receive beamforming vector \mathbf{v}_k . We can therefore optimize the beamforming separately for each k :

$$\begin{aligned} \text{argmax}_{\mathbf{v}_k: \|\mathbf{v}_k\|^2=1} & \frac{\frac{q_k}{\sigma^2} |\mathbf{h}_k^H \mathbf{v}_k|^2}{\sum_{i \neq k} \frac{q_i}{\sigma^2} |\mathbf{h}_i^H \mathbf{v}_k|^2 + \mathbf{v}_k^H \mathbf{I}_N \mathbf{v}_k} \\ &= \frac{\left(\mathbf{I}_N + \sum_{i=1}^K \frac{q_i}{\sigma^2} \mathbf{h}_i \mathbf{h}_i^H \right)^{-1} \mathbf{h}_k}{\left\| \left(\mathbf{I}_N + \sum_{i=1}^K \frac{q_i}{\sigma^2} \mathbf{h}_i \mathbf{h}_i^H \right)^{-1} \mathbf{h}_k \right\|}. \end{aligned} \quad (16)$$

The solution follows since this is the maximization of a generalized Rayleigh quotient [7]. Note that the same receive beamforming is optimal irrespective of which function of the uplink SINRs we want to optimize. In fact, (16) also minimizes the mean squared error (MSE) between the transmitted signal and the processed received signal, thus it is known as the Wiener filter and minimum MSE (MMSE) filter [9].

The optimal transmit and receive beamforming have the same structure; the Wiener filter is obtained from (10) by setting λ_k equal to the uplink transmit power q_k . This parameter choice is only optimal

lecture NOTES continued

for the downlink in symmetric scenarios, as discussed later. In general, the parameters are different because the uplink signals pass through different channels (thus, the uplink is affected by variations in the channel norms), while everything that reaches a user in the downlink has passed through a single channel [4].

HEURISTIC TRANSMIT BEAMFORMING

It is generally hard to find the optimal λ -parameters, but the beamforming structure in (10) and (11) serves as a foundation for heuristic beamforming; that is, we can select the parameters judiciously and hope for close-to-optimal beamforming. If we make all the parameters equal, $\lambda_k = \lambda$ for all k , we obtain

$$W = \left(I_N + \frac{\lambda}{\sigma^2} H H^H \right)^{-1} H P^{\frac{1}{2}} \\ = H \left(I_K + \frac{\lambda}{\sigma^2} H^H H \right)^{-1} P^{\frac{1}{2}}. \quad (17)$$

The heuristic beamforming in (17) is known as *regularized ZFBF* [10] since the identity matrix acts as a regularization of the ZFBF in (14). Regularization is a common way to achieve numerical stability and robustness to channel uncertainty. Since there is only a single parameter λ

in regularized ZFBF, it can be optimized for a certain transmission scenario by conventional line search.

The sum property $\sum_{i=1}^K \lambda_i = P$ suggests that we set the parameter in regularized ZFBF equal to the average transmit power: $\lambda = P/K$. This parameter choice has a simple interpretation, because the corresponding beamforming directions $\left(I_N + \sum_{i=1}^K P/(\sigma^2 K) h_i h_i^H \right)^{-1} h_k$ are the ones that maximize the ratio of the desired signal power to the noise power plus the interference power caused to other users; in other words,

$$\operatorname{argmax}_{\tilde{w}_k: \|\tilde{w}_k\|^2=1} \frac{\frac{P}{K\sigma^2} |h_k^H \tilde{w}_k|^2}{\sum_{i \neq k} \frac{P}{K\sigma^2} |h_i^H \tilde{w}_k|^2 + 1} \\ = \frac{\left(I_N + \sum_{i=1}^K \frac{P}{K\sigma^2} h_i h_i^H \right)^{-1} h_k}{\left\| \left(I_N + \sum_{i=1}^K \frac{P}{K\sigma^2} h_i h_i^H \right)^{-1} h_k \right\|}. \quad (18)$$

This heuristic performance metric is identical to maximization of the uplink SINR in (15) for equal uplink powers $q_i = P/K$. Hence, (18) is solved, similar to (16), as a generalized Rayleigh quotient. The idea of maximizing the metric in (18)

has been proposed independently by many authors and the resulting beamforming has received many different names. The earliest work might be [11] from 1995, where the authors suggested beamforming “such that the quotient of the mean power of the desired contribution to the undesired contributions is maximized.” Due to the relationship to receive beamforming, this scheme is also known as *transmit Wiener filter* [9], *signal-to-leakage-and-noise ratio beamforming* [12], *transmit MMSE beamforming*, and *virtual SINR beamforming*; see [7, Remark 3.2] for a further historical background.

The heuristic beamforming direction in (18) is truly optimal only in special cases. For example, consider a symmetric scenario where the channels are equally strong and have well-separated directivity, while the utility function in (P2) is symmetric with respect to $\text{SINR}_1, \dots, \text{SINR}_K$. It then makes sense to let the λ -parameters be symmetric as well, which implies $\lambda_k = P/K$ for all k since $\sum_{i=1}^K \lambda_i = P$. In other words, the reason that the transmit MMSE beamforming performs well is that it satisfies the optimal beamforming structure—at least in symmetric scenarios. In general,

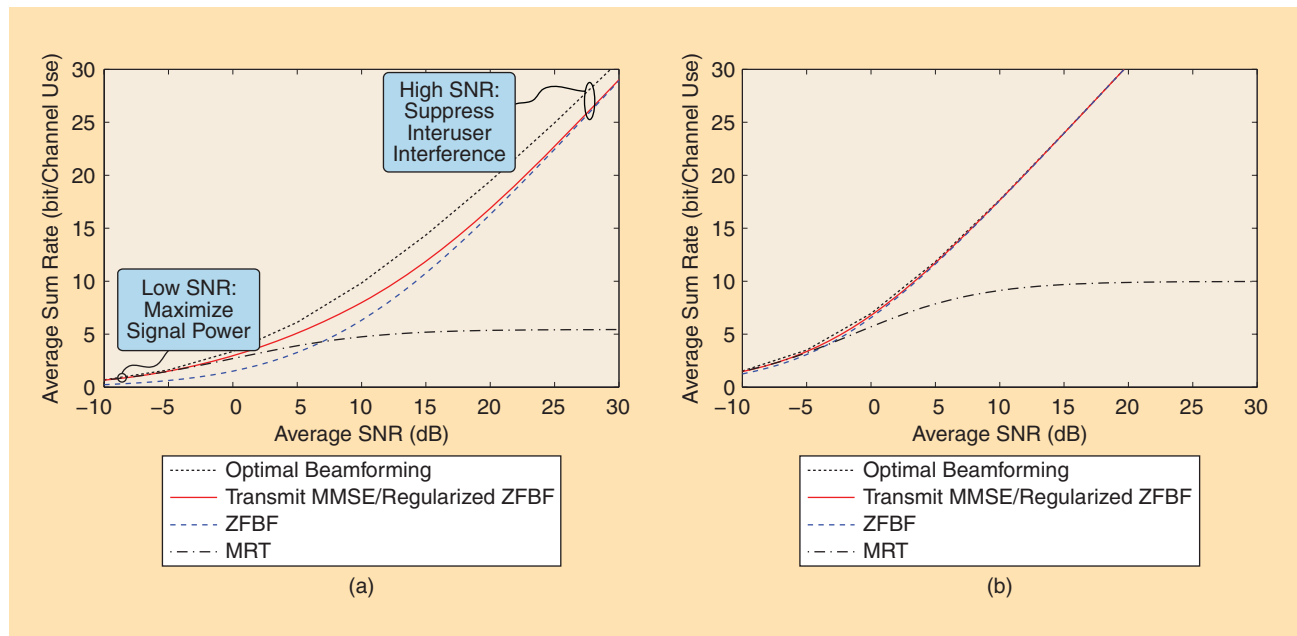


[FIG3] The average sum rate for $K = 4$ users as a function of the average SNR. Heuristic beamforming can perform closely to the optimal beamforming, particularly when there are many more antennas than users. Transmit MMSE/regularized ZFBF always performs better, or equally well, as MRT and ZFBF. (a) $N = 4$ antennas. (b) $N = 12$ antennas.

we need all the K degrees of freedom provided by $\lambda_1, \dots, \lambda_K$ to find the optimal beamforming, because the single parameter in regularized ZFBF does not provide enough degrees of freedom to manage asymmetric user channel conditions and utility functions.

The properties of MRT, ZFBF, and transmit MMSE beamforming are illustrated by simulation in Figure 3. We consider $K = 4$ users and (P2) with the sum rate as utility function: $f(\text{SINR}_1, \dots, \text{SINR}_4) = \sum_{k=1}^4 \log_2(1 + \text{SINR}_k)$. The simulation results are averaged over random circularly symmetric complex Gaussian channel realizations, $\mathbf{h}_k \sim \mathcal{CN}(0, \mathbf{I}_N)$, and the SNR is measured as P/σ^2 . The optimal beamforming is computed by the branch-reduce-and-bound algorithm in [7] whose computational complexity grows exponentially with K . This huge complexity stands in contrast to the closed-form heuristic beamforming directions that are combined with a closed-form power allocation scheme from [7, Theorem 3.16].

Figure 3 shows the simulation results for (a) $N = 4$ and (b) $N = 12$ transmit antennas. In the former case, we observe that MRT is near optimal at low SNRs, while ZFBF is asymptotically optimal at high SNRs. Transmit MMSE beamforming is a more versatile scheme that combines the respective asymptotic properties of MRT and ZFBF with good performance at intermediate SNRs. However, there is still a significant gap to the optimal solution, which is only bridged by fine-tuning the $K = 4$ parameters $\lambda_1, \dots, \lambda_4$ (with an exponential complexity in K). In the case of $N = 12$, there are many more antennas than users, which makes the need for fine-tuning much smaller; transmit MMSE beamforming is near optimal in the entire SNR range, which is an important observation for systems with very large antenna arrays [3] (these systems are often referred to as massive MIMO). Figure 3 was generated using MATLAB; the code is available for download in [13].

EXTENSIONS

Next, we briefly describe extensions to scenarios with multiple BSs and practical power constraints.

MULTIPLE COOPERATING BASE STATIONS

Suppose the N transmit antennas are distributed over multiple cooperating BSs. A key difference from (P2) is that only a subset of the BSs transmits to each user, which has the advantage of not having to distribute all users' data to all BSs. This is equivalent to letting only a subset of the antennas transmit to each user. We describe the association by a diagonal matrix $\mathbf{D}_k = \text{diag}(d_{k,1}, \dots, d_{k,N})$, where $d_{k,n} = 1$ if antenna n transmits to user k and $d_{k,n} = 0$ otherwise [7]. The effective beamforming vector of user k is $\mathbf{D}_k \mathbf{w}_k$ instead of \mathbf{w}_k . By plugging this into the derivations, the optimal beamforming in (10) becomes

$$\begin{aligned} & \mathbf{D}_k \mathbf{w}_k^* \\ &= \sqrt{p_k} \frac{\left(\mathbf{I}_N + \sum_{i=1}^K \frac{\lambda_i}{\sigma^2} \mathbf{D}_k^H \mathbf{h}_i \mathbf{h}_i^H \mathbf{D}_k \right)^{-1} \mathbf{D}_k^H \mathbf{h}_k}{\left\| \left(\mathbf{I}_N + \sum_{i=1}^K \frac{\lambda_i}{\sigma^2} \mathbf{D}_k^H \mathbf{h}_i \mathbf{h}_i^H \mathbf{D}_k \right)^{-1} \mathbf{D}_k^H \mathbf{h}_k \right\|} \\ & \text{for } k = 1, \dots, K \end{aligned} \quad (19)$$

for some positive parameters $\lambda_1, \dots, \lambda_K$. The balancing between high signal power and low interference leakage now takes place only among the antennas that actually transmit to the particular user.

GENERAL POWER AND SHAPING CONSTRAINTS

Practical systems are constrained not only in terms of the total transmit power, as in (P1) and (P2), but also in other respects; for example, maximal per-antenna power, limited power per BS, regulatory limits on the equivalent isotropic radiated power, and interference suppression toward other systems. Such constraints can be well described by having L quadratic constraints of the form

$$\sum_{k=1}^K \mathbf{w}_k^H \mathbf{Q}_{\ell,k} \mathbf{w}_k \leq P_{\ell} \quad \text{for } \ell = 1, \dots, L, \quad (20)$$

where the positive semidefinite weighting matrix $\mathbf{Q}_{\ell,k} \in \mathbb{C}^{N \times N}$ describes a subspace where the power is limited by a constant $P_{\ell} \geq 0$. The total power constraint in (P2) is given by $L = 1$ and $\mathbf{Q}_{1,k} = \mathbf{I}_N$ for all k , while per-antenna constraints are given by $L = N$ and $\mathbf{Q}_{\ell,k}$ being nonzero only at

the ℓ th diagonal element. The weighting matrices are user specific and can be used for precise interference shaping; for example, the interference leakage at user i is limited to P_i if we set $\mathbf{Q}_{\ell,k} = \mathbf{h}_i \mathbf{h}_i^H$ for $k \neq i$ and $\mathbf{Q}_{\ell,i} = 0$.

If the power constraints are plugged into (P2), it is proved in [6] and [7] that the optimal beamforming is

$$\mathbf{W}^* = \left(\sum_{\ell=1}^L \mu_{\ell} \mathbf{Q}_{\ell,k} + \frac{1}{\sigma^2} \mathbf{H} \mathbf{H}^H \right)^{-1} \mathbf{H} \mathbf{P}^{\frac{1}{2}}, \quad (21)$$

where the L new parameters $\mu_1, \dots, \mu_L \geq 0$ describe the importance of shaping the beamforming to each power constraint; if μ_{ℓ} is large, very little power is transmitted into the subspace of $\mathbf{Q}_{\ell,k}$. On the contrary, inactive power constraints have $\mu_{\ell} = 0$ and, thus, have no impact on the optimal beamforming. One can show that the parameters satisfy $\sum_{i=1}^K \lambda_i = P_{\max}$ and $\sum_{\ell=1}^L P_{\ell} \mu_{\ell} = P_{\max}$ where $P_{\max} = \max_{\ell} P_{\ell}$ [7].

LESSONS LEARNED AND FUTURE AVENUES

It is difficult to compute the optimal multiuser transmit beamforming, but the solution has a simple and intuitive structure with only one design parameter per user. This fundamental property has enabled many researchers to propose heuristic beamforming schemes—there are many names for essentially the same simple scheme. The optimal beamforming maximizes the received signal powers at low SNRs, minimizes the interference leakage at high SNRs, and balances between these conflicting goals at intermediate SNRs.

The optimal beamforming structure can be extended to practical multicell scenarios, as briefly described in this lecture note. Alternative beamforming parameterizations based on local channel state information (CSI) or transceiver hardware impairments can be found in [7]. Some open problems in this field are the robustness to imperfect CSI, multistream beamforming to multiantenna users, multicasting where each signal is intended for a group of users, and adaptive λ -parameter selection based on the utility function.

lecture **NOTES** continued**ACKNOWLEDGMENTS**

This work was supported by the International Postdoc Grant 2012-228 from the Swedish Research Council and by the European Research Council (ERC) under the European Community's Seventh Framework Programme (FP7/20072013)/ERC grant 228044.

AUTHORS

Emil Björnson (emil.bjornson@liu.se) is an assistant professor in the Department of Electrical Engineering, Linköping University, Sweden. He is also a joint postdoctoral researcher at Supélec, France, and at the KTH Royal Institute of Technology, Sweden.

Mats Bengtsson (mats.bengtsson@ee.kth.se) is an associate professor in the Department of Signal Processing, KTH Royal Institute of Technology, Sweden.

Björn Ottersten (bjorn.ottersten@ee.kth.se) is a professor in the Department of Signal Processing, KTH Royal Institute of Technology, Sweden, and also the director for the Interdisciplinary

Centre for Security, Reliability and Trust, University of Luxembourg.

REPRODUCIBLE RESEARCH

This lecture note has supplementary, downloadable material available in [13], provided by the authors. The material includes MATLAB code that can reproduce all the simulation results. Contact Emil Björnson for further questions about this work.

REFERENCES

- [1] A. Gershman, N. Sidiropoulos, S. Shahbazpanahi, M. Bengtsson, and B. Ottersten, "Convex optimization-based beamforming," *IEEE Signal Processing Mag.*, vol. 27, no. 3, pp. 62–75, 2010.
- [2] Y.-F. Liu, Y.-H. Dai, and Z.-Q. Luo, "Coordinated beamforming for MISO interference channel: Complexity analysis and efficient algorithms," *IEEE Trans. Signal Processing*, vol. 59, no. 3, pp. 1142–1157, 2011.
- [3] F. Rusek, D. Persson, B. Lau, E. Larsson, T. Marzetta, O. Edfors, and F. Tufvesson, "Scaling up MIMO: Opportunities and challenges with very large arrays," *IEEE Signal Processing Mag.*, vol. 30, no. 1, pp. 40–60, 2013.
- [4] M. Bengtsson and B. Ottersten, "Optimal and suboptimal transmit beamforming," in *Handbook of Antennas in Wireless Communications*, L. C. Godara, Ed. Boca Raton, FL: CRC Press, pp. 18–18-33, 2001.

[5] A. Wiesel, Y. Eldar, and S. Shamai, "Linear precoding via conic optimization for fixed MIMO receivers," *IEEE Trans. Signal Processing*, vol. 54, no. 1, pp. 161–176, 2006.

[6] W. Yu and T. Lan, "Transmitter optimization for the multi-antenna downlink with per-antenna power constraints," *IEEE Trans. Signal Processing*, vol. 55, no. 6, pp. 2646–2660, 2007.

[7] E. Björnson and E. Jorswieck, "Optimal resource allocation in coordinated multi-cell systems," *Found. Trends Commun. Inform. Theory*, vol. 9, no. 2–3, pp. 113–381, 2013.

[8] T. Lo, "Maximum ratio transmission," *IEEE Trans. Commun.*, vol. 47, no. 10, pp. 1458–1461, 1999.

[9] M. Joham, W. Utschick, and J. Nosssek, "Linear transmit processing in MIMO communications systems," *IEEE Trans. Signal Processing*, vol. 53, no. 8, pp. 2700–2712, 2005.

[10] C. Peel, B. Hochwald, and A. Swindlehurst, "A vector-perturbation technique for near-capacity multiantenna multiuser communication—Part I: Channel inversion and regularization," *IEEE Trans. Commun.*, vol. 53, no. 1, pp. 195–202, 2005.

[11] P. Zetterberg and B. Ottersten, "The spectrum efficiency of a base station antenna array system for spatially selective transmission," *IEEE Trans. Veh. Technol.*, vol. 44, no. 3, pp. 651–660, 1995.

[12] M. Sadek, A. Tarighat, and A. Sayed, "A leakage-based precoding scheme for downlink multi-user MIMO channels," *IEEE Trans. Wireless Commun.*, vol. 6, no. 5, pp. 1711–1721, 2007.

[13] E. Björnson, M. Bengtsson, and B. Ottersten. MATLAB code [Online]. Available: <https://github.com/emilbjornson/optimal-beamforming>

SPspecial **REPORTS** (continued from page 14)

has been on diabetes. A glucose meter has been out on the market for many years, and we have gone through at least one revision in that standard and we're working on a second revision right now. We're also working with an eHealth group at the University of Toronto that is developing a glucose monitor and insulin pump.

IEEE SPM: Batteries are always an issue, but probably more so with portable, or wearable, medical devices. Is this being addressed from a technical and/or standards development perspective?

Kirwan: Batteries are always an issue. As consumers, we turn off Wi-Fi and Bluetooth because we know it's draining our battery. We need a better standard. But there are a lot of things happening now, and oneM2M is a good example of what we can do to help mobile devices in the future. Just looking at Continua; most of

our certified devices have the Bluetooth transport in them; I would say 60–70%. So, as I already indicated, we're seeing manufacturers moving away from the classic Bluetooth to Bluetooth Low Energy devices. But let's say I get out of the hospital and I have a blood pressure monitor and maybe some other medical device, my phone is going to be dead before long. The difference between the technologies between classic Bluetooth and Bluetooth Low Energy is that the radio is always on versus the radio is always off. If the radio is always off, it comes on at a timed interval. It comes on when it has to. It's supposedly more efficient. That's the difference with medical devices. With more of these [Bluetooth Low Energy-based] products going through the certification process, it's only a matter of time before we see more of them on the market as real consumer products.

IEEE SPM: Any special events we should watch out for that focus on mHealth this year and into 2015?

Kirwan: Continua will be back on track with our mHealth summits this year, holding three events with Plugfests over the remainder of 2014. Two of the events will be held in conjunction with mHealth Summit conferences, bringing new opportunities to increase Continua's visibility as an immediate benefit of our new collaboration under the PCHA umbrella. We will also colocate the Continua Summer Summit with the Open Mobile Alliance.

The Plugfest dates will be announced shortly. Due to the timing of the currently scheduled events, we will move Continua's AsiaPac Summit to spring 2015.

Editor's Note: This interview was conducted by Ron Schneiderman, a regular contributor to *SPM*.

SP

Jinchang Ren, Jaime Zabalza, Stephen Marshall,
and Jiangbin Zheng

Effective Feature Extraction and Data Reduction in Remote Sensing Using Hyperspectral Imaging

With numerous and contiguous spectral bands acquired from visible light (400–1,000 nm) to (near) infrared (1,000–1,700 nm and over), hyperspectral imaging (HSI) can potentially identify different objects by detecting minor changes in temperature, moisture, and chemical content. As a result, HSI has been widely applied in a number of application areas, including remote sensing [1]. HSI data contains two-dimensional (2-D) spatial and one-dimensional spectral information, and naturally forms a three-dimensional (3-D) hypercube with a high spectral resolution in nanometers that enables robust discrimination of ground features. However, new challenges arise in dealing with extremely large data sets. For a hypercube with relatively small spatial dimension of 600×400 pixels at 16 bits-per-band-per-pixel, the data volume becomes 120 MB for 250 spectral bands. In some cases, this large data volume can be linearly increased when multiple hypercubes are acquired across time to monitor system dynamics in consecutive time instants. When the ratio between the feature dimension (spectral bands) and the number of data samples (in vector-based pixels) is vastly different, high-dimensional data suffers from the well-known curse of dimensionality. For feature extraction and dimensionality reduction, principal components analysis (PCA) is widely used in HSI [2], where the number of extracted components is significantly reduced compared to the original feature dimension, i.e., the number of spectral bands. For effective analysis of large-scale

data in HSI, conventional PCA faces three main challenges:

- obtain the covariance matrix in extremely large spatial dimension, which can lead to software tools such as MATLAB running out of memory
- cope with the high computational cost required for analysis of large data sets
- retain locally structured elements that only appear in a small number of bands (mainly local structures) for improved discriminating ability when feature bands are globally extracted as principal components.

This article discusses several variations and extensions of conventional PCA to address the aforementioned challenges. These variations and extensions include slicing the HSI data for efficient computation of the covariance matrix similarly done in 2-D-PCA analysis [3] and grouping the spectral data to preserve the local structures and further speedup the process to determine the covariance matrix [4]. In addition, we also discuss some non-PCA-based approaches for feature extraction and data reduction, based on techniques such as band selection, random projection, singular value decomposition, and machine-learning approaches such as the support vector machine (SVM) [2], [5], [6].

FEATURE EXTRACTION USING PCA AND ITS VARIATIONS

PCA has been widely used for unsupervised feature extraction and data reduction [2], [7]. Through orthogonal projection and truncation of the transformed feature data, PCA can successfully remove correlation inherent in the data.

For a hypercube with F spectral bands and a spatial size of $R \times C$ (Figure 1),

where R and C are the number of rows and columns, respectively, conventional PCA first converts the data into an $F \times S$ matrix (\mathbf{I}), where $S = RC$. Then, the covariance matrix of \mathbf{I} , $\mathbf{\Lambda}$, is obtained as follows: eigendecomposition is followed by data projection to determine the principal components. Due to the extremely large size of S , which can be over 100 kB, practical difficulties arise when directly determining $\mathbf{\Lambda}$ from \mathbf{I} . To solve these problems, 2-D-PCA inspired data slicing PCA (SPCA) [3] along with segmented PCA (Seg-PCA) [4] are used.

DATA SLICING PCA

Rather than taking all spectral vectors in \mathbf{I} together, SPCA (Figure 1) treats each spectral vector \mathbf{I}_n separately when determining the corresponding covariance matrix $\mathbf{\Lambda}_n$, where $n \in [1, S]$. For each $\mathbf{I}_n \in \mathfrak{R}^{F \times 1}$, its associated partial covariance matrix is obtained as $\mathbf{I}_n \mathbf{I}_n^T \in \mathfrak{R}^{F \times F}$, and the overall covariance matrix $\mathbf{\Lambda}$ is determined as the sum of all partial covariance matrices by

$$\mathbf{\Lambda} = \frac{1}{S} \sum_{n=1}^{S=RC} \mathbf{I}_n \mathbf{I}_n^T. \quad (1)$$

SPCA is equivalent to PCA in determining the covariance matrix. The fundamental difference is that the calculation of $\mathbf{\Lambda}$ is implemented by a series of S independent partial covariance matrices. As such, the memory requirement is reduced from $F \times S$ to $F \times 1$. In addition to this, these partial covariance matrices can be separately calculated in parallel to improve efficiency.

SEGMENTED PCA

Although the spectral data in HSI naturally form long vectors, the input spectral data can be grouped to produce a

Digital Object Identifier 10.1109/MSP.2014.2312071

Date of publication: 13 June 2014

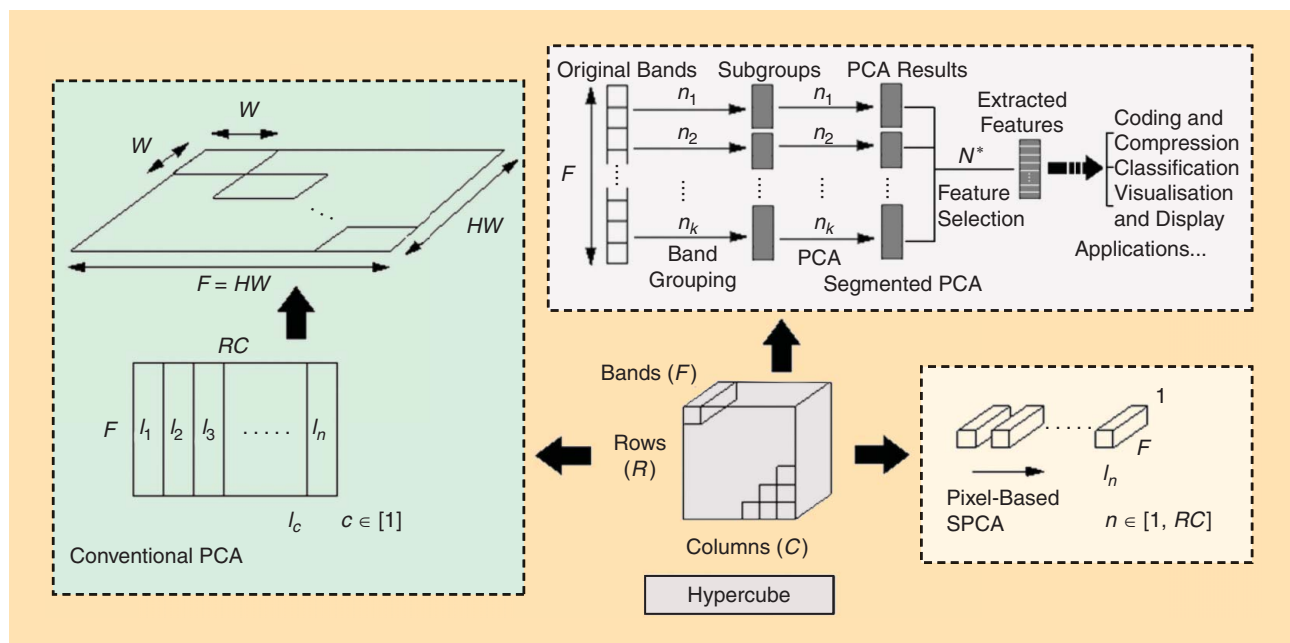


[FIG1] Diagrams of conventional PCA in comparison with the SPCA and Seg-PCA.

series of small vectors for fast calculation of PCA in each group while enabling extraction of local structures from each group. As shown in Figure 1, in Seg-PCA each of the S spectral vectors is grouped to form k subvectors. For each subvector, the size of its covariance matrix is reduced to $n_k \times n_k$.

For a particular group $b \in [1, k]$, let $\mathbf{i}_{mb} = [i_{1m} \ i_{2m} \ \dots \ i_{n_b m}]^T$ denote the corresponding small spectral vector formed from the original F bands, where $m \in [1, S]$, and Λ_b is the covariance matrix. Then, Λ_b can be determined as

$$\Lambda_b = \frac{1}{S} \sum_{m=1}^S \mathbf{i}_{mb} \mathbf{i}_{mb}^T, \quad (2)$$

where again S denotes the spatial size of the hypercube. Also note that $\mathbf{i}_{mb} \mathbf{i}_{mb}^T$ is the partial covariance matrix obtained from the grouped spectral vector \mathbf{i}_{mb} .

For a given spectral vector $\mathbf{i}_n \in \mathcal{R}^{F \times 1}$, conventional PCA extracts all the principal components from the F bands. In contrast, Seg-PCA divides \mathbf{i}_n into H groups and ensures that variable numbers of components are extracted from each group. As a result, Seg-PCA has the potential to preserve some local spectral structures, which are nondominant and thus are discarded

in conventional PCA. Such local structures provide additional values to Seg-PCA for superior discrimination ability as explained below.

In Seg-PCA, as illustrated in Figure 1, each spectral vector of F bands is grouped into H groups or K groups as shown in Figure 1. When $H = 1$, Seg-PCA defaults to SPCA, which is equivalent to the conventional PCA. In fact, the performance of the Seg-PCA is strongly dependent on how the bands are grouped, as it affects how much additional information can be extracted to improve the conventional PCA.

In one particular case where all groups contain the same number of W bands, $HW = F$, the covariance matrices from different groups share the same dimension. As a result, they can be summed to form one covariance matrix $\Lambda_{\text{Seg-PCA}}$. This can further simplify the eigendecomposition procedure for better efficiency, as only one matrix rather than k must be processed

$$\Lambda_{\text{Seg-PCA}} = \sum_{b=1}^k \Lambda_b. \quad (3)$$

In conventional PCA, using SPCA for example, the covariance matrix in (1) can be rewritten as follows, where $\mathbf{a}_n = [a_{1n}, a_{2n}, \dots, a_{fn}]^T$:

$$\begin{aligned} \Lambda_{\text{SPCA}} &= \frac{1}{S} \sum_{n=1}^S \mathbf{i}_n \mathbf{i}_n^T \\ &= \frac{1}{S} \sum_{n=1}^S \begin{bmatrix} \mathbf{a}_{1n} \mathbf{a}_{1n}^T & \mathbf{a}_{1n} \mathbf{a}_{2n}^T & \dots & \mathbf{a}_{1n} \mathbf{a}_{fn}^T \\ \mathbf{a}_{2n} \mathbf{a}_{1n}^T & \mathbf{a}_{2n} \mathbf{a}_{2n}^T & \dots & \mathbf{a}_{2n} \mathbf{a}_{fn}^T \\ \vdots & \vdots & \ddots & \vdots \\ \mathbf{a}_{fn} \mathbf{a}_{1n}^T & \mathbf{a}_{fn} \mathbf{a}_{2n}^T & \dots & \mathbf{a}_{fn} \mathbf{a}_{fn}^T \end{bmatrix}. \end{aligned} \quad (4)$$

For the particular case in Seg-PCA where all groups have the same number of bands, the covariance matrix can be further derived as

$$\begin{aligned} \Lambda_{\text{Seg-PCA}} &= \sum_{b=1}^k \Lambda_b \\ &= \frac{1}{S} \sum_{n=1}^S (\mathbf{a}_{1n} \mathbf{a}_{1n}^T + \mathbf{a}_{2n} \mathbf{a}_{2n}^T + \dots + \mathbf{a}_{fn} \mathbf{a}_{fn}^T). \end{aligned} \quad (5)$$

From (4) and (5), it is straightforward to demonstrate that $\Lambda_{\text{Seg-PCA}}$ is formed by accumulating the $W \times W$ sections in the main diagonal of Λ_{SPCA} , the original covariance matrix. This is also illustrated in Figure 1 for comparison. Note that in a real hypercube, uneven band groupings are used to allow variable numbers of bands to be contained in different groups. However, this leads to the challenging problem of grouping bands for feature characterization, which is discussed in the following sections.

FEATURE EXTRACTION USING NON-PCA-BASED APPROACHES

For non-PCA-based feature extraction and dimensionality reduction, the most commonly used approaches are based on band selection [5], machine learning [6], and steepest ascent search [7]. As adjacent spectral bands in HSI usually contain a large degree of redundant information, these approaches tend to select individual spectral bands rather than PCA components for data classification.

In these approaches, bands that contain less discriminatory information are discarded, which results in a much reduced number of remaining bands. Usually, the discriminatory information is reflected by how different a band is in comparison to adjacent bands. To determine the degree of similarity between two (band) images, a number of approaches can be used including distance measurement, mutual information, and the structural similarity measurement (SSIM) [2], [5].

For any two band images A_m and A_n , the simplest distance-based similarity is given below to measure an average distance/similarity over all pixels

$$S_d(A_m, A_n) = 1 - \frac{\sum_{i=1}^X \sum_{j=1}^Y |A_m(i, j) - A_n(i, j)|^\lambda}{\sum_{i=1}^X \sum_{j=1}^Y [\max(A_m(i, j), A_n(i, j))]^\lambda}, \quad (6)$$

where $\lambda > 0$ and (i, j) are the spatial coordinate indices of the two images satisfying $i \in [1, X]$ and $j \in [1, Y]$; $X \times Y$ denotes the spatial dimension of the band images.

In contrast, mutual information-based similarity is determined by the image histograms [2], [5]. By treating the spectral images as random variables, their associated mutual information can be determined as follows:

$$I(A_m, A_n) = H(A_m) + H(A_n) - H(A_m, A_n), \quad (7)$$

where $H(A_m)$ and $H(A_n)$ are the entropy of A_m and A_n , and $H(A_m, A_n)$ is their joint entropy.

$$H(A_m) = - \sum_{a \in A_m} p(a) \log p(a). \quad (8)$$

The SSIM [8] contains three factors, including consistency in terms of luminance $l(A_m, A_n)$, contrast $c(A_m, A_n)$, and structure $s(A_m, A_n)$ defined as follows:

$$\begin{aligned} l(A_m, A_n) &= \frac{2\mu_m \mu_n + C_1}{\mu_m^2 + \mu_n^2 + C_1} \\ c(A_m, A_n) &= \frac{2\sigma_m \sigma_n + C_2}{\sigma_m^2 + \sigma_n^2 + C_2} \\ s(A_m, A_n) &= \frac{\sigma_{mn} + C_3}{\sigma_m \sigma_n + C_3} \end{aligned} \quad (9)$$

$$\text{SSIM}(A_m, A_n) = l^\alpha(A_m, A_n) c^\beta(A_m, A_n) s^\gamma(A_m, A_n), \quad (10)$$

where (μ_m, μ_n) and (σ_m, σ_n) are the mean intensity and the standard deviation of the band images A_m and A_n , respectively; $C_1 - C_3$ are constants; and α, β, γ are nonnegative weights. In the particular case where $\alpha = \beta = \gamma = 1$ and $C_2 = 2C_3$, SSIM can be further simplified as

$$\begin{aligned} \text{SSIM}(A_m, A_n) &= \frac{(2\mu_m \mu_n + C_1)(2\sigma_{mn} + C_2)}{(\mu_m^2 + \mu_n^2 + C_1)(\sigma_m^2 + \sigma_n^2 + C_2)}. \end{aligned} \quad (11)$$

Due to the inclusion of a consistency measurement in terms of luminance, contrast, and structural similarity, SSIM is found to produce more consistent similarity measurements than distance and mutual information-based approaches

[9]. For the 92AV3C data set as described in detail in the next section, SSIM-based band similarity maps are shown in Figure 2. As can be seen, bands are naturally divided into similar groups, with exceptions to bands just over 100 and 150 where adjacent bands show low similarity to each other. These are noisy bands that contain very little useful information, hence the low correlation with adjacent bands.

Based on the similarity maps mentioned earlier, band groups and the key bands can be easily determined by thresholding [3] or the Jeffries–Matusita interclass distance [7] with the steepest ascent search strategy [2], [7]. For machine-learning-based approaches, ground truth information is usually used to determine the discriminatory ability of bands in any classification-based tests.

PERFORMANCE EVALUATION AND ANALYSIS

We compare the performance of SPCA and Seg-PCA with conventional PCA using the publicly available hyperspectral data set 92AV3C from the original Indian Pines [10]. The 92AV3C data set was collected by the AVIRIS instrument over an agricultural study site in Northwest Indiana [10] for land cover classification in remote sensing applications. The hyperspectral data set contains 220 spectral reflectance bands in the wavelength range of 400–2,500 nm, and the spatial size is

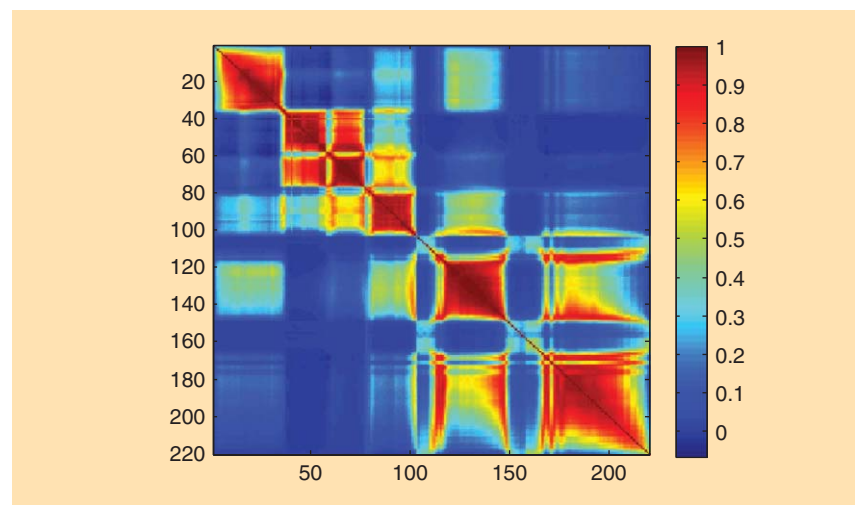


[FIG2] The correlation matrix among the band images of the 92AV3C data set.

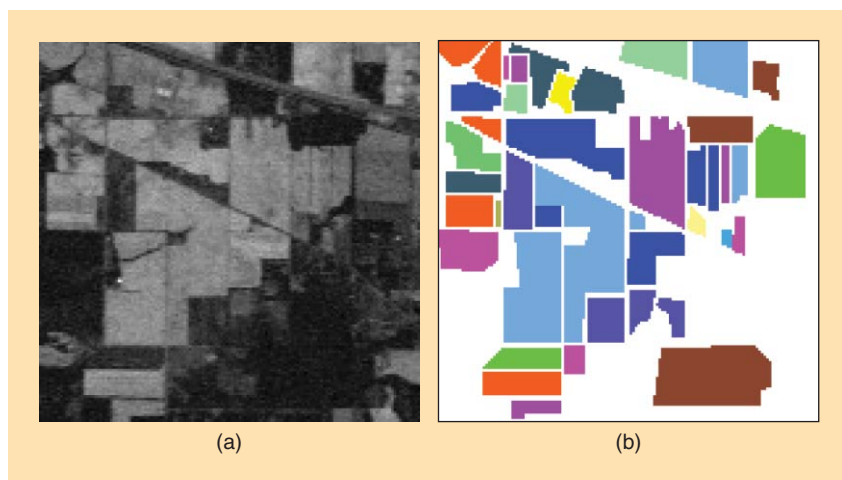


[FIG3] (a) One sample band image and (b) the ground truth of land cover of the 92AV3C data set. (Images used courtesy of [10].)

[TABLE 1] COMPARISONS OF COMPUTATIONAL COST.

STAGES/APPROACHES	COVARIANCE MATRIX	EIGENPROBLEM	DATA PROJECTION
PCA/SPCA	$O(SH^2 W^2)$	$O(H^3 W^3)$	$O(SHWK)$
Seg-PCA	$O(SHW^2)$	$O(HW^3)$	$O(SWK)$
SAVING FACTOR	H	H^2	H

21,025 (145×145) pixels. The data set contains different land cover classes corresponding to agriculture, forest, vegetation, and buildings. One sample band and the ground truth of the 16 land cover classes are illustrated in Figure 3. Disregarding the white regions that are unclassified background, the other colored regions in the ground truth refer to alfalfa, corn (three types), wheat, grass (three types), oats, woods, soybeans (three types), hay, and two others.

FEATURE EXTRACTION AND DATA CLASSIFICATION

SVM has been widely used for hyperspectral image classification [6], [7]. The implementation using the bSVM library [11] is employed for performance assessment. As a supervised classifier, SVM relies on training data for model optimization. In the experiments, the principal components extracted from the original spectral data using the conventional PCA, SPCA and Seg-PCA approaches are used as features for the SVM. For the labeled pixels in the data set, 30% of them are used for training the SVM and the remaining 70%

for testing. The kernel function used for SVM is the radial basis function, whose parameters, the penalty (c), and the gamma (γ), were optimized in the training process through a grid search of possible combinations of these parameters.

As suggested in the literature [5], [7], the noisy bands covering the region of water absorption (104–108, 150–163, 220) are removed from the spectral vectors before applying PCA for feature extraction. To this end, the effective number of spectral bands for the data sets is reduced from 220 to 200. In total, four groups of features are used for comparison. The first is referred to as the *whole spectral band (WSB)*, in which the total 200 spectral bands are used directly as features. This is taken as a baseline approach for benchmarking. The remaining three groups use principal components as features, extracted from the conventional PCA, SPCA, and Seg-PCA approaches, respectively.

For each group of features as samples, ten experiments were carried out with data samples randomly selected for training and testing. No data sample overlap

was allowed in the training set and testing set. The average testing result over these tests and the corresponding standard deviation of classification accuracy were obtained and reported below for evaluation and assessment.

PERFORMANCE ASSESSMENT

We assess performance in terms of reduction of computation cost, memory requirement, and improvement of classification accuracy.

The computation costs of the SPCA and Seg-PCA are compared against those of the conventional PCA in Table 1, for the three stages involved, where S and K refer, respectively, to the number of samples (pixels) and the number of principal components extracted. Since the computational cost for PCA and SPCA is the same, they are put together to be compared with Seg-PCA. The saving factor of computational cost for Seg-PCA is H or H^3 in comparison to conventional PCA and SPCA. With $H = 10$ and $K = 30$, the number of multiply-accumulates required in PCA/SPCA is $9.75e8$, where in Seg-PCA it is reduced to $9.67e7$. In effect, the computational cost has reduced to 9.92%. In other words, Seg-PCA has achieved a saving factor of ten, i.e., an order of magnitude for the hyperspectral remote sensing data set used.

In Table 2, memory requirements for PCA, SPCA, and Seg-PCA over different stages are compared. SPCA only reduces memory requirement in the first stage when the covariance matrix is obtained. The other two stages require the same amount of memory as the conventional PCA. Seg-PCA has significantly lower memory requirements, and the minimum saving factor achieved is H^2 . When $H = 10$ Seg-PCA only requires 1% of the memory compared to the conventional PCA.

With local structures extracted over the spectral domain, Seg-PCA has great potential to improve the efficacy in feature extraction resulting in higher discrimination power and better classification. With $H = 10$, ($W = 20$), the classification results using various numbers of principal components are plotted in Figure 4, where K covers a large

[TABLE 2] A COMPARISON OF MEMORY REQUIREMENTS IN PCA, SPCA, AND SEG-PCA AT DIFFERENT STAGES.

STAGES/ APPROACHES	COVARIANCE COMPUTATION	COVARIANCE MATRIX SIZE	PROJECTION MATRIX SIZE	PROJECTION MULTIPLICATION
PCA	$S \times HW$	$HW \times HW$	$HW \times K$	$SHW \times HWK$
SPCA	$HW \times 1$	$HW \times HW$	$HW \times K$	$SHW \times HW$
SAVING FACTOR	S	1	1	1
Seg-PCA	$S \times W$	$W \times W$	$W \times K/H$	$HW \times WK/H$
SAVING FACTOR	H	H^2	H^2	SH^2

range from ten to 110. First, Seg-PCA is found to consistently outperform conventional PCA (and also SPCA). As can be seen, Seg-PCA significantly improves on the conventional PCA when the number of components is less than 110, i.e., 50% of the dimensionality of original features. When K is ten and over, Seg-PCA achieves comparable or even slightly better results in comparison to WSB for classification, a significant advantage for feature extraction as the dimensionality of features used in WSB is 200.

NON-PCA-BASED APPROACHES

The mutual information-based band selection approach [5], SVM-based approach [6], and the steepest ascent search-based approach [7] are compared in this group of experiments, along with the PCA-based methods. Again SVM is used as the preferred classifier yet under 60% training ratio. The results are summarized in Table 3 for comparison. As one can see, PCA-based approaches have generated reasonably good results, where Seg-PCA is found to be the best among the five approaches evaluated. The SVM-based approach outperforms conventional PCA and the steepest ascent search-based approach, and the mutual information-based approach is found to be the poorest performing in this group of tests.

EFFECT OF NOISE

Due to atmospheric water absorption and other effects, the hyperspectral images obtained may contain severe noise, where the corresponding band image is effectively useless as it has no correlation to any adjacent bands (see Figure 2). As a result, noise removal becomes a very important issue. Without

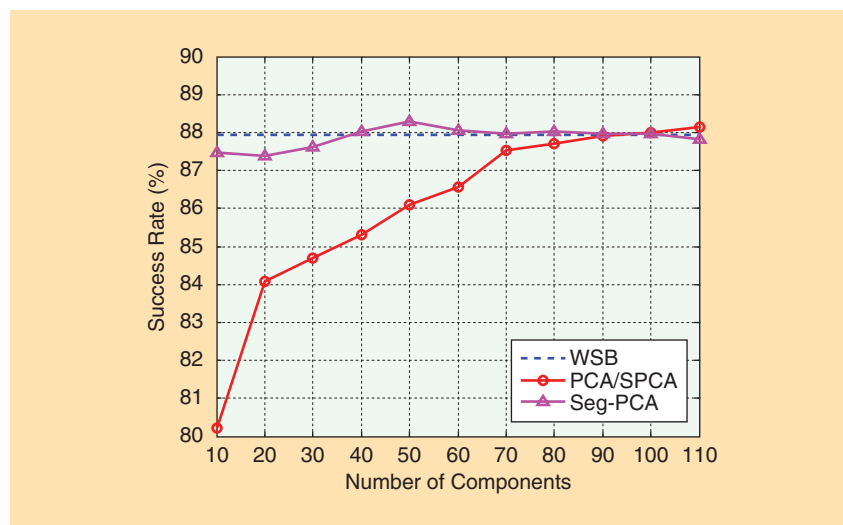


[FIG4] The classification results for the 92AV3C data set from PCA/SPCA and Seg-PCA in benchmarking with WSB approach under various numbers of principal components used, where the training ratio is 30%.

[TABLE 3] A COMPARISON OF THE OVERALL ACCURACY OF DIFFERENT APPROACHES UNDER A VARIOUS NUMBER OF FEATURES USED FOR CLASSIFICATION.

METHODS	PCA	Seg-PCA [4]	MUTUAL INFORMATION [5]	SVM-BASED BAND SELECTION [6]	STEEPEST ASCENT SEARCH METHOD [7]
10	86.76	91.40	73.06	87.55	85.79
20	89.56	92.49	73.95	90.68	87.92
30	89.17	92.61	76.58	91.03	89.45

noisy band removal, the classification accuracy achieved for the 92AV3C data set by PCA with ten components is only around 70%, in comparison to nearly 87% obtained in Table 3. Furthermore, some researchers also apply noise removal in the spatial domain, using the known wavelet shrinkage approach [12]. After removal of the noisy bands, it is found that this pre-processing can further improve the overall classification accuracy by 2–3% [12].

CONCLUSIONS

Although PCA has been widely used for feature extraction and data reduction, it suffers from three main drawbacks: high computational cost, large memory requirement, and low efficacy in processing large data sets such as HSI. This article analyzed two variations of PCA, specifically SPCA and Seg-PCA. Seg-PCA can further improve classification accuracy while significantly reducing the computational cost and memory requirement, without

applications **CORNER** continued

requiring prior knowledge. There is potential to apply similar feature extraction and data reduction techniques in application areas beyond HSI when the analysis of large-dimensional data sets is required, such as magnetic resonance imaging and digital video processing.

RESOURCES

For hyperspectral remote sensing, a series of sensors have been applied in the world, which include AVIRIS [10], ROSIS [13], and HYDICE [10] as well as many others such as TRWIS, CASI, OKSI AVS, MERIS, Hyperio, HICO, CHRIS, NEON, and TERN. Detailed specifications in terms of the spectral range and spectral/spatial resolution etc. for these sensors are summarized in [14] and [15].

For the AVIRIS sensor, the data were acquired since the early 1990s, and they can be obtained from NASA by accessing the link http://aviris.jpl.nasa.gov/data/get_aviris_data.html. Alternatively, some associated data sets such as 92AV3C, Salinas, and Cuprite can be downloaded online from [10] and/or [13]. For the ROSIS sensor, the Pavia Center and Pavia University data sets can be obtained from [13]. In addition, the DC Mall data set from the HYDICE sensor is also available online [10]. Note that for 92AV3C, Salinas, the Pavia Center, and the Pavia University data sets, there are available ground truth to facilitate objective assessment in data classification-based applications.

AUTHORS

Jinchang Ren (Jinchang.Ren@strath.ac.uk) is the deputy director of the Hyperspectral Imaging Centre in the University of Strathclyde, Glasgow, United Kingdom.

Jaime Zabalza (J.Zabalza@strath.ac.uk) is currently working toward his Ph.D. degree in the Department of Electronic and Electrical Engineering, University of Strathclyde, United Kingdom.

Stephen Marshall (Stephen.Marshall@strath.ac.uk) is a professor with the Department of Electronic and Electrical Engineering at the University of Strathclyde, United Kingdom. He is a fellow of the Institute of Engineering and Technology.

Jiangbin Zheng (zhengjb@nwpu.edu.cn) is currently a professor with the School of Software and Microelectronics, Northwestern Polytechnical University, Xi'an, China.

REFERENCES

- [1] R. Dianat and S. Kasaei, "Dimension reduction of optical remote sensing images via minimum change rate deviation method," *IEEE Trans. Geosci. Remote Sensing*, vol. 48, no. 1, pp. 198–206, Jan. 2010.
- [2] X. Jia, B.-C. Kuo, and M. Crawford, "Feature mining for hyperspectral image classification," *Proc. IEEE*, vol. 101, no. 3, pp. 676–697, Mar. 2013.
- [3] J. Yang, D. Zhang, A. F. Frangi, and J.-Y. Yang, "Two-dimensional PCA: A new approach to appearance-based face representation and recognition," *IEEE Trans. Pattern Anal. Mach. Intell.*, vol. 26, no. 1, pp. 131–137, Jan. 2004.
- [4] X. Jia, and J. A. Richards, "Segmented principal components transformation for efficient hyperspectral remote sensing image display and classification," *IEEE Trans. Geosci. Remote Sensing*, vol. 37, no. 1, pp. 538–542, 1999.

[5] B. Guo, S. Gunn, R. Damper, and J. Nelson, "Band selection for hyperspectral image classification using mutual information," *IEEE Geosci. Remote Sensing Lett.*, vol. 3, no. 4, pp. 522–526, 2006.

[6] M. Pal and G. M. Foody, "Feature selection for classification of hyperspectral data by SVM," *IEEE Trans. Geosci. Remote Sensing*, vol. 48, no. 5, pp. 2297–2307, 2010.

[7] F. Melgani and L. Bruzzone, "Classification of hyperspectral remote sensing images with SVMs," *IEEE Trans. Geosci. Remote Sensing*, vol. 42, no. 8, pp. 1778–1790, Aug. 2004.

[8] Z. Wang, A. C. Bovik, H. R. Sheikh, and E. P. Somanelli, "Image quality assessment: From error visibility to structural similarity," *IEEE Trans. Image Processing*, vol. 13, no. 4, pp. 600–612, 2004.

[9] D. P. Widemann, "Dimensionality reduction for hyperspectral data," Ph.D. dissertation, Dept. Math., University of Maryland, 2008.

[10] (1992, June 12). Pursue's University multispec site: Aviris image north-south flightline, Indiana. [Online]. Available: <https://engineering.purdue.edu/~biehl/MultiSpec/hyperspectral.html>

[11] C.-W. Hsu and C.-J. Lin. (2012, June 18). bSVM multiclass classifier 2.08. [Online]. Available: <http://www.csie.ntu.edu.tw/~cjlin/bsvm/>

[12] B. Demir, S. Erturk, and M. K. Gullu, "Hyperspectral image classification using denoising of intrinsic mode functions," *IEEE Geosci. Remote Sensing Lett.*, vol. 8, no. 2, pp. 220–224, 2011.

[13] Comput. Intell. Group, Univ. Basque Country. Hyperspectral remote sensing scenes. Online datasets. [Online]. Available: http://www.ehu.es/ccwintco/index.php/Hyperspectral_Remote_Sensing_Scenes

[14] (2013, Aug. 14). GISResources. Fundamentals of hyperspectral remote sensing. [Online]. Available: <http://www.gisresources.com/fundamentals-of-hyperspectral-remote-sensing-2/>

[15] (2013, Aug. 23). HySpeed Computing. Remote sensing data access, A review of online resources for hyperspectral imagery. [Online]. Available: <http://hyspeedblog.wordpress.com/2013/04/23/remote-sensing-data-access-a-review-of-online-resources-for-hyperspectral-imagery/>



moving?

You don't want to miss any issue of this magazine!

change your address

BY E-MAIL: address-change@ieee.org

BY PHONE: +1 800 678 IEEE (4333) in the U.S.A.
or +1 732 981 0060 outside the U.S.A.

ONLINE: www.ieee.org, click on quick links, change contact info

BY FAX: +1 732 562 5445

Be sure to have your member number available.

D. Robert Iskander

Signal Processing in Visual Optics

often finish my digital signal processing lecture on Fourier transformation asking students to think of a Fourier transform application that is close to them. The answers I usually get are “it’s in my cell phone” or “in my laptop.” “It is much close to your skin,” I probe further. Rarely, I get the expected answer that the eye is essentially a Fourier transform operator. Hence, the human eye is an excellent object to study for a signal processing practitioner.

The eye, despite being extraordinarily well developed through evolution, is not an ideal optical system and produces retinal images of moderate quality. On the other hand, a simple textbook comparison of the eye to a man-made optical instrument, such as a camera, for example, is totally unjust. The eye is a complicated, dynamic, and robust optical system [1]. The image of a distant object needs to travel through a thin, few micrometers thick layer of tear film, cornea, aqueous humour, pupil, crystalline lens with a gradient refractive index, before it falls on the photosensitive retina at the back of the eye. All of the eye elements, which the rays that form the image of a distant object pass, are dynamic in nature and are not fully synchronized with each other. Figure 1 depicts the considered eye elements and the major signals that affect their performance.

First, the eye globe, as a whole, performs complicated micromovements in lateral as well as longitudinal directions. Tear film dynamically changes the optical characteristics of the eye from a blink to another [2]. The cornea, despite its name being derived from a horn, is not a rigid body and is suggested to undergo slow dynamic changes in central curvature,

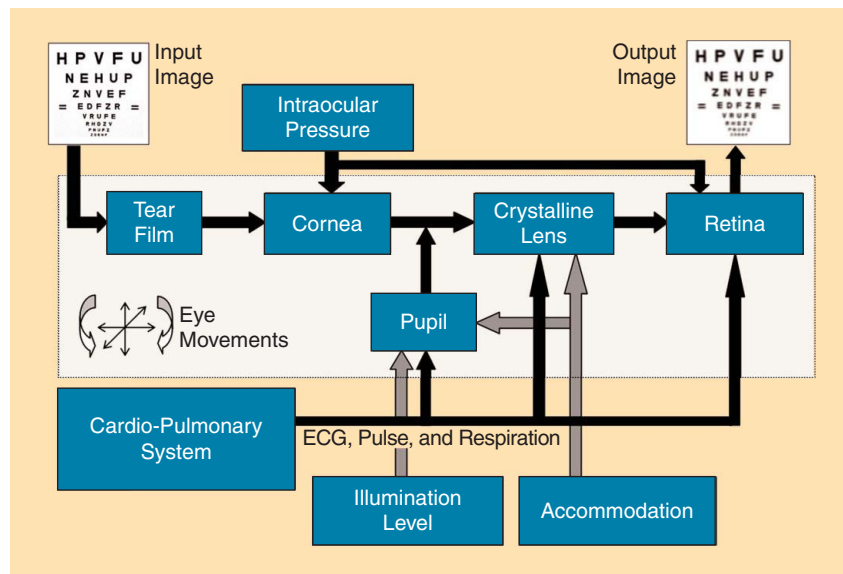


[FIG1] The human eye as a dynamic system.

possibly due to eye’s accommodation (i.e., changes in its focal point). The shape and size of the pupil are not fixed; they vary with light intensity and level of accommodation. Pupil size undergoes small microfluctuations called hippus (pupillary athetosis). Additionally, the center of the pupil is not concentric with the geometrical center of the cornea. Hence, with changes in size its relevant position to cornea also changes. This is an important factor when relating optical characteristics of the cornea to those of the whole eye.

The crystalline lens is a flexible eye element that allows changing the eye’s focal point. In a young eye, those changes can reach over a dozen diopters. The accommodative status of the crystalline lens is additionally modulated by the signals from the cardiopulmonary system [3]. At the end of their paths, the rays forming the image of an object fall on a dynamic retina, connected with the cardiopulmonary system, which may also undergo slow diurnal structural changes in its choroid [4].

All of the eye’s elements, described above, together with signals associated with accommodation, pupillary response, and those of cardiopulmonary system lead to a static retinal image that is far from ideal at a given point of time. However, due to the dynamic nature of all those elements, the human eye is able to resolve images with high acuity of about 1 min of arc mainly because of the match between moderate optical image quality and the resolution of the retinal mosaic [1]. The actual image that a human being can resolve also depends on neural processes occurring in the retina and the brain. Those could involve elements of stochastic resonance where the naturally occurring eye vibrations may result in an improved visual quality [5], [6].

Some aspects of the dynamics in optical characteristics of the eye, particularly those related to changes in the tear film structure and microfluctuations of the steady-state accommodation, have been considered. The latter can be associated

with the refractive status of the eye from which emmetropization mechanisms (i.e., processes that optimize the eye's optics) could be learned. However, the wealth of information available when examining the dynamic nature of optical characteristics of the eye has not been fully exploited. Challenges exist to develop analytic methodologies that would adequately account for all such variations and their interdependencies with the major physiological signals of the human body. To achieve this goal, an overall system of the eye's optics that takes into account the aberration dynamics needs to be considered. This column summarizes the recent endeavors undertaken in search of adequate characterization of the human eye's optics that involves application of various levels of signal processing tools. In particular, we focus on temporal changes in tear film and natural microfluctuations in a steady-state accommodation—the two factors that have the greatest influence on optical quality of the human eye.

DATA ACQUISITION

Some progress in the development of instrumentation for acquisition of the signals shown in Figure 1 has already been made. For example, the movements associated with the eye/head interface can be measured with high-speed cameras, optical distance sensors, or ultrasonic sensors. The kinetics of tear film can be assessed with high-speed videokeratoscopy, interferometry, wavefront sensing, or retroillumination techniques [2], [7]. Videokeratoscopy is the current standard for measuring corneal topography but reflective-based systems such as the Placido disk videokeratoscope are being utilized for assessing tear film surface quality. Interferometric techniques are used to measure the thickness of the tear film lipid layer or the quality of its surface as is the case with lateral shearing interferometry [2]. Wavefront sensing, usually based on the Shack–Hartmann principle, is the current standard for measuring the eye's optical aberrations. It can also be utilized to assess tear film quality within the pupil area [3]. Similar assessment area can be obtained with the retroillumination technique in which an external light source is used to illuminate the retina that,

subsequently, retroilluminates the cornea and the tear film [7].

The dynamics of the anterior cornea can be currently assessed with high-speed videokeratoscopy. In the future, the anterior and posterior corneal surfaces could be evaluated with dynamic Scheimpflug imaging or dynamic spectral optical coherence tomography—techniques currently well developed for static acquisition of those surfaces.

Scheimpflug imaging is a well-established technique in which the lens plane is not parallel to the image plane. This allows achieving a well-focused image of a wide cross-section of the cornea extending to the corneoscleral region. Optical coherence tomography, particularly the spectral domain based, became the standard for imaging both anterior and posterior segments of the eye.

The effect of the intraocular pressure (IOP) on corneal surface can be assessed by measuring temporal variations in IOP using dynamic contour tonometry [8]. Further, the changes in pupil size and shape and their relation to the geometric center of the cornea can be simply assessed with high-speed pupillometry and appropriate image processing routines for estimating the corneal limbus. The dynamics of the crystalline lens, those associated with accommodation, and those related to the cardiopulmonary system can be assessed using a combined system of a wavefront sensor and a bioamplifier with sensors for measuring pulse, respiration, and the electric heart activity [9]. Finally, the dynamics related to the retina can be assessed by measuring fundus pulsation [10].

Although there are no instruments currently available that would acquire a complete dynamic “picture” of the eye's optical and physiological characteristics, some progress has been made in this direction. For example, a combined topographer/wavefront sensors instrument has been recently commercially realized. Several ophthalmic instruments include dynamic measurement of the pupil size and its position with respect to the cornea. There is also a growing body of laboratory settings where researchers try to combine several devices to assess correlation

(coherence) between the parameters (signals) estimated from each of the considered instruments [7], [9].

Problems associated with acquisition of dynamic data range from prosaic storage shortages and limits in computing power, as in the case of the three-dimensional optical coherence tomography, to more complex associated with limits in optical technology and lack of robust algorithms for data processing. The latest is of interest to signal processing community.

TEAR FILM

The tear film is the first optical element of the eye that the rays forming the image of an object in the field of view encounter. The tear film broadly comprises three distinct layers, an outer lipid layer, a middle aqueous layer, and an inner mucin layer. It renews with every blink and will eventually rupture/evaporate if blinking does not occur. At the air/tear film interface the rays undergo the strongest refraction (from about $n = 1$ to about $n = 1.336$). Hence, the stability of tear film surface smoothness is essential for the retinal image to have good quality.

Currently accepted assessment of tear film includes a range of clinical diagnostic methods that are time-consuming and unreliable. They are also inadequate to study the kinetics of tear film and their influence on visual performance of the eye [2]. Recently, more attention has been given to the developments of noninvasive methods for tear film surface analysis such as repeated measure videokeratography, high-speed videokeratoscopy, dynamic wavefront sensing, and interferometry. There are also attempts of combining several techniques as in the case of wavefront sensing and retroillumination [7]. A recent study comparing several noninvasive measurement technologies indicated that high-speed videokeratoscopy appears to be the most precise method for measuring tear film surface quality while lateral shearing interferometry appears to be the most sensitive method for analyzing tear film kinetics [2].

One of the important parameters characterizing tear film quality, particularly in the diagnosis of dry eye syndrome, is the tear film break-up time. In clinical

practice, it is measured with a stop watch by observing postblink tear film thinning patterns in a slit-lamp biomicroscope after instillation of fluorescein into the eye. The method is both invasive (i.e., instillation of small amount of fluorescein to the eye is required) and nonphysiological as it requires the patient to keep their eyes open for a period of time significantly exceeding that of an average interblink interval. Noninvasive methods of tear film assessment resolve the first problem while robust estimation techniques applied to the acquired dynamic measurements help resolve the other [11]. Noninvasive measurement techniques that acquire dynamic data in natural blinking conditions bring several other parameters such as the tear film build-up time, tear film thinning rate, and the predicted tear film break-up time. For those, methods of data fitting involving iterative orthogonal least square procedures and information criteria had to be developed [12].

Measurement and modeling of tear film surface kinetics is important for studying the loss of retinal image quality associated with poor tear film, but their main purposes are to help diagnosing dry eye syndrome, and study the efficacy of tear film substitutes and biocompatibility of contact lens material.

MICROFLUCTUATIONS IN STEADY-STATE ACCOMMODATION

The eye displays small movements even in a steady viewing condition. This particular phenomenon is not limited to the eye globe but also occurs in individual components of the eye such as the pupil, crystalline lens, and retina (choroid). This results in the optical characteristics of the eye to exhibit some temporal variations, the magnitude of which is not large. Such variations are referred to as microfluctuations in steady-state accommodation [3]. The first works on the character of measured dynamics of the eye's monochromatic aberrations revealed their nonstationary character and possible correlation with the signals of the cardiopulmonary system [3]. Utilizing a set of metrics derived from a time-frequency coherence estimator, it was later confirmed that there exist periods of time during which the coherence between

aberration dynamics and signals of cardiopulmonary systems is very high and periods when quite opposite occurs [9]. This finding suggests that the microfluctuations in a steady-state accommodation are the result of not only the dynamics associated with crystalline lens—an idea well established earlier—but also to those related to choroidal pulsation. It has been hypothesized that the observed high coherence levels may be associated with the crystalline lens micromovements being in phase with those of choroid.

There were also attempts to model the individual aberration components, now standardly expressed as time-varying coefficients of a Zernike polynomial expansion to the dynamically measured wavefront aberrations [3], [13], [14]. Those models ranged from simple parametric autoregressive (AR) and AR moving-average (ARMA) processes, to amplitude modulation-frequency modulation (AM-FM) signals, to more intricate approaches involving wavelet-based multifractal analysis and chaos theory. For example, Hampson and Mallen [13] have found that the aberration dynamics cannot be characterized by a single fractal dimension. They showed that the most frequently found Hölder exponent for the root mean square (RMS) wavefront error averaged across subjects was 0.31, indicating that the aberration dynamics are antipersistent ($H < 1/2$). In their latest developments [14], they showed that aberrations

dynamics can be well modeled as a chaotic process with the attractor embedding dimension equal to three and the average Lyapunov exponent of the RMS wavefront error of $0.44 \mu\text{m/s}$. These recent developments are very interesting and indicate how intricate the problem of adequate modeling of eye's visual optics is.

A VIBRATING EYE?

The more we study the dynamics of the human eye's optical system, the more questions arise. Taking into account all individual elements of the eye and the range of unsynchronized physiological signals of mechanical and electrical nature that affect their performance, how is it possible to achieve good retinal image quality? Are the elements of stochastic resonance truly involved in the eye's operation? Is the only reason that we see so well because of the properly selected resolution of our photoreceptors? How then does the eye cope with both transversal and longitudinal changes in the retinal image?

One previously unconsidered aspect of human visual system can be related to an old study of Lohmann and Paris [15] who have shown that, under certain conditions, the transfer function of a defocused lens can be considerably improved by introducing to a system a certain amount of longitudinal vibrations. Contrarily, such improvement could not be demonstrated in the case of transverse vibrations. A simple simulation demonstrates that using a

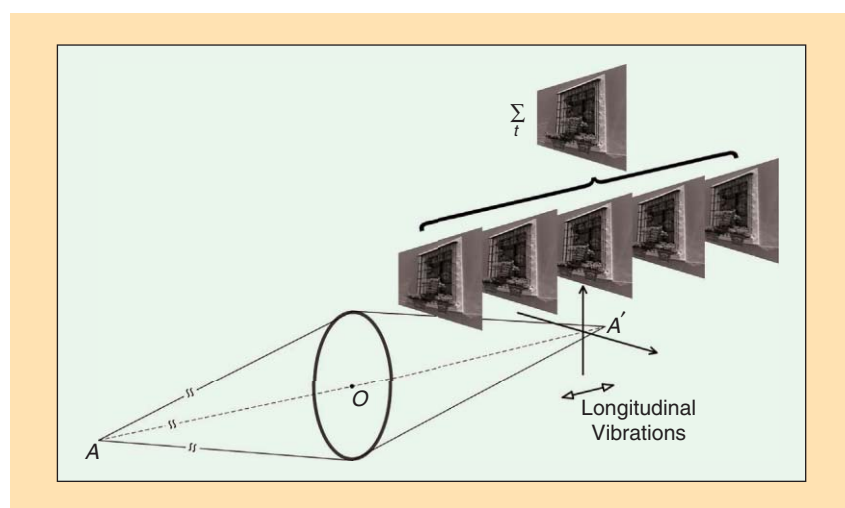


[FIG2] Longitudinal vibrations at a point away from focus improve the overall image quality.

life SCIENCES continued

low level of defocus, say about ± 0.25 of a diopter and allowing for longitudinal vibrations of a similar order can result in a threefold increase in the eye's visual Strehl ratio—a popular metric of retinal image quality [16]. Such levels of defocus are typically encountered in emmetropic subjects (i.e., those exhibiting good vision without any corrective implements). Figure 2 depicts the concept of improving integrated image quality with longitudinal vibrations, provided that the retinal image plane is not at the focal point. Whether the temporal summation of longitudinal vibrations truly occurs in the human eye is yet to be proved. For this, wavefront sensors equipped with high speed (exceeding the Nyquist frequency of 120 Hz) and sensitive enough cameras need to be employed.

The optical system of the human eye presents challenges for future generations of signal processing professionals. Current approaches to study its dynamics are often reduced to an application of the off-the-shelf signal processing tools to a limited aspect of the system. However, a more comprehensive approach that integrates all available information in some form of data fusion is needed to fully understand all its intricacies. Gaining such knowledge

would benefit not only the visual optic community but also those interested in computer and machine vision.

AUTHOR

D. Robert Iskander (robert.iskander@pwr.edu.pl) is a professor of biomedical signal processing at the Institute of Biomedical Engineering and Instrumentation, Wrocław University of Technology, Poland.

REFERENCES

- [1] P. Artal, A. Benito, and J. Taberner, "The human eye is an example of robust optical design," *J. Vis.*, vol. 10, no. 6, pt. 1, pp. 1–7, 2006.
- [2] D. H. Szczesna, D. Alonso-Caneiro, D. R. Iskander, S. A. Read, and M. J. Collins, "Lateral shearing interferometry, dynamic wavefront sensing, and high-speed videokeratometry for non-invasive assessment of tear film surface characteristics: A comparative study," *J. Biomed. Opt.*, vol. 15, no. 3, p. 037005, 2010.
- [3] D. R. Iskander, M. J. Collins, M. R. Morelande, and M. Zhu, "Analyzing the dynamic wavefront aberrations in human eye," *IEEE Trans. Biomed. Eng.*, vol. 51, no. 11, pp. 1969–1980, 2004.
- [4] S. A. Read, M. J. Collins, and D. R. Iskander, "Diurnal variation of axial length, intraocular pressure and anterior eye biometrics," *Invest. Ophthalmol. Vis. Sci.*, vol. 49, no. 7, pp. 2911–2918, 2008.
- [5] M. H. Hennig, N. J. Kerscher, K. Funke, and F. Wörgötter, "Stochastic resonance in visual cortical neurons: Does the eye-tremor actually improve visual acuity?" *Neurocomputing*, vol. 44–46, pp. 115–120, 2002.
- [6] M.-O. Hongler, Y. L. de Meneses, A. Beyeler, and J. Jacot, "The resonant retina: Exploiting vibration noise to optimally detect edges in an image," *IEEE*

Trans. Pattern Anal. Mach. Intel., vol. 25, no. 9, pp. 1051–1062, 2003.

[7] N. L. Himebaugh, J. Nam, A. Bradley, H. Liu, L. N. Thibos, and C. G. Begley, "Scale and spatial distribution of aberrations associated with tear breakup," *Optom. Vis. Sci.*, vol. 89, no. 11, pp. 1590–1600, 2012.

[8] E. M. Hoffmann, F. H. Grus, and N. Pfeiffer, "Intraocular pressure and ocular pulse amplitude using dynamic contour tonometry and contact lens tonometry," *BMC Ophthalmol.*, vol. 4, no. 4, pp. 1–7, 2004.

[9] M. Muma, D. R. Iskander, and M. J. Collins, "The role of cardiopulmonary signals in the dynamics of eye's wavefront aberrations," *IEEE Trans. Biomed. Eng.*, vol. 57, no. 2, pp. 373–383, 2010.

[10] L. F. Schmetterer, F. Lexer, C. J. Unfried, H. Sattmann, and A. F. Fercher, "Topical measurement of fundus pulsations," *Opt. Eng.*, vol. 34, no. 3, pp. 711–716, 1995.

[11] D. H. Szczesna and D. R. Iskander, "Robust estimation of tear film surface quality in lateral shearing interferometry," *J. Biomed. Opt.*, vol. 14, no. 6, p. 064039, 2009.

[12] D. H. Szczesna and D. R. Iskander, "Lateral shearing interferometry: A technique for complete temporal analysis of tear film surface kinetics," *Optom. Vis. Sci.*, vol. 87, no. 7, pp. 513517, 2010.

[13] K. M. Hampson and E. A. H. Mallen, "Multifactorial nature of ocular aberration dynamics of the human eye," *Biomed. Opt. Exp.*, vol. 2, no. 3, pp. 464–477, 2011.

[14] K. M. Hampson and E. A. H. Mallen, "Chaos in ocular aberration dynamics of the human eye," *Biomed. Opt. Exp.*, vol. 3, no. 5, pp. 863–877, 2012.

[15] A. W. Lohmann and D. P. Paris, "Influence of longitudinal vibrations on image quality," *Appl. Opt.*, vol. 4, no. 4, pp. 393–397, 1965.

[16] D. R. Iskander, "Computational aspects of the visual Strehl ratio," *Optom. Vis. Sci.*, vol. 83, no. 1, pp. 57–59, 2006.

SP

from the GUEST EDITORS (continued from page 15)

Zhu and Bamler provide a further insight into SAR tomography, and their article demonstrates the ability of compressive sensing to achieve vertical super-resolution with data acquired by SAR systems operating in very high horizontal resolutions modes.

Still in the context of SAR interferometry, the article by Baseline et al. investigates methods based on the use of contextual information and addresses statistical methods to solve the multichannel interferometric SAR phase unwrapping problem for digital elevation model generation.

The article by Deledalle et al. covers the methods of filtering multichannel SAR data, represented by interferometric, polarimetric, or interferometric/polarimetric, to preserve preservation of texture and structures.

SAR polarimetry, the topic of the article by Chen et al., provides insights in

polarimetric target decomposition techniques for the interpretation of scattering mechanisms, including extension and fusion with interferometry.

Solimene et al.'s contribution deals with a unified treatment from the mathematical viewpoint of SAR imaging algorithms and discusses their generalizations to handle unconventional scenarios, such as through-wall imaging, imaging of urban canyons, and underground tunnel detection.

A further contribution to the imaging of buried targets is provided by the article by Kedzierawski et al., which addresses the topic of airborne ground penetrating radar (GPR), a combination of SAR and GPR, based on the use of time-reversal data processing algorithms.

Finally, Leigsnering et al. deal with the problem of scatterings and multipath when using SAR for imaging of building

interiors. The article discusses both multipath mitigation and exploitation techniques and shows how to perform the latter with compressed observations.

We would like to express our deep gratitude to the many individuals who made this special issue of *SPM* possible. We thank all authors who submitted proposals and all reviewers whose recommendations significantly helped in improving the selected articles. We are also grateful to Abdelhak Zoubir, *SPM's* editor-in-chief, and we are indebted to Fulvio Gini, special issues area editor, for his constant support and guidance throughout the solicitation and reviewing process, as well as to Rebecca Wollman for her valuable administrative assistance.

SP

[dates **AHEAD**]

Please send calendar submissions to:
Dates Ahead, c/o Jessica Barragué
IEEE Signal Processing Magazine
445 Hoes Lane
Piscataway, NJ 08855 USA
e-mail: j.barrague@ieee.org
(Colored conference title indicates
SP-sponsored conference.)

2014**[JUNE]**

**IEEE Sensor Array and Multichannel
Signal Processing Workshop (SAM)**
22–25 June, A Caruña, Spain.
URL: <http://www.gtcc.udc.es/sam2014/>

**15th IEEE International Workshop
on Signal Processing Advances in
Wireless Communications (SPAWC)**
22–25 June, Toronto, Canada.
General Cochairs: Tim Davidson and Wei Yu
URL: <http://www.spawc2014.info/joomla30/>

**IEEE Statistical Signal Processing
Workshop (SSP)**
29 June–2 July, Gold Coast, Australia.
General Cochairs: Rob Evans and
Abd-Krim Seghouane
URL: <http://www.ee.unimelb.edu.au/SSP2014/index.html>

[JULY]

**2nd IEEE China Summit and
International Conference on Signal
and Information Processing (ChinaSIP)**
9–13 July, Xi'an, China.
General Chairs: Mingyi He and Kung Yao
URL: <http://www.chinasip2014.org/CfP.htm>

**IEEE International Conference
on Multimedia and Expo (ICME)**
14–18 July, Chengdu, China.
General Cochairs: Touradj Ebrahimi,
Shipeng Li, Houjun Wang, and Jie Yang
URL: <http://www.icme2014.org/>

Digital Object Identifier 10.1109/MSP.2014.2311180
Date of publication: 13 June 2014

[AUGUST]

**2014 International Conference on
Digital Signal Processing (DSP)**
20–23 August, Hong Kong.
General Chairs: Yong Ching Lim, Daniel P.K.
Lun, A.N. Skodras, and Danilo Mandic
URL: <http://www.dsp2014.org/>

**11th IEEE International Conference
on Advanced Video and Signal-Based
Surveillance (AVSS)**
26–29 August, Seoul, South Korea.
General Chair: Hanseok Ko
General Cochair: Jin Young Choi
URL: <http://www.avss2014.org/>

[SEPTEMBER]

**22nd European Signal Processing
Conference (EUSIPCO)**
1–5 September, Lisbon, Portugal.
Honorary Chair: Carlos Salema
General Chair: Leonel Sousa
URL: <http://www.eusipco2014.org/>

**2014 Sensor Signal Processing for
Defence (SSPD)**
8–9 September, Edinburgh, United Kingdom.
General Chairs: Mike Davies, Paul Thomas,
and Jonathon Chambers
URL: <http://www.see.ed.ac.uk/drupal/udrc/sspd/>

**24th IEEE International Workshop on
Machine Learning for Signal Processing
(MLSP)**
21–24 September, Reims, France.
General Chair: Mamadou Mboup
URL: <http://mlsp2014.conwiz.dk/home.htm>

**16th IEEE International Workshop on
Multimedia Signal Processing (MMSP)**
22–24 September, Jakarta, Indonesia.
General Chairs: Susanto Rahardja and
Zhengyou Zhang
URL: <http://mmsp2014.ilearning.me/call-for-paper/>

[OCTOBER]

**IEEE Workshop on Signal Processing
Systems (SIPS)**
20–23 October, Belfast, Ireland.

[DECEMBER]

**IEEE Global Conference on Signal and
Information Processing (GlobalSIP)**
3–5 December, Atlanta, Georgia.
General Chairs: Geoffrey Li and Fred Juang
URL: <http://renyi.ece.iastate.edu/globalsip2014/>

**IEEE International Workshop on
Information Forensics and Security (WIFS)**
3–5 December, Atlanta, Georgia.
General Chairs: Yan (Lindsay) Sun and
Vicky H. Zhao
URL: <http://ieeewifs.org/>

**IEEE Spoken Language Technology
Workshop (SLT)**
6–9 December, South Lake Tahoe, California.
General Chairs: Murat Akbacak
and John Hansen

**2014 Asia-Pacific Signal and Information
Processing Association Annual Summit
and Conference (APSIPA)**
9–12 December, Chiang Mai, Thailand.
Honorary Cochairs: Sadaoki Furui,
K.J. Ray Liu, and Prayoot Akkarakethalin
General Cochairs: Kosin Chamnongthai,
C.-C. Jay Kuo, and Hitoshi Kiyu
URL: <http://www.apsipa2014.org/home/>

2015**[APRIL]**

**IEEE International Conference
on Acoustics, Speech, and
Signal Processing (ICASSP)**
19–24 April, Brisbane, Australia.
General Cochairs: Vaughan Clarkson
and Jonathan Manton
URL: <http://icassp2015.org/>

[SEPTEMBER]

**IEEE International Conference
on Image Processing (ICIP)**
28 September–1 October, Quebec City,
Quebec, Canada.

[advertisers INDEX]

The Advertisers Index contained in this issue is compiled as a service to our readers and advertisers: the publisher is not liable for errors or omissions although every effort is made to ensure its accuracy. Be sure to let our advertisers know you found them through *IEEE Signal Processing Magazine*.

ADVERTISER	PAGE	URL	PHONE
IEEE Marketing Department	7	www.ieee.org/digitalsubscriptions	
IEEE MDL/Marketing	3	www.ieee.org/go/trymdl	
Mathworks	CVR 4	www.mathworks.com/accelerate	+1 508 647 7040
Mini-Circuits	CVR 2, 5, CVR 3	www.minicircuits.com	+1 718 934 4500

[advertising SALES OFFICES]

James A. Vick
Sr. Director, Advertising
Phone: +1 212 419 7767;
Fax: +1 212 419 7589
jv.ieeemedia@ieee.org

Marion Delaney
Advertising Sales Director
Phone: +1 415 863 4717;
Fax: +1 415 863 4717
md.ieeemedia@ieee.org

Susan E. Schneiderman
Business Development Manager
Phone: +1 732 562 3946;
Fax: +1 732 981 1855
ss.ieeemedia@ieee.org

Product Advertising
MIDATLANTIC
Lisa Rinaldo
Phone: +1 732 772 0160;
Fax: +1 732 772 0164
lr.ieeemedia@ieee.org
NY, NJ, PA, DE, MD, DC, KY, WV

**NEW ENGLAND/SOUTH CENTRAL/
EASTERN CANADA**
Jody Estabrook
Phone: +1 774 283 4528;
Fax: +1 774 283 4527
je.ieeemedia@ieee.org
ME, VT, NH, MA, RI, CT, AR, LA, OK, TX
Canada: Quebec, Nova Scotia,
Newfoundland, Prince Edward Island,
New Brunswick

SOUTHEAST
Thomas Flynn
Phone: +1 770 645 2944;
Fax: +1 770 993 4423
tf.ieeemedia@ieee.org
VA, NC, SC, GA, FL, AL, MS, TN

Digital Object Identifier 10.1109/MSP.2013.2290963

MIDWEST/CENTRAL CANADA
Dave Jones
Phone: +1 708 442 5633;
Fax: +1 708 442 7620
dj.ieeemedia@ieee.org
IL, IA, KS, MN, MO, NE, ND,
SD, WI, OH
Canada: Manitoba,
Saskatchewan, Alberta

**MIDWEST/ ONTARIO,
CANADA**
Will Hamilton
Phone: +1 269 381 2156;
Fax: +1 269 381 2556
wh.ieeemedia@ieee.org
IN, MI, Canada: Ontario

**WEST COAST/MOUNTAIN STATES/
WESTERN CANADA**
Marshall Rubin
Phone: +1 818 888 2407;
Fax: +1 818 888 4907
mr.ieeemedia@ieee.org
AZ, CO, HI, NM, NV, UT, AK, ID, MT,
WY, OR, WA, CA. Canada: British
Columbia

**EUROPE/AFRICA/MIDDLE EAST
ASIA/FAR EAST/PACIFIC RIM**
Louise Smith
Phone: +44 1875 825 700;
Fax: +44 1875 825 701
les.ieeemedia@ieee.org
Europe, Africa, Middle East
Asia, Far East, Pacific Rim, Australia,
New Zealand

Recruitment Advertising
MIDATLANTIC
Lisa Rinaldo
Phone: +1 732 772 0160;
Fax: +1 732 772 0164
lr.ieeemedia@ieee.org
NY, NJ, CT, PA, DE, MD, DC, KY, WV

NEW ENGLAND/EASTERN CANADA
Liza Reich
Phone: +1 212 419 7578;
Fax: +1 212 419 7589
e.reich@ieee.org
ME, VT, NH, MA, RI, Canada: Quebec,
Nova Scotia, Prince Edward Island,
Newfoundland, New Brunswick

SOUTHEAST
Cathy Flynn
Phone: +1 770 645 2944;
Fax: +1 770 993 4423
cf.ieeemedia@ieee.org
VA, NC, SC, GA, FL, AL, MS, TN

**MIDWEST/SOUTH CENTRAL/
CENTRAL CANADA**
Darcy Giovino
Phone: +224 616 3034;
Fax: +1 847 729 4269
dg.ieeemedia@ieee.org
AR, IL, IN, IA, KS, LA, MI, MN, MO, NE,
ND, SD, OH, OK, TX, WI, Canada:
Ontario, Manitoba, Saskatchewan, Alberta

**WEST COAST/SOUTHWEST/
MOUNTAIN STATES/ASIA**
Tim Matteson
Phone: +1 310 836 4064;
Fax: +1 310 836 4067
tm.ieeemedia@ieee.org
AZ, CO, HI, NV, NM, UT, CA, AK, ID, MT,
WY, OR, WA, Canada: British Columbia

EUROPE/AFRICA/MIDDLE EAST
Louise Smith
Phone: +44 1875 825 700;
Fax: +44 1875 825 701
les.ieeemedia@ieee.org
Europe, Africa, Middle East



photo courtesy of the U.S. Military & NASA

ULTRA-REL[®] 10 MHz to 6 GHz CERAMIC MMIC AMPLIFIERS

Low NF 0.5 dB High IP3 up to 38 dBm Low DC current 65 mA **\$4⁹⁵** ea. (qty 20)

When failure is not an option. Our new CMA MMIC amplifiers deliver outstanding performance in a rugged, nitrogen-filled, hermetic LTCC design, just 0.045" high. These models are so tough, they've qualified for use under MIL environmental conditions:

Robust performance across wide bandwidths makes them ideal for instrumentation, or anywhere long-term reliability adds bottom-line value. Go to minicircuits.com for all the details today, and get them in your hands as soon as tomorrow!

MIL Qualifications (see website for complete list and details)

- Gross and Fine Leak HTOL (1700 hours+ @ +105°C)
- Mechanical Shock Thermal Shock
- Vibration Steam Aging
- Acceleration Solder Heat Resistance
- PIND Autoclave (and more)

Electrical Specifications (-55 to +105°C)



3 x 3 x 1.14 mm

Model	Freq. (GHz)	Gain (dB)	P _{OUT} (dBm)	IP3 (dBm)	NF (dB)	DC (V)	Price \$ ea. (qty 20)
CMA-62+	0.01-6	15	19	33	5	5	4.95
CMA-63+	0.01-6	20	18	32	4	5	4.95
CMA-545+	0.05-6	15	20	37	1	3	4.95
NEW CMA-5043+	0.05-4	18	20	33	0.8	5	4.95
NEW CMA-54SG1+	0.4-2.2	32	23	36	0.9	5	5.45
NEW CMA-162LN+	0.7-1.6	23	19	30	0.5	4	4.95
NEW CMA-252LN+	1.5-2.5	17	18	30	1	4	4.95

RoHS compliant



www.minicircuits.com P.O. Box 350166, Brooklyn, NY 11235-0003 (718) 934-4500 sales@minicircuits.com

503 Rev E



Find it at
mathworks.com/accelerate
datasheet
video example
trial request

GENERATE HDL CODE AUTOMATICALLY

from

MATLAB and Simulink



© 2012 The MathWorks, Inc.

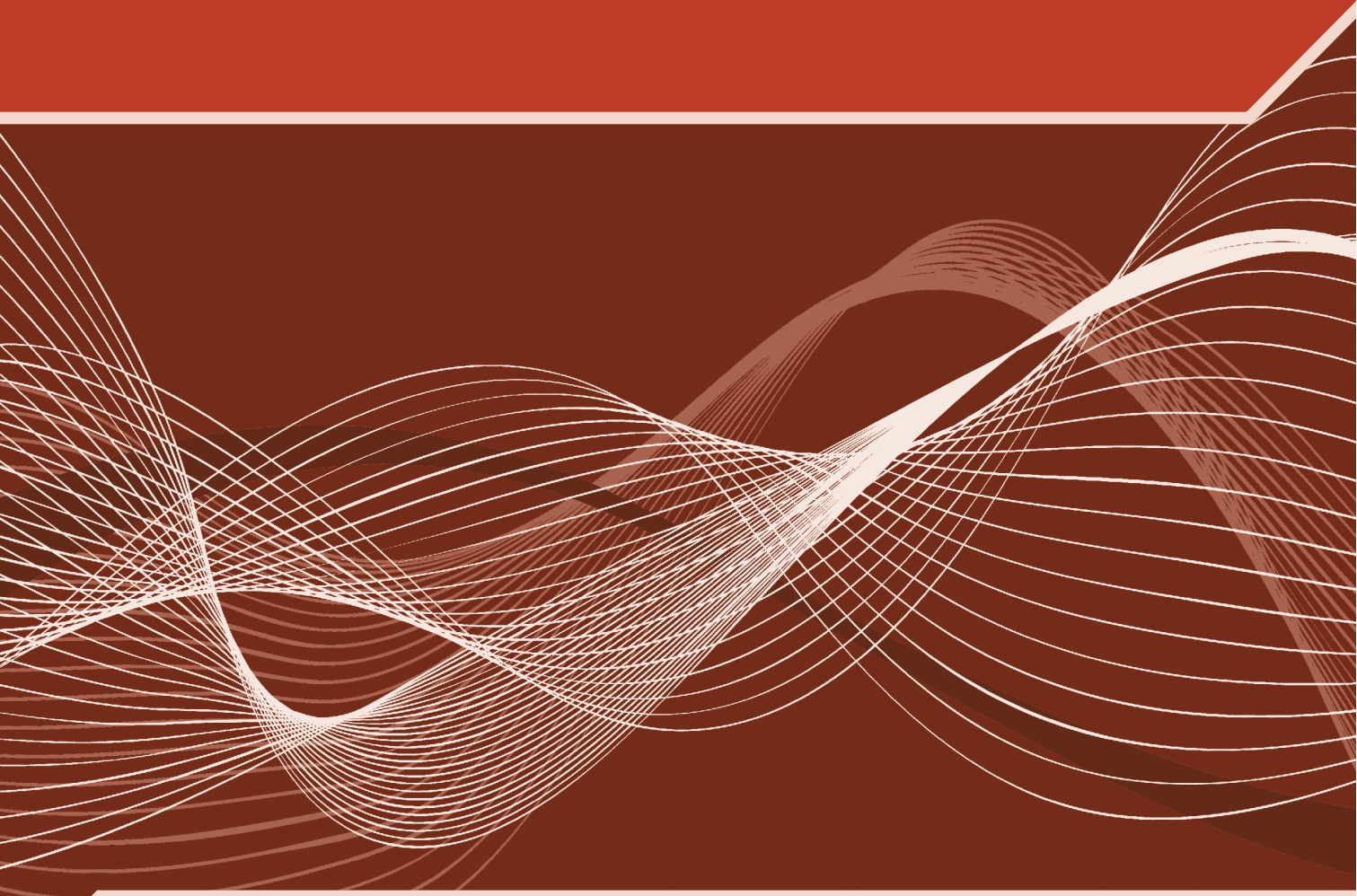
HDL CODER™ automatically converts Simulink models and MATLAB algorithms directly into Verilog and VHDL code for FPGAs or ASIC designs. The code is bit-true, cycle-accurate and synthesizable.

MATLAB®
& SIMULINK®

IEEE SIGNAL PROCESSING SOCIETY

CONTENT GAZETTE

[ISSN 2167-5023]



JULY 2014



2014 Spoken Language Technology Workshop

December 7-10, 2014 • South Lake Tahoe, Nevada, USA



IEEE

IEEE
Signal Processing Society

Organizing Committee

Co-chairs:

Murat Akbacak, Microsoft
John Hansen, UT Dallas

Finance Chair:

Ozlem Kalinli, Sony

Advisory board:

Bhuvana Ramabhadran, IBM
Gokhan Tur, Microsoft
Yang Liu, UT Dallas

Technical Co-chairs:

Steve Young, Cambridge
Pascale Fung, HKUST
Dilek Hakkani Tur, Microsoft
Haizhou Li, I²R

Publicity Co-chairs:

Julia Hirschberg, Columbia
Agustin Gravano, UBA

Publications Chair:

Shri Narayanan, USC

Local Organizers:

Nikki Mirghafori, ICSI Berkeley
Yun Lei, SRI International

Demo Co-chairs:

Alex Rudnicky, CMU
Sachin Kajarekar, Apple

Panel Co-chairs:

Larry Heck, Microsoft
Mazin Gilbert, AT&T

Europe Liaisons:

Isabel Trancoso, INESC ID
Hermann Ney, RWTH Aachen

Asia Liaisons:

Lin Shan Lee, NTU
Sadaoki Furui, TIT

NIPS Liaison:

Li Deng, Microsoft

Sponsorship Co-chairs:

Jerome Bellagarda, Apple
Xiao Li, Facebook
Ananth Sankar, Microsoft

The Fifth IEEE Workshop on Spoken Language Technology (SLT 2014) will be held in South Lake Tahoe, Nevada, on Dec 7-10, 2014. The main theme of the workshop will be "machine learning in spoken language technologies". The workshop goals include increasing both intra and inter community interaction, by means of keynote/guest speakers from the ML community, online panel discussions, miniSIGs, and highlight sessions.

Topics

Submission of papers in all areas of spoken language technology is encouraged, with emphasis on the following topics:

Traditional topic coverage:

Speech recognition and synthesis	Spoken language databases
Spoken language understanding	Speaker/language recognition
Spoken dialog systems	Multimodal processing
Spoken document summarization	Human/computer interaction
Machine translation for speech	Assistive technologies
Question answering from speech	Natural Language Processing
Speech data mining	Educational and healthcare applications
Spoken document retrieval	

Emerging areas: Large scale spoken language understanding; massive data resources for SLT; unsupervised methods in SLT; capturing and representing world knowledge in SLT; web search with SLT; SLT in social networks; multimedia applications; intelligent environments.

Venue, Information and Registration

SLT 2014 will take place in South Lake Tahoe, a town located on the shore of Lake Tahoe, right on the CA-NV state line and easily accessible by plane or car. The workshop venue will be Harvey's Lake Tahoe Casino/Hotel, located within walking distance from the town center and the Heavenly ski resort. Registration and information: www.slt2014.org

Important Dates

Paper Submission:	July 21, 2014
Notification of Acceptance:	September 5, 2014
Demo Submission:	September 2014
Demo Acceptance:	October 2014
Special Sessions / Special Interest Group Proposal submission:	TBD
Early registration deadline:	October 17, 2014
Workshop:	December 7-10, 2014

Submission Procedure

Prospective authors are invited to submit full-length, 4-6 page papers, including figures and references, to the SLT 2014 web site: www.slt2014.org

Supported by



International Speech
Communication Association



IEEE TRANSACTIONS ON SIGNAL PROCESSING

A PUBLICATION OF THE IEEE SIGNAL PROCESSING SOCIETY



www.signalprocessingsociety.org

Indexed in PubMed® and MEDLINE®, products of the United States National Library of Medicine



MAY 15, 2014

VOLUME 62

NUMBER 10

ITPRED

(ISSN 1053-587X)

REGULAR PAPERS

A Flexible NISC-Based LDPC Decoder http://dx.doi.org/10.1109/TSP.2014.2311964	<i>B. Le Gal, C. Jego, and C. Leroux</i>	2469
Accuracy vs. Resolution in Radio Tomography http://dx.doi.org/10.1109/TSP.2014.2311969	<i>R. K. Martin, A. Folkerts, and T. Heintz</i>	2480
Scaled Radix-2/8 Algorithm for Efficient Computation of Length- $N = 2^m$ DFTs http://dx.doi.org/10.1109/TSP.2014.2310434	<i>W. Zheng, K. Li, and K. Li</i>	2492
An Hybrid Cramér-Rao Bound in Closed Form for Direction-of-Arrival Estimation by an “Acoustic Vector Sensor” With Gain-Phase Uncertainties http://dx.doi.org/10.1109/TSP.2014.2310431	<i>P. K. Tam, K. T. Wong, and Y. Song</i>	2504
Optimal Design of Cosine Modulated Nonuniform Linear Phase FIR Filter Bank via Both Stretching and Shifting Frequency Response of Single Prototype Filter http://dx.doi.org/10.1109/TSP.2014.2312326	<i>B. W.-K. Ling, C. Y.-F. Ho, K.-L. Teo, W.-C. Siu, J. Cao, and Q. Dai</i>	2517
Distributed Localization of Coverage Holes Using Topological Persistence http://dx.doi.org/10.1109/TSP.2014.2314063	<i>H. Chintakunta and H. Krim</i>	2531

IEEE TRANSACTIONS ON SIGNAL PROCESSING (ISSN 1053-587X) is published semimonthly by the Institute of Electrical and Electronics Engineers, Inc. Responsibility for the contents rests upon the authors and not upon the IEEE, the Society/Council, or its members. **IEEE Corporate Office:** 3 Park Avenue, 17th Floor, New York, NY 10016-5997. **IEEE Operations Center:** 445 Hoes Lane, Piscataway, NJ 08854-4141. **NJ Telephone:** +1 732 981 0060. **Price/Publication Information:** Individual copies: IEEE Members \$20.00 (first copy only), nonmembers \$569.00 per copy. (Note: Postage and handling charge not included.) Member and nonmember subscription prices available upon request. **Copyright and Reprint Permissions:** Abstracting is permitted with credit to the source. Libraries are permitted to photocopy for private use of patrons, provided the per-copy fee of \$31.00 is paid through the Copyright Clearance Center, 222 Rosewood Drive, Danvers, MA 01923. For all other copying, reprint, or republication permission, write to Copyrights and Permissions Department, IEEE Publications Administration, 445 Hoes Lane, Piscataway, NJ 08854-4141. Copyright © 2014 by the Institute of Electrical and Electronics Engineers, Inc. All rights reserved. Periodicals Postage Paid at New York, NY and at additional mailing offices. **Postmaster:** Send address changes to IEEE TRANSACTIONS ON SIGNAL PROCESSING, IEEE, 445 Hoes Lane, Piscataway, NJ 08854-4141. GST Registration No. 125634188. CPC Sales Agreement #40013087. Return undeliverable Canada addresses to: Pitney Bowes IMEX, P.O. Box 4332, Stanton Rd., Toronto, ON M5W 3J4, Canada. IEEE prohibits discrimination, harassment and bullying. For more information visit <http://www.ieee.org/nondiscrimination>. Printed in U.S.A.



Nested Vector-Sensor Array Processing via Tensor Modeling http://dx.doi.org/10.1109/TSP.2014.2314437	<i>K. Han and A. Nehorai</i>	2542
Analytical Construction and Fast Computation of Frequency Warping Operators and Dual Frame http://dx.doi.org/10.1109/TSP.2014.2309552	<i>S. Caporale and N. Speciale</i>	2554
Linearization of Time-Varying Nonlinear Systems Using A Modified Linear Iterative Method http://dx.doi.org/10.1109/TSP.2014.2311965 ..	<i>M. Hotz and C. Vogel</i>	2566
Efficient Closed-Form Algorithms for AOA Based Self-Localization of Sensor Nodes Using Auxiliary Variables http://dx.doi.org/10.1109/TSP.2014.2314064	<i>H.-J. Shao, X.-P. Zhang, and Z. Wang</i>	2580
A Phase-Reconstruction Technique for Low-Power Centimeter-Accurate Mobile Positioning http://dx.doi.org/10.1109/TSP.2014.2311967 ..	<i>K. M. Pesyna, Z. M. Kassas, R. W. Heath, and T. E. Humphreys</i>	2595
Analytical Performance Assessment of Multi-Dimensional Matrix- and Tensor-Based ESPRIT-Type Algorithms http://dx.doi.org/10.1109/TSP.2014.2313530	<i>F. Roemer, M. Haardt, and G. Del Galdo</i>	2611
Sequential Bayesian Estimation With Censored Data for Multi-Sensor Systems http://dx.doi.org/10.1109/TSP.2014.2315163	<i>Y. Zheng, R. Niu, and P. K. Varshney</i>	2626
A New Technique for INS/GNSS Attitude and Parameter Estimation Using Online Optimization http://dx.doi.org/10.1109/TSP.2014.2312317	<i>Y. Wu, J. Wang, and D. Hu</i>	2642
Resource Allocation in MIMO Radar With Multiple Targets for Non-Coherent Localization http://dx.doi.org/10.1109/TSP.2014.2315169 ..	<i>N. Garcia, A. M. Haimovich, M. Coulon, and M. Lops</i>	2656
Electrocardiogram Signal Modeling With Adaptive Parameter Estimation Using Sequential Bayesian Methods http://dx.doi.org/10.1109/TSP.2014.2312316	<i>S. Edla, N. Kovvali, and A. Papandreou-Suppappola</i>	2667
Distributed Inference With M-Ary Quantized Data in the Presence of Byzantine Attacks http://dx.doi.org/10.1109/TSP.2014.2314072	<i>V. S. S. Nadendla, Y. S. Han, and P. K. Varshney</i>	2681
A Low Complexity-High Throughput QC-LDPC Encoder http://dx.doi.org/10.1109/TSP.2014.2314435	<i>A. Mahdi and V. Paliouras</i>	2696
Explicit Causal Recursive Estimators for Continuous-Time Bivariate Markov Chains http://dx.doi.org/10.1109/TSP.2014.2314434	<i>B. L. Mark and Y. Ephraim</i>	2709
MMSE-SLNR Precoding for Multi-Antenna Cognitive Radio http://dx.doi.org/10.1109/TSP.2014.2314442	<i>Y. Richter and I. Bergel</i>	2719
Statistical Framework for Optimization in the Multi-User MIMO Uplink With ZF-DFE http://dx.doi.org/10.1109/TSP.2014.2314067	<i>S. Järmyr, B. Ottersten, and E. A. Jorswieck</i>	2730

IEEE TRANSACTIONS ON SIGNAL PROCESSING

A PUBLICATION OF THE IEEE SIGNAL PROCESSING SOCIETY



www.signalprocessingsociety.org

Indexed in PubMed® and MEDLINE®, products of the United States National Library of Medicine



MAY 15, 2014

VOLUME 62

NUMBER 10

ITPRED

(ISSN 1053-587X)

REGULAR PAPERS

Biomedical Signal Processing

Electrocardiogram Signal Modeling With Adaptive Parameter Estimation Using Sequential Bayesian Methods

<http://dx.doi.org/10.1109/TSP.2014.2312316> *S. Edla, N. Kovvali, and A. Papandreou-Suppappola* 2667

Design and Implementation of Signal Processing Systems

Scaled Radix-2/8 Algorithm for Efficient Computation of Length- $N = 2^m$ DFTs <http://dx.doi.org/10.1109/TSP.2014.2310434>

..... *W. Zheng, K. Li, and K. Li* 2492

A Low Complexity-High Throughput QC-LDPC Encoder <http://dx.doi.org/10.1109/TSP.2014.2314435>

..... *A. Mahdi and V. Paliouras* 2696

Digital and Multirate Signal Processing

Optimal Design of Cosine Modulated Nonuniform Linear Phase FIR Filter Bank via Both Stretching and Shifting Frequency Response of Single Prototype Filter <http://dx.doi.org/10.1109/TSP.2014.2312326>

..... *B. W.-K. Ling, C. Y.-F. Ho, K.-L. Teo, W.-C. Siu, J. Cao, and Q. Dai* 2517

Analytical Construction and Fast Computation of Frequency Warping Operators and Dual Frame

<http://dx.doi.org/10.1109/TSP.2014.2309552> *S. Caporale and N. Speciale* 2554

IEEE TRANSACTIONS ON SIGNAL PROCESSING (ISSN 1053-587X) is published semimonthly by the Institute of Electrical and Electronics Engineers, Inc. Responsibility for the contents rests upon the authors and not upon the IEEE, the Society/Council, or its members. **IEEE Corporate Office:** 3 Park Avenue, 17th Floor, New York, NY 10016-5997. **IEEE Operations Center:** 445 Hoes Lane, Piscataway, NJ 08854-4141. **NJ Telephone:** +1 732 981 0060. **Price/Publication Information:** Individual copies: IEEE Members \$20.00 (first copy only), nonmembers \$569.00 per copy. (Note: Postage and handling charge not included.) Member and nonmember subscription prices available upon request. **Copyright and Reprint Permissions:** Abstracting is permitted with credit to the source. Libraries are permitted to photocopy for private use of patrons, provided the per-copy fee of \$31.00 is paid through the Copyright Clearance Center, 222 Rosewood Drive, Danvers, MA 01923. For all other copying, reprint, or republication permission, write to Copyrights and Permissions Department, IEEE Publications Administration, 445 Hoes Lane, Piscataway, NJ 08854-4141. Copyright © 2014 by the Institute of Electrical and Electronics Engineers, Inc. All rights reserved. Periodicals Postage Paid at New York, NY and at additional mailing offices. **Postmaster:** Send address changes to IEEE TRANSACTIONS ON SIGNAL PROCESSING, IEEE, 445 Hoes Lane, Piscataway, NJ 08854-4141. GST Registration No. 125634188. CPC Sales Agreement #40013087. Return undeliverable Canada addresses to: Pitney Bowes IMEX, P.O. Box 4332, Stanton Rd., Toronto, ON M5W 3J4, Canada. IEEE prohibits discrimination, harassment and bullying. For more information visit <http://www.ieee.org/nondiscrimination>. Printed in U.S.A.



<i>Implementation of Signal Processing Systems</i>	
A Flexible NISC-Based LDPC Decoder http://dx.doi.org/10.1109/TSP.2014.2311964	B. Le Gal, C. Jego, and C. Leroux 2469
<i>Signal Processing for Networks</i>	
Distributed Localization of Coverage Holes Using Topological Persistence http://dx.doi.org/10.1109/TSP.2014.2314063	H. Chintakunta and H. Krim 2531
Statistical Framework for Optimization in the Multi-User MIMO Uplink With ZF-DFE http://dx.doi.org/10.1109/TSP.2014.2314067	S. Järmyr, B. Ottersten, and E. A. Jorswieck 2730
<i>Other Areas and Applications</i>	
Linearization of Time-Varying Nonlinear Systems Using A Modified Linear Iterative Method http://dx.doi.org/10.1109/TSP.2014.2311965 ..	M. Hotz and C. Vogel 2566
<i>Radar and Sonar Signal Processing</i>	
Resource Allocation in MIMO Radar With Multiple Targets for Non-Coherent Localization http://dx.doi.org/10.1109/TSP.2014.2315169 ..	N. Garcia, A. M. Haimovich, M. Coulon, and M. Lops 2656
<i>Sensor Array and Multichannel Processing</i>	
An Hybrid Cramér-Rao Bound in Closed Form for Direction-of-Arrival Estimation by an “Acoustic Vector Sensor” With Gain-Phase Uncertainties http://dx.doi.org/10.1109/TSP.2014.2310431	P. K. Tam, K. T. Wong, and Y. Song 2504
Nested Vector-Sensor Array Processing via Tensor Modeling http://dx.doi.org/10.1109/TSP.2014.2314437	K. Han and A. Nehorai 2542
Analytical Performance Assessment of Multi-Dimensional Matrix- and Tensor-Based ESPRIT-Type Algorithms http://dx.doi.org/10.1109/TSP.2014.2313530	F. Roemer, M. Haardt, and G. Del Galdo 2611
<i>Signal Processing for Sensor Networks</i>	
Distributed Inference With M-Ary Quantized Data in the Presence of Byzantine Attacks http://dx.doi.org/10.1109/TSP.2014.2314072	V. S. S. Nadendla, Y. S. Han, and P. K. Varshney 2681
Sequential Bayesian Estimation With Censored Data for Multi-Sensor Systems http://dx.doi.org/10.1109/TSP.2014.2315163	Y. Zheng, R. Niu, and P. K. Varshney 2626
<i>Signal Processing for Communications</i>	
MMSE-SLNR Precoding for Multi-Antenna Cognitive Radio http://dx.doi.org/10.1109/TSP.2014.2314442	Y. Richter and I. Bergel 2719
<i>Statistical Signal Processing</i>	
A Phase-Reconstruction Technique for Low-Power Centimeter-Accurate Mobile Positioning http://dx.doi.org/10.1109/TSP.2014.2311967 ..	K. M. Pesyna, Z. M. Kassas, R. W. Heath, and T. E. Humphreys 2595
Explicit Causal Recursive Estimators for Continuous-Time Bivariate Markov Chains http://dx.doi.org/10.1109/TSP.2014.2314434	B. L. Mark and Y. Ephraim 2709
A New Technique for INS/GNSS Attitude and Parameter Estimation Using Online Optimization http://dx.doi.org/10.1109/TSP.2014.2312317	Y. Wu, J. Wang, and D. Hu 2642
Efficient Closed-Form Algorithms for AOA Based Self-Localization of Sensor Nodes Using Auxiliary Variables http://dx.doi.org/10.1109/TSP.2014.2314064	H.-J. Shao, X.-P. Zhang, and Z. Wang 2580
Accuracy vs. Resolution in Radio Tomography http://dx.doi.org/10.1109/TSP.2014.2311969	R. K. Martin, A. Folkerts, and T. Heintl 2480

IEEE TRANSACTIONS ON SIGNAL PROCESSING

A PUBLICATION OF THE IEEE SIGNAL PROCESSING SOCIETY



www.signalprocessingsociety.org

Indexed in PubMed® and MEDLINE®, products of the United States National Library of Medicine



JUNE 1, 2014

VOLUME 62

NUMBER 11

ITPRED

(ISSN 1053-587X)

REGULAR PAPERS

General Parameterized Time-Frequency Transform http://dx.doi.org/10.1109/TSP.2014.2314061	2751
..... <i>Y. Yang, Z. K. Peng, X. J. Dong, W. M. Zhang, and G. Meng</i>	
Online Dictionary Learning for Kernel LMS http://dx.doi.org/10.1109/TSP.2014.2318132	2765
..... <i>W. Gao, J. Chen, C. Richard, and J. Huang</i>	
General Non-Orthogonal Constrained ICA http://dx.doi.org/10.1109/TSP.2014.2318136	2778
..... <i>P. A. Rodriguez, M. Anderson, X.-L. Li, and T. Adali</i>	
Quadrature Compressive Sampling for Radar Signals http://dx.doi.org/10.1109/TSP.2014.2315168	2787
..... <i>F. Xi, S. Chen, and Z. Liu</i>	
Forest Sparsity for Multi-Channel Compressive Sensing http://dx.doi.org/10.1109/TSP.2014.2318138	2803
..... <i>C. Chen, Y. Li, and J. Huang</i>	
An EM Algorithm for Multipath State Estimation in OTHR Target Tracking http://dx.doi.org/10.1109/TSP.2014.2318134	2814
..... <i>H. Lan, Y. Liang, Q. Pan, F. Yang, and C. Guan</i>	
Recursive Algorithm for Sliding Walsh Hadamard Transform http://dx.doi.org/10.1109/TSP.2014.2316146	2827
..... <i>C.-S. Park</i>	
Cooperative Synchronization in Wireless Networks http://dx.doi.org/yes	2837
..... <i>B. Etzlinger, H. Wymeersch, and A. Springer</i>	

IEEE TRANSACTIONS ON SIGNAL PROCESSING (ISSN 1053-587X) is published semimonthly by the Institute of Electrical and Electronics Engineers, Inc. Responsibility for the contents rests upon the authors and not upon the IEEE, the Society/Council, or its members. **IEEE Corporate Office:** 3 Park Avenue, 17th Floor, New York, NY 10016-5997. **IEEE Operations Center:** 445 Hoes Lane, Piscataway, NJ 08854-4141. **NJ Telephone:** +1 732 981 0060. **Price/Publication Information:** Individual copies: IEEE Members \$20.00 (first copy only), nonmembers \$569.00 per copy. (Note: Postage and handling charge not included.) Member and nonmember subscription prices available upon request. **Copyright and Reprint Permissions:** Abstracting is permitted with credit to the source. Libraries are permitted to photocopy for private use of patrons, provided the per-copy fee of \$31.00 is paid through the Copyright Clearance Center, 222 Rosewood Drive, Danvers, MA 01923. For all other copying, reprint, or republication permission, write to Copyrights and Permissions Department, IEEE Publications Administration, 445 Hoes Lane, Piscataway, NJ 08854-4141. Copyright © 2014 by the Institute of Electrical and Electronics Engineers, Inc. All rights reserved. Periodicals Postage Paid at New York, NY and at additional mailing offices. **Postmaster:** Send address changes to IEEE TRANSACTIONS ON SIGNAL PROCESSING, IEEE, 445 Hoes Lane, Piscataway, NJ 08854-4141. GST Registration No. 125634188. CPC Sales Agreement #40013087. Return undeliverable Canada addresses to: Pitney Bowes IMEX, P.O. Box 4332, Stanton Rd., Toronto, ON M5W 3J4, Canada. IEEE prohibits discrimination, harassment and bullying. For more information visit <http://www.ieee.org/nondiscrimination>. Printed in U.S.A.



Deterministic Construction of Sparse Sensing Matrices via Finite Geometry http://dx.doi.org/10.1109/TSP.2014.2318140	2850
..... <i>S. Li and G. Ge</i>	
Scalar Quantization for Estimation: From An Asymptotic Design to a Practical Solution http://dx.doi.org/10.1109/TSP.2014.2313528	2860
..... <i>R. Cabral Farias and J.-M. Brossier</i>	
Bayesian Spectral Analysis With Student-t Noise http://dx.doi.org/10.1109/TSP.2014.2315164	2871
..... <i>J. Christmas</i>	
Semi-Supervised Multiresolution Classification Using Adaptive Graph Filtering With Application to Indirect Bridge Structural Health Monitoring http://dx.doi.org/10.1109/TSP.2014.2319775	2879
..... <i>S. Chen, F. Cerda, P. Rizzo, J. Bielak, J. H. Garrett, and J. Kovačević</i>	
Blind Separation of Multi-Dimensional Components via Subspace Decomposition: Performance Analysis http://dx.doi.org/10.1109/TSP.2014.2319774	2894
..... <i>D. Lahat, J.-F. Cardoso, and H. Messer</i>	
Bayesian Group-Sparse Modeling and Variational Inference http://dx.doi.org/10.1109/TSP.2014.2319772	2906
..... <i>S. D. Babacan, S. Nakajima, and M. N. Do</i>	
Codebook-Based Opportunistic Interference Alignment http://dx.doi.org/10.1109/TSP.2014.2313525	2922
..... <i>H. J. Yang, B. C. Jung, W.-Y. Shin, and A. Paulraj</i>	
Laplace Transform of Product of Generalized Marcum Q, Bessel I, and Power Functions With Applications http://dx.doi.org/10.1109/TSP.2014.2316162	2938
..... <i>N. Y. Ermolova and O. Tirkkonen</i>	
Ambiguity Function Analysis for UMTS-Based Passive Multistatic Radar http://dx.doi.org/10.1109/TSP.2014.2319776	2945
..... <i>S. Gogineni, M. Rangaswamy, B. D. Rigling, and A. Nehorai</i>	
Reduced Mean-Square Error Quadratic Inverse Spectrum Estimator http://dx.doi.org/10.1109/TSP.2014.2320462	2958
..... <i>K. Q. Lepage and D. J. Thomson</i>	
Unbiased Recursive Least-Squares Estimation Utilizing Dichotomous Coordinate-Descent Iterations http://dx.doi.org/	2973
..... <i>R. Arablouei, K. Doğançay, and T. Adalı</i>	
A New Decomposition Method for Multiuser DC-Programming and Its Applications http://dx.doi.org/	2984
..... <i>A. Alvarado, G. Scutari, and J.-S. Pang</i>	
Detection in Passive MIMO Radar Networks http://dx.doi.org/	2999
..... <i>D. E. Hack, L. K. Patton, B. Himed, and M. A. Saville</i>	
Centralized Passive MIMO Radar Detection Without Direct-Path Reference Signals http://dx.doi.org/	3013
..... <i>D. E. Hack, L. K. Patton, B. Himed, and M. A. Saville</i>	

IEEE TRANSACTIONS ON SIGNAL PROCESSING

A PUBLICATION OF THE IEEE SIGNAL PROCESSING SOCIETY



www.signalprocessingsociety.org

Indexed in PubMed® and MEDLINE®, products of the United States National Library of Medicine



JUNE 1, 2014

VOLUME 62

NUMBER 11

ITPRED

(ISSN 1053-587X)

REGULAR PAPERS

Adaptive Signal Processing

Unbiased Recursive Least-Squares Estimation Utilizing Dichotomous Coordinate-Descent Iterations
<http://dx.doi.org/10.1109/TSP.2014.2316162> R. Arablouei, K. Doğançay, and T. Adalı 2973

Digital and Multirate Signal Processing

Forest Sparsity for Multi-Channel Compressive Sensing <http://dx.doi.org/10.1109/TSP.2014.2318138> C. Chen, Y. Li, and J. Huang 2803

Quadrature Compressive Sampling for Radar Signals <http://dx.doi.org/10.1109/TSP.2014.2315168> F. Xi, S. Chen, and Z. Liu 2787

General Parameterized Time-Frequency Transform <http://dx.doi.org/10.1109/TSP.2014.2314061>
 Y. Yang, Z. K. Peng, X. J. Dong, W. M. Zhang, and G. Meng 2751

Semi-Supervised Multiresolution Classification Using Adaptive Graph Filtering With Application to Indirect Bridge
 Structural Health Monitoring <http://dx.doi.org/10.1109/TSP.2014.2313528>
 S. Chen, F. Cerda, P. Rizzo, J. Bielak, J. H. Garrett, and J. Kovačević 2879

Multidimensional Signal Processing

Recursive Algorithm for Sliding Walsh Hadamard Transform <http://dx.doi.org/10.1109/TSP.2014.2316146> C.-S. Park 2827

IEEE TRANSACTIONS ON SIGNAL PROCESSING (ISSN 1053-587X) is published semimonthly by the Institute of Electrical and Electronics Engineers, Inc. Responsibility for the contents rests upon the authors and not upon the IEEE, the Society/Council, or its members. **IEEE Corporate Office:** 3 Park Avenue, 17th Floor, New York, NY 10016-5997. **IEEE Operations Center:** 445 Hoes Lane, Piscataway, NJ 08854-4141. **NJ Telephone:** +1 732 981 0060. **Price/Publication Information:** Individual copies: IEEE Members \$20.00 (first copy only), nonmembers \$569.00 per copy. (Note: Postage and handling charge not included.) Member and nonmember subscription prices available upon request. **Copyright and Reprint Permissions:** Abstracting is permitted with credit to the source. Libraries are permitted to photocopy for private use of patrons, provided the per-copy fee of \$31.00 is paid through the Copyright Clearance Center, 222 Rosewood Drive, Danvers, MA 01923. For all other copying, reprint, or republication permission, write to Copyrights and Permissions Department, IEEE Publications Administration, 445 Hoes Lane, Piscataway, NJ 08854-4141. Copyright © 2014 by the Institute of Electrical and Electronics Engineers, Inc. All rights reserved. Periodicals Postage Paid at New York, NY and at additional mailing offices. **Postmaster:** Send address changes to IEEE TRANSACTIONS ON SIGNAL PROCESSING, IEEE, 445 Hoes Lane, Piscataway, NJ 08854-4141. GST Registration No. 125634188. CPC Sales Agreement #40013087. Return undeliverable Canada addresses to: Pitney Bowes IMEX, P.O. Box 4332, Stanton Rd., Toronto, ON M5W 3J4, Canada. IEEE prohibits discrimination, harassment and bullying. For more information visit <http://www.ieee.org/nondiscrimination>. Printed in U.S.A.



<i>Machine Learning</i>	
Bayesian Spectral Analysis With Student-t Noise http://dx.doi.org/10.1109/TSP.2014.2316139	J. Christmas 2871
General Non-Orthogonal Constrained ICA http://dx.doi.org/10.1109/TSP.2014.2318136	P. A. Rodriguez, M. Anderson, X.-L. Li, and T. Adali 2778
<i>Signal Processing for Networks</i>	
Online Dictionary Learning for Kernel LMS http://dx.doi.org/10.1109/TSP.2014.2318132	W. Gao, J. Chen, C. Richard, and J. Huang 2765
<i>Optimization Methods for Signal Processing</i>	
A New Decomposition Method for Multiuser DC-Programming and Its Applications http://dx.doi.org/10.1109/TSP.2014.2315167	A. Alvarado, G. Scutari, and J.-S. Pang 2984
<i>Radar and Sonar Signal Processing</i>	
Centralized Passive MIMO Radar Detection Without Direct-Path Reference Signals http://dx.doi.org/10.1109/TSP.2014.2320462	D. E. Hack, L. K. Patton, B. Himed, and M. A. Saville 3013
<i>Sensor Array and Multichannel Processing</i>	
Deterministic Construction of Sparse Sensing Matrices via Finite Geometry http://dx.doi.org/10.1109/TSP.2014.2318139	S. Li and G. Ge 2850
Ambiguity Function Analysis for UMTS-Based Passive Multistatic Radar http://dx.doi.org/10.1109/TSP.2014.2318135	S. Gogineni, M. Rangaswamy, B. D. Rigling, and A. Nehorai 2945
Detection in Passive MIMO Radar Networks http://dx.doi.org/10.1109/TSP.2014.2319776	D. E. Hack, L. K. Patton, B. Himed, and M. A. Saville 2999
<i>Signal Processing for Sensor Networks</i>	
Cooperative Synchronization in Wireless Networks http://dx.doi.org/10.1109/TSP.2014.2313531	B. Etxlinger, H. Wymeersch, and A. Springer 2837
<i>Signal Processing for Communications</i>	
Codebook-Based Opportunistic Interference Alignment http://dx.doi.org/10.1109/TSP.2014.2319774	H. J. Yang, B. C. Jung, W.-Y. Shin, and A. Paulraj 2922
Laplace Transform of Product of Generalized Marcum Q, Bessel I, and Power Functions With Applications http://dx.doi.org/10.1109/TSP.2014.2319772	N. Y. Ermolova and O. Tirkkonen 2938
<i>Statistical Signal Processing</i>	
Scalar Quantization for Estimation: From An Asymptotic Design to a Practical Solution http://dx.doi.org/10.1109/TSP.2014.2318140	R. Cabral Farias and J.-M. Brossier 2860
Bayesian Group-Sparse Modeling and Variational Inference http://dx.doi.org/10.1109/TSP.2014.2319775	S. D. Babacan, S. Nakajima, and M. N. Do 2906
Reduced Mean-Square Error Quadratic Inverse Spectrum Estimator http://dx.doi.org/10.1109/TSP.2014.2313525	K. Q. Lepage and D. J. Thomson 2958
Blind Separation of Multi-Dimensional Components via Subspace Decomposition: Performance Analysis http://dx.doi.org/10.1109/TSP.2014.2315164	D. Lahat, J.-F. Cardoso, and H. Messer 2894
An EM Algorithm for Multipath State Estimation in OTHR Target Tracking http://dx.doi.org/10.1109/TSP.2014.2318134	H. Lan, Y. Liang, Q. Pan, F. Yang, and C. Guan 2814

IEEE TRANSACTIONS ON SIGNAL PROCESSING

A PUBLICATION OF THE IEEE SIGNAL PROCESSING SOCIETY



www.signalprocessingsociety.org

Indexed in PubMed® and MEDLINE®, products of the United States National Library of Medicine



JUNE 15, 2014

VOLUME 62

NUMBER 12

ITPRED

(ISSN 1053-587X)

REGULAR PAPERS

Consensus-based Distributed Particle Filtering With Distributed Proposal Adaptation http://dx.doi.org/10.1109/TSP.2014.2319777	3029
..... <i>O. Hlinka, F. Hlawatsch, and P. M. Djurić</i>	
Discrete Signal Processing on Graphs: Frequency Analysis http://dx.doi.org/10.1109/TSP.2014.2321121	3042
..... <i>A. Sandryhaila and J. M. F. Moura</i>	
Optimal Periodic Sensor Scheduling in Networks of Dynamical Systems http://dx.doi.org/10.1109/TSP.2014.2320455	3055
..... <i>S. Liu, M. Fardad, P. K. Varshney, and E. Masazade</i>	
Collective Ratings for Online Communities With Strategic Users http://dx.doi.org/10.1109/TSP.2014.2320457	3069
..... <i>Y. Zhang and M. van der Schaar</i>	
SUMIS: Near-Optimal Soft-In Soft-Out MIMO Detection With Low and Fixed Complexity http://dx.doi.org/10.1109/TSP.2014.2303945 ..	3084
..... <i>M. Čirkić and E. G. Larsson</i>	

IEEE TRANSACTIONS ON SIGNAL PROCESSING (ISSN 1053-587X) is published semimonthly by the Institute of Electrical and Electronics Engineers, Inc. Responsibility for the contents rests upon the authors and not upon the IEEE, the Society/Council, or its members. **IEEE Corporate Office:** 3 Park Avenue, 17th Floor, New York, NY 10016-5997. **IEEE Operations Center:** 445 Hoes Lane, Piscataway, NJ 08854-4141. **NJ Telephone:** +1 732 981 0060. **Price/Publication Information:** Individual copies: IEEE Members \$20.00 (first copy only), nonmembers \$569.00 per copy. (Note: Postage and handling charge not included.) Member and nonmember subscription prices available upon request. **Copyright and Reprint Permissions:** Abstracting is permitted with credit to the source. Libraries are permitted to photocopy for private use of patrons, provided the per-copy fee of \$31.00 is paid through the Copyright Clearance Center, 222 Rosewood Drive, Danvers, MA 01923. For all other copying, reprint, or republication permission, write to Copyrights and Permissions Department, IEEE Publications Administration, 445 Hoes Lane, Piscataway, NJ 08854-4141. Copyright © 2014 by the Institute of Electrical and Electronics Engineers, Inc. All rights reserved. Periodicals Postage Paid at New York, NY and at additional mailing offices. **Postmaster:** Send address changes to IEEE TRANSACTIONS ON SIGNAL PROCESSING, IEEE, 445 Hoes Lane, Piscataway, NJ 08854-4141. GST Registration No. 125634188. CPC Sales Agreement #40013087. Return undeliverable Canada addresses to: Pitney Bowes IMEX, P.O. Box 4332, Stanton Rd., Toronto, ON M5W 3J4, Canada. IEEE prohibits discrimination, harassment and bullying. For more information visit <http://www.ieee.org/nondiscrimination>. Printed in U.S.A.



Distributed State Estimation With Dimension Reduction Preprocessing http://dx.doi.org/10.1109/TSP.2014.2323021	3098
..... <i>H. Ma, Y.-H. Yang, Y. Chen, K. J. R. Liu, and Q. Wang</i>	
Data-Aided Channel Estimation in Large Antenna Systems http://dx.doi.org/10.1109/TSP.2014.2321120	3111
..... <i>J. Ma and L. Ping</i>	
Direct Construction of Superoscillations http://dx.doi.org/10.1109/TSP.2014.2321119	3125
..... <i>D. G. Lee and P. J. S. G. Ferreira</i>	
Geolocation by Direction of Arrival Using Arrays With Unknown Orientation http://dx.doi.org/10.1109/TSP.2014.2321109	3135
..... <i>O. Jean and A. J. Weiss</i>	
Fixed-Lag Smoothing for Bayes Optimal Knowledge Exploitation in Target Tracking http://dx.doi.org/10.1109/TSP.2014.2321731	3143
..... <i>F. Papi, M. Bocquel, M. Podt, and Y. Boers</i>	
On Optimal Gaussian Signaling in MIMO Relay Channels With Partial Decode-and-Forward http://dx.doi.org/10.1109/TSP.2014.2321737 ..	3153
..... <i>C. Hellings, L. Gerdes, L. Weiland, and W. Utschick</i>	
An Efficient Partial-Sum Network Architecture for Semi-Parallel Polar Codes Decoder Implementation http://dx.doi.org/10.1109/TSP.2014.2319773	3165
..... <i>Y. Fan and C.-Y. Tsui</i>	
Sequential Distributed Detection in Energy-Constrained Wireless Sensor Networks http://dx.doi.org/10.1109/TSP.2014.2320458	3180
..... <i>Y. Yilmaz and X. Wang</i>	
Radar Target Profiling and Recognition Based on TSI-Optimized Compressive Sensing Kernel http://dx.doi.org/10.1109/TSP.2014.2323022	3194
..... <i>Y. Gu, N. A. Goodman, and A. Ashok</i>	
Distributed Detection in Tree Topologies With Byzantines http://dx.doi.org/10.1109/TSP.2014.2321735	3208
..... <i>B. Kailkhura, S. Brahma, Y. S. Han, and P. K. Varshney</i>	
Approximate Subspace-Based Iterative Adaptive Approach for Fast Two-Dimensional Spectral Estimation http://dx.doi.org/10.1109/TSP.2014.2320460	3220
..... <i>W. Sun, H. C. So, Y. Chen, L.-T. Huang, and L. Huang</i>	
Optimal Energy Allocation for Energy Harvesting Transmitters With Hybrid Energy Storage and Processing Cost http://dx.doi.org/10.1109/TSP.2014.2321733	3232
..... <i>O. Ozel, K. Shahzad, and S. Ulukus</i>	
The Labeled Multi-Bernoulli Filter http://dx.doi.org/10.1109/TSP.2014.2323064	3246
..... <i>S. Reuter, B.-T. Vo, B.-N. Vo, and K. Dietmayer</i>	
Distributed Compressive CSIT Estimation and Feedback for FDD Multi-User Massive MIMO Systems http://dx.doi.org/10.1109/TSP.2014.2324991	3261
..... <i>X. Rao and V. K. N. Lau</i>	
An Adaptive Approach to Learn Overcomplete Dictionaries With Efficient Numbers of Elements http://dx.doi.org/10.1109/TSP.2014.2324994	3272
..... <i>M. Marsousi, K. Abhari, P. Babyn, and J. Alirezaie</i>	
<hr/>	
EDICS—Editors' Information Classification Scheme http://dx.doi.org/10.1109/TSP.2014.2326451	3284
Information for Authors http://dx.doi.org/10.1109/TSP.2014.2326452	3286

IEEE TRANSACTIONS ON SIGNAL PROCESSING

A PUBLICATION OF THE IEEE SIGNAL PROCESSING SOCIETY



www.signalprocessingsociety.org

Indexed in PubMed® and MEDLINE®, products of the United States National Library of Medicine



JUNE 15, 2014

VOLUME 62

NUMBER 12

ITPRED

(ISSN 1053-587X)

REGULAR PAPERS

<i>Design and Implementation of Signal Processing Systems</i>	
An Efficient Partial-Sum Network Architecture for Semi-Parallel Polar Codes Decoder Implementation http://dx.doi.org/10.1109/TSP.2014.2319773	<i>Y. Fan and C.-Y. Tsui</i> 3165
<i>Digital and Multirate Signal Processing</i>	
Direct Construction of Supercorrelations http://dx.doi.org/10.1109/TSP.2014.2321119	<i>D. G. Lee and P. J. S. G. Ferreira</i> 3125
<i>Machine Learning</i>	
An Adaptive Approach to Learn Overcomplete Dictionaries With Efficient Numbers of Elements http://dx.doi.org/10.1109/TSP.2014.2324994	<i>M. Marsousi, K. Abhari, P. Babyn, and J. Alirezaie</i> 3272
<i>Signal Processing for Networks</i>	
Consensus-based Distributed Particle Filtering With Distributed Proposal Adaptation http://dx.doi.org/10.1109/TSP.2014.2319777	<i>O. Hlinka, F. Hlawatsch, and P. M. Djurić</i> 3029
Distributed Detection in Tree Topologies With Byzantines http://dx.doi.org/10.1109/TSP.2014.2321735	<i>B. Kailkhura, S. Brahma, Y. S. Han, and P. K. Varshney</i> 3208
Distributed State Estimation With Dimension Reduction Preprocessing http://dx.doi.org/10.1109/TSP.2014.2323021	<i>H. Ma, Y.-H. Yang, Y. Chen, K. J. R. Liu, and Q. Wang</i> 3098
Collective Ratings for Online Communities With Strategic Users http://dx.doi.org/10.1109/TSP.2014.2320457	<i>Y. Zhang and M. van der Schaar</i> 3069

IEEE TRANSACTIONS ON SIGNAL PROCESSING (ISSN 1053-587X) is published semimonthly by the Institute of Electrical and Electronics Engineers, Inc. Responsibility for the contents rests upon the authors and not upon the IEEE, the Society/Council, or its members. **IEEE Corporate Office:** 3 Park Avenue, 17th Floor, New York, NY 10016-5997. **IEEE Operations Center:** 445 Hoes Lane, Piscataway, NJ 08854-4141. **NJ Telephone:** +1 732 981 0060. **Price/Publication Information:** Individual copies: IEEE Members \$20.00 (first copy only), nonmembers \$569.00 per copy. (Note: Postage and handling charge not included.) Member and nonmember subscription prices available upon request. **Copyright and Reprint Permissions:** Abstracting is permitted with credit to the source. Libraries are permitted to photocopy for private use of patrons, provided the per-copy fee of \$31.00 is paid through the Copyright Clearance Center, 222 Rosewood Drive, Danvers, MA 01923. For all other copying, reprint, or republication permission, write to Copyrights and Permissions Department, IEEE Publications Administration, 445 Hoes Lane, Piscataway, NJ 08854-4141. Copyright © 2014 by the Institute of Electrical and Electronics Engineers, Inc. All rights reserved. Periodicals Postage Paid at New York, NY and at additional mailing offices. **Postmaster:** Send address changes to IEEE TRANSACTIONS ON SIGNAL PROCESSING, IEEE, 445 Hoes Lane, Piscataway, NJ 08854-4141. GST Registration No. 125634188. CPC Sales Agreement #40013087. Return undeliverable Canada addresses to: Pitney Bowes IMEX, P.O. Box 4332, Stanton Rd., Toronto, ON M5W 3J4, Canada. IEEE prohibits discrimination, harassment and bullying. For more information visit <http://www.ieee.org/nondiscrimination>. Printed in U.S.A.



<i>Other Areas and Applications</i>	
Discrete Signal Processing on Graphs: Frequency Analysis http://dx.doi.org/10.1109/TSP.2014.2321121	3042
<i>A. Sandryhaila and J. M. F. Moura</i>	
<i>Radar and Sonar Signal Processing</i>	
Radar Target Profiling and Recognition Based on TSI-Optimized Compressive Sensing Kernel http://dx.doi.org/10.1109/TSP.2014.2320460	3194
<i>Y. Gu, N. A. Goodman, and A. Ashok</i>	
<i>Sensor Array and Multichannel Processing</i>	
Approximate Subspace-Based Iterative Adaptive Approach for Fast Two-Dimensional Spectral Estimation http://dx.doi.org/10.1109/TSP.2014.2320460	3220
<i>W. Sun, H. C. So, Y. Chen, L.-T. Huang, and L. Huang</i>	
<i>Signal Processing for Sensor Networks</i>	
SUMIS: Near-Optimal Soft-In Soft-Out MIMO Detection With Low and Fixed Complexity http://dx.doi.org/10.1109/TSP.2014.2303945 ..	3084
<i>M. Čirkić and E. G. Larsson</i>	
Optimal Periodic Sensor Scheduling in Networks of Dynamical Systems http://dx.doi.org/10.1109/TSP.2014.2320455	3055
<i>S. Liu, M. Fardad, P. K. Varshney, and E. Masazade</i>	
<i>Signal Processing for Communications</i>	
Optimal Energy Allocation for Energy Harvesting Transmitters With Hybrid Energy Storage and Processing Cost http://dx.doi.org/10.1109/TSP.2014.2321733	3232
<i>O. Ozel, K. Shahzad, and S. Ulukus</i>	
Data-Aided Channel Estimation in Large Antenna Systems http://dx.doi.org/10.1109/TSP.2014.2321120	3111
<i>J. Ma and L. Ping</i>	
Distributed Compressive CSIT Estimation and Feedback for FDD Multi-User Massive MIMO Systems http://dx.doi.org/10.1109/TSP.2014.2324991	3261
<i>X. Rao and V. K. N. Lau</i>	
On Optimal Gaussian Signaling in MIMO Relay Channels With Partial Decode-and-Forward http://dx.doi.org/10.1109/TSP.2014.2321737 ..	3153
<i>C. Hellings, L. Gerdes, L. Weiland, and W. Utschick</i>	
<i>Statistical Signal Processing</i>	
Fixed-Lag Smoothing for Bayes Optimal Knowledge Exploitation in Target Tracking http://dx.doi.org/10.1109/TSP.2014.2321731	3143
<i>F. Papi, M. Bocquel, M. Podt, and Y. Boers</i>	
Sequential Distributed Detection in Energy-Constrained Wireless Sensor Networks http://dx.doi.org/10.1109/TSP.2014.2320458	3180
<i>Y. Yilmaz and X. Wang</i>	
The Labeled Multi-Bernoulli Filter http://dx.doi.org/10.1109/TSP.2014.2323064	3246
<i>S. Reuter, B.-T. Vo, B.-N. Vo, and K. Dietmayer</i>	
Geolocation by Direction of Arrival Using Arrays With Unknown Orientation http://dx.doi.org/10.1109/TSP.2014.2321109	3135
<i>O. Jean and A. J. Weiss</i>	
<hr/>	
EDICS—Editors' Information Classification Scheme http://dx.doi.org/10.1109/TSP.2014.2326451	3284
Information for Authors http://dx.doi.org/10.1109/TSP.2014.2326452	3285
<hr/>	

IEEE/ACM TRANSACTIONS ON AUDIO, SPEECH, AND LANGUAGE PROCESSING

A PUBLICATION OF THE IEEE SIGNAL PROCESSING SOCIETY



Association for
Computing Machinery

www.signalprocessingsociety.org

Indexed in PubMed® and MEDLINE®, products of the United States National Library of Medicine



MAY 2014

VOLUME 22

NUMBER 5

ITASFA

(ISSN 2329-9290)

REGULAR PAPERS

- Discriminatively Trained Sparse Inverse Covariance Matrices for Speech Recognition <http://dx.doi.org/10.1109/TASLP.2014.2312548> *W. Zhang and P. Fung* 873
- Spoken Knowledge Organization by Semantic Structuring and a Prototype Course Lecture System for Personalized Learning <http://dx.doi.org/10.1109/TASLP.2014.2310993> *H.-y. Lee, S.-R. Shiang, C.-f. Yeh, Y.-N. Chen, Y. Huang, S.-Y. Kong, and L.-s. Lee* 883
- Speech Enhancement with EMD and Hurst-Based Mode Selection <http://dx.doi.org/10.1109/TASLP.2014.2312541> *L. Zǎo, R. Coelho, and P. Flandrin* 899

IEEE TRANSACTIONS ON AUDIO, SPEECH, AND LANGUAGE PROCESSING (ISSN 2329-9290) is published bimonthly in print and monthly online by the Institute of Electrical and Electronics Engineers, Inc. Responsibility for the contents rests upon the authors and not upon the IEEE, the Society/Council, or its members. **IEEE Corporate Office:** 3 Park Avenue, 17th Floor, New York, NY 10016-5997. **IEEE Operations Center:** 445 Hoes Lane, Piscataway, NJ 08854-4141. **NJ Telephone:** +1 732 981 0060. **Price/Publication Information:** Individual copies: IEEE Members \$20.00 (first copy only), nonmembers \$307.00 per copy. (Note: Postage and handling charge not included.) Member and nonmember subscription prices available upon request. **Copyright and Reprint Permissions:** Abstracting is permitted with credit to the source. Libraries are permitted to photocopy for private use of patrons, provided the per-copy fee of \$31.00 is paid through the Copyright Clearance Center, 222 Rosewood Drive, Danvers, MA 01923. For all other copying, reprint, or republication permission, write to Copyrights and Permissions Department, IEEE Publications Administration, 445 Hoes Lane, Piscataway, NJ 08854-4141. Copyright © 2014 by the Institute of Electrical and Electronics Engineers, Inc. All rights reserved. Periodicals Postage Paid at New York, NY and at additional mailing offices. **Postmaster:** Send address changes to IEEE TRANSACTIONS ON AUDIO, SPEECH, AND LANGUAGE PROCESSING, IEEE, 445 Hoes Lane, Piscataway, NJ 08854-4141. GST Registration No. 125634188. CPC Sales Agreement #40013087. Return undeliverable Canada addresses to: Pitney Bowes IMEX, P.O. Box 4332, Stanton Rd., Toronto, ON M5W 3J4, Canada. IEEE prohibits discrimination, harassment and bullying. For more information visit <http://www.ieee.org/nondiscrimination>. Printed in U.S.A.



Stable 1-Norm Error Minimization Based Linear Predictors for Speech Modeling http://dx.doi.org/10.1109/TASLP.2014.2311324	912
..... <i>D. Giacobello, Christensen, T. L. Jensen, M. N. Murthi, S. H. Jensen, and M. Moonen</i>	
Multichannel Noise Reduction in the Karhunen-Loève Expansion Domain http://dx.doi.org/10.1109/TASLP.2014.2311299	923
..... <i>Y. Lacouture-Parodi, E. A. P. Habets, J. Chen, and J. Benesty</i>	
Blind Spectral Weighting for Robust Speaker Identification under Reverberation Mismatch http://dx.doi.org/10.1109/TASLP.2014.2311329 ..	937
..... <i>S. O. Sadjadi and J. H. Hansen</i>	
Query-by-Example Spoken Term Detection using Frequency Domain Linear Prediction and Non-Segmental Dynamic Time Warping http://dx.doi.org/10.1109/TASLP.2014.2311322	946
..... <i>G. Mantena, S. Achanta, and K. Prahallad</i>	
On Over-Determined Frequency Domain BSS http://dx.doi.org/10.1109/TASLP.2014.2307166	956
..... <i>C. Osterwise and S. L. Grant</i>	
Noise Reduction in the Spherical Harmonic Domain Using a Tradeoff Beamformer and Narrowband DOA Estimates http://dx.doi.org/10.1109/TASLP.2014.2311925	967
..... <i>D. P. Jarrett, M. Taseska, E. A. P. Habets, and P. A. Naylor</i>	
Natural Language Generation as Incremental Planning Under Uncertainty: Adaptive Information Presentation for Statistical Dialogue Systems http://dx.doi.org/10.1109/TASLP.2014.2315271	979
..... <i>V. Rieser, O. Lemon, and S. Keizer</i>	

CORRESPONDENCE

Comments on “Complete Parallel Narrowband Active Noise Control Systems” http://dx.doi.org/10.1109/TASLP.2014.2311319	995
..... <i>J. Cheer and S. J. Elliott</i>	

IEEE/ACM TRANSACTIONS ON AUDIO, SPEECH, AND LANGUAGE PROCESSING

A PUBLICATION OF THE IEEE SIGNAL PROCESSING SOCIETY



www.signalprocessingsociety.org

Indexed in PubMed® and MEDLINE®, products of the United States National Library of Medicine



MAY 2014

VOLUME 22

NUMBER 5

ITASFA

(ISSN 2329-9290)

REGULAR PAPERS

Audio Source Separation and Enhancement

On Over-Determined Frequency Domain BSS http://dx.doi.org/10.1109/TASLP.2014.2307166	<i>C. Osterwise and S. L. Grant</i>	956
Noise Reduction in the Spherical Harmonic Domain Using a Tradeoff Beamformer and Narrowband DOA Estimates http://dx.doi.org/10.1109/TASLP.2014.2311925	<i>D. P. Jarrett, M. Taseska, E. A. P. Habets, and P. A. Naylor</i>	967

IEEE TRANSACTIONS ON AUDIO, SPEECH, AND LANGUAGE PROCESSING (ISSN 2329-9290) is published bimonthly in print and monthly online by the Institute of Electrical and Electronics Engineers, Inc. Responsibility for the contents rests upon the authors and not upon the IEEE, the Society/Council, or its members. **IEEE Corporate Office:** 3 Park Avenue, 17th Floor, New York, NY 10016-5997. **IEEE Operations Center:** 445 Hoes Lane, Piscataway, NJ 08854-4141. **NJ Telephone:** +1 732 981 0060. **Price/Publication Information:** Individual copies: IEEE Members \$20.00 (first copy only), nonmembers \$307.00 per copy. (Note: Postage and handling charge not included.) Member and nonmember subscription prices available upon request. **Copyright and Reprint Permissions:** Abstracting is permitted with credit to the source. Libraries are permitted to photocopy for private use of patrons, provided the per-copy fee of \$31.00 is paid through the Copyright Clearance Center, 222 Rosewood Drive, Danvers, MA 01923. For all other copying, reprint, or republication permission, write to Copyrights and Permissions Department, IEEE Publications Administration, 445 Hoes Lane, Piscataway, NJ 08854-4141. Copyright © 2014 by the Institute of Electrical and Electronics Engineers, Inc. All rights reserved. Periodicals Postage Paid at New York, NY and at additional mailing offices. **Postmaster:** Send address changes to IEEE TRANSACTIONS ON AUDIO, SPEECH, AND LANGUAGE PROCESSING, IEEE, 445 Hoes Lane, Piscataway, NJ 08854-4141. GST Registration No. 125634188. CPC Sales Agreement #40013087. Return undeliverable Canada addresses to: Pitney Bowes IMEX, P.O. Box 4332, Stanton Rd., Toronto, ON M5W 3J4, Canada. IEEE prohibits discrimination, harassment and bullying. For more information visit <http://www.ieee.org/nondiscrimination>. Printed in U.S.A.



Speech Analysis

Stable 1-Norm Error Minimization Based Linear Predictors for Speech Modeling <http://dx.doi.org/10.1109/TASLP.2014.2311324>
 *D. Giacobello, Christensen, T. L. Jensen, M. N. Murthi, S. H. Jensen, and M. Moonen* 912

Speech Enhancement

Multichannel Noise Reduction in the Karhunen-Loève Expansion Domain <http://dx.doi.org/10.1109/TASLP.2014.2311299>
 *Y. Lacouture-Parodi, E. A. P. Habets, J. Chen, and J. Benesty* 923

Speech Enhancement with EMD and Hurst-Based Mode Selection <http://dx.doi.org/10.1109/TASLP.2014.2312541>
 *L. Zǎo, R. Coelho, and P. Flandrin* 899

Acoustic Modeling for Automatic Speech Recognition

Discriminatively Trained Sparse Inverse Covariance Matrices for Speech Recognition <http://dx.doi.org/10.1109/TASLP.2014.2312548>
 *W. Zhang and P. Fung* 873

Speaker Recognition and Characterization

Blind Spectral Weighting for Robust Speaker Identification under Reverberation Mismatch <http://dx.doi.org/10.1109/TASLP.2014.2311329> ..
 *S. O. Sadjadi and J. H. Hansen* 937

Spoken Language Understanding and Computational Semantics

Spoken Knowledge Organization by Semantic Structuring and a Prototype Course Lecture System for Personalized Learning <http://dx.doi.org/10.1109/TASLP.2014.2310993>
 *H.-y. Lee, S.-R. Shiang, C.-f. Yeh, Y.-N. Chen, Y. Huang, S.-Y. Kong, and L.-s. Lee* 883

Discourse and Dialog

Natural Language Generation as Incremental Planning Under Uncertainty: Adaptive Information Presentation for Statistical Dialogue Systems <http://dx.doi.org/10.1109/TASLP.2014.2315271> *V. Rieser, O. Lemon, and S. Keizer* 979

Speech Data Mining and Document Retrieval

Query-by-Example Spoken Term Detection using Frequency Domain Linear Prediction and Non-Segmental Dynamic Time Warping <http://dx.doi.org/10.1109/TASLP.2014.2311322> *G. Mantena, S. Achanta, and K. Prahallad* 946

 CORRESPONDENCE
Active Noise Control, Echo Reduction and Feedback Reduction

Comments on “Complete Parallel Narrowband Active Noise Control Systems” <http://dx.doi.org/10.1109/TASLP.2014.2311319>
 *J. Cheer and S. J. Elliott* 995

IEEE/ACM TRANSACTIONS ON AUDIO, SPEECH, AND LANGUAGE PROCESSING

A PUBLICATION OF THE IEEE SIGNAL PROCESSING SOCIETY



www.signalprocessingsociety.org

Indexed in PubMed® and MEDLINE®, products of the United States National Library of Medicine



JUNE 2014

VOLUME 22

NUMBER 6

ITASFA

(ISSN 2329-9290)

REGULAR PAPERS

Musical Source Clustering and Identification in Polyphonic Audio http://dx.doi.org/10.1109/TASLP.2014.2313404	<i>V. Arora and L. Behera</i>	1003
Design of Minimax Broadband Beamformers that are Robust to Microphone Gain, Phase, and Position Errors http://dx.doi.org/10.1109/TASLP.2014.2315044	<i>R. C. Nongpiur</i>	1013
Binaural Signal Processing Motivated Generalized Analytic Signal Construction and AM-FM Demodulation http://dx.doi.org/10.1109/TASLP.2014.2316376	<i>A. Venkitaraman and C. S. Seelamantula</i>	1023

IEEE TRANSACTIONS ON AUDIO, SPEECH, AND LANGUAGE PROCESSING (ISSN 2329-9290) is published bimonthly in print and monthly online by the Institute of Electrical and Electronics Engineers, Inc. Responsibility for the contents rests upon the authors and not upon the IEEE, the Society/Council, or its members. **IEEE Corporate Office:** 3 Park Avenue, 17th Floor, New York, NY 10016-5997. **IEEE Operations Center:** 445 Hoes Lane, Piscataway, NJ 08854-4141. **NJ Telephone:** +1 732 981 0060. **Price/Publication Information:** Individual copies: IEEE Members \$20.00 (first copy only), nonmembers \$307.00 per copy. (Note: Postage and handling charge not included.) Member and nonmember subscription prices available upon request. **Copyright and Reprint Permissions:** Abstracting is permitted with credit to the source. Libraries are permitted to photocopy for private use of patrons, provided the per-copy fee of \$31.00 is paid through the Copyright Clearance Center, 222 Rosewood Drive, Danvers, MA 01923. For all other copying, reprint, or republication permission, write to Copyrights and Permissions Department, IEEE Publications Administration, 445 Hoes Lane, Piscataway, NJ 08854-4141. Copyright © 2014 by the Institute of Electrical and Electronics Engineers, Inc. All rights reserved. Periodicals Postage Paid at New York, NY and at additional mailing offices. **Postmaster:** Send address changes to IEEE TRANSACTIONS ON AUDIO, SPEECH, AND LANGUAGE PROCESSING, IEEE, 445 Hoes Lane, Piscataway, NJ 08854-4141. GST Registration No. 125634188. CPC Sales Agreement #40013087. Return undeliverable Canada addresses to: Pitney Bowes IMEX, P.O. Box 4332, Stanton Rd., Toronto, ON M5W 3J4, Canada. IEEE prohibits discrimination, harassment and bullying. For more information visit <http://www.ieee.org/nondiscrimination>. Printed in U.S.A.

Memory-Enhanced Neural Networks and NMF for Robust ASR http://dx.doi.org/10.1109/TASLP.2014.2318514	1037
..... <i>J. T. Geiger, F. Weninger, J. F. Gemmeke, M. Wöllmer, B. Schuller, and G. Rigoll</i>	
Memory Proportionate APA with Individual Activation Factors for Acoustic Echo Cancellation http://dx.doi.org/10.1109/TASLP.2014.2318519	1047
..... <i>H. Zhao, Y. Yu, S. Gao, X. Zeng, and Z. He</i>	
Multiview Supervised Dictionary Learning in Speech Emotion Recognition http://dx.doi.org/10.1109/TASLP.2014.2319157	1056
..... <i>M. J. Gangeh, P. Fewzee, A. Ghodsi, M. S. Kamel, and F. Karray</i>	
Dual-Microphone Voice Activity Detection Technique Based on Two-Step Power Level Difference Ratio http://dx.doi.org/10.1109/TASLP.2014.2313917	1069
..... <i>J.-H. Choi and J.-H. Chang</i>	
A Geometric Approach to Sound Source Localization from Time-Delay Estimates http://dx.doi.org/10.1109/TASLP.2014.2317989	1082
..... <i>X. Alameda-Pineda and R. Horaud</i>	
Minimum Mutual Information-Based Linearly Constrained Broadband Signal Extraction http://dx.doi.org/10.1109/TASLP.2014.2319155	1096
..... <i>K. Reindl, S. Meier, H. Barfuss, and W. Kellermann</i>	
<hr/>	
EDICS—Editor’s Information and Classification Scheme http://dx.doi.org/10.1109/TASLP.2014.2325655	1109
Information for Authors http://dx.doi.org/10.1109/TASLP.2014.2325656	1111

CALL FOR PAPERS

IEEE/ACM Transactions on Audio, Speech and Language Processing - Special issue on continuous-space and related methods in natural language processing

Natural Language Processing (NLP) aims to analyze, understand, and generate languages that humans use naturally. Significant progress in NLP has been achieved in recent years, addressing important and practical real-world problems, enabling mass deployment of large-scale systems. New machine learning paradigms such as deep learning and continuous space methods have contributed to inferring language patterns from increasingly large real-world data and to making predictions about new data more accurate.

One of the challenges in NLP is to represent language in a form that can be processed effectively by computing algorithms. Words in sequence are traditionally treated as discrete symbols, which has its advantages and limitations. The research on continuous space methods provides a promising alternative that describes words and their semantic and syntactic relationships in a different way. In continuous space language modeling, we represent words with real-valued vectors. In this way, conditional probability distributions of words can be learned and expressed as smooth functions of these vectors; similar words are therefore described as neighbors in a continuous space. A Neural Network Language Model is a typical example of such continuous space methods.

Building on the success of acoustic and statistical language modeling, research on artificial (deep) neural networks and continuous space models in general has seen significant progress in mitigating data sparseness, incorporating longer contexts, and modeling morphological, syntactic and semantic relationships across words. As a result, continuous space models are now embedded in many state-of-the-art speech recognition and machine translation systems. This special issue provides a forum to discuss the latest findings on research problems related to the application of continuous space and related models in NLP. We invite papers on various NLP topics, including but not limited to

- * Automatic speech recognition
- * Speaker recognition
- * Language modeling
- * Machine translation
- * Spoken language understanding
- * Spoken document retrieval
- * Text mining
- * Computational semantics
- * Morphological analysis
- * Syntactic parsing
- * Discourse and dialogue
- * Machine learning methods

The authors are required to follow the Author's Guide for manuscript submission to the IEEE /ACM Transactions on Audio, Speech, and Language Processing at

<http://www.signalprocessingsociety.org/publications/periodicals/taslp/taslp-author-information>

- * Submission deadline: Jul. 15, 2014
- * Notification of first round review: Oct. 1, 2014
- * Notification of acceptance: Dec. 1, 2014
- * Final manuscripts due: Dec. 15, 2015

For further information, please contact the guest editors,

- * Haizhou Li, Institute for Infocomm Research, Singapore
- * Marcello Federico, FBK, Italy
- * Xiaodong He, Microsoft Research, USA
- * Helen Meng, The Chinese University of Hong Kong, China
- * Isabel Trancoso, INESC-ID and Instituto Superior Técnico, University of Lisbon, Portugal

IEEE TRANSACTIONS ON IMAGE PROCESSING

A PUBLICATION OF THE IEEE SIGNAL PROCESSING SOCIETY



www.signalprocessingsociety.org

Indexed in PubMed® and MEDLINE®, products of the United States National Library of Medicine



MAY 2014

VOLUME 23

NUMBER 5

IPRE4

(ISSN 1057-7149)

PAPERS

Saliency Tree: A Novel Saliency Detection Framework http://dx.doi.org/10.1109/TIP.2014.2307434	<i>Z. Liu, W. Zou, and O. L. Meur</i>	1937
LBP-Based Edge-Texture Features for Object Recognition http://dx.doi.org/10.1109/TIP.2014.2310123	<i>A. Satpathy, X. Jiang, and H.-L. Eng</i>	1953
Fast Space-Varying Convolution Using Matrix Source Coding With Applications to Camera Stray Light Reduction http://dx.doi.org/10.1109/TIP.2014.2311657	<i>J. Wei, C. A. Bouman, and J. P. Allebach</i>	1965
Statistical Model of Quantized DCT Coefficients: Application in the Steganalysis of Jsteg Algorithm http://dx.doi.org/10.1109/TIP.2014.2310126	<i>T. H. Thai, R. Cogranne, and F. Retraint</i>	1980
Spatial Pooling of Heterogeneous Features for Image Classification http://dx.doi.org/10.1109/TIP.2014.2310117	<i>L. Xie, Q. Tian, M. Wang, and B. Zhang</i>	1994
Heterogeneous Domain Adaptation and Classification by Exploiting the Correlation Subspace http://dx.doi.org/10.1109/TIP.2014.2310992 ..	<i>Y.-R. Yeh, C.-H. Huang, and Y.-C. F. Wang</i>	2009
Click Prediction for Web Image Reranking Using Multimodal Sparse Coding http://dx.doi.org/10.1109/TIP.2014.2311377	<i>J. Yu, Y. Rui, and D. Tao</i>	2019
Images as Occlusions of Textures: A Framework for Segmentation http://dx.doi.org/10.1109/TIP.2014.2307475	<i>M. T. McCann, D. G. Mixon, M. C. Fickus, C. A. Castro, J. A. Ozolek, and J. Kovačević</i>	2033
Cross-Indexing of Binary SIFT Codes for Large-Scale Image Search http://dx.doi.org/10.1109/TIP.2014.2312283	<i>Z. Liu, H. Li, L. Zhang, W. Zhou, and Q. Tian</i>	2047
Image-Difference Prediction: From Color to Spectral http://dx.doi.org/10.1109/TIP.2014.2311373	<i>S. L. Moan and P. Urban</i>	2058
Full-Reference Quality Estimation for Images With Different Spatial Resolutions http://dx.doi.org/10.1109/TIP.2014.2310991	<i>A. M. Demirtas, A. R. Reibman, and H. Jafarkhani</i>	2069
Saliency-Based Selection of Gradient Vector Flow Paths for Content Aware Image Resizing http://dx.doi.org/10.1109/TIP.2014.2312649 ...	<i>S. Battiato, G. M. Farinella, G. Puglisi, and D. Ravi</i>	2081
Single-Image Superresolution of Natural Stochastic Textures Based on Fractional Brownian Motion http://dx.doi.org/10.1109/TIP.2014.2312284	<i>I. Zachevsky and Y. Y. (Josh) Zeevi</i>	2096



Online Global Transfer for Automatic Figure-Ground Segmentation http://dx.doi.org/10.1109/TIP.2014.2312287	W. Zou, C. Bai, K. Kpalma, and J. Ronsin	2109
Learning Joint Intensity-Depth Sparse Representations http://dx.doi.org/10.1109/TIP.2014.2312645	I. Tošić and S. Drewes	2122
A Regularized Approach for Geodesic-Based Semisupervised Multimanifold Learning http://dx.doi.org/10.1109/TIP.2014.2312643	M. Fan, X. Zhang, Z. Lin, Z. Zhang, and H. Bao	2133
Residual Component Analysis of Hyperspectral Images-Application to Joint Nonlinear Unmixing and Nonlinearity Detection http://dx.doi.org/10.1109/TIP.2014.2312616	Y. Altmann, N. Dobigeon, S. McLaughlin, and J.-Y. Tourneret	2148
MsLRR: A Unified Multiscale Low-Rank Representation for Image Segmentation http://dx.doi.org/10.1109/TIP.2014.2297027	X. Liu, Q. Xu, J. Ma, H. Jin, and Y. Zhang	2159
MIMO Radar 3D Imaging Based on Combined Amplitude and Total Variation Cost Function With Sequential Order One Negative Exponential Form http://dx.doi.org/10.1109/TIP.2014.2311735	C. Ma, T. S. Yeo, Y. Zhao, and J. Feng	2168
Persistent Aerial Video Registration and Fast Multi-View Mosaicing http://dx.doi.org/10.1109/TIP.2014.2313183	E. Molina and Z. Zhu	2184
FeatureMatch: A General ANNF Estimation Technique and Its Applications http://dx.doi.org/10.1109/TIP.2014.2309436	S. A. Ramakanth and R. V. Babu	2193
Modeling the Time-Varying Subjective Quality of HTTP Video Streams With Rate Adaptations http://dx.doi.org/10.1109/TIP.2014.2312613	C. Chen, L. K. Choi, G. de Veciana, C. Caramanis, R. W. Heath, and A. C. Bovik	2206
Nonlinear Transform for Robust Dense Block-Based Motion Estimation http://dx.doi.org/10.1109/TIP.2014.2314023	R. Xu, D. Taubman, and A. T. Naman	2222
Actively Learning Human Gaze Shifting Paths for Semantics-Aware Photo Cropping http://dx.doi.org/10.1109/TIP.2014.2311658	L. Zhang, Y. Gao, R. Ji, Y. Xia, Q. Dai, and X. Li	2235
Gaussian Copula Multivariate Modeling for Texture Image Retrieval Using Wavelet Transforms http://dx.doi.org/10.1109/TIP.2014.2313232	N.-E. Lasmar and Y. Berthoumieu	2246
Coding Visual Features Extracted From Video Sequences http://dx.doi.org/10.1109/TIP.2014.2312617	L. Baroffio, M. Cesana, A. Redondi, M. Tagliasacchi, and S. Tubaro	2262
A Fuzzy-Rule-Based Approach for Single Frame Super Resolution http://dx.doi.org/10.1109/TIP.2014.2312289	P. Purkait, N. R. Pal, and B. Chanda	2277
A Probabilistic Graph-Based Framework for Plug-and-Play Multi-Cue Visual Tracking http://dx.doi.org/10.1109/TIP.2014.2312286	S. Feldman-Haber and Y. Keller	2291
Anisotropic Scattered Data Interpolation for Pushbroom Image Rectification http://dx.doi.org/10.1109/TIP.2014.2316377	E. Ringaby, O. Friman, P.-E. Forssén, T. O. Opsahl, T. V. Haavardsholm, and I. Kåsen	2302
Model-Based Edge Detector for Spectral Imagery Using Sparse Spatospectral Masks http://dx.doi.org/10.1109/TIP.2014.2315154	B. S. Paskaleva, S. E. Godoy, W.-Y. Jang, S. C. Bender, S. Krishna, and M. M. Hayat	2315
Discriminability Limits in Spatio-Temporal Stereo Block Matching http://dx.doi.org/10.1109/TIP.2014.2316420	A. K. Jain and T. Q. Nguyen	2328
A Compact Representation for Compressing Converted Stereo Videos http://dx.doi.org/10.1109/TIP.2014.2315958	Z. Zhang, C. Zhou, R. Wang, Y. Wang, and W. Gao	2343
Robust Object Tracking via Sparse Collaborative Appearance Model http://dx.doi.org/10.1109/TIP.2014.2313227	W. Zhong, H. Lu, and M.-H. Yang	2356
Comparison of Image Patches Using Local Moment Invariants http://dx.doi.org/10.1109/TIP.2014.2315923	A. Sit and D. Kihara	2369
Derivative-Based Scale Invariant Image Feature Detector With Error Resilience http://dx.doi.org/10.1109/TIP.2014.2315959	P. Mainali, G. Lafruit, K. Tack, L. V. Gool, and R. Lauwereins	2380
Segmentation-Driven Image Registration-Application to 4D DCE-MRI Recordings of the Moving Kidneys http://dx.doi.org/10.1109/TIP.2014.2315155	E. Hodneland, E. A. Hanson, A. Lundervold, J. Modersitzki, E. Eikefjord, and A. Z. Munthe-Kaas	2392
A Sequential Framework for Image Change Detection http://dx.doi.org/10.1109/TIP.2014.2309432	A. J. Lingg, E. Zelnio, F. Garber, and B. D. Rigling	2405

IEEE TRANSACTIONS ON IMAGE PROCESSING

A PUBLICATION OF THE IEEE SIGNAL PROCESSING SOCIETY



www.signalprocessingsociety.org

Indexed in PubMed® and MEDLINE®, products of the United States National Library of Medicine



MAY 2014

VOLUME 23

NUMBER 5

IIPRE4

(ISSN 1057-7149)

PAPERS

Statistical-Model Based Methods

- Statistical Model of Quantized DCT Coefficients: Application in the Steganalysis of Jsteg Algorithm <http://dx.doi.org/10.1109/TIP.2014.2310126> T. H. Thai, R. Cogranne, and F. Retraint 1980
- A Regularized Approach for Geodesic-Based Semisupervised Multimanifold Learning <http://dx.doi.org/10.1109/TIP.2014.2312643> M. Fan, X. Zhang, Z. Lin, Z. Zhang, and H. Bao 2133
- Gaussian Copula Multivariate Modeling for Texture Image Retrieval Using Wavelet Transforms <http://dx.doi.org/10.1109/TIP.2014.2313232> N.-E. Lasmara and Y. Berthoumieu 2246

Structural-Model Based Methods

- Saliency Tree: A Novel Saliency Detection Framework <http://dx.doi.org/10.1109/TIP.2014.2307434> Z. Liu, W. Zou, and O. L. Meur 1937
- Image and Video Representation*
- LBP-Based Edge-Texture Features for Object Recognition <http://dx.doi.org/10.1109/TIP.2014.2310123> A. Satpathy, X. Jiang, and H.-L. Eng 1953
- Spatial Pooling of Heterogeneous Features for Image Classification <http://dx.doi.org/10.1109/TIP.2014.2310117> L. Xie, Q. Tian, M. Wang, and B. Zhang 1994
- Learning Joint Intensity-Depth Sparse Representations <http://dx.doi.org/10.1109/TIP.2014.2312645> I. Tošić and S. Drewes 2122
- MsLRR: A Unified Multiscale Low-Rank Representation for Image Segmentation <http://dx.doi.org/10.1109/TIP.2014.2297027> X. Liu, Q. Xu, J. Ma, H. Jin, and Y. Zhang 2159
- A Compact Representation for Compressing Converted Stereo Videos <http://dx.doi.org/10.1109/TIP.2014.2315958> Z. Zhang, C. Zhou, R. Wang, Y. Wang, and W. Gao 2343
- Comparison of Image Patches Using Local Moment Invariants <http://dx.doi.org/10.1109/TIP.2014.2315923> A. Sit and D. Kihara 2369

Perception and Quality Models for Images and Video

- Image-Difference Prediction: From Color to Spectral <http://dx.doi.org/10.1109/TIP.2014.2311373> S. L. Moan and P. Urban 2058
- Full-Reference Quality Estimation for Images With Different Spatial Resolutions <http://dx.doi.org/10.1109/TIP.2014.2310991> A. M. Demirtas, A. R. Reibman, and H. Jafarkhani 2069
- Modeling the Time-Varying Subjective Quality of HTTP Video Streams With Rate Adaptations <http://dx.doi.org/10.1109/TIP.2014.2312613> C. Chen, L. K. Choi, G. de Veciana, C. Caramanis, R. W. Heath, and A. C. Bovik 2206
- Actively Learning Human Gaze Shifting Paths for Semantics-Aware Photo Cropping <http://dx.doi.org/10.1109/TIP.2014.2311658> L. Zhang, Y. Gao, R. Ji, Y. Xia, Q. Dai, and X. Li 2235



<i>Restoration and Enhancement</i>	
Fast Space-Varying Convolution Using Matrix Source Coding With Applications to Camera Stray Light Reduction http://dx.doi.org/10.1109/TIP.2014.2311657	J. Wei, C. A. Bouman, and J. P. Allebach 1965
Saliency-Based Selection of Gradient Vector Flow Paths for Content Aware Image Resizing http://dx.doi.org/10.1109/TIP.2014.2312649	S. Battiato, G. M. Farinella, G. Puglisi, and D. Ravi 2081
<i>Interpolation, Super-Resolution, and Mosaicing</i>	
Single-Image Superresolution of Natural Stochastic Textures Based on Fractional Brownian Motion http://dx.doi.org/10.1109/TIP.2014.2312284	I. Zachevsky and Y. Y. (Josh) Zeevi 2096
A Fuzzy-Rule-Based Approach for Single Frame Super Resolution http://dx.doi.org/10.1109/TIP.2014.2312289	P. Purkait, N. R. Pal, and B. Chanda 2277
<i>Image and Video Multimedia Communications</i>	
Nonlinear Transform for Robust Dense Block-Based Motion Estimation http://dx.doi.org/10.1109/TIP.2014.2314023	R. Xu, D. Taubman, and A. T. Naman 2222
<i>Color and Multispectral Imaging</i>	
Anisotropic Scattered Data Interpolation for Pushbroom Image Rectification http://dx.doi.org/10.1109/TIP.2014.2316377	E. Ringaby, O. Friman, P.-E. Forssén, T. O. Opsahl, T. V. Haavardsholm, and I. Kåsen 2302
Derivative-Based Scale Invariant Image Feature Detector With Error Resilience http://dx.doi.org/10.1109/TIP.2014.2315959	P. Mainali, G. Lafruit, K. Tack, L. V. Gool, and R. Lauwereins 2380
<i>Stereoscopic and Multiview Processing and Display</i>	
Persistent Aerial Video Registration and Fast Multi-View Mosaicing http://dx.doi.org/10.1109/TIP.2014.2313183	E. Molina and Z. Zhu 2184
Discriminability Limits in Spatio-Temporal Stereo Block Matching http://dx.doi.org/10.1109/TIP.2014.2316420	A. K. Jain and T. Q. Nguyen 2328
<i>Magnetic Resonance Imaging</i>	
Segmentation-Driven Image Registration-Application to 4D DCE-MRI Recordings of the Moving Kidneys http://dx.doi.org/10.1109/TIP.2014.2315155 ..	E. Hodneland, E. A. Hanson, A. Lundervold, J. Modersitzki, E. Eikefjord, and A. Z. Munthe-Kaas 2392
<i>Radar Imaging, Remote Sensing, and Geophysical Imaging</i>	
Residual Component Analysis of Hyperspectral Images-Application to Joint Nonlinear Unmixing and Nonlinearity Detection http://dx.doi.org/10.1109/TIP.2014.2312616	Y. Altmann, N. Dobigeon, S. McLaughlin, and J.-Y. Tourneret 2148
MIMO Radar 3D Imaging Based on Combined Amplitude and Total Variation Cost Function With Sequential Order One Negative Exponential Form http://dx.doi.org/10.1109/TIP.2014.2311735	C. Ma, T. S. Yeo, Y. Zhao, and J. Feng 2168
Model-Based Edge Detector for Spectral Imagery Using Sparse Spatiospectral Masks http://dx.doi.org/10.1109/TIP.2014.2315154	B. S. Paskaleva, S. E. Godoy, W.-Y. Jang, S. C. Bender, S. Krishna, and M. M. Hayat 2315
A Sequential Framework for Image Change Detection http://dx.doi.org/10.1109/TIP.2014.2309432	A. J. Lingg, E. Zelnio, F. Garber, and B. D. Rigling 2405
<i>Region, Boundary, and Shape Analysis</i>	
Images as Occlusions of Textures: A Framework for Segmentation http://dx.doi.org/10.1109/TIP.2014.2307475	M. T. McCann, D. G. Mixon, M. C. Fickus, C. A. Castro, J. A. Ozolek, and J. Kovačević 2033
Online Glocal Transfer for Automatic Figure-Ground Segmentation http://dx.doi.org/10.1109/TIP.2014.2312287	W. Zou, C. Bai, K. Kpalma, and J. Ronsin 2109
<i>Image and Video Interpretation and Understanding</i>	
Heterogeneous Domain Adaptation and Classification by Exploiting the Correlation Subspace http://dx.doi.org/10.1109/TIP.2014.2310992	Y.-R. Yeh, C.-H. Huang, and Y.-C. F. Wang 2009
A Probabilistic Graph-Based Framework for Plug-and-Play Multi-Cue Visual Tracking http://dx.doi.org/10.1109/TIP.2014.2312286	S. Feldman-Haber and Y. Keller 2291
Robust Object Tracking via Sparse Collaborative Appearance Model http://dx.doi.org/10.1109/TIP.2014.2313227	W. Zhong, H. Lu, and M.-H. Yang 2356
<i>Image and Video Storage and Retrieval</i>	
Click Prediction for Web Image Reranking Using Multimodal Sparse Coding http://dx.doi.org/10.1109/TIP.2014.2311377	J. Yu, Y. Rui, and D. Tao 2019
Cross-Indexing of Binary SIFT Codes for Large-Scale Image Search http://dx.doi.org/10.1109/TIP.2014.2312283	Z. Liu, H. Li, L. Zhang, W. Zhou, and Q. Tian 2047
Coding Visual Features Extracted From Video Sequences http://dx.doi.org/10.1109/TIP.2014.2312617	L. Baroffio, M. Cesana, A. Redondi, M. Tagliasacchi, and S. Tubaro 2262
<i>Image and Video Synthesis, Rendering, and Visualization</i>	
FeatureMatch: A General ANNF Estimation Technique and Its Applications http://dx.doi.org/10.1109/TIP.2014.2309436	S. A. Ramakanth and R. V. Babu 2193

IEEE TRANSACTIONS ON IMAGE PROCESSING

A PUBLICATION OF THE IEEE SIGNAL PROCESSING SOCIETY



www.signalprocessingsociety.org

Indexed in PubMed® and MEDLINE®, products of the United States National Library of Medicine



JUNE 2014

VOLUME 23

NUMBER 6

IIPRE4

(ISSN 1057-7149)

PAPERS

Generalized Higher Degree Total Variation (HDTV) Regularization http://dx.doi.org/10.1109/TIP.2014.2315156	2423
..... <i>Y. Hu, G. Ongie, S. Ramani, and M. Jacob</i>	
Common Feature Discriminant Analysis for Matching Infrared Face Images to Optical Face Images http://dx.doi.org/10.1109/TIP.2014.2315920	2436
..... <i>Z. Li, D. Gong, Y. Qiao, and D. Tao</i>	
A Locally Adaptive System for the Fusion of Objective Quality Measures http://dx.doi.org/10.1109/TIP.2014.2316379	2446
..... <i>A. Barri, A. Dooms, B. Jansen, and P. Schelkens</i>	
Gradient Histogram Estimation and Preservation for Texture Enhanced Image Denoising http://dx.doi.org/10.1109/TIP.2014.2316423	2459
..... <i>W. Zuo, L. Zhang, C. Song, D. Zhang, and H. Gao</i>	
Q-STAR: A Perceptual Video Quality Model Considering Impact of Spatial, Temporal, and Amplitude Resolutions http://dx.doi.org/10.1109/TIP.2014.2303636	2473
..... <i>Y.-F. Ou, Y. Xue, and Y. Wang</i>	
Passive Synthetic Aperture Hitchhiker Imaging of Ground Moving Targets-Part 1: Image Formation and Velocity Estimation http://dx.doi.org/10.1109/TIP.2014.2302682	2487
..... <i>S. Wacks and B. Yazıcı</i>	
Image Reconstruction From Double Random Projection http://dx.doi.org/10.1109/TIP.2014.2316642	2501
..... <i>Q. Zhang and R. J. Plemmons</i>	
Cascade Category-Aware Visual Search http://dx.doi.org/10.1109/TIP.2014.2317986	2514
..... <i>S. Zhang, Q. Tian, Q. Huang, W. Gao, and Y. Rui</i>	
Distributed Dictionary Learning for Sparse Representation in Sensor Networks http://dx.doi.org/10.1109/TIP.2014.2316373	2528
..... <i>J. Liang, M. Zhang, X. Zeng, and G. Yu</i>	
Local Learned Dictionaries Optimized to Edge Orientation for Inverse Halftoning http://dx.doi.org/10.1109/TIP.2014.2319732	2542
..... <i>C.-H. Son and H. Choo</i>	
Combining LBP Difference and Feature Correlation for Texture Description http://dx.doi.org/10.1109/TIP.2014.2316640	2557
..... <i>X. Hong, G. Zhao, M. Pietikäinen, and X. Chen</i>	
A Statistical Prediction Model Based on Sparse Representations for Single Image Super-Resolution http://dx.doi.org/10.1109/TIP.2014.2305844	2569
..... <i>T. Peleg and M. Elad</i>	
Receptive Fields Selection for Binary Feature Description http://dx.doi.org/10.1109/TIP.2014.2317981	2583
..... <i>B. Fan, Q. Kong, T. Trzcinski, Z. Wang, C. Pan, and P. Fua</i>	



A Regularized Model-Based Optimization Framework for Pan-Sharpener	http://dx.doi.org/10.1109/TIP.2014.2316641	<i>H. A. Aly and G. Sharma</i>	2596
Light Illumination and Detection Patterns for Fluorescence Diffuse Optical Tomography Based on Compressive Sensing	http://dx.doi.org/10.1109/TIP.2014.2300756	<i>A. Jin, B. Yazıcı, and V. Ntziachristos</i>	2609
Saliency Detection for Stereoscopic Images	http://dx.doi.org/10.1109/TIP.2014.2305100	<i>Y. Fang, J. Wang, M. Narwaria, P. L. Callet, and W. Lin</i>	2625
On Scanning Linear Barcodes From Out-of-Focus Blurred Images: A Spatial Domain Dynamic Template Matching Approach	http://dx.doi.org/10.1109/TIP.2014.2319579	<i>L. Chen, H. Man, and H. Jia</i>	2637
Mixed Noise Removal by Weighted Encoding With Sparse Nonlocal Regularization	http://dx.doi.org/10.1109/TIP.2014.2317985	<i>J. Jiang, L. Zhang, and J. Yang</i>	2651
Unsupervised Post-Nonlinear Unmixing of Hyperspectral Images Using a Hamiltonian Monte Carlo Algorithm	http://dx.doi.org/10.1109/TIP.2014.2314022	<i>Y. Altmann, N. Dobigeon, and J.-Y. Tourneret</i>	2663
An Iterative Compensation Approach Without Linearization of Projector Responses for Multiple-Projector System	http://dx.doi.org/10.1109/TIP.2014.2317979	<i>I. Miyagawa, Y. Sugaya, H. Arai, and M. Morimoto</i>	2676
High-Dimensional Camera Shake Removal With Given Depth Map	http://dx.doi.org/10.1109/TIP.2014.2320368	<i>T. Yue, J. Suo, and Q. Dai</i>	2688
Heterogeneity Image Patch Index and Its Application to Consumer Video Summarization	http://dx.doi.org/10.1109/TIP.2014.2320814	<i>C. T. Dang and H. Radha</i>	2704
Sparse Spatial Coding: A Novel Approach to Visual Recognition	http://dx.doi.org/10.1109/TIP.2014.2317988	<i>G. L. Oliveira, E. R. Nascimento, A. W. Vieira, and M. F. M. Campos</i>	2719
Weighted KPCA Degree of Homogeneity Amended Nonclassical Receptive Field Inhibition Model for Salient Contour Extraction in Low-Light-Level Image	http://dx.doi.org/10.1109/TIP.2014.2312647	<i>Y. Zhang, J. Han, J. Yue, and L.-F. Bai</i>	2732

TECHNICAL CORRESPONDENCE

Reversible Symmetric Nonexpansive Convolution: An Effective Image Boundary Processing for M-Channel Lifting-Based Linear-Phase Filter Banks	http://dx.doi.org/10.1109/TIP.2014.2312647	<i>T. Suzuki and M. Ikehara</i>	2744
---	---	-------	---------------------------------	------

COMMENTS AND CORRECTIONS

Erratum to “An Unbiased Risk Estimator for Image Denoising in the Presence of Mixed Poisson-Gaussian Noise”	http://dx.doi.org/10.1109/TIP.2014.2320453	<i>Y. Le Montagner, E. D. Angelini, and J.-C. Olivo-Marin</i>	2750
Erratum to “Tree Filtering: Efficient Structure-Preserving Smoothing With a Minimum Spanning Tree”	http://dx.doi.org/10.1109/TIP.2014.2320452	<i>L. Bao, Y. Song, and Q. Yang</i>	2751
EDICS-Editor’s Information Classification Scheme	http://dx.doi.org/10.1109/TIP.2014.2325638		2752
Information for Authors	http://dx.doi.org/10.1109/TIP.2014.2325637		2753

IEEE TRANSACTIONS ON IMAGE PROCESSING

A PUBLICATION OF THE IEEE SIGNAL PROCESSING SOCIETY



www.signalprocessingsociety.org

Indexed in PubMed® and MEDLINE®, products of the United States National Library of Medicine



JUNE 2014

VOLUME 23

NUMBER 6

IIPRE4

(ISSN 1057-7149)

PAPERS

<i>Image and Video Sensing and Acquisition</i>	
Weighted KPCA Degree of Homogeneity Amended Nonclassical Receptive Field Inhibition Model for Salient Contour Extraction in Low-Light-Level Image http://dx.doi.org/10.1109/TIP.2014.2317987	<i>Y. Zhang, J. Han, J. Yue, and L.-F. Bai</i> 2732
<i>Image and Video Representation</i>	
Distributed Dictionary Learning for Sparse Representation in Sensor Networks http://dx.doi.org/10.1109/TIP.2014.2316373	<i>J. Liang, M. Zhang, X. Zeng, and G. Yu</i> 2528
Combining LBP Difference and Feature Correlation for Texture Description http://dx.doi.org/10.1109/TIP.2014.2316640	<i>X. Hong, G. Zhao, M. Pietikäinen, and X. Chen</i> 2557
Receptive Fields Selection for Binary Feature Description http://dx.doi.org/10.1109/TIP.2014.2317981	<i>B. Fan, Q. Kong, T. Trzcinski, Z. Wang, C. Pan, and P. Fua</i> 2583
<i>Perception and Quality Models for Images and Video</i>	
A Locally Adaptive System for the Fusion of Objective Quality Measures http://dx.doi.org/10.1109/TIP.2014.2316379	<i>A. Barri, A. Dooms, B. Jansen, and P. Schelkens</i> 2446
Q-STAR: A Perceptual Video Quality Model Considering Impact of Spatial, Temporal, and Amplitude Resolutions http://dx.doi.org/10.1109/TIP.2014.2303636	<i>Y.-F. Ou, Y. Xue, and Y. Wang</i> 2473
Saliency Detection for Stereoscopic Images http://dx.doi.org/10.1109/TIP.2014.2305100 ...	<i>Y. Fang, J. Wang, M. Narwaria, P. L. Callet, and W. Lin</i> 2625
<i>Restoration and Enhancement</i>	
Gradient Histogram Estimation and Preservation for Texture Enhanced Image Denoising http://dx.doi.org/10.1109/TIP.2014.2316423	<i>W. Zuo, L. Zhang, C. Song, D. Zhang, and H. Gao</i> 2459
Mixed Noise Removal by Weighted Encoding With Sparse Nonlocal Regularization http://dx.doi.org/10.1109/TIP.2014.2317985	<i>J. Jiang, L. Zhang, and J. Yang</i> 2651
High-Dimensional Camera Shake Removal With Given Depth Map http://dx.doi.org/10.1109/TIP.2014.2320368	<i>T. Yue, J. Suo, and Q. Dai</i> 2688
<i>Interpolation, Super-Resolution, and Mosaicing</i>	
A Statistical Prediction Model Based on Sparse Representations for Single Image Super-Resolution http://dx.doi.org/10.1109/TIP.2014.2305844 ...	<i>T. Peleg and M. Elad</i> 2569



<i>Printing and Halftoning</i>	
Local Learned Dictionaries Optimized to Edge Orientation for Inverse Halftoning http://dx.doi.org/10.1109/TIP.2014.2319732	2542
<i>Scanned Document Analysis, Processing, and Coding</i>	
On Scanning Linear Barcodes From Out-of-Focus Blurred Images: A Spatial Domain Dynamic Template Matching Approach http://dx.doi.org/10.1109/TIP.2014.2319579	2637
<i>Stereoscopic and Multiview Processing and Display</i>	
An Iterative Compensation Approach Without Linearization of Projector Responses for Multiple-Projector System http://dx.doi.org/10.1109/TIP.2014.2317979	2676
<i>Tomographic Imaging</i>	
Passive Synthetic Aperture Hitchhiker Imaging of Ground Moving Targets-Part 1: Image Formation and Velocity Estimation http://dx.doi.org/10.1109/TIP.2014.2302682	2487
Light Illumination and Detection Patterns for Fluorescence Diffuse Optical Tomography Based on Compressive Sensing http://dx.doi.org/10.1109/TIP.2014.2300756	2609
<i>Magnetic Resonance Imaging</i>	
Generalized Higher Degree Total Variation (HDTV) Regularization http://dx.doi.org/10.1109/TIP.2014.2315156	2423
<i>Radar Imaging, Remote Sensing, and Geophysical Imaging</i>	
Image Reconstruction From Double Random Projection http://dx.doi.org/10.1109/TIP.2014.2316642	2501
A Regularized Model-Based Optimization Framework for Pan-Sharpness http://dx.doi.org/10.1109/TIP.2014.2316641	2596
Unsupervised Post-Nonlinear Unmixing of Hyperspectral Images Using a Hamiltonian Monte Carlo Algorithm http://dx.doi.org/10.1109/TIP.2014.2314022	2663
<i>Image and Video Interpretation and Understanding</i>	
Heterogeneity Image Patch Index and Its Application to Consumer Video Summarization http://dx.doi.org/10.1109/TIP.2014.2320814	2704
Sparse Spatial Coding: A Novel Approach to Visual Recognition http://dx.doi.org/10.1109/TIP.2014.2317988	2719
<i>Image and Video Biometric Analysis</i>	
Common Feature Discriminant Analysis for Matching Infrared Face Images to Optical Face Images http://dx.doi.org/10.1109/TIP.2014.2315920 ..	2436
<i>Image and Video Storage and Retrieval</i>	
Cascade Category-Aware Visual Search http://dx.doi.org/10.1109/TIP.2014.2317986	2514
<hr/>	
TECHNICAL CORRESPONDENCE	
<i>Lossy Coding of Images and Video</i>	
Reversible Symmetric Nonexpansive Convolution: An Effective Image Boundary Processing for M-Channel Lifting-Based Linear-Phase Filter Banks http://dx.doi.org/10.1109/TIP.2014.2312647	2744
<hr/>	
COMMENTS AND CORRECTIONS	
Erratum to "An Unbiased Risk Estimator for Image Denoising in the Presence of Mixed Poisson-Gaussian Noise" http://dx.doi.org/10.1109/TIP.2014.2320453	2750
Erratum to "Tree Filtering: Efficient Structure-Preserving Smoothing With a Minimum Spanning Tree" http://dx.doi.org/10.1109/TIP.2014.2320452	2751
EDICS-Editor's Information Classification Scheme http://dx.doi.org/10.1109/TIP.2014.2325638	2752
Information for Authors http://dx.doi.org/10.1109/TIP.2014.2325637	2753

IEEE TRANSACTIONS ON INFORMATION FORENSICS AND SECURITY

A PUBLICATION OF THE IEEE SIGNAL PROCESSING SOCIETY



www.signalprocessingsociety.org

MAY 2014

VOLUME 9

NUMBER 5

ITIFA6

(ISSN 1556-6013)

OVERVIEW ARTICLE

Brain Waves for Automatic Biometric-Based User Recognition <http://dx.doi.org/10.1109/TIFS.2014.2308640> *P. Campisi and D. La Rocca* 782

REGULAR PAPERS

Video Steganalysis Against Motion Vector-Based Steganography by Adding or Subtracting One Motion Vector Value
<http://dx.doi.org/10.1109/TIFS.2014.2308633> *K. Wang, H. Zhao, and H. Wang* 741

Effect of Image Downsampling on Steganographic Security <http://dx.doi.org/10.1109/TIFS.2014.2309054> *J. Kodovský and J. Fridrich* 752

CP-ABE With Constant-Size Keys for Lightweight Devices <http://dx.doi.org/10.1109/TIFS.2014.2309858>
..... *F. Guo, Y. Mu, W. Susilo, D. S. Wong, and V. Varadharajan* 763

Defense Against Primary User Emulation Attacks in Cognitive Radio Networks Using Advanced Encryption Standard
<http://dx.doi.org/10.1109/TIFS.2014.2310355> *A. Alahmadi, M. Abdelhakim, J. Ren, and T. Li* 772

Secure Transmission Using MIMO Precoding <http://dx.doi.org/10.1109/TIFS.2014.2309211> *C.-H. Lin, S.-H. Tsai, and Y.-P. Lin* 801

Uniform Embedding for Efficient JPEG Steganography <http://dx.doi.org/10.1109/TIFS.2014.2312817> *L. Guo, J. Ni, and Y. Q. Shi* 814

3D Assisted Face Recognition: Dealing With Expression Variations <http://dx.doi.org/10.1109/TIFS.2014.2309851>
..... *N. Erdogmus and J.-L. Dugelay* 826

Amplify-and-Forward Compressed Sensing as a Physical-Layer Secrecy Solution in Wireless Sensor Networks
<http://dx.doi.org/10.1109/TIFS.2014.2309855> *J. E. Barceló-Lladó, A. Morell, and G. Seco-Granados* 839

Unraveling the Effect of Textured Contact Lenses on Iris Recognition <http://dx.doi.org/10.1109/TIFS.2014.2313025>
..... *D. Yadav, N. Kohli, J. S. Doyle, Jr., R. Singh, M. Vatsa, and K. W. Bowyer* 851

Adaptively Splitted GMM With Feedback Improvement for the Task of Background Subtraction
<http://dx.doi.org/10.1109/TIFS.2014.2313919> *R. H. Evangelio, M. Pätzold, I. Keller, and T. Sikora* 863

The Spammed Code Offset Method <http://dx.doi.org/10.1109/TIFS.2014.2312851> *B. Škorić and N. de Vreede* 875



IEEE TRANSACTIONS ON INFORMATION FORENSICS AND SECURITY

A PUBLICATION OF THE IEEE SIGNAL PROCESSING SOCIETY



www.signalprocessingsociety.org

MAY 2014

VOLUME 9

NUMBER 5

ITIFA6

(ISSN 1556-6013)

OVERVIEW ARTICLE

Brain Waves for Automatic Biometric-Based User Recognition <http://dx.doi.org/10.1109/TIFS.2014.2308640> *P. Campisi and D. La Rocca* 782

REGULAR PAPERS

- Anonymization and Data Privacy*
- The Spammed Code Offset Method <http://dx.doi.org/10.1109/TIFS.2014.2312851> *B. Škorić and N. de Vreede* 875
- Applied Cryptography*
- CP-ABE With Constant-Size Keys for Lightweight Devices <http://dx.doi.org/10.1109/TIFS.2014.2309858> *F. Guo, Y. Mu, W. Susilo, D. S. Wong, and V. Varadharajan* 763
- Biometrics*
- 3D Assisted Face Recognition: Dealing With Expression Variations <http://dx.doi.org/10.1109/TIFS.2014.2309851> *N. Erdogmus and J.-L. Dugelay* 826
- Unraveling the Effect of Textured Contact Lenses on Iris Recognition <http://dx.doi.org/10.1109/TIFS.2014.2313025> *D. Yadav, N. Kohli, J. S. Doyle, Jr., R. Singh, M. Vatsa, and K. W. Bowyer* 851
- Communication and Physical-Layer Security*
- Secure Transmission Using MIMO Precoding <http://dx.doi.org/10.1109/TIFS.2014.2309211> *C.-H. Lin, S.-H. Tsai, and Y.-P. Lin* 801
- Amplify-and-Forward Compressed Sensing as a Physical-Layer Secrecy Solution in Wireless Sensor Networks <http://dx.doi.org/10.1109/TIFS.2014.2309855> *J. E. Barceló-Lladó, A. Morell, and G. Seco-Granados* 839
- Network Security*
- Defense Against Primary User Emulation Attacks in Cognitive Radio Networks Using Advanced Encryption Standard <http://dx.doi.org/10.1109/TIFS.2014.2310355> *A. Alahmadi, M. Abdelhakim, J. Ren, and T. Li* 772



Steganography and Covert Communications

Video Steganalysis Against Motion Vector-Based Steganography by Adding or Subtracting One Motion Vector Value http://dx.doi.org/10.1109/TIFS.2014.2308633	<i>K. Wang, H. Zhao, and H. Wang</i>	741
Effect of Image Downsampling on Steganographic Security http://dx.doi.org/10.1109/TIFS.2014.2309054	<i>J. Kodovský and J. Fridrich</i>	752
Uniform Embedding for Efficient JPEG Steganography http://dx.doi.org/10.1109/TIFS.2014.2312817	<i>L. Guo, J. Ni, and Y. Q. Shi</i>	814

Surveillance

Adaptively Splitted GMM With Feedback Improvement for the Task of Background Subtraction http://dx.doi.org/10.1109/TIFS.2014.2313919	<i>R. H. Evangelio, M. Pätzold, I. Keller, and T. Sikora</i>	863
---	--	-----

IEEE TRANSACTIONS ON INFORMATION FORENSICS AND SECURITY

A PUBLICATION OF THE IEEE SIGNAL PROCESSING SOCIETY



www.signalprocessingsociety.org

JUNE 2014

VOLUME 9

NUMBER 6

ITIFA6

(ISSN 1556-6013)

PAPERS

Captcha as Graphical Passwords—A New Security Primitive Based on Hard AI Problems http://dx.doi.org/10.1109/TIFS.2014.2312547	<i>B. B. Zhu, J. Yan, G. Bao, M. Yang, and N. Xu</i>	891
Active Content Fingerprinting http://dx.doi.org/10.1109/TIFS.2014.2315531	<i>F. Farhadzadeh and S. Voloshynovskiy</i>	905
Exploiting Process Variations and Programming Sensitivity of Phase Change Memory for Reconfigurable Physical Unclonable Functions http://dx.doi.org/10.1109/TIFS.2014.2315743	<i>L. Zhang, Z. H. Kong, C.-H. Chang, A. Cabrini, and G. Torelli</i>	921
Online Signature Verification on Mobile Devices http://dx.doi.org/10.1109/TIFS.2014.2316472	<i>N. Sae-Bae and N. Memon</i>	933
A New Sketch Method for Measuring Host Connection Degree Distribution http://dx.doi.org/10.1109/TIFS.2014.2312544	<i>P. Wang, X. Guan, J. Zhao, J. Tao, and T. Qin</i>	948
A Robust Grouping Proof Protocol for RFID EPC C1G2 Tags http://dx.doi.org/10.1109/TIFS.2014.2316338	<i>S. Sundaresan, R. Doss, S. Piramuthu, and W. Zhou</i>	961
SybilBelief: A Semi-Supervised Learning Approach for Structure-Based Sybil Detection http://dx.doi.org/10.1109/TIFS.2014.2316975	<i>N. Z. Gong, M. Frank, and P. Mittal</i>	976
Detection of Abnormal Visual Events via Global Optical Flow Orientation Histogram http://dx.doi.org/10.1109/TIFS.2014.2315971	<i>T. Wang and H. Snoussi</i>	988
Exploiting the Incomplete Diffusion Feature: A Specialized Analytical Side-Channel Attack Against the AES and Its Application to Microcontroller Implementations http://dx.doi.org/10.1109/TIFS.2014.2315534	<i>S. Guo, X. Zhao, F. Zhang, T. Wang, Z. Shi, F.-X. Standaert, and C. Ma</i>	999
Thermal Facial Analysis for Deception Detection http://dx.doi.org/10.1109/TIFS.2014.2317309	<i>B. A. Rajoub and R. Zwigelaar</i>	1015
Keyless Authentication in a Noisy Model http://dx.doi.org/10.1109/TIFS.2014.2320634	<i>S. Jiang</i>	1024

EDICS—Editor's Information Classification Scheme http://dx.doi.org/10.1109/TIFS.2014.10.1109/TIFS.2014.2323174	1034
Information for Authors http://dx.doi.org/10.1109/TIFS.2014.2323173	1035

ANNOUNCEMENTS

Call for Papers—IEEE TRANSACTIONS ON INFORMATION FORENSICS AND SECURITY http://dx.doi.org/10.1109/TIFS.2014.2324431	1037
Call for Papers—IEEE JOURNAL OF SELECTED TOPICS IN SIGNAL PROCESSING http://dx.doi.org/10.1109/TIFS.2014.2323156	1038
Call for Papers—IEEE JOURNAL OF SELECTED TOPICS IN SIGNAL PROCESSING http://dx.doi.org/10.1109/TIFS.2014.2323157	1039
IEEE Open Access Publishing http://dx.doi.org/10.1109/TIFS.2014.2323159	1040



IEEE TRANSACTIONS ON INFORMATION FORENSICS AND SECURITY

A PUBLICATION OF THE IEEE SIGNAL PROCESSING SOCIETY



www.signalprocessingsociety.org

JUNE 2014

VOLUME 9

NUMBER 6

ITIFA6

(ISSN 1556-6013)

PAPERS

Applied Cryptography

- Exploiting the Incomplete Diffusion Feature: A Specialized Analytical Side-Channel Attack Against the AES and Its Application to Microcontroller Implementations <http://dx.doi.org/10.1109/TIFS.2014.2315534> *S. Guo, X. Zhao, F. Zhang, T. Wang, Z. Shi, F.-X. Standaert, and C. Ma* 999

Biometrics

- Online Signature Verification on Mobile Devices <http://dx.doi.org/10.1109/TIFS.2014.2316472> *N. Sae-Bae and N. Memon* 933

Forensics Analysis

- Thermal Facial Analysis for Deception Detection <http://dx.doi.org/10.1109/TIFS.2014.2317309> *B. A. Rajoub and R. Zwigelaar* 1015

Hardware Security

- Exploiting Process Variations and Programming Sensitivity of Phase Change Memory for Reconfigurable Physical Unclonable Functions <http://dx.doi.org/10.1109/TIFS.2014.2315743> *L. Zhang, Z. H. Kong, C.-H. Chang, A. Cabrini, and G. Torelli* 921

Information Theoretic Security

- Captcha as Graphical Passwords-A New Security Primitive Based on Hard AI Problems <http://dx.doi.org/10.1109/TIFS.2014.2312547> *B. B. Zhu, J. Yan, G. Bao, M. Yang, and N. Xu* 891
- Keyless Authentication in a Noisy Model <http://dx.doi.org/10.1109/TIFS.2014.2320634> *S. Jiang* 1024
-



<i>Multimedia Content Hash</i>	
Active Content Fingerprinting http://dx.doi.org/10.1109/TIFS.2014.2315531	<i>F. Farhadzadeh and S. Voloshynovskiy</i> 905
<i>Network Security</i>	
A New Sketch Method for Measuring Host Connection Degree Distribution http://dx.doi.org/10.1109/TIFS.2014.2312544	<i>P. Wang, X. Guan, J. Zhao, J. Tao, and T. Qin</i> 948
SybilBelief: A Semi-Supervised Learning Approach for Structure-Based Sybil Detection http://dx.doi.org/10.1109/TIFS.2014.2316975	<i>N. Z. Gong, M. Frank, and P. Mittal</i> 976
<i>Security of Large Networked Systems</i>	
A Robust Grouping Proof Protocol for RFID EPC C1G2 Tags http://dx.doi.org/10.1109/TIFS.2014.2316338	<i>S. Sundaresan, R. Doss, S. Piramuthu, and W. Zhou</i> 961
<i>Surveillance</i>	
Detection of Abnormal Visual Events via Global Optical Flow Orientation Histogram http://dx.doi.org/10.1109/TIFS.2014.2315971	<i>T. Wang and H. Snoussi</i> 988
<hr/>	
EDICS—Editor’s Information Classification Scheme http://dx.doi.org/10.1109/TIFS.2014.2323174	1034
Information for Authors http://dx.doi.org/10.1109/TIFS.2014.2323173	1035
<hr/>	
ANNOUNCEMENTS	
Call for Papers—IEEE TRANSACTIONS ON INFORMATION FORENSICS AND SECURITY http://dx.doi.org/10.1109/TIFS.2014.2324431	1037
Call for Papers—IEEE JOURNAL OF SELECTED TOPICS IN SIGNAL PROCESSING http://dx.doi.org/10.1109/TIFS.2014.2323156	1038
Call for Papers—IEEE JOURNAL OF SELECTED TOPICS IN SIGNAL PROCESSING http://dx.doi.org/10.1109/TIFS.2014.2323157	1039
IEEE Open Access Publishing http://dx.doi.org/10.1109/TIFS.2014.2323159	1040
<hr/>	

CALL FOR PAPERS
IEEE TRANSACTIONS ON INFORMATION FORENSICS AND SECURITY
Special Issue on Biometric Spoofing and Countermeasures

Guest Editors

Nicholas Evans	EURECOM, France (evans@eurecom.fr)
Sébastien Marcel	Idiap Research Institute, Switzerland (marcel@idiap.ch)
Arun Ross	Michigan State University, USA (rossarun@cse.msu.edu)
Stan Z. Li	Chinese Academy of Sciences, China (szli@nlpr.ia.ac.cn)

While biometrics technology has revolutionized approaches to person authentication and has evolved to play a critical role in personal, national and global security, the potential for the technology to be fooled or ‘spoofed’ is widely acknowledged. Efforts to study such threats and to develop countermeasures are now well underway resulting in some promising solutions. While progress with respect to each biometric modality has attained varying degrees of maturity, there are some notable shortcomings in research methodologies. Current spoofing studies focus on specific, known attacks. Existing countermeasures designed to detect and deflect such attacks are often based on unrealistic *a priori* knowledge and typically learned using training data produced using exactly the same spoofing method that is to be detected. Current countermeasures thus have questionable application in practical scenarios where the nature of the attack can never be known. This special issue will focus on the latest research on the topic of biometric spoofing and countermeasures, with a particular emphasis on novel methodologies and generalized spoofing countermeasures that have the potential to protect biometric systems against varying or previously unseen attacks. The aim is to further the state-of-the-art in this field, to stimulate interactions between the biometrics and information forensic communities, to encourage the development of reliable methodologies in spoofing and countermeasure assessment and solutions, and to promote the development of generalized countermeasures. Papers on biometric obfuscation (e.g., fingerprint or face alteration) and relevant countermeasures will also be considered in the special issue. Novel contributions related to both traditional biometric modalities such as face, iris, fingerprint, and voice, and other modalities such as vasculature and electrophysiological signals will be considered. The focus includes, but is not limited to, the following topics related to spoofing and anti-spoofing countermeasures in biometrics:

- vulnerability analysis with an emphasis on previously unconsidered spoofing attacks;
- theoretical models for attack vectors;
- advanced machine learning and pattern recognition algorithms for anti-spoofing;
- information theoretic approaches to quantify spoofing vulnerability;
- spoofing and anti-spoofing in mobile devices;
- generalized countermeasures;
- challenge-response countermeasures;
- sensor-based solutions to spoof attacks;
- biometric obfuscation schemes;
- information forensic approaches to spoofing detection;
- new evaluation protocols, datasets, and performance metrics;
- reproducible research (public databases, open source software and experimental setups).

Submission Procedure: Manuscripts are to be submitted according to the Information for Authors at <http://www.signalprocessingsociety.org/publications/periodicals/forensics/forensics-authors-info/> using the IEEE online manuscript system, Manuscript Central. Papers must not have appeared or be under review elsewhere. Manuscripts by the guest editors submitted to this SI will be handled by the EIC of IEEE-TIFS.

Schedule:

Submission deadline: 1st July 2014
First Review: 15th September 2014
Revisions Due: 1st November 2014
Final Decision: 15th December 2014
Final manuscript due: 15th January 2015
Tentative publication date: 1st April 2015

General Chairs

Vaughan Clarkson
University of Queensland
Jonathan Manton
University of Melbourne

Technical Program Chairs

Doug Cochran
Arizona State University
Doug Gray
University of Adelaide

Finance Chair

Lang White
University of Adelaide

Special Session Chairs

Robert Calderbank
Duke University
Stephen Howard
DSTO

Tutorials Chair

Daniel Palomar
Hong Kong University of S&T

Local Arrangements Chair

Andrew Bradley
University of Queensland

Registration Chair

Paul Teal
Victoria University of Wellington

Publicity Chair

Matt McKay
Hong Kong University of S&T

Publication Chair

Leif Hanlen
NICTA

Exhibits Chair

Iain Collings
CSIRO

Student Paper Contest Chair

Nikos Sidiropoulos
University of Minnesota

Conference Managers

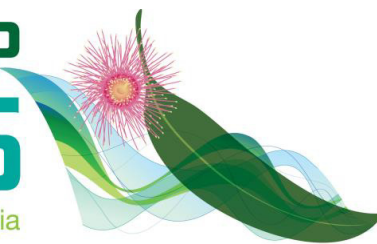
Registration & Program Enquiries:
Conference Management Services, Inc
3833 S Texas Ave, Ste 221,
Bryan TX 77802, USA

General Enquiries:

arinex pty limited
S3, The Precinct, 12 Browning St
Brisbane QLD 4101, Australia
Ph: +61 2 9265 0700
Email: icassp2015@arinex.com.au

ICASSP 2015

Brisbane Australia



First Call for Papers

ICASSP 2015

2015 IEEE International Conference on Acoustics,
Speech, and Signal Processing (ICASSP)
Brisbane Convention & Exhibition Centre
April 19 – 24, 2015 • Brisbane, Australia

www.ICASSP2015.org

The 40th International Conference on Acoustics, Speech, and Signal Processing (ICASSP) will be held in the Brisbane Convention & Exhibition Centre, Brisbane, Australia, between April 19th and 24th, 2015. ICASSP is the world's largest and most comprehensive technical conference focused on signal processing and its applications. The conference will feature world-class speakers, tutorials, exhibits, and over 120 lecture and poster sessions. Topics include but are not limited to:

Audio and acoustic signal processing	Multimedia signal processing
Bio- imaging and biomedical signal processing	Sensor array & multichannel signal processing
Signal processing education	Design /implementation of signal processing systems
Speech processing	Signal processing for communications & networking
Industry technology tracks	Image, video & multidimensional signal processing
Information forensics and security	Signal processing theory & methods
Machine learning for signal processing	Spoken language processing
Localisation and tracking	Remote sensing signal processing

Brisbane – Australia's New World City: Brisbane provides a beautiful location for ICASSP 2015 with its picturesque winding river, attractive modern buildings, thriving retail centre, excellent restaurants and year-round pleasant weather. Brisbane is a city of alluring character, from its distinctive architecture (the charming "Queenslanders" and workers' cottages that line inner-suburban streets) to its swimming beach right in the middle of the central business district. As the capital of Queensland, Australia's "Sunshine State", Brisbane is an ideal gateway to the world-famous beaches and theme parks of the Gold and Sunshine Coasts, the rainforests of the islands and hinterlands, and the Great Barrier Reef.

Submission of Papers: Prospective authors are invited to submit full-length papers, with up to four pages for technical content including figures and possible references, and with one additional optional 5th page containing only references. A selection of best papers will be made by the ICASSP 2015 committee upon recommendations from Technical Committees.

Notice: The IEEE Signal Processing Society enforces a "no-show" policy. Any accepted paper included in the final program is expected to have at least one author or qualified proxy attend and present the paper at the conference. Authors of the accepted papers included in the final program who do not attend the conference will be subscribed to a "No-Show List", compiled by the Society. The "no-show" papers will not be published by IEEE on IEEEXplore or other public access forums, but these papers will be distributed as part of the on-site electronic proceedings and the copyright of these papers will belong to the IEEE.

Tutorial and Special Sessions Proposals: Tutorials will be held on April 19 and 20. Brief proposals should be submitted by August 17, 2014, to tutorials@icassp2015.org and must include title, outline, contact information, biography and selected publications for the presenter(s), and a description of the tutorial and material to be distributed to participants. Special sessions proposals should be submitted by August 17, 2014, to specialsessions@icassp2015.org and must include a topical title, rationale, session outline, contact information, and a list of invited papers. Refer to the ICASSP 2015 website for additional information.

Important Deadlines:

Special session & tutorial proposals due	Sunday, August 17 th 2014
Notification of special session & tutorial acceptance	Sunday, September 7 th 2014
Submission of regular papers	Sunday, October 5 th 2014
Early registration opens	Monday, January 12 th 2015
Notification of paper acceptance	Wednesday, January 14 th 2015
Revised paper upload	Friday, February 13 th 2015
Author registration	Friday, February 13 th 2015



IEEE TRANSACTIONS ON *MULTIMEDIA*

A PUBLICATION OF
THE IEEE CIRCUITS AND SYSTEMS SOCIETY
THE IEEE SIGNAL PROCESSING SOCIETY
THE IEEE COMMUNICATIONS SOCIETY
THE IEEE COMPUTER SOCIETY



<http://www.signalprocessingsociety.org/tmm/>

JUNE 2014

VOLUME 16

NUMBER 4

ITMUF8

(ISSN 1520-9210)

OVERVIEW PAPER

Cloud Mobile Media: Reflections and Outlook <http://dx.doi.org/10.1109/TMM.2014.2315596>
..... *Y. Wen, X. Zhu, J. J. P. C. Rodrigues, and C. W. Chen* 885

REGULAR PAPERS

Audio/Video Analysis and Synthesis

Video Object Co-Segmentation via Subspace Clustering and Quadratic Pseudo-Boolean Optimization in an MRF
Framework <http://dx.doi.org/10.1109/TMM.2014.2306393> *C. Wang, Y. Guo, J. Zhu, L. Wang, and W. Wang* 903

Sport Type Classification of Mobile Videos <http://dx.doi.org/10.1109/TMM.2014.2307552>
..... *F. Cricri, M. J. Roininen, J. Leppänen, S. Mate, I. D. D. Curcio, S. Uhlmann, and M. Gabbouj* 917

Compression and Coding

Efficient H.264/AVC Video Coding with Adaptive Transforms <http://dx.doi.org/10.1109/TMM.2014.2305579>
..... *M. Wang, K. N. Ngan, and L. Xu* 933

An H.264 High-Profile Intra-Prediction with Adaptive Selection Between the Parallel and Pipelined Executions of
Prediction Modes <http://dx.doi.org/10.1109/TMM.2014.2306396> *C. E. Rhee, T. S. Kim, and H.-J. Lee* 947

Stationary Probability Model for Microscopic Parallelism in JPEG2000 <http://dx.doi.org/10.1109/TMM.2014.2307553>
..... *F. Aulí-Llinàs and M. W. Marcellin* 960

3-D Audio/Video Processing

Physical Metaphor for Streaming Media Retargeting <http://dx.doi.org/10.1109/TMM.2014.2305917>
..... *R. Gallea, E. Ardizzone, and R. Pirrone* 971

Sparse Signal Processing

Image Similarity Using Sparse Representation and Compression Distance <http://dx.doi.org/10.1109/TMM.2014.2306175>
..... *T. Guha and R. K. Ward* 980



Display Technology for Multimedia

Corruptive Artifacts Suppression for Example-Based Color Transfer <http://dx.doi.org/10.1109/TMM.2014.2305914> Z. Su, K. Zeng, L. Liu, B. Li, and X. Luo 988

System Software for Multimedia

Variational Bayesian Methods For Multimedia Problems <http://dx.doi.org/10.1109/TMM.2014.2307692> Z. Chen, S. D. Babacan, R. Molina, and A. K. Katsaggelos 1000

Multimodal Human-Human and Human-Computer Dialog

Hire me: Computational Inference of Hirability in Employment Interviews Based on Nonverbal Behavior <http://dx.doi.org/10.1109/TMM.2014.2307169> L. S. Nguyen, D. Frauendorfer, M. S. Mast, and D. Gatica-Perez 1018

Multimodal Human-Machine Interfaces and Interaction

Simultaneous-Speaker Voice Activity Detection and Localization Using Mid-Fusion of SVM and HMMs <http://dx.doi.org/10.1109/TMM.2014.2306632> V. P. Minotto, C. R. Jung, and B. Lee 1032

Multimedia Interfaces and Interaction

Self-Sorting Map: An Efficient Algorithm for Presenting Multimedia Data in Structured Layouts <http://dx.doi.org/10.1109/TMM.2014.2306183> G. Strong and M. Gong 1045

Knowledge and Semantics Modeling for Multimedia Databases

A Cross-Modal Approach for Extracting Semantic Relationships Between Concepts Using Tagged Images <http://dx.doi.org/10.1109/TMM.2014.2306655> M. Katsurai, T. Ogawa, and M. Haseyama 1059

Multimedia Search and Retrieval

Corpus Development for Affective Video Indexing <http://dx.doi.org/10.1109/TMM.2014.2305573> M. Soleymani, M. Larson, T. Pun, and A. Hanjalic 1075

Discrete Cosine Transform Locality-Sensitive Hashes for Face Retrieval <http://dx.doi.org/10.1109/TMM.2014.2305633> M. Kafai, K. Eshghi, and B. Bhanu 1090

Contextual Query Expansion for Image Retrieval <http://dx.doi.org/10.1109/TMM.2014.2305909> H. Xie, Y. Zhang, J. Tan, L. Guo, and J. Li 1104

Image Attribute Adaptation <http://dx.doi.org/10.1109/TMM.2014.2306092> Y. Han, Y. Yang, Z. Ma, H. Shen, N. Sebe, and X. Zhou 1115

A Prior-Free Weighting Scheme for Binary Code Ranking <http://dx.doi.org/10.1109/TMM.2014.2306392> Y. Zhang, L. Zhang, and Q. Tian 1127

Wireless/Mobile Multimedia

An Adaptive Mechanism for Optimal Content Download in Wireless Networks <http://dx.doi.org/10.1109/TMM.2014.2307155> I. de Fez and J. C. Guerri 1140

Multimedia Algorithms, Systems, and Interfaces

PicWords: Render a Picture by Packing Keywords <http://dx.doi.org/10.1109/TMM.2014.2305635> Z. Hu, S. Liu, J. Jiang, R. Hong, M. Wang, and S. Yan 1156

Regularity Preserved Superpixels and Supervoxels <http://dx.doi.org/10.1109/TMM.2014.2305571> H. Fu, X. Cao, D. Tang, Y. Han, and D. Xu 1165

CORRESPONDENCE

Wireless/Mobile Multimedia

Interruption Probability of Wireless Video Streaming With Limited Video Lengths <http://dx.doi.org/10.1109/TMM.2014.2306656> A. Anttonen and A. Mämmelä 1176

EDICS—Editors Classification Scheme <http://dx.doi.org/10.1109/TMM.2014.2322433> 1181

Information for Authors <http://dx.doi.org/10.1109/TMM.2014.2322434> 1182

IEEE JOURNAL OF SELECTED TOPICS IN SIGNAL PROCESSING



www.ieee.org/sp/index.html

JUNE 2014

VOLUME 8

NUMBER 3

IJSTGY

(ISSN 1932-4553)

EDITORIAL

Introduction to the Issue on Perception Inspired Video Processing http://dx.doi.org/10.1109/IJSTSP.2014.2318078	355
..... <i>H. Kalva, A. Bovik, H. Chen, K. Egiazarian, and Z. Wang</i>	

PAPERS

Evoked Neural Responses to Events in Video http://dx.doi.org/10.1109/IJSTSP.2014.2313022	358
..... <i>D. Rosenthal, P. DeGuzman, L. C. Parra, and P. Sajda</i>	
Using Electroencephalography to Measure Perceived Video Quality http://dx.doi.org/10.1109/IJSTSP.2014.2313026	366
..... <i>S. Arndt, J.-N. Antons, R. Schleicher, S. Möller, and G. Curio</i>	
Objective Quality Assessment for Image Retargeting Based on Perceptual Geometric Distortion and Information Loss http://dx.doi.org/10.1109/IJSTSP.2014.2311884	377
..... <i>C.-C. Hsu, C.-W. Lin, Y. Fang, and W. Lin</i>	
Mobile Video Perception: New Insights and Adaptation Strategies http://dx.doi.org/10.1109/IJSTSP.2014.2313456	390
..... <i>J. Xue and C. W. Chen</i>	
Visual Attention Model Aided Non-Uniform Asymmetric Coding of Stereoscopic Video http://dx.doi.org/10.1109/IJSTSP.2014.2313717	402
..... <i>E. Ekmekcioglu, V. De Silva, P. T. Pesch, and A. Kondoz</i>	
3D Visual Discomfort Prediction: Vergence, Foveation, and the Physiological Optics of Accommodation http://dx.doi.org/10.1109/IJSTSP.2014.2311885	415
..... <i>J. Park, S. Lee, and A. C. Bovik</i>	
Perceptual Principles for Video Classification With Slow Feature Analysis http://dx.doi.org/10.1109/IJSTSP.2014.2315742	428
..... <i>C. Thériault, N. Thome, M. Cord, and P. Pérez</i>	
A Retina-Based Perceptually Lossless Limit and a Gaussian Foveation Scheme With Loss Control http://dx.doi.org/10.1109/IJSTSP.2014.2315716	438
..... <i>A. L. N. Targino da Costa and M. N. Do</i>	
Coherency Based Spatio-Temporal Saliency Detection for Video Object Segmentation http://dx.doi.org/10.1109/IJSTSP.2014.2315874	454
..... <i>D. Mahapatra, S. O. Gilani, and M. K. Saini</i>	
Perception-Oriented Methodology for Robust Motion Estimation Design http://dx.doi.org/10.1109/IJSTSP.2014.2317289	463
..... <i>A. Heinrich, R. J. van der Vleuten, and G. de Haan</i>	
Region-of-Interest Based Conversational HEVC Coding with Hierarchical Perception Model of Face http://dx.doi.org/10.1109/IJSTSP.2014.2314864	475
..... <i>M. Xu, X. Deng, S. Li, and Z. Wang</i>	
Gamut Mapping in Cinematography Through Perceptually-Based Contrast Modification http://dx.doi.org/10.1109/IJSTSP.2014.2313182	490
..... <i>S. W. Zamir, J. Vazquez-Corral, and M. Bertalmio</i>	



Information for Authors <http://dx.doi.org/10.1109/JSTSP.2014.2322300> 504

ANNOUNCEMENTS

Call for Papers—Special Issue on Spatial Audio <http://dx.doi.org/10.1109/JSTSP.2014.2322303> 506

Call for Papers—Special Issue on Signal Processing for Big Data <http://dx.doi.org/10.1109/JSTSP.2014.2322304> 507

Call for Papers—Special issue on Advances in Hyperspectral Data Processing and Analysis <http://dx.doi.org/10.1109/JSTSP.2014.2322305> ..

..... 508

IEEE

SIGNAL PROCESSING LETTERS

A PUBLICATION OF THE IEEE SIGNAL PROCESSING SOCIETY


www.ieee.org/sp/index.html

JUNE 2014

VOLUME 21

NUMBER 6

ISPLEM

(ISSN 1070-9908)

LETTERS

On the Complementarity of Phone Posterior Probabilities for Improved Speaker Recognition http://dx.doi.org/10.1109/LSP.2014.2312213 ..	649
..... <i>M. Diez, A. Varona, M. Penagarikano, L. J. Rodriguez-Fuentes, and G. Bordel</i>	
New Steady-State Analysis Results of Variable Step-Size LMS Algorithm With Different Noise Distributions	653
http://dx.doi.org/10.1109/LSP.2013.2291404	
..... <i>S. Zhang and J. Zhang</i>	
Tongue Contour Reconstruction from Optical and Electrical Palatography http://dx.doi.org/10.1109/LSP.2014.2312456	658
..... <i>R. Mumtaz, S. Preuß, C. Neuschaefer-Rube, C. Hey, R. Sader, and P. Birkholz</i>	
Time-of-Flight Depth Camera Motion Blur Detection and Deblurring http://dx.doi.org/10.1109/LSP.2014.2312384	663
..... <i>S. Lee</i>	
Study of the Mainlobe Misorientation of the First-Order Steerable Differential Array in the Presence of Microphone Gain and Phase Errors http://dx.doi.org/10.1109/LSP.2014.2312729	667
..... <i>X. Wu, H. Chen, J. Zhou, and T. Guo</i>	
Consensus Bernoulli Filter for Distributed Detection and Tracking using Multi-Static Doppler Shifts	672
http://dx.doi.org/10.1109/LSP.2014.2313177	
..... <i>M. B. Guldogan</i>	
A Non-Parametric Motion Model for Foreground Detection in Camera Jitter Scenes http://dx.doi.org/10.1109/LSP.2014.2312371	677
..... <i>J. Liao, R. Dong, B. Li, and Q. Chen</i>	
Robust Digital Image Reconstruction via the Discrete Fourier Slice Theorem http://dx.doi.org/10.1109/LSP.2014.2313341	682
..... <i>S. S. Chandra, N. Normand, A. Kingston, J. Guédon, and I. Svalbe</i>	
Parameterized AdaBoost: Introducing a Parameter to Speed Up the Training of Real AdaBoost	687
http://dx.doi.org/10.1109/LSP.2014.2313570	
..... <i>S. Wu and H. Nagahashi</i>	
Time-Varying Multicomponent Signal Modeling for Analysis of Surface EMG Data http://dx.doi.org/10.1109/LSP.2014.2313880	692
..... <i>M. Zivanovic</i>	

IEEE SIGNAL PROCESSING LETTERS (ISSN 1070-9908) is published quarterly in print and monthly online by the Institute of Electrical and Electronics Engineers, Inc. Responsibility for the contents rests upon the authors and not upon the IEEE, the Society/Council, or its members. **IEEE Corporate Office:** 3 Park Avenue, 17th Floor, New York, NY 10016-5997. **IEEE Operations Center:** 445 Hoes Lane, Piscataway, NJ 08854-4141. **NJ Telephone:** +1 732 981 0060. **Price/Publication Information:** Individual copies: IEEE Members \$20.00 (first copy only), nonmembers \$304.00 per copy. (Note: Postage and handling charge not included.) Member and nonmember subscription prices available upon request. Available in microfiche and microfilm. **Copyright and Reprint Permissions:** Abstracting is permitted with credit to the source. Libraries are permitted to photocopy for private use of patrons, provided the per-copy fee indicated in the code at the bottom of the first page is paid through the Copyright Clearance Center, 222 Rosewood Drive, Danvers, MA 01923. For all other copying, reprint, or republication permission, write to Copyrights and Permissions Department, IEEE Publications Administration, 445 Hoes Lane, Piscataway, NJ 08854-4141. Copyright © 2014 by the Institute of Electrical and Electronics Engineers, Inc. All rights reserved. Periodicals Postage at New York, NY and at additional mailing offices. **Postmaster:** Send address changes to IEEE SIGNAL PROCESSING LETTERS, IEEE, 445 Hoes Lane, Piscataway, NJ 08854-4141. GST Registration No. 125634188. CPC Sales Agreement #40013087. Return undeliverable Canada addresses to: Pitney Bowes IMEX, P.O. Box 4332, Stanton Rd., Toronto, ON M5W 3J4, Canada. IEEE prohibits discrimination, harassment and bullying. For more information visit <http://www.ieee.org/nondiscrimination>. Printed in U.S.A.



Scene-Adaptive Hierarchical Data Association for Multiple Objects Tracking http://dx.doi.org/10.1109/LSP.2014.2313853	697
..... <i>C. Wang, H. Liu, and Y. Gao</i>	
Probabilistic Linear Discriminant Analysis for Acoustic Modeling http://dx.doi.org/10.1109/LSP.2014.2313410	702
..... <i>L. Lu and S. Renals</i>	
Bayesian Texture and Instrument Parameter Estimation From Blurred and Noisy Images Using MCMC http://dx.doi.org/10.1109/LSP.2014.2313274	707
..... <i>C. Vacar, J. F. Giovannelli, and Y. Berthoumieu</i>	
Enhancement in Spectral Efficiency using Transmit-side Channel Shortener for MISO-OFDM Systems http://dx.doi.org/10.1109/LSP.2014.2313885	712
..... <i>I. Singh and K. Giridhar</i>	
Depth Motion Detection—A Novel RS-Trigger Temporal Logic based Method http://dx.doi.org/10.1109/LSP.2014.2313345	717
..... <i>C. Wang, H. Liu, and L. Ma</i>	
Optimal Viterbi Based Total Variation Sequence Detection (TVSD) For Robust Image/Video Decoding In Wireless Sensor Networks http://dx.doi.org/10.1109/LSP.2014.2313887	722
..... <i>A. Kudeshia and A. K. Jagannatham</i>	
Bernoulli Forward-Backward Smoothing for Track-Before-Detect http://dx.doi.org/10.1109/LSP.2014.2310137	727
..... <i>S. Wong, B.-T. Vo, and F. Papi</i>	
Recursive Prediction for Joint Spatial and Temporal Prediction in Video Coding http://dx.doi.org/10.1109/LSP.2014.2314215	732
..... <i>F. Kamisli</i>	
A Grid-Less Approach to Underdetermined Direction of Arrival Estimation Via Low Rank Matrix Denoising http://dx.doi.org/10.1109/LSP.2014.2314175	737
..... <i>P. Pal and P. P. Vaidyanathan</i>	
A Differentiable Approximation Approach to Contrast-Aware Image Fusion http://dx.doi.org/10.1109/LSP.2014.2314647	742
..... <i>K. Hara, K. Inoue, and K. Urahama</i>	
On Localization of A Non-Cooperative Target with Non-Coherent Binary Detectors http://dx.doi.org/10.1109/LSP.2014.2314220	746
..... <i>A. Shoari and A. Seyedi</i>	
A Fast Approach for No-Reference Image Sharpness Assessment Based on Maximum Local Variation http://dx.doi.org/10.1109/LSP.2014.2314487	751
..... <i>K. Bahrami and A. C. Kot</i>	
Modulation Discovery Over Arbitrary Additive Noise Channels Based on the Richardson-Lucy Algorithm http://dx.doi.org/10.1109/LSP.2014.2314695	756
..... <i>B. Dulek, O. Ozdemir, P. K. Varshney, and W. Su</i>	
Super-Resolution Compressed Sensing: An Iterative Reweighted Algorithm for Joint Parameter Learning and Sparse Signal Recovery http://dx.doi.org/10.1109/LSP.2014.2316004	761
..... <i>J. Fang, J. Li, Y. Shen, H. Li, and S. Li</i>	
Random Parameter EM-Based Kalman Filter (REKF) for Joint Symbol Detection and Channel Estimation in Fast Fading STTC MIMO Systems http://dx.doi.org/10.1109/LSP.2014.2316538	766
..... <i>A. Mishra, R. Gayathri, and A. K. Jagannatham</i>	
<hr/>	
Information for Authors http://dx.doi.org/10.1109/LSP.2014.2319553	771
EDICS—Editors' Information Classification Scheme http://dx.doi.org/10.1109/LSP.2014.2319551	773
<hr/>	
ANNOUNCEMENTS	
Call for Papers—IEEE JOURNAL OF SELECTED TOPICS IN SIGNAL PROCESSING Issue on Spatial Audio http://dx.doi.org/10.1109/LSP.2014.2320433	774
Call for Papers—IEEE JOURNAL OF SELECTED TOPICS IN SIGNAL PROCESSING Issue on Signal Processing for Big Data http://dx.doi.org/10.1109/LSP.2014.2320434	775
Call for Papers—IEEE JOURNAL OF SELECTED TOPICS IN SIGNAL PROCESSING Issue on Advances in Hyperspectral Data Processing and Analysis http://dx.doi.org/10.1109/LSP.2014.2320432	776

IEEE

SIGNAL PROCESSING LETTERS

A PUBLICATION OF THE IEEE SIGNAL PROCESSING SOCIETY


www.ieee.org/sp/index.html

JUNE 2014

VOLUME 21

NUMBER 6

ISPLEM

(ISSN 1070-9908)

LETTERS

Audio and Acoustic Signal Processing

Study of the Mainlobe Misorientation of the First-Order Steerable Differential Array in the Presence of Microphone Gain and Phase Errors <http://dx.doi.org/10.1109/LSP.2014.2312729> X. Wu, H. Chen, J. Zhou, and T. Guo 667

Biomedical Signal Processing

Tongue Contour Reconstruction from Optical and Electrical Palatography <http://dx.doi.org/10.1109/LSP.2014.2312456> R. Mumtaz, S. Preuß, C. Neuschaefer-Rube, C. Hey, R. Sader, and P. Birkholz 658

Time-Varying Multicomponent Signal Modeling for Analysis of Surface EMG Data <http://dx.doi.org/10.1109/LSP.2014.2313880> M. Zivanovic 692

Image and Multidimensional Signal Processing

Time-of-Flight Depth Camera Motion Blur Detection and Deblurring <http://dx.doi.org/10.1109/LSP.2014.2312384> S. Lee 663

A Non-Parametric Motion Model for Foreground Detection in Camera Jitter Scenes <http://dx.doi.org/10.1109/LSP.2014.2312371> J. Liao, R. Dong, B. Li, and Q. Chen 677

Robust Digital Image Reconstruction via the Discrete Fourier Slice Theorem <http://dx.doi.org/10.1109/LSP.2014.2313341> S. S. Chandra, N. Normand, A. Kingston, J. Guédon, and I. Svalbe 682

Depth Motion Detection—A Novel RS-Trigger Temporal Logic based Method <http://dx.doi.org/10.1109/LSP.2014.2313345> C. Wang, H. Liu, and L. Ma 717

Optimal Viterbi Based Total Variation Sequence Detection (TVSD) For Robust Image/Video Decoding In Wireless Sensor Networks <http://dx.doi.org/10.1109/LSP.2014.2313887> A. Kudeshia and A. K. Jagannatham 722

Recursive Prediction for Joint Spatial and Temporal Prediction in Video Coding <http://dx.doi.org/10.1109/LSP.2014.2314215> F. Kamisli 732

A Differentiable Approximation Approach to Contrast-Aware Image Fusion <http://dx.doi.org/10.1109/LSP.2014.2314647> K. Hara, K. Inoue, and K. Urahama 742

A Fast Approach for No-Reference Image Sharpness Assessment Based on Maximum Local Variation <http://dx.doi.org/10.1109/LSP.2014.2314487> K. Bahrami and A. C. Kot 751

Modulation Discovery Over Arbitrary Additive Noise Channels Based on the Richardson-Lucy Algorithm <http://dx.doi.org/10.1109/LSP.2014.2314695> B. Dulek, O. Ozdemir, P. K. Varshney, and W. Su 756

IEEE SIGNAL PROCESSING LETTERS (ISSN 1070-9908) is published quarterly in print and monthly online by the Institute of Electrical and Electronics Engineers, Inc. Responsibility for the contents rests upon the authors and not upon the IEEE, the Society/Council, or its members. **IEEE Corporate Office:** 3 Park Avenue, 17th Floor, New York, NY 10016-5997. **IEEE Operations Center:** 445 Hoes Lane, Piscataway, NJ 08854-4141. **NJ Telephone:** +1 732 981 0060. **Price/Publication Information:** Individual copies: IEEE Members \$20.00 (first copy only), nonmembers \$304.00 per copy. (Note: Postage and handling charge not included.) Member and nonmember subscription prices available upon request. Available in microfiche and microfilm. **Copyright and Reprint Permissions:** Abstracting is permitted with credit to the source. Libraries are permitted to photocopy for private use of patrons, provided the per-copy fee indicated in the code at the bottom of the first page is paid through the Copyright Clearance Center, 222 Rosewood Drive, Danvers, MA 01923. For all other copying, reprint, or republication permission, write to Copyrights and Permissions Department, IEEE Publications Administration, 445 Hoes Lane, Piscataway, NJ 08854-4141. Copyright © 2014 by the Institute of Electrical and Electronics Engineers, Inc. All rights reserved. Periodicals Postage at New York, NY and at additional mailing offices. **Postmaster:** Send address changes to IEEE SIGNAL PROCESSING LETTERS, IEEE, 445 Hoes Lane, Piscataway, NJ 08854-4141. GST Registration No. 125634188. CPC Sales Agreement #40013087. Return undeliverable Canada addresses to: Pitney Bowes IMEX, P.O. Box 4332, Stanton Rd., Toronto, ON M5W 3J4, Canada. IEEE prohibits discrimination, harassment and bullying. For more information visit <http://www.ieee.org/nondiscrimination>. Printed in U.S.A.



Machine Learning and Statistical Signal Processing

Scene-Adaptive Hierarchical Data Association for Multiple Objects Tracking <http://dx.doi.org/10.1109/LSP.2014.2313853> *C. Wang, H. Liu, and Y. Gao* 697

Super-Resolution Compressed Sensing: An Iterative Reweighted Algorithm for Joint Parameter Learning and Sparse Signal Recovery <http://dx.doi.org/10.1109/LSP.2014.2316004> *J. Fang, J. Li, Y. Shen, H. Li, and S. Li* 761

Sensor Array and Multichannel Signal Processing

A Grid-Less Approach to Underdetermined Direction of Arrival Estimation Via Low Rank Matrix Denoising <http://dx.doi.org/10.1109/LSP.2014.2314175> *P. Pal and P. P. Vaidyanathan* 737

On Localization of A Non-Cooperative Target with Non-Coherent Binary Detectors <http://dx.doi.org/10.1109/LSP.2014.2314220> *A. Shoari and A. Seyedi* 746

Signal Processing for Communications

Enhancement in Spectral Efficiency using Transmit-side Channel Shortener for MISO-OFDM Systems <http://dx.doi.org/10.1109/LSP.2014.2313885> *I. Singh and K. Giridhar* 712

Random Parameter EM-Based Kalman Filter (REKF) for Joint Symbol Detection and Channel Estimation in Fast Fading STTC MIMO Systems <http://dx.doi.org/10.1109/LSP.2014.2316538> *A. Mishra, R. Gayathri, and A. K. Jagannatham* 766

Speech Processing

On the Complementarity of Phone Posterior Probabilities for Improved Speaker Recognition <http://dx.doi.org/10.1109/LSP.2014.2312213> .. *M. Diez, A. Varona, M. Penagarikano, L. J. Rodriguez-Fuentes, and G. Bordel* 649

Probabilistic Linear Discriminant Analysis for Acoustic Modeling <http://dx.doi.org/10.1109/LSP.2014.2313410> *L. Lu and S. Renals* 702

Statistical and Adaptive Signal Processing

New Steady-State Analysis Results of Variable Step-Size LMS Algorithm With Different Noise Distributions <http://dx.doi.org/10.1109/LSP.2013.2291404> *S. Zhang and J. Zhang* 653

Consensus Bernoulli Filter for Distributed Detection and Tracking using Multi-Static Doppler Shifts <http://dx.doi.org/10.1109/LSP.2014.2313177> *M. B. Guldogan* 672

Parameterized AdaBoost: Introducing a Parameter to Speed Up the Training of Real AdaBoost <http://dx.doi.org/10.1109/LSP.2014.2313570> *S. Wu and H. Nagahashi* 687

Bayesian Texture and Instrument Parameter Estimation From Blurred and Noisy Images Using MCMC <http://dx.doi.org/10.1109/LSP.2014.2313274> *C. Vacar, J. F. Giovannelli, and Y. Berthoumieu* 707

Bernoulli Forward-Backward Smoothing for Track-Before-Detect <http://dx.doi.org/10.1109/LSP.2014.2310137> *S. Wong, B.-T. Vo, and F. Papi* 727

Information for Authors <http://dx.doi.org/10.1109/LSP.2014.2319553> 771

EDICS—Editors' Information Classification Scheme <http://dx.doi.org/10.1109/LSP.2014.2319551> 773

ANNOUNCEMENTS

Call for Papers—IEEE JOURNAL OF SELECTED TOPICS IN SIGNAL PROCESSING Issue on Spatial Audio <http://dx.doi.org/10.1109/LSP.2014.2320433> 774

Call for Papers—IEEE JOURNAL OF SELECTED TOPICS IN SIGNAL PROCESSING Issue on Signal Processing for Big Data <http://dx.doi.org/10.1109/LSP.2014.2320434> 775

Call for Papers—IEEE JOURNAL OF SELECTED TOPICS IN SIGNAL PROCESSING Issue on Advances in Hyperspectral Data Processing and Analysis <http://dx.doi.org/10.1109/LSP.2014.2320432> 776

IEEE

SIGNAL PROCESSING LETTERS

A PUBLICATION OF THE IEEE SIGNAL PROCESSING SOCIETY


www.ieee.org/sp/index.html

JULY 2014

VOLUME 21

NUMBER 7

ISPLEM

(ISSN 1070-9908)

Editorial http://dx.doi.org/10.1109/LSP.2014.2318131	<i>P. Willett</i>	781
<i>Digital and Multirate Signal Processing</i>		
Orthogonal Wavelet Filters with Minimum RMS Bandwidth http://dx.doi.org/10.1109/LSP.2014.2318691	<i>D. B. H. Tay, Z. Lin, and S. Murugesan</i>	819
A Reed-Solomon Code Based Measurement Matrix with Small Coherence http://dx.doi.org/10.1109/LSP.2014.2314281	<i>M. M. Mohades, A. Mohades, and A. Tadaion</i>	839
Dynamically-Sampled Bivariate Empirical Mode Decomposition http://dx.doi.org/10.1109/LSP.2014.2317773	<i>N. Rehman, M. W. Sajdar, U. Rehman, and D. P. Mandic</i>	857
<i>Image and Multidimensional Signal Processing</i>		
Exploring Facial Asymmetry Using Optical Flow http://dx.doi.org/10.1109/LSP.2014.2316918	<i>J. Chen, C. Yang, Y. Deng, G. Zhang, and G. Su</i>	792
A Parametric Model for Describing the Correlation Between Single Color Images and Depth Maps http://dx.doi.org/10.1109/LSP.2013.2283851	<i>Y. Wang, R. Wang, and Q. Dai</i>	800
Discrete Anamorphic Transform for Image Compression http://dx.doi.org/10.1109/LSP.2014.2319586	<i>M. H. Asghari and B. Jalali</i>	829
Fast Synopsis for Moving Objects Using Compressed Video http://dx.doi.org/10.1109/LSP.2014.2317754	<i>R. Zhong, R. Hu, Z. Wang, and S. Wang</i>	834
Co-Learned Multi-View Spectral Clustering for Face Recognition Based on Image Sets http://dx.doi.org/10.1109/LSP.2014.2319817	<i>L. Huang, J. Lu, and Y.-P. Tan</i>	875
Exposure-Robust Alignment of Differently Exposed Images http://dx.doi.org/10.1109/LSP.2014.2318302	<i>S. Wu, Z. Li, J. Zheng, and Z. Zhu</i>	885
Effective Estimation of Image Rotation Angle Using Spectral Method http://dx.doi.org/10.1109/LSP.2014.2320503	<i>C. Chen, J. Ni, and Z. Shen</i>	890

IEEE SIGNAL PROCESSING LETTERS (ISSN 1070-9908) is published quarterly in print and monthly online by the Institute of Electrical and Electronics Engineers, Inc. Responsibility for the contents rests upon the authors and not upon the IEEE, the Society/Council, or its members. **IEEE Corporate Office:** 3 Park Avenue, 17th Floor, New York, NY 10016-5997. **IEEE Operations Center:** 445 Hoes Lane, Piscataway, NJ 08854-4141. **NJ Telephone:** +1 732 981 0060. **Price/Publication Information:** Individual copies: IEEE Members \$20.00 (first copy only), nonmembers \$304.00 per copy. (Note: Postage and handling charge not included.) Member and nonmember subscription prices available upon request. Available in microfiche and microfilm. **Copyright and Reprint Permissions:** Abstracting is permitted with credit to the source. Libraries are permitted to photocopy for private use of patrons, provided the per-copy fee indicated in the code at the bottom of the first page is paid through the Copyright Clearance Center, 222 Rosewood Drive, Danvers, MA 01923. For all other copying, reprint, or republication permission, write to Copyrights and Permissions Department, IEEE Publications Administration, 445 Hoes Lane, Piscataway, NJ 08854-4141. Copyright © 2014 by the Institute of Electrical and Electronics Engineers, Inc. All rights reserved. Periodicals Postage at New York, NY and at additional mailing offices. **Postmaster:** Send address changes to IEEE SIGNAL PROCESSING LETTERS, IEEE, 445 Hoes Lane, Piscataway, NJ 08854-4141. GST Registration No. 125634188. CPC Sales Agreement #40013087. Return undeliverable Canada addresses to: Pitney Bowes IMEX, P.O. Box 4332, Stanton Rd., Toronto, ON M5W 3J4, Canada. IEEE prohibits discrimination, harassment and bullying. For more information visit <http://www.ieee.org/nondiscrimination>. Printed in U.S.A.



Machine Learning and Statistical Signal Processing

A Lossless Tagged Visual Cryptography Scheme <http://dx.doi.org/10.1109/LSP.2014.2317706> X. Wang, Q. Pei, and H. Li 853

Multimedia Signal Processing

An Asymmetric Matching Method for a Robust Binary Audio Fingerprinting <http://dx.doi.org/10.1109/LSP.2014.2310237> J. S. Seo 844

Sensor Array and Multichannel Signal Processing

Uncensored Indoor Positioning <http://dx.doi.org/10.1109/LSP.2014.2317787> M. F. Mansour and D. W. Waters 824

Adaptive Detection of Point-Like Targets in the Presence of Homogeneous Clutter and Subspace Interference <http://dx.doi.org/10.1109/LSP.2014.2309434> A. Aubry, A. De Maio, D. Orlando, and M. Piezzo 848

Sub-Array Weighting UN-MUSIC: A Unified Framework and Optimal Weighting Strategy <http://dx.doi.org/10.1109/LSP.2014.2312848> ... X. Zhang, Y. Li, X. Yang, T. Long, and L. Zheng 871

New Results on Fractional QCQP with Applications to Radar Steering Direction Estimation <http://dx.doi.org/10.1109/LSP.2014.2320300> .. A. De Maio and Y. Huang 895

Signal Processing for Communications

On Symbol-Wise Variational Bayesian CSI Estimation and Detection for Distributed Antenna Systems Subjected to Multiple Unknown Jammers <http://dx.doi.org/10.1109/LSP.2014.2315529> K. Zhong and S. Li 782

Application of Full-Duplex Wireless Technique into Secure MIMO Communication: Achievable Secrecy Rate based Optimization <http://dx.doi.org/10.1109/LSP.2014.2316999> Y. Zhou, Z. Z. Xiang, Y. Zhu, and Z. Xue 804

Noise Interpolation for Unique Word OFDM <http://dx.doi.org/10.1109/LSP.2014.2317512> A. Onic and M. Huemer 814

Low Complexity Equalization of HCM Systems with DPFFT Demodulation over Doubly-Selective Channels <http://dx.doi.org/10.1109/LSP.2014.2311128> Y. Li, X. Sha, F.-C. Zheng, and K. Wang 862

Statistical and Adaptive Signal Processing

Parallel Consensus on Likelihoods and Priors for Networked Nonlinear Filtering <http://dx.doi.org/10.1109/LSP.2014.2316258> G. Battistelli, L. Chisci, and C. Fantacci 787

A Lower Bound for the Fisher Information Measure <http://dx.doi.org/10.1109/LSP.2014.2316008> M. Stein, A. Mezghani, and J. A. Nossek 796

Variable Tap-Length LMS Algorithm Based on Adaptive Parameters for TDL Structure Adaption <http://dx.doi.org/10.1109/LSP.2014.2317752> D. Xu, B. Yin, W. Wang, and W. Zhu 809

Information-Preserving Transformations for Signal Parameter Estimation <http://dx.doi.org/10.1109/LSP.2014.2315537> M. Stein, M. Castañeda, A. Mezghani, and J. A. Nossek 870

Steady-State Mean-Square Error Analysis for Adaptive Filtering under the Maximum Correntropy Criterion <http://dx.doi.org/10.1109/LSP.2014.2319308> B. Chen, L. Xing, J. Liang, N. Zheng, and J. C. Príncipe 880

Modeling Dependencies in Multiple Parallel Data Streams with Hyperdimensional Computing <http://dx.doi.org/10.1109/LSP.2014.2320573> O. Räsänen and S. Kakouros 899

IEEE

SIGNAL PROCESSING LETTERS

A PUBLICATION OF THE IEEE SIGNAL PROCESSING SOCIETY


www.ieee.org/sp/index.html

JULY 2014

VOLUME 21

NUMBER 7

ISPLEM

(ISSN 1070-9908)

 Editorial <http://dx.doi.org/10.1109/LSP.2014.2318131> *P. Willett* 781

LETTERS

On Symbol-Wise Variational Bayesian CSI Estimation and Detection for Distributed Antenna Systems Subjected to Multiple Unknown Jammers http://dx.doi.org/10.1109/LSP.2014.2315529	<i>K. Zhong and S. Li</i>	782
Parallel Consensus on Likelihoods and Priors for Networked Nonlinear Filtering http://dx.doi.org/10.1109/LSP.2014.2316258	<i>G. Battistelli, L. Chisci, and C. Fantacci</i>	787
Exploring Facial Asymmetry Using Optical Flow http://dx.doi.org/10.1109/LSP.2014.2316918	<i>J. Chen, C. Yang, Y. Deng, G. Zhang, and G. Su</i>	792
A Lower Bound for the Fisher Information Measure http://dx.doi.org/10.1109/LSP.2014.2316008	<i>M. Stein, A. Mezghani, and J. A. Nossek</i>	796
A Parametric Model for Describing the Correlation Between Single Color Images and Depth Maps http://dx.doi.org/10.1109/LSP.2013.2283851	<i>Y. Wang, R. Wang, and Q. Dai</i>	800
Application of Full-Duplex Wireless Technique into Secure MIMO Communication: Achievable Secrecy Rate based Optimization http://dx.doi.org/10.1109/LSP.2014.2316999	<i>Y. Zhou, Z. Z. Xiang, Y. Zhu, and Z. Xue</i>	804
Variable Tap-Length LMS Algorithm Based on Adaptive Parameters for TDL Structure Adaption http://dx.doi.org/10.1109/LSP.2014.2317752	<i>D. Xu, B. Yin, W. Wang, and W. Zhu</i>	809
Noise Interpolation for Unique Word OFDM http://dx.doi.org/10.1109/LSP.2014.2317512	<i>A. Onic and M. Huemer</i>	814
Orthogonal Wavelet Filters with Minimum RMS Bandwidth http://dx.doi.org/10.1109/LSP.2014.2318691	<i>D. B. H. Tay, Z. Lin, and S. Murguesan</i>	819
Uncensored Indoor Positioning http://dx.doi.org/10.1109/LSP.2014.2317787	<i>M. F. Mansour and D. W. Waters</i>	824

IEEE SIGNAL PROCESSING LETTERS (ISSN 1070-9908) is published quarterly in print and monthly online by the Institute of Electrical and Electronics Engineers, Inc. Responsibility for the contents rests upon the authors and not upon the IEEE, the Society/Council, or its members. **IEEE Corporate Office:** 3 Park Avenue, 17th Floor, New York, NY 10016-5997. **IEEE Operations Center:** 445 Hoes Lane, Piscataway, NJ 08854-4141. **NJ Telephone:** +1 732 981 0060. **Price/Publication Information:** Individual copies: IEEE Members \$20.00 (first copy only), nonmembers \$304.00 per copy. (Note: Postage and handling charge not included.) Member and nonmember subscription prices available upon request. Available in microfiche and microfilm. **Copyright and Reprint Permissions:** Abstracting is permitted with credit to the source. Libraries are permitted to photocopy for private use of patrons, provided the per-copy fee indicated in the code at the bottom of the first page is paid through the Copyright Clearance Center, 222 Rosewood Drive, Danvers, MA 01923. For all other copying, reprint, or republication permission, write to Copyrights and Permissions Department, IEEE Publications Administration, 445 Hoes Lane, Piscataway, NJ 08854-4141. Copyright © 2014 by the Institute of Electrical and Electronics Engineers, Inc. All rights reserved. Periodicals Postage at New York, NY and at additional mailing offices. **Postmaster:** Send address changes to IEEE SIGNAL PROCESSING LETTERS, IEEE, 445 Hoes Lane, Piscataway, NJ 08854-4141. GST Registration No. 125634188. CPC Sales Agreement #40013087. Return undeliverable Canada addresses to: Pitney Bowes IMEX, P.O. Box 4332, Stanton Rd., Toronto, ON M5W 3J4, Canada. IEEE prohibits discrimination, harassment and bullying. For more information visit <http://www.ieee.org/nondiscrimination>. Printed in U.S.A.



Discrete Anamorphic Transform for Image Compression http://dx.doi.org/10.1109/LSP.2014.2319586	<i>M. H. Asghari and B. Jalali</i>	829
Fast Synopsis for Moving Objects Using Compressed Video http://dx.doi.org/10.1109/LSP.2014.2317754	<i>R. Zhong, R. Hu, Z. Wang, and S. Wang</i>	834
A Reed-Solomon Code Based Measurement Matrix with Small Coherence http://dx.doi.org/10.1109/LSP.2014.2314281	<i>M. M. Mohades, A. Mohades, and A. Tadaion</i>	839
An Asymmetric Matching Method for a Robust Binary Audio Fingerprinting http://dx.doi.org/10.1109/LSP.2014.2310237	<i>J. S. Seo</i>	844
Adaptive Detection of Point-Like Targets in the Presence of Homogeneous Clutter and Subspace Interference http://dx.doi.org/10.1109/LSP.2014.2309434	<i>A. Aubry, A. De Maio, D. Orlando, and M. Piezzo</i>	848
A Lossless Tagged Visual Cryptography Scheme http://dx.doi.org/10.1109/LSP.2014.2317706	<i>X. Wang, Q. Pei, and H. Li</i>	853
Dynamically-Sampled Bivariate Empirical Mode Decomposition http://dx.doi.org/10.1109/LSP.2014.2317773	<i>N. Rehman, M. W. Safdar, U. Rehman, and D. P. Mandic</i>	857
Low Complexity Equalization of HCM Systems with DPPFFT Demodulation over Doubly-Selective Channels http://dx.doi.org/10.1109/LSP.2014.2311128	<i>Y. Li, X. Sha, F.-C. Zheng, and K. Wang</i>	862
Information-Preserving Transformations for Signal Parameter Estimation http://dx.doi.org/10.1109/LSP.2014.2315537	<i>M. Stein, M. Castañeda, A. Mezghani, and J. A. Nossek</i>	866
Sub-Array Weighting UN-MUSIC: A Unified Framework and Optimal Weighting Strategy http://dx.doi.org/10.1109/LSP.2014.2312848 ...	<i>X. Zhang, Y. Li, X. Yang, T. Long, and L. Zheng</i>	871
Co-Learned Multi-View Spectral Clustering for Face Recognition Based on Image Sets http://dx.doi.org/10.1109/LSP.2014.2319817	<i>L. Huang, J. Lu, and Y.-P. Tan</i>	875
Steady-State Mean-Square Error Analysis for Adaptive Filtering under the Maximum Correntropy Criterion http://dx.doi.org/10.1109/LSP.2014.2319308	<i>B. Chen, L. Xing, J. Liang, N. Zheng, and J. C. Príncipe</i>	880
Exposure-Robust Alignment of Differently Exposed Images http://dx.doi.org/10.1109/LSP.2014.2318302	<i>S. Wu, Z. Li, J. Zheng, and Z. Zhu</i>	885
Effective Estimation of Image Rotation Angle Using Spectral Method http://dx.doi.org/10.1109/LSP.2014.2320503	<i>C. Chen, J. Ni, and Z. Shen</i>	890
New Results on Fractional QCQP with Applications to Radar Steering Direction Estimation http://dx.doi.org/10.1109/LSP.2014.2320300 ..	<i>A. De Maio and Y. Huang</i>	895
Modeling Dependencies in Multiple Parallel Data Streams with Hyperdimensional Computing http://dx.doi.org/10.1109/LSP.2014.2320573	<i>O. Räsänen and S. Kakouros</i>	899

IEEE

SIGNAL PROCESSING LETTERS

A PUBLICATION OF THE IEEE SIGNAL PROCESSING SOCIETY


www.ieee.org/sp/index.html

AUGUST 2014

VOLUME 21

NUMBER 8

ISPLEM

(ISSN 1070-9908)

LETTERS

Object Tracking via Robust Multitask Sparse Representation http://dx.doi.org/10.1109/LSP.2014.2320291	<i>Y. Bai and M. Tang</i>	909
Numerical Synthesis of an Optimal Low-Sidelobe Beam Pattern for a Microphone Array http://dx.doi.org/10.1109/LSP.2014.2320916	<i>Y. Hur, Y.-C. Park, J. S. Abel, and D. H. Youn</i>	914
Learning Structural Regularity for Evaluating Blocking Artifacts in JPEG Images http://dx.doi.org/10.1109/LSP.2014.2320743	<i>L. Li, W. Lin, and H. Zhu</i>	918
Artifact Removal from Single-Trial ERPs using Non-Gaussian Stochastic Volatility Models and Particle Filter http://dx.doi.org/10.1109/LSP.2014.2321000	<i>C.-M. Ting, S.-H. Salleh, Z. M. Zainuddin, and A. Bahar</i>	923
Steady-State Performance of Non-Negative Least-Mean-Square Algorithm and Its Variants http://dx.doi.org/10.1109/LSP.2014.2320944	<i>J. Chen, J. C. M. Bermudez, and C. Richard</i>	928
A Time-Frequency Hybrid Downmixing Method for AC-3 Decoding http://dx.doi.org/10.1109/LSP.2014.2321061	<i>H. Li, Y. Wang, and P. Li</i>	933
Accurate Static Region Classification Using Multiple Cues for ARO Detection http://dx.doi.org/10.1109/LSP.2014.2320676	<i>J. Kim and D. Kim</i>	937
A GMM Post-Filter for Residual Crosstalk Suppression in Blind Source Separation http://dx.doi.org/10.1109/LSP.2014.2317761	<i>B. Liu, V. G. Reju, A. W. H. Khong, and V. V. Reddy</i>	942
Robust Transceiver for AF MIMO Relaying with Direct Link: A Globally Optimal Solution http://dx.doi.org/10.1109/LSP.2014.2321414	<i>H. Shen, W. Xu, and C. Zhao</i>	947
Sparse Representation of Monogenic Signal: With Application to Target Recognition in SAR Images http://dx.doi.org/10.1109/LSP.2014.2321565	<i>G. Dong, N. Wang, and G. Kuang</i>	952

IEEE SIGNAL PROCESSING LETTERS (ISSN 1070-9908) is published quarterly in print and monthly online by the Institute of Electrical and Electronics Engineers, Inc. Responsibility for the contents rests upon the authors and not upon the IEEE, the Society/Council, or its members. **IEEE Corporate Office:** 3 Park Avenue, 17th Floor, New York, NY 10016-5997. **IEEE Operations Center:** 445 Hoes Lane, Piscataway, NJ 08854-4141. **NJ Telephone:** +1 732 981 0060. **Price/Publication Information:** Individual copies: IEEE Members \$20.00 (first copy only), nonmembers \$304.00 per copy. (Note: Postage and handling charge not included.) Member and nonmember subscription prices available upon request. Available in microfiche and microfilm. **Copyright and Reprint Permissions:** Abstracting is permitted with credit to the source. Libraries are permitted to photocopy for private use of patrons, provided the per-copy fee indicated in the code at the bottom of the first page is paid through the Copyright Clearance Center, 222 Rosewood Drive, Danvers, MA 01923. For all other copying, reprint, or republication permission, write to Copyrights and Permissions Department, IEEE Publications Administration, 445 Hoes Lane, Piscataway, NJ 08854-4141. Copyright © 2014 by the Institute of Electrical and Electronics Engineers, Inc. All rights reserved. Periodicals Postage at New York, NY and at additional mailing offices. **Postmaster:** Send address changes to IEEE SIGNAL PROCESSING LETTERS, IEEE, 445 Hoes Lane, Piscataway, NJ 08854-4141. GST Registration No. 125634188. CPC Sales Agreement #40013087. Return undeliverable Canada addresses to: Pitney Bowes IMEX, P.O. Box 4332, Stanton Rd., Toronto, ON M5W 3J4, Canada. IEEE prohibits discrimination, harassment and bullying. For more information visit <http://www.ieee.org/nondiscrimination>. Printed in U.S.A.



IEEE

SIGNAL PROCESSING LETTERS

A PUBLICATION OF THE IEEE SIGNAL PROCESSING SOCIETY


www.ieee.org/sp/index.html

AUGUST 2014

VOLUME 21

NUMBER 8

ISPLEM

(ISSN 1070-9908)

LETTERS

Audio and Acoustic Signal Processing

Numerical Synthesis of an Optimal Low-Sidelobe Beam Pattern for a Microphone Array <http://dx.doi.org/10.1109/LSP.2014.2320916> *Y. Hur, Y.-C. Park, J. S. Abel, and D. H. Youn* 914

A GMM Post-Filter for Residual Crosstalk Suppression in Blind Source Separation <http://dx.doi.org/10.1109/LSP.2014.2317761> *B. Liu, V. G. Reju, A. W. H. Khong, and V. V. Reddy* 942

Biomedical Signal Processing

Artifact Removal from Single-Trial ERPs using Non-Gaussian Stochastic Volatility Models and Particle Filter <http://dx.doi.org/10.1109/LSP.2014.2321000> *C.-M. Ting, S.-H. Salleh, Z. M. Zainuddin, and A. Bahar* 923

Digital and Multirate Signal Processing

A Time-Frequency Hybrid Downmixing Method for AC-3 Decoding <http://dx.doi.org/10.1109/LSP.2014.2321061> *H. Li, Y. Wang, and P. Li* 933

Efficient Iterative Estimation of the Parameters of a Damped Complex Exponential in Noise <http://dx.doi.org/10.1109/LSP.2014.2320927> .. *E. Aboutanios and S. Ye* 975

Automated Recovery of Compressedly Observed Sparse Signals From Smooth Background <http://dx.doi.org/10.1109/LSP.2014.2321256> .. *Z. Chen, R. Molina, and A. K. Katsaggelos* 1012

Large Margin Dimensionality Reduction for Action Similarity Labeling <http://dx.doi.org/10.1109/LSP.2014.2320530> *X. Peng, Y. Qiao, Q. Peng, and Q. Wang* 1022

IEEE SIGNAL PROCESSING LETTERS (ISSN 1070-9908) is published quarterly in print and monthly online by the Institute of Electrical and Electronics Engineers, Inc. Responsibility for the contents rests upon the authors and not upon the IEEE, the Society/Council, or its members. **IEEE Corporate Office:** 3 Park Avenue, 17th Floor, New York, NY 10016-5997. **IEEE Operations Center:** 445 Hoes Lane, Piscataway, NJ 08854-4141. **NJ Telephone:** +1 732 981 0060. **Price/Publication Information:** Individual copies: IEEE Members \$20.00 (first copy only), nonmembers \$304.00 per copy. (Note: Postage and handling charge not included.) Member and nonmember subscription prices available upon request. Available in microfiche and microfilm. **Copyright and Reprint Permissions:** Abstracting is permitted with credit to the source. Libraries are permitted to photocopy for private use of patrons, provided the per-copy fee indicated in the code at the bottom of the first page is paid through the Copyright Clearance Center, 222 Rosewood Drive, Danvers, MA 01923. For all other copying, reprint, or republication permission, write to Copyrights and Permissions Department, IEEE Publications Administration, 445 Hoes Lane, Piscataway, NJ 08854-4141. Copyright © 2014 by the Institute of Electrical and Electronics Engineers, Inc. All rights reserved. Periodicals Postage at New York, NY and at additional mailing offices. **Postmaster:** Send address changes to IEEE SIGNAL PROCESSING LETTERS, IEEE, 445 Hoes Lane, Piscataway, NJ 08854-4141. GST Registration No. 125634188. CPC Sales Agreement #40013087. Return undeliverable Canada addresses to: Pitney Bowes IMEX, P.O. Box 4332, Stanton Rd., Toronto, ON M5W 3J4, Canada. IEEE prohibits discrimination, harassment and bullying. For more information visit <http://www.ieee.org/nondiscrimination>. Printed in U.S.A.



Image and Multidimensional Signal Processing

Object Tracking via Robust Multitask Sparse Representation http://dx.doi.org/10.1109/LSP.2014.2320291	<i>Y. Bai and M. Tang</i>	909
Learning Structural Regularity for Evaluating Blocking Artifacts in JPEG Images http://dx.doi.org/10.1109/LSP.2014.2320743	<i>L. Li, W. Lin, and H. Zhu</i>	918
Accurate Static Region Classification Using Multiple Cues for ARO Detection http://dx.doi.org/10.1109/LSP.2014.2320676	<i>J. Kim and D. Kim</i>	937
Sparse Representation of Monogenic Signal: With Application to Target Recognition in SAR Images http://dx.doi.org/10.1109/LSP.2014.2321565	<i>G. Dong, N. Wang, and G. Kuang</i>	952
Robust Keypoint Detection Using Higher-Order Scale Space Derivatives: Application to Image Retrieval http://dx.doi.org/10.1109/LSP.2014.2321755	<i>U. Park, J. Park, and A. K. Jain</i>	962
Viewpoint-Aware Representation for Sketch-Based 3D Model Retrieval http://dx.doi.org/10.1109/LSP.2014.2321764	<i>C. Zou, C. Wang, Y. Wen, L. Zhang, and J. Liu</i>	966
A Generic Proximal Algorithm for Convex Optimization—Application to Total Variation Minimization http://dx.doi.org/10.1109/LSP.2014.2322123	<i>L. Condat</i>	985

Machine Learning and Statistical Signal Processing

Reducing Basis Mismatch in Harmonic Signal Recovery via Alternating Convex Search http://dx.doi.org/10.1109/LSP.2014.2322444	<i>J. M. Nichols, A. K. Oh, and R. M. Willett</i>	1007
---	---	------

Multimedia Signal Processing

PMFS: A Perceptual Modulated Feature Similarity Metric for Stereoscopic Image Quality Assessment http://dx.doi.org/10.1109/LSP.2014.2320956	<i>W. Zhou, G. Jiang, M. Yu, F. Shao, and Z. Peng</i>	1003
--	---	------

Sensor Array and Multichannel Signal Processing

Orthogonal Space Projection (OSP) Processing for Adaptive Interference Cancellation http://dx.doi.org/10.1109/LSP.2014.2319317	<i>E. J. Holder</i>	980
---	---------------------	-----

Signal Processing for Communications

Robust Transceiver for AF MIMO Relaying with Direct Link: A Globally Optimal Solution http://dx.doi.org/10.1109/LSP.2014.2321414 ..	<i>H. Shen, W. Xu, and C. Zhao</i>	947
Linearized Robust Beamforming for Two-Way Relay Systems http://dx.doi.org/10.1109/LSP.2014.2322118	<i>A. Aziz, C. Thron, S. Cui, and C. Georgiades</i>	1017

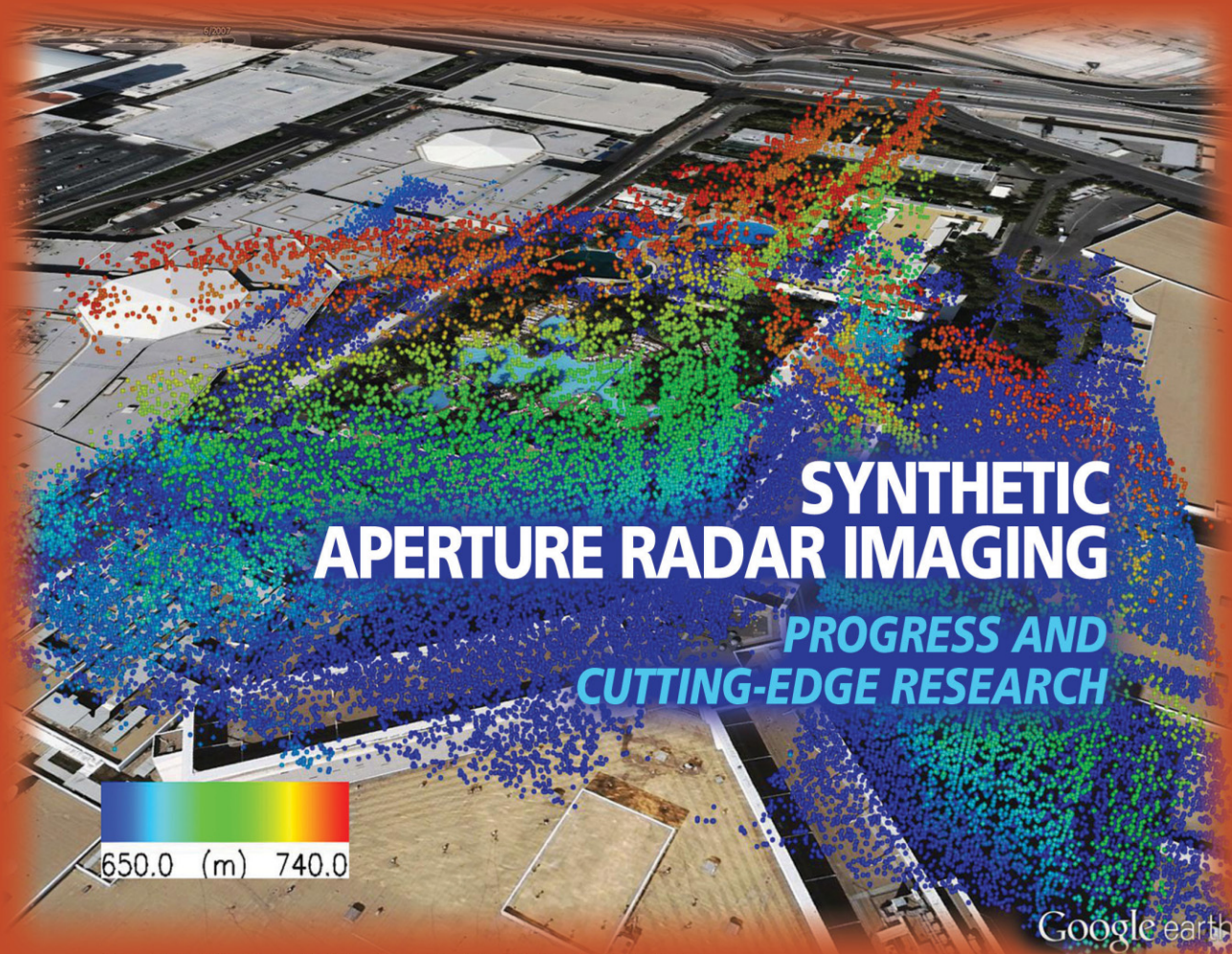
Statistical and Adaptive Signal Processing

Steady-State Performance of Non-Negative Least-Mean-Square Algorithm and Its Variants http://dx.doi.org/10.1109/LSP.2014.2320944 ...	<i>J. Chen, J. C. M. Bermudez, and C. Richard</i>	928
Determining the Existence of Objects in an Image and Its Application to Image Thumbnailing http://dx.doi.org/10.1109/LSP.2014.2321751 ..	<i>J. Choi, C. Jung, J. Lee, and C. Kim</i>	957
A Computationally Efficient Subspace Algorithm for 2-D DOA Estimation with L-shaped Array http://dx.doi.org/10.1109/LSP.2014.2321791	<i>N. Xi and L. Liping</i>	971
Condition Number-Constrained Matrix Approximation With Applications to Signal Estimation in Communication Systems http://dx.doi.org/10.1109/LSP.2014.2322113	<i>J. Tong, Q. Guo, S. Tong, J. Xi, and Y. Yu</i>	990
Asymptotic Performance of Categorical Decision Making with Random Thresholds http://dx.doi.org/10.1109/LSP.2014.2321474	<i>T. Wimalajeewa and P. K. Varshney</i>	994
Multichannel Detection of an Unknown Rank-N Signal Using Uncalibrated Receivers http://dx.doi.org/10.1109/LSP.2014.2322514	<i>D. E. Hack, C. W. Rossler, and L. K. Patton</i>	998

IEEE SignalProcessing

MAGAZINE

[VOLUME 31 NUMBER 4 JULY 2014]



SYNTHETIC APERTURE RADAR IMAGING

PROGRESS AND
CUTTING-EDGE RESEARCH

650.0 (m) 740.0

LONG-WAVE INFRARED HYPERSPECTRAL
REMOTE SENSING OF CHEMICAL CLOUDS

EFFECTIVE FEATURE EXTRACTION AND
DATA REDUCTION IN REMOTE SENSING USING HSI

OPTIMAL MULTIUSER TRANSMIT BEAMFORMING

IEEE
Signal Processing Society

IEEE

CONTENTS

[VOLUME 31 NUMBER 4]

SPECIAL SECTION—SYNTHETIC APERTURE RADAR IMAGING

15 FROM THE GUEST EDITORS

Joachim Ender, Moeness G. Amin,
Gianfranco Fornaro,
and Paul A. Rosen

16 WIDE-ANGLE SYNTHETIC APERTURE RADAR IMAGING

Joshua N. Ash, Emre Ertin,
Lee C. Potter, and Edmund G. Zelnio

27 SPARSITY-DRIVEN SYNTHETIC APERTURE RADAR IMAGING

Müjdat Çetin, Ivana Stojanović,
N. Özben Önhon, Kush R. Varshney,
Sadeq Samadi, W. Clem Karl,
and Alan S. Willsky

41 TOMOGRAPHIC PROCESSING OF INTERFEROMETRIC SAR DATA

Gianfranco Fornaro, Fabrizio
Lombardini, Antonio Pauciuolo,
Diego Reale, and Federico Viviani

51 SUPERRESOLVING SAR TOMOGRAPHY FOR MULTIDIMENSIONAL IMAGING OF URBAN AREAS

Xiao Xiang Zhu and Richard Bamler

59 CONTEXTUAL INFORMATION-BASED MULTICHANNEL SYNTHETIC APERTURE RADAR INTERFEROMETRY

Fabio Baselice, Giampaolo Ferraioli,
Vito Pascazio, and Gilda Schirinzi

69 EXPLOITING PATCH SIMILARITY FOR SAR IMAGE PROCESSING

Charles-Alban Deledalle,
Loïc Denis, Giovanni Poggi,
Florence Tupin, and Luisa Verdoliva

79 MODELING AND INTERPRETATION OF SCATTERING MECHANISMS IN POLARIMETRIC SYNTHETIC APERTURE RADAR

Si-Wei Chen, Yong-Zhen Li,
Xue-Song Wang, Shun-Ping Xiao,
and Motoyuki Sato

90 SAR IMAGING ALGORITHMS AND SOME UNCONVENTIONAL APPLICATIONS

Raffaele Solimene, Iliara Catapano,
Gianluca Gennarelli, Antonio Cuccaro,
Angela Dell'Aversano,
and Francesco Soldovieri

99 THE TIME-REVERSAL TECHNIQUE FOR SAR FOCUSING OF BURIED TARGETS

Robert Kedzierawski,
Jean-Marc Le Caillec,
and Witold Czarnecki

110 MULTIPATH EXPLOITATION AND SUPPRESSION FOR SAR IMAGING OF BUILDING INTERIORS

Michael Leigsnering,
Moeness G. Amin, Fauzia Ahmad,
and Abdelhak M. Zoubir

FEATURE

120 LONG-WAVE INFRARED HYPERSPECTRAL REMOTE SENSING OF CHEMICAL CLOUDS

Dimitris G. Manolakis,
Steven E. Golowich,
and Robert S. DiPietro

COLUMNS

4 FROM THE EDITOR

Signal Processing: Is it Time
to Change the Society's Name?
Abdelhak Zoubir

6 PRESIDENT'S MESSAGE

At the Forefront in Technical
Publications
Alex Acero

8 READER'S CHOICE

Top Downloads in IEEE *Xplore*

10 SPECIAL REPORTS

Signal Processing: On the Edge
of Astronomy's New Frontier
John Edwards

Health Alliance Boosts Influence
in Standards Development
Ron Schneiderman

142 LECTURE NOTES

Optimal Multiuser Transmit
Beamforming: A Difficult Problem
with a Simple Solution Structure
Emil Björnson, Mats Bengtsson,
and Björn Ottersten

149 APPLICATIONS CORNER

Effective Feature Extraction and Data
Reduction in Remote Sensing Using
Hyperspectral Imaging
Jinchang Ren, Jaime Zabalza,
Stephen Marshall, and Jiangbin Zheng

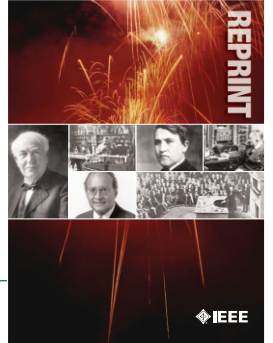
155 LIFE SCIENCES

Signal Processing in Visual Optics
D. Robert Iskander

DEPARTMENT

159 DATES AHEAD

Digital Object Identifier 10.1109/MSP.2014.2311859



IEEE ORDER FORM FOR REPRINTS

Purchasing IEEE Papers in Print is easy, cost-effective and quick.

Complete this form, tear it out, and either fax it (24 hours a day) to 732-981-8062 or mail it back to us.

PLEASE FILL OUT THE FOLLOWING

Author: _____

Publication Title: _____

Paper Title: _____

RETURN THIS FORM TO:
 IEEE Publishing Services
 445 Hoes Lane
 Box 1331
 Piscataway, NJ 08855-1331
Call Reprint Department at (732) 562-3941
for questions regarding this form
(732) 981-8062 - FAX

PLEASE SEND ME

- 50 100 200 300 400 500 or _____ (in multiples of 50) reprints.
- YES NO Self-covering/title page required. COVER PRICE: \$74 per 100, \$39 per 50.
- \$58.00 Air Freight must be added for all orders being shipped outside the U.S.
- \$18.50 must be added for all USA shipments to cover the cost of UPS shipping and handling.

PAYMENT

Check enclosed. Payable on a bank in the USA.

Charge my: Visa Mastercard Amex Diners Club

Account # _____ Exp. date _____

Cardholder's Name (please print): _____

Bill me (you must attach a purchase order) Purchase Order Number _____

Send Reprints to: _____ Bill to address, if different: _____

Because information and papers are gathered from various sources, there may be a delay in receiving your reprint request. This is especially true with postconference publications. Please provide us with contact information if you would like notification of a delay of more than 12 weeks.

Telephone: _____ Fax: _____ Email Address: _____

2011 REPRINT PRICES (without covers)

Number of Text Pages

	1-4	5-8	9-12	13-16	17-20	21-24	25-28	29-32	33-36	37-40	41-44	45-48
50	\$126	\$211	\$243	\$245	\$285	\$340	\$371	\$408	\$440	\$477	\$510	\$543
100	\$242	\$423	\$476	\$492	\$570	\$680	\$742	\$817	\$885	\$953	\$1021	\$1088

Larger quantities can be ordered. Email reprints@ieee.org with specific details.

Tax Applies on shipments of regular reprints to CA, DC, FL, MI, NJ, NY, OH and Canada (GST Registration no. 12534188).
 Prices are based on black & white printing. Please call us for full color price quote, if applicable.

Authorized Signature: _____ Date: _____



2014 IEEE MEMBERSHIP APPLICATION

(students and graduate students must apply online)



Start your membership immediately: Join online www.ieee.org/join

Please complete both sides of this form, typing or **printing in capital letters**. Use only English characters and abbreviate only if more than 40 characters and spaces per line. We regret that incomplete applications cannot be processed.

1 Name & Contact Information

Please PRINT your name as you want it to appear on your membership card and IEEE correspondence. As a key identifier for the IEEE database, circle your last/surname.

Male Female Date of birth (Day/Month/Year) ____/____/____

Title First/Given Name Middle Last/Family Surname

▼ Primary Address Home Business (All IEEE mail sent here)

Street Address

City State/Province

Postal Code Country

Primary Phone

Primary E-mail

▼ Secondary Address Home Business

Company Name Department/Division

Street Address City State/Province

Postal Code Country

Secondary Phone

Secondary E-mail

To better serve our members and supplement member dues, your postal mailing address is made available to carefully selected organizations to provide you with information on technical services, continuing education, and conferences. Your e-mail address is not rented by IEEE. Please check box only if you do not want to receive these postal mailings to the selected address.

2 Attestation

I have graduated from a three- to five-year academic program with a university-level degree. Yes No

This program is in one of the following fields of study:

- Engineering
- Computer Sciences and Information Technologies
- Physical Sciences
- Biological and Medical Sciences
- Mathematics
- Technical Communications, Education, Management, Law and Policy
- Other (please specify): _____

This academic institution or program is accredited in the country where the institution is located. Yes No Do not know

I have _____ years of professional experience in teaching, creating, developing, practicing, or managing within the following field:

- Engineering
- Computer Sciences and Information Technologies
- Physical Sciences
- Biological and Medical Sciences
- Mathematics
- Technical Communications, Education, Management, Law and Policy
- Other (please specify): _____

3 Please Tell Us About Yourself

Select the numbered option that best describes yourself. This information is used by IEEE magazines to verify their annual circulation. Please enter numbered selections in the boxes provided.

A. Primary line of business

1. Computers
2. Computer peripheral equipment
3. Software
4. Office and business machines
5. Test, measurement and instrumentation equipment
6. Communications systems and equipment
7. Navigation and guidance systems and equipment
8. Consumer electronics/appliances
9. Industrial equipment, controls and systems
10. ICs and microprocessors
11. Semiconductors, components, sub-assemblies, materials and supplies
12. Aircraft, missiles, space and ground support equipment
13. Oceanography and support equipment
14. Medical electronic equipment
15. OEM incorporating electronics in their end product (not elsewhere classified)
16. Independent and university research, test and design laboratories and consultants (not connected with a mfg. co.)
17. Government agencies and armed forces
18. Companies using and/or incorporating any electronic products in their manufacturing, processing, research or development activities
19. Telecommunications services, telephone (including cellular)
20. Broadcast services (TV, cable, radio)
21. Transportation services (airline, railroad, etc.)
22. Computer and communications and data processing services
23. Power production, generation, transmission and distribution
24. Other commercial users of electrical, electronic equipment and services (not elsewhere classified)
25. Distributor (reseller, wholesaler, retailer)
26. University, college/other educational institutions, libraries
27. Retired
28. Other _____

B. Principal job function

- | | |
|--|---|
| 1. General and corporate management | 9. Design/development engineering—digital |
| 2. Engineering management | 10. Hardware engineering |
| 3. Project engineering management | 11. Software design/development |
| 4. Research and development management | 12. Computer science |
| 5. Design engineering management— <u>analog</u> | 13. Science/physics/mathematics |
| 6. Design engineering management— <u>digital</u> | 14. Engineering (not elsewhere specified) |
| 7. Research and development engineering | 15. Marketing/sales/purchasing |
| 8. Design/development engineering— <u>analog</u> | 16. Consulting |
| | 17. Education/teaching |
| | 18. Retired |
| | 19. Other _____ |

C. Principal responsibility

- | | |
|--|-----------------------|
| 1. Engineering and scientific management | 6. Education/teaching |
| 2. Management other than engineering | 7. Consulting |
| 3. Engineering design | 8. Retired |
| 4. Engineering | 9. Other _____ |
| 5. Software: science/mngmnt/engineering | |

D. Title

- | | |
|--|--------------------------------|
| 1. Chairman of the Board/President/CEO | 10. Design Engineering Manager |
| 2. Owner/Partner | 11. Design Engineer |
| 3. General Manager | 12. Hardware Engineer |
| 4. VP Operations | 13. Software Engineer |
| 5. VP Engineering/Dir. Engineering | 14. Computer Scientist |
| 6. Chief Engineer/Chief Scientist | 15. Dean/Professor/Instructor |
| 7. Engineering Management | 16. Consultant |
| 8. Scientific Management | 17. Retired |
| 9. Member of Technical Staff | 18. Other _____ |

Are you now or were you ever a member of IEEE?

Yes No If yes, provide, if known:

Membership Number Grade Year Expired

4 Please Sign Your Application

I hereby apply for IEEE membership and agree to be governed by the IEEE Constitution, Bylaws, and Code of Ethics. I understand that IEEE will communicate with me regarding my individual membership and all related benefits. **Application must be signed.**

Signature _____ Date _____ *Over Please*

Information for Authors

(Updated March 2012)

The IEEE TRANSACTIONS are published monthly covering advances in the theory and application of signal processing. The scope is reflected in the EDICS: the Editor's Information and Classification Scheme. Please consider the journal with the most appropriate scope for your submission.

Authors are encouraged to submit manuscripts of Regular papers (papers which provide a complete disclosure of a technical premise), or Correspondences (brief items that describe a use for or magnify the meaning of a single technical point, or provide comment on a paper previously published in the TRANSACTIONS). Submissions/resubmissions must be previously unpublished and may not be under consideration elsewhere.

Every manuscript must (a) provide a clearly defined statement of the problem being addressed, (b) state why it is important to solve the problem, and (c) give an indication as to how the current solution fits into the history of the problem.

By submission/resubmission of your manuscript to this TRANSACTIONS, you are acknowledging that you accept the rules established for publication of manuscripts, including agreement to pay all overlength page charges, color charges, and any other charges and fees associated with publication of the manuscript. Such charges are not negotiable and cannot be suspended.

New and revised manuscripts should be prepared following the "New Manuscript Submission" guidelines below, and submitted to the online manuscript system ScholarOne Manuscripts. After acceptance, finalized manuscripts should be prepared following the "Final Manuscript Submission Guidelines" below. Do not send original submissions or revisions directly to the Editor-in-Chief or Associate Editors; they will access your manuscript electronically via the ScholarOne Manuscripts system.

New Manuscript Submission. Please follow the next steps.

1. *Account in ScholarOne Manuscripts.* If necessary, create an account in the on-line submission system ScholarOne Manuscripts. Please check first if you already have an existing account which is based on your e-mail address and may have been created for you when you reviewed or authored a previous paper.
2. *Electronic Manuscript.* Prepare a PDF file containing your manuscript in double-spaced format (one full blank line between lines of type) using a font size of 11 points or larger, having a margin of at least 1 inch on all sides. For a regular paper, the manuscript may not exceed 30 double-spaced pages, including title; names of authors and their complete contact information; abstract; text; all images, figures and tables; and all references. Upload your manuscript as a PDF file "manuscript.pdf" to the ScholarOne Manuscripts site, then proofread your submission, confirming that all figures and equations are visible in your document before you "SUBMIT" your manuscript. Proofreading is critical; once you submit your manuscript, the manuscript cannot be changed in any way. You may also submit your manuscript as a PostScript or MS Word file. The system has the capability of converting your files to PDF, however it is your responsibility to confirm that the conversion is correct and there are no font or graphics issues prior to completing the submission process.
3. *Double-Column Version of Manuscript.* You are required to also submit a roughly formatted version of the manuscript in single-spaced, double column IEEE format (10 points for a regular submission or 9 points for a Correspondence) using the IEEE style files (it is allowed to let long equations stick out). *If accepted for publication*, over length page charges are levied beginning with the 11th published page of your manuscript. You are, therefore, advised to be conservative in your submission. This double-column version submitted will serve as a confirmation of the approximate publication length of the manuscript and gives an additional confirmation of your understanding that over length page charges will be paid when billed upon publication.

Upload this version of the manuscript as a PDF file "double.pdf" to the ScholarOneManuscripts site.

4. *Additional Material for Review.* Please upload pdf versions of all items in the reference list which are not publicly available, such as unpublished (submitted) papers. Other materials for review such as supplementary tables and figures, audio fragments and QuickTime movies may be uploaded as well. Reviewers will be able to view these files only if they have the appropriate software on their computers. Use short filenames without spaces or special characters. When the upload of each file is completed, you will be asked to provide a description of that file.
5. *Submission.* After uploading all files and proofreading them, submit your manuscript by clicking "Submit." A confirmation of the successful submission will open on screen containing the manuscript tracking number and will be followed with an e-mail confirmation to the corresponding and all contributing authors. Once you click "Submit," your manuscript cannot be changed in any way.

6. *Copyright Form and Consent Form.* By policy, IEEE owns the copyright to the technical contributions it publishes on behalf of the interests of the IEEE, its authors, and their employers; and to facilitate the appropriate reuse of this material by others. To comply with the IEEE copyright policies, authors are required to sign and submit a completed "IEEE Copyright and Consent Form" prior to publication by the IEEE.

The IEEE recommends authors to use an effective electronic copyright form (eCF) tool within the ScholarOne Manuscripts system. You will be redirected to the "IEEE Electronic Copyright Form" wizard at the end of your original submission; please simply sign the eCF by typing your name at the proper location and click on the "Submit" button.

Correspondence Items. Correspondence items are short disclosures with a reduced scope or significance that typically describe a use for or magnify the meaning of a single technical point, or provide brief comments on material previously published in the TRANSACTIONS. These items may not exceed 12 pages in double-spaced format (3 pages for Comments), using 11 point type, with margins of 1 inch minimum on all sides, and including: title, names and contact information for authors, abstract, text, references, and an appropriate number of illustrations and/or tables. Correspondence items are submitted in the same way as regular manuscripts (see "New Manuscript Submission" above for instructions).

Manuscript Length. Papers published on or after 1 January 2007 can now be up to 10 pages, and any paper in excess of 10 pages will be subject to over length page charges. The IEEE Signal Processing Society has determined that the standard manuscript length shall be no more than 10 published pages (double-column format, 10 point type) for a regular submission, or 6 published pages (9 point type) for a Correspondence item, respectively. Manuscripts that exceed these limits will incur mandatory over length page charges, as discussed below. Since changes recommended as a result of peer review may require additions to the manuscript, it is strongly recommended that you practice economy in preparing original submissions.

Exceptions to the 30-page (regular paper) or 12-page (Correspondences) manuscript length may, under extraordinary circumstances, be granted by the Editor-in-Chief. However, such exception does not obviate your requirement to pay any and all over length or additional charges that attach to the manuscript.

Resubmission of Previously Rejected Manuscripts. Authors of rejected manuscripts are allowed to resubmit their manuscripts only once. The Signal Processing Society strongly discourages resubmission of rejected manuscripts more than once. At the time of submission, you will be asked whether you consider your manuscript to be a new submission or a resubmission of an earlier rejected manuscript. If you choose to submit a new version of your manuscript, you will be asked to submit supporting documents detailing how your new version addresses all of the reviewers' comments.

Full details of the resubmission process can be found in the Signal Processing Society "Policy and Procedures Manual" at <http://www.signalprocessingsociety.org/about/governance/policy-procedure/>. Also, please refer to the decision letter and your Author Center on the on-line submission system.

Author Misconduct.

Author Misconduct Policy: Plagiarism includes copying someone else's work without appropriate credit, using someone else's work without clear delineation of citation, and the uncited reuse of an authors previously published work that also involves other authors. Plagiarism is unacceptable.

Self-plagiarism involves the verbatim copying or reuse of an authors own prior work without appropriate citation; it is also unacceptable. Self-plagiarism includes duplicate submission of a single journal manuscript to two different journals, and submission of two different journal manuscripts which overlap substantially in language or technical contribution.

Authors may only submit original work that has not appeared elsewhere in a journal publication, nor is under review for another journal publication. Limited overlap with prior journal publications with a common author is allowed only if it is necessary for the readability of the paper. If authors have used their own previously published work as a basis for a new submission, they are required to cite the previous work and very briefly indicate how the new submission offers substantively novel contributions beyond those of the previously published work.

It is acceptable for conference papers to be used as the basis for a more fully developed journal submission. Still, authors are required to cite related prior work; the papers cannot be identical; and the journal publication must include novel aspects.

Author Misconduct Procedures: The procedures that will be used by the Signal Processing Society in the investigation of author misconduct allegations are described in the IEEE SPS Policies and Procedures Manual.

Author Misconduct Sanctions: The IEEE Signal Processing Society will apply the following sanctions in any case of plagiarism, or in cases of self-plagiarism that involve an overlap of more than 25% with another journal manuscript:

- 1) immediate rejection of the manuscript in question;
- 2) immediate withdrawal of all other submitted manuscripts by any of the authors, submitted to any of the Society's publications (journals, conferences, workshops), except for manuscripts that also involve innocent co-authors; immediate withdrawal of all other submitted manuscripts by any of the authors, submitted to any of the Society's publications (journals, conferences, workshops), except for manuscripts that also involve innocent co-authors;
- 3) prohibition against each of the authors for any new submissions, either individually, in combination with the authors of the plagiarizing manuscript, or in combination with new co-authors, to all of the Society's publications (journals, conferences, workshops). The prohibition shall continue for one year from notice of suspension.

Further, plagiarism and self-plagiarism may also be actionable by the IEEE under the rules of Member Conduct.

Submission Format.

Authors are encouraged to prepare manuscripts employing the on-line style files developed by IEEE. All manuscripts accepted for publication will require the authors to make final submission employing these style files. The style files are available on the web at http://www.ieee.org/publications_standards/publications/authors/authors_journals.html#sect2 under "Template for all Transactions." (LaTeX and MS Word).

Authors using LaTeX: the two PDF versions of the manuscript needed for submission can both be produced by the IEEEtran.cls style file. A double-spaced document is generated by including `\documentclass[11pt,draftcls,onecolumn]{IEEEtran}` as the first line of the manuscript source file, and a single-spaced double-column document for estimating the publication page charges via `\documentclass[10pt,twocolumn,twoside]{IEEEtran}` for a regular submission, or `\documentclass[9pt,twocolumn,twoside]{IEEEtran}` for a Correspondence item.

- **Title page and abstract:** The first page of the manuscript shall contain the title, names and contact information for all authors (full mailing address, institutional affiliations, phone, fax, and e-mail), the abstract, and the EDICS. An asterisk * should be placed next to the name of the Corresponding Author who will serve as the main point of contact for the manuscript during the review and publication processes.

An abstract should have not more than 200 words for a regular paper, or 50 words for a Correspondence item. The abstract should indicate the scope of the paper or Correspondence, and summarize the author's conclusions. This will make the abstract, by itself, a useful tool for information retrieval.

- **EDICS:** All submissions must be classified by the author with an EDICS (Editors' Information Classification Scheme) selected from the list of EDICS published online at <http://www.signalprocessingsociety.org/publications/periodicals/tsp/TSP-EDICS/>
- **NOTE:** EDICS are necessary to begin the peer review process. Upon submission of a new manuscript, please choose the EDICS categories that best suit your manuscript. Failure to do so will likely result in a delay of the peer review process.
- The EDICS category should appear on the first page—i.e., the title and abstract page—of the manuscript.
- **Illustrations and tables:** Each figure and table should have a caption that is intelligible without requiring reference to the text. Illustrations/tables may be worked into the text of a newly-submitted manuscript, or placed at the end of the manuscript. (However, for the final submission, illustrations/tables must be submitted separately and not interwoven with the text.)

Illustrations in color may be used but, unless the final publishing will be in color, the author is responsible that the corresponding grayscale figure is understandable.

In preparing your illustrations, note that in the printing process, most illustrations are reduced to single-column width to conserve space. This may result in as much as a 4:1 reduction from the original. Therefore, make sure that all words are in a type size that will reduce to a minimum of 9 points or 3/16 inch high in the printed version. Only the major grid lines on graphs should be indicated.

- **Abbreviations:** This TRANSACTIONS follows the practices of the IEEE on units and abbreviations, as outlined in the Institute's published standards. See http://www.ieee.org/portal/cms_docs_iportals/iportals/publications/authors/transjnl/aunifo07.pdf for details.
- **Mathematics:** All mathematical expressions must be legible. Do not give derivations that are easily found in the literature; merely cite the reference.

Final Manuscript Submission Guidelines.

Upon formal acceptance of a manuscript for publication, instructions for providing the final materials required for publication will be sent to the Corresponding Author. Finalized manuscripts should be prepared in LaTeX or MS Word, and are required to use the style files established by IEEE, available at http://www.ieee.org/publications_standards/publications/authors/authors_journals.html#sect2.

Instructions for preparing files for electronic submission are as follows:

- Files must be self-contained; that is, there can be no pointers to your system setup.
- Include a header to identify the name of the TRANSACTIONS, the name of the author, and the software used to format the manuscript.
- Do not import graphics files into the text file of your finalized manuscript (although this is acceptable for your initial submission). If submitting on disk, use a separate disk for graphics files.
- Do not create special macros.
- Do not send PostScript files of the text.
- File names should be lower case.
- Graphics files should be separate from the text, and not contain the caption text, but include callouts like "(a)," "(b)."
- Graphics file names should be lower case and named fig1.eps, fig2.tif, etc.
- Supported graphics types are EPS, PS, TIFF, or graphics created using Word, Powerpoint, Excel or PDF. Not acceptable is GIF, JPEG, WMF, PNG, BMP or any other format (JPEG is accepted for author photographs only). The provided resolution needs to be at least 600 dpi (400 dpi for color).
- Please indicate explicitly if certain illustrations should be printed in color; note that this will be at the expense of the author. Without other indications, color graphics will appear in color in the online version, but will be converted to grayscale in the print version.

Additional instructions for preparing, verifying the quality, and submitting graphics are available via http://www.ieee.org/publications_standards/publications/authors/authors_journals.html.

Multimedia Materials.

IEEE Xplore can publish multimedia files and Matlab code along with your paper. Alternatively, you can provide the links to such files in a README file that appears on Xplore along with your paper. For details, please see http://www.ieee.org/publications_standards/publications/authors/authors_journals.html#sect6 under "Multimedia." To make your work reproducible by others, the TRANSACTIONS encourages you to submit all files that can recreate the figures in your paper.

Page Charges.

Voluntary Page Charges. Upon acceptance of a manuscript for publication, the author(s) or his/her/their company or institution will be asked to pay a charge of \$110 per page to cover part of the cost of publication of the first ten pages that comprise the standard length (six pages, in the case of Correspondences).

Mandatory Page Charges. The author(s) or his/her/their company or institution will be billed \$220 per each page in excess of the first ten published pages for regular papers and six published pages for correspondence items. These are mandatory page charges and the author(s) will be held responsible for them. They are not negotiable or voluntary. The author(s) signifies his willingness to pay these charges simply by submitting his/her/their manuscript to the TRANSACTIONS. The Publisher holds the right to withhold publication under any circumstance, as well as publication of the current or future submissions of authors who have outstanding mandatory page charge debt.

Color Charges. Color figures which appear in color only in the electronic (Xplore) version can be used free of charge. In this case, the figure will be printed in the hardcopy version in grayscale, and the author is responsible that the corresponding grayscale figure is intelligible. Color reproduction in print is expensive, and all charges for color are the responsibility of the author. The estimated costs are as follows. There will be a charge of \$62.50 for each figure; this charge may be subject to change without notification. In addition, there are printing preparation charges which may be estimated as follows: color reproductions on four or fewer pages of the manuscript: a total of approximately \$1045; color reproductions on five pages through eight pages: a total of approximately \$2090; color reproductions on nine through 12 pages: a total of approximately \$3135, and so on. Payment of fees on color reproduction is not negotiable or voluntary, and the author's agreement to publish the manuscript in the TRANSACTIONS is considered acceptance of this requirement.

To find the Information for Authors for IEEE Signal Processing Letters, the IEEE Journal of Selected Topics in Signal Processing or the IEEE Signal Processing Magazine, please refer to the IEEE Signal Processing website at www.signalprocessingsociety.org.

2014 IEEE SIGNAL PROCESSING SOCIETY MEMBERSHIP APPLICATION

(Current and reinstating IEEE members joining SPS complete areas 1, 2, 8, 9.)
 Mail to: IEEE OPERATIONS CENTER, ATTN: Louis Curcio, Member and Geographic Activities, 445 Hoes Lane, Piscataway, New Jersey 08854 USA
 or Fax to (732) 981-0225 (credit card payments only.)
 For info call (732) 981-0060 or 1 (800) 678-IEEE or E-mail: new.membership@ieee.org



1. PERSONAL INFORMATION

NAME AS IT SHOULD APPEAR ON IEEE MAILINGS: SEND MAIL TO: Home Address OR Business/School Address
 If not indicated, mail will be sent to home address. Note: Enter your name as you wish it to appear on membership card and all correspondence.
PLEASE PRINT Do not exceed 40 characters or spaces per line. Abbreviate as needed. Please circle your last/surname as a key identifier for the IEEE database.

TITLE	FIRST OR GIVEN NAME	MIDDLE NAME	SURNAME/LAST NAME
HOME ADDRESS			
CITY		STATE/PROVINCE	POSTAL CODE
			COUNTRY

2. Are you now or were you ever a member of IEEE? Yes No
 If yes, please provide, if known:

MEMBERSHIP NUMBER _____
 Grade _____ Year Membership Expired: _____

3. BUSINESS/PROFESSIONAL INFORMATION

Company Name _____
 Department/Division _____
 Title/Position _____ Years in Current Position _____
 Years in the Profession Since Graduation _____ PE State/Province _____
 Street Address _____
 City _____ State/Province _____ Postal Code _____ Country _____

4. EDUCATION A baccalaureate degree from an IEEE recognized educational program assures assignment of "Member" grade. For others, additional information and references may be necessary for grade assignment.

A. Baccalaureate Degree Received _____ Program/Course of Study _____
 College/University _____ Campus _____
 State/Province _____ Country _____ Mo./Yr. Degree Received _____

B. Highest Technical Degree Received _____ Program/Course of Study _____
 College/University _____ Campus _____
 State/Province _____ Country _____ Mo./Yr. Degree Received _____

5. Full signature of applicant _____

6. DEMOGRAPHIC INFORMATION – ALL APPLICANTS -

Date Of Birth _____ Male Female
 Day _____ Month _____ Year _____

7. CONTACT INFORMATION

Office Phone/Office Fax _____ Home Phone/Home Fax _____
 Office E-Mail _____ Home E-Mail _____

8. 2014 IEEE MEMBER RATES

IEEE DUES	16 Aug-28 Feb Pay Full Year	1 Mar-15 Aug 14 Pay Half Year**
Residence		
United States	\$187.00 <input type="checkbox"/>	\$93.50 <input type="checkbox"/>
Canada (incl. GST)	\$168.10 <input type="checkbox"/>	\$84.05 <input type="checkbox"/>
Canada (incl. HST for NB, NF and ON)	\$179.46 <input type="checkbox"/>	\$89.73 <input type="checkbox"/>
Canada (incl. HST for Nova Scotia)	\$182.30 <input type="checkbox"/>	\$91.15 <input type="checkbox"/>
Canada (incl. HST for PEI)	\$180.88 <input type="checkbox"/>	\$90.44 <input type="checkbox"/>
Africa, Europe, Middle East	\$155.00 <input type="checkbox"/>	\$77.50 <input type="checkbox"/>
Latin America	\$146.00 <input type="checkbox"/>	\$73.00 <input type="checkbox"/>
Asia, Pacific	\$147.00 <input type="checkbox"/>	\$73.50 <input type="checkbox"/>

Canadian Taxes (GST/HST): All supplies, which include dues, Society membership fees, online products and publications (except CD-ROM and DVD media), shipped to locations within Canada are subject to the GST of 5% or the HST of 13%, 14% or 15%, depending on the Province to which the materials are shipped. GST and HST do not apply to Regional Assessments. (IEEE Canadian Business Number 12563 4188 RT0001)
Value Added Tax (VAT) in the European Union: In accordance with the European Union Council Directives 2002/38/EC and 77/388/EEC amended by Council Regulation (EC)792/2002, IEEE is required to charge and collect VAT on electronic/digitized products sold to private consumers that reside in the European Union. The VAT rate applied is the EU member country standard rate where the consumer is resident. (IEEE's VAT registration number is EU826000081)
U.S. Sales Taxes: Please add applicable state and local sales and use tax on orders shipped to **Alabama, Arizona, California, Colorado, District of Columbia, Florida, Georgia, Illinois, Indiana, Kentucky, Massachusetts, Maryland, Michigan, Minnesota, Missouri, New Jersey, New Mexico, New York, North Carolina, Ohio, Oklahoma, West Virginia, Wisconsin.** Customers claiming a tax exemption must include an appropriate and properly completed tax-exemption certificate with their first order.



2014 SPS MEMBER RATES

	16 Aug-28 Feb Pay Full Year	1 Mar-15 Aug Pay Half Year
Signal Processing Society Membership Fee*	\$ 20.00 <input type="checkbox"/>	\$ 10.00 <input type="checkbox"/>
Fee includes: IEEE Signal Processing Magazine (electronic and digital), Inside Signal Processing eNewsletter (electronic) and IEEE Signal Processing Society Content Gazette (electronic).		
Add \$15 to enhance SPS Membership and also receive:	\$ 15.00 <input type="checkbox"/>	\$ 7.50 <input type="checkbox"/>
IEEE Signal Processing Magazine (print) and SPS Digital Library: online access to Signal Processing Magazine, Signal Processing Letters, Journal of Selected Topics in Signal Processing, Trans. on Audio, Speech, and Language Processing, Trans. on Image Processing, Trans. on Information Forensics and Security and Trans. on Signal Processing.		
<i>Publications available only with SPS membership:</i>		
Signal Processing, IEEE Transactions on:	Print \$190.00 <input type="checkbox"/>	\$95.00 <input type="checkbox"/>
Audio, Speech, and Language Proc., IEEE/ACM Trans. on:	Print \$145.00 <input type="checkbox"/>	\$72.50 <input type="checkbox"/>
Image Processing, IEEE Transactions on:	Print \$188.00 <input type="checkbox"/>	\$94.00 <input type="checkbox"/>
Information Forensics and Security, IEEE Trans. on:	Print \$163.00 <input type="checkbox"/>	\$81.50 <input type="checkbox"/>
IEEE Journal of Selected Topics in Signal Processing:	Print \$160.00 <input type="checkbox"/>	\$80.00 <input type="checkbox"/>
Affective Computing, IEEE Transactions on:	Electronic \$33.00 <input type="checkbox"/>	\$16.50 <input type="checkbox"/>
Biomedical and Health Informatics, IEEE Journal of:	Print \$55.00 <input type="checkbox"/>	\$27.50 <input type="checkbox"/>
	Electronic \$40.00 <input type="checkbox"/>	\$20.00 <input type="checkbox"/>
	Print & Electronic \$65.00 <input type="checkbox"/>	\$32.50 <input type="checkbox"/>
IEEE Cloud Computing	Electronic and Digital \$39.00 <input type="checkbox"/>	\$19.50 <input type="checkbox"/>
Computing in Science & Engineering:	Electronic and Digital \$45.00 <input type="checkbox"/>	\$22.50 <input type="checkbox"/>
	Print & Electronic \$49.00 <input type="checkbox"/>	\$24.50 <input type="checkbox"/>
Medical Imaging, IEEE Transactions on:	Print \$74.00 <input type="checkbox"/>	\$37.00 <input type="checkbox"/>
	Electronic \$53.00 <input type="checkbox"/>	\$26.50 <input type="checkbox"/>
	Print & Electronic \$89.00 <input type="checkbox"/>	\$44.50 <input type="checkbox"/>
Mobile Computing, IEEE Trans. on:	ELE/Print Abstract/CD-ROM \$36.00 <input type="checkbox"/>	\$18.00 <input type="checkbox"/>
Multimedia, IEEE Transactions on:	Electronic \$42.00 <input type="checkbox"/>	\$21.00 <input type="checkbox"/>
IEEE MultiMedia Magazine:	Electronic and Digital \$45.00 <input type="checkbox"/>	\$22.50 <input type="checkbox"/>
	Print & Electronic \$49.00 <input type="checkbox"/>	\$24.50 <input type="checkbox"/>
Network Science and Engrg, IEEE Trans. on:	Electronic \$32.00 <input type="checkbox"/>	\$16.00 <input type="checkbox"/>
IEEE Reviews in Biomedical Engineering:	Print \$25.00 <input type="checkbox"/>	\$12.50 <input type="checkbox"/>
	Electronic \$25.00 <input type="checkbox"/>	\$12.50 <input type="checkbox"/>
	Print & Electronic \$40.00 <input type="checkbox"/>	\$20.00 <input type="checkbox"/>
IEEE Security and Privacy Magazine:	Electronic and Digital \$45.00 <input type="checkbox"/>	\$22.50 <input type="checkbox"/>
	Print and Electronic \$49.00 <input type="checkbox"/>	\$24.50 <input type="checkbox"/>
IEEE Biometrics Compendium	Online \$30.00 <input type="checkbox"/>	\$15.00 <input type="checkbox"/>
IEEE Sensors Journal:	Print \$150.00 <input type="checkbox"/>	\$75.00 <input type="checkbox"/>
	Electronic \$50.00 <input type="checkbox"/>	\$25.00 <input type="checkbox"/>
	Print & Electronic \$190.00 <input type="checkbox"/>	\$95.00 <input type="checkbox"/>
Smart Grid, IEEE Transactions on:	Print \$100.00 <input type="checkbox"/>	\$50.00 <input type="checkbox"/>
	Electronic \$40.00 <input type="checkbox"/>	\$20.00 <input type="checkbox"/>
	Print & Electronic \$120.00 <input type="checkbox"/>	\$60.00 <input type="checkbox"/>
IEEE Transactions on Engineering Management:	Print & Electronic \$39.00 <input type="checkbox"/>	\$19.50 <input type="checkbox"/>
IEEE Engineering Management Review:	Print & Electronic \$29.00 <input type="checkbox"/>	\$14.50 <input type="checkbox"/>
IEEE Technology Management Package:	Print & Electronic \$60.00 <input type="checkbox"/>	\$30.00 <input type="checkbox"/>
Wireless Communications, IEEE Transactions on:	Print \$87.00 <input type="checkbox"/>	\$43.50 <input type="checkbox"/>
	Electronic \$42.00 <input type="checkbox"/>	\$21.00 <input type="checkbox"/>
	Print & Electronic \$87.00 <input type="checkbox"/>	\$43.50 <input type="checkbox"/>
IEEE Wireless Communications Letters:	Print \$80.00 <input type="checkbox"/>	\$40.00 <input type="checkbox"/>
	Electronic \$18.00 <input type="checkbox"/>	\$9.00 <input type="checkbox"/>
	Print & Electronic \$95.00 <input type="checkbox"/>	\$47.50 <input type="checkbox"/>

*IEEE membership required or requested
 Affiliate application to join SP Society only. Amount Paid \$ _____

9. IEEE Membership Dues (See pricing in Section 8)

Signal Processing Society Fees \$ _____
 Canadian residents pay 5% GST or 13% HST
 Reg. No. 125634188 on Society payment(s) & pubs only Tax \$ _____
AMOUNT PAID WITH APPLICATION TOTAL \$ _____

Prices subject to change without notice.
 Check or money order enclosed Payable to IEEE on a U.S. Bank
 American Express VISA MasterCard
 Diners Club

Exp. Date	Mo./Yr.								
Cardholder's Digit Zip Code Billing Statement Address/USA Only									

Full signature of applicant using credit card _____ Date _____

10. WERE YOU REFERRED?

Yes No If yes, please provide the following information:
 Member Recruiter Name: _____
 IEEE Recruiter's Member Number (Required): _____



2014 IEEE International Workshop on Genomic Signal Processing and Statistics at **GlobalSIP**

Atlanta, Georgia, USA, December 3-5, 2014

The 2014 Workshop on Genomic Signal Processing and Statistics (**GENSIPS'14**) will join the 2014 IEEE Global Conference on Signal and Information Processing (**GlobalSIP'14**) to be held in Atlanta on Dec. 3-5, 2014. **GENSIPS'14** will continually provide a forum for researchers in signal processing, bioinformatics, computational biology, and biostatistics to share the state-of-art advances in the fast growing genomics, proteomics, metabolomics, lipidomics, and metagenomics areas and to tackle the challenges of high dimensionality, high heterogeneity, and high complexity.

Papers on unpublished original research are solicited. Topics of interest include, and not limited to:

- Big data analytics for genomics, proteomics, metabolomics, lipidomics, and metagenomics data
- Next generation sequencing data compression
- Genomics sequencing signal quality control
- Analysis methods for SNP/genotype/epigenetic data
- Dynamic modeling of regulatory and signaling networks
- Single-cell & cellular heterogeneity analysis
- Integration of multi-modality omic data
- Genomics and protein array image analysis
- Statistical signal processing of sequencing data
- Computational and statistical analysis of meta-genomics
- Cancer genomics, Neuro genomics, Cardio genomics
- Environmental genomics and toxicogenomics
- Functions of microRNA and non-coding RNAs
- Crowd-sourcing for novel biomarker discovery methods
- Sequencing alignment and assembly
- Cloud-based -omic data analysis & storage
- Genomics text data processing
- -omic data visualization
- Structural and comparative genomics
- Epigenetics and DNA Methylation analysis
- Translational bioinformatics
- Gene expression pattern recognition
- Pharmaco-genomics
- Plant genomics
- Bioinformatics of health monitoring
- Molecular interaction and pathways

Prospective authors should submit to GENSISP 2014 by EDAS <http://edas.info/newPaper.php?c=17341>. Please use 2-column IEEE template available at <http://www.ieeeglobalsip.org/formatting.html>) for paper up to 4 pages. The key dates are:

Paper submission deadline	July 25th, 2014
Notification of Acceptance	Sept. 15th, 2014
Camera Ready paper due	Oct.15th, 2014
GENSIPS'14	December 3-5, 2014

Selected papers will be invited to submit to **IEEE Journal of Biomedical and Health Informatics**, and other journal(s) for peer-review and publication.

Workshop Co-Chairs:

Peng Qiu, Ph.D.

Biomedical Engineering, Georgia Institute of Technology & Emory University

May D. Wang, Ph.D.

Biomedical Engineering and Electrical and Computer Engineering,
Georgia Institute of Technology & Emory University

